Deterministic coupling of single color centers to monolithic photonic crystal cavities in single crystal diamond

Dissertation

**zur Erlangung des Grades
des Doktors der Naturwissenschaften
der Naturwissenschaftlich-Technischen Fakultät II
– Physik und Mechatronik –
der Universität des Saarlandes**

von

Janine Simone Riedrich-Möller

Saarbrücken

2014

Tag des Kolloquiums:	17.12.2014
Dekan:	Univ.-Prof. Dr.-Ing. Georg Frey
Mitglieder des Prüfungsausschusses:	Univ.-Prof. Dr. Romanus Dyczij-Edlinger Univ.-Prof. Dr. rer. nat. Christoph Becher Univ.-Prof. Dr. rer. nat. Oliver Benson Univ.-Prof. Dr. rer. nat. Stephan Götzinger Dr. rer. nat. Eva Wollrab

Für meine Familie

Abstract

This thesis demonstrates the deterministic coupling of single optically active nitrogen-vacancy (NV) and silicon-vacancy (SiV) color centers to monolithic photonic crystal cavities (PhC) realized in single crystal diamond. To this end, we develop a fabrication technique for 300 nm-thick free-standing diamond membranes, and their subsequent patterning using focused ion beam milling. This allows us to observe PhC modes of high optical quality factors ($Q = 1,200$) and small mode volumes ($1(\lambda/n)$) in single crystal diamond for the first time. For controlled coupling of single color centers to PhC modes, we develop a method for frequency-tuning the monolithic cavities, and for controlling the emitter-cavity positioning based on two approaches. The first approach involves targeted implantation of nitrogen ions at the center of PhCs fabricated in ultra-pure diamond. Using confocal spectroscopy, we confirm the successful creation of a few NV centers within the PhCs. The second approach is based on a tailored fabrication process of PhCs around pre-characterized single SiV centers. The controlled coupling to the nanocavity allows for the demonstration of resonant enhancement of the spontaneous emission rate of a single SiV center by a factor of 2.7, along with a 19-fold increase in intensity. The results of this work are promising for future applications in quantum information science, such as the realization of efficient cavity-enhanced single photon sources, or spin-photon interfaces for the use in quantum networks.

Zusammenfassung

Diese Dissertation demonstriert die kontrollierte Ankopplung einzelner optisch aktiver Stickstoff- (NV) und Silizium-Fehlstellen (SiV) Farbzentren an einen monolithischen photonischen Kristallresonator (PhC), hergestellt in einkristallinem Diamant. Zu diesem Zweck entwickeln wir ein Verfahren zur Fabrikation 300 nm-dünner Diamantmembranen und deren gezielter Strukturierung mittels fokussierten Ionenstrahl-Abtrags. Damit werden erstmals optische Moden hoher Güte ($Q = 1200$) und kleiner Modenvolumina ($1(\lambda/n)$) für PhCs in einkristallinem Diamant nachgewiesen. Zur gezielten Ankopplung einzelner Farbzentren entwickeln wir eine Methode zur Frequenzabstimmung der monolithischen PhCs und zur kontrollierten Emitter-Resonator Positionierung basierend auf zwei Ansätzen: Der erste Ansatz besteht in der gezielten Implantation von Stickstoffionen in die Mitte eines PhCs aus hochreinem Diamant. Mittels Konfokalspektroskopie wird die erfolgreiche Erzeugung einiger weniger NV Zentren in den PhCs zweifelsfrei nachgewiesen. Im zweiten Ansatz wird ein PhC um die Position eines einzelnen, voruntersuchten SiV Zentrums strukturiert. Die gezielte Ankopplung ermöglicht die Überhöhung der Spontanemissionsrate einzelner SiVs um einen Faktor 2,7 bei gleichzeitiger 19-facher Intensitätserhöhung. Die Ergebnisse dieser Arbeit sind vielversprechend im Hinblick auf Anwendungen in der Quanteninformationsverarbeitung wie z.B. der Realisierung effizienter Einzelphotonenquellen und Spin-Photon Schnittstellen eingebettet in einem Quantennetzwerk.

Contents

Chapter 1

Introduction

The vision to build a quantum computer that solves specific numeric tasks, such as large database search (Grover algorithm) [1] or integer factorization of large numbers (Shor algorithm) [2], much faster than any classical computer, and that allows for the simulation of complex quantum systems [3] has stimulated active and vital scientific research in the last several decades. This has lead to tremendous progress in quantum information processing, ranging from the initialization, control, storage and readout of individual quantum systems, over the implementation of the first quantum algorithms, to the vision of a quantum network [4] or quantum internet [5] that connects distant quantum nodes and converts information from one quantum system to another. Quantum communication permits secret sharing between distant nodes with, in principle, complete security that is guaranteed by the laws of quantum mechanics. Beyond the initial motivation, quantum science has led to tremendous progress in quantum metrology, which allows for time measurement with unprecedented high precision, in sensing applications, and in imaging technologies.

In contrast to classical bit numbers, a quantum mechanical bit, also referred to as a qubit, can simultaneously exist in an arbitrary superposition of discrete quantum states, which are usually realized in a two-level system. The time during which the superposition state is maintained before interaction with the environment disturbs its phase is referred to as the coherence time. By integrating multiple qubits to form a quantum register, the superposition principle allows for entanglement of individual qubits. Entanglement is a unique quantum mechanical phenomena that is responsible for the power of quantum parallelism.

For the realization of a quantum computer, a qubit has to meet five criteria that have been formulated by D. DiVincenzo [6]:

1. A scalable physical system of well characterized qubits.
2. The ability of initialization of the qubit.
3. Relevant long coherence times much longer than the gate operation time.
4. A “universal set” of quantum gate operations.

5. The ability to readout the qubit state.

Isolated atoms and ions have been established as qubits with long coherence times and well defined optical transitions. They can be trapped using electromagnetic fields in a high vacuum that protects them from the environment. The invention of the Paul- and Penning traps, used to trap single ions, has been awarded with the Nobel prize in physics in 1989. Moreover, trapped ions and atoms can be manipulated using optical, microwave and radio-frequency fields and together with the collective motion of an array of atoms or ions, this has enabled the demonstration of a two-ion controlled NOT-gate [7], the key ingredient for quantum computing with trapped ions [8]. For a review on quantum simulations with trapped ions see e.g. [9]. The seminal experiments on single trapped atoms, ions, and photons were awarded with the Nobel prize in physics in 2012 for Serge Haroche and David Wineland.

Since then, other systems based on solid-state devices have been established as qubits such as quantum dots or color centers in diamond. Moreover, mesoscopic systems such as superconducting qubits or nanomechanical resonators that act as single quantum systems are also investigated as qubits. Each system has its advantages and disadvantages and up to now it is unclear which will ultimately prove successful.

One challenge to all these quantum systems is scaling to large numbers of qubits. One proposal is to distribute the computation between different quantum nodes, i.e. quantum registers, storage units, etc., and to interconnect them via optical channels [4,10]. Moreover, the implementation of such a quantum network or quantum internet [5] would allow for the connection of individual quantum computers, and would enable secure communication between distant nodes. A quantum network consists of stationary quantum nodes (stationary qubits) where quantum information is generated, processed, and stored, and quantum channels to link individual quantum nodes and transport quantum information from one site to another. The optical transfer of information is based on single photons (flying qubits), which are well suited due to their long coherence times, arising from their non-interacting nature and the availability of low-loss optical fibers and efficient detectors [5, 11].

In this work, we focus on single color centers in diamond for applications in quantum information science. Color centers are optically active point defects in the diamond lattice. These artificial atoms feature tightly localized electronic states within the large band gap of diamond. The two most prominent color centers are the nitrogen-vacancy (NV) center and the silicon-vacancy (SiV) center, which consist of a nitrogen or silicon atom, respectively, and a lattice vacancy next to it. Both centers are known as bright and efficient single photon sources, which have already been used for secure quantum communication schemes such as quantum key distribution (QKD) [12]. The huge interest in these centers for quantum information processing stems mainly from their electronic ground state spins that can be optically addressed [13–17]. For the NV center, the electronic spin ground state exhibits extraordinarily long coherence times (up to seconds) and it can be coupled via the hyperfine interaction to long-lived nuclear spin states of ^{14}N and adjacent ^{13}C atoms in the diamond lattice. This highlights the NV center among other color centers as a long-lived spin qubit well suited as a stationary qubit, for implementations in a quantum register to store information and perform quantum

gate operations on the spin state. Similarly, for the SiV center, there is recent evidence that its electronic spin state can be coupled to long-lived nuclear ^{29}Si spin states [17]. Additionally, due to the optical access of the electronic spin states, both color centers are interesting as spin-photon interfaces, which mediate the interaction between long-lived electronic or nuclear spin states used as stationary qubits and single photons for long distance transmission in a quantum network [18], or for quantum computing [19]. A summary of recent experimental progress in the implementation of these theoretical proposals will be given below. The efforts to utilize color centers in diamond for quantum information processing (QIP) can be divided into three groups [20]:

1. Secure quantum communication based on color centers as single photon sources
2. QIP based on entanglement and coherent interaction between neighboring NV centers
3. QIP based on long-range entanglement between distant NV centers via single photons within a quantum optical network

In the following, we summarize the first demonstrations of secure communication experiments based on QKD using single NV and SiV centers as single photon sources. Additionally, we present major achievements in quantum computing, and establishing a quantum network based on the NV center as a long-lived spin qubit.

Quantum key distribution based on color centers as single photon sources

In 2000, two groups independently demonstrated single photon emission from single NV centers [21, 22], and in 2004, optical access to the electronic ground state spin was discovered [13, 14]. Since then, the NV center has advanced to become the most investigated color center in diamond. The NV center has a relatively long excited state lifetime of 12 ns [23]. Unfortunately, due to strong electron-phonon coupling, the spectrum of the NV center is rather broad, extending over 100 nm, of which only 3-4% is emitted into the zero-phonon line (ZPL) at 637 nm. For applications in free-space quantum communication, this necessitates tight filtering of the NV center emission.

In contrast to the NV center, the SiV center has been investigated as bright and narrow-band single photon source [24, 25] with short excited state lifetime of 1.28 ns [26] and with a ZPL at 738 nm into which up to 80% [25] of the photons are emitted. In low-strain diamond, multiple intrinsically identical SiV centers have been located [26] that enabled the demonstration of Hong-Ou-Mandel interference on a beam splitter, proving indistinguishable single photon emission from two separate SiV centers at low temperatures [27].

Single photons emitted from NV as well as SiV centers have been used successfully to demonstrate quantum key distribution based on BB84 protocols [12] for tap-proof communication. The information was encoded in the polarization state of the transmitted single photons. Using single NV centers in nanodiamonds under pulsed excitation, Beveratos et al. [28] implemented QKD in free space over 50 m at night, whereas Alléaume et al. [29] performed the experiment in daylight between two buildings separated

by 30 m. These results showed that the usage of single photons for QKD has measurable advantages over established attenuated laser pulses when the transmission loss exceeds 10 dB [29]. Assuming a typical transmission of light through air of $0.4\,\mathrm{dB\,km^{-1}}$ [30,31], this would correspond to a distance exceeding 25 km. Leifgen et al. [30] demonstrated for the first time QKD under laboratory conditions using single SiV centers in nanodiamonds as single photon sources, and compared them to the performance of NV centers. These proof-of-principle experiments mark the beginning of the usage of single color centers in diamond for secure communication based on QKD.

NV center for quantum information processing

Besides their application as efficient single photon sources, the great interest in the NV and SiV centers stems from their electronic spin states that can be optically initialized and read out. While for the SiV center, investigations on electronic spin manipulation have started very recently [15–17], including possible access to ^{29}Si nuclear spin via the hyperfine interaction [17], optical access to the electronic ground state spin of the NV center has been a known and daily routine in laboratory experiments for about ten years [13,14]. Since then, multiple seminal experiments have highlighted the NV center as ideal solid-state spin qubit with extraordinarily long coherence times, well suited for quantum information processing and quantum computation applications.

Most of the interesting properties are associated with the negatively charged NV center, whose electronic ground state is a spin triplet state ($S = 1$) with long-lived spin sublevels ($m_s = \pm 1, 0$). The peculiarity of the NV center stems from the fact that the electronic spin state can be optically initialized and read out [32], even at room temperature, via spin-selective transitions through intermediate, metastable states. After a few optical cycles under off resonant excitation, the spin state is prepared in its $m_s = 0$ state. Single-shot readout of the electronic spin state was achieved using resonant excitation at low temperatures [33]. Once initialized, the electronic spin transitions can be manipulated and gate operations can be performed within nanoseconds [34,35] using microwave striplines directly integrated on the sample.

The coherence time determines the time over which the spin coherently evolves and can interact with the applied fields. In isotopically purified diamonds, coherence times up to several milliseconds at room temperature have been reported [36]. In standard isotopic diamond, comparable coherence times are achieved using "dynamical decoupling" techniques [34,37,38] that periodically flip the spin, such that its temporal evolution is reversed and effectively decoupled from the disturbances of the diamond lattice. Using dynamical decoupling, spin coherence times of milliseconds [34, 37, 38] at room temperature, and nearly one second at 77 K [39], have been achieved in standard isotopic diamond. Given GHz-manipulation rates [34, 35], this allows for millions of operations before the spin state dephases.

The main source of decoherence is coupling to nuclear spins of ^{13}C atoms in the diamond lattice. However, the hyperfine interaction is not only a source of loss but also provides the chance to achieve even longer coherence times by coupling the NV electronic spin state to nuclear spins of nearby ^{13}C atoms [40], or of the ^{14}N atom [41]

forming the NV center. Applying narrow-band microwave pulses acting as a conditional NOT-gate that flips the electronic spin state conditional on the state of the nuclear spin has allowed for single-shot readout of single [41] and multiple nuclear spins [42] under ambient conditions. Using nuclear spins as qubits with coherence times of one second [40] and manipulation times of microseconds enabled the realization of quantum memories [43], quantum gate operations [44], quantum algorithms for fast searching (Grover algorithm) [44], and multi-qubit quantum registers with implemented quantum error correction [45, 46] at room temperature.

The first attempts to integrate multiple qubits have been based on coupling adjacent NV centers with one another via dipole interaction between their electronic spins. Entanglement of the electronic spin states of two NV centers separated by 10 nm [47, 48] and entanglement swapping from the electronic to the ^{15}N nuclear spin state [48] have been demonstrated. Large scale targeted creation of single NV centers separated by small distances might be achieved using high-resolution ion-implantation [49].

Long-range entanglement between NV centers in a quantum optical network

The challenge remains to extend the quantum system from a small number of qubits to large scale networks of spin-based quantum registers using single photons as flying qubits. Here, the NV center stands out among other spin qubits due to its capability as a single photon source. Recent experiments have implemented the NV center as a spin-photon interface that allows one to entangle the spin state and the polarization state of emitted single photons. Spin-photon entanglement is key to the generation of large distance entanglement between the spin states of two independent NV centers, and moreover, to establishing scalable optical quantum networks. This approach requires the emission of single, indistinguishable photons by the individual NV centers and quantum interference of the photons on a beam-splitter.

The first component for the realization of optical connections is spin-photon entanglement. For the first time, entanglement between the spin state and the polarization of emitted photons has been demonstrated by driving spin-selective optical transitions of the NV center at low temperatures [50]. To entangle two separate NV centers, the emitted photons must be indistinguishable, so that they coherently interfere on a beam splitter. Stark-tuning of the NV emission lines via external electric fields and tight filtering of a single fine structure line allowed for the observation of Hong-Ou-Mandel interference behind the beam splitter of single, indistinguishable photons originating from different NV centers [51, 52]. These initial demonstrations paved the way for entanglement of the electronic spin states of two NV centers located in two independent cryostats [53]. Long-distance entanglement of two NV centers was an enormous step that can be combined with initialization, single-shot read out and local entanglement operations between the NV electronic spin and nearby long-lived nuclear spins. This has pioneered extended quantum networks, including quantum repeaters, and deterministic long-distance teleportation. Unconditional teleportation has recently been achieved using photon-mediated long-distance entanglement between the electronic spins of two separate NV centers, where the source qubit is encoded in the nuclear spin state [54].

Although there has been amazing progress toward the implementation of single color centers in quantum communication, quantum computation, and quantum networks, most of the schemes suffer from poor collection efficiencies of single photons. Moreover, the broad bandwidth and small branching ratio of the NV emission into the ZPL necessitate tight filtering to discriminate single photon emission from background contributions [28–30], and to ensure indistinguishability of single photons [53]. For the demonstration of long-distance entanglement of two NV centers [53], tight filtering entailed a poor success rate of one entangled pair in 12 million attempts [53], which necessitated an integration time of 158 h. Although SiV emission is much narrower compared to the broadband NV spectrum, SiV centers in nanodiamonds suffer from fairly low quantum efficiencies, in the range of a few percent [55]. The spectral properties of single color centers as well as the single photon count rates and generation of entangled photon pairs can be significantly improved by coupling the single emitters to an optical nanocavity.

Cavity coupling to single color centers in diamond

A single emitter decays spontaneously by interaction with the vacuum field. This interaction can be strongly enhanced by coupling the single emitter to a cavity. This has major consequences on the emission properties of the color center. Depending on the coupling strength compared to losses, we can distinguish between weak and strong coupling.

In the weak coupling regime, light-matter interaction is dominated by the incoherent loss processes. However, the interaction is sufficiently strong to enhance the rate at which single photons are emitted by the color center. The modification of spontaneous emission via cavity-coupling was first described by E. Purcell in 1946 [56]. Moreover, the emission process becomes directive in the direction of the cavity mode, allowing for significantly larger collection efficiencies.

In the strong coupling regime, when the coupling strength exceeds losses, coherent interaction between the color center and the cavity field becomes possible. In that regime, the emitter and cavity field are no longer treated separately but form one combined hybrid system. Strongly coupled light-matter interaction allows for direct transfer of the spin coherence from the color center onto the state of the photon emitted into the cavity mode.

There exist multiple theoretical proposals for coupling of color centers to small cavities requiring either weak or strong coupling. However, experimental state-of-the-art cavity structures designed for coupling to color centers in diamond do not allow for entry into the strong coupling regime. Therefore, we focus here on proposals intended for weak coupling.

Theoretical studies on single NV [57] and SiV centers [58] in diamond coupled weakly to a photonic crystal nanocavity (see below) predict cavity-enhanced single photon emission, with significantly reduced excited state lifetimes of the emitter, and preferential emission into the ZPL with a linewidth strongly reduced via cavity-coupling. At the

same time, the emission into phonon side bands is significantly suppressed. Moreover, greatly enhanced radiative decay rates into the ZPL transition yield improved quantum efficiencies of single color centers. Cavity-enhanced single photon emission would allow quantum key distribution at high bit rates over distances up to 150 km in open air experiments using color centers in diamond as single photon sources [58].

Besides improved single photon emission, cavity-enhanced readout schemes of the NV ground state spin based on spin state-selective reflectivity measurements have been proposed [59]. Theses schemes are based on a single NV center incorporated in a low-Q photonic crystal cavity (see below) that is fed by a nearby waveguide. By monitoring the reflectivity signal of weak probe light coupled through the waveguide, the spin state of the NV center can be deduced. The advantage of this scheme is that it requires much less excitation intensity and fewer optical cycles for readout than standard schemes. This reduces the probability of spin-flip transitions and decoherence by optical pumping.

The schemes for spin-selective reflectivity monitoring have been extended to non-demolition measurement schemes that allow for the creation of entanglement of the NV spin with the emitted photons [60]. Again, this proposal requires only weak coupling of the NV center to a small size cavity with a moderate cavity lifetime.

Another theoretical proposal [61] studied deterministic and robust entanglement generation between two NV centers located in a photonic crystal cavity. The key element of this proposal [61] is to use a Λ-scheme between long-lived spin ground states of the NV center. One transition of the Λ-system is coupled to a photonic crystal cavity mode. This allows for entanglement between two NV spin states, both placed in the same photonic crystal cavity and coupled to the cavity field.

Based on entanglement generation between individual NV centers, there exist sophisticated proposals that range from the realization of fault-tolerant quantum repeaters [62] requiring long distance entanglement, to fault-tolerant quantum computing [18].

In order to achieve large coupling strengths between the emitter and the cavity mode, and strong enhancement of the spontaneous emission rate, cavity structures are required that exhibit long cavity lifetimes, characterized by the quality factor Q, and small mode volumes V. To date, coupling between single color centers and nanocavities has been realized in various systems [63–66] that can be classified into two main categories: the hybrid approach and the monolithic all-diamond approach. Hybrid implementations typically involve single color centers hosted in nanodiamonds, or incorporated near the surface of single crystal diamond substrates that are coupled to the evanescent field of cavity structures fabricated in non-diamond materials such as gallium phosphide, silica, or polystyrene. Recent experiments include hybrid coupling to whispering gallery mode resonators such as polystyrene microspheres [67, 68], silica microtoroids [69] or -spheres [70], and gallium phosphide microdisks or -rings [71–74], as well as coupling to two-dimensional photonic crystal cavities fabricated in gallium phosphide [75–77] or silicon nitride [78]. Moreover, small size Fabry-Pérot cavities [79–82] have been used for hybrid coupling to single NV centers in nanodiamonds. While hybrid schemes are straightforward to implement, they often suffer from reduced overlap between cavity field and NV dipole, as well as from inferior spectral properties of NV centers hosted

in nanodiamonds or located closed to a surface. On the other hand, the monolithic all-diamond approach is based on optical cavity structures directly fabricated in single crystal diamond. This approach allows for direct incorporation of single color centers at the field maximum of the cavity modes. Several monolithic cavity designs have been realized in diamond, ranging from whispering gallery mode resonators such as microrings [83, 84] or microdisks [85], to one- and two-dimensional photonic crystal cavities in diamond [86–90].

In this work, we focus on monolithic two-dimensional photonic crystal cavities directly fabricated in thin diamond membranes. They consist of a periodic array of air holes with one or several missing holes at the center forming the cavity. Light propagation and confinement in photonic crystals rely on distributed Bragg reflections at the edge of the air holes. Mathematically, this is described by the photonic band structure, which has a band gap in a certain frequency range given the right structural parameters. Light propagation with frequencies inside the band gap is hindered through the periodic material and the light is tightly localized inside the cavity defect region. Photonic crystal cavities are well suited for efficient coupling to color centers as they exhibit extremely small mode volumes, on the order of one cubic wavelength, and high quality factors. Moreover, they offer the ability for large scale integration of multiple components, such as cavities, waveguides, and out-couplers, on one chip.

Scope of this thesis

This thesis aims at controlled coupling of single color centers to photonic crystal cavities realized in single crystal diamond membranes. To achieve this goal, multiple techniques have to be combined, including numerical simulations, nano-fabrication, optical confocal microscopy, and theoretical analysis of cavity-coupling. At the beginning of this thesis, no techniques for the fabrication of nanometer-size structures in single crystal diamond were available, and no tuning techniques existed that allowed for frequency matching the cavity mode to a specific emission line. Moreover, only a few theoretical design studies on photonic crystal cavities in diamond existed.

After a brief introduction on cavity-coupling, color centers in diamond and our experimental setup, we perform numerical simulations yielding optimized photonic crystal geometries with high quality factors and small mode volumes. To realize the simulated structures in diamond, the first challenge is the fabrication of thin free-standing membranes in high-quality single crystal diamond and subsequent patterning of nanometer-size structures. To test the performances of the fabricated structures, and for proof-of-principle experiments, diamond films containing large ensembles of SiV centers are used. We develop a tuning technique that allows, for the first time, for frequency tuning a diamond-based photonic crystal cavity. The developed processes are the basis for the subsequent coupling experiments to single color centers. In order to couple a single color center to a nanocavity, several challenges have to be tackled. These are the exact positioning and alignment of the emitter with respect to the cavity electric field, and the ability to spectrally tune the cavity modes in resonance with the emission line. We achieve exact positioning using two approaches. The first approach involves the fabri-

cation of photonic crystal cavities in ultra-pure diamond, and targeted implantation of nitrogen ions at the center of the cavity structure. The second approach starts with a diamond membrane containing single SiV centers. Using positioning markers, a photonic crystal cavity is structured around it. In combination with cavity tuning, this allows for deterministic coupling of a photonic crystal cavity to a single color centers in diamond. Analyzing the internal population dynamics, we demonstrate Purcell enhancement and inhibition as well as the modification of the radiative quantum efficiency of single color centers in diamond.

Outline of this thesis

Chapter 2 introduces the basic theoretical model, the Jaynes-Cummings model, describing light-matter interaction in the framework of cavity quantum electrodynamics. From the model, we deduce two limiting cases: strong and weak (Purcell) coupling. Moreover, the chapter gives a brief overview of the different approaches pursued for cavity-coupling to single color centers in diamond.

Chapter 3 reviews the spectral properties of the NV and SiV centers, as well as their electronic and vibrational structures, and the process of optical spin polarization of the NV electronic spin state.

Chapter 4 presents the confocal microscope setup used to locate single color centers in the diamond membrane, to analyze their spectral properties, to prove single-emitter character using a Hanbury-Brown and Twiss interferometer, and to measure the excited state lifetime.

Chapter 5 introduces the concept of photonic crystal cavities, with the focus on two-dimensional periodic arrangements of air holes etched in a thin diamond slab. We present the numerical techniques used to calculate photonic band structures and to simulate field distributions confined in photonic crystal cavities, as well as to calculate quality factors and mode volumes. By carefully choosing the defect structure and optimizing the design, we reach small size cavity structures with high cavity Q-factors.

Chapter 6 presents the techniques to fabricate photonic crystal cavities in diamond. We use two different starting materials: diamond films that contain single SiV centers and SiV ensembles, and ultra-pure diamond membranes intended for targeted implantation of nitrogen. The fabrication process involves plasma etching to obtain a free-standing diamond membrane, that is subsequently patterned using a focused beam of gallium ions. Lattice damages and gallium impurities are removed via an extensive post-processing step, that allows for the observation of photonic crystal cavity modes in the spectrum. We deduce the experimental quality factors and discuss possible limitations.

Chapter 7 concerns coupling a photonic crystal cavity to an ensemble of SiV centers. We develop a tuning technique that successively shifts the cavity modes into resonance with the SiV emission line. In resonance, we observe an intensity enhancement of the emission line that we analyze by taking into account spectral and spatial ensemble averaging, as well as different dipole orientations of the SiV centers.

Chapter 8 is dedicated to targeted creation of single NV centers via ion-implantation at the center of photonic crystal cavities realized in ultra-pure diamond. We present the

implantation setup, which is based on a combined system of a nitrogen ion beam and an atomic force microscope. A nanohole in the tip serves as an aperture for the ion beam. After high temperature annealing, we verify the successful creation of single NV centers at the cavity center and evaluate the creation efficiency. To describe cavity coupling to a broad-band emitter such as the NV center, we adopt an extended Jaynes-Cummings model developed by Auffèves et al. [91, 92] and Albrecht et al. [80, 81], to determine a generalized Purcell factor for the implanted NV centers coupled to photonic crystal cavities.

Chapter 9 focuses on deterministic structuring of a photonic crystal cavity around a pre-characterized single SiV center using positioning markers. We analyze the emission properties and internal population dynamics of the single SiV centers before and after patterning, and evaluate inhibition of the spontaneous emission rate due to the reduced local density of states. Tuning the cavity modes into resonance, we demonstrate controlled coupling to the narrow SiV emission line. In resonance, we measure the excited state lifetime and deduce the Purcell enhancement. Moreover, we evaluate a possible change in the emitters quantum efficiency, and demonstrate polarization control via cavity coupling.

Chapter 2

Emitter-cavity coupling

The interaction of a single emitter with the quantized electromagnetic field confined in an optical cavity is described in the framework of cavity quantum electrodynamics (cavity QED) (see e.g. [93, 94]). In a representative model, a two-level atom is coupled to the quantized radiation field confined in an optical resonator. The dynamics of the system are described by the Jaynes-Cummings Hamiltonian including contributions of the atom, the cavity field and an interaction term describing atom-photon coupling. Taking into account dissipation out of the cavity and non-resonant decay of the atom, one distinguishes two limiting cases: Weak and strong coupling. Weak coupling leads to the modification of spontaneous emission, whereas strong coupling is characterized by a coherent exchange of an energy quanta, i.e. a photon, between the atom and the cavity mode. In the last two decades, laboratory experiments have been able to mimic this ideal system using for example single atoms or ions in Fabry-Pérot resonators [95–100], single quantum dots in semiconductor microcavities [101–110] or cooper-pair boxes in superconducting circuits [111]. In 2012, the field of cavity QED was awarded with the Nobel prize to Serge Haroche and David Wineland on their seminal experiments of light-matter interaction involving single atoms and photons in cavities [112, 113].

We begin this chapter by defining the key parameters characterizing atom-cavity coupling, before we briefly introduce the Jaynes-Cummings model including dissipation. Using the example of single color centers in diamond, e.g. the silicon-vacancy and nitrogen-vacancy center, we estimate the required cavity specifications in order to observe weak or strong coupling to solid-state cavities. Finally, we give an overview of state-of-the-art cavity-coupling experiments involving color centers in diamond allowing to put the results of the present thesis in the context of current research.

2.1 Two-level atom coupled to an optical cavity

To describe light-matter interaction, we consider a single two-level atom involving a ground state $|g\rangle$ and an excited state $|e\rangle$ coupled to the electromagnetic field confined in an optical cavity (Fig. 2.1). The interaction strength between a single emitter and

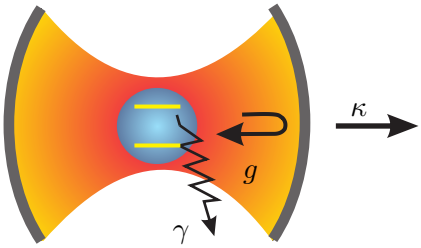

Figure 2.1: Single two-level atom coupled to a cavity mode including losses. The coupling constant is denoted by g, while the non-resonant decay rate of the atom is symbolized by γ and the cavity loss rate by κ.

the light field is governed by three parameters: The cavity loss rate κ, the non-resonant atomic decay rate γ and the coupling constant g. These parameters will be briefly introduced in the following.

- **Cavity photon decay rate κ:** The cavity decay rate κ determines the temporal loss rate of photons out of the cavity given by

$$\kappa = \frac{\omega}{Q}. \tag{2.1}$$

  Here, Q denotes the dimensionless quality factor also referred as Q-factor which characterizes the temporal confinement of the resonant field limited e.g. by non-perfect mirror reflectivity or absorption losses. The quality factor is defined by the resonance frequency ω and the cavity linewidth $\Delta\omega$:

$$Q = \frac{\omega}{\Delta\omega} \tag{2.2}$$

  Besides the temporal confinement, the spatial confinement of the cavity mode essentially influences emitter-cavity coupling. It is given by the mode volume V [114]:

$$V = \frac{\int \varepsilon(\vec{r})|\vec{E}(\vec{r})|^2 d^3r}{\max\{\varepsilon(\vec{r})|\vec{E}(\vec{r})|^2\}}, \tag{2.3}$$

  where $\epsilon(\vec{r})$ is the permittivity of the dielectric material within the cavity and $\vec{E}(\vec{r})$ denotes the electric field of the cavity mode.

- **Non-resonant atomic decay rate γ:** The non-resonant atomic decay rate can have various origins: The emitted photons might be radiated in a direction that does not coincide with the cavity mode. This effect is strongly influenced by the specific cavity geometry. Alternatively, the atom might decay to other levels, e.g. to higher vibrational atomic levels, whose transition frequencies do not match the resonant frequency of the cavity mode. This loss contribution can be minimized by choosing single emitters with high branching ratios into one specific transition. A third possibility might be that the excited atom undergoes non-radiative decay

induced e.g. by scattering processes. To reduce non-radiative decay, it is important to choose single emitters with a high radiative quantum yield η_{qe} defined as the sum over all radiative transition rates compared to the overall decay rate.

- **Coupling constant g:** The coupling rate g governs the interaction strength between the atom and the vacuum field confined in the cavity. The coupling rate g is given by the dipole moment $\hat{d}$ associated with the atomic transition between the excited state and ground state and the cavity electric field operator $\hat{E}$ divided by the Planck's constant [115]:

$$g = \frac{|\langle -\hat{d} \cdot \hat{E} \rangle|}{\hbar} \tag{2.4}$$

Considering the magnitude $E_{\mathrm{vac}} = \sqrt{\hbar\omega/2\epsilon_0 n^2 V}$ [115] of the vacuum field in the cavity mode, the coupling constant g is given by:

$$g = \sqrt{\frac{\omega}{2\hbar n^2 \epsilon_0 V}} \cdot |d|, \tag{2.5}$$

where $n = \sqrt{\epsilon}$ is the refractive index of the medium within the cavity, ϵ_0 is the vacuum permittivity and V is the mode volume defined by equation (2.3). Hence, to achieve a large coupling strength, it is favorable to choose a cavity design with a very small mode volume, as g scales as $1/\sqrt{V}$.

Please note that the definitions of the cavity loss rate κ and the spontaneous decay rate γ differ from the usual definitions $\tilde{\kappa}, \tilde{\gamma}$ given in standard textbooks on atomic physics by a factor of two: $\tilde{\kappa} = \omega/2Q$ and $\tilde{\gamma} = \gamma/2$. In atomic physics, one typically considers the decay of coherence that is twice as fast as the decay of population that we study in this work. Our definition is conform with a recent publication [80] on cavity-coupling to a single NV center and their theoretical model adopted later in this work.

The three parameters g, κ, γ define the time-scale of atom-cavity coupling and allow for the classification into two regimes of light-matter interaction with completely different dynamics. Before we proceed with this classification, we briefly introduce the theoretical description of atom-cavity coupling governed by the Jaynes-Cummings model assuming an ideal lossless system. In a second step, we include dissipation in the mathematical model to account for cavity losses and spontaneous decay of the atom.

Jaynes-Cummings model

The interaction of a single two-level atom with a quantized electromagnetic field confined to an optical cavity is given by the Jaynes-Cummings Hamiltonian [116–118]:

$$\hat{\mathcal{H}}_{JC} = \hat{\mathcal{H}}_{\mathrm{atom}} + \hat{\mathcal{H}}_{\mathrm{cav}} + \hat{\mathcal{H}}_{\mathrm{int}} \tag{2.6}$$

The Hamiltonian of the unperturbed two-level atom is given by:

$$\hat{\mathcal{H}}_{\mathrm{atom}} = \hbar\omega_a \hat{\sigma}_z, \tag{2.7}$$

with $\hat{\sigma}_z = (|e\rangle\langle e| - |g\rangle\langle g|)/2$ being the projector operator onto the excited $|e\rangle$ and ground state $|g\rangle$ of the atom with an energetic difference of $\hbar\omega_a$.
The Hamiltonian of the quantized field is described by:

$$\hat{\mathcal{H}}_{\text{cav}} = \hbar\omega_c \hat{a}^\dagger \hat{a}, \tag{2.8}$$

with $\hat{a}^\dagger$ and $\hat{a}$ being the creation and annihilation operators of photons in the cavity with $\hat{a}|m\rangle = \sqrt{m}|m-1\rangle$ and ω_c being the angular frequency of the resonator.
In the dipole approximation, the atom-photon interaction is determined by the Hamiltonian:

$$\hat{\mathcal{H}}_{\text{int}} = -\hat{d} \cdot \hat{E}, \tag{2.9}$$

including the two-level atomic dipole operator $\hat{d} = \vec{d}\hat{\sigma}^\dagger + \vec{d}^*\hat{\sigma}$ and the electric field operator $\hat{E} = \vec{E}(\vec{r})\hat{a} - \vec{E}^*(\vec{r})\hat{a}^\dagger$, where $\hat{\sigma}^\dagger = |e\rangle\langle g|$ and $\hat{\sigma} = |g\rangle\langle e|$ are the atomic raising and lowering operators. The spatially varying electric field amplitude $\vec{E}(\vec{r}) = E_{\text{vac}}\vec{e}_E(\vec{r})$ is characterized by the vacuum field amplitude and the unit direction vector $\vec{e}_E(\vec{r})$. In the rotating wave approximation, the interaction Hamiltonian is given by [117]:

$$\hat{\mathcal{H}}_{\text{int}} = \hbar g \hat{\sigma}^\dagger \hat{a} + \hbar g^* \hat{a}^\dagger \hat{\sigma}, \tag{2.10}$$

with the coupling constant g introduced via equations (2.4)-(2.5). The eigenstates $|e, m\rangle$ and $|g, m\rangle$ of the non-interacting atom-cavity Hamiltonians $\hat{\mathcal{H}}_{\text{atom}} + \hat{\mathcal{H}}_{\text{cav}}$ are referred as bare states with eigenenergies $\mathcal{E}_{e,m} = \hbar(m\omega_a + \omega_c/2)$ and $\mathcal{E}_{g,m} = \hbar(m\omega_a - \omega_c/2)$. They are constructed via the tensor product of the atomic excited $|e\rangle$ and ground state $|g\rangle$ and the cavity photon number states $|m\rangle$, with $m \geq 1$. In the basis of the bare atom and cavity states $|e, m-1\rangle$ (atom in excited state and $m-1$ photons are present in the cavity) and $|g, m\rangle$ (atom in ground state and m photons in the cavity), the new eigenstates $|m, +\rangle$, $|m, -\rangle$ of the coupled atom-cavity system governed by the Jaynes-Cummings Hamiltonian $\hat{\mathcal{H}}_{JC}$ can be expressed as follows [118]:

$$|m, +\rangle = \cos\theta_m |g, m\rangle + \sin\theta_m |e, m-1\rangle \tag{2.11}$$

$$|m, -\rangle = \sin\theta_m |g, m\rangle - \cos\theta_m |e, m-1\rangle \tag{2.12}$$

The eigenstates $|m, +\rangle$, $|m, -\rangle$ of the hybrid atom-cavity system are referred to as *dressed states* with the coupling angle θ_m defined by [118] [1]:

$$\tan^2\theta_m = \frac{\Omega_m + \Delta}{\Omega_m - \Delta}, \tag{2.13}$$

where $\Delta = \omega_a - \omega_c$ denotes the atom-cavity detuning and Ω_m is the *Rabi-frequency*:

$$\Omega_m = \sqrt{\Delta^2 + 4g^2 m} \tag{2.14}$$

By expressing the dressed states in the basis of the atom and cavity modes, we find that the energy oscillates coherently between the two states $|g, m\rangle$, $|e, m-1\rangle$ with a frequency Ω_m. Physically, this means that the excited atom emits a photon into the

[1] Here, we use $\sin\theta_m = \tan\theta_m/\sqrt{1+\tan^2\theta_m}$ and $\cos\theta_m = 1/\sqrt{1+\tan^2\theta_m}$

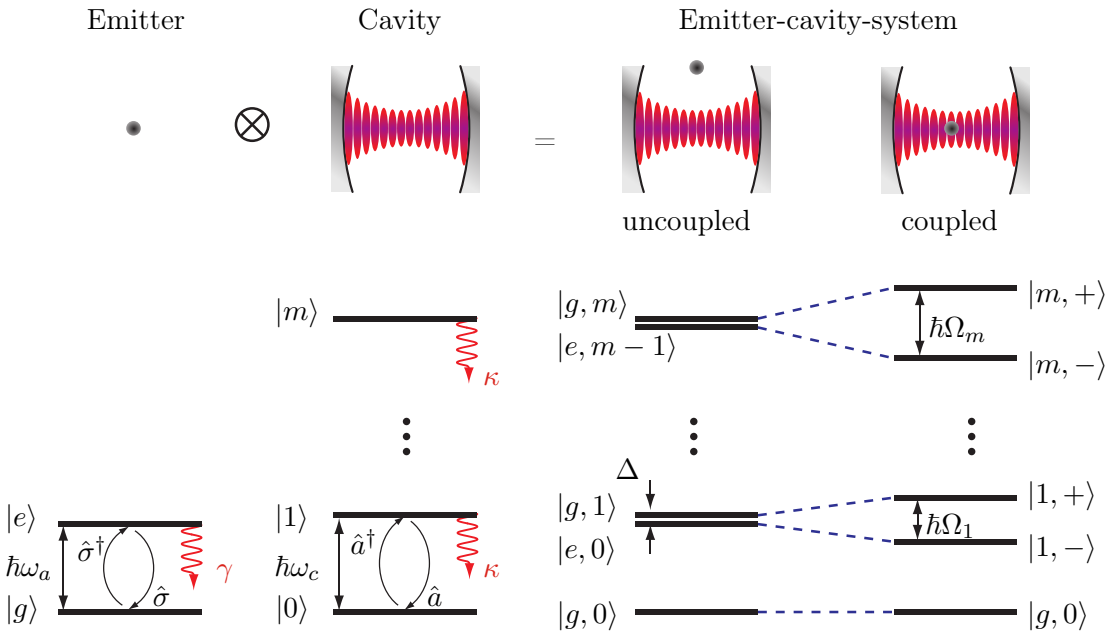

Figure 2.2: Jaynes-Cummings model: A single emitter described by a two-level system with an excited state $|e\rangle$ and a ground state $|g\rangle$ couples to a quantized electromagnetic field confined within a cavity. The cavity states are given by the photon number states $|m\rangle$ with $m \geq 1$. In the uncoupled case, the bare states are given by the tensor product $|g,m\rangle$ and $|e,m\rangle$. The eigenstates of the coupled emitter-cavity system are referred to as dressed states, whose eigenenergies are separated by the Rabi-frequency Ω_m. (After [119])

cavity mode that is later reabsorbed by the emitter. The corresponding eigenenergies are given by:

$$\mathcal{E}_{m,\pm} = \hbar\left(m\omega_a - \frac{\omega_c}{2}\right) \pm \frac{\hbar}{2}\Omega_m \tag{2.15}$$

Figure 2.2 shows the energy level scheme of the bare atom-cavity states as well as of the dressed atom-cavity system. When the atom is resonantly coupled to the cavity ($\Delta = 0$), the dressed states are energy doublets separated by $\hbar\Omega_m = 2\sqrt{m}\hbar g$. For an empty resonator ($m = 1$), we obtain an energy splitting of $\hbar\Omega_1 = 2\hbar g$. This splitting is often referred as normal-mode splitting or vacuum Rabi splitting and arises from the interaction of the atom with the vacuum field in the cavity.

Dissipative Jaynes-Cummings Hamiltonian

The Jaynes-Cummings Hamiltonian describes a reversible process of coherent energy exchange between the atom and the cavity field. However, in the experiment, we have to include dissipation, i.e. coupling to a reservoir. The origins of dissipation are either leakage of photons out of the cavity at a rate κ or spontaneous emission of the excited atom at a rate γ. In chapter 8, we will extend the standard model to further dissipation

terms such as pure dephasing or higher vibrational levels of the NV center. However, for now, we restrict to the principal loss rates κ and γ. Our derivation follows [118]. The system subjected to dissipation is conveniently described in terms of the density operator $\hat{\rho}$ governed by the master equation

$$\frac{d\hat{\rho}}{dt} = -\frac{i}{\hbar}[\hat{\mathcal{H}}, \hat{\rho}] + \mathcal{L}_{\text{diss}}(\hat{\rho}), \tag{2.16}$$

where $\mathcal{L}_{\text{diss}}(\hat{\rho})$ describes the dissipation operator in the Lindblad form expressed by the collapse operators $\hat{C}_k$:

$$\mathcal{L}_{\text{diss}}(\hat{\rho}) = \frac{1}{2}\sum_k (2\hat{C}_k\hat{\rho}\hat{C}_k^\dagger - \hat{\rho}\hat{C}_k^\dagger\hat{C}_k - \hat{C}_k^\dagger\hat{C}_k\hat{\rho}). \tag{2.17}$$

The collapse operator of spontaneous emission is given by $\hat{C}_{\text{spont}} = \sqrt{\gamma}\hat{\sigma}$, while the collapse operator of cavity decay is determined by $\hat{C}_{\text{cav}} = \sqrt{\kappa}\hat{a}$. Using the collapse operators for spontaneous emission and cavity decay, the master equation can be rewritten:

$$\frac{d\hat{\rho}}{dt} = -\frac{i}{\hbar}[\hat{\mathcal{H}}_{\text{eff}}, \hat{\rho}] + \gamma\hat{\sigma}\hat{\rho}\hat{\sigma}^\dagger + \kappa\hat{a}\hat{\rho}\hat{a}^\dagger, \tag{2.18}$$

with an effective Hamiltonian:

$$\hat{\mathcal{H}}_{\text{eff}} = \hat{\mathcal{H}}_{JC} - \frac{i\hbar}{2}\left(\gamma\hat{\sigma}\hat{\sigma}^\dagger + \kappa\hat{a}\hat{a}^\dagger\right). \tag{2.19}$$

In the basis of the bare atom cavity states $|e, m-1\rangle$ and $|g, m\rangle$, the eigenvalues of the dissipative system are given by:

$$\mathcal{E}_{m,\pm}^{\text{diss}} = \hbar\left(m\omega_a - \frac{\omega_c}{2}\right) \pm \frac{\hbar}{2}\Omega_m^{\text{diss}} - i\hbar\left[\kappa\left(m - \frac{1}{2}\right) + \frac{\gamma}{2}\right], \tag{2.20}$$

with the complex Rabi-frequency Ω_m^{diss} including dissipation:

$$\Omega_m^{\text{diss}} = \sqrt{[\Delta^2 - i(\gamma - \kappa)]^2 + 4g^2 m}. \tag{2.21}$$

The real part of the complex eigenvalue (2.20) determines the energy $\mathcal{E}_{m,\pm}^r$ of the coupled states, whereas the imaginary part governs the dissipation rate $\gamma_{m,\pm}$ such that

$$\mathcal{E}_{m,\pm}^{\text{diss}} = \mathcal{E}_{m,\pm}^r - i\hbar\gamma_{m,\pm}. \tag{2.22}$$

Depending on the rates g, κ and γ, we distinguish between the strong coupling limit, if $2g \gg (\gamma, \kappa)$ and the weak coupling regime, if $2g \ll (\gamma, \kappa)$. For these intervals, the Rabi-frequency given by equation (2.21) becomes either real valued or purely imaginary, respectively. In the strong coupling regime, the coupling rate between the atom and cavity mode is much faster than the loss rates κ and γ. In that case, a photon emitted by the atom into the cavity mode can be re-absorbed by the atom before it is lost. This regime allows for the study of coherent interaction between the atom-cavity field. In contrast, in the weak coupling regime also referred to as Purcell regime, the loss rates dominate the interaction such that photon emission is an irreversible process. However, in this regime the spontaneous emission rate of the atom can be significantly altered. Here, we discuss the characteristic properties of the two regimes for the resonant case $\Delta = 0$.

Strong coupling regime

In the limit $2g \gg (\kappa, \gamma)$, the solution resembles to the lossless case without dissipation as discussed before. As the coupling constant g exceeds the loss rates, light-matter interaction becomes a reversible process. The coherent exchange of a photon between the cavity and the atom happens at the Rabi-frequency Ω_m^{diss}:

$$\Omega_m^{\text{diss}} = \sqrt{4g^2 m - (\gamma - \kappa)^2}. \tag{2.23}$$

The energy coherently oscillates between the states $|g, m\rangle$ and $|e, m-1\rangle$ at the Rabi-frequency. The eigenstates of the coupled system are dressed states of the emitter and cavity field with energy levels separated by $\hbar\Omega_m^{\text{diss}}$. In the experiment, the energy splitting of the eigenstates results in two resonant peaks in the spectrum under weak optical probing. In solid-state systems, the emission line of the single emitter is often tuned into resonance with the cavity mode giving rise to the typical anti-crossing of the strongly coupled emitter-cavity states.

Weak coupling (Purcell) regime

In the limit $2g \ll (\kappa, \gamma)$, dissipation dominates the time evolution of the system and hinders Rabi oscillations to occur. In the weak coupling limit, we distinguish between two regimes: If the cavity loss rate determines the dynamics, i.e. $\kappa \gg (\gamma, 2g)$, we refer to this regime as *bad cavity regime*, whereas if the atomic loss rate dominates, i.e. $\gamma \gg (\kappa, 2g)$, we refer to this limit as *bad emitter regime*. For typical solid state implementations like ours, the cavity decay rate is two to three orders of magnitude larger than the spontaneous emission rate. Hence, we operate in the bad cavity regime. In this limit, the eigenvalues are given by [118]:

$$\mathcal{E}_{m,+}^{\text{diss}} = \hbar\omega\left(m - \frac{1}{2}\right) - i\hbar\left[\kappa\left(1 + \frac{4g^2}{\kappa^2}\right)(m-1) + \gamma\left(1 + \frac{4g^2}{\kappa\gamma}\right)\right] \tag{2.24}$$

$$\mathcal{E}_{m,-}^{\text{diss}} = \hbar\omega\left(m - \frac{1}{2}\right) - i\hbar\kappa\left(1 - \frac{4g^2}{\kappa^2}\right)m. \tag{2.25}$$

Eigenstates of the system are the bare cavity and atom states and for zero detuning, the states are degenerate. Although irreversible losses are dominant, light-matter interaction in the weak coupling regime results in a modification of the spontaneous emission rate and the cavity decay rate:

$$\gamma_{\text{cav}} = \gamma\left(1 + \frac{4g^2}{\gamma\kappa}\right) \tag{2.26}$$

$$\kappa_{\text{cav}} = \kappa\left(1 - \frac{4g^2}{\kappa^2}\right). \tag{2.27}$$

The cavity decay rate κ is slightly modified in the presence of the emitter by a factor $4g^2/\kappa^2$. At the same time, the spontaneous emission rate of the atom can be enhanced

or inhibited by a factor referred to as the Purcell factor:

$$F_P = \frac{4g^2}{\gamma\kappa}. \tag{2.28}$$

The total spontaneous emission rate $\gamma_{\text{cav}} = \gamma + \gamma_{\text{on}}$ is given by the sum of the bulk atomic decay rate γ and the on resonance spontaneous emission rate $\gamma_{\text{on}} = \gamma F_P$ enhanced or inhibited by the cavity Purcell factor. For an emitter placed in a homogeneous medium with refractive index n, the bulk decay rate γ is given by [115, 120]:

$$\gamma = \frac{1}{3}\frac{n\omega^3|d|^2}{\pi\hbar\epsilon_0 c^3}, \tag{2.29}$$

where the prefactor $1/3$ accounts for a random dipole orientation. Taking into account definition (2.5), the coupling constant g can be expressed by:

$$g = \sqrt{\frac{3}{16\pi^2}\,\frac{\gamma\,\omega}{V}\,\left(\frac{\lambda}{n}\right)^3}. \tag{2.30}$$

Together, with the cavity decay rate κ given by equation (2.1), the Purcell factor yields:

$$F_P = \frac{\gamma_{\text{on}}}{\gamma} = \frac{3}{4\pi^2}\frac{Q}{V}\left(\frac{\lambda}{n}\right)^3. \tag{2.31}$$

This equation was first derived by E. Purcell in 1946 [56] to describe the enhancement of spontaneous emission via cavity-coupling. The Purcell factor is a convenient figure of merit that characterizes cavity-coupling and allows for the comparison between different cavity designs. A Purcell factor $F_P > 1$ implies enhancement of the spontaneous emission rate, while $F_P < 1$ symbolizes inhibition of the decay rate. In order to achieve large Purcell enhancement, cavity designs should be chosen with a high ratio Q/V implying a high quality factor and a small mode volume. In chapter 5, we will see that the enhancement of the emission rate is related to a high local density of states at the resonant frequency of the cavity mode. In contrast, if the local density of states is significantly reduced, as it is the case e.g. for frequencies within the photonic band gap, the transition rate is suppressed as there are no modes into which the atom can emit.

Please note that the Purcell factor has been derived under the constraint that the atomic emission linewidth is much narrower than the cavity linewidth [121]. Moreover, equation (2.31) defines an ideal Purcell factor assuming the emitter to be placed at the field antinode of the cavity mode with the emission frequency coinciding with the cavity mode $\omega = \omega_c$ and its dipole moment oriented along the field. In chapter 5, we derive a more general expression of the Purcell factor starting from Fermi's Golden Rule, including spatial and spectral detuning and the dipole orientation of the emitter.

Related to the Purcell factor, we define the spontaneous emission coupling factor β [115]:

$$\beta = \frac{F_P}{1 + F_P}. \tag{2.32}$$

The β-factor determines the ratio of photons emitted into the cavity mode compared to the total number of photons released by the emitter. Ideally, the spontaneous emission coupling factor would be equal to unity guaranteeing directive channeling of all photons into the cavity mode. However, in a realistic cavity, the β-factor is smaller than one and approaches unity only for large Purcell factors F_P.

Cavity specifications for weak and strong coupling to color centers in diamond

Up to now, we have introduced the formal mathematical criteria to achieve strong or weak cavity-coupling to an ideal two-level atom. In this thesis, we focus on coupling a small photonic cavity to single optically active defect centers in diamond. Assuming realistic excited state lifetimes and emission linewidths, we here exemplarily evaluate the required cavity specifications, i.e. quality factors and mode volumes, for weak and strong coupling to prominent color centers in diamond, namely the silicon- and nitrogen-vacancy center. As indicated above, for typical solid state cavity-coupling experiments, we have $\kappa \gg \gamma$. Therefore, to enter the strong coupling regime, we have to fullfill the condition $2g \gg \kappa$.

First, let's consider the case of a single SiV center with a zero-phonon line at 738 nm coupled to a photonic crystal cavity. For SiV centers in low-strained single crystal diamond, an excited state lifetime of 1.28 ns [26] has been determined at room temperature yielding $\gamma = 770\,\mathrm{MHz}$. Taking into account the definition of the cavity decay $\kappa = \omega/Q$ (eq. (2.1)) and expression (2.30) for the coupling constant g, we find the following condition to enter the strong coupling regime:

$$\frac{Q}{\sqrt{V}} \gg \sqrt{\frac{4\pi^2\omega}{3\gamma}}. \tag{2.33}$$

Assuming a modal volume of the photonic crystal cavity of $V = 1\,(\lambda/n)^3$, which is state-of-the-art of current photonic crystal cavities in diamond, this puts a lower limit to the quality factor of $Q \gg 6,600$ ($\kappa \ll 390\,\mathrm{GHz}$). In the case of a single NV center with a zero-phonon line at 637 nm and an excited state lifetime of typically 12 ns [23], corresponding to $\gamma = 83\,\mathrm{MHz}$, a quality factor of $Q \gg 20,000$ ($\kappa \ll 140\,\mathrm{GHz}$) would be required to observe strong coupling.

The cavity structures realized in this thesis do not achieve quality factors exceeding 1,200. Therefore, we are sure to operate in the weak coupling regime. For effective Purcell enhancement, the cavity linewidth has to be larger than the emission line [121]. At room temperature, SiV centers exhibit extraordinarily narrow zero-phonon linewidths down to 0.7 nm [25] (at 738 nm). This linewidth puts an upper limit on the cavity Q-factor of $Q \ll 1,000$. Together with the extremely small mode volume of diamond-based photonic crystal cavities of around one cubic wavelength, Purcell factors as high as $F_P \approx 80$ could be achieved coming along with up to $\beta \approx 98.8\%$ of the emitted photons channeled into the cavity mode.

We would like to emphasize that in our simple estimation, we assume ideal emitters to deduce the minimum and maximum cavity quality factors required for strong and

weak coupling. However, in the experiment, the exact position of the solid state emitter and its dipole orientation with respect to the maximum cavity electric field as well as the spectral detuning of the emitter-cavity lines play a crucial role for efficient coupling. Moreover, for real emitters, the actual radiative quantum efficiency and the ZPL branching ratio have to be taken into account. The detailed analysis of cavity-coupling including all these contributions as well as the determination of the quantum efficiency of single SiV centers and the theoretical description of cavity-coupling to broad-band emitters such as the NV centers are subject to the present thesis.

2.2 Cavity-coupling experiments in solid-state systems

Seminal experiments reported weak and strong coupling of single emitters to a cavity. The first observation of the Purcell effect at optical frequencies was made by Heinzen et al. [122] using Yb atoms in Fabry-Pérot cavities. Measuring lifetime shortening via Purcell coupling to macroscopic Fabry-Pérot cavities is challenging due to the requirement of high Q-factors and small mode volumes. Therefore, one of the clearest demonstrations of Purcell enhancement has been performed using solid-state microcavities such as dielectric contrast micropillars, whispering gallery mode resonators or photonic crystal cavities [123] as they offer high Q/V ratios. Here, we name some of the seminal experiments performed with single quantum dots and give a brief overview over current progress in cavity-coupling to color centers in diamond.

Cavity-coupling experiments with quantum dots

The emission of quantum dots has been Purcell enhanced using GaAs/AlAs micropillars [101,102], GaAs microdisks [103] and photonic crystals [104] fabricated in GaAs. Similar cavity designs (micropillars [105, 106], -disks [107] and photonic crystal cavities [108]) have been used subsequently to demonstrate strong coupling to single quantum dots. Moreover, inhibition of spontaneous emission has been reported for single quantum dots embedded in a GaAs nanowire [124]. Semiconductor fabrication techniques are developed to such an extend that even deterministic coupling of single quantum dots to photonic crystal cavities has been achieved [109, 110]. In these experiments [109, 110], a single quantum dot could be located via atomic force microscopy at the sample surface by growing stacks of tracer dots on top of the original quantum dot. Once identified, a photonic crystal cavity has been fabricated around the single emitter and the cavity modes were shifted into resonance via temperature tuning. This allowed for the observation of deterministic strong coupling. All these experiments required cryogenic temperatures.

Cavity-coupling experiments with color centers in diamond

In recent years, color centers in diamond have attracted much interest due to their long-lived electronic spin states even at room temperature and their prospects for efficient spin-photon interfaces when coupled to a cavity. To date, coupling experiments to

single color centers in diamond have been reported for various cavity systems that can be divided in two main categories: The hybrid approach and the monolithic all-diamond approach. For a review of cavity-coupling to color centers in diamond see e.g. [63–65]. We briefly present recent coupling experiments and discuss the advantages and remaining challenges of the two concepts.

Hybrid approach

In the hybrid approach [66], single color centers incorporated in nanodiamond particles or single crystal diamond are coupled to the evanescent field of a non-diamond cavity structure fabricated e.g. of gallium phosphide, silica or polystyrene. Hybrid approaches are straightforward to implement and profit from highly developed processing techniques of semiconductor materials enabling high-Q cavity structures.

Interestingly, the first experiment [125] on hybrid coupling between nanodiamonds containing NV centers that were drop-coated on a silica microsphere claimed to observe strong coupling. The whispering gallery modes and the NV ZPL were tuned into resonance via temperature variation from 6 to 12 K. Up to now, the results, i.e. the demonstration of strong coupling, were not reproduced by any other group.

In recent years, several precise positioning techniques based on scanning near field tips [67, 68], atomic force microscopy tips [75, 78, 126–129], tapered fibers [69] or thin tungsten tips incorporated in a scanning electron microscope [77, 130] have been developed that allow for picking up a preselected nanodiamond and place it on top of a non-diamond resonator. First experiments reported the modulation of the broad-band spectrum of nitrogen-vacancy centers via evanescent coupling to whispering gallery mode resonators such as polystyrene microspheres [67, 68], silica microtoroids [69] or -spheres [70] and gallium phosphide microdisks [71] .

Controlled enhancement of the zero-phonon line intensity was demonstrated for single NV centers in nanodiamonds when coupled to photonic crystal cavities fabricated in silicon nitride [78] or gallium phosphide [75–77]. Wolters et al. [75] observed intensity enhancement of the ZPL by a factor of 12 when placing a preselected nanodiamond with a single NV center on top of a GaP three missing hole photonic crystal cavity with $Q = 1,000$ and $V = 0.75(\lambda/n)^3$. Moreover, they demonstrated tuning of the cavity modes to the ZPL wavelength by local oxidation of the GaP material via laser irradiation. Unfortunately, upon tuning the cavity quality factor decreased to $Q = 600$.

To overcome the drawback of weak emitter-field overlap due to evanescent coupling, van der Sar et al. [77] placed a nanodiamond inside an air hole of a GaP photonic crystal cavity. The cavity design, consisting of a square lattice of air holes with one hole defect at the center, was chosen such that the mode field maximum was located within the air hole. No tuning technique was applied to shift the cavity mode with $Q = 3,800$ into resonance with the NV ZPL, but the mode was blue detuned by several nanometers. When the nanodiamond containing a single NV center was placed in the photonic crystal air hole, the resonant mode was fed by the broad-band NV luminescence and could be clearly distinguished in the spectrum.

Instead of displacing the nanodiamond, Englund et al. [76] pursued the inverse

approach and positioned a GaP photonic crystal cavity above diamond particles dispersed on a cover slip. When the three missing hole cavity with $Q = 550 - 600$ and $V = 0.74(\lambda/n)^3$ was positioned directly above a nanodiamond containing a single NV center, they measured an intensity increase by a factor of ~ 4 coming along with a lifetime reduction of the NV excited state from 16.4 ns to 12.7 ns. However, they stated that the lifetime reduction was primarily attributed to the increased refractive index surrounding the NV center. Analyzing the intensity enhancement and lifetime change, they deduced a spectrally resolved Purcell factor of 7.

Alternatively to solid state devices, single NV centers in nanodiamonds have also been coupled to Fabry-Pérot [79] and fiber-based microcavities [80–82], consisting of curved mirrors written at the end-facet of an optical fiber. These resonators can be easily and widely frequency tuned and allow for direct fiber-based in- and out-coupling of single photon emission. By coupling broad-band NV centers to fiber-based cavities, phonon-assisted cavity feeding was observed and theoretically described [80]. Within this framework, an extended model of Purcell enhancement of broad-band emitters such as the NV center was developed [80].

NV centers incorporated in nanodiamonds often suffer from material strain or poor spectral properties, e.g. spectral diffusion induced by charge fluctuations originating from non-diamond phases, defects or the presence of a nearby surface. Moreover, the orientation of the NV dipole moment in the nanodiamond is unknown and can neither be controlled nor aligned to the cavity field in these experiments. These limitations can be overcome by using single crystal diamond as host material for color centers in diamond. First attempts of implementing single crystal diamond in hybrid coupling schemes have been performed. Large ensembles of NV centers incorporated in single crystal diamond nanopillars, that were fabricated via reactive ion etching, were coupled to a silica microsphere with $Q = 2 \times 10^6$ and $V = 4,080(\lambda/n)^3$ positioned above the pillar [70]. The NV emission was modulated by the whispering gallery modes that were in- and out-coupled of the microsphere using a tapered fiber opposite to the nanopillar [70].

Other experiments by Barclay and Fu et al. [72–74] were based on NV centers implanted near the surface in pure single crystal diamond. On top of the diamond, GaP microrings and microdisks were fabricated with quality factors of $Q = 3,500-9,000$ [72–74] and $V = 3-18(\lambda/n)^3$ [72,74]. Measurements were performed at room [72] and cryogenic temperatures [73,74]. By condensing xenon gas onto the structures at low temperatures, cavity modes were tuned by $1.5-3$ nm onto the NV ZPL and the cavity-coupled emission was collected using either a tapered fiber [73] or a microscope objective [74]. On resonance, a lifetime reduction from 11.6 ns to 9.7 ns [74] was observed for single NV centers at cryogenic temperatures coming along with an intensity increase in the ZPL signal by a factor of 6 [74]. In contrast, no lifetime change was observed for NV ensembles probably prevented by ensemble averaging effects [73].

All these experiments aim at Purcell enhancement of the spontaneous emission rate by coupling to a high-Q cavity mode. It is noteworthy that inhibition of spontaneous emission of a single NV center has equally been demonstrated recently [131]. Incorporating nanodiamonds containing single NV centers in a three-dimensional photonic crystal

of self-assembled polystyrene spheres, the NV excited state lifetime was increased by 30% when the photonic band gap overlaps with the NV emission spectrum [131].

The hybrid approach is a flexible and versatile tool. The integration of single NV centers in nanodiamonds or single crystal diamond to non-diamond cavities have enabled successful demonstration of intensity inhibition and enhancement as well as lifetime reduction via Purcell coupling. However, the observed coupling strengths are moderate and mostly limited by the inability to position the color centers at the field maximum. Moreover, the scheme suffers from random dipole orientation and poor spectral properties of NV centers hosted in nanodiamonds due to spectral diffusion and material strain as well as from significant degradation in the cavity Q-factor due to scattering losses in the presence of nanodiamonds or -pillars. These limitations might be overcome by implementing direct integration and coupling of single color centers to monolithic all-diamond cavities.

All-diamond approach

The monolithic all-diamond approach is based on cavity structures that are directly fabricated in diamond. The challenge here is the fabrication of free-standing single crystal diamond membranes and the precise patterning of the diamond material. In recent years, diamond processing techniques have been developed and improved based on (inductively coupled) reactive ion etching (ICP-RIE) in an oxygen plasma or focused ion beam (FIB) milling with gallium ions. In the last few years, these new capabilities enabled the realization of high-Q whispering gallery mode resonators as well as photonic crystal cavity structures in single crystal diamond.

Faraon et al. [83] fabricated microrings and -disks via ICP-RIE in single crystal diamond attached to a silica substrate. By cooling the sample to cryogenic temperatures and condensation of xenon gas, the cavity modes with $Q \approx 4,000$ and $V = 17-32(\lambda/n)^3$ could be tuned into resonance with the ZPL of single NV centers. In resonance, an increase in the photoluminescence signal by a factor of 5 and a lifetime reduction from 11.1 ns to 8.3 ns were observed. Taking into account the ZPL branching ratio of 3%, the authors deduced a Purcell factor of 11.

Similar microrings were realized by Hausmann et al. [84]. The emission of a single NV center incorporated in the microring was collected with an overall efficiency of 10% using a nearby optical waveguide with grating in- and out-couplers.

Besides the resonant enhancement of NV emission, microdisk cavities with $Q = 2,200$ were also used for coupling to ensembles of silicon-vacancy centers. Lee et al. [85] reported a lifetime decrease from 1.8 ns to 1.48 ns of SiV ensembles that were incorporated into microdisks and compared to ensemble emission next to the structure.

The first photonic crystal cavities intended for coupling to NV centers were fabricated in suspended nanocrystalline diamond films using reactive ion etching [132]. However, due to pronounced absorption and scattering losses in nanocrystalline diamond, the quality factors were limited to 600.

Within the framework of this thesis, I was the first who realized one- and two-dimensional photonic crystal cavities in single crystal diamond using an unique material

system of diamond films grown on a sacrificial substrate. The diamond was patterned using FIB. In our publication [86], I demonstrated for the first time cavity tuning via oxidation in air and observed a room-temperature resonant intensity enhancement of the ZPL of incorporated ensembles of SiV centers by a factor of 3. Details on this experiment are presented in chapter 7.

Subsequently, Faraon et al. [87] demonstrated coupling of single NV centers to a two-dimensional photonic crystal cavity with $Q = 3,000$ and $V = 0.88(\lambda/n)^3$ patterned via ICP-RIE. Using gas condensation at cryogenic temperatures, the cavity frequency was matched to the NV ZPL. The intensity was resonantly enhanced by a factor of 26 coming along with a lifetime reduction from 13.7 ns to 4.0 ns. Considering the ZPL branching ratio, the authors of [87] deduced a Purcell factor of 69, which is the largest Purcell enhancement of a single color center reported up to date.

Equally using ICP-RIE etching, one-dimensional photonic crystal cavities with incorporated single NV centers have been realized in single crystal diamond [88, 90]. Cavity tuning was accomplished via heat oxidation and gas condensation at low temperatures. With a quality factor of $Q = 1,600$ and a mode volume of $V = 3.7(\lambda/n)^3$, Hausmann et al. [88] measured an intensity increase of the NV ZPL by a factor of 7.

Significantly larger Purcell enhancement of single NV centers was demonstrated by Li et al. [90] using one-dimensional ladder-type cavities. With $Q = 3,300$, they measured a lifetime reduction of a randomly coupled NV center from 18.4 ns to 6.7 ns via cavity coupling, while preserving long spin coherence times of 230 μs of the NV center [90]. In the same publication [90], the authors reported record quality factors up to 10,000 for diamond-based photonic crystal cavities.

All these experiments relied on random positioning of color centers within the monolithic cavity structures and the emitter-cavity systems were post-selected after fabrication for optimum coupling. Within the framework of this thesis, two approaches for deterministic coupling of single color centers to monolithic photonic crystal cavities in diamond have been developed. The first approach relies on targeted implantation of N^+ ions at the cavity center through a nanohole in an AFM tip, while the second solution uses fabrication of a photonic crystal cavity around a preselected SiV center. Details on these experiments are given in chapters 8 and 9.

A related idea was recently presented in a conference contribution [133], where the authors proposed to use a small hole in a silicon mask as an aperture upon N^+ implantation at the center of a cavity structure.

Although technically more demanding than the hybrid approach, cavity-coupling to a monolithic all-diamond cavity seems to be the concept of choice, as it allows for optimal emitter-field overlap, for well-defined orientations of the emitter dipole moment and for spectral tuning of the cavity modes. With advancing progress of precise patterning techniques, growth of high-quality diamond films and high-resolution implantation schemes, deterministic coupling of a single color center to diamond-based microcavities and the possible observation of strong coupling is within reach.

This chapter provided the basic theoretical description of coupling a two-level single emitter to a cavity structure of high quality factor and small mode volume. The here

introduced mathematical framework is essential to derive figure of merits characterizing light-matter interaction including cavity loss and spontaneous decay. Moreover, it is the basis for computations on the local density of states, the spontaneous emission rate and the Purcell factor of designed microcavities via the radiated power. In chapter 5, we derive a relation between the four parameters and present simulations on photonic crystal structures in diamond. For convenience, the emitter was modeled by a two-level atom that decays exclusively radiatively via a narrow-band transition. In chapters 7 and 9, we refine the here introduced Purcell factor to explain experimentally observed intensity enhancement and lifetime reduction when a photonic crystal cavity mode is tuned into resonance with the narrow-band emission of an ensemble and single SiV centers. Thereby, we take into account the emission properties of real emitters such as the radiative quantum yield and non-resonant decay rates, i.e. phonon side bands, of the SiV centers as well as the the actual emitter position, dipole orientation and spectral detuning from the cavity mode. For broad-band emitters such as the NV center with emission lines exceeding the cavity linewidth, the standard Purcell model fails. In chapter 8, we further extend the dissipative Jaynes-Cummings model and include higher order vibrational levels and additional loss terms such as pure dephasing to calculate cavity-coupling to the broad band NV center.

Chapter 3

Color centers in diamond

This chapter introduces the optical and spin properties of the nitrogen-vacancy (NV) and silicon-vacancy (SiV) color center in diamond that are used in this thesis as single photon sources for coupling experiments to diamond-based photonic crystal cavities. We start by introducing diamond as a host material for optically active defect centers. As a next step, selected color centers are presented that have been investigated in recent years as single photon sources. Among them the nitrogen-vacancy and the silicon-vacancy center are the most prominent and most investigated defect centers. The NV center is famous for its long-lived spin states that can be optically initialized and read out. The drawback of the NV center is its broad-band emission spectrum. The SiV center has been investigated as efficient narrow-band single photon source. Moreover, very recent experiments on the SiV center show strong evidence of an optically accessible spin. Here, we introduce the main properties of both centers including the emission spectrum, the dipole orientation as well as the electronic and vibronic level structure. Moreover, the scheme to optically initialize and readout the electronic spin state of the NV center is discussed as well as recent experiments on the SiV electronic spin. Finally, we introduce a simple three-level system of the electronic structure to deduce the internal population dynamics and the excited state lifetime of the color centers from experimental power-dependent intensity auto-correlation measurements.

3.1 Diamond

For building devices that enable the incorporation of single emitters and take advantage of quantum mechanical properties such as long coherence times, diamond seems to be the material of choice. Diamond consists of a tetrahedral arrangement of carbon atoms, which are bound over sp^3 hybrid orbitals in a face centered cubic (fcc) crystal lattice. The primitive Bravais cell consists of two basis carbon atoms situated at $(0, 0, 0)a$ and $(1/4, 1/4, 1/4)a$ with a lattice constant $a = 3.567\,\text{Å}$. Hence, the structure can be seen as two face centered cubic crystals displaced by $(1/4, 1/4, 1/4)a$. A schematic of the diamond crystal structure is shown in figure 3.1(a).

Due to its covalent bonds, diamond is the hardest naturally occurring material widely applied as cutting tool for industrial applications. It exhibits high thermal conductivity, 5 times larger than copper and therefore is often used as a heat spreader. In the visible spectral range, diamond has a high refractive index of $n = 2.4$ well suited for the realization of small cavity structures that rely on dielectric index contrast. Diamond has an excellent mechanical stiffness with a high Young's modulus of 1,000 GPa and a Poisson's ratio of 0.1, ideal for the realization of mechanical resonators with high frequency. Moreover, due to its bio-compatibility, diamond seems to be a promising platform for various medical applications.

Diamond has the widest optical band gap of all known solids extending over 5.5 eV [134]. This makes it transparent from the ultraviolet (220 nm) to the far-infrared (2.5 μm). Being transparent over a wide spectral region, diamond is an ideal host material for various optically active lattice or impurity defects forming discrete energy levels inside the band gap of diamond. Natural diamond typically contains large amounts of impurity atoms that hinder the localization of isolated optical centers. In contrast, artificial diamond can be synthesized with high purity representing an ideal host material for single optically active defect centers.

There exist two common production methods of synthetic diamond: The high pressure high temperature (HPHT) approach and chemical vapor deposition (CVD). In a HPHT process, graphite is transformed in a hydraulic press under pressures up to several gigapascal and temperatures up to 1,500°C into diamond which is the more stable phase under these extreme conditions [135–138]. The transformation process is accelerated by addition of a catalyst, e.g. metals such as nickel or iron. Typically, this method suffers from high nitrogen content yielding yellow colored diamond. However, very recently upon recrystallization via a temperature gradient, the synthesis of very pure HPHT diamond has been reported [139]. A second method to deposit synthetic diamond is chemical vapor deposition [140]: In a plasma process, diamond is grown on various substrates using methane-hydrogen gas mixtures. The most common CVD methods use either strong microwave fields or hot filaments to created the plasma (for a review see e.g. [141]). Typically, single crystal diamond can only be grown on single crystal diamond substrate, e.g. on HPHT substrates. This process is referred to as homoepitaxial growth. However, recent studies investigate the deposition on non-diamond substrates such as iridium [142] or platinum [143]. This synthesis is referred as heteroepitaxial growth which allows for the deposition of thin quasi single crystal diamond films on sacrificial substrates that can be easily removed after growth. For that reason, heteroepitaxial diamond films are particularly interesting for the realization of thin free-standing diamond membranes. Besides single crystal diamond samples, single isolated nanodiamonds containing only few down to one optically active defect center have attracted much attention in recent years as fluorescence markers for biological and life science applications [144, 145]. These nanodiamonds can be grown via CVD process on non-diamond substrates [25], produced via detonation synthesis [146] or via disintegration of diamond films [147].

We distinguish between different crystallinities of diamond, ranging from mono or single crystal diamond over polycrystalline to nanocrystalline diamond films. Poly- and

nanocrystalline films consisting of isolated diamond grains with sp^2 hybridized grain boundaries and graphite-like inclusions. These non-diamond phases give rise to material absorption and scattering losses strongly limiting the performances of any optical device. To overcome absorption and scattering losses, we here focus on single crystal diamond. A measure of the diamond quality is the Raman spectrum. High-quality single crystal diamond with low intrinsic strain exhibits a Raman line at $1332.5\,\mathrm{cm}^{-1}$ [134], that might shift in the presence of strain. In contrast, sp^2 bonded disordered carbon phases or graphite-like inclusions can be revealed by broad Raman peaks around $1360\,\mathrm{cm}^{-1}$ (D-band of disordered carbon) and around $1560\,\mathrm{cm}^{-1}$ (G-band of graphite) [134].

Diamond is typically classified in type I and II depending on the presence or absence of nitrogen impurities that can be detected using i.e. IR absorption spectroscopy [148, 149]. Type I diamond with significant nitrogen concentrations is further subdivided according to the arrangement of nitrogen impurities [150]: Type Ia diamond contains aggregated nitrogen clusters, while in type Ib diamond, single isolated nitrogen atoms are incorporated. Type II diamond has no measurable content of nitrogen and is further divided according to the concentration of boron impurities: Type IIa lacks of significant boron concentration, whereas IIb diamond contains boron impurities that are thought to be isolated atoms replacing carbon atoms in the diamond lattice. Type IIb diamond is known for its electrical conductivity as a direct consequence of the boron concentration. In recent years, ultra-pure diamond referred to as "electronic grade" became available with a nitrogen concentration $N_s^0 < 5\,\mathrm{ppb}$ and a boron concentration $B < 1\,\mathrm{ppb}$ [151] ($1\,\mathrm{ppb} = 1$ part per billion $< 1.7 \times 10^{14}\,\mathrm{cm}^{-3}$). Besides synthesis of ultra-pure diamond, isotopically enriched diamond referred to as "quantum grade" with a ^{13}C content $< 0.3\%$ and a nitrogen impurity concentration $N_s^0 < 0.05\,\mathrm{ppb}$ has been engineered [36, 152] to allow for ultralong spin coherence times of paramagnetic optically active defect centers hosted in the diamond (namely the nitrogen-vacancy center, see below).

3.2 Color centers in diamond

Due to its wide band gap and its associated transparency window covering the ultraviolet to the far-infrared spectral range, diamond is an excellent host material for single optically active defect centers. These lattice or impurity defects in diamond are referred to as *color centers*. The name is motivated by the fact that in large concentrations these defect centers are responsible for the coloration of the diamond gemstone. The reason is that defect centers provoke discrete energy levels within the band gap of diamond. In large concentration, the induced characteristic absorption of light results in coloration of the diamond in complementary color to the absorbed light. In very dilute concentration, isolated single color centers have been investigated as sources of single photons.

The requirements for an efficient, easy-to-handle single photon source based on solid state emitters are: a narrow emission line, photostability, room temperature operation, high count rates, well defined polarized emission, small lifetime and high radiative quantum efficiency as well as the ability for deterministic creation, e.g. via ion implantation or controlled growth conditions. These criteria would enable the generation of

single photons on-demand. Moreover, emission wavelengths in the near-infrared spectral range are desirable where highly efficient silicon avalanche photo diodes for single photon detection and low-loss fibers with high transmission are available.

Among the more than 500 known color centers in diamond [134] only a few of them have been investigated as single photon sources. For a review of color centers in diamond as single photon emitters and their versatile applications see e.g. [64, 153]. The most investigated and prominent color center is the NV center, that consists of a substitutional nitrogen atom and a lattice vacancy next to it. The NV center is highly interesting for quantum information applications due to its long-lived electronic spin state that can be initialized and readout optically. The drawback of the NV center is its more than 100 nm broad emission spectrum. The brightest color center up-to-date with a very narrow emission line is the SiV center formed by a silicon impurity and a lattice vacancy next to it. Analogous to the NV center, recent experiments demonstrated optical initialization and readout of the electronic spin of individual SiV centers. Before we go ahead in presenting in more detail the electronic structure as well as the optical and spin properties of the NV and SiV center, we would like to briefly introduce other color centers that have been investigated as efficient, narrow-band, room temperature single photon sources.

Chromium-related center: Chromium-related defect centers in single crystal diamond and nanodiamonds have been investigated. They reveal zero-phonon lines between 740-790 nm, narrow linewidths down to 4 nm [154, 155] and high count rates up to 3.2×10^6 counts/s at saturation [156]. For centers in single crystal diamond, short excited state lifetimes of 0.92 ns and high radiative quantum efficiencies of 0.3 have been detected [157]. In nanodiamonds, these properties strongly differ from center to center [158] probably due to the presence of material strain and random dipole orientations. The exact configuration and formation of the chromium-related centers within the diamond lattice is still under debate [159]. For chromium-related centers, wide tunability upon external electric fields have been demonstrated [155].

NiSi center: It was suggested that nickel together with silicon forms optically active complexes. After nickel-silicon co-implantation into single crystal diamond [160] and nanodiamonds [161] as well as after nickel implantation into silicon-rich nanodiamonds, bright emission lines at $767 - 775$ nm with count rates up to 2×10^5 counts/s [160] and short excited state lifetimes of $1.1 - 2.0$ ns have been detected.

NE8 center: Besides nickel-silicon complexes, nickel-nitrogen related optically active centers have been investigated as single photon sources. The NE8 center is the most prominent nickel-related defect center. It involves one nickel atom, two vacancies and four nitrogen atoms giving rise to a narrow ZPL at $780-802$ nm with linewidths between $1.2-2.0$ nm and with weak phonon side band contributions [162–164]. Single NE8 centers have been identified in natural diamond [162, 163] and CVD grown diamond films [164] exhibiting excited state lifetimes between $1.2 - 11.5$ ns and large radiative quantum efficiencies of $0.5 - 0.7$ [162, 163]. However, as the defect center involves multiple defect

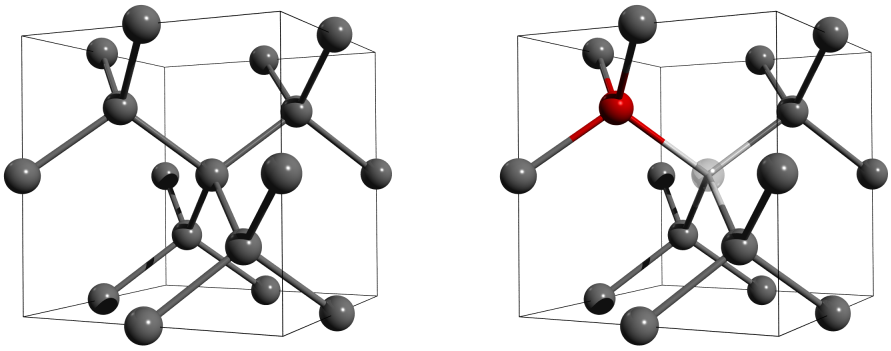

(a) Diamond lattice (b) NV center

Figure 3.1: Crystal structure of diamond and of the NV center: (a) The diamond lattice is a face centered crystal structure with a two-atomic basis at (0, 0, 0)a and (1/4, 1/4, 1/4)a. Gray spheres: carbon atoms. (b) A NV center is formed by replacing two carbon atoms by one nitrogen impurity atom (red sphere) and a vacancy (white sphere) next to it.

atoms and vacancies, deterministic creation of the NE8 complex via ion implantation has not yet been achieved.

3.3 Nitrogen-vacancy center

Besides the ability of single photon generation, the NV center stands out among all color centers because of its long lived electronic spin that can be prepared optically [165] and readout [166, 167] even at room temperature. This highlights the NV center as possible solid state spin qubit suitable for quantum information processing.

The NV center is a point defect within diamond consisting of a nitrogen atom replacing one carbon atom and a lattice vacancy next to it (Fig. 3.1(b)). The nitrogen-vacancy pair is oriented along the ⟨111⟩ diamond axes. The point group symmetry is $C_{3\nu}$. The NV center can be incorporated into the diamond during CVD growth, via electron irradiation or nitrogen ion implantation and subsequent annealing. At temperatures above 600°C [168], lattice vacancies generated by electron irradiation or ion implantation become mobile, diffuse towards substitutional nitrogen atoms and form optically active NV centers.

NV emission spectrum

The defect center induces discrete energy levels with radiative transitions inside the large band gap of diamond. Two optically active charge states of the NV center are known, the neutral charge state NV^0 with a ZPL at 575 nm and the negatively charged NV^- center with a ZPL at 637 nm. The different ZPLs allow for the discrimination of the two charge states. Beyond the ZPL, the NV^0 and NV^- exhibit broad phonon

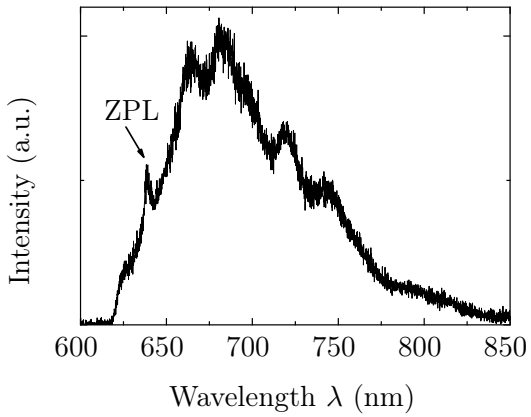

Figure 3.2: Room temperature emission spectrum of a single NV^- center: The NV^- spectrum exhibits a ZPL at 637 nm and a broad phonon side band extending over 100 nm to longer wavelengths. Measurement performed by A. Bommer [174]; reproduced with permission.

side bands extending by more than 100 nm from the ZPL to higher/lower wavelengths in emission/absorption. An additional infrared ZPL at 1042 nm has been associated to the NV^- center [169]. Figure 3.2 exemplarily shows the room temperature emission spectrum of a single NV^- center under 532 nm excitation. The spectrum reveals that only 3% of the photons are emitted into the ZPL at 637 nm (see also [80,83,125,170]). At cryogenic temperatures, temperature-dependent homogeneous broadening mechanisms are frozen out and the ZPL linewidth significantly narrows and becomes much more pronounced [171,172]. At low temperatures under resonant excitation, a Fourier limited linewidth of $\Delta\nu = 13$ MHz of the NV^- ZPL has been demonstrated [173] (excited state lifetime of $T_1 = 12$ ns [23], $\Delta\nu T_1 = 2\pi$).

Both NV^0 and NV^- charge states have been demonstrated as efficient single photon sources operating at room temperature [21, 22, 175]. Due to its extraordinary spin and optical properties, we focus in the following on the negatively charged NV^- center and start by briefly introducing its electronic structure..

Electronic structure

There are six electrons associated to the NV^- center: one from each adjacent carbon atom, two from the nitrogen atom and one acquired from a nearby donor determining the negative charge state [176]. Based on *ab initio* calculations and group theoretical considerations, the molecular orbitals (MO) of the NV^- center can be constructed yielding two (a_1, a_1') orbitals and one degenerate pair of (e_x, e_y) orbitals [177–179]. The molecular orbitals (a_1, e_x, e_y) are highly localized within the diamond band gap, whereas the lowest a_1' MO is completely filled with electrons and lies within the valence band of diamond. We will ignore the a_1' orbital in the following and discuss the configuration of the remaining four electrons. The molecular model of the ground and the excited state and the occupation are depicted in figure 3.3(a). In the lowest energetic

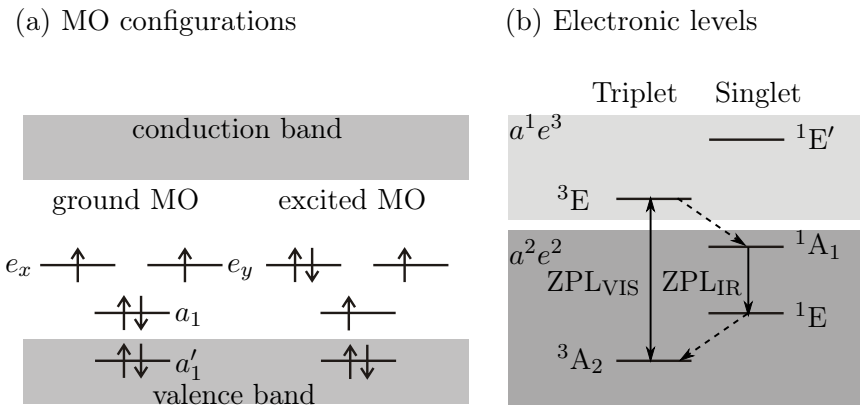

Figure 3.3: Electronic structure of the NV^- center: (a) Configurations of the ground and excited molecular orbitals. (b) The ground state MO configuration a^2e^2 gives rise to one triplet state $^3A_2$ at lowest energy and to two singlet states $^1A_1$ and ^1E. The excited MO configuration a^1e^3 results in one triplet state ^3E and one high-energetic singlet state $^1E'$. The triplet states $^3A_2$ and ^3E form the ground and the excited state of the NV^- center with intermediate singlet states $^1A_1$ and ^1E in between. The transition from ^3E to $^3A_2$ is associated with the ZPL at 637 nm, whereas the decay between $^1A_1$ and ^1E gives rise to the infrared ZPL at 1042 nm. Solid arrows: radiative transitions, dotted arrows: non-radiative transitions. (After [81])

MO configuration, the a_1 MO is completely filled and the two remaining unpaired electron spins occupy the (e_x, e_y) MOs. This configuration gives rise to one triplet state $^3A_2$ ($S = 1$) and two singlet states ^1E and $^1A_1$ ($S = 0$). The energy of the triplet state $^3A_2$ is the lowest and forms the ground state of the NV^- center (Fig. 3.3(b)). This assignment of $^3A_2$ as the NV^- ground state has been confirmed by various measurements such as uniaxial stress [168], spectral hole burning [180], magnetic circular dichroism [180], optically detected magnetic resonance (ODMR) [181], spin-locking [181] and spin cross-relaxation [182] studies as well as electron paramagnetic resonance (EPR) measurements without optical illumination [183, 184]. The radiative transition between the two singlet states $^1A_1$ to ^1E gives rise to the infrared zero-phonon line at 1042 nm [169]. By transferring one electron from the a_1 orbital to (e_x, e_y), the first excited MO configuration is reached. This configuration results in one triplet state ^3E and one singlet state $^1E'$ with a higher energy. The triplet state ^3E is considered as the excited state of the NV^- center, with the transition from ^3E to $^3A_2$ defining the NV^- zero-phonon line at 637 nm. The high-energetic singlet state $^1E'$ has no relevance in the later discussion and will be ignored in the following.

Infrared transition

Besides the ground and excited state, the electronic structure of the NV^- center comprises two intermediate singlet states that were first confirmed by the observation of the infrared transition at 1042 nm under optical excitation [169]. The absence of any Zee-

man splitting suggests that the transition occurred between two spin singlet states [169]. The intensity of the infrared transition is weak reaching only 10^{-3} compared to the visible band [176]. The weakness of the infrared fluorescence band is probably attributed to strong competing non-radiative recombination rates between the singlet states [185]. The upper shelving state has a relative short lifetime of 0.9 ns [186], whereas the lifetime of the lower intermediate state is significantly longer and depends strongly on temperature yielding 462 ns at 4.4 K, 219 ns at 295 K and 142 ns at 450 K [186]. Using uniaxial stress measurements along different crystallographic directions assigned the upper level to the $^1A_1$ singlet state and the lower level to the ^1E singlet state [176, 187]. There is recent evidence that the ^1E level is subjected to a dynamic Jahn-Teller effect (c.f. page 40) giving rise to a vibronic side band at 115 cm^{-1} above the ^1E state [176]. However, detailed knowledge on the vibronic side band of the infrared transition as well as the relative energy of the singlet states with respect to the ground and excited triplet states is yet missing. Moreover, the response to electric and magnetic fields is not yet well understood.

Fine structure of the ground state

At zero magnetic field, the ground state $^3A_2$ of the NV^- center splits into two spin sub-levels $m_s = 0$ and $m_s = \pm 1$ separated by $D_{gs} = 2.88$ GHz [188, 189] (Fig. 3.4). The fine structure splitting was first measured via EPR [188] and supported by Raman heterodyne electron nuclear double resonance (ENDOR) measurements [190] and double nuclear magnetic resonance [191]. After some initial debate, the splitting could be attributed to first order electronic spin-spin interaction [165, 192]. In contrast, contributions of spin-orbit coupling are small [192]. In the presence of strain, the degeneracy of the $m_s = \pm 1$ state is further lifted. Moreover, by applying external magnetic and electric fields, Zeeman and Stark field splittings of the fine structure components have been observed for the NV^- ground state [193–195]. However, compared to the excited state, the impact of the Stark shift on the ground state fine structure is several orders of magnitude smaller (compare [195] and [196]).

Fine structure of the excited state

Recently, the fine structure of the excited state could directly be observed at low temperature using photoexcitation spectroscopy of single NV^- centers with narrow optical linewidths [197, 198]. At low temperature, the excited state fine structure is determined by spin-orbit coupling, spin-spin interaction and perturbations resulting from local material strain. The impact of the individual contributions on the excited state energy level is schematically shown in figure 3.4. Axial spin-orbit coupling splits the ^3E excited state into three twofold degenerate, equally separated levels. The doublet ($\mathcal{E}$) associated to the $m_s = 0$ state is not displaced, whereas the ($\mathcal{E}'$) and ($\mathcal{A}_1$, $\mathcal{A}_2$) levels are shifted by $\pm\lambda_z$ down or up in energy [197, 199]. In contrast, the effect of transverse spin-orbit coupling λ_{xy} is weak [198]. Spin-spin interaction induces a shift of the states proportional to D_{es} and lifts the degeneracy of the ($\mathcal{A}_1$, $\mathcal{A}_2$) levels displacing them by $\pm\Delta$. Hence,

(a) Low temperature fine structure (b) Room temperature fine structure

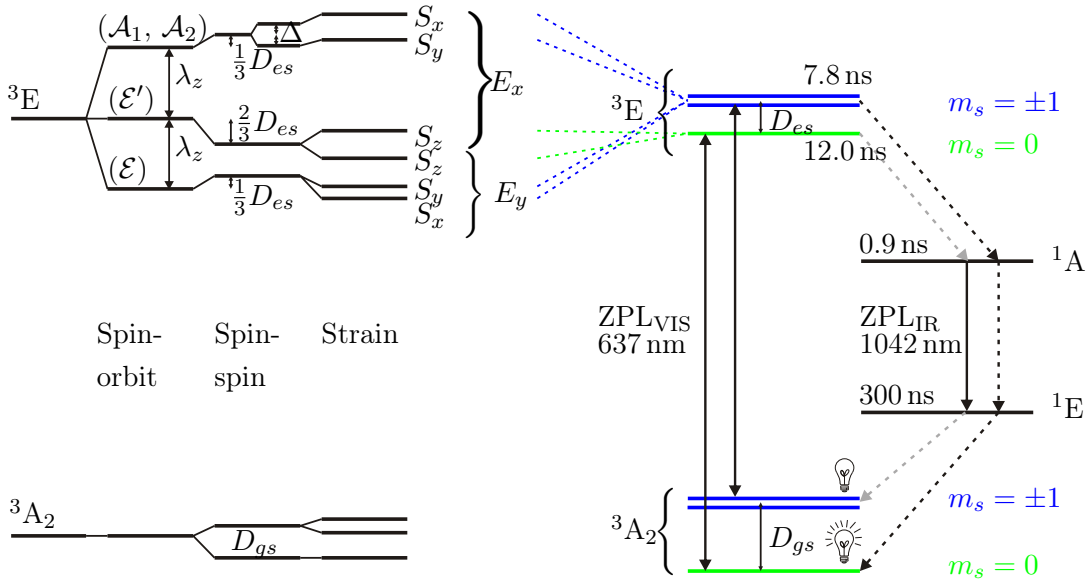

Figure 3.4: Low and room temperature fine structure of the ground ^{3}A$_2$ and excited state ^{3}E of the NV$^-$ center. (a) At low temperatures, the fine structure of the ^{3}E excited state is subjected to spin-spin interaction, spin-orbit coupling and perturbations resulting from material strain, lifting the degeneracy and shifting the sub levels apart. The six resulting spin states are ground in two orbital branches E_x and E_y. The ground state ^{3}A$_2$ fine structure at low temperatures is affected by spin-orbit coupling and material strain. However, compared to the excited state, the magnitude of the level shifting is significantly smaller. (b) With increasing temperature, the ^{3}E fine structure is subjected to averaging of both orbital branches mediated by phonons resulting in an average state solely subjected to spin-spin interaction. At room temperatures, the excited and the ground state exhibit zero-field splitting of 1.42 and 2.88 GHz, respectively, between the $m_s = 0$ and $m_s = \pm 1$ spin sublevels. Dotted lines: non-radiative decays, gray dotted lines: weak non-radiative decays.

the low-temperature fine structure of the NV^- center hosted in low-strain diamond is determined by the four parameters $\lambda_z = 5.5\,\mathrm{GHz}$, $D_{es} = 1.42\,\mathrm{GHz}$, $\Delta = 3.1\,\mathrm{GHz}$ [197] and $\lambda_{xy} = 0.2\,\mathrm{GHz}$ [198].

In the presence of material strain, the energy levels are further shifted apart. Local axial material strain displaces all energy levels, whereas non-axial strain lowers the symmetry and lifts the degeneracy of the $(\mathcal{E})$, $(\mathcal{E}')$ states. The six resulting spin states can be grouped into two orbital branches E_x and E_y of the excited state, each comprising three spin states S_x, S_y, S_z [197,198]. In the lower branch E_x, the spin states are strongly mixed in the presence of strain. For specific strain fields, two level anti-crossing was observed, resulting in optical spin-flip transitions, when the lower branch is excited [197]. In contrast, the upper branch E_y retains the optical spin selection rules [197].

At room-temperature, ODMR studies on single NV^- centers and ensembles revealed a zero-field splitting of 1.42 GHz of the excited state ^{3}E [172,193,194] that was found to be independent on local material strain [197]. The strong temperature dependence of the ^{3}E excited state fine structure has been attributed to phonon mediated orbital averaging [199]. With increasing temperature, electron-phonon coupling becomes important. As electron-phonon coupling only affects the orbital states and leaves the spin projections unchanged, the phonon transitions will distribute population between the orbital states belonging to the same spin-subset [177,199]. Moreover, due to spin-spin coupling of the $m_s = \pm 1$ spin states, the population will also be distributed between theses spin sub-levels. The decoupling of orbit and spin results in an averaged state at room temperature that is solely subjected to spin-spin interaction. Spin-spin coupling gives rise to a single zero-field splitting of $D_{es} = 1.42\,\mathrm{GHz}$ between the $m_s = \pm 1$ and $m_s = 0$ sub-levels of the ^{3}E fine structure [177,199] that was observed in the experiments.

Besides the splitting due to spin-spin interaction, spin-orbit coupling and intrinsic material strain, the influence of static electric [195,198] and magnetic fields [177,199] on the fine structure at low temperature has been investigated experimentally and theoretically. Via Stark effect or Zeeman splitting, the fine structure components of the NV ZPL could be tuned and spin-flip and spin-conserved transitions could selectively be excited.

Dipole orientation

The transition from the ^{3}E excited to the $^3A_2$ ground state is allowed for two orthogonal dipoles lying in the plane perpendicular to the NV symmetry axis [172,200]. Figure 3.5 depicts the crystal structure of the NV center with the symmetry axis $\parallel$ [111] and the transition dipoles $X \parallel [\bar{1}\bar{1}2]$ and $Y \parallel [1\bar{1}0]$ [172]. In low-strain diamond, the transition dipole moments have the same strength resulting in complex polarization characteristics contrary to other color centers exhibiting linear polarized emission. In the presence of strain, the two dipoles might rotate in the (111) diamond plane away from these specific crystallographic axes [201]. In general, the NV symmetry axis can be oriented along four possible crystal directions [111], $[1\bar{1}1]$, $[\bar{1}11]$ and $[\bar{1}\bar{1}1]$. The specific orientation of an individual center could be determined by monitoring the emission profiles of the two dipole moments under polarized excitation [202].

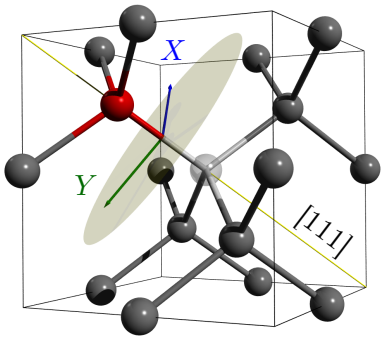

Figure 3.5: NV dipole orientation: The (X, Y) transition dipoles of the NV center are oriented in the (111) plane perpendicular to the NV symmetry axis. Green arrow: X dipole $\parallel [\bar{1}\bar{1}2]$, blue arrow: Y dipole $\parallel [1\bar{1}0]$, yellow line: NV symmetry axis $\parallel [111]$.

Spin initialization and readout

One of the most outstanding properties of the NV^- center is the ability to optically prepare and read out the electronic ground state spin. This highlights the NV^- center among other color centers as a spin qubit for quantum information applications [50, 203, 204]. The process of optical spin preparation relies on the non-radiative decay paths through the intermediate singlet states. We focus on room temperature spin readout as depicted in figure 3.4(b). The decay from the excited triplet state ^3E to the intermediate singlet state $^1A_1$ is spin-selective with the non-radiative shelving rate from the ^3E $m_s = \pm 1$ sub level being much stronger than from the ^3E $m_s = 0$ level. The population between the two singlet states $^1A_1$ and ^1E decays non-radiatively or radiatively giving rise to the infrared ZPL at 1042 nm. The transition from the lower singlet state ^1E to the NV^- ground state $^3A_2$ is also spin selective but here with a preferential non-radiative decay into the $^3A_2$ $m_s = 0$ sub level. Hence, after a few optical cycles the NV^- center is spin polarized into the $m_s = 0$ ground state sub level [165, 205, 206].

The larger non-radiative transition rates from the $m_s = \pm 1$ excited state sub levels lead to differences in the optical emission intensity and to different excited state lifetimes of the two spin sub sets. It was estimated that the non-radiative decay rate out of the ^3E $m_s = \pm 1$ state is at least 0.5 of the ^3E radiative decay rate [165], whereas the non-radiative transition from the ^3E $m_s = 0$ level is expected to be negligible. As the non-radiative decay paths into the shelving states compete with the direct radiative ZPL transition from the ^3E excited triplet to the $^3A_2$ ground state, we expect that the spin projections with the weakest non-radiative decay will appear brightest and vice versa. Hence, if the NV^- center is originally prepared in the $m_s = \pm 1$ sub level, the high probability for the electron to decay into the long-lived intermediate singlet state results in less fluorescence signal detected on the ZPL at 637 nm. Due to the weak intensity, we refer to the $m_s = \pm 1$ state as the "dark" state. In contrast, if the NV^- center is prepared in the $m_s = 0$ sub level, the ZPL fluorescence signal is strong due to

negligible non-radiative decay. Therefore, we refer to the $m_s = 0$ sub state as "bright" state. In the experiment, the unknown spin state is optically readout by comparing the integrated fluorescence signal upon optical excitation with calibration measurements performed on well prepared $m_s = 0$ and $m_s = \pm 1$ spin states [207]. It should be noted that readout of the spin state requires illumination of the center which, given enough time and intensity, will repolarize the spin and lose the spin information. To overcome this problem, cavity-enhanced spin readout schemes have been proposed that require much less excitation intensity [59].

Besides the difference in the fluorescence signal, the spin-selective transition into the shelving state gives rise to different excited state lifetimes of the spin sub levels. Due to the important non-radiative decay rates, we would expect a reduced lifetime of the ^{3}E $m_s = \pm 1$ excited spin state compared to the ^{3}E $m_s = 0$ sub set. Indeed, lifetime measurements of the individual ^{3}E spin levels performed on single NV$^-$ centers in bulk revealed a lifetime of $12.0 - 13.7$ ns for the $m_s = 0$ spin state and $7.3 - 7.8$ ns for the $m_s = \pm 1$ sub set [173, 208]. The excited state lifetime of NV$^-$ centers in nanodiamonds are typically twice as large as in bulk diamond yielding $23 - 25$ ns [194, 209] due to the reduced local density of states in the nanoparticles. Also for nanodiamond host materials, different lifetimes of the individual spin sub levels have been detected: For the $m_s = 0$ state, a lifetime of 23 ns was reported for single NV$^-$ centers, whereas the $m_s = \pm 1$ state revealed a decay time of 12.7 ns [194].

The spin dynamics of the NV$^-$ center occur between different spin sub levels of the triplet states. In general, one distinguishes three different time scales over which the spin stays in a certain state before it undergoes spin-flip or starts to lose its phase [210]. The spin relaxation time $\mathcal{T}_1$ characterizes losses due to population decay (spin-flip). The homogeneous dephasing time $\mathcal{T}_2$ commonly referred to as "coherence time" is limited by fluctuating interactions resulting in a phase change. In contrast, $\mathcal{T}_2^*$ is the inhomogeneous dephasing time averaged over an ensemble of quantum systems. The inhomogeneous dephasing time $\mathcal{T}_2^*$ is also used for single NV$^-$ centers to account for variations of the system over time.

The ground state spin of the NV center has the longest spin coherence time $\mathcal{T}_2$ of all electronic spins in solids exceeding 1.8 ms for isotopically purified diamond [36]. The long spin coherence time allows for coupling the NV ground state spin to electronic or nuclear spins of nearby carbon atoms in the diamond lattice, to resolve and manipulate them [47, 203, 204, 211, 212].

Vibrational structure

The optical, electronic and spin properties of the NV center are strongly affected by lattice vibrations. Due to slightly different atomic arrangements in the ground and excited state, the emission and absorption of photons is accompanied by lattice vibrations. In the simplest approximation, the vibrational modes are modeled by harmonic oscillations of the nuclei between equilibrium coordinates q associated with the electronic states. This harmonic oscillator approximation is referred as the Huang-Rhys model. In the framework of this model, the ground and excited states take the form of harmonic

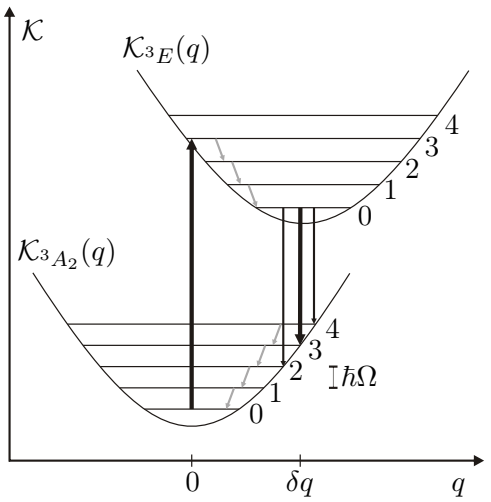

Figure 3.6: Huang-Rhys model of the vibrational transitions in the Frank-Condon picture: The harmonic potential $\mathcal{K}_{^3E}(q)$ of the excited state is displaced at equilibrium by δq with respect to the ground state potential $\mathcal{K}_{^3A_2}(q)$. The recombination originating at δq marks the most probable transition (thick black arrow) from the fundamental ^{3}E vibrational level to one of the vibrational levels of the ^{3}A$_2$ ground state followed by non-radiative transitions to the equilibrium position $q = 0$. The number of vibrational quanta involved in an optical transition are determined by the Huang-Rhys factor S. The excitation proceeds vice versa. Vertical black arrows: optical transitions, gray arrows: non-radiative transitions.

potentials $\mathcal{K}_{^3A_2}$ and $\mathcal{K}_{^3E}$ [213]:

$$\mathcal{K}_{^3A_2} = \frac{1}{2}\Omega^2 q^2 \tag{3.1}$$

$$\mathcal{K}_{^3E} = C_{^3E} + aq + \frac{1}{2}(\Omega^2 + b)q^2 \tag{3.2}$$

$$= C_{^3E} - C_R + \frac{1}{2}(\Omega^2 + b)(q - \delta q)^2. \tag{3.3}$$

Given these potentials, the vibrational modes of the ground and excited states are described as harmonic states at discrete energies $\hbar\Omega(\nu + \frac{1}{2})$ and $\hbar\sqrt{\Omega^2 + b}(\nu + \frac{1}{2})$, respectively, where ν and Ω are the vibrational occupation and the vibrational frequency. The term aq describes the linear nuclear displacement of the excited state configuration with respect to the ground state equilibrium ($q = 0$), whereas the quadratic term bq^2 represents the vibrational frequency shift due to a redistribution of the electronic charge between the electronic states. From the linear and quadratic coupling parameters a and b, we determine $\delta q = -a/(\Omega^2 + b)$ being the equilibrium displacement of the ^{3}E state and $C_R = a^2/2(\Omega^2 + b) = S\hbar\sqrt{\Omega^2 + b}$ [213] the relaxation energy, where S is referred to as the *Huang-Rhys factor*. The harmonic potentials and states are schematically shown in figure 3.6, with the excited state potential being shifted by the equilibrium displacement δq with respect to the ground state potential.

Applying the Franck-Condon principle, the most probable electronic transition from the excited ^{3}E state to the ground state $^3A_2$ originates from the fundamental vibrational ^{3}E state at δq into higher vibrational levels of the $^3A_2$ ground state followed by non-radiative relaxation to the fundamental $^3A_2$ vibrational level that effectively displaces the nuclei to the ground state equilibrium coordinate. The excitation from $^3A_2$ to ^{3}E proceeds vice versa. The Huang-Rhys factor S physically describes the mean number of vibrational quanta involved in the optical transition. For the NV center, the Huang-Rhys factor is typically $S = 3.76$ and the energy of the ground state vibrational mode is $\hbar\Omega = 65\,\text{meV}$ [168, 214]. The most probable transition originating from δq marks the maximum in the emission spectrum at $\hbar\omega = \hbar\omega_{\text{ZPL}} - S\hbar\Omega$, shifted to longer wavelengths with respect to the ZPL. Other transitions are less probable and less intense. For the NV^- center, we expect maximum intensity at 1.7 eV (728 nm). In absorption, an excitation energy of $\hbar\omega = \hbar\omega_{\text{ZPL}} + S\hbar\Omega = 2.19\,\text{eV}$ (565 nm) efficiently excites the NV center, which corresponds well with the 532 nm excitation wavelength widely used for off resonant excitation.

A second measure of the electronic-vibrational coupling is the Debye-Waller factor D_w, which is related to the Huang-Rhys factor via $D_w = \exp(-S)$. The Debye-Waller factor determines the ratio of photons emitted into the zero-phonon line compared to the overall emission. Due to the poor ZPL branching ratio, the Debye-Waller factor of the NV center amounts only $D_w = 2 - 4\%$ [80, 83, 125, 170].

Line broadening mechanisms of the zero-phonon line

According to the Heisenberg uncertainty principle $\Delta\nu T_1 > 2\pi$, the lifetime of the excited state T_1 induces a fundamental limit to the linewidth $\Delta\nu$ of a specific transition. For single NV^- centers in single crystal diamond cooled down to cryogenic temperatures, Fourier limited linewidths of 13 MHz [173] have been detected under resonant excitation considering an excited state lifetime of $T_1 = 12\,\text{ns}$. However, in most of the experiments, the measured linewidths are considerably broadened. For the NV^- center, one distinguishes two main broadening mechanisms: inhomogeneous broadening due to spectral diffusion and homogeneous broadening due to a dynamic Jahn-Teller effect in the excited state of the NV^- center. In the following, we briefly introduce the two mechanisms.

Dynamic Jahn-Teller effect: As discussed above, the excited state of the NV^- center is orbitally degenerate. This degeneracy is energetically unfavorable and will undergo distortion to retain an atomic arrangement with lower symmetry and lower energy, thereby lifting the orbital degeneracy. Orbital degeneracy lifting due to lattice distortion is the key statement of the Jahn-Teller effect [215]. We distinguish between the static Jahn-Teller effect induced by static distortion resulting in a lowered symmetry of the defect and dynamic Jahn-Teller effect by entangling vibrational and electronic states [216]. There is recent experimental evidence that the NV^- center is subjected to a dynamic Jahn-Teller effect [216–218], whereas static Jahn-Teller effect is excluded [214]. Electron-vibration interaction of the excited ^{3}E state with vibrations of e symmetry induces population transfer between E_x and E_y orbital levels through a two-phonon

Raman process [217]. Fu et al. [217] found that this excited-state population transfer results in a temperature dependent ZPL width $\Delta\nu$ increasing with T^5 for temperatures below 100 K. The Raman process induces dephasing of the optical transition and an increase in the optical linewidth [217]. Because of the temperature dependence, the linewidth broadening due to Jahn-Teller effect can be minimized by cooling the sample to cryogenic temperatures.

Spectral diffusion: Spectral diffusion is associated to electrostatic fluctuations that originate from ionized impurities like isolated substitutional nitrogen (electron donor) in the diamond or defects near an etched surface. These impurities or defects trap or release charges upon green laser excitation [166, 219, 220]. A single elementary charge at a distance of several nanometers can shift the excited state of the NV^- center via DC Stark effect by several hundred GHz [219]. It is assumed that spectral diffusion occurs in the form of jumps of the narrow NV^- emission line to random positions within a broad envelope. The random jitter of the emission line leads to inhomogeneous broadening of the NV ZPL with a Gaussian envelope. The spectral diffusion rate per photon is temperature independent in the range from 5 K to 20 K and independent of the excitation power [219]. However, the jump rate dramatically depends on the excitation wavelength. With increasing excitation wavelength in the range of 510-580 nm the spectral diffusion rate decreases [219]. The authors measured an abrupt change in the jump rate at an excitation wavelength of 540 nm (2.3 eV), which they attributed to deep charge traps with an ionization energy close to 2.3 eV. The optical ionization energy of substitutional nitrogen, considered as the main source of spectral diffusion, was found to be 2.2 eV, whereas the thermal activation energy is 1.7 eV [221].

3.4 Silicon-vacancy center

Besides the NV center, the silicon-vacancy (SiV) center has been investigated as efficient single photon source operating at room temperature with narrow emission lines, small excited state lifetime of 1.28 ns [26] and record count rates up to 6.2×10^6 counts/s [55]. Very recently, the generation of indistinguishable photons from two separated SiV centers has been demonstrated in a Hong-Ou-Mandel interference experiment [27]. Moreover, recent steps towards optical access to the electronic spin state have raised the exciting possibility to use the SiV center as a spin qubit [15–17].

The SiV center is created by substituting two carbon atoms of the diamond lattice by a silicon impurity and a vacancy nearby. The silicon atom relaxes to the interstitial lattice site in between the two former carbon sites [222]. This so called "split-vacancy" configuration [222] gives rise to a D_{3d} symmetry with the two vacant sites and the silicon atom aligned along the $\langle 111 \rangle$ diamond axes. A schematic of the SiV center in the diamond lattice is displayed in figure 3.7.

SiV centers have successfully been incorporated during CVD growth in nanodiamonds [25] and single-crystal diamond films (c.f. chapter 6). Moreover, single SiV centers can be created via Si implantation into pure diamond and subsequent high tem-

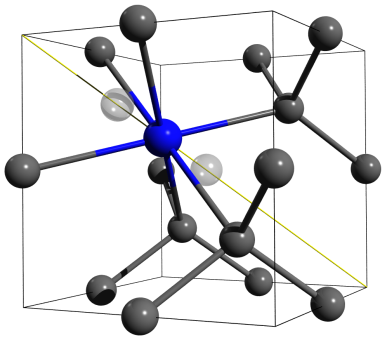

Figure 3.7: Crystal structure of the SiV center embedded into the diamond lattice: The Si impurity atom (blue sphere) relaxes to an interstitial position between two vacant sites (white spheres) forming a "split-vacancy" configuration aligned along the [111] crystallographic axis (yellow line).

perature annealing [24, 223].

Two different charge states of the SiV center have been investigated experimentally: The neutral SiV^0 center with a zero-phonon transition at 1.31 eV (946 nm) [224] was identified using EPR measurements with a ground state spin of $S = 1$. The negative SiV^- center exhibits a zero-phonon line at 1.68 eV (738 nm) and has been associated with a $S = 1/2$ ground state [222, 223]. Due to its high brightness and the possible ability for optical readout of the excited state spin [15], we here focus on the negative SiV^- center. We start to present the optical emission spectrum before we briefly discuss the electronic structure.

SiV emission spectrum

Figure 3.8 exemplarily shows the room temperature spectrum of a single SiV^- center hosted in a single-crystal diamond membrane fabricated within the framework of this thesis. Even under ambient conditions, the SiV^- spectrum exhibits a narrow ZPL around 738 nm with linewidths down to 0.7 nm [25] into which up to 80% of the photons are emitted [25]. In low-strain ultra-pure single crystal diamond, multiple identical SiV^- centers with impressively small variations in the ZPL wavelength have been observed [225, 226]. However, in the presence of material strain, the ZPL position of the SiV^- center might deviate from the ideal spectral position at 738 nm. For single SiV^- centers in strained nanodiamonds, ZPL wavelengths in the range of $730 - 750$ nm have been reported [25, 227].

For single SiV centers, a Huang-Rhys factor of 0.24 has been found corresponding to a Debye-Waller factor of $D_w = 0.8$ [25]. Hence, electron-phonon coupling is very weak resulting in low contributions of the phonon side bands. This highlights the SiV^- center as an efficient, narrow-band single photon source compared to the broad-band emission of the NV center. A detailed view of the SiV^- phonon side bands is shown

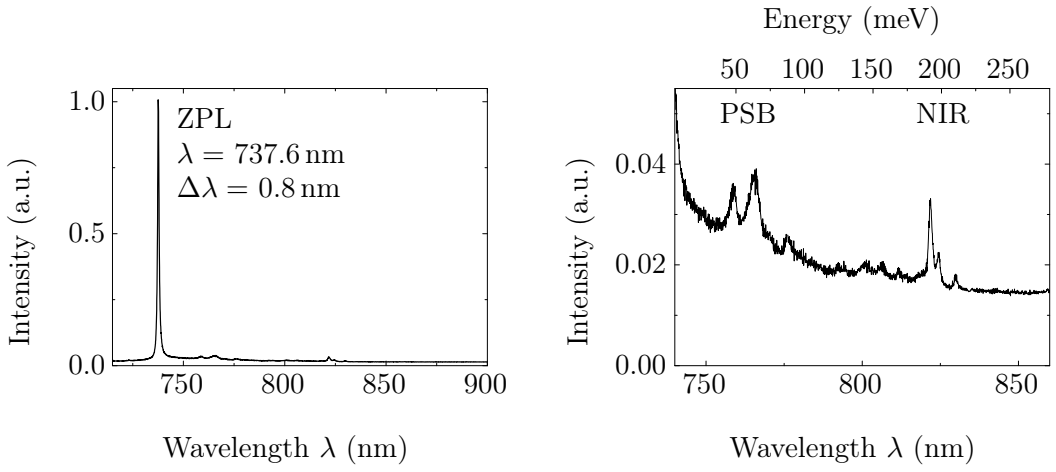

(a) SiV^- spectrum

(b) SiV^- phonon side band

Figure 3.8: Room temperature emission spectrum of a single SiV^- center in a single-crystal diamond membrane: (a) The SiV^- spectrum reveals a pronounced ZPL at 737.6 nm with a narrow linewidth $\Delta\lambda = 0.8\,\mathrm{nm}$ into which up to 80% of the photons are emitted. (b) Detailed view of the phonon side band (PSB) region for energies between $0 - 165\,\mathrm{meV}$ (ZPL to 810 nm) and of the near-infrared transition (NIR) at $820 - 840\,\mathrm{nm}$. The spectra (a,b) are normalized to the ZPL maximum.

in figure 3.8(b). The one-phonon region extends from $0 - 165\,\mathrm{meV}$ (ZPL to 810 nm) with remarkably narrow side band features. Very recently, the narrow side band at 64 meV has been attributed to a local vibrational mode of the Si atom along the [111] crystal direction [226]. Beyond the one-phonon region, narrow lines around $820 - 840\,\mathrm{nm}$ are observed in the spectrum [227, 228]. These lines have been tentatively attributed to electronic transitions additional to the ZPL involving the same ground state as the ZPL and further excited levels [228]. Interestingly, the near-infrared lines have only been reported for SiV^- centers hosted in strained nanodiamonds, whereas in low-strain single crystal diamond these features were not detected. This observation is related to the electronic structure of the SiV^- center. As will be discussed below, the near-infrared line has been associated to the transition between an intermediated shelving state and the ground state which is parity forbidden for an undistorted lattice but becomes partially allowed in the presence of strain [229].

Electronic structure

Very recently, first theoretical models on the electronic structure of the SiV center have been developed [229, 230]. However, the experimental confirmation of these proposals is still partially lacking. Here, we present the current state of knowledge on the electronic structure of the SiV^- center following [229] without any claim to completeness.

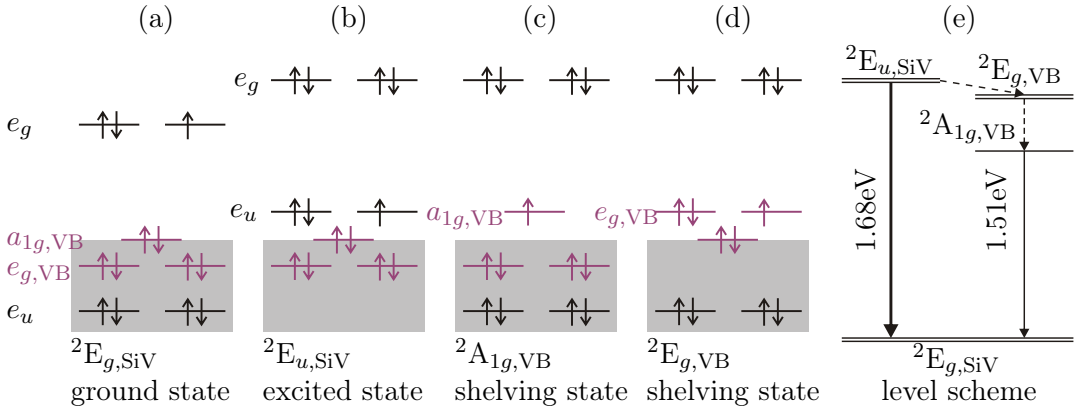

Figure 3.9: Molecular orbital configurations and electronic structure of the SiV^- center (after [229, 230]): (a) The ground state MO configuration $e_u^4\, e_g^3$ induces the SiV^- ground state ^2E_g. Black: SiV MOs, purple: valance band (VB) orbitals. (b) Excited MO configuration $e_u^3\, e_g^4$ forming the ^2E_u excite state. (c,d) Due to the presence of the SiV center, the VB orbitals ($a_{1g,\mathrm{VB}}$, $e_{g,\mathrm{VB}}$) are disturbed and transfer an electron to the SiV e_g MO. This electron transfer gives rise to two intermediate states $^2A_{1g}$ and ^2E_g tentatively attributed to shelving states. (e) Electronic level scheme of the SiV^- center.

The negative SiV^- center is associated with 11 electrons: six electrons originating from the dangling bonds of the vacant lattice sites, four electrons originating from the silicon atom and one electron from a nearby donor determining the negative charge state. Using group theory and *ab initio* calculations, the molecular orbitals of the SiV center have been determined: a_{1g}, a_{2u}, e_u, e_g (sorted by energy in ascending order). Please note due to the inversion symmetry of the SiV defect, we here distinguish between even ("gerade", subscript g) and odd ("ungerade", subscript u) MOs. The lowest energetic MOs, a_{1g} and a_{2u}, are completely filled with electrons and will be ignored in the following. The ground state MO configuration is obtained when four of the seven remaining electrons occupy the e_u MO and three electrons occupy the highest-energetic e_g MO (black levels in Fig. 3.9(a)). *Ab initio* simulations [229] suggest that in the ground state configuration, the e_u MO lies within the valance band of the diamond host material, whereas the e_g state is situated 0.8 eV above the valance band edge. The electronic configuration gives rise to the ^2E_g ground state of the SiV^- center (Fig. 3.9(e)). By promoting one electron from e_u to e_g, the excited MO configuration is obtained (black levels in Fig. 3.9(b)). The electron transfer rises the energy of e_u above the valance band edge and increases the e_g energy [229]. This MO configuration results in the ^2E_u excited state of the SiV^- center. The transition from excited state ^2E_u to ground state ^2E_g is associated with the pronounced ZPL with an evaluated energy of 1.72 eV which is in reasonable agreement with the experimentally observed 1.68 eV. Furthermore, simulations [229] reveal that the valance band (VB) molecular orbitals are strongly disturbed by the presence of the SiV^- center. Promoting one electron from the VB orbitals $a_{1g,\mathrm{VB}}$ or $e_{g,\mathrm{VB}}$ to the e_g MO shifts the valence band orbital containing the

hole into the band gap (purple levels in Fig. 3.9(c,d)). The resulting states $^2A_{1g}$ and ^2E_g are tentatively attributed to the shelving states of the SiV^- center. In low-strain diamond, assuming perfect inversion symmetry, the optical transition from these shelving states to the ground state is parity forbidden. In the presence of strain, the inversion symmetry of the SiV structure might be distorted, lifting the parity and allowing for radiative transition from the shelving state to the SiV^- ground state. The calculated transition energy 1.59 eV is very close to the recently observed near-infrared electronic transition of 1.51 eV (823 nm) reported for single SiV^- centers hosted in strained nanodiamonds [228]. Interestingly, the near-infrared transition was not yet observed for SiV^- centers in low-strain single crystal diamond [226, 230], supporting the assumption that the parity forbidden transition is lifted solely in the presence of strain. However, independent cross-correlation measurements on the ZPL and the near-infrared transition of a single SiV^- center excluded a possible involvement of a metastable shelving state to the near-infrared line [228]. Therefore, further detailed experiments are required to elucidate and confirm the theoretical prediction on the exact nature and energetic position of the shelving state within the band gap. To describe our experimental data, we model the SiV^- electronic structure as an effective three level system with one ^2E_g ground, one ^2E_u excited and an $^2A_{1g}$ intermediate shelving state. The resulting rate equation model is presented in the next section 3.5.

Fine structure of the ground and excited state

When cooled down to cryogenic temperatures, the SiV^- fine structure reveals four lines that have been assigned to doublet levels of the ground and excited states which split by 48 GHz (0.20 meV) and 259 GHz (1.07 meV), respectively [26, 223, 231, 232]. A schematic of the SiV^- fine structure is shown in figure 3.10. Detailed theoretical analysis [223] of measured spectra under presence of magnetic fields revealed that the splitting is mostly attributed to spin-orbit interaction with weak contributions of dynamic Jahn-Teller effect [223]. Early photoluminescence measurements [231, 233] on SiV^- ensembles at cryogenic temperatures revealed a 12-line fine structure near 1.68 eV that can be divided into three groups each containing four lines. The relative intensity of the three subgroups is correlated with the natural abundance of 0.922, 0.047 and 0.030 of the three silicon isotopes ^{28}Si, ^{29}Si and ^{30}Si [231]. Very recently, the isotopic shift of ~ 80 GHz has been confirmed for single SiV^- centers hosted in low-strain single crystal diamond allowing for the unambiguous identification of the silicon isotope of an individual SiV^- center [226]. This enables to select ^{29}Si isotopes which are known to have a nuclear spin $I = 1/2$, whereas the most abundant ^{28}Si has no nuclear spin. Hyperfine splitting of ^{29}Si nuclear spin has recently been observed for the first time [17]. Nuclear spins are expected to have superior coherence properties and would be ideal qubits for quantum information processing applications [17].

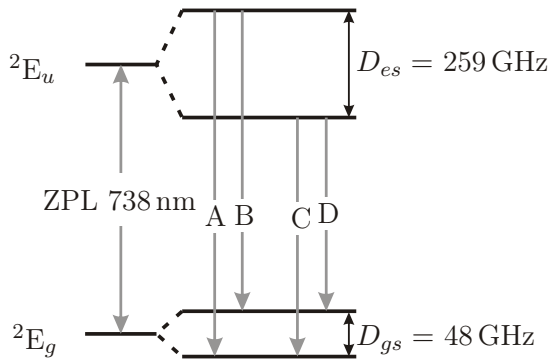

Figure 3.10: Fine structure of the SiV^- center at low temperature: The ^2E_g ground and ^2E_u excited state split by $D_{gs} = 48\,GHz$ and $D_{es} = 259\,GHz$, respectively, giving rise to four transitions referred to as A, B, C and D. The splitting is mainly attributed to spin-orbit coupling.

Dipole orientation

Group theoretical calculations predict an orientation of the SiV^- dipole along the $\langle 111 \rangle$ diamond axes [222]. This expectation has recently been verified via polarization analysis of the ZPL emission at room and cryogenic temperature [26, 223, 225]. At room temperature, a linear polarization of the SiV^- ZPL along the $\langle 111 \rangle$ crystallographic axis has been found in low-strain diamond [26]. At cryogenic temperatures, the four fine structure lines split into two mutually orthogonal, linearly polarized sub sets with the polarization of the two inner lines oriented parallel to each other and perpendicular to the two outer lines. All lines are polarized along the $\langle 111 \rangle$ directions [223, 225]. The inner lines have been attributed to a dipole $d_\parallel$ aligned along the $\langle 111 \rangle$ axis, whereas the outer lines have been assigned to a dipole $d_\perp$ perpendicular to the $\langle 111 \rangle$ direction [223, 225]. From the intensity ratio, it was concluded that $d_\parallel$ being the dominant dipole four times stronger than $d_\perp$ [223, 225]. Under the influence of strain, theoretical simulations predict [223] that the polarization axis might rotate away from the $\langle 111 \rangle$ direction explaining observations on single SiV^- centers in strained nanodiamonds revealing linear polarization along the $\langle 110 \rangle$ direction [227].

Optical spin readout

Besides the ability to emit linearly polarized single photons at a high count rate under ambient conditions, the SiV^- center is expected to be used as a spin qubit whose spin state can be optically accessed [15, 17]. In the presence of an external magnetic field, the spin sublevels are subjected to Zeeman splitting as recently been observed for single centers and ensembles of SiVs in low-strain single crystal diamond and nanodiamonds [15, 223]. Using resonant excitation under finite magnetic field, spin-selective population and relaxation between excited state sublevels with the same spin projection have been demonstrated. The spin-tagged resonant fluorescence enable direct optical

access, initialization and control of the electronic spin of individual SiV^- centers [15,17].

The spin dephasing time of the SiV^- ground state has recently been measured using coherent population trapping [16,17]. By applying a magnetic field inclined with respect to the quantization axis [111] of the SiV center, a Λ scheme was created between different spin states. By simultaneously driving the two transitions of the Λ system, the spin is optically pumped in a coherent superposition of the two involved ground state sub levels. As a consequence the fluorescence from the shared excited state decreases when the two lasers are tuned into resonance with the Λ-transitions. From the dip in the recorded fluorescence signal, the spin coherence time of the SiV^- ground state has been determined to be $\mathcal{T}_2^* = 45\,\text{ns}$ [16] or $\mathcal{T}_2^* = 35\,\text{ns}$ [17]. As in this thesis, we only investigate negatively charged SiV centers, we omit the minus sign in the following and refer to the SiV^- center simply as SiV center.

3.5 Internal population dynamics

In the experiment, it is essential to prove single emitter character of the color centers under investigation. This can be accomplished by measuring the intensity auto-correlation function $g^{(2)}$ that we briefly introduce here. The emission of single photons is a purely quantum mechanical process that has no analog in classical physics. The $g^{(2)}$ function measured at various excitation powers allows for further insight into the internal population dynamics of a single color center. In a first approximation, the NV and SiV center are modeled as three-level systems including a ground state, an excited state and one intermediate metastable state. The inter-system decay rates and excited state lifetime as well as resultant parameters such as the radiative quantum efficiency are deduced from this simple model.

Intensity auto-correlation function $g^{(2)}$

To prove the single emitter character and to deduce the internal population dynamics of a single color center, we perform intensity auto-correlation measurements, also referred to as $g^{(2)}$ measurements. For a classical and non-classical light source, the intensity auto-correlation function is defined as:

$$g^{(2)}(\tau) = \frac{\langle I(t)I(t+\tau)\rangle}{\langle I(t)\rangle^2}, \tag{3.4}$$

where $\langle\cdot\rangle$ indicates the time average and $I(t)$ and $I(t+\tau)$ are the intensities registered at times t and $t+\tau$, respectively. A rigorous derivation of the $g^{(2)}$ function based on quantum electrodynamics can be found e.g. in [234] and will not be reproduced. Here, we give a more intuitive explanation of the intensity-correlation function. In the experiment, the $g^{(2)}$ function is measured using a Hanbury-Brown and Twiss (HBT) interferometer that consists of a beam splitter and two photon detectors, one at each output port (c.f. chapter 4). In the case of a single quantum emitter approximated by a two-level system, the excitation and relaxation cycle takes a finite time and hence the probability to register two photons at the same time ($\tau = 0$) is ideally zero, i.e.

$g^{(2)}(0) = 0$. The absence of any correlation events at $\tau = 0$ is referred as antibunching. In a more rigorous derivation [234], one can show that for antibunched light, we have:

$$g^{(2)}(0) = 1 - \frac{1}{m} < 1, \tag{3.5}$$

where m is the number of emitters present in the laser focus. For two emitters ($m = 2$) with equal intensity, we obtain $g^{(2)}(0) = 0.5$. Hence, the condition $g^{(2)}(0) < 0.5$ reveals the presence of a single emitter. For large delay times τ, the $g^{(2)}$ function approaches a constant value of unity. This fact is used in this work for normalization of the raw data such that the measured correlation histograms retain $g^{(2)}(\tau) = 1$ for large τ.

In the discussion above, we have seen that in theory the $g^{(2)}$ function should vanish at zero time delay in the case of a single emitter. However, in the experiment, this is hardly observed due to background contributions originating from the diamond host material as well as because of the limited temporal resolution of the single photon counters. Let s be the count rate of the single photon source and b the background contribution, we define the factor p_f giving the probability that a detected photon originates from the single emitter:

$$p_f = \frac{s}{s+b} \tag{3.6}$$

Here, p_f is related to the signal-to-noise ratio that can be determined by measuring the count rate or the integrated spectral intensity at the emitter position and next to it. To account for uncorrelated background contributions to the antibunching dip, we fit the correlation measurements with the following $g_b^{(2)}$ function [22]:

$$g_b^{(2)}(\tau) = 1 + (g^{(2)}(\tau) - 1)\, p_f^2. \tag{3.7}$$

The actual $g^{(2)}$ correlation function corrected for random coincidences is then obtained by simply reversing equation (3.7) [22]:

$$g^{(2)}(\tau) = [g_b^{(2)}(\tau) - (1 - p_f^2)]/p_f^2. \tag{3.8}$$

A second cause for a non-vanishing $g^{(2)}(0)$ is the finite temporal resolution of our single photon counters. In chapter 4, we will see that the detected $g^{(2)}$ functions are given by a convolution of the actual signal with the temporal response function of our detection device. We account for the temporal uncertainty of the detectors by measuring the instrument response function of our setup and including it in the fit routine of the intensity-correlation functions.

Three-level model

The detected $g^{(2)}$ correlation not only allows for the confirmation of single emitter character but gives furthermore insight into the internal population dynamics of a single color center under investigation. Based on the detected $g^{(2)}$ correlation as a function of the excitation power, we derive a simple model of the SiV center. In section 3.4, we have seen that the SiV center can be modeled as an effective three-level system involving the

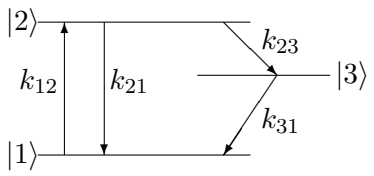

Figure 3.11: Three-level model to evaluate the population dynamics of the SiV center.

$^2\mathrm{E}_g$ ground state $|1\rangle$, the $^2\mathrm{E}_u$ excited state $|2\rangle$ and one $^1\mathrm{A}_{1g}$ intermediate state (shelving state) $|3\rangle$ with a longer lifetime. A schematic of the three-level system is depicted in figure 3.11. The transition rates between the states are indicated by arrows. Here, k_{12} and k_{21} denote the pump rate and the spontaneous decay rate from ground state to the excited state and vice versa. The photons emitted via the radiative transition k_{21} are detected in the experiments. The shelving state is populated at a rate k_{23} and relaxes back to the ground state at rate k_{31}. As long as the populations is "trapped" in the shelving state, no photons are detected on the radiative transition k_{21}. Neglecting all coherence, the population dynamics of the three-level system are governed by the following rate equations [235]:

$$\begin{aligned} \frac{dn_1}{dt} &= n_2k_{21} - n_1k_{12} + n_3k_{31} \\ \frac{dn_2}{dt} &= -n_2k_{21} + n_1k_{12} - n_2k_{23} \\ \frac{dn_3}{dt} &= n_2k_{23} - n_3k_{31}, \end{aligned} \tag{3.9}$$

where n_j, with $j = \{1, 2, 3\}$, are the populations of the three energy levels. Assuming the system to be in the ground state at $t = 0$ ($n_1(0) = 1$, $n_2(0) = n_3(0) = 0$) and that the sum over all populations $n_1 + n_2 + n_3 = 1$, the solution to the differential equations yields the population of the excited state $n_2(t)$, as well as the $g^{(2)}$ function defined by $n_2(t)/n_2(t \to \infty)$ [21]:

$$g^{(2)}(\tau) = 1 - (1 + a)\, e^{-|\tau|/\tau_1} + a\, e^{-|\tau|/\tau_2}. \tag{3.10}$$

The parameters τ_1, τ_2 and a are given by

$$\tau_{1,2} = 2/(A \pm \sqrt{A^2 - 4B}) \tag{3.11}$$

$$A = k_{12} + k_{21} + k_{23} + k_{31} \tag{3.12}$$

$$B = k_{12}k_{23} + k_{12}k_{31} + k_{21}k_{31} + k_{23}k_{31} \tag{3.13}$$

$$a = \frac{1 - \tau_2 k_{31}}{k_{31}\,(\tau_2 - \tau_1)}. \tag{3.14}$$

This expression has first been applied to dye molecules [235]. The parameters τ_1 and τ_2 represent the times governing the antibunching and the bunching behavior of the $g^{(2)}$ function. The parameter a is a measure for the impact of the shelving state. For $a = 0$, the system behaves like a two-level model.

In the experiment we proceed as follows: We measure the $g^{(2)}$ function for various excitation powers and fit them via equation (3.10) or (3.7) to extract τ_1, τ_2 and a. To deduce the internal population dynamics from the fit parameters, several assumptions on the dependence of the decay rates k_{12}, k_{21}, k_{23} and k_{31} on the excitation power P have to be made. Here, we follow the model proposed for single SiV centers in references [25, 55, 228]. We assume a linear dependence of the pump rate k_{12} to the excited state on the off resonant excitation power P. This is reasonable, as relaxation processes between vibrational sublevels of the excited state are expected to be very fast such that the excitation process solely depends on the pump power. Furthermore, we assume constant rate coefficients k_{21}, k_{23} and a power dependent de-shelving rate k_{31} following a saturation law [25, 55, 228]:

$$k_{12} = \sigma P, \qquad k_{21} = \text{const}, \qquad k_{23} = \text{const}, \qquad k_{31} = \frac{d \cdot P}{P + c} + k_{31}^0 \tag{3.15}$$

The rate coefficients k_{21}, k_{23}, k_{31}^0 and d that govern the population dynamics of the SiV color center are determined from the limiting values of τ_1, τ_2 and a under the assumption $k_{21} + k_{23} > k_{31}^0$ [25]:

$$k_{31}^0 = \frac{1}{\tau_2^0} \tag{3.16}$$

$$d = \frac{1}{\tau_2^\infty \, (a^\infty + 1)} - \frac{1}{\tau_2^0} \tag{3.17}$$

$$k_{23} = \frac{1}{\tau_2^\infty} \cdot \frac{a^\infty}{a^\infty + 1} \tag{3.18}$$

$$k_{21} = \frac{1}{\tau_1^0} - k_{23} \tag{3.19}$$

Here the superscript $^\infty$ denotes the value for high excitation powers P and ^{0} for vanishing excitation powers. The parameters σ governing the excitation rate and the de-shelving parameter c are determined from the power dependent fits of the parameters τ_1, τ_2 and a according to equations (3.11)-(3.14).

Besides the inter-system decay rates, the excited state lifetime can be evaluated from this model. The extrapolation of the τ_1 parameter for vanishing excitation powers gives the lifetime T_1 of the excited state $|2\rangle$ such that: $\lim_{P \to 0} \tau_1 = T_1$ [21,236]. This relation will be widely used in our experiments to evaluate e.g. a possible lifetime change when coupling a single color center to a cavity mode.

Saturation measurement

One essential figure of merit to characterize the efficiency of a single photon source is the maximum obtainable count rate. By detecting the count rate $I(P)$ as a function of the excitation power P, we obtain the so called saturation curve, which can be fitted according to [21, 25]

$$I(P) = I^\infty \frac{P}{P + P_{\text{sat}}}. \tag{3.20}$$

At high excitation powers, the count rate converges to a constant value I^{∞} referred to as the saturation count rate, whereas P_{sat} denotes the saturation pump power.

In the following, we relate the experimental saturation count rate to the excited steady state population n_2^{∞} and the radiative transition rate deduced from the three-level model. In the steady state, all time derivatives in equations (3.9) vanish. By taking into account the normalization condition $n_1 + n_2 + n_3 = 1$, we obtain the excited state population as a function of the transition rates $k_{12}(P)$, k_{21}, k_{23} and $k_{31}(P)$:

$$n_2(P) = \frac{k_{12}(P)k_{31}(P)}{k_{31}(P)(k_{21} + k_{23} + k_{12}(P)) + k_{23}k_{12}(P)}. \tag{3.21}$$

The product of the excited state population and the spontaneous emission rate $n_2(P)k_{21}$ is proportional to the photon count rate $I(P)$ of the single emitter under investigation. In the limit $P \to \infty$, the steady state population of the excited state is given by:

$$n_2^{\infty} = \lim_{P\to\infty} n_2(P) = \frac{1}{1 + \dfrac{k_{23}}{d + k_{31}^0}}. \tag{3.22}$$

By taking into account, the overall detection efficiency η_{det} of the optical setup as well as the radiative quantum efficiency η_{qe} (defined as the ratio of the radiative decay rates to the overall transition rates) of the emitter and the spontaneous decay rate k_{21}, the maximum obtainable photon count rate I^{∞} at saturation can be determined:

$$I^{\infty} = \eta_{\mathrm{det}}\eta_{\mathrm{qe}} n_2^{\infty} k_{12}. \tag{3.23}$$

In the experiment, the detection efficiency of the setup η_{det} and the saturation count rate I^{∞} can be measured. Moreover, the steady state population n_2^{∞} and the spontaneous decay rate k_{21} can be deduced from the internal population dynamics. Including these four parameters, equation (3.23) allows for the evaluation of the internal quantum efficiency η_{qe} of the investigated single color center. Detailed knowledge of the quantum efficiency is essential to evaluate the enhancement or inhibition of the spontaneous emission rate via cavity-coupling.

This chapter discussed the extraordinary optical and spin properties of the nitrogen- and silicon-vacancy center that are subsequently used as single photon sources incorporated in diamond. We introduced a simple three-level model that allows us to evaluate the internal population dynamics from power-dependent intensity correlation measurements. The model is widely used in this thesis to deduce a possible modification of the spontaneous emission rate and the excited state lifetime when single color centers are coupled to a photonic crystal cavity directly fabricated in diamond.

Chapter 4

Experimental setup

In the following chapter, we briefly introduce the experimental setup used to identify and characterize single color centers and photonic crystal cavity modes. In this work two similarly constructed confocal microscope setups are used that are both connected either to a grating spectrometer to spectrally analyze the fluorescence light or to a Hanbury Brown and Twiss interferometer to measure the intensity auto-correlation function $g^{(2)}$ of the emitted photons as well as the excited state lifetime of color centers under pulsed excitation. The first setup is solely used for room temperature experiments under continuous wave illumination. In the following, we will refer to this setup as "Lab 1". The second setup additionally allows for pulsed excitation and cooling the sample to liquid helium temperatures. We will refer to the cryogenic temperature setup as "Lab 2". We briefly describe the applied components before we analyze in detail the spatial resolution as well as the detection efficiency of each confocal setup. For time-correlated single photon counting experiments, we introduce the Hanbury Brown and Twiss interferometer and discuss the impact of its temporal resolution on the measured $g^{(2)}$ functions and excited state lifetimes.

4.1 Confocal setup for spectroscopy at room temperature

Confocal detection is based on the fact that only a small volume of the sample is illuminated by focused laser light. The fluorescence signal and scattered laser light originating from the focal volume are collected using an objective. After being separated from the laser light by a beam splitter, the fluorescence is focused by a lens on a pinhole used as a spatial filter in front of a detector. Light not originating from the focal area will not be able to pass through the detection pinhole and will be rejected. Confocal microscopy allows for a high spatial resolution as well as reduced background contributions. An extended image of the sample can be obtained by raster scanning the sample with respect to the fixed beam path and recording the fluorescence signal for each pixel. For an overview of confocal optical microscopy the reader is referred to reference [237].

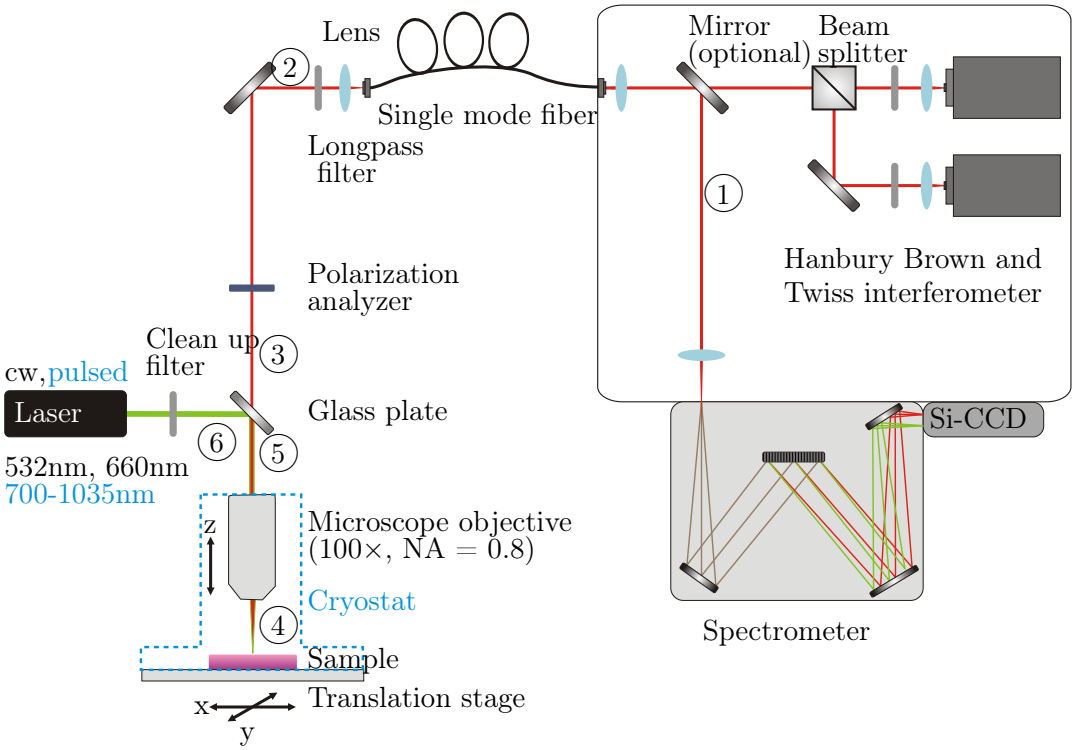

Figure 4.1: Confocal microscopy setup for spectroscopy of single color centers in diamond: Two similar confocal setups are used in this work: One operates solely at room temperature, whereas the second setup also allows for measurements at cryogenic temperatures and pulsed laser excitation. The supplemental components of the second setup are marked by blue dashed lines.

In the following, we present the basic components of the confocal microscope setup "Lab 1" designed for room temperature spectroscopy of single color centers under continuous wave laser excitation and cavity coupling experiments. Figure 4.1 shows a schematic of the confocal system. The setup is equipped with two continuous wave lasers: one diode-pumped solid-state laser (Linos, Nano 250-532-100) at a wavelength of 532 nm and with a specified output power of 100 mW for NV center excitation and Raman spectroscopy as well as a diode laser (Schäfter-Kirchhoff, 58FCM) at an emission wavelength of 660 nm and with a specified output power of 25 mW for SiV excitation. After passing through a clean up filter, the excitation laser is focused by a 100× microscope objective (Olympus, LMPlanFL N 100×) with a numerical aperture of 0.8 onto the sample. The fluorescence is collected by the same objective. The objective as well as the sample are mounted on a z- or (x, y)-translation stage (Newport, M-VP-25XL), respectively, in order to adjust the focus position and to laterally scan the sample with respect to the fixed laser beam. A glass plate and long-pass filters separate the excitation light from the fluorescence before it is coupled into a single mode fiber (Thorlabs, SM600) with a core diameter of 4.3 μm. The single mode fiber simultaneously serves as

a pinhole for the confocal detection. In the detection path, a linear polarization analyzer can be placed to investigate the emission polarization properties. The fluorescence is spectrally analyzed by a grating spectrometer (Princeton Instruments, Acton Research SP 2500) connected to a liquid nitrogen cooled CCD camera (Princeton Instruments, Spec-10). A grating with 600 grooves/mm yielding a resolution of 0.14 nm [238] is applied for room temperature analysis. Furthermore, to perform intensity auto-correlation measurements, the setup is equipped with a Hanbury Brown and Twiss interferometer involving two silicon avalanche photo diodes (PicoQuant, τ-SPAD-100) with a quantum efficiency of $> 60\%$ specified in the wavelength range of $600 - 800$ nm, a dark count rate of < 100 cts/s and a typical dead time of < 70 ns [239].

Detection efficiency

To relate the count rate detected by the avalanche photo diodes (APD) to the actual number of photons emitted by a single color center, it is crucial to know the detection efficiency of our setup. To this end, the transmission of the applied components is measured for continuous wave laser light at a wavelength of 764 nm, corresponding to the emission wavelength of a single SiV center investigated later in this work in chapter 9. The laser power is measured at specific positions within the confocal setup marked by numbers 1 to 6 in figure 4.1. The glass plate used to separate the excitation laser light from the fluorescence reflects only a fraction of 0.02 ($6 \rightarrow 5$) of the excitation laser but transmits > 0.95 ($5 \rightarrow 3$) of the fluorescence light. The transmission of the microscope objective is 0.60 ± 0.02 ($4 \rightarrow 5$). The collected light passes the detection path with a throughput of 0.88 ± 0.03 ($3 \rightarrow 2$) before it is filtered using two longpass filters and coupled into a single mode fiber with a combined transmission of 0.40 ± 0.02 ($2 \rightarrow 1$). Including the specified quantum efficiency of the APDs of ~ 0.65 at 764 nm and the transmission of the beam splitter cube of > 0.90 in the Hanbury Brown and Twiss setup, the overall detection efficiency of our confocal setup can be estimated to be 0.14 ± 0.02 at a wavelength of 764 nm. As different bandpass filters in front of the APDs are used in the experiments, the transmission of those filters has not been included in the present analysis but will be considered and mentioned in the relevant chapters.

Spatial resolution of the confocal setup

The spatial resolution of an optical system describes the ability to separate two point-like objects. Mapping a radiating point source by an optical system from its source to its imaging plane is mathematically described by the point-spread function (PSF, for detailed analysis see e.g. [120]). In the case of a confocal microscope, the point spread function of the overall setup is composed of individual PSFs describing the focusing of the Gaussian excitation beam into the sample plane as well as the collection of the fluorescence light by the objective. In practice, the PSF is determined by exciting and imaging a point source, e.g. a single color center hosted in a nanodiamond, using confocal laser scanning microscopy. Once the PSF is determined, the resolution of the setup can be calculated according to the following criterion defined by Webb [237]:

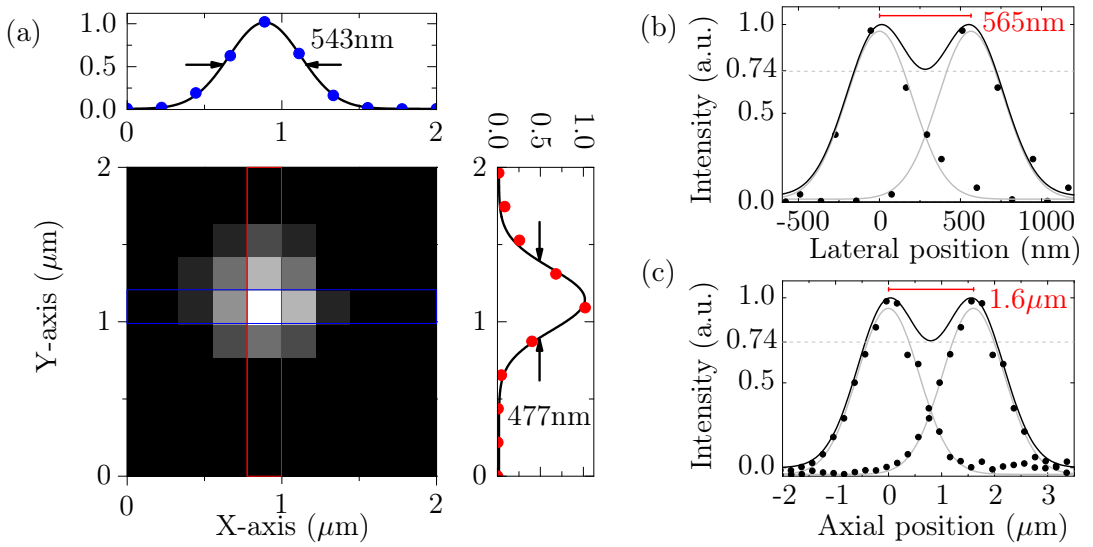

Figure 4.2: Spatial resolution of the confocal setup: (a) Fluorescence scan of a single SiV center in a nanodiamond and lateral intensity profiles fitted with Gaussian functions with a FWHM of 543 nm and 477 nm in x-, y-direction. (b,c) The minimal distance when the dip between two Gaussians with a FWHM of 477 nm (1.36 μm) reaches 26% of the maximum intensity determines the lateral (axial) resolution of our confocal setup to be 565 nm (1.6 μm).

Two emitters can be resolved if the relative intensity dip between the two point-spread functions is 26% of the maximum intensity. We will use this criterion to deduce in the following the experimental spatial resolution of our confocal microscope setup. To this end, we identify a single SiV center hosted in a nanodiamond as a bright localized spot in the fluorescence scan. To determine the width, the intensity profiles are fitted with a Gaussian function. Figure 4.2(a) shows the fluorescence scan of a single SiV center and the lateral intensity profiles with full widths at half maximum (FWHM) of 543 nm and 477 nm in the x- and y-direction, respectively. Furthermore, the axial intensity profile is measured by scanning the axial position of the microscope objective in z-direction. Fitting the axial intensity profile by a Gaussian yields a FWHM of 1.36 μm. By numerically calculating the minimal distance when the dip between two Gaussians with a FWHM of 477 nm (1.36 μm) reaches 26% of the maximum intensity, we determine the lateral (axial) resolution of our setup to be

$$r_{\text{lat}} = 565\,\text{nm} \qquad r_{\text{axial}} = 1.6\,\mu\text{m} \tag{4.1}$$

An illustration of the resolution criterion defined by Webb for our experimental settings in the lateral and axial directions is shown in figure 4.2(b,c).

To obtain single photon emission, we have to assure that only one emitter is present in the laser focus. As the diamond membranes with a low density of SiV centers used in our experiments contain on average 2 SiV centers per $20\times20\,\mu\text{m}^2$ (c.f. chapter 9), the lateral resolution of our confocal microscope setup is sufficient to investigate single color centers.

Furthermore, as the thickness of the diamond membranes is typically $300-400\,\mathrm{nm}$, the axial resolution of our confocal setup plays only a minor role. Hence, the confocal microscope setup presented above is well suited for the detection and characterization of single SiV and NV centers in diamond.

4.2 Confocal setup for spectroscopy at cryogenic temperatures

In this work, we use a second similarly constructed confocal microscope setup "Lab 2" designed for spectroscopy at cryogenic temperatures and pulsed excitation of single color centers. For lifetime measurements, the setup is equipped with a femtosecond Titanium:sapphire laser (Spectra Physics, Tsunami) with a repetition rate of 80 MHz and a tuning range of $700-1035\,\mathrm{nm}$. Furthermore, two continuous wave lasers are available for excitation of SiV centers and NV centers: a Titanium:sapphire laser (Sirah GmbH, Matisse TX) with a tuning range between $675-1010\,\mathrm{nm}$ and a frequency-doubled Nd:YVO_4 laser (Spectra Physics, Millennia) at a wavelength of 532 nm. Both Titanium:sapphire lasers are externally pumped by the frequency-doubled Nd:YVO_4 laser. The excitation light is focused on the sample by a $100\times$ microscope objective (Olympus, LMPlanFL N $100\times$) with a numerical aperture of 0.8. Both the microscope objective and the sample are integrated in an evacuated cryostat chamber. To perform measurements down to liquid helium temperatures, the sample is mounted on the cold finger of a continuous flow cryostat (Janis Research, ST-500LN). All specified temperatures are measured on the cold finger. To adjust the focus position, the microscope objective is mounted on a z-translation stage, whereas the sample is placed on a (x, y)-translation stage (Newport, M-UMR8.25) to laterally scan the sample with respect to the fixed laser spot using a motorized actuator (Newport, LTA-HL). Outside the cryostat chamber, the excitation and fluorescence light is separated by a glass plate and by longpass filters. The collected light is coupled into a single mode fiber (Thorlabs, SM600) with a core diameter of $4.3\,\mu\mathrm{m}$ used as a confocal pinhole and is spectrally analyzed by a grating spectrometer (Horiba Jobin Yvon, iHR 550) connected to a liquid nitrogen cooled CCD camera (Horibo Jobin Yvon, Symphony BIDD). Depending on the required precision, three gratings with either 600 grooves/mm, 1200 grooves/mm or 1800 grooves/mm are available with a maximum specified resolution of 0.22 nm, 0.10 nm or 0.06 nm at 500 nm, respectively. Furthermore, the spectrally filtered count rate can be correlated using a Hanbury Brown and Twiss interferometer equipped with two silicon avalanche photo diodes (Perkin Elmer, SPCM-AQR-14) with a specified typical detection efficiency of 65% at wavelengths between $600-750\,\mathrm{nm}$, a specified dark count rate of 100 cts/s and a dead time of 60 ns.

Detection efficiency

Similar to the setup described in section 4.1, we determine the detection efficiency of the second confocal microscope setup used for spectroscopy at cryogenic temperatures

and lifetime measurements. The transmission through the components for pulsed laser light at a wavelength of 764 nm and with a repetition rate of 80 MHz is determined by measuring the laser power at specific positions within the setup marked by numbers 1 to 5 in figure 4.1. The microscope objective has a transmission of 0.48 ± 0.02 ($5 \rightarrow 4$). The collected fluorescence passes the detection path ($3 \rightarrow 2$) with a throughput of 0.91 ± 0.02 before it is filtered by two longpass filters and coupled into a single mode fiber with a combined transmission of 0.60 ± 0.06 ($2 \rightarrow 1$). Including the specified quantum efficiency of the APDs of 0.65 and the transmission of the beam splitter cube > 0.90 in the Hanbury Brown and Twiss interferometer, we obtain an overall detection efficiency of 0.15 ± 0.02. Please note that the transmission of bandpass filters mounted in the HBT interferometer is not included in our calculation, as various filters have been used in the experiments. The transmission of the individual filters will be considered in the relevant sections.

Resolution of confocal setup

We determine the spatial resolution of the confocal setup using the same procedure as described in section 4.1. From the fluorescence scan of a single SiV center hosted in a nanodiamond that has been continuously excited at 700 nm and detected within the spectral window of $730 - 750$ nm we extract the lateral intensity profiles that are fitted with Gaussian functions with a FWHM of 497 nm and 539 nm in the x- and y-direction, respectively. Similarly, by scanning the objective in z-direction, we obtain the axial intensity profile that is fitted by a Gaussian with a FWHM of 1.42 μm. Using the criterion defined by Webb (c.f. section 4.1), we obtain the lateral and axial resolution of the second confocal microscope setup:

$$r_{\text{lat}} = 589\,\text{nm} \qquad r_{\text{axial}} = 1.67\,\mu\text{m}, \tag{4.2}$$

The spatial resolution of the second confocal setup designed for spectroscopy at cryogenic temperatures is comparable to the spatial resolution of the room temperature setup. The slight discrepancy is attributed to differences in the fine adjustment of the setup during the measurement. The spatial resolution of both setups is sufficiently high to identify and analyze single color centers in diamond.

4.3 Hanbury Brown and Twiss interferometer

The Hanbury Brown and Twiss (HBT) interferometer is used to measure the $g^{(2)}$ autocorrelation function to prove single emitter character. Originally used in astronomy, the first interferometer was published by Robert Hanbury Brown and Richard Q. Twiss in 1956 to correlate photons emitted by bright stars [240, 241]. Nowadays, the HBT interferometer is widely used in quantum optics to reveal non-classical emission of a light source. The fluorescence light is coupled via the single mode fiber into the HBT setup and passes a non-polarizing nominal 50 : 50 beam splitter cube (Lab 1: Lens Optics, Lab 2: B. Halle Nachfl. GmbH, TWK1). In both arms of the interferometer the

fluorescence light is filtered using bandpass filters before it is focused by a 50 mm focal lens on the active area of two silicon avalanche photo diodes (APD, Lab 1: PicoQuant, τ-SPAD-100, Lab 2: Perkin Elmer, SPCM-AQR-14). The APDs are operated in "Geiger-mode": A single impinging photon creates a charge carrier in the active region that triggers an avalanche pulse of electrons. The specified dead times of the photo diodes are 70 ns (Lab 1) and 60 ns (Lab 2) before the next photon can be detected. The individual current pulses are analyzed by the Time-Correlated Single Photon Counting (TCSPC) electronics (Lab 1: Dotfast Consulting, Time Tag Module, Lab 2: PicoQuant, PicoHarp 300) with two input channels each connected to an APD. The time-correlation electronics is operated in the Time-Tagged Time-Resolved (TTTR) mode: The arrival times of individual photon events are recorded for both channels via PicoHarp 300 software. Later, the lists of the two channels are correlated to deduce the $g^{(2)}$ function as well as the mean count rate of a single emitter.

Temporal resolution of the HBT setup

In an ideal system, the photon arrival times could be determined with infinitely high precision. In practice, however, the temporal resolution of the APDs and electronics is finite. The main source of limitation is a non-constant time delay between the arrival of a photon on the detection area of the APD and the subsequent output of an electrical pulse. This so called "timing jitter" of the APD can be determined by measuring the instrument response function (IRF) of the HBT setup. To this end, the auto-correlation of attenuated Titanium:sapphire laser pulses with a repetition rate of 80 MHz is measured. The laser has a specified pulse duration of 100 fs. However, after passing through several optical elements, the pulse duration is increased to some picoseconds [242]. The detected pulse train characterizing the HBT response function can be fitted by Gaussians:

$$\mathrm{IRF}(t) = \frac{A}{\sqrt{2\pi}\,\sigma} \exp\left(-\frac{(t-t_c)^2}{2\sigma^2}\right), \tag{4.3}$$

where A denotes the amplitude and t_c the central position of the detected pulses. The temporal resolution is given by the half width σ of the Gaussian taken at its $1/\sqrt{e}$ maximum value. For the room temperature setup (Lab 1) a temporal resolution of $\sigma = 296\,\mathrm{ps}$[1] [238] (PicoQuant, τ-SPAD-100 + Dotfast Consulting, Time Tag Module) is measured, whereas the cryogenic temperature setup (Lab 2) has a timing jitter of $\sigma = 354\,\mathrm{ps}$[2] [243] (Perkin Elmer, SPCM-AQR-14 + PicoQuant, PicoHarp 300). The measured temporal resolution of the HBT setups is mainly limited by the timing uncertainty of the APDs introduced in the conversion of a single photon to an electrical pulse. Compared to the jitter of the electronics of 78 ps [238] (Lab 1) and $< 12\,\mathrm{ps}$ [239] (Lab 2), respectively, the APD response function is 4 to 30 times larger.

When measuring the intensity correlation of a single photon source, the detected

[1] Lab 1: The fitted FWHM of the Gaussian HBT instrument response function is 698 ps

[2] Lab 2: The fitted FWHM of the Gaussian HBT instrument response function is 835 ps

signal $g^{(2)}_{\mathrm{det}}$ is a convolution of the actual $g^{(2)}_b$ function with the IRF of the HBT setup:

$$g^{(2)}_{\mathrm{det}}(\tau) = \mathrm{IRF}(\tau) * g^{(2)}_b(\tau) = \int_{-\infty}^{\infty} \mathrm{IRF}(t)\, g^{(2)}_b(\tau - t)\, dt \tag{4.4}$$

Assuming a Gaussian HBT response function according to equation (4.3) and taking into account $g^{(2)}_b(\tau) = 1 + p_f^2(-(1+a)\, e^{-|\tau-\tau_0|/\tau_1} + a\, e^{-|\tau-\tau_0|/\tau_2})$ including background contributions (c.f. eqs. (3.10) and (3.10) in section 3.5), we obtain an expression for the detected intensity correlation function:

$$\begin{aligned} g^{(2)}_{\mathrm{det}}(\tau) = 1 - p_f^2(1+a)\frac{1}{2}\Bigg\{ & e^{-\frac{\tau-\tau_0}{\tau_1}+\frac{\sigma^2}{2\tau_1^2}} \left(1 + \mathrm{erf}\left(\frac{1}{\sqrt{2}\sigma}\left(\tau - \tau_0 - \frac{\sigma^2}{\tau_1}\right)\right)\right) \\ & + e^{\frac{\tau-\tau_0}{\tau_1}+\frac{\sigma^2}{2\tau_1^2}} \left(1 - \mathrm{erf}\left(\frac{1}{\sqrt{2}\sigma}\left(\tau - \tau_0 - \frac{\sigma^2}{\tau_1}\right)\right)\right)\Bigg\} \\ + p_f^2 a\frac{1}{2}\Bigg\{ & e^{-\frac{\tau-\tau_0}{\tau_2}+\frac{\sigma^2}{2\tau_2^2}} \left(1 + \mathrm{erf}\left(\frac{1}{\sqrt{2}\sigma}\left(\tau - \tau_0 - \frac{\sigma^2}{\tau_2}\right)\right)\right) \\ & + e^{\frac{\tau-\tau_0}{\tau_2}+\frac{\sigma^2}{2\tau_2^2}} \left(1 - \mathrm{erf}\left(\frac{1}{\sqrt{2}\sigma}\left(\tau - \tau_0 - \frac{\sigma^2}{\tau_2}\right)\right)\right)\Bigg\} \end{aligned} \tag{4.5}$$

Where $\mathrm{erf}(\cdot)$ denotes the error function[3]. In the experiments, the measured intensity correlation functions are fitted using the above equation to obtain the parameters τ_1, τ_2 and a corrected for the HBT response function.

The impact of the APD timing jitter on the measured intensity correlation function becomes important in the case of fast decay times approaching the temporal resolution. In figure 4.3(a) the convolution of the IRF with ideal $g^{(2)}$ functions is shown for various τ_1 times given in units of the temporal resolution σ. Here, we disregard any background contribution ($p_f^2 = 1$) and bunching dynamics ($a = 0$) of the $g^{(2)}$ function at longer time scales. If the time τ_1 is large compared to σ, the influence of the IRF is negligible and $g^{(2)}(0) \approx 0$. However, as soon as τ_1 becomes comparable to the temporal resolution of the setup, the anti-bunching dip at zero time delay does not vanish. A quantitative analysis is shown in figure 4.3(b) where $g^{(2)}(0)$ is plotted as a function of the τ_1 time for a given temporal resolution $\sigma = 296\,\mathrm{ps}$. For long τ_1 times around 12 ns corresponding to a typical lifetime of the NV^- ZPL measured in bulk diamond, the anti-bunching dip drops below 0.023. In contrast, in the case of fast decaying SiV centers, the impact of the IRF becomes important and $g^{(2)}(0)$ significantly raises for short τ_1 times. For $\tau_1 = 1\,\mathrm{ns}$ corresponding to the excited state lifetime of SiV centers observed in unstrained bulk diamond [26], $g^{(2)}(0)$ does not drop beyond 0.2. The effect becomes even worse for times in the picosecond range. For the shortest decay time $\tau_1 = 180\,\mathrm{ps}$ detected in this

[3]The error function is defined as

$$\mathrm{erf}(x) = \sqrt{\frac{2}{\pi}} \int_0^x e^{-\xi^2}\, d\xi$$

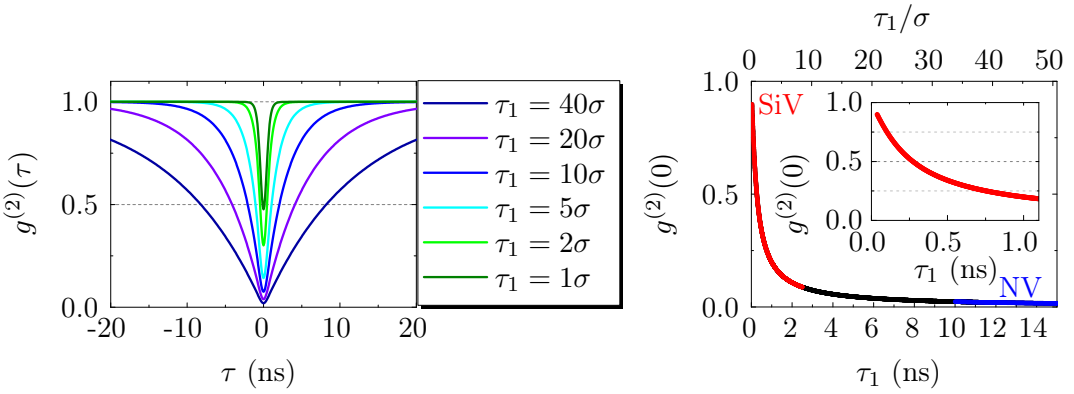

Figure 4.3: Impact of the APD timing jitter on the anti-bunching dip of the $g^{(2)}$ function: (a) Intensity correlation function for various times τ_1 ($a = 0$, $p_f^2 = 1$) convoluted with the HBT response function. τ_1 is given in units of the temporal resolution σ. (b) Intensity correlation at zero time delay $g^{(2)}(0)$ as a function of τ_1 for a fixed resolution $\sigma = 296\,\text{ps}$. For long τ_1 times comparable to the lifetime of the NV^- center (marked in blue) $g^{(2)}(0) \approx 0$, whereas for short τ_1 times in the case of SiV centers (marked in red) $g^{(2)}(0) > 0$. The inset shows a zoom into $g^{(2)}(0)$ for short times τ_1.

work (c.f. chapter 9), the anti-bunching dip reaches only $g^{(2)}(0) = 0.6$. If not corrected for the APD timing jitter, this color center would not have been identified as a single emitter. Therefore, it is essential to take into account the HBT response in the analysis of the measured $g^{(2)}$ function.

4.4 Lifetime measurements

By coupling a single color center to a photonic crystal cavity, its spontaneous emission rate and the associated lifetime of the excited state can strongly be modified according to the Purcell effect. In this section, we present the experimental tools to measure the excited state lifetime of a single emitter. Excited by a short laser pulse, a single color center spontaneously emits a photon after a certain time delay and with a certain probability depending on the lifetime of the excited state. To measure the probability of single photon emission as a function of time, we perform time-correlated single photon counting (TCSPC) experiments. To this end, a single color center is repetitively excited by laser pulses with a pulse width much shorter than the excited state lifetime of the emitter. The time difference between the excitation pulse and the subsequent single photon emission is registered over many cycles and plotted in a histogram.

For pulsed excitation of a SiV center, the confocal microscope setup "Lab 2" described in section 4.2 is equipped with a Titanium:sapphire laser (Spectra Physics, Tsunami) tunable in the wavelength range of $700 - 1035\,\text{nm}$ with a repetition rate of 80 MHz. In combination with the HBT setup described above, this allows for time-resolved fluores-

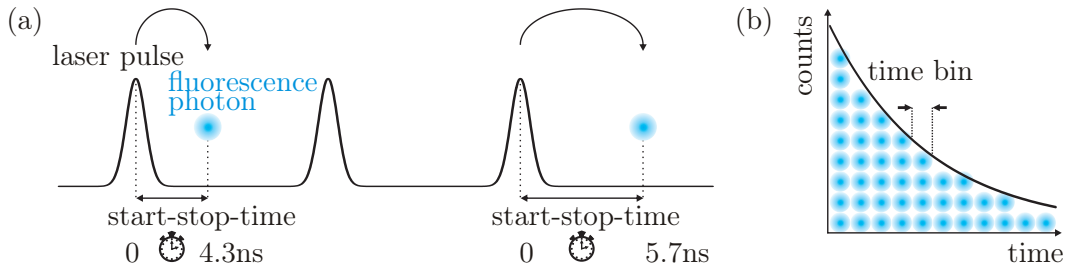

Figure 4.4: Time-correlated single photon counting to measure the excited state lifetime of a single emitter (after [244]): (a) The arrival times of emitted photons are registered with respect to the short laser pulses periodically exciting the single color center. (b) The number of photons that arrive after a certain time delay and within a time bin are recorded in a histogram. The envelope follows an exponential decay with a decay time T_1 corresponding to the excited state lifetime of the emitter.

cence spectroscopy. As a reference for the timing, the electrical synchronization signal of the excitation pulses supplied by a fast photo diode is connected to the first channel of the TCSPC electronics. The arrival times of the fluorescence photons emitted by the repetitively excited single color center are detected by an APD that is connected to the second channel of the TCSPC electronics (Fig. 4.4(a)). The TCSPC electronics correlates the arrival times with respect to the excitation laser and records the number of photons registered per time interval ("time bin") after a certain time delay. A histogram of the photon arrival times whose envelope represents the exponential time decay of the fluorescence signal after a short excitation is shown in figure 4.4(b). Fitting the temporal decay with an exponential function

$$s(t) = \begin{cases} s_1 + s_0 \exp\left(-\frac{(t-t_s)}{T_1}\right) & , t \geq t_s \\ 0 & , t \leq t_s \end{cases} , \tag{4.6}$$

we obtain the excited state lifetime T_1 of the single color center under investigation.

To guarantee that the color center is excited at a well defined time and only once per cycle, the duration of the excitation pulse must be short with respect to the lifetime of the excited state. In our experiments, the shortest lifetime of a single SiV center is measured to be 440 ps (c.f. chapter 9), thereby being much longer than the pulse duration which is at maximum on the order of some picoseconds after passing through several optical elements introducing a pulse broadening [242]. Furthermore, the probability for multiphoton emission per cycle must be low. The reason for this is the dead time of the APD of 60 ns. If the number of photons per cycle would be typically > 1, only the first photon would be registered by the system whereas the following ones are missed. As the count rate of the investigated SiV centers is $< 0.01\%$ compared to the laser repetition rate, we can be sure that the probability of multiphoton emission per cycle is extremely small.

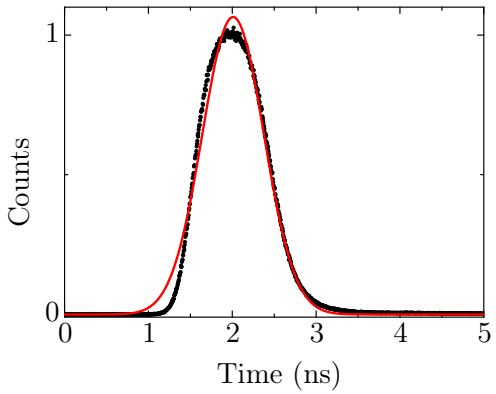

Figure 4.5: Instrument response function of the confocal setup "Lab 2" under pulsed excitation: The response function (•) can be approximated by a Gaussian (red solid line) according to equation (4.3) with a width of $\sigma = 367\,\mathrm{ps}$.

Temporal resolution of lifetime measurements

An exponential decay time of the photon emission probability as schematically shown in figure 4.4(b) can only be detected for an ideal system involving an infinitely sharp excitation pulse and infinitely accurate detectors and electronics. However, in practice, the individual components of our setup lead to a deviation from this ideal result. The most critical limitation is the timing accuracy of the APDs, with a temporal resolution of 354 ps, whereas the broadening of the excitation pulse to some picoseconds [242] and the timing jitter of the electronics $< 12\,\mathrm{ps}$ [239] can be neglected. The overall timing precision for detection of the arrival time of a single photon is characterized by the instrument response function of the setup. We measure the instrument response function by replacing the sample in our confocal setup with a dielectric planar mirror. The reflected pulsed laser light is detected by the APD and time-correlated to the electrical synchronization signal supplied by the photo diode. Please note that this is different to the detection of the HBT response function (c.f. page 59), where we time-correlated the signal of two APDs. By measuring the TCSPC signal of the reflected laser pulses with respect to the trigger signal, we obtain the response function of our confocal setup under pulsed excitation that is shown in figure 4.5. The detected pulse train can be approximated by Gaussian functions given by equation (4.3) with a half width of $\sigma = 367\,\mathrm{ps}$[4] at $1/\sqrt{e}$ maximum count rate. As the width of the IRF is comparable to the timing jitter of the APDs of 354 ps, the temporal precision of the APDs can be identified as the main limiting factor of the timing resolution of the whole setup under pulsed excitation.

The time-correlated signal $y(t)$ obtained in the experiment when periodically exciting a single color center is a convolution of the setup response function with the actual exponential decay of the fluorescence intensity described by equation (4.6). Using the approximation of the IRF by a Gaussian function, the convolution with the exponential

[4]The FWHM of the IRF of the confocal microscope setup under pulsed excitation is 864 ps.

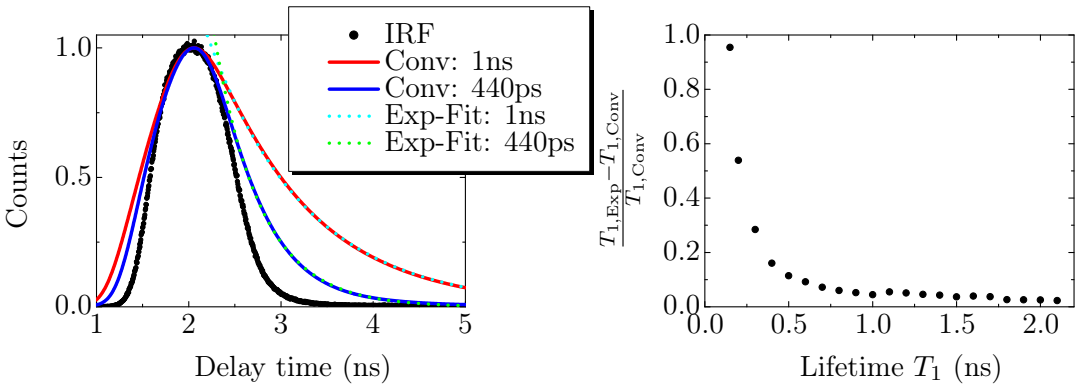

Figure 4.6: Impact of the instrument response function (IRF) on the measured lifetime: (a) Convolution of the setup IRF with two exponential functions with decay times of $T_1 = 440\,\mathrm{ps}$ and $T_1 = 1\,\mathrm{ns}$ (solid lines). For comparison the IRF (•) and exponential fits (dotted lines) to the convolution are shown. For clarity, all curves have been normalized. (b) Relative error $\frac{T_{1,\mathrm{Exp}}-T_{1,\mathrm{Conv}}}{T_{1,\mathrm{Conv}}}$ of the excited state lifetime determined either by an exponential fit or fitting the data with the convolution given by equation (4.7).

decay yields:

$$\begin{aligned} y(t) &= \mathrm{IRF}(t) * s(t) = \int_{-\infty}^{\infty} \mathrm{IRF}(t')\, s(t-t')\, dt' \\ &= \frac{A}{2}\left[s_1 \,\mathrm{erf}\left(\frac{1}{\sqrt{2}\,\sigma}(t - t_s - t_c)\right)\right. \\ &\left. + s_0 \,\exp\left(-\frac{t-t_s-t_c}{T_1} + \frac{\sigma^2}{2\,T_1^2}\right) \mathrm{erf}\left(\frac{1}{\sqrt{2}\,\sigma}(t-t_s-t_c) - \frac{\sigma}{\sqrt{2}\,T_1}\right)\right] \end{aligned} \tag{4.7}$$

In the experiment, to obtain the exponential decay time T_1 corresponding to the lifetime of the excited state the measured data are fitted using either equation (4.7) or by direct convolution of the measured IRF with an exponential function using mathematical software analysis [5]. Figure 4.6(a) shows exemplarily the convolution of the measured IRF of our setup with exponential functions with time decay constants of $T_1 = 440\,\mathrm{ps}$ and $T_1 = 1.0\,\mathrm{ns}$, corresponding to the shortest lifetime of a single SiV center measured in this work (c.f. chapter 9) and the excited state lifetime of single SiVs observed in unstrained bulk diamond [26], respectively. The measured IRF and exponential fits to the convolution curves is plotted for comparison. The convolution of both curves are centered around $t_0 + t_c$, where t_0 is the shift of the exponential according to equation (4.6) and t_c is the position of the IRF maximum. For $t > t_0 + t_c$ the signal is dominated by the exponential decay whereas for $t < t_0 + t_c$ it is mostly determined by the IRF. Fitting the data for $t > t_0 + t_c$ with an exponential function and neglecting the setup response leads to a relative error that is plotted in figure 4.6(b). For long decay times $T_1 \geq 1\,\mathrm{ns}$ the impact of the IRF is negligible yielding a relative error of $< 5\%$. However,

[5] Matlab, Mathworks

for small decay times comparable to the temporal resolution of the setup the influence of the IRF becomes important: Ignoring the impact of the response function for $T_1 = 440\,\text{ps}$ already leads to an error of 15% and increases rapidly to $> 50\%$ for $T_1 = 200\,\text{ps}$.

To summarize, in this chapter we described two confocal microscopy setups "Lab 1" and "Lab 2" designed for cavity coupling experiments and spectroscopy of single color centers in diamond at room temperature and cryogenic temperatures. The spatial resolution of the confocal setups in the lateral and axial direction is 565 nm and 1.6 μm (Lab 1) and 589 nm and 1.67 μm (Lab 2), respectively. Each confocal setup can be connected either to a grating spectrometer for spectral analysis of the fluorescence or to a Hanbury Brown and Twiss interferometer to perform intensity auto-correlation measurements with a temporal resolution of 296 ps (Lab 1) and 354 ps (Lab 2). Furthermore, using pulsed laser excitation, the second setup allows for lifetime measurements of single SiV centers with a temporal resolution of 367 ps. For all correlation setups, instrument-response functions have been determined which have to be used in the experiments of this thesis to yield deconvoluted fluorescence lifetimes and $g^{(2)}$ functions.

Chapter 5

Photonic crystal cavities

This chapter provides the theoretical background for the propagation and the confinement of light in photonic crystals. Photonic crystals are often considered as semiconductors for light. Analogous to solid-state crystals in which the interaction of the electronic wave function with the periodic potential of the atomic lattice gives rise to an electronic band structure with band gaps for certain energies, the periodic variation of the refractive index results in a band structure for photons propagating through the dielectric material. The periodic interaction entails a photonic band gap in which certain frequencies are forbidden. Furthermore, by intentionally introducing line or point defects in the periodic lattice, localized modes with frequencies inside the band gap are created. The associated electromagnetic fields are tightly confined in the defect region by virtue of being prohibited in the surrounding lattice. For this reason, photonic crystal devices enable extraordinary localization of electromagnetic fields in tiny volumes as well as efficient and compact control and guidance of light in matter together with the ability for compact chip-integration of various components. Moreover, by coupling a single emitter to a cavity field, its spontaneous emission rate can be significantly enhanced or inhibited which is known as the Purcell effect [56]. The inhibition of spontaneous emission in periodic structures was first studied by Bykov in 1972 [245, 246]. Five years later, two seminal papers by Yablonovitch [247] and John [248] introduced the concept of photonic band gap materials. The appearance of a band gap as well as the confinement of light substantially depend on the dimensionality of the crystal, i.e. in how many spatial directions (one, two or three) the crystal's unit cell is replicated. Three-dimensional structures offer complete photonic band gaps independent of the polarization or propagation direction of light. Yablonovitch [247] proposed a three-dimensional photonic crystal design in which the photonic and electronic band structure overlapped in frequency. Thereby, the spontaneous emission from electron-hole recombinations could be suppressed and the performances of semiconductor lasers or solar cells would be strongly improved. At the same time, John [248] suggested to use three-dimensional periodic structures for the localization of light in dielectric materials. With the advance of nanofabrication techniques it was possible to demonstrate the inhibition of spontaneous emission from quantum dots embedded in a three-dimensional

photonic crystal [249–251]. However, the fabrication of structures with a periodic replication in three spatial directions is extremely challenging. An adequate alternative are photonic crystal slabs with a two-dimensional in-plane periodicity and finite height in the vertical direction. Three-dimensional light confinement is achieved via a combination of the photonic band gap effect and total internal reflection. For photonic crystal slab structures in gallium arsenide, strong cavity-coupling to a single quantum dot has already been demonstrated [108, 110]. Moreover, Purcell enhancement of a single nitrogen-vacancy center coupled to a two-dimensional photonic crystal cavity in diamond has been shown [87]. For a review of spontaneous emission control in three- and two-dimensional photonic crystals see [123]. Modification of color centers' spontaneous emission has also been achieved in one-dimensional photonic crystal cavities [88, 90], consisting of a patterned waveguide cavity fabricated in diamond. Besides their ability for tight confinement of optical modes, one-dimensional photonic crystal cavities have attracted significant interest in recent years, as they simultaneously allow for localization of mechanical modes. This gives rise to a complete new field of opto-mechanical coupling [252–254]. These structures exhibit band gaps for both photons and phonons and thus enable simultaneous confinement and efficient coupling of optical and vibrational modes of the structure. Optimized designs achieving coupling strength in the MHz regime have recently been proposed for diamond [255].

In this chapter, we mainly focus on two-dimensional photonic crystal slabs that consist of a triangular lattice of air holes in diamond. Starting from Maxwell's equations, we derive an eigenvalue equation for the electric and magnetic fields that allows for the subsequent computation of the photonic band structure. Moreover, we provide the theoretical framework for Purcell inhibition and enhancement of spontaneous emission in periodic materials that is related to a strong modification of the local density of states. By numerically solving the eigenvalue equation, we obtain the photonic band diagram. From purely two-dimensional systems, we derive essential properties, e.g. the appearance of a frequency gap. Realistic structures are modeled by introducing a finite slab thickness. We present an extended band diagram that accounts for dissipation losses in the vertical direction. The photonic band gap is the key property for the realization of integrated waveguides and cavities. In our simulations, we focus on line defects formed by omitting one line of holes and point defects created by zero, one or several missing holes. The cavity structures are characterized by their field distributions, resonant frequencies, quality factors and mode volumes. We propose an alternative method to compute the cavity quality factor and apply an efficient optimization procedure to boost the Q-factor by one order of magnitude. Finally, we present the simulation techniques used to compute the band structures as well as the near and far fields of the cavity modes.

5.1 Maxwell's equations and master equation

Starting from Maxwell's equations, we derive an eigenvalue problem for the electric and magnetic field in a mixed dielectric medium. The mathematical description follows

reference [256]. The propagation of light in a dielectric material, e.g. a photonic crystal, is governed by the macroscopic Maxwell's equations given in SI (système international) units

$$\begin{aligned} \vec{\nabla} \cdot \vec{B} &= 0 \qquad & \vec{\nabla} \times \vec{E} + \frac{\partial \vec{B}}{\partial t} &= 0 \\ \vec{\nabla} \cdot \vec{D} &= \rho \qquad & \vec{\nabla} \times \vec{H} - \frac{\partial \vec{D}}{\partial t} &= \vec{J} \end{aligned} \tag{5.1}$$

where $\vec{E}$ and $\vec{H}$ are the electric and magnetic fields, $\vec{D}$ and $\vec{B}$ are the displacement and magnetic induction fields and ρ and $\vec{J}$ are the free charge and current densities, respectively. In the following, we restrict our analysis to dielectric materials, where neither free charges ($\rho = 0$) nor light sources ($\vec{J} = 0$) are present. The material consisting of regions of homogeneous media is described by the dielectric function $\varepsilon(\vec{r}, \omega)$, where $\vec{r}$ is the position vector and ω the frequency. To appropriately describe the propagation of light through a photonic crystal, we make the following assumptions for the dielectric function:

- The material is macroscopic and isotrope. Hence, the dielectric function $\varepsilon(\vec{r}, \omega)$ is a scalar.
- The material is not dispersive. Therefore, any explicit frequency dependence of the dielectric constant $\varepsilon(\vec{r})$ can be ignored.
- The field strengths are sufficiently small meaning that the relation between $\vec{D}$ and $\vec{E}$ as well as between $\vec{B}$ and $\vec{H}$ is linear: $\vec{D}(\vec{r}) = \varepsilon_0 \varepsilon(\vec{r}) \vec{E}(\vec{r})$ and $\vec{B}(\vec{r}) = \mu_0 \mu(\vec{r}) \vec{H}(\vec{r})$, where ε_0, μ_0 are the vacuum permittivity and permeability and $\mu(\vec{r})$ is the relative magnetic permeability. For diamond $\mu(\vec{r}) \approx 1$.
- The material is transparent resulting in purely real and positive $\varepsilon(\vec{r})$.

With all these assumptions, Maxwell's equations (5.1) become

$$\begin{aligned} \vec{\nabla} \cdot \vec{H}(\vec{r}, t) &= 0 \qquad & \vec{\nabla} \times \vec{E}(\vec{r}, t) + \mu_0 \frac{\partial \vec{H}(\vec{r}, t)}{\partial t} &= 0 \\ \vec{\nabla} \cdot \varepsilon(\vec{r}) \vec{E}(\vec{r}, t) &= 0 \qquad & \vec{\nabla} \times \vec{H}(\vec{r}, t) - \varepsilon_0 \varepsilon(\vec{r}) \frac{\partial \vec{E}(\vec{r}, t)}{\partial t} &= 0. \end{aligned} \tag{5.2}$$

The two divergence equations $\vec{\nabla} \cdot \vec{H}(\vec{r}) = 0$ and $\vec{\nabla} \cdot \varepsilon(\vec{r}) \vec{E}(\vec{r}) = 0$ signify the absence of sources or sinks of electromagnetic fields in this medium. Equivalently, these equations indicate that the electric fields are *transverse*. In the case of plane waves $\vec{H} = \vec{a} \exp(-i\vec{k} \cdot \vec{r})$ or $\vec{D} = \vec{a} \exp(-i\vec{k} \cdot \vec{r})$, for some wave vector $\vec{k}$, it results that $\vec{a} \cdot \vec{k} = 0$. This means that the electromagnetic field vector is perpendicular to the direction of propagation.

Because Maxwell's equations are linear, we can separate the time and spatial dependence by expanding the fields in harmonic modes: $\vec{H}(\vec{r}, t) = \vec{H}(\vec{r}) e^{-i\omega t}$ and $\vec{E}(\vec{r}, t) = \vec{E}(\vec{r}) e^{-i\omega t}$. For harmonic modes, Maxwell's equations become time independent and the

electric and magnetic field can be decoupled, yielding the following master equation for the magnetic field $\vec{H}$:

$$\vec{\nabla} \times \left(\frac{1}{\varepsilon(\vec{r})} \vec{\nabla} \times \vec{H}(\vec{r}) \right) = \left(\frac{\omega}{c} \right)^2 \vec{H}(\vec{r}), \tag{5.3}$$

where c is the vacuum speed of light. In the same way, the master equation for the electrical field $\vec{E}$ can be derived:

$$\vec{\nabla} \times \vec{\nabla} \times \vec{E}(\vec{r}) = \left(\frac{\omega}{c} \right)^2 \varepsilon(\vec{r}) \vec{E}(\vec{r}). \tag{5.4}$$

The strategy is to solve one of the eigenvalue problems (5.3) or (5.4) for a given structure $\varepsilon(\vec{r})$ to find the modes $\vec{H}(\vec{r})$ and $\vec{E}(\vec{r})$ and the corresponding eigenfrequencies ω. It is sufficient to solve only one eigenvalue equation, as the electric and magnetic field are related via

$$\vec{H}(\vec{r}) = -\frac{i}{\omega \mu_0} \vec{\nabla} \times \vec{E}(\vec{r}) \qquad \text{and} \qquad \vec{E}(\vec{r}) = \frac{i}{\omega \varepsilon_0 \varepsilon(\vec{r})} \vec{\nabla} \times \vec{H}(\vec{r}) \tag{5.5}$$

In the following, we will focus on solving equation (5.3) for the magnetic field. For that purpose we define the linear operator $\hat{\Theta}$ so that

$$\hat{\Theta} \vec{H}(\vec{r}) \equiv \vec{\nabla} \times \left(\varepsilon(\vec{r})^{-1} \vec{\nabla} \times \vec{H}(\vec{r}) \right). \tag{5.6}$$

It is essential to note, that the operator $\hat{\Theta}$ is Hermitian[1], implicating the following key properties to the electromagnetic solutions:

- The eigenvalues $(\omega/c)^2$ of $\hat{\Theta}$ are real and positive.
- The eigenfunctions associated to different eigenvalues $(\omega/c)^2$ are orthogonal.

The orthonormality condition of two eigenfunctions $\vec{H}_m$, $\vec{H}_n$ or $\vec{E}_m$, $\vec{E}_n$ is defined as

$$\langle \vec{H}_m, \vec{H}_n \rangle = \int d^3 r \vec{H}_m^*(\vec{r}) \cdot \vec{H}_n(\vec{r}) = \delta_{mn}, \tag{5.7}$$

$$\langle \vec{E}_m, \varepsilon \, \vec{E}_n \rangle = \int d^3 r \vec{E}_m^*(\vec{r}) \cdot \varepsilon(\vec{r}) \vec{E}_n(\vec{r}) = \delta_{mn}, \tag{5.8}$$

where δ_{mn} is the Kronecker's delta, that is $\delta_{mn} = 1$ for $m = n$ and $\delta_{mn} = 0$ for $m \neq n$. The different definitions of the orthonormality condition arise from the two transverse Maxwell's equations (5.2) of the magnetic and electric field.

Please note that the operator $\varepsilon^{-1} \vec{\nabla} \times \vec{\nabla} \times$ given in equation (5.4) is not Hermitian [256]. However, if we include the relative permeability $\mu(\vec{r}) \neq 1$ in the master equation, the eigenvalue problems (5.3), (5.4) can be rewritten:

$$\frac{1}{\mu(\vec{r})} \vec{\nabla} \times \left(\frac{1}{\varepsilon(\vec{r})} \vec{\nabla} \times \vec{H}(\vec{r}) \right) = \left(\frac{\omega}{c} \right)^2 \vec{H}(\vec{r}), \quad \vec{\nabla} \cdot \mu(\vec{r}) \vec{H}(\vec{r}) = 0 \tag{5.9}$$

[1] An operator $\hat{\Theta}$ is Hermitian if $\langle \vec{F}, \hat{\Theta} \vec{G} \rangle = \langle \hat{\Theta} \vec{F}, \vec{G} \rangle$, where $\langle \vec{F}, \vec{G} \rangle = \int d^3 r \, \vec{F}^* \cdot \vec{G}$ denotes the inner product of two vector fields $\vec{F}$ and $\vec{G}$.

$$\frac{1}{\varepsilon(\vec{r})}\vec{\nabla}\times\left(\frac{1}{\mu(\vec{r})}\vec{\nabla}\times\vec{E}(\vec{r})\right)=\left(\frac{\omega}{c}\right)^2\vec{E}(\vec{r}),\quad \vec{\nabla}\cdot\varepsilon(\vec{r})\,\vec{E}(\vec{r})=0 \tag{5.10}$$

The operators $\hat{\Theta}_\mu$ and $\hat{\Xi}_\mu$ given by

$$\hat{\Theta}_\mu\vec{H}(\vec{r})=\frac{1}{\mu(\vec{r})}\vec{\nabla}\times\left(\frac{1}{\varepsilon(\vec{r})}\vec{\nabla}\times\vec{H}(\vec{r})\right) \tag{5.11}$$

$$\hat{\Xi}_\mu\vec{E}(\vec{r})=\frac{1}{\varepsilon(\vec{r})}\vec{\nabla}\times\left(\frac{1}{\mu(\vec{r})}\vec{\nabla}\times\vec{E}(\vec{r})\right) \tag{5.12}$$

are both Hermitian [257]. In the following, we will mainly focus on equation (5.3) to describe the propagation of light through a photonic crystal. However, for some analytical calculations, such as the derivation of the variational theorem or of the local density of states, it is more convenient to use either equation (5.4) or (5.12).

5.1.1 Variational theorem

The harmonic modes propagating through a dielectric medium can have complicated field patterns. However, as a general principle the modes tend to concentrate the electric field energy in regions of high dielectric constant while remaining orthogonal to the modes with lower frequencies. This principle can be derived from the electromagnetic variational theorem: The smallest eigenvalue $(\omega_0/c)^2$ and the lowest-frequency mode correspond to the field pattern that minimizes the energy functional U_f:

$$U_f(\vec{H})\equiv\frac{\langle\vec{H},\hat{\Theta}\vec{H}\rangle}{\langle\vec{H},\vec{H}\rangle}. \tag{5.13}$$

Considering a small perturbation $\delta\vec{H}$ added to the field $\vec{H}$, one can show that the resulting small change in δU_f is zero only if $\vec{H}$ is an eigenvector of $\hat{\Theta}$ [2]. The lowest-frequency eigenmode $\vec{H}_0$ to the eigenvalue $(\omega_0/c)^2$ minimizes U_f. The next low-frequency mode will again minimize U_f in a subspace of modes that are orthogonal to the fundamental mode $\vec{H}_0$.

The energy functional can be rewritten in terms of the electric field $\vec{E}$, by substituting equations (5.5) and (5.6) into equation (5.13) and rewriting the denominator considering $(\omega/c)^2\langle\vec{H},\vec{H}\rangle=\langle\vec{H},\hat{\Theta}\vec{H}\rangle=\int d^3r\,\varepsilon^{-1}|\vec{\nabla}\times\vec{H}|^2$ and equation (5.5). For the energy functional we obtain:

$$U_f(\vec{E})=\frac{\int d^3r\,|\vec{\nabla}\times\vec{E}(\vec{r})|^2}{\int d^3r\,\varepsilon(\vec{r})|\vec{E}(\vec{r})|^2}. \tag{5.14}$$

[2] Considering the difference $\delta U_f(\vec{H})=U_f(\vec{H}+\delta\vec{H})-U_f(\vec{H})$ and ignoring terms higher than first order in $\delta\vec{H}$, we can approximate $\delta U_f\approx\left[(\delta\vec{H},\vec{G})+(\vec{G},\delta\vec{H})\right]/2$, where the gradient $\vec{G}$ is given by

$$\vec{G}(\vec{H})=\frac{2}{\langle\vec{H},\vec{H}\rangle}\left(\hat{\Theta}\vec{H}-\left[\frac{\langle\vec{H},\hat{\Theta}\vec{H}\rangle}{\langle\vec{H},\vec{H}\rangle}\right]\vec{H}\right).$$

At the minimum, δU_f vanishes for every perturbation $\delta\vec{H}$ if the quantity in parenthesis on the right hand side is zero. This is equivalent to the fact that $\vec{H}$ must be an eigenvector of $\hat{\Theta}$.

The energy functional is minimized when the electric field is concentrated in regions of high dielectric constant thereby maximizing the denominator and when the nominator is minimized by reducing the amount of oscillations while remaining orthogonal to lower-frequency modes.

5.1.2 Scale invariance of Maxwell's equations

In electrodynamics, there is no fundamental length scale and the solution for a given problem can easily be scaled up or down in dimension and frequency. This key property of Maxwell's equations has major consequences for designing photonic crystal structures. In the following, we will show the scale invariance of Maxwell's equations. As a starting point, we consider the master equation (5.3) for the magnetic field $\vec{H}$. Supposing that the dielectric material will be stressed or compressed by a factor s, this would lead to a changed dielectric function: $\varepsilon'(\vec{r}) = \varepsilon(\vec{r}/s)$. Applying the variable transformation $\vec{r} = \vec{r}\,'/s$ and $\vec{\nabla} = \vec{\nabla}'s$, we derive the following master equation with a different scale:

$$\vec{\nabla}' \times \left(\frac{1}{\varepsilon(\vec{r}\,'/s)} \vec{\nabla}' \times \vec{H}(\vec{r}\,'/s) \right) = \left(\frac{\omega}{cs} \right)^2 \vec{H}(\vec{r}\,'/s). \tag{5.15}$$

This is just again the master equation for a scaled dielectric function $\varepsilon'(\vec{r}) = \varepsilon(\vec{r}\,'/s)$ with the modified eigenmode $\vec{H}'(\vec{r}\,') = \vec{H}(\vec{r}\,'/s)$ and a scaled frequency $\omega' = \omega/s$. Thus, the new mode profile and its frequency can be obtained by simply rescaling the old profile and its frequency. The scale invariance of Maxwell's equations is essential for practical applications: once the solution to a problem is calculated, the solutions to all other length scales can easily be derived. Due to the rescaling property of Maxwell's equations, the dimension of the structures are typically not given in absolute values but rather in units of the dimensionless *lattice constant* a. For the same reasons, all frequencies ω and wave vectors k are given in dimensionless units $2\pi c/a$ and $2\pi/a$, where c denotes the speed of light. The dimensionless frequency ω is equivalent to a/λ, where λ is the vacuum wavelength. New designs of photonic crystal structures can be easily applied to any desired wavelength range, e.g. to the NV or SiV emission lines, by adjusting the lattice constant. We will widely use the scale invariance when designing photonic crystal structures in diamond.

In this section, we provided the basic equations and fundamental properties of electromagnetic fields in periodic structures. Starting from Maxwell's equations, we derived a Hermitian eigenvalue problem that will be simplified in the subsequent section by taking into account the symmetry of the periodic lattice.

5.2 Maxwell's eigenvalue problem and symmetry analysis

The propagation of light through periodic structures with length scales on the order of the wavelength is profoundly different from the homogeneous case. This fact is well known from solid-state physics, where the periodic potential of atoms arranged in a crystal is responsible for the formation of energy bands and band gaps of electronic states in

semiconductors, metals and insulators. Equivalently, a periodic variation of the refractive index of the dielectric medium leads to the formation of frequency bands and band gaps for electromagnetic states in the photonic crystal. To appropriately describe the periodic dielectric function, we recall the formalism of the reciprocal lattice known from solid-state physics and identify the first Brillouin zone for the two-dimensional triangular lattice that will be used throughout the text. In order to compute the eigenfrequencies and eigenstates for a given periodic structure, we restrict the eigenvalue problem (5.3), derived in the previous section, to a single unit cell of the lattice. For that purpose, we investigate the invariance of the structure under translational, rotational and mirror symmetry. Here, we focus on a two-dimensional triangular lattice of air holes in diamond. We will see that the discrete translational symmetry of the two-dimensional photonic lattice provokes a discrete spectrum of eigenfrequencies, referred to as the *photonic band structure*. Moreover, mirror reflection symmetries enable us to classify the electromagnetic fields in the crystal into two different polarizations, for which the band structure can be calculated independently. The definition of the real and reciprocal lattice is taken from reference [258], whereas the symmetry analysis and mathematical description of Maxwell's eigenvalue problem follow reference [256].

Photonic lattice and Brillouin zone

In this section, we review the framework of real space, reciprocal lattices and the Brillouin zone known from solid-state physics to appropriately describe the two-dimensional photonic crystal structure. An ideal crystal is defined by a periodic repetition of a basic building block. This elementary unit is commonly referred as the *unit cell*. Such unit cell may be reproduced in one, two or three dimensions in space. Here, we focus on two-dimensional photonic crystals consisting of air holes in diamond periodically replicated in the (x, y)-plane with no extend in the vertical z-direction. The two primitive lattice vectors $\vec{a}_1$ and $\vec{a}_2$ define the edges of a triangular unit cell with one air hole at the center (see blue region in Fig. 5.1(a)):

$$\vec{a}_1 = 0.5a\,\vec{e}_x + \sqrt{3}/2a\,\vec{e}_y \qquad \vec{a}_2 = 0.5a\,\vec{e}_x - \sqrt{3}/2a\,\vec{e}_y. \tag{5.16}$$

Here, $a = |\vec{a}_1| = |\vec{a}_2|$ denotes the *lattice constant* and $\vec{e}_x$, $\vec{e}_y$ define the Cartesian unit vectors along the x- and y-axis. By replicating the unit cell in space by multiples of the primitive lattice vectors, $\vec{a}_1$, $\vec{a}_2$, a triangular *photonic lattice* can be constructed. Any arbitrary point $\vec{r}\,'$ in the crystal structure can be considered identical to a corresponding point $\vec{r}\,'$ within a chosen unit cell, differing only by a lattice vector $\vec{R}$:

$$\vec{r}\,' = \vec{r} + \vec{R}, \qquad \text{with} \quad \vec{R} = m_1\,\vec{a}_1 + m_2\,\vec{a}_2, \tag{5.17}$$

where $m_1, m_2 \in \mathbb{Z}$. As a consequence, we can restrict the complete analysis of the crystal to points within a single unit cell.

For future analysis and the calculation of the band structure as a function of the wave vector $\vec{k}$, it is essential to Fourier transform the structure to the reciprocal space domain, i.e. into k-space. Given a set of lattice vectors $\vec{a}_1$ and $\vec{a}_2$, the corresponding primitive

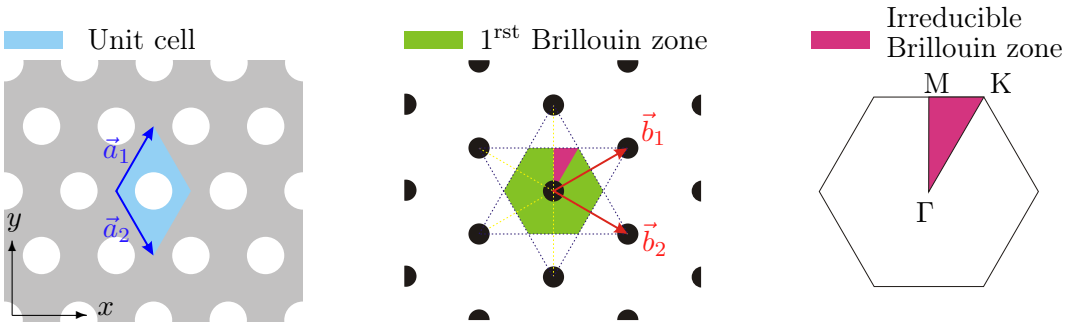

(a) Real lattice (b) Reciprocal lattice (c) 1rst Brillouin zone

Figure 5.1: The two-dimensional triangular lattice in real and reciprocal space: (a) The vectors $\vec{a}_1$, $\vec{a}_2$ define the unit cell (blue area) in real space. Gray: diamond, white: air holes. (b) The reciprocal lattice vectors $\vec{b}_1$, $\vec{b}_2$ are given by $\vec{a}_i \cdot \vec{b}_j = 2\pi\delta_{ij}$. The green area marks the first Brillouin zone defining the unit cell of the reciprocal lattice. (c) The irreducible Brillouin zone (pink area) comprises all nonredundant wave vectors under sixfold rotational symmetry. The three vertices of the irreducible Brillouin zone are the Γ, M and K point.

vectors $\vec{b}_1$ and $\vec{b}_2$ of the reciprocal lattice are defined by the relation $\vec{a}_i \cdot \vec{b}_j = 2\pi\delta_{ij}$, where δ_{ij} denotes the Kronecker's delta. The primitive reciprocal lattice vectors $\vec{b}_1$, $\vec{b}_2$ define the unit cell in Fourier space. For a triangular lattice with the lattice vector $\vec{a}_1$, $\vec{a}_2$ defined by equation (5.16), we obtain the following primitive reciprocal vectors:

$$\vec{b}_1 = 4\pi/(\sqrt{3}a) \cdot (\sqrt{3}/2\,\vec{e}_x + 0.5\,\vec{e}_y) \qquad \vec{b}_2 = 4\pi/(\sqrt{3}a) \cdot (\sqrt{3}/2\,\vec{e}_x - 0.5\,\vec{e}_y), \tag{5.18}$$

with the absolute values $|\vec{b}_1| = |\vec{b}_2| = 4\pi/(\sqrt{3}a)$. A schematic of the reciprocal space is displayed in figure 5.1(b). The whole Fourier lattice can be constructed by translating the unit cell by multiples of $\vec{b}_1$, $\vec{b}_2$. Analogous to real space, we define the reciprocal lattice vector $\vec{G}$ that relates any wave vector $\vec{k}'$ to a corresponding wave vector $\vec{k}$ within the unit cell in Fourier space, such that:

$$\vec{k}' = \vec{k} + \vec{G}, \qquad \text{with} \quad \vec{G} = v_1\,\vec{b}_1 + v_2\,\vec{b}_2, \tag{5.19}$$

where $v_1, v_2 \in \mathbb{Z}$. Hence, we can restrict our Fourier space analysis to a finite zone of wave vectors $\vec{k}$. This finite zone or unit cell in reciprocal space is called the *first Brillouin zone*. The first Brillouin zone of the triangular lattice is shown by the green area in figure 5.1(b). This unit cell of the reciprocal space can be constructed as follows: From the center point defined as the origin, we draw connecting lines to the other lattice points. The perpendicular bisectors define the boundary of the first Brillouin zone. In the following section, we will see that due to the discrete translational symmetry of the photonic lattice, we can restrict the calculation of the band structure to wave vectors within the reciprocal unit cell. Moreover, due to the sixfold rotational symmetry of the triangular lattice, it is sufficient to limit the calculation to wave vectors in the *irreducible Brillouin zone* (pink area in Fig. 5.1(b)), that can not be reconstructed

by sixfold rotation. The edge of the irreducible Brillouin zone is defined by the three vertices Γ, M and K:

$$\Gamma = \vec{0}, \qquad M = 0.5\,\vec{b}_1, \qquad K = \frac{1}{3}\,\vec{b}_1 + \frac{1}{3}\,\vec{b}_2. \tag{5.20}$$

A close up of the irreducible Brillouin zone with the three vertices Γ, M and K is shown by the pink area in figure 5.1(c). In the following, the definition of the irreducible Brillouin zone is essential for the calculation of the photonic band structure. Based on symmetry analysis, we will see that the calculation of eigenmodes of the photonic lattice can be restricted to wave vectors along the lines connecting the points Γ, M and K.

Discrete translational symmetry

Above, we have seen that the triangular lattice is invariant under discrete translation by the lattice vector $\vec{R}$. For each $\vec{R}$, we can define a translation operator $\hat{T}_{\vec{R}}$ which, when applied to a vector or scalar function $f(\vec{r})$, shifts the argument by $\vec{R}$:

$$\hat{T}_{\vec{R}}\, f(\vec{r}) = f(\vec{r} + \vec{R}). \tag{5.21}$$

When applied to the dielectric function of the triangular lattice, we obtain $\hat{T}_{\vec{R}}\,\varepsilon(\vec{r}) = \varepsilon(\vec{r} + \vec{R}) = \varepsilon(\vec{r})$. As the structure at position $\vec{r}$ and $\vec{r} + \vec{R}$ is identical, the associated electromagnetic solutions are equally invariant under discrete translation by a vector $\vec{R}$. Mathematically speaking, the operator $\hat{\Theta}$ (c.f. eq. (5.3)), that determines the electromagnetic solutions for a given dielectric function, commutes with the translation operator $\hat{T}_{\vec{R}}$: $[\hat{\Theta}, \hat{T}_{\vec{R}}] = 0$. If two operators commute, there exists a set of common eigenfunctions that are solutions for both operators. The eigenfunctions of the translation operator are plane waves given by:

$$\hat{T}_{\vec{R}}\, e^{i\vec{k}\cdot\vec{r}} = e^{i\vec{k}\cdot(\vec{r}+\vec{R})} = \left(e^{i\vec{k}\cdot\vec{R}}\right)\, e^{i\vec{k}\cdot\vec{r}}. \tag{5.22}$$

The eigenfunctions $e^{i\vec{k}\cdot\vec{r}}$ are degenerate, as the modes associated with the wave vectors $\vec{k}$ and $\vec{k} + \vec{G}$ have the same eigenvalue $e^{i\vec{k}\cdot\vec{R}}$. Here, we used the relation $\vec{G}\cdot\vec{R} = 2\pi p$, with $p \in \mathbb{Z}$. Since the linear combination of the degenerate eigenfunctions $e^{i(\vec{k}+\vec{G})\cdot\vec{r}}$ for different reciprocal lattice vectors $\vec{G}$ is itself an eigenfunction with the same eigenvalue, we can decompose the magnetic field into eigenfunctions of the photonic lattice, given by:

$$\vec{H}_{m,\vec{k}}(\vec{r}) = \sum_{\{\vec{G}\}} \vec{h}_{m,\vec{k}+\vec{G}}\, e^{i\vec{r}\cdot(\vec{k}+\vec{G})} = e^{i\vec{r}\cdot\vec{k}} \sum_{\{\vec{G}\}} \vec{h}_{m,\vec{k}+\vec{G}}\, e^{i\vec{r}\cdot\vec{G}} = e^{i\vec{r}\cdot\vec{k}}\, \vec{u}_{\vec{k}}(\vec{r}). \tag{5.23}$$

The index m denotes the *band number*. The coefficients $\vec{h}_{m,\vec{k}+\vec{G}}$ are determined by solving Maxwell's equations. The function $\vec{u}_{\vec{k}}(\vec{r})$ is a periodic function $\vec{u}_{\vec{k}}(\vec{r}) = \vec{u}_{\vec{k}}(\vec{r}+\vec{R})$. The electromagnetic modes propagating through a periodic dielectric material are plane waves modulated by the function $\vec{u}_{\vec{k}}(\vec{r})$ that shares the periodicity of the photonic lattice.

The result $\vec{H}_{m,\vec{k}}(\vec{r}) = e^{i\vec{r}\cdot\vec{k}}\,\vec{u}_{\vec{k}}(\vec{r})$ is commonly known as *Bloch's theorem* in solid state physics. One key fact about Bloch states is that the eigenstates associated with wave vectors $\vec{k}$ and $\vec{k}+\vec{G}$ are identical and thus the same must hold for the eigenfrequencies $\omega_m(\vec{k}) = \omega_m(\vec{k}+\vec{G})$. Therefore, we can restrict the eigenfrequency calculation to wave vectors $\vec{k}$ within the first Brillouin zone of the reciprocal lattice.

Photonic band structure, Maxwell's eigenvalue problem

From general symmetry analysis, we have derived that the electromagnetic modes of a photonic crystal with a discrete translational symmetry in two-dimensions can be written as Bloch states that are composed of a plane wave multiplied with a periodic function $\vec{u}_{\vec{k}}(\vec{r})$. When inserting the Bloch state $\vec{H}_{\vec{k}} = e^{i\vec{k}\cdot\vec{r}}\vec{u}_{\vec{k}}(\vec{r})$ into the master equation (5.3), we can derive an eigenvalue problem for $\vec{u}_{\vec{k}}(\vec{r})$:

$$\hat{\Theta}_{\vec{k}}\vec{u}_{\vec{k}}(\vec{r}) = (i\vec{k}+\vec{\nabla})\times\frac{1}{\varepsilon(\vec{r})}(i\vec{k}+\vec{\nabla})\times\vec{u}_{\vec{k}}(\vec{r}) = (\omega(\vec{k})/c)^2\vec{u}_{\vec{k}}(\vec{r}). \tag{5.24}$$

Here we have defined a new Hermitian operator $\hat{\Theta}_{\vec{k}}$ depending on $\vec{k}$. The function $\vec{u}_{\vec{k}}(\vec{r})$ has to fulfill the transversality relation $(i\vec{k}+\vec{\nabla})\vec{u}_{\vec{k}}(\vec{r}) = 0$. Due to the periodicity relation $\vec{u}_{\vec{k}}(\vec{r}) = \vec{u}_{\vec{k}}(\vec{r}+\vec{R})$, we can restrict our analysis to a single unit cell of the photonic lattice and to wave vectors within the first Brillouin zone (see previous section). Similarly to the quantum-mechanical problem of a particle in a box, restricting a Hermitian eigenvalue problem to a finite volume leads to a discrete spectrum of eigenvalues. Therefore, we expect to find for each wave vector $\vec{k}$ a finite set of modes with discretely spaced frequencies, which are labeled according to the band index m. For a fixed band number m, the frequency $\omega_m(\vec{k})$ obtained by solving equation (5.24) varies continuously when the wave vector $\vec{k}$ is continuously changed. Displaying the calculated frequencies $\omega_m(\vec{k})$ as a function of the wave vector $\vec{k}$ in the Brillouin zone, we obtain the *band structure* of the photonic crystal. In practice, to calculate the band structure for a given photonic crystal described by $\varepsilon(\vec{r})$, we use computational techniques, e.g. the freely available software package *MIT Photonic-Bands (mpb)* [259, 260] that is described in section 5.7.1.

Rotational symmetry

Besides the discrete translational symmetry the triangular lattice has a sixfold rotational symmetry. This means that upon rotation by an angle of $\alpha = 60°$ around the axis normal to the photonic crystal plane, the exact configuration of the crystal is reproduced. To rotate a vector field $\vec{f}(\vec{r})$ by an angle α, we define the operator $\hat{O}_{\mathcal{R}}$ as

$$\hat{O}_{\mathcal{R}}\vec{f}(\vec{r}) = \mathcal{R}\vec{f}(\mathcal{R}^{-1}\vec{r}). \tag{5.25}$$

The vector field $\vec{f}$ is rotated with $\mathcal{R}$ to give $\vec{f}' = \mathcal{R}\vec{f}$ and the argument $\vec{r}$ is rotated by $\mathcal{R}^{-1}$ yielding $\vec{r}' = \mathcal{R}^{-1}\vec{r}$. If the structure is invariant under rotation by $\mathcal{R}$, we can

conclude that $[\hat{\Theta}, \hat{O}_{\mathcal{R}}] = 0$. Using the commutator relation, we deduce

$$\hat{\Theta}(\hat{O}_{\mathcal{R}}\vec{H}_{m,\vec{k}}) = \hat{O}_{\vec{G}R}(\hat{\Theta}\vec{H}_{m,\vec{k}}) = \left(\frac{\omega_m(\vec{k})}{c}\right)^2 (\hat{O}_{\mathcal{R}}\vec{H}_{m,\vec{k}}). \tag{5.26}$$

The rotated state $\hat{O}_{\mathcal{R}}\vec{H}_{m,\vec{k}}$ is another Bloch state with a rotated wave vector $\mathcal{R}\vec{k}$[3]. Furthermore, equation (5.26) shows that the rotated mode $\hat{O}_{\mathcal{R}}\vec{H}_{m,\vec{k}}$ is just as well a solution to the master equation (5.24) with the same eigenvalue $(\omega_m(\mathcal{R}\vec{k})/c)^2 = (\omega_m(\vec{k})/c)^2$ as $\vec{H}_{m,\vec{k}}$. This means that the eigenfrequencies ω_m associated with the wave vector $\vec{k}$ and the rotated wave vector $\mathcal{R}\vec{k}$ are the same. Therefore, we can restrict the calculation of eigenfrequencies to wave vectors in a small part of the Brillouin zone that can not be restored by the sixfold rotational symmetry of the lattice. This reduced part is referred to as the *irreducible Brillouin zone* (c.f. page 73 in section 5.2).

According to the extremum principle known from complex functional analysis, the maxima and minima of a function in a domain are to be found on the boundary of that domain. This is especially valid for harmonic functions. From the maxima and minima of the lattice eigenfrequencies, important properties of the photonic band structure, e.g. the existence of a photonic band gap, can be deduced. Therefore, it is sufficient to restrict the calculation of the eigenfrequencies $\omega_m(\vec{k})$ to wave vectors $\vec{k}$ along the boundary of the irreducible Brillouin zone, connecting the points Γ, M and K in reciprocal space (c.f. Fig. 5.1(c)).

Mirror symmetry and TM- and TE-modes

Mirror reflection symmetry in two-dimensional photonic crystals allows us to classify the modes in two distinct polarizations and enables to separate the eigenequation (5.24) for $\hat{\Theta}_{\vec{k}}$ into two individual equations one for each polarization. The two-dimensional photonic crystal structure shown in figure 5.2 is symmetric upon reflections in the (x, y), (y, z) and (x, z)-planes. In the following, we will focus on reflections with respect to the (x, y)-plane, but the mathematical descriptions can easily be transferred to other mirror planes. The reflection of a vector $\vec{r}$ with respect to the (x, y)-plane is mathematically described by: $M_z(x, y, z) = (x, y, -z)$, where M_z changes the sign of the z-component and leaves x, y unchanged. To describe the transformation of electromagnetic fields under mirror reflection with respect to the (x, y)-plane, we define the mirror reflection operator $\hat{O}_{M_z}$. When applied to the z-component of a vector field $\vec{f}(\vec{r})$, e.g. the electric field $\vec{E}$, f_z is inverted with a minus sign, whereas a pseudo vector field, e.g. the magnetic field $\vec{H}$, is transformed with a plus sign:

$$\text{vector:}\quad \hat{O}_{M_z} f_z(\vec{r}) = -f_z(M_z\vec{r}) \tag{5.28}$$

[3]To prove this, we show that the rotated state is an eigenvector of the discrete translation operator:

$$\hat{T}_{\vec{R}}(\hat{O}_{\mathcal{R}}\vec{H}_{m,\vec{k}}) = e^{i\mathcal{R}\vec{k}\cdot\vec{R}}(\hat{O}_{\mathcal{R}}\vec{H}_{m,\vec{k}}). \tag{5.27}$$

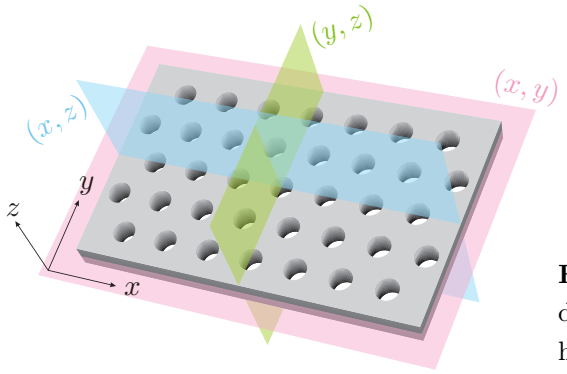

Figure 5.2: Mirror symmetry planes of a two dimensional photonic crystal with a finite slab height in z-direction.

$$\text{pseudo vector:}\quad \hat{O}_{M_z} f_z(\vec{r}) = +f_z(M_z\vec{r}) \tag{5.29}$$

We refer to a vector field as $+z$-*mode* with respect to the (x, y)-plane, when it is invariant under reflection $\hat{O}_{M_z} f_z(\vec{r}) = f_z(\vec{r})$, whereas it is called $-z$-*mode*, when it transforms with a minus sign $\hat{O}_{M_z} f_z(\vec{r}) = -f_z(\vec{r})$. In our simulations (c.f. section 5.7), we use this classification in $\pm z$-modes, and equivalently in $\pm x$ and $\pm y$ modes, in order to specify the symmetry of the modes. The above definition is in accordance with the one given in the book by Joannopoulos [256]. In contrast to this, most of the experimental publications [86, 132] on photonic crystals classify the cavity modes in *even* and *odd* modes. Unfortunately, there is no uniform classification of even and odd modes in literature. In order to be conform with references [86,132,261,262] investigating photonic crystal waveguides and cavities that are similar to those studied in this thesis, we define $+z$-*modes* as *odd* and $-z$-*modes* as *even* modes. Although this definition is at first sight counter intuitive, we keep this classification throughout the thesis in order to allow for comparison to other experimental as well as to theoretical studies. Based on our definition, we obtain for the electromagnetic fields:

	odd or $(+z)$	*even* or $(-z)$
vector:	$E_z(M_z\vec{r}) = -E_z(\vec{r})$	$E_z(M_z\vec{r}) = E_z(\vec{r})$
pseudo vector:	$H_z(M_z\vec{r}) = H_z(\vec{r})$	$H_z(M_z\vec{r}) = -H_z(\vec{r})$

(5.30)

Similarly, the operators $\hat{O}_{M_x}$ and $\hat{O}_{M_y}$ describe the transformation of a (pseudo)-vector field upon reflection in the (y, z) and (x, z)-plane, respectively. Under those mirror reflections, the x- and y-components of the electromagnetic fields transform as follows:

	odd or $(+x)$	*even* or $(-x)$
vector:	$E_x(M_x\vec{r}) = -E_x(\vec{r})$	$E_x(M_x\vec{r}) = E_x(\vec{r})$
pseudo vector:	$H_x(M_x\vec{r}) = H_x(\vec{r})$	$H_x(M_x\vec{r}) = -H_x(\vec{r})$

(5.31)

	odd or $(+y)$	*even* or $(-y)$
vector:	$E_y(M_y\vec{r}) = -E_y(\vec{r})$	$E_y(M_y\vec{r}) = E_y(\vec{r})$
pseudo vector:	$H_y(M_y\vec{r}) = H_y(\vec{r})$	$H_y(M_y\vec{r}) = -H_y(\vec{r})$

(5.32)

We have to keep in mind that the electromagnetic fields do not transform independently but they are related according to equations (5.5). Hence, if the H_z component is even (odd) under the reflection with respect to the (x, y)-plane, E_x and E_y also transform with a minus (plus) sign according to equations (5.5). Similarly, if the E_z component is even (odd) with respect to (x, y) reflections, H_x and H_y equally transform with a plus (minus) sign. In the case of two-dimensional photonic crystals defined in the (x, y)-plane, the structure is invariant under reflections: $M_z\, z = z = 0$. Likewise, for wave vectors $\vec{k}_{||}$ in the two-dimensional Brillouin zone, we have $M_z\vec{k}_{||} = \vec{k}_{||}$. According to the relations (5.30), for any odd mode, we get $E_z(x, y, z = 0) = -E_z(x, y, -z = 0)$. Hence, the E_z component must vanish at $z = 0$ and thereby also H_x and H_y. The only persisting components are E_x, E_y, H_z in the case of odd modes. Similarly, in the case of even modes, H_z, E_x and E_y vanish and H_x, H_y and E_z remain.

The modes for every two-dimensional photonic crystal can be classified into two distinct polarizations: either (E_x, E_y, H_z) or (H_x, H_y, E_z). As the electric field is confined to the (x, y)-plane, we call the former modes *transverse electric (TE)* modes, whereas the latter are termed *transverse magnetic (TM)* modes with the magnetic field components being confined in the (x, y)-plane. The classification of the modes according to their polarization allows us to solve the eigenequation for $\hat{\Theta}_{\vec{k}}$ and to calculate the band structure independently for TE- and TM-modes. However, please note that this is only valid in the case of two-dimensional photonic crystals, where we have $M_z z = z$ and $M_z\vec{k}_{||} = \vec{k}_{||}$. For two-dimensional structures with a finite slab thickness in z-direction, this separation of polarizations is not valid anymore for every wave vector. However, the modes can still be classified as even and odd modes as will be addressed in section 5.4.2. Before we proceed by numerically solving the derived eigenvalue equation for $\hat{\Theta}_{\vec{k}}$ in order to compute the photonic band diagram for two-dimensional periodic structures (c.f. section 5.4), we introduce the local density of states, which is essential for the description of light inhibition and enhancement in photonic crystals.

5.3 Local density of states

The two earliest papers [247, 248] on photonic band gap materials highlight their ability of dramatically alter the emission properties of a single emitter hosted in it. The emission modification arises from the difference in the local density of states within the crystal compared to bulk material. Yablonovitch [247] anticipated the inhibition of spontaneous emission when placing the emitter in a three-dimensional photonic crystal structure with a complete band gap at the emitter's transition frequency. In contrast, John [248] focused on the localization of light due to disorder, e.g. a point or line defect, in an otherwise periodic dielectric material. The defect induces sharp Bragg resonances in the local density of states at frequencies within the band gap of the periodic lattice. In this section, we review the concept of the local density of optical states determining the radiation dynamics of a fluorescent source placed in a photonic lattice. Mathematically, the spontaneous emission rate and the local density of states are related via Fermi's Golden Rule. The local density of states, used in Fermi's Golden Rule, arises from a

semi-classical analysis of the atom-field interaction, in which the atom is treated quantum mechanically and the electromagnetic fields classically. Based on classical Maxwell's equations, we deduce a relation between the radiated power of a dipole source and the local density of states of the surrounding medium. Moreover, the impact of the local density of states on the spontaneous emission rate of a two-level atom is derived. By normalizing the spontaneous emission rate of a single emitter placed within the crystal to its emission properties in bulk, we can derive the Purcell factor. The Purcell factor determines the inhibition or enhancement of the emission rate as a function of the atom's spatial and spectral position and dipole orientation. The mathematical definitions and descriptions in this section follow references [120, 257].

Definition of (local) density of states

The density of states (DOS) defines the number of optical states per frequency interval $[\omega, \omega + d\omega]$ at each emission frequency ω of the fluorescent source hosted in the material. The density of states is given by

$$DOS(\omega) = \sum_m \delta(\omega - \omega_m). \tag{5.33}$$

Here, the delta function $\delta(\omega - \omega_m)$ filters the relevant emission frequencies ω_m from the collection of optical states. The integral over all frequencies $\int DOS(\omega)\, d\omega$ counts the number of modes in the integration interval.

For applications in quantum optics, it is necessary to specify the density of states at the position $\vec{r}$ of a single atom placed in the photonic crystal. If an excited atom, hosted in a photonic crystal, decays via a single-photon process, the photon has to be emitted into a mode supported by the photonic lattice. The local coupling of the atomic dipole moment $\vec{d}$ to the photonic crystal modes $\vec{E}_m$ determines the decay rate of the excited atom. The number of existing modes and the coupling to the photonic crystal modes are expressed by the local density of states (LDOS). If we normalize the crystal eigenfields such that $\int \vec{E}^*(\vec{r})\, \varepsilon(\vec{r})\, \vec{E}(\vec{r}) d^3r = 1$, we can define the local density of states projected on the atomic dipole moment by [4]:

$$LDOS(\vec{r}, \omega, \vec{e}_d) = \sum_m \delta(\omega - \omega_m)\, \varepsilon(\vec{r}) |\langle \vec{E}_m(\vec{r}), \vec{e}_d \rangle|^2. \tag{5.34}$$

Here, $\langle \cdot, \cdot \rangle$ is the inner product, $\vec{e}_d$ denotes the unit vector pointing along the transition dipole moment orientation and $\vec{E}_m$ is the m^{th} electric eigenmode obtained by solving

[4] The local density of states $LDOS(\vec{r}, \omega, \vec{e}_d)$ gives a measure of the density of states $DOS(\omega)$ weighted by the energy density of each mode's electric field at position $\vec{r}$ and in the direction of the dipole $\vec{d}$. Equivalently, one could define the LDOS weighted by the magnetic field energy $\mu |\langle \vec{H}_m, \vec{e}_d \rangle|^2$ with the normalization $\int \mu |\vec{H}|^2 = 1$. However, many physical phenomena, e.g. the spontaneous emission rate of an atom, are related to electric dipole sources. Therefore, the LDOS based on the electric field distribution is more convenient for us.

Maxwell's eigenvalue problem for a given photonic crystal structure. Due to the position dependency of the LDOS, the location of the emitter in the photonic crystal might be crucial for the success of quantum optical experiments. When integrating the local density of states over all possible dipole positions $\vec{r}$ and summing over all dipole orientations $\vec{d}$, we again obtain the total density of states DOS:

$$DOS(\omega) = \sum_{\vec{d}} \int LDOS(\vec{r}, \omega, \vec{e}_d)\, d^3r. \tag{5.35}$$

The local density of states is of central importance for understanding the classical radiation of a dipole source as well as quantum mechanical phenomena of light-matter interaction, e.g. single-photon emission by an atom. Using a semiclassical approach, we show in the following that both the power radiated by a classical dipole source and the spontaneous emission rate of atoms are connected to the local density of states.

Local density of states and radiated power

Starting from Maxwell's equations, we derive a relationship between the local density of states and the power radiated by a current source $\vec{J}$ hosted in a dielectric material. This relation is widely used in practice to compute the local density of states by inserting a dipole source and performing Fourier transforms of the radiated electromagnetic fields [263–268]. Including an electric point source, Maxwell's equations are given by

$$\vec{\nabla} \times \vec{H}(\vec{r}, t) = \varepsilon_0 \varepsilon(\vec{r}) \frac{\partial \vec{E}(\vec{r}, t)}{\partial t} + \vec{J}(\vec{r}, t) \tag{5.36}$$

$$\vec{\nabla} \times \vec{E}(\vec{r}, t) = -\mu_0 \mu(\vec{r}) \frac{\partial \vec{H}(\vec{r}, t)}{\partial t}. \tag{5.37}$$

Assuming time-harmonic electromagnetic fields $\vec{H}(\vec{r}, t) = \vec{H}(\vec{r})\, e^{-i\omega t}$, $\vec{E}(\vec{r}, t) = \vec{E}(\vec{r})\, e^{-i\omega t}$ and an electric current source $\vec{J}(\vec{r}, t) = \vec{J}(\vec{r})\, e^{-i\omega t}$, equations (5.36)-(5.37) can be decoupled and we obtain the following problem for the electric field:

$$\left(\hat{\Xi}_\mu - \left(\frac{\omega}{c} \right)^2 \right) \vec{E}(\vec{r}) = \frac{i\omega}{c^2 \varepsilon_0} \frac{\vec{J}(\vec{r})}{\varepsilon(\vec{r})}. \tag{5.38}$$

Here, we applied the definition of the Hermitian operator Ξ_μ given by equation (5.12). According to Poynting's theorem, the total radiated power is equal to the time-averaged work of the electric field done on the electric current [269]:

$$P = -\frac{1}{2} \mathfrak{Re} \int \vec{E}^*(\vec{r}) \cdot \vec{J}(\vec{r})\, d^3r = -\frac{1}{2} \mathfrak{Re} \langle \vec{E}, \vec{J} \rangle, \tag{5.39}$$

where $\langle \cdot, \cdot \rangle$ denotes the inner product. As a next step, we expand the electric current $\vec{J}$ and the electric field $\vec{E}$ in the basis of the photonic crystal modes $\vec{E}_m$ associated to the eigenfrequencies ω_m [257]:

$$\frac{\vec{J}(\vec{r})}{\varepsilon(\vec{r})} = \sum_m \langle \vec{E}_m(\vec{r}), \vec{J}(\vec{r}) \rangle\, \vec{E}_m(\vec{r}) \tag{5.40}$$

$$\vec{E}(\vec{r}) = \sum_m \frac{i\omega}{\varepsilon_0} \frac{\langle \vec{E}_m(\vec{r}), \vec{J}(\vec{r})\rangle \, \vec{E}_m(\vec{r})}{\omega_m^2 - \omega^2}. \tag{5.41}$$

Thereby, we take advantage of the orthogonality relation (5.8) of the cavity modes as well as of the eigenequation $\Xi_\mu \vec{E}_m = (\omega_m/c)^2 \vec{E}_m$ and equation (5.38). Unfortunately, we cannot directly substitute equations (5.40) and (5.41) into the expression (5.39) for the radiated power P. First of all, the denominator vanishes for $\omega_m = \omega$ and hence $\vec{E}(\vec{r})$ diverges. Second, $\vec{E}(\vec{r})$ is purely imaginary which results in $\mathfrak{Re}\langle \vec{E}, \vec{J}\rangle = 0$. To overcome these singularities, we consider a lossy system by introducing a complex eigenfrequency $\omega_c = \omega_m - i\eta_m/2$ with an imaginary part $\eta_m > 0$, for which the equation can be solved. Finally, we take the limit $\eta_m \to 0$. For a current source placed in a lossless medium, the radiated power is given by [257]:

$$P = \frac{\pi}{4\varepsilon_0} \sum_m |\langle \vec{E}_m(\vec{r}), \vec{J}(\vec{r})\rangle|^2 \delta(\omega - \omega_m). \tag{5.42}$$

In contrast, if we assume small losses $\eta_m \ll \omega_m$, the frequency dependence of the modes is no longer described by delta functions but governed by a Lorentzian function that models the spectral broadening. The power radiated by the current source placed in a dissipative medium is then given by [257]:

$$P = \frac{1}{8\varepsilon_0} \sum_m \frac{\eta_m \, |\langle \vec{E}_m(\vec{r}), \vec{J}(\vec{r})\rangle|^2}{(\omega - \omega_m)^2 + (\eta_m/2)^2}. \tag{5.43}$$

Hence, the radiated power is determined by the sum over all leaky modes, described by Lorentzian functions, multiplied by the overlap integral $|\int \vec{E}_m(\vec{r}) \cdot \vec{J}(\vec{r}) \, d^3r|^2$. In the limit $\eta_m \to 0$, we retrieve equation (5.42) by considering that the delta distribution can be approached by a Lorentzian: $\lim_{\eta_m \to 0} (\eta_m/2)/((\omega - \omega_m)^2 + (\eta_m/2)^2) = \pi\delta(\omega - \omega_m)$.

Given equation (5.42), a relation between the radiated power and the local density of states can be derived. Let us consider a time-harmonic current source $\vec{J}(\vec{r}, t) = \vec{J}(\vec{r}) \, e^{-i\omega t}$ with

$$\vec{J}(\vec{r}) = \vec{d}\,\delta(\vec{r} - \vec{r}_0), \quad \text{with } \vec{d} = d\,\vec{e}_d. \tag{5.44}$$

To the lowest order, the current source $\vec{J}$ can be thought of an oscillating dipole positioned at $\vec{r}_0$ with d and $\vec{e}_d$ being the magnitude and the direction of the dipole moment $\vec{d}$. Temporarily, we assume a unit-amplitude $d = 1$. Substituting the definition (5.44) of the point-dipole source in equation (5.42), we obtain $|\langle \vec{E}_m(\vec{r}), \vec{J}(\vec{r})\rangle|^2 = |\langle \vec{E}_m(\vec{r}_0), \vec{e}_d\rangle|^2$. Comparing equation (5.42) and equation (5.34), we find the following relation between the radiated power and the LDOS for a point-source in a lossless medium:

$$LDOS(\vec{r}_0, \omega, \vec{e}_d) = \frac{4}{\pi} \, \varepsilon_0 \, \varepsilon(\vec{r}_0) P(\vec{r}_0, \omega, \vec{e}_d). \tag{5.45}$$

The argument $\vec{e}_d$ indicates that the local density of states and the radiated power depend on the specific orientation of the dipole moment. According to equation (5.45), the local density of states is proportional to the power radiated by a point-dipole source differing only by a factor of $4\,\varepsilon_0 \varepsilon(\vec{r}_0)/\pi$.

Based on equation (5.45), we can compute the local density of states by simulating the radiated power emitted by a dipole source. To this end, we place a point-dipole source $J(\vec{r},t) = d(t)\,\vec{d}\,\delta(\vec{r}-\vec{r}_0)$ at a point $\vec{r}_0$ within the photonic crystal lattice, with a polarization along the unit vector $\vec{e}_d$ and an impulsive amplitude distribution $d(t)$ that vanishes for long times t. The LDOS spectrum is obtained by accumulating the frequency dependent Fourier transform $\tilde{E}_d(\vec{r}_0,\omega) = \mathrm{FT}[\vec{E}(\vec{r}_0,t)\cdot\vec{e}_d]$ of the electric field $\vec{E}(\vec{r}_0,t)$ projected on the polarization axis $\vec{e}_d$ of the dipole moment and multiplied by the Fourier transform $\tilde{d}(\omega) = \mathrm{FT}[d(t)]$ of the source amplitude distribution $d(t)$ [257]:

$$LDOS(\vec{r}_0,\omega,\vec{e}_d) = -\frac{2}{\pi}\varepsilon_0\varepsilon(\vec{r}_0)\frac{\mathfrak{Re}\{\tilde{E}_d^*(\vec{r}_0,\omega)\,\tilde{d}(\omega)\}}{|\tilde{d}(\omega)|^2}. \tag{5.46}$$

In order to retrieve the power emitted by a unit-amplitude dipole, we normalize the LDOS in equation (5.46) by the pulse spectrum $\tilde{d}(\omega)$. Typically, we are interested in the modification of the LDOS by a photonic crystal structure with respect to a homogeneous medium. In this case, we simulate the LDOS twice and divide the two. All normalization factors such as $|\tilde{d}(\omega)|^2$ cancel each other, when calculating the ratio. In section 5.4, we compute the LDOS using finite-difference time-domain (FDTD) simulations for two-dimensional photonic crystal lattices and photonic crystal slab structures.

Local density of states and spontaneous emission rate

Since Purcell's fundamental work [56], we know that the radiative properties of an atom can be significantly modified by the surrounding medium. When placed in a resonant electric device, the spontaneous decay rate of a single emitter can be enhanced compared to its free-space decay rate. To experimentally observe the Purcell effect, one requires a physical device whose dimensions are on the order of the wavelength of light, as it is the case for photonic crystals. Using quantum electrodynamics, we here derive the spontaneous decay rate γ for a two-level quantum system and relate it to the local density of states of the surrounding medium. The mathematical description is based on reference [120].

Here we consider a two-level atom with one excited state $|e\rangle$ and several ground state levels $|g\rangle$ with identical energies. The combined emitter-field system undergoes a transition from the initial state $|i\rangle$ to the final state $|f\rangle$ under emission of a single photon. The spontaneous emission rate γ is determined by Fermi's Golden Rule:

$$\gamma = \frac{2\pi}{\hbar^2}\sum_f |\langle f|\hat{H}_{int}|i\rangle|^2\,\delta(\omega_i-\omega_f). \tag{5.47}$$

Here, $\hat{H}_{int} = -\hat{d}\cdot\hat{E}$ is the interaction Hamiltonian in the dipole approximation, with $\hat{d}$ being the atomic dipole operator and $\hat{E}$ the electric field operator. In a next step, we develop the electric field operator as a sum of complex modes $\vec{E}_m^+ = (\vec{E}_m^-)^*$ associated to frequencies ω_m [120]:

$$\hat{E} = \sum_m \left[\vec{E}_m^+\hat{a}_m(t) + \vec{E}_m^-\hat{a}_m^\dagger(t)\right], \tag{5.48}$$

where

$$\hat{a}_m^\dagger(t) = \hat{a}_m^\dagger(0)\exp(i\omega_m t), \qquad \hat{a}_m(t) = \hat{a}_m(0)\exp(-i\omega_m t). \tag{5.49}$$

The quantities $\hat{a}_m^\dagger$, $\hat{a}_m$ are the photon creation and annihilation operators, respectively. The dipole operator $\hat{d}$ of the two-level atom with the ground state $|g\rangle$ and excited state $|e\rangle$ can be written as [120]

$$\hat{d} = \vec{d}\left(|e\rangle\langle g| + |g\rangle\langle e|\right). \tag{5.50}$$

To determine the transition rate, we define the initial $|i\rangle$ and excited state $|f\rangle$ of the combined emitter-field system as:

$$|i\rangle = |e, 0\rangle \qquad |f\rangle = |g, 1_{\omega_m}\rangle, \tag{5.51}$$

where $|e, 0\rangle$ means that the atom is initially excited and no photon being present in the field, whereas $|g, 1_{\omega_m}\rangle$ symbolizes the atomic ground state and the one-photon state of the field with a frequency $\omega_0 = (E_e - E_g)/\hbar$. Here, E_e, E_g are the energies of the atomic excited and the ground state, respectively. Substituting the expansions of the electric field and dipole operator into Fermi's Golden Rule for the defined initial and final state of the system, we obtain for the spontaneous emission rate γ [120]:

$$\gamma = \frac{2\pi}{\hbar^2}\sum_m \left[\vec{d}\cdot(\vec{E}_m^+\vec{E}_m^-)\cdot\vec{d}\right]\,\delta(\omega_0 - \omega_m). \tag{5.52}$$

It is convenient to express the electric field modes in terms of normal modes $\vec{u}_m$ defined as [120]

$$\vec{E}_m^+ = \sqrt{\frac{\hbar\omega_m}{2\varepsilon_0}}\vec{u}_m, \qquad \vec{E}_m^- = \sqrt{\frac{\hbar\omega_m}{2\varepsilon_0}}\vec{u}_m^*. \tag{5.53}$$

Considering the definition of normal modes and the dipole moment $\vec{d} = d\vec{e}_d$ with an amplitude d aligned along the unit-vector $\vec{e}_d$, the decay rate can be written as

$$\gamma = \frac{\pi\omega_0}{\hbar\varepsilon_0}|d|^2\sum_m \left[\vec{e}_d\cdot(\vec{u}_m\vec{u}_m^*)\cdot\vec{e}_d\right]\,\delta(\omega_0 - \omega_m). \tag{5.54}$$

If we compare the derived spontaneous emission rate with equation (5.34), we can identify the local density of states with

$$LDOS(\vec{r}_0, \omega_0, \vec{e}_d) = \varepsilon(\vec{r}_0)\sum_m \left[\vec{e}_d\cdot(\vec{u}_m\vec{u}_m^*)\cdot\vec{e}_d\right]\,\delta(\omega_0 - \omega_m). \tag{5.55}$$

The spontaneous emission rate is hence proportional to the local density of states calculated at the emitter's position $\vec{r}_0$ divided by the dielectric function $\varepsilon(\vec{r}_0)$:

$$\gamma = \frac{\pi\omega_0}{\hbar\varepsilon_0}|d|^2\frac{1}{\varepsilon(\vec{r}_0)}LDOS(\vec{r}_0, \omega_0, \vec{e}_d) \tag{5.56}$$

We emphasize that according to our definitions the spontaneous emission rate is proportional to the ratio $LDOS(\vec{r}_0, \omega_0, \vec{e}_d)/\,\varepsilon(\vec{r}_0)$ including the LDOS as well as the dielectric function at position $\vec{r}_0$. This is conform with previous findings reported in literature [270]

where the LDOS is expressed in terms of the dyadic Green's function $\overleftrightarrow{G}$[5]. The analogy between the quantum analysis of spontaneous emission and the classical dipole radiation picture can be found in references [120, 265].

In the definition of the spontaneous emission rate above, we assumed a delta-like emission spectrum at a fixed frequency ω_0. In the case of an atomic transition i with a finite linewidth η_i given by a Lorentzian function centered at a transition frequency ω_i, the spontaneous emission rate is determined by [257, 265]:

$$\gamma = \frac{\omega_i}{\hbar\varepsilon_0}|d|^2 \int \frac{1}{\varepsilon(\vec{r}_i)} LDOS(\vec{r}_i, \omega, \vec{e}_d) \frac{\eta_i/2}{(\omega-\omega_i)^2 + (\eta_i/2)^2}\, d\omega, \tag{5.57}$$

where $\vec{r}_i$ denotes the emitter's position. Including a finite emission linewidth in the analysis, the spontaneous emission rate is not just given by the local density of states at ω_i, but it has to be multiplied by the Lorentzian emission spectrum of the dipole source. The above description could also be derived by taking the temporal Fourier transform of a current source with an exponentially decaying amplitude $\vec{J}(\vec{r},t) = d\vec{e}_d\delta(\vec{r}-\vec{r}_0)\, e^{-i\omega_i t-\eta_i t/2}$. In the limit for vanishing η_i, $\lim_{\eta_i\to 0}(\eta_i/2)/((\omega-\omega_i)^2+(\eta_i/2)^2) = \pi\,\delta(\omega-\omega_i)$, equation (5.57) converges to (5.56). If the emitter's linewidth η_i is much smaller than any feature size in the LDOS spectrum, it is often reasonable to simply use the $LDOS(\vec{r}_i, \omega_i, \vec{e}_d)$ [257].

Once we have found the dependency of γ on the LDOS, we can now derive a correlation between the atomic spontaneous transition rate and the power radiated by the emitter. To this end, we substitute equation (5.45), linking the radiated power with the local density of states, into expression (5.56). For the spontaneous decay rate, we find

$$\gamma = \frac{4\omega_0}{\hbar}|d|^2 P(\vec{r}_0, \omega_0, \vec{e}_d). \tag{5.58}$$

Hence, the spontaneous emission rate is exactly proportional to the radiated power. Normalized to the free-space emission properties, the enhancement or inhibition of the quantum spontaneous emission rate can be easily derived from the radiated power:

$$\frac{\gamma}{\gamma_0} = \frac{P}{P_0}. \tag{5.59}$$

This important relationship has been widely applied to compute the Purcell factor by solving classical Maxwell's equations [263–268]. In connection with periodic photonic crystal slabs, we will use equation (5.59) to evaluate the inhibition of the spontaneous emission rate for a single emitter placed inside a periodic structure by simulating the radiated power in all three spatial directions (c.f. page 100).

5.3.1 Purcell factor

The Purcell factor is defined as the spontaneous emission rate of an emitter placed in an inhomogeneous medium, e.g. a photonic crystal lattice or a cavity, divided by the

[5]The dyadic Green's function is obtained by solving $(\Xi_\mu - (\omega/c)^2)\,\overleftrightarrow{G}\,(\vec{r},\vec{r}_0) = \overleftrightarrow{I}\,\delta(\vec{r}-\vec{r}_0)$, with the unit dyad $\overleftrightarrow{I}$.

spontaneous emission rate in bulk material. To derive the Purcell factor, we consider a single cavity mode coupled to a single emitter at position $\vec{r}_0$, with dipole moment $\vec{d}$ and an atomic-like transition rate at frequency ω_0 given by equation (5.58). To obtain a compact and clear description, we make several assumptions. First, we suppose that the local density of states of the cavity is dominated by one photonic crystal mode at frequency $\omega_m = \omega_{\text{cav}}$ with a finite linewidth η_{cav} described by a Lorentzian spectrum given by equation (5.43). Secondly, we express the resonance linewidth η_{cav} by the dimensionless quality factor Q: $\eta_{\text{cav}} = \omega_{\text{cav}}/Q$. As a third step, we consider normalized electric fields $\vec{e}_E(\vec{r}) = \alpha_E \vec{E}(\vec{r})$, where $\vec{e}_E$ denotes the unit vector pointing along the electric field direction and α_E is the normalization constant. From $\int \varepsilon(\vec{r})|\alpha_E \vec{E}(\vec{r})|^2 d^3r = 1$ (c.f. eq. (5.8)), we obtain the normalization constant $|\alpha_E|^2 = (\int \varepsilon(\vec{r})|\vec{E}(\vec{r})|^2 d^3r)^{-1}$ [114]. With these three assumptions, the spontaneous emission rate of an emitter placed at position $\vec{r}_0$ in the photonic lattice is given by:

$$\gamma = \frac{|d|^2}{\hbar\varepsilon_0} \cdot \frac{2Q}{1 + 4Q^2(\frac{\omega_0}{\omega_{\text{cav}}} - 1)^2} \cdot \frac{\max\{\varepsilon(\vec{r})|\vec{E}(\vec{r})|^2\}}{\int \varepsilon(\vec{r})|\vec{E}(\vec{r})|^2 d^3r} \cdot \frac{|\vec{E}(\vec{r}_0)|^2 \ |\langle \vec{e}_d \cdot \vec{e}_E \rangle|^2}{\max\{\varepsilon(\vec{r})|\vec{E}(\vec{r})|^2\}}. \tag{5.60}$$

Here, we have multiplied the nominator and denominator with $\max\{\varepsilon(\vec{r})|\vec{E}(\vec{r})|^2\}$, representing the maximum of the electric field energy in the simulation volume. According to definition (2.3) in chapter 2, we identity the term:

$$V = \frac{\int \varepsilon(\vec{r})|\vec{E}(\vec{r})|^2 d^3r}{\max\{\varepsilon(\vec{r})|\vec{E}(\vec{r})|^2\}}. \tag{5.61}$$

as the modal volume V. To deduce the Purcell factor, we normalize the spontaneous emission rate of the same emitter hosted in bulk with refractive index n [120]:

$$\gamma_0 = \frac{n\omega^3|d|^2}{3\pi\hbar\varepsilon_0 c^3}. \tag{5.62}$$

The Purcell factor F_{cav} is given by:

$$F_{\text{cav}} = \frac{\gamma}{\gamma_0} = \frac{3}{4\pi^2}\frac{Q}{V}\left(\frac{\lambda}{n}\right)^3 \cdot \frac{1}{1 + 4Q^2(\frac{\omega_0}{\omega_{\text{cav}}} - 1)^2} \cdot \frac{|\vec{E}(\vec{r}_0)|^2}{\max|\vec{E}(\vec{r})|^2} \cdot |\langle \vec{e}_d \cdot \vec{e}_E \rangle|^2 . \tag{5.63}$$

Thereby, we set $\max\{\varepsilon(\vec{r})|\vec{E}(\vec{r})|^2\} = n^2 \max|\vec{E}(\vec{r})|^2$, assuming the field maximum to be concentrated in the high index material. This is guaranteed by the variational theorem (c.f. section 5.1.1). The terms $R_\lambda = (1 + 4Q^2(\frac{\omega_0}{\omega_{\text{cav}}} - 1)^2)^{-1}$ and $R_r = |\vec{E}(\vec{r}_0)|^2/\max|\vec{E}(\vec{r})|^2$ account for the spectral and spatial misalignment of the emitter at position $\vec{r}_0$ with respect to the maximum of the cavity electric field, whereas the factor $R_d = |\langle \vec{e}_d \cdot \vec{e}_E \rangle|^2$ considers the orientation of the emitter's dipole moment with respect to the polarization of the resonant electric field. Please note that we here suggested an atomic linewidth being much narrower than the cavity linewidth. For an emitter spectrally and spatially aligned with the cavity mode and with a dipole moment parallel to the electric field, we obtain the ideal Purcell factor F_P [56]:

$$F_P = \frac{3}{4\pi^2}\frac{Q}{V}\left(\frac{\lambda}{n}\right)^3. \tag{5.64}$$

The ideal Purcell factor is the important figure of merit to compare theoretical predictions of different cavity designs or to evaluate the maximum enhancement of the spontaneous emission rate. However, in the experiments, non-ideal contributions R_λ, R_r, R_d have to be necessarily taken into account to correctly determine the cavity coupling strength. In the experimental chapters 7 and 9, we will widely use equation (5.63) to appropriately evaluate the enhancement of the spontaneous emission rate of an ensemble and single SiV centers via cavity-coupling to a photonic cavity mode. Please note that we here assumed the linewidth of the emitter to be much smaller than the cavity mode. In the case of narrow-band emission of single SiV centers, this condition is fulfilled. However, for broad-band NV centers, the assumption of an atomic-like transition does not hold any longer. In chapter 8, we present an extended model of a generalized Purcell factor that appropriately describes cavity-coupling to broad-band emitters.

Most commonly, we are not interested in absolute values but rather in the relative increase or decrease of the spontaneous emission rate. To compute Purcell enhancement, we therefore typically perform two simulations, the first one with the dipole source placed in the photonic lattice and the second one with the same source hosted in a homogeneous diamond slab and divide the two results. In this work, we focus on color centers in diamond as single emitter within the photonic structures. These solid state emitter are naturally hosted in diamond material. Therefore, in accordance with the experiments, we solely consider point-dipole sources in our simulations that are situated in dielectric material. In that case, the contribution of the dielectric function in equation (5.45) cancels when evaluating the relative modification of the local density of states. This enables us to easily relate the four essential quantities governing light emission in periodic crystals as well as in cavity structures:

$$\frac{LDOS}{LDOS_0} = \frac{P}{P_0} = \frac{\gamma}{\gamma_0} = F_{\text{cav}}. \tag{5.65}$$

In the following section 5.4, we will use this relationship to compute the Purcell factor as well as the local density of states of the photonic crystal lattice.

5.4 Photonic band structure

In this section, we compute the photonic band structure by numerically solving eigenequation (5.24) of the electromagnetic fields derived in paragraph 5.2. Section 5.4.1 refers to purely two-dimensional systems with no extend in the vertical direction, whereas in section 5.4.2, we include a finite slab thickness in our simulations. From the two-dimensional computations, we derive essential properties like a vanishing density of states in a certain frequency range, referred as the *photonic band gap*. Light with frequencies inside the band gap is hindered to propagate through the periodic material but is reflected. Thereby, the band gap effect enables the realization of highly-reflective mirrors and tiny cavity structures in photonic crystals.

The appearance and the width of the photonic band gap depend on several material and geometrical parameters such as the refractive index contrast, the lattice type and the

hole or rod radius as well as on the polarization of light. We discuss the impact of these parameters on the band structure and derive an optimal lattice geometry consisting of a triangular arrangement of air holes in diamond. We elucidate the physical origin for the appearance of a photonic frequency gap based on the variational principle and the classification in TE- and TM-modes. Although fundamental properties could be derived from a purely two-dimensional system, the third dimension has to be necessarily taken into account when considering experimental structures. We investigate the impact of a finite slab thickness and present an extended band diagram that accounts for wave vector components radiating in the surrounding air by introducing the so called *light cone*. Moreover, the finite height entails a modified classification of the polarization, as well as a non-zero local density of states depending on both position and polarization of the emitter.

5.4.1 Band structure of a two-dimensional photonic crystal

In this section, we investigate the photonic band structure of a two-dimensional photonic crystal with a discrete translational symmetry in the (x, y) plane and no or equivalently infinite extend in the z-direction. The purely two-dimensional definition is equivalent to a continuous translational symmetry with infinite size in z-direction.

Various two-dimensional photonic crystals of different lattice types ranging from a triangular arrangement of air holes to a square lattice of dielectric rods of diverse sizes and shapes have been theoretically investigated and experimentally fabricated in high and low-ε materials in the past decades. Before, we start our analysis and simulations of photonic band structures, we would like to specify the material and geometrical properties, we will focus on throughout this work.

In general, the higher the refractive index contrast of the photonic crystal structure, the larger the width of the photonic band gap can be. For two-dimensional photonic crystals realized in silicon or gallium arsenide with refractive indices of $n = 3.4$ and $n = 3.5$, large gap widths have been predicted for only one specific polarization of light [256] as well as for all polarization of light [271, 272]. Photonic crystals realized in silicon, gallium or aluminum arsenide are well suited to control the transition rate of quantum dots [109, 110, 267, 273] with emission wavelengths in the infrared spectral range where these semiconductor materials are transparent. In this work, in contrast, we focus on photonic crystals directly fabricated in a diamond membrane, that enable efficient coupling to optically active color centers incorporated or implanted into the diamond. Therefore, all simulations in this work are performed for a refractive index of $n = 2.4$ of bulk diamond. As diamond is transparent for light ranging from the UV to infrared spectral range, we here assume a real-valued dielectric constant. In section 6.5, we will discuss the impact of material absorption on the performances of our fabricated structures. To this end, we will include absorption losses in our simulations by implementing a complex dielectric function, where the imaginary part determines the absorption coefficient of the diamond material. Details on these simulations can also be found in our publication [274].

In addition to the refractive index contrast, the lattice type has a substantial impact

on the appearance of a photonic band gap. In previous work [275], several lattice types like square and triangular lattices of air holes in diamond have been investigated. The largest band gap is achieved for a triangular arrangement of air holes in diamond. Hence, in this work, we will focus on this specific lattice type.

For a triangular lattice of air holes, the hole size has a strong impact on the width of the frequency gap. The impact of the hole radius will be simulated and discussed in this section.

Besides the material and geometrical parameters, the appearance of a photonic band gap depends on the polarization of light propagating through the periodic material. We will investigated the physical origin of the band gap by analyzing the electric field energy distribution both for TE- and TM-polarized light in high- and low-index materials.

The photonic band gap

To solve the eigenvalue problem (5.24) and to calculate the photonic band structure, we use the freely available software package *MIT Photonic-Bands* (*mpb*) [259, 260] based on a plane wave expansion method (for details see section 5.7.1). In figure 5.3(a), the eigenfrequencies of the two-dimensional air hole lattice in diamond are plotted as a function of the wave vectors $\vec{k}$ along the edge of the irreducible Brillouin zone connecting the points Γ, M, K to Γ (see inset). The radius of the air holes is chosen to be $R = 0.28\,a$ according to our publication [274] yielding optimal light confinement within the smallest photonic crystal cavity realized in diamond. Here, a is the lattice constant. According to the symmetry with respect to the (x, y)-plane, the calculated modes are classified as transverse electric (TE) and transverse magnetic (TM) modes (c.f. page 77 in section 5.2) and the eigenfrequencies are calculated independently for each polarization. In the case of TE-modes, a frequency gap is observed between the first ($m = 1$) and second order ($m = 2$) band marked by the yellow shaded region in figure 5.3(a). This means that regardless of the wave vector $\vec{k}$, no eigenfrequency is found in the range of $\omega \in [0.292, 0.343] \times 2\pi c/a$. This frequency gap is called the *photonic band gap*.

To better understand the physical meaning of the frequency gap, we simulate the projected local density of states. To this end, we insert a dipole source at the center of the photonic crystal unit cell with either transverse electric or magnetic polarization. For detection, we define a box surrounding the photonic crystal lattice and calculate the Fourier transform of the radiated electromagnetic fields detected at the box surface (c.f. eq. (5.46) in section 5.3). The obtained total radiated power is normalized it to the bulk value. Figure 5.3(b) shows the TE and TM density of states of a two-dimensional photonic crystal. Over the whole frequency range, the local density of states is drastically altered compared to its value in a homogenous medium. For a TE-polarized source, the density of states vanishes for frequencies inside the band gap. Hence, there are no states, supported by the geometry, in the frequency range $\omega \in [0.292, 0.343] \times 2\pi c/a$. In contrast, in the case of a TM-polarized mode, the density of states exhibits a finite value in the considered frequency range. Due to the absence of any states in the TE band gap, an atom, with its electric dipole moment oriented in the plane of the photonic lattice, can not emit any photons as there are no Bloch modes in

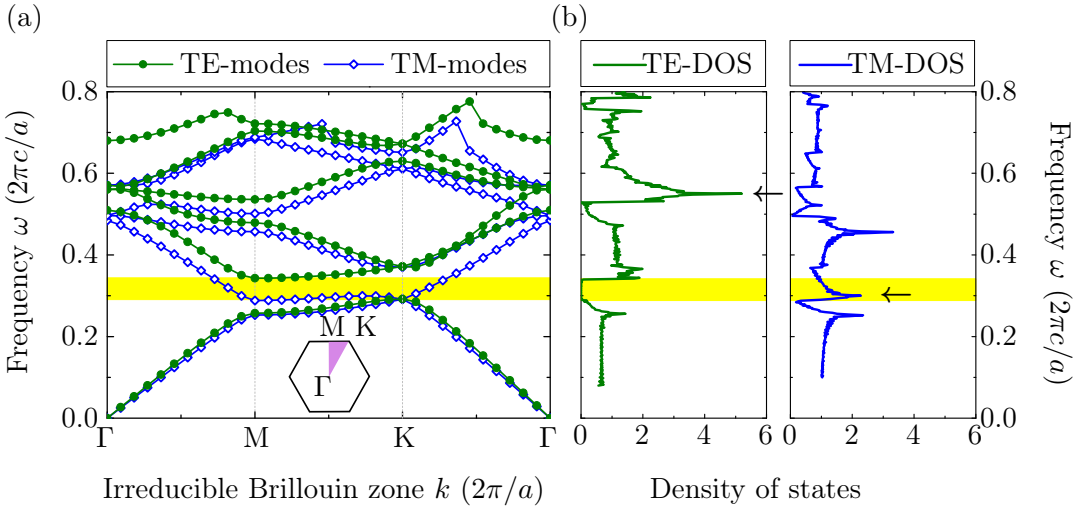

Figure 5.3: Photonic band structure and density of states of a two-dimensional triangular photonic lattice of air holes in diamond: (a) The band diagram of TE- and TM-modes is calculated for wave vectors $\vec{k}$ along the edge of the irreducible Brillouin zone connecting the points Γ, M, K, Γ. For TE-modes a band gap (yellow region) appears between the first and second band. (b) Density of states calculated for a dipole source with either TE- or TM-polarization hosted at the center of the photonic crystal. The density of states has been normalized to the value for homogenous material.

this frequency range to which it can couple. Hence, the spontaneous emission rate of the atom is strongly inhibited. In contrast, if its dipole moment is oriented perpendicular to the crystal, photons can be emitted into Bloch modes of the photonic crystal due to the finite density of states for TM-modes.

In the classical picture, a vanishing density of states implicates that light with frequencies inside the band gap can not propagate through the material but is reflected. The refractive index contrast between the diamond material and the air holes leads to distributed Bragg reflections at the hole edges. Plane waves with frequencies in the band gap interfere destructively such that no light can be transmitted through the material but is completely reflected. Hence, independent on the propagation direction, the photonic crystal acts as a frequency-specific and polarization-specific highly-reflective mirror for light with frequencies in the photonic band gap. This essential property enables the realization of tiny nano-cavities within photonic lattices (c.f. section 5.5).

Before we proceed with the explanation of the physical origin of the band gap, we would like to discuss two peculiarities of the density of optical states of a two-dimensional photonic crystal. Besides the frequencies inside the band gap, we observe several singularities in the local density of states, whenever a cutoff frequency is approached (or in general, at points of zero group velocity $d\omega/dk = 0$). For example, at the band edge or at a frequency of $\omega = 0.558 \times 2\pi c/a$ (marked by small arrows in Fig. 5.3(b)), the TE density of states in figure 5.3(b) is significantly increased compared to the bulk quantity.

These singularities are known from solid state physics as *Van Hove singularities* [276]. When an atom, with a transition frequency equal to a cutoff frequency, is placed in the photonic lattice, its spontaneous emission rate can be strongly enhanced. Moreover, these phenomena have been exploited in the realization of distributed feed back lasers in photonic crystal material [277].

Please note that in the above discussion, the terms "local density of states" and "density of states" have be used as synonyms. Indeed, in the case of a two-dimensional photonic crystal, infinitely extending in the (x, y) plane, the local density of states is independent of the position of the emitter [278–280]. Hence, for a fixed polarization, the local density of states equals the total density of states. Therefore, it is valid to use both terms equivalently. However, the situation is totally different for photonic crystal structures with a finite extend in one or several spatial directions. In that case, the position of the emitter within the lattice is crucial and we necessarily have to focus on the local density of states to appropriately describe the spontaneous emission by an atom.

Physical origin of the photonic band gap

To understand the physical origin of the photonic band gap (c.f. Fig 5.4(a)), we consider the electric field energy $\varepsilon|\vec{E}|^2$ distribution of the states $m = 1$ and $m = 2$ immediately above and below the band gap. According to the electromagnetic variational theorem as discussed in section 5.1.1, low-frequency modes concentrate their electric field energy in high-ε material. The frequency is increased if the electric fields are located in low-ε material, i.e. air. To quantify the degree of concentration of electric fields in high-index material, we define the concentration factor:

$$\text{concentration factor} = \frac{\int_{\text{dia}} \varepsilon(\vec{r})\,|\vec{E}(\vec{r})|^2\,d^3r}{\int \varepsilon(\vec{r})\,|\vec{E}(\vec{r})|^2\,d^3r}. \tag{5.66}$$

The integral in the numerator is restricted to high index material, i.e. diamond, whereas the integral in the denominator is defined over the whole unit cell. The first order TE-like mode $m = 1$ concentrates 96% of its electric field energy in regions of high dielectric constant, i.e. in diamond. Energetically favorable, this results in a low frequency of the fundamental mode. In contrast, as the next order mode $m = 2$ is orthogonal with respect to the first order mode, its electric field expends to low-index material, i.e. air holes (Fig. 5.4(b)), and only 72% of the electric field energy is still concentrated in diamond. Thus, the mode energy is significantly enhanced yielding to a higher frequency. The difference in frequency of the two modes induced by the energy concentration in high and low-index regions gives rise to the photonic band gap. As the electric field energy of the band below the photonic frequency gap is mainly concentrated in dielectric material, it is often referred to as the *dielectric band* or *valence band*. On the other hand, the band above the frequency gap is called the *air band* or *conduction band* as its electric field energy is mainly localized within the air holes. The terms "valence band" and "conduction band" are chosen analogous to the electronic band structure of semiconductors.

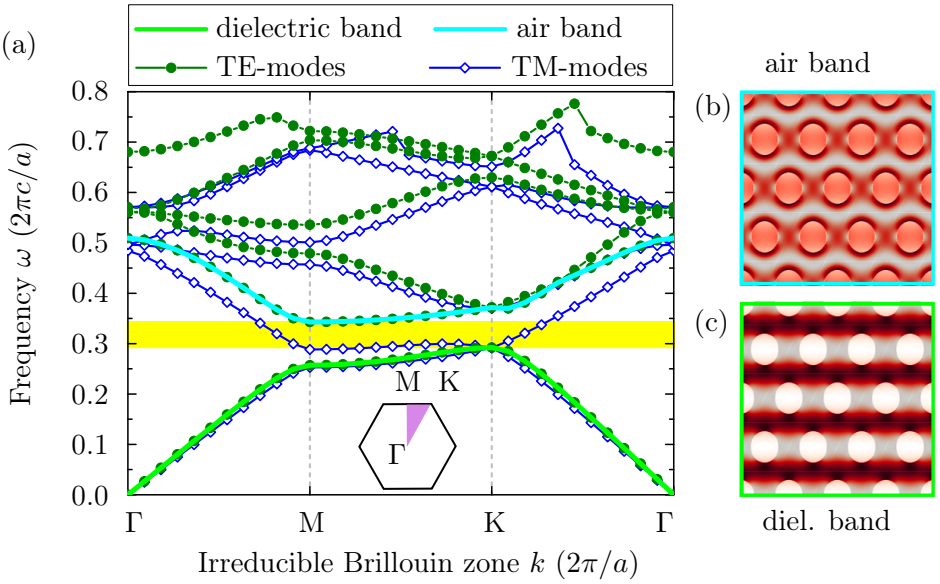

Figure 5.4: Band structure of a two-dimensional triangular photonic crystal in diamond: (a) The band diagram of TE- and TM-modes. The first and second TE-band below and above the frequency gap (yellow region) are denoted dielectric and air band, respectively. (b,c) Electric field energy $\varepsilon|\vec{E}|^2$ calculated at the M-point of the (b) air and (c) dielectric band. Color scale: gray: diamond, white: air holes and red: high electric field energy. In the simulations, an air hole radius of $R = 0.28\,a$ is assumed.

In figure 5.4(a), it can be seen that the band structures of TE- and TM-modes are very different. There is a band gap for TE-modes but not for TM-modes. The reason is the discontinuous behavior of electromagnetic fields at material interfaces. When the fields cross a dielectric boundary, the electric field energy density $\varepsilon|\vec{E}|^2$ will decrease or increase discontinuously depending on the polarization of the electric field vector. In the case of TE-modes, the electric field lines are in plane and can be concentrated in the dielectric material between the air holes without passing dielectric interfaces. Hence, a high concentration of the electric energy density in the dielectric material is possible, giving rise to a large band gap. On the other hand, the electric field lines of TM-modes point in the vertical direction and do not necessarily cross the dielectric boundaries. Hence, the electric energy density of both the dielectric (concentration factor: 98%) and air band (concentration factor: 93%) are mainly localized in high dielectric regions leading to comparable frequencies. As the frequency does not significantly change from one band to the other the appearance of a band gap is hindered. In general, one could say, that TM band gaps are favored in a lattice of isolated high-ε regions, and TE band gaps are favored in a connected lattice. Sophisticated designs have been proposed for two-dimensional photonic crystals enabling the simultaneous appearance of frequency gaps for TE- and TM-modes [281–285]. However, all simulations have been performed for high index materials such as silicon or gallium arsenide and can not easily be applied

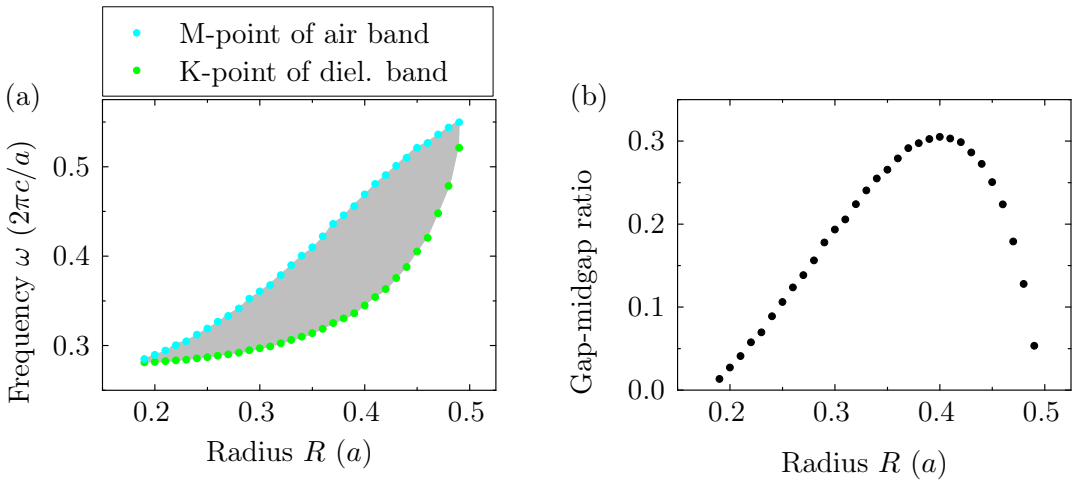

Figure 5.5: Gap map and gap-midgap ratio of a triangular photonic lattice of air holes in diamond: (a) Gap map: The lower (●) and upper bound (●) of the photonic band gap calculated at the K- and M-point of the dielectric and air band, respectively, are plotted as a function of the hole radius R of the photonic structure. (b) Gap-midgap ratio: The width of the band gap normalized to the central frequency of the band gap in dependence of the radius R.

to diamond. Moreover, most of the proposed designs exhibit complete band gaps only between higher order frequency bands which is not favorable for the realization of cavity structures.

Impact of the air hole radius R on the band gap

The extend of the photonic band gap can be characterized by the *gap-midgap ratio* which is given by the frequency width normalized to the frequency at the gap center. We will use the defined gap-midgap ratio in the following to investigate the dependence of the photonic band gap on the hole radius R of a two-dimensional triangular arrangement of air holes in diamond. The simulations to calculate the band structure are two-dimensional. Please note that the gap-midgap ratio is size independent. If the system is scaled up or down, all frequencies are scaled accordingly as discussed in section 5.1.2 but the gap-midgap ratio remains the same. For every hole radius R, the upper and lower bounds of the photonic band gap are extracted from the band structure calculated for TE-modes at the K and M points of the irreducible Brillouin zone. The boundary values plotted as a function of the radius R is called the *gap map* of the photonic structure shown in figure 5.5(a). Additionally, the gap-midgap ratio of the photonic band gap in dependence of the air hole radius R is displayed in figure 5.5(b). At small radii of $R = 0.2\,a$ a band gap for TE-modes start to appear in the band structure between the first and second order band. With increasing radii the band gap shifts to higher frequencies and widens until the maximal gap-midgap ratio of 0.3 is achieved at a radius of $R = 0.4\,a$. Larger air holes have a strong impact on the frequency of the air band with its energy

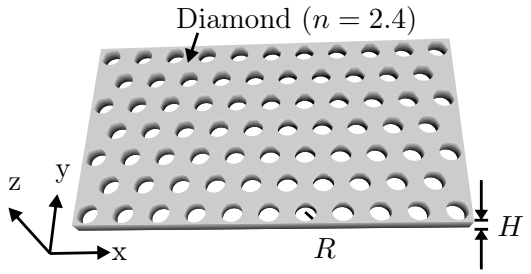

Figure 5.6: Schematic of a photonic crystal slab consisting of a triangular lattice of air holes with radius R in the horizontal (x, y)-plane and a finite thickness H in the vertical z-direction.

density mainly localized in the air holes. For radii exceeding $0.4\,a$ the width of the band gap significantly decreases. For large radii the connected dielectric material regions become very narrow which significantly influences the dielectric band increasing strongly in frequency and closing the band gap. In practice, fabricated photonic crystal structures are not purely two-dimensional but have a finite extend in the vertical direction. For lattices with a finite thickness, smaller radii are often favorable as besides the gap size radiation losses into the surrounding medium must be taken into account.

Most of the studies on two-dimensional photonic lattices have been performed for round air holes. Indeed, the size of the band gap depends on the hole shape. However, a round shape of the air holes is not a prerequisite for the appearance of a photonic band gap. In literature, various other geometries ranging from triangular [286] to hexagonal holes [287] have been studied for triangular lattices. For square lattices, even more fancy air hole designs have been simulated yielding large band gaps [288].

5.4.2 Band structure of a photonic crystal slab

In the previous section, we already derived essential properties of photonic band diagrams, e.g. the appearance of a frequency gap, from a purely two-dimensional analysis. However, to appropriately describe the behavior of fabricated structures, the third dimension has to be included in our calculation. The introduction of the vertical direction implicates a qualitatively new behavior for the guidance and confinement of modes in a photonic crystal, that will be addressed in the following.

Three-dimensional photonic crystals with a complete band gap enable perfect reflection of light irrespective of its propagation direction and its polarization. This is essential for the realization of highly reflective mirrors or microcavities with ultra long storage times as the light can be localized in all three dimensions. However, in practice, the fabrication of three-dimensional photonic crystal structures is challenging especially in diamond. An alternative approach is to use two-dimensional *photonic crystal slab* structures with a periodic arrangement of air holes of radius R in the horizontal (x, y)-plane and a finite slab thickness H in the vertical z-direction (Fig. 5.6). Planar photonic crystal slabs combine two advantages of a technically feasible fabrication and light localization in three dimensions. In the horizontal plane, light is confined due to the photonic band gap effect, whereas in the vertical direction it is guided in the slab by total internal reflection. However, the confinement due to total internal reflection is not perfect but some part of the light is radiated out of the slab. We introduce an expended

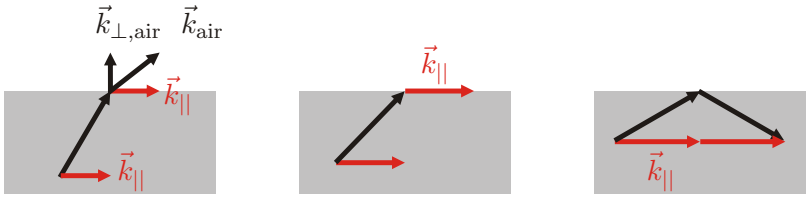

Light cone	Light line	Guided modes
$\lvert\vec{k}_{\parallel}\rvert < \omega/c$	$\lvert\vec{k}_{\parallel}\rvert = \omega/c$	$\lvert\vec{k}_{\parallel}\rvert > \omega/c$

Figure 5.7: Illustration of guided and leaky modes: Depending on the in-plane wave vector $\vec{k}_{||}$, light is radiated in the surrounding air according to Snell's law for $|\vec{k}_{||}| < \omega/c$, propagates parallel to the air diamond interface for $|\vec{k}_{||}| = \omega/c$ (light line) or is guided in the diamond slab for $|\vec{k}_{||}| > \omega/c$.

concept of the photonic band structure that takes into account the leaky components as well as the surrounding material. Moreover, the finite thickness demands a more general classification of the modes with respect to their mirror symmetry in the (x, y)-plane. Finally, we will study the impact of the slab thickness on the width of the band gap.

Light cone

Light in a two-dimensional photonic crystal slab suspended in air can be localized due to the band gap effect in the horizontal plane and by *index guiding*, a generalization of total internal reflection, in the vertical direction. However, the localization in the vertical direction is not perfect. A fraction of light escapes out of the slab according to Snell's law and is radiated into the environment. The other part is confined in the slab by total internal reflection due to the higher refractive index of diamond compared to the surrounding air. All modes confined in the slab decay exponentially in air. The two cases can be distinguished on the basis of the in-plane wave vector $\vec{k}_{||}$ of the light. The key fact is that $\vec{k}_{||}$ is conserved at the diamond-air interface. By projecting every wave vector in the surrounding medium on its in-plane component, a map of radiated and confined states can be created referred to as the *projected band structure*. Before discussing in detail the band structure of a photonic crystal slab, we consider in the following three limiting cases for $\vec{k}_{||}$.

- **Leaky modes** $|\vec{k}_{||}| < \omega/c$: The modes, radiated out of the slab according to Snell's law and extended into air, resemble to free-space plane waves with a wave vector $\vec{k}_{\mathrm{air}} = \vec{k}_{||,\mathrm{air}} + \vec{k}_{\perp,\mathrm{air}}$ in air that is decomposed of an in-plane component $\vec{k}_{||,\mathrm{air}}$ parallel to the diamond-air interface and a perpendicular component $\vec{k}_{\perp,\mathrm{air}}$. The associated eigenfrequency $\omega = c|\vec{k}_{\mathrm{air}}|$ of the mode is given by:

$$\omega = c\sqrt{|\vec{k}_{||,\mathrm{air}}|^2 + |\vec{k}_{\perp,\mathrm{air}}|^2}, \tag{5.67}$$

  with c being the speed of light in air. According to Snell's law, the component $\vec{k}_{||}$ is

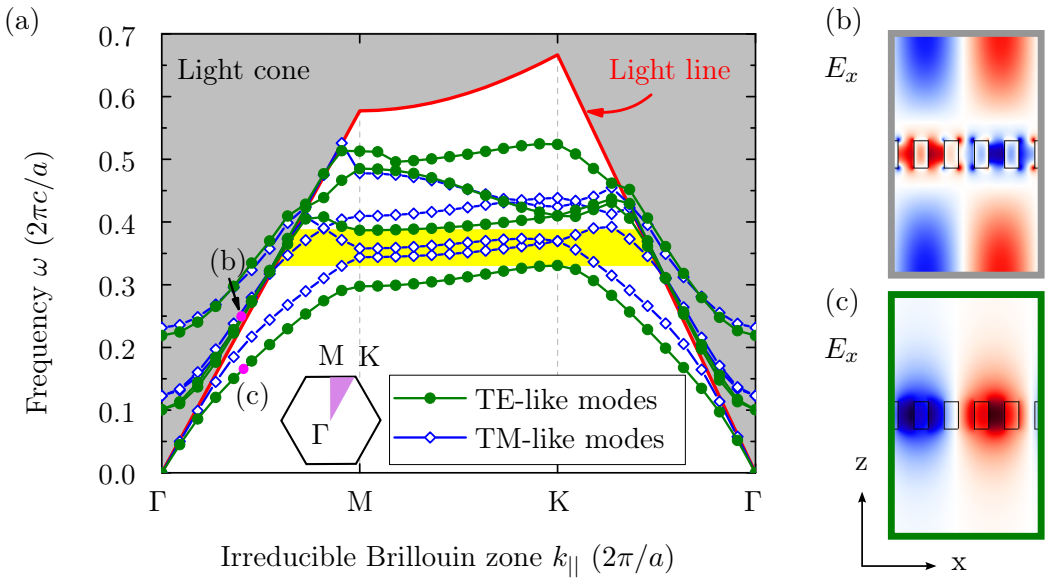

Figure 5.8: Band structure of a photonic crystal slab with finite height ($R = 0.28\,a$, $H = 0.91\,a$): (a) The TE- (green) and TM-like (blue) modes in the white region are confined in the photonic crystal slab, whereas the gray region indicates the light cone with the continuum of leaky modes. (b,c) Cross sections of the E_x component calculated for specific $(\omega, k_{||})$ indicated by points (b) and (c) in the band structure. (b) Leaky modes are radiated in the vertical direction, whereas (c) index guided modes are localized within the slab and exponentially decay in the surrounding air.

continuous at the air-diamond interface: $\vec{k}_{||,\text{air}} = \vec{k}_{||,\text{diamond}} = \vec{k}_{||}$. The modes that escape from the slab have a non-vanishing component $\vec{k}_{\perp,\text{diamond}} \geq 0$. Thus, for the eigenfrequency we obtain $\omega \geq c|\vec{k}_{||}|$. This relation defines the *light cone*, gray shaded region in figure 5.8(a). The continuum of modes with wave vectors in the light cone are radiated into the surrounding. These modes are called *leaky modes*. The *projected band structure* enables to display the leaky modes as a function of the in-plane wave vector $\vec{k}_{||}$.

- **Light line** $|\vec{k}_{||}| = \omega/c$: The limiting case between radiated and guided modes is defined by the relation $|\vec{k}_{||}| = \omega/c$, referred to as the *light line* in the projected band structure (red line in Fig. 5.8(a)). As $|\vec{k}_{\perp,\text{air}}| = 0$, the modes, escaping from the slab with wave vectors defined by the light line, propagate parallel to the slab.

- **Guided modes** $|\vec{k}_{||}| > \omega/c$: For light impinging at a shallow angle of incidence on the interface the in-plane wave vector is $|\vec{k}_{||}| > \omega/c$. These modes are totally internally reflected at the interface and are confined in the slab via *index guiding*. Due to the localization of modes, we obtain discrete bands $\omega_m(|\vec{k}_{||}|)$ (white region in Fig. 5.8(a)) below the light line. The only solutions in air have a purely

imaginary wave vector component $\vec{k}_{\perp,\mathrm{air}} = \pm i\sqrt{k_{||}^2 - \omega^2/c^2}$, corresponding to fields that exponentially decay away from the slab. These modes are called *evanescent modes*.

Projected band structure

As an example, we calculate the eigenfrequencies of a triangular photonic crystal slab with an air hole radius of $R = 0.28\,a$ and a slab thickness of $h = 0.91\,a$ as a function of the in-plane wave vector $\vec{k}_{||}$ along the edge of the irreducible Brillouin zone comprising the Γ, M, K-points. The resulting projected band structure is shown in figure 5.8(a). The gray region marks the light cone of all leaky modes whereas the white region defines all index-guided modes confined within the slab. The two cases are separated by the light line shown in red. Figures 5.8(b,c) show vertical cross section of the E_x field distributions in the slab and the surrounding air. In the case of leaky modes, most of the light escapes from the slab and is radiated in the vertical direction (Fig. 5.8(b)). In contrast, the E_x field of a guided mode is localized within the slab and exponentially decays in the surrounding air (Fig. 5.8(c)). Below the light line, the calculated eigenfrequencies form a set of discrete bands whose associated modes are distinguished according to their mirror symmetry in the (x, y)-plane. Odd modes are called *TE-like* modes, whereas even modes are referred to as *TM-like* modes. The nomenclature is based on the classification in TE- and TM-polarization introduced by equation (5.30) in section 5.2 for two-dimensional photonic crystals. The separation of modes upon reflection in the (x, y)-plane is discussed in more detail in the next section. In the band diagram, we observe a photonic band gap for TE-like modes with a lower bound at $\omega = 0.3307 \times 2\pi c/a$ determined at the K-point of the irreducible Brillouin zone and an upper bound at $\omega = 0.3868 \times 2\pi c/a$ calculated at the M-point. For TM-like modes no band gap is observed. In contrast to the band structure of a two-dimensional photonic crystal, the band gap does not extend across all in-plane wave vectors but is limited to frequencies below the light line. However, the incomplete band gap is still suitable for the realization of highly reflective in-plane mirrors and cavity structures to confine light in tiny small volumes (see section 5.5).

TE- and TM-like modes

Due to the finite slab thickness the modes can no longer be distinguished in purely TE and TM polarization which is only valid in the case of two-dimensional photonic crystals (c.f. page 77 in section 5.2) or equivalently photonic crystal slabs with an infinite slab thickness in the z-direction. However, the modes confined in a photonic crystal slab can still be separated in *even* and *odd* modes according to their reflection symmetry with respect to the (x, y) mirror plane. Figure 5.9 shows electromagnetic field components calculated in a vertical cross section of the slab and the surrounding air. In the case of odd modes, the E_z, H_x and H_y components cancel out at the slab center ($z = 0$), whereas for even modes, the E_x, E_y and H_z fields vanish in the middle of the slab. The reason is that at the slab center the condition $M_z\vec{k} = \vec{k}$ defined on page 77 in section

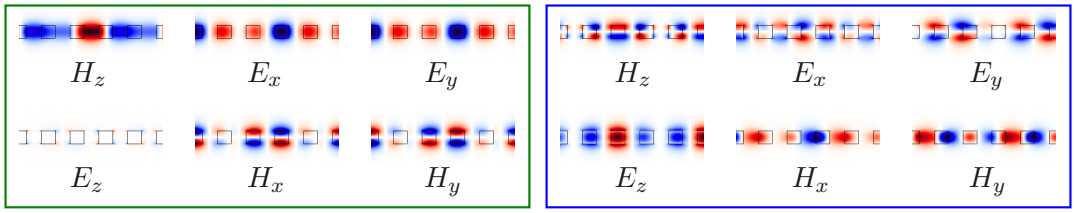

(a) TE-like mode (b) TM-like mode

Figure 5.9: Cross section of the electromagnetic field components of TE- and TM-like guided modes: (a) For TE-like modes the H_z, E_x, E_y components have an antinode at the slab center, whereas the E_z, H_x, H_y components vanish at $z = 0$. (b) For TM-like modes it is vice versa: H_z, E_x, E_y have a node at the slab center, whereas E_z, H_x, H_y show an antinode. The vertical direction in the pictures defines the z-axis.

5.2 is still fulfilled for $k_z = 0$ and hence odd modes show a TE-like polarization and even modes are TM-like at $z = 0$. In section 5.7.3, we will see that the cancellation of specific field components has major consequences on the polarization of even (odd) modes in the far field yielding linear polarized emission along the y- (x-) direction.

Impact of the slab thickness

The slab thickness has a major impact on the existence of a photonic band gap for its guided modes. Figure 5.10 shows the gap map and gap-midgap ratio as a function of the slab height H calculated for a triangular photonic crystal slab with air hole radii of $R = 0.28\,a$. If the slab is too thin, the dielectric and air band are only weakly guided, exhibiting high frequencies just below and close to the light line and only a small frequency gap opens between these states (Fig. 5.10). With increasing thickness, the band gap is shifted to smaller frequencies and the gap-midgap ratio reaches a constant level of 16% for heights between $H = 0.9\,a - 1.8\,a$. If the slab is too thick ($H > 1.8\,a$), higher order modes with additional horizontal nodal planes (inset in Fig. 5.10(b)) enter the band gap. The upper bound of the gap abruptly drops yielding a drastic decrease in the gap size.

The largest band gap is expected to be obtained when the thickness equals half the wavelength in matter [289]: $H_{\text{opt}} = \lambda/2\sqrt{\varepsilon_{\text{eff}}} = a/2\omega\sqrt{\varepsilon_{\text{eff}}}$, with $\omega = a/\lambda$ and ε_{eff} being the effective dielectric constant. If the thickness is much smaller than H_{opt} light is only weakly confined. If the thickness exceeds one wavelength, higher order modes are easily created via additional nodal planes. The wavelength mentioned here refers to the wavelength in an effective dielectric medium given by the dielectric function $\varepsilon(\vec{r})$ weighted by the electromagnetic fields. The effective dielectric constant ε_{eff} strongly depends on the polarization of the mode. TE-like modes are mainly localized in high dielectric material, whereas TM-like modes are mostly concentrated in low index material. For TE-like modes the dielectric function is weighted with the electric field confined in the

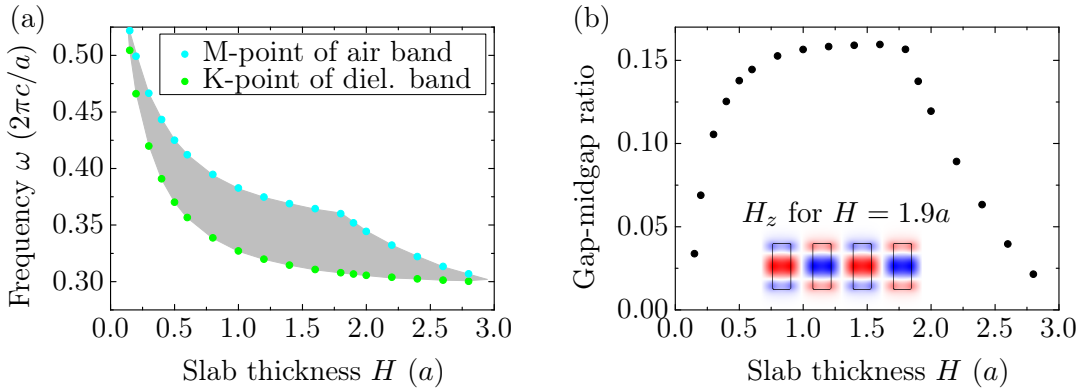

Figure 5.10: Gap map and gap-midgap ratio as a function of the slab thickness H calculated for a triangular photonic crystal slab of air holes ($R = 0.28\,a$) in diamond: (a) Gap map: The lower and upper bound of the photonic band gap are calculated at the K- and M-point of the dielectric and air band, respectively. (b) Gap-midgap ratio: The width of the band gap normalized to the central frequency is almost constant for slab thicknesses between $H = 0.9\,a - 1.8\,a$. For large heights $H > 1.8\,a$, the gap size abruptly decreases due to the creation of higher order modes with additional horizontal nodal planes that enter the frequency gap. The inset shows the vertical cross section of the H_z component calculated at the M-point of the air band for $H = 1.9\,a$.

slab [289]:

$$\varepsilon_{\text{eff}}^{\text{TE}} = \frac{\int_{\text{slab}} \varepsilon(\vec{r})|\vec{E}(\vec{r})|^2 d^3r}{\int_{\text{slab}} |\vec{E}(\vec{r})|^2 d^3r}. \tag{5.68}$$

Using the electric field distribution of the fundamental mode calculated at the K-point of the irreducible Brillouin zone for a triangular photonic crystal in diamond ($R = 0.28\,a$, $\omega = 0.3307 \times 2\pi c/a$), we obtain an effective dielectric constant of $\varepsilon_{\text{eff}}^{\text{TE}} = 5.27$. This value is slightly smaller than the dielectric constant $\varepsilon = 5.76$ of bulk diamond. Taking into account the effective dielectric constant, we obtain an optimal slab thickness of $H_{\text{opt}} = 0.8\,a$, which is in the range of constant gap size. It should be noted that the size of the band gap is an important criteria for the choice of the slab thickness. However, depending on the application, additional factors have to be considered. For example, for the localization of light in a cavity, it might be suitable to apply a slightly larger slab thickness in order to obtain longer cavity decay times (see section 5.5.2). Therefore, it is often better to optimize the parameters such as the slab thickness and the air hole radii based on the actual structure of interest, rather than indirectly by increasing the gap size. However, the thickness calculated by the effective dielectric constant is a good starting point for the fine-tuning process.

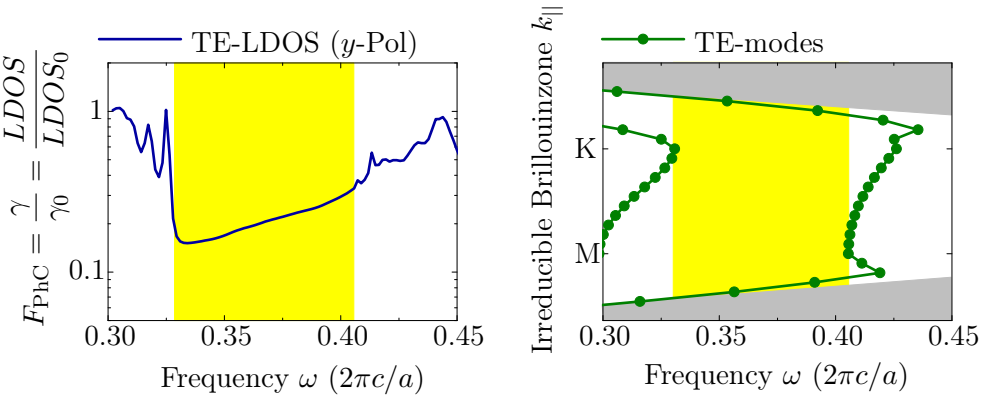

Figure 5.11: (a) Purcell factor F_{PhC} and local density of states as a function of the frequency calculated for a y-polarized TE-dipole source at the center of a photonic crystal slab. The data are normalized by the result of a homogeneous diamond slab (subscript 0). (b) Band diagram for TE-like modes. Yellow region marks the band gap. Simulation parameters: $R = 0.31\,a$, $H = 1.1\,a$, lattice size 16×11 air holes.

LDOS and Purcell factor of the finite photonic crystal slab

In section 5.4, we have seen that the appearance of a photonic band gap implicates a vanishing local density of states. A current source placed within the periodic lattice would radiate zero power at any frequency within the stop band, since there are no modes to which it can couple. However, this observation is only valid for infinite periodic structures like purely two-dimensional photonic lattices with periodic boundary conditions. When passing to three-dimensional structures with a finite thickness surrounded by an air region or with a limited number of hole periods, the local density of states becomes nonzero in the band gap. This is attributed to the non-ideal confinement of light in the slab structure. The evanescent tail of the field produced by the dipole source leaks out of the photonic crystal and radiates into air. Hence, the fields emitted by the dipole source can couple to lossy components inside the light cone, which results in a nonzero density of states for frequencies in the band gap. In the following, we compute the local density of states and the spontaneous emission rate of an emitter placed in a photonic crystal slab using FDTD methods (c.f. section 5.7.2). Thereby, we profit from the proportionality relation (5.65) between LDOS, γ and the power radiated by a dipole source. To characterize the change in the spontaneous emission rate, we define the *Purcell factor of the photonic crystal lattice* $F_{\mathrm{PhC}} = \gamma/\gamma_0$, where γ_0 denotes the decay rate in a homogeneous diamond membrane. In our simulations, we insert a dipole source with electric transverse y-polarization at the center of the photonic lattice and detect the radiated power P passing through six faces of a virtual box comprising the photonic structure and the source (c.f. Fig. 5.40(a) in section 5.7.3). For normalization, the reference power P_0 is computed by rerunning the simulation with the dipole source hosted in a homogeneous diamond slab instead of the photonic crystal structure. The obtained normalized power P/P_0 equals the modification of the local density of states $LDOS/LDOS_0$ and the spontaneous emission rate γ/γ_0. Figure 5.11(a) shows the LDOS spectrum com-

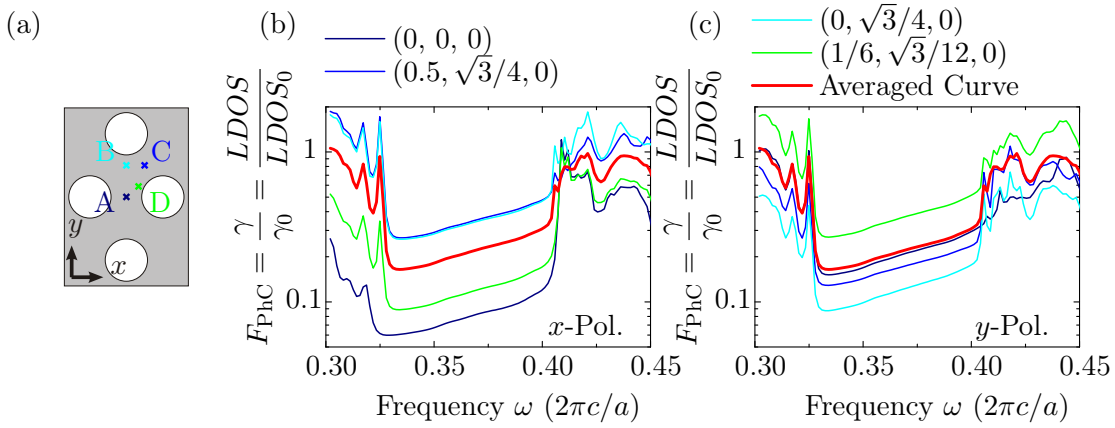

Figure 5.12: The spontaneous emission rate, normalized by that of a homogeneous diamond slab, as a function of frequency for (a) various dipole positions *A*-*D* in the photonic lattice: (b) x-polarized dipole and (c) y-polarized dipole.

puted for a photonic crystal diamond slab with hole radii $R = 0.31\,a$ and a thickness of $H = 1.1\,a$. The lattice has a finite extend in the (x, y)-plane consisting of 16×11 lines of air holes. For comparison, the first and second TE-like bands are displayed in figure 5.11(b) with the frequency gap marked by the yellow region. For frequencies within the band gap, the local density of states is significantly diminished compared to the bulk value and consequently, the spontaneous emission rate of a single color center placed within the photonic crystal is strongly inhibited by the Purcell factor F_{PhC}. However, compared to an ideal two-dimensional cyrstal with infinite extend in the (x, y)-plane, the LDOS spectrum of a photonic crystal slab does not vanish in the stop band. Due to the finite extend of the crystal slab, the dipole emission can couple to leaky components within the light cone resulting in vertical radiation losses and in a nonzero LDOS.

In the experiment, the exact position of a single color center might deviate from the origin of the unit cell and the orientation of its dipole moment might vary between different fabricated photonic crystal structures. Therefore, as a next step, we investigate the dependence of the LDOS on the position within the crystal unit cell and on the polarization properties of the emitter. Figure 5.12(b,c) shows the normalized radiated power emitted by a transverse electric dipole source polarized along the x- or y-direction and placed at four different positions A, B, C, D (Fig. 5.12(a)) [268] within the periodic photonic crystal lattice of radius $R = 0.31\,a$ and a thickness $H = 1.1\,a$. If the emitter is placed at the origin $(0, 0, 0)$ with its dipole moment polarized along the x-axis, its spontaneous emission rate is significantly decreased compared to the bulk value by a factor of $F_{\mathrm{PhC},x} = 0.09$ at a frequency $\omega = 0.375 \times 2\pi c/a$, whereas for y-polarization, we obtain $F_{\mathrm{PhC},y} = 0.22$. In contrast, when the dipole source is slightly displaced along the y-axis at $(0, \sqrt{3}/4, 0)$, the inhibition factor of x-polarized light is $F_{\mathrm{PhC},x} = 0.36$ and for y-polarization, $F_{\mathrm{PhC},y} = 0.13$. For single color centers, the actual position within the unit cell and orientation of its dipole moment have an important impact on the LDOS and hence on the spontaneous emission rate.

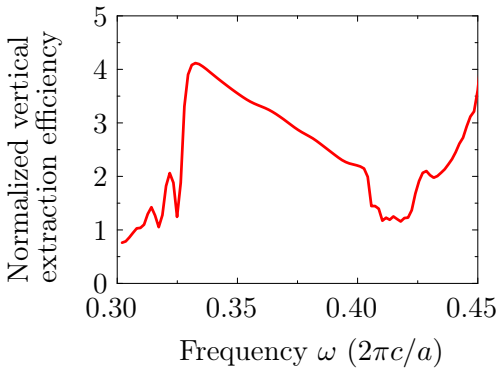

Figure 5.13: Vertical extraction efficiency as a function of frequency of a photonic crystal slab compared to a homogeneous diamond membrane. Due to the band gap effect, the in-plane light propagation is prohibited and the emission is channeled into the vertical direction.

In contrast, in the case of large ensembles of color centers centers with different dipole orientations hosted within the photonic crystal, it is more convenient to calculate an averaged Purcell factor (red curve in Fig. 5.12(b,c)). Averaged over all four positions and dipole orientations, we obtain an inhibition factor of the photonic crystal lattice $F_{\mathrm{PhC}} = 0.23$ at a frequency of $\omega = 0.375 \times 2\pi c/a$. This value slightly varies with frequency. For example, at $\omega = 0.380 \times 2\pi c/a$, the Purcell factor is $F_{\mathrm{PhC}} = 0.25$. In our calculations, we assumed a perfect dipole source which undergoes solely radiative transitions. However, in the experiment, non-radiative transitions of the emitter play a substantial role that might limit the achievable Purcell-factor. In chapter 9, we will see that inhibition of the spontaneous emission rate can be observed for single color centers when placed in a two-dimensional photonic crystal slab.

Besides the suppression of the spontaneous emission rate, the structuring of a photonic crystal lattice in a slab has a second effect: efficient light extraction in the vertical direction. The photonic band gap effect prohibits propagation of light in the plane of the photonic crystal slab. Light originally distributed in the plane of the homogeneous diamond membrane is channeled in the vertical direction when the diamond slab is patterned with a photonic lattice of air holes [267, 268]. Hence, the out-of-plane extraction of light is expected to be much more efficient due to the photonic lattice. Using FDTD methods, we simulate the fraction P_z/P_{tot} of the vertically radiated power in relation to the total power P_{tot}. Figure 5.13 shows that the extraction efficiency of a photonic crystal slab is enhanced by a factor of two to four when normalizing it to the one of a homogeneous diamond slab. The enhancement of the vertical extraction efficiency is almost independent of the emitter's position within the crystal unit cell. In our experiments, we will see that the diamond background fluorescence on the photonic crystal structure is much more pronounced compared to the unstructured membrane. We attribute this increase to the intensified vertical emission at the periodic lattice.

5.5 Photonic crystal cavities and waveguides

The appearance of a frequency gap in the band diagram is the most important feature of photonic crystals. As explained above, the band gap effect forbids the propagation of light through the crystal as there are no states to which it can couple. In other words, the periodic structure acts as a frequency- and polarization-specific mirror based on distributed Bragg reflections at the edge of the air holes forming the lattice. This essential property can be exploited to guide or tightly localize light in defect structures within the photonic crystal lattice. By introducing a line or point defect in the periodic photonic lattice, e.g. by removing one line of holes or just a single hole, we create waveguides or cavities that are effectively surrounded by reflecting walls. The resulting localized modes associated to the waveguide or cavity structure form discrete states inside the band gap of the surrounding unperturbed crystal with their electromagnetic field distributions tightly confined to the defect region. The localization of light relies on distributed Bragg reflections in the horizontal plane and on index guiding in the vertical direction. In this section, we present different waveguide and cavity designs with mode frequencies inside the band gap. The field distributions of the guided and resonant modes as well as the cavity quality factors and mode volumes are computed using *finite-difference time-domain* simulations (*FDTD*, for details on the algorithm see section 5.7.2). Terminating a linear waveguide on both ends by highly reflective photonic lattices, large size cavities are created whose resonant frequency range and mode profiles strongly resemble to the original waveguide modes. We illustrate in detail the relation between linear and point defects in photonic crystals.

5.5.1 Waveguides: Line defects in photonic crystals

By introducing linear defects, e.g. by omitting a line of holes in the periodic lattice, low-loss nano-scale waveguides can be realized in photonic crystals for light at optical wavelengths. Waveguides are important elements in optical integrated circuits as they allow for the transmission of electromagnetic fields between various devices and components in interconnected systems. The modification of a linear sequence of unit cells results in discrete guided bands lying inside the band gap of the otherwise periodic photonic lattice. Light that propagates along the waveguide with frequencies given by the dispersion curve inside the band gap is strongly confined to the line defect and can be guided with high transmission even around sharp corners [290]. In the following, we will discuss the different kinds of guided modes in the waveguide.

Let us consider a line of missing holes along the x-direction in a triangular photonic crystal slab of air holes in diamond as depicted in the inset of figure 5.14. To calculate the waveguide dispersion properties, we define a unit cell for the linear defect geometry that consists of six air hole periods in the y-direction with one missing hole at the center and a lateral extend of one lattice constant in the x-direction. By replicating the defined unit cell by $\vec{R} = m\,a\,\vec{e}_x$, $m \in \mathbb{Z}$, along the x-axis, the whole waveguide geometry can be constructed. We emphasize that the unit cell of the waveguide structure is not reproduced along the y-axis due to the break of translational symmetry in that

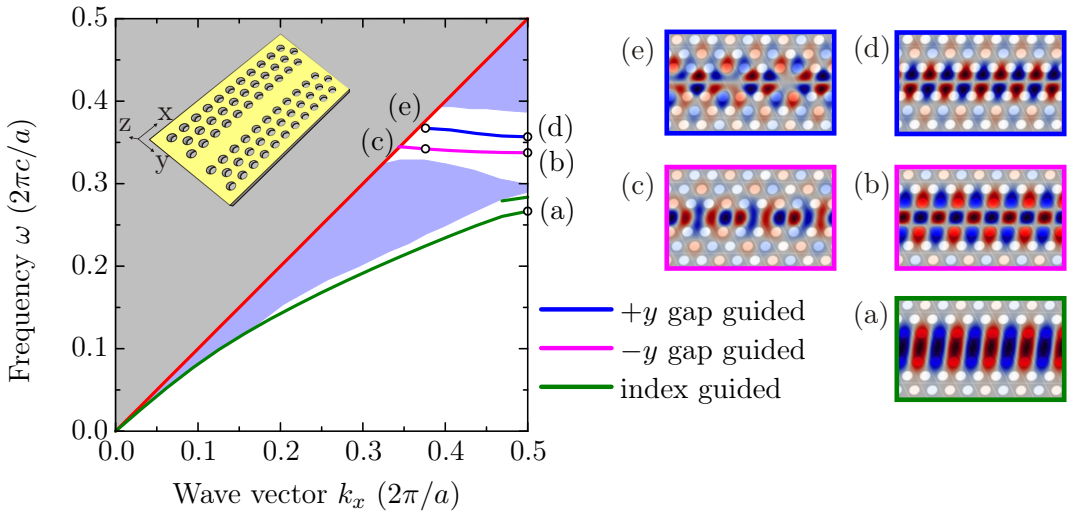

Figure 5.14: Projected band structure of TE-like modes for a linear waveguide in a photonic crystal slab in diamond: Below the light cone (gray shaded region), guided modes (blue and pink solid lines) inside the band gap as well as index guided modes (green solid lines) are formed. The guided modes are classified as $\pm y$ according to their mirror reflection symmetry at $y = 0$. Extended TE-like states of the crystal are shown by purple shaded regions. Inset: waveguide structure formed by one line of missing holes along the x-axis of the triangular photonic crystal slab. (a-e) H_z field distributions of the guided modes corresponding to the (a-e) labeled points in the band structure.

direction by the line defect. The discrete translational symmetry of the structure along the x-direction allows for expressing the magnetic field as Bloch modes

$$\vec{H}_{m,k_x}(x,y) = \vec{u}_{k_x}(x,y)\, e^{ix\cdot k_x}, \tag{5.69}$$

with k_x being the Bloch wave number and $\vec{u}_{k_x}(x,y) = \vec{u}_{k_x}(x+a,y)$ being the Bloch periodic function in x. By numerically solving the eigenvalue equation (5.24) for the Bloch state (5.69), we calculate the projected band structure of the waveguide as a function of the Bloch wave vector k_x in the propagation direction of the light field. Figure 5.14 shows the projected waveguide band structure for TE-like polarized light propagating along the photonic crystal waveguide with an air hole radius of $R = 0.28\,a$ and a slab thickness of $H = 0.91\,a$. Similarly to the band structures of photonic crystal slabs, discussed in section 5.4.2, all wave vectors with $k_x < \omega/c$ define the light cone of radiation modes extending in the vertical z-direction into the surrounding air. Beneath the light cone, the line defect pulls down discrete guided modes from the upper air band into the TE-like band gap of the surrounding lattice. The guided modes are vertically localized in the slab by index guiding. In the horizontal direction, the waveguide modes are confined to the linear lattice defect via the band gap effect and decay within the surrounding crystal. The waveguide supports two guided modes (blue and pink solid lines) in the band gap whose field distributions are shown in figure 5.14(b)-(e). However,

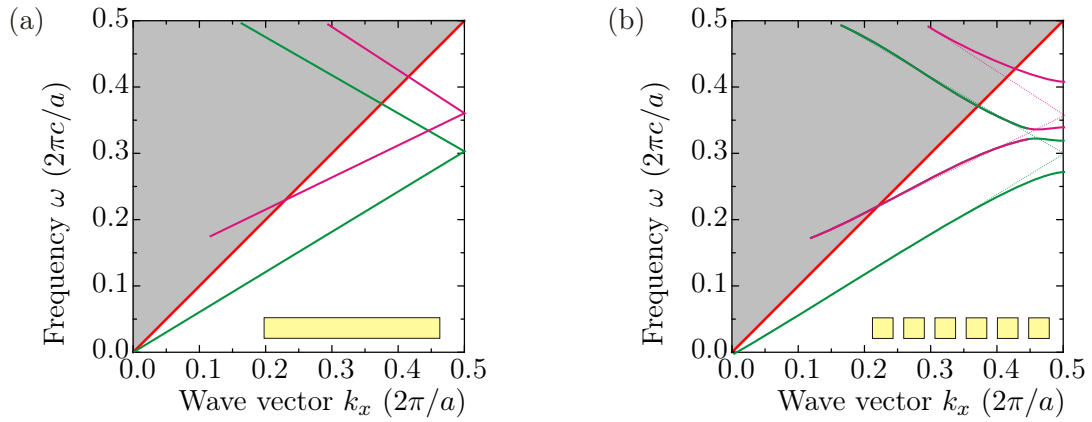

Figure 5.15: Schematic diagram of anti-crossing: (a) A one-dimensional homogeneous waveguide (see inset) supports several guided modes shown by pink and green solid lines that are reflected at the edge of the Brillouin zone at $k_x = 0.5 \times 2\pi/a$ and intersect with each other. (b) In a one-dimensional periodic photonic waveguide, the modes couple and repel each other at the intersection point. A mode gap opens between the two hybrid bands that originate from bands of different symmetry. As a consequence, the field distribution of a hybrid band continuously changes from one pattern to the other with increasing k_x.

the modes with frequencies inside the band gap are not the only modes guided by the line defect. As the dielectric waveguide has a higher refractive index than the surrounding photonic lattice, the line defect additionally supports *index guided modes* at low frequencies indicated by the green solid line in the band structure. The associated field distribution of the index guided mode is shown in figure 5.14(a). All modes that are not localized in the waveguide but freely propagating within the crystal are indicated by the purple shaded region in figure 5.14. These modes are denoted *extended modes* of the crystal. As the waveguide modes are symmetric under mirror reflections in the (x, z)-plane, they can be classified in $+y$ and $-y$-modes. The H_z component, plotted in figure 5.14, has a node along $y = 0$ for $+y$-modes and an antinode for $-y$-modes. According to references [261, 262], the fundamental waveguide mode (pink solid line in Fig. 5.14) and the index guided mode (green solid line in Fig. 5.14) have even symmetries with respect to the (x, z)-plane, whereas the higher order waveguide mode (blue solid line in Fig. 5.14) has an odd symmetry [256, 291].

What is striking in figure 5.14 is the drastic change in the waveguide mode profile calculated for specific pairs (ω, k_x) along the dispersion curves indicated by (b) and (c) and similarly by (d) and (e). Although (b) and (c) belong to the same waveguide mode, the mode profile at (b) has two additional nodes along the x-axis. The origin of the mode profile change is an anti-crossing of the bands [256] schematically illustrated in figure 5.15 for the case of a one-dimensional waveguide. The waveguide modes can be considered as a mixture of guided modes of a homogeneous waveguide and their replica folded at the edge of the Brillouin zone. If two modes exhibit the same symmetry they can couple and repel each other, which results in a degeneracy lifting and a mode gap

opens at the intersection points [261,292]. The band repulsion is referred as anti-crossing of the modes. On the contrary, modes with different symmetries can not couple and their crossing have no effect on their dispersion curves. Due to the anti-crossing effect, the field distribution of a specific band continuously changes with increasing k_x, as the waveguide band originates from several states with different mode pattern. Later in this section, we will see that by restricting the waveguide mode to a finite volume, a set of cavity modes is created. The field profiles confined in large size cavity structures equally show a considerable change with increasing resonant frequency which is attributed to the anti-crossing effect of the original waveguide mode.

5.5.2 Cavities: Point defects in photonic crystals

In the previous section, we have shown that light can be guided along linear defects in the photonic lattice. By using point instead of line defects, e.g. by omitting one or several holes, light can be tightly localized in the defect region. The symmetry break due to the structural defect creates localized states inside the photonic band gap of the original crystal. Due to the photonic band gap effect, the unperturbed surrounding photonic lattice acts as a highly reflective mirror for light with frequencies inside the band gap. By introducing a point defect, we create a tiny cavity that is effectively surrounded by reflecting walls. The light can not propagate through the periodic lattice but is localized in the defect region. The localization of the cavity modes is characterized by four important properties: its frequency ω, its symmetry, its quality factor Q and its mode volume V. The mode volume V, given by equation (5.61) in section 5.3.1, describes the spatial confinement, whereas the quality factor Q is the dimensionless lifetime of the cavity mode denoting the number of optical periods that pass before the energy decays by $e^{-2\pi}$ [256]. Here, we will present different cavity designs based on the removal of zero, one or several holes in the photonic lattice. The field distributions of the cavity modes are classified according to their mirror symmetry and the cavity quality factors and mode volumes are computed using finite-difference time-domain algorithms. Moreover, we show that large size cavity structures can be approximated by a linear waveguide that is ended on both sides by highly reflective photonic lattices. Using the simple Fabry-Pérot model, the resonant frequencies, the mode profiles and even the quality factors of the cavity modes can be derived from the waveguide properties discussed in the previous section 5.5.1.

Donor and acceptor modes

If the perfect periodicity of the photonic lattice is intentionally broken by a local defect, the Bloch modes of the crystal are disturbed and local electromagnetic modes are induced within the forbidden band gap. The periodicity can be lifted either by removal or addition of extra material, e.g by increasing or decreasing of one or several air holes at the center of the structure: (1) By material removal the electric field energy previously localized in dielectric material of the unperturbed crystal is now confined in air. According to the electromagnetic variational theorem, this leads to an increase in

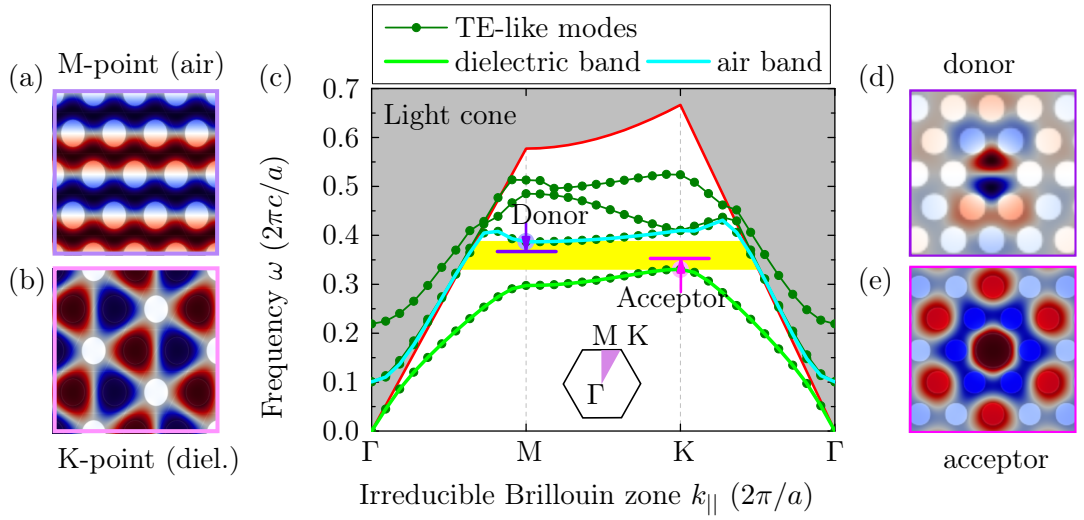

Figure 5.16: Donor and acceptor modes within the band gap in a photonic crystal slab: (c) By removing the central air hole a donor mode is pulled from the M-point of the air band (second band) into the band gap of the triangular photonic crystal slab, whereas an acceptor mode is pushed from the K-point of the dielectric band (first band) into the band gap with increasing hole size. (a,b) H_z fields taken at the M- and K-point of the air and dielectric band, respectively. (d,e) The H_z components of the donor and acceptor mode, respectively.

frequency. The perturbation of the Bloch modes, originating from the K-point of the dielectric band, leads to localized modes which are pushed into the band gap from the lower dielectric band. In accordance to solid state physics, these modes are referred as *acceptor modes* [293, 294]. (2) In contrast, by adding extra material, the electric field components, that have previously been confined in air, are now localized in dielectric material which leads to a decrease in frequency. The associated defect modes originate from Bloch modes at the M-point of the air band whose frequency is lowered by the defect and form new states inside the band gap. We call these defect modes *donor modes* [293,294]. Figure 5.16 illustrates the creation of acceptor and donor states within the band gap. Enlarging the radius of the central air hole leads to the creation of an acceptor state within the frequency gap (Fig. 5.16(c)). The field distribution of the acceptor state is primary localized in the central air (Fig. 5.16(e)). For comparison the field simulated at the K-point of the dielectric band is displayed in figure 5.16(b). On the other hand, by removing the central air hole, a donor mode is created in the band gap whose field distribution is tightly confined in the dielectric defect region (Fig. 5.16(d)). For reference, the field taken at the M-point of the air band is shown in figure 5.16(a).

For emitter-cavity coupling experiments of a single color center to a photonic crystal cavity, a donor type defect, created by filling one or several holes of the photonic lattice, would be optimal. The introduced additional material enables positioning of a single color center at the cavity center. Moreover, the maxima of the cavity elec-

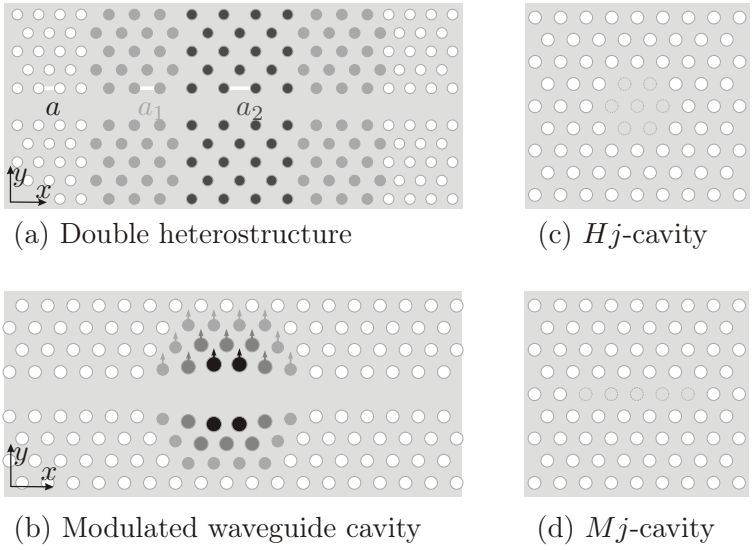

(a) Double heterostructure (c) Hj-cavity

(b) Modulated waveguide cavity (d) Mj-cavity

Figure 5.17: Various donor type cavity designs in two-dimensional photonic crystals: (a) Double heterostructure and (b) modulated waveguide cavity, where a cavity is created (a) by modification of the lattice constant in sections of the photonic crystal or (b) by variation of the air hole radii and positions. (c) Small-size Hj-cavity and (d) Mj-cavity, where the cavity is introduced by omitting (c) one or several concentric rings of holes or (d) one or several holes aligned in a row. The index j indicates the number of missing concentric rings or the number of missing holes in a row.

tric field distribution of donor modes are localized in high dielectric material ideally at the emitter's position which is an essential prerequisite for efficient Purcell coupling (c.f. section 5.3). Several donor type cavity designs in two-dimensional photonic crystals have been proposed ranging from small size structures to modulated waveguide geometries. Figure 5.17 shows two modulated waveguide designs, referred to as double heterostructure (Fig. 5.17(a)) and modulated waveguide cavity (Fig. 5.17(b)), where cavities are introduced by changing the lattice constant or the air hole radii and positions in sections next to a photonic crystal waveguide. For diamond, high quality factors of $Q = 10^5 - 10^6$ have been predicted for these waveguide cavities with modal volumes of $V = 1.77\,(\lambda/n)^3$ [295]. For double heterostructures in silicon, record Q-factors of 9×10^6 have been experimentally achieved [296]. Cavity designs with smaller mode volumes can be achieved by removing one or several holes at the center of the photonic crystal. If the holes are removed in concentric rings from the cavity center, we refer to this defect type as Hj-cavity [297–299] (Fig. 5.17(c)), whereas if the missing holes are aligned in a row along the x-axis, the defect is called Mj-cavity [300, 301] (Fig. 5.17(d)). The attached index $j \in \mathbb{N}_0$ indicates the number of missing concentric rings or the number of missing holes aligned in a row to form the cavity structures.

In this work, we focus on linear donor type Mj defects created by removing zero, one or several holes at the center of a triangular photonic crystal slab of air holes in

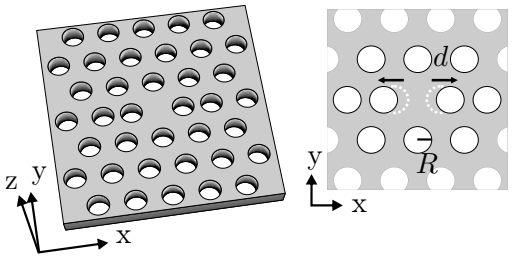

Figure 5.18: M0-cavity design: The smallest photonic crystal cavity is created by shifting two adjacent holes by a distance d outwards along the x-axis. The air hole radius is R.

diamond. All cavity structures introduce donor type states within the band gap pushed down from the M-point of the upper air band. In the case of the M0-cavity, a defect is introduced by shifting two adjacent holes by a distance d apart. The small M0-cavity creates one single localized mode with its frequency in close vicinity to the upper bound of the band gap, whereas extended defect structures, e.g. the M7-cavity, generate several discrete states localized deep in the forbidden band gap. In the following sections, we present the structural design of the M0-, M1- and Mj-cavity ($j > 2$) as well as the localized electromagnetic field distributions of the resonant modes.

M0-cavity

The smallest cavity structure that can be realized in a two-dimensional photonic crystal slab is a M0-cavity, where the defect is created by shifting two adjacent holes by a distance d outwards along the x-direction (Fig. 5.18) [274, 301, 302]. M0-cavities in combination with a nearby waveguide have been used for the realization of nanolasers that allow for high extraction efficiencies [303]. In the simulations, we assume an air hole radius $R = 0.28\,a$, a diamond slab thickness $H = 0.91\,a$ and a displacement of the inner holes $d = 0.14\,a$. The hole displacement gives rise to one single localized donor state within the band gap with a resonant frequency $\omega = 0.3782 \times 2\pi c/a$ near the upper air band (c.f. Fig. 5.23). The associated electromagnetic field is tightly localized in the defect region yielding an ultra-low modal volume of $V = 0.35(\lambda/n)^3$ and a high cavity quality factor of $Q = 14,520$. Figure 5.19 shows the E_x, E_y and H_z field distributions of the M0-cavity mode in the (x, y)-plane and the H_z component in the (x, z)-plane. The mode profiles show only very few nodal planes. Upon mirror reflection in the planes at $x = 0$, $y = 0$ and $z = 0$, the electromagnetic field components E_x, E_y and H_z of the M0-cavity mode transform as follows:

$$\begin{aligned} E_x(M_x\vec{r}) &= +E_x(\vec{r}) \\ E_y(M_y\vec{r}) &= +E_y(\vec{r}) \\ H_z(M_z\vec{r}) &= +H_z(\vec{r}), \end{aligned} \tag{5.70}$$

where $M_x(x, y, z) = (-x, y, z)$, $M_y(x, y, z) = (x, -y, z)$ and $M_z(x, y, z) = (x, y, -z)$ denote reflections of a vector $\vec{r}$ in the (y, z)-, (x, z)- and (x, y)-plane, respectively. As the electric field transforms like a vector field, the M0-cavity mode has an even reflection symmetry $(-x - y)$ with respect to the planes at $x = 0$ and $y = 0$ (c.f. eqs. (5.30)-(5.32) in section 5.2). The magnetic field H_z (pseudo-vector) exhibits an odd symmetry

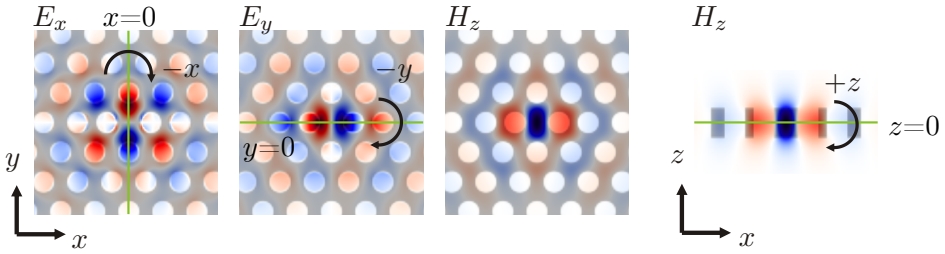

Figure 5.19: Electromagnetic field components E_x, E_y and H_z of the M0-cavity mode in diamond: The symmetry planes at $x = 0$, $y = 0$ and $z = 0$ are indicated by green lines. According to the E_x, E_y components in the (x, y)-plane, the M0 mode has an even symmetry (-x-y) with respect to the $x = 0$ and $y = 0$ planes. In contrast, the H_z field (pseudo-vector) is odd ($+z$) with respect to the $z = 0$ plane indicating a TE-like M0 mode.

($+z$) with respect to the plane at $z = 0$. Because the E_x and E_y field have the same amplitude and exhibit both a node either along the x- or y-axis, we would expect no clearly linear polarization of the M0-mode but rather an unpolarized angular profile in the experiment. Moreover, the E_x and E_y fields are pronounced in the photonic crystal plane, whereas the H_x and H_y fields vanish at $z = 0$ (not shown). Hence, according to the classification given on page 97, the M0-cavity mode is classified as a TE-like mode.

Above, the figures of merit Q, V and ω characterizing the M0-cavity have been simulated for a specific geometry. However, due to intrinsic fabrication tolerances, it is extremely challenging in practice to exactly match the given structural specifications. In the following, we study the dependency of the quality factor and resonance frequency on the structural parameters of the M0-cavity, i.e. the air hole radius R, the shift d creating the defect and the slab thickness H. To this end, we start with the parameter set given above: $R = 0.28\,a$, $d = 0.14\,a$ and $H = 0.91\,a$ and simulate the Q-factor and the frequency ω as a function of the air hole radius R, while keeping the parameters d and H fixed. Figure 5.20(a) reveals a variation in Q ranging from 11,700 to 21,400 when changing R between $0.25\,a$ an $0.29\,a$ with the maximum in Q obtained for $R = 0.26\,a$. At the same time, the resonance frequency of the M0-cavity mode strongly raises with increasing hole sizes from $\omega = 0.3609 \times 2\pi c/a$ to $0.3841 \times 2\pi c/a$. Assuming a lattice constant of $a = 280\,\text{nm}$, an enlargement in R by 1 nm would implicate a shift of the resonant wavelength by 4.2 nm to smaller values. As a second step, we resume the radius $R = 0.26\,a$ yielding the maximum Q-factor and the slab thickness $H = 0.91$ and vary the shift d. Similar to the hole radius, figure 5.20(b) displays a significant change in Q from 15,300 to 24,000 for modified shifts d. However, the impact on the resonant wavelength is much less pronounced: Increasing d by 1 nm leads to a red shift of the resonance by 1 nm. Finally, we investigate the influence of the slab thickness for fixed parameters $R = 0.26\,a$ and $d = 0.14\,a$ (Fig. 5.20(c)). In the range of $H = 0.9\,a - 0.94\,a$, an almost constant quality factor of $Q \approx 24,500$ is obtained, that drops to 18,400 for $H = 0.95\,a$. The slab thickness has a weak influence on the resonant wavelength. Diminishing H by 2 nm (1 nm from the top and bottom surface), results in a wavelength shift of 0.9 nm.

To summarize, both the air hole radius R and the shift d have a strong impact on

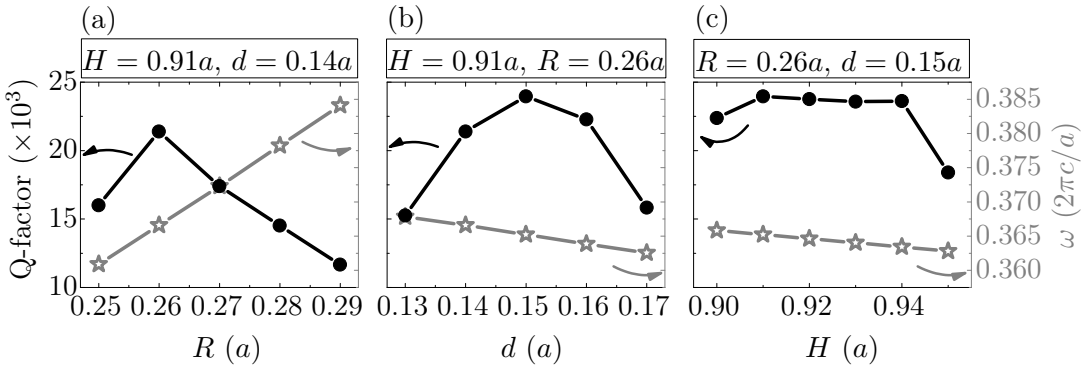

Figure 5.20: Dependence of the Q-factor and resonance frequency ω of the M0-cavity mode on (a) the hole radius R, (b) the shift d and (c) the slab thickness H. The parameters, which are kept fixed during the simulations, are given above the diagrams.

the quality factor of M0-cavity mode, whereas the dependency on the slab thickness is less critical. By varying the three parameters, we found a maximum quality factor of 24,500. In section 5.6.2, we apply an efficient optimization procedure that allows for further boost of the quality factor of the M0-cavity by one order of magnitude without increasing the mode volume. The method is based on a variation of the holes' radii around the defect such that the field gently decay in the crystals.

The frequency dependence of the cavity modes on the air hole radius of the structure is widely used in practice to fine tune the mode frequency. Using a digital etching technique which successively increases the air holes, the resonances of the photonic crystal can be shifted to higher frequencies and smaller wavelengths. We will discuss the tuning ability as a function of the radius and other tuning techniques in more detail in chapters 7 and 9 in the context of photonic crystal cavities realized in thin diamond membranes.

M1-cavity

The M1-cavity is created by removal of one single central air hole in the triangular photonic lattice [304, 305]. The generated donor type cavity modes are tightly localized in the defect region with modal volumes of around one cubic wavelength. The M1-cavity has been used in various applications ranging from electrically and optically pumped photonic crystal lasers [306–308] to low-threshold nanolasers [309, 310]. Moreover, M1-cavity designs reaching large Q/V ratios have been proposed [311], well suited for emitter-cavity coupling. In this context, an one-hole defect cavity in a square lattice has been deterministically positioned around a single quantum dot [109, 312]. Single-point defects have also been used for in-plane integrated optical circuits, where a cavity is coupled to a linear photonic crystal waveguide, enabling the realization of add-drop filters [313]. For coupling of single color centers in diamond, various M1 defects have been designed, reaching quality factors of $Q > 6 \times 10^4$ and modal volumes on the order of one cubic wavelength [275, 314, 315].

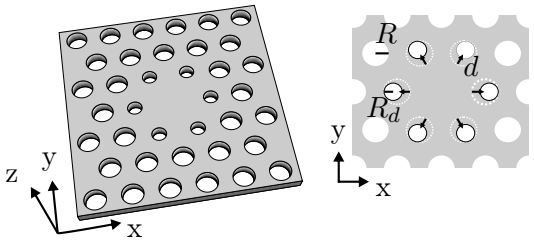

Figure 5.21: Modified M1-cavity: The radius of the six nearest-neighbor holes are reduced to R_d and the hole positions are shifted along the symmetry lines away from the center by a distance d. R denotes the air hole radius of the unperturbed lattice.

The removal of a single hole at the center of the photonic crystal preserves the sixfold symmetry of the triangular photonic lattice. This means that by rotating the structure by 60° through the center of the cavity, the geometry remains the same. The rotational symmetry gives rise to unique highly symmetric modes tightly localized to the M1 defect. In the unmodified single-hole defect cavity, only two doubly degenerate dipole modes exist within the band gap [304, 305, 316, 317]. For an air hole radius $R = 0.28\,a$ of the photonic lattice and a slab thickness of $H = 0.91\,a$, we find two orthogonally polarized degenerate dipole modes with resonant frequencies $\omega = 0.3660 \times 2\pi c/a$ and $\omega = 0.3661 \times 2\pi c/a$ (c.f. Fig. 5.23). The slight deviation in frequency of the degenerate modes arises from numerical uncertainties induced by finite mesh discretization (for details on the numerical simulations see section 5.7.2). The M1-cavity modes exhibit a modest quality factor of $Q = 204$ and a small mode volume of $V = 0.5(\lambda/n)^3$.

However, apart from the dipole modes, the M1-cavity design supports higher order modes as well. Via modulation of the structural design, the dielectric defect area is slightly enlarged and additional modes enter the photonic band gap from the upper air band. Figure 5.21 shows the modified M1-cavity design with preserved sixfold rotational symmetry. The six nearest-neighboring air holes are shifted away from the cavity center by a distance d along the lines of symmetry after their radii have been reduced from R to R_d. In the simulation, we assume the following parameters: $R = 0.35\,a$, $R_d = 0.25\,a$, $d = 0.1\,a$, a slab thickness $H = 0.91\,a$ and a refractive index of bulk diamond of $n = 2.4$. Depending on their field profile, the resonant modes localized in the single-

Mode	ω $(2\pi c/a)$	Q	V $((\lambda/n)^3)$	symmetry
Dipole	0.3600	3,200	0.62	$+x-y$
Dipole	0.3600	3,000	0.61	$-x+y$
Hexapole	0.3878	3,300	1.13	$-x+y$
Quadrupole	0.3963	5,300	0.91	$-x-y$
Quadrupole	0.3969	5,200	0.93	$+x+y$
Monopole	0.4313	900	1.02	$-x+y$

Table 5.1: Resonant frequencies, quality factors and mode volumes of higher order modes confined in the modified M1-cavity in diamond with $R = 0.35\,a$, $R_d = 0.25\,a$, $d = 0.1\,a$ and $H = 0.91\,a$.

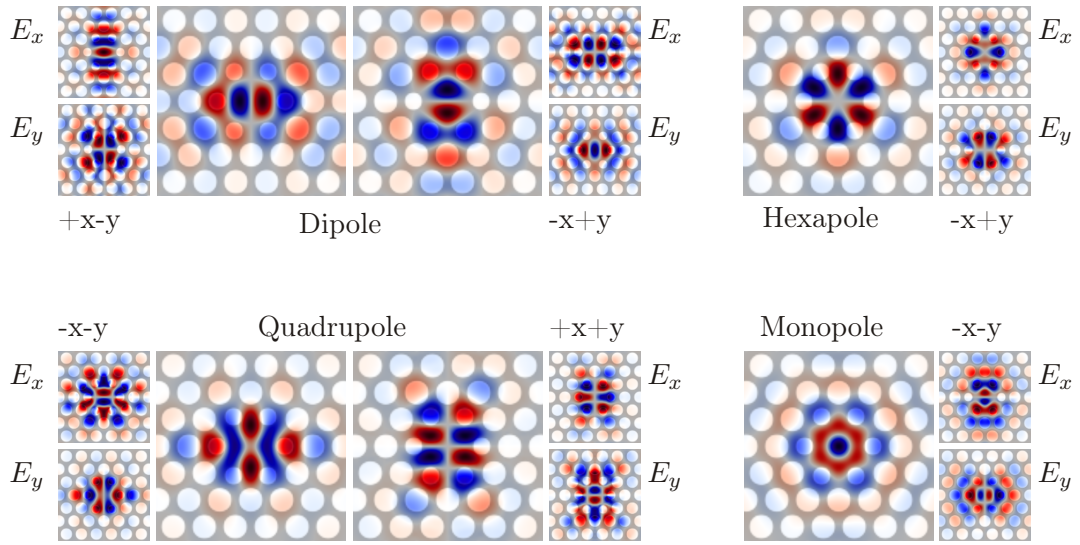

Figure 5.22: Resonant cavity modes of a modified M1-cavity in diamond: The large images show the H_z field and the small pictures the E_x and E_y electric field components of TE-like M1-cavity modes. The dipole and quadrupole modes are doubly degenerate, whereas the hexapole and monopole modes are non-degenerate. The symmetry of each mode with respect to mirror reflections in the (y, z)- and (x, z)-plane are indicated by $\pm x \pm y$, where the minus (plus) sign indicates an even (odd) symmetry. In the simulations, the structural parameters are set to $R = 0.35\,a$, $R_d = 0.25\,a$, $d = 0.1\,a$ and $H = 0.91\,a$.

defect region are classified in four main categories [316–319]: (1) doubly degenerate dipole modes, (2) doubly degenerate quadrupole modes as well as non-degenerate (3) hexapole and (4) monopole modes. The resonant frequencies, the quality factors and the mode volumes of the modes supported by the modified M1-cavity are summarized in table 5.1. The E_x, E_y, H_z components of the TE-like M1-cavity modes are shown in figure 5.22. The classification of the modes upon mirror reflection in the (y, z)- and (x, z)-plane are indicated by $\pm x \pm y$, where a minus (plus) sign indicates an even (odd) symmetry upon mirror reflection, respectively. The dipole modes are invariant under 360° rotation, whereas quadrupole modes return to the same state until 180° rotation has been applied. In the case of dipole and quadrupole modes, a new state is obtained when adding to a given mode its 60°-rotated analogon. As there exist two mutually orthogonal basis states, the modes are called doubly degenerate [319]. On the other hand, in the case of the monopole and hexapole modes, the identical state or identically zero is obtained when adding to a given mode its 60°-rotated counterpart. Hence, monopole and hexapole modes are non-degenerate states [319]. The degeneracy of the dipole and quadrupole modes can easily be lifted by modifying the size or position of two holes diagonally opposed with respect to the cavity center. In practice, small local fabrication errors already lead to a degeneracy break. The electric field distribution of both dipole and monopole modes is concentrated at the cavity center, which makes them

well suited for emitter-cavity coupling experiments. For nanolaser applications, different designs relying on the dipole- [307], monopole- [306, 308] and hexapole-mode [309, 310] have been realized. In the experiment, the different M1-modes can be distinguished via polarization analysis [310, 320, 321]. The two dipole modes are expected to be linearly polarized, mutually orthogonal. The monopole mode is expected to have no clearly preferred polarization direction. The hexapole mode is theoretically unpolarized and the quadrupole modes should show a four-fold emission pattern [316, 317]. However, due to fabrication imperfection, the hexapole and quadrupole mode profiles can be disturbed resulting in a linear emission polarization [310, 316]. In section 5.7.3, we will compute the polarization properties and far-field emission profiles of different M1-cavity modes.

Several missing hole cavity

In the previous section, we discussed the spectral properties and field distributions of small size cavity structures such as the M0- and M1-cavity. In this section, we focus on large size cavity structures, where several holes ($j \geq 2$) aligned along the x-axis of the photonic lattice are removed. To describe the mode profile and spectral frequency range of the cavity modes, we will approximate large size cavity structures as a fraction of a linear waveguide that is terminated on both ends by highly reflective photonic lattices. Using this approximation, fundamental properties of large size cavity structures are deduced from the waveguide modes discussed in section 5.5.1. To study the impact of the defect size on the spectral properties of the cavity modes, we successively increase the number j of missing holes while keeping the air hole radius $R = 0.28\,a$ of the photonic lattice and the slab thickness $H = 0.91\,a$ fixed. Here, we only focus on TE-like modes. Furthermore, the modes are classified in $\pm y$ according to their mirror symmetry under reflection in the (x, z)-plane. Figure 5.23 shows the resonant frequencies of the $+y$ modes and the three lowest order $-y$ modes localized within the band gap of the surrounding unperturbed lattice as a function of the number j of missing holes creating a defect. For larger defect sizes, the number of resonant modes increases. In the case of the M0-cavity with the smallest defect size, we find only one mode with a frequency near the upper air band. For the M1-cavity, two degenerate dipole modes with orthogonal symmetry ($+x - y$ and $-x + y$) are found with frequencies localized deeper in the photonic band gap. When the number of missing holes raises further, the frequency of the $-y$-modes drops and new $-y$-modes are introduced from the upper air band. In contrast, the $+y$-modes split up into several modes. For large defect sizes ($j \geq 6$) the resonant frequency of the fundamental $-y$-mode seems to approach a lower bound at $\omega = 0.3375 \times 2\pi c/a$. Strikingly, the resonant frequencies of $-y$-modes cover almost the whole band gap, ranging from the upper air band to a lower limit of $\omega = 0.3375 \times 2\pi c/a$. In contrast, the $+y$-modes are limited to the spectral interval $\omega = [0.3579, 0.3748] \times 2\pi c/a$. The reason can be found by approximating large size cavity structures as a fraction of a linear waveguide that is ended on both sides by highly reflective photonic crystal lattices [322]. Due to the band gap effect, the original waveguide mode can not propagate through the crystal but is back reflected at the ends, interferes with the incoming light and discrete

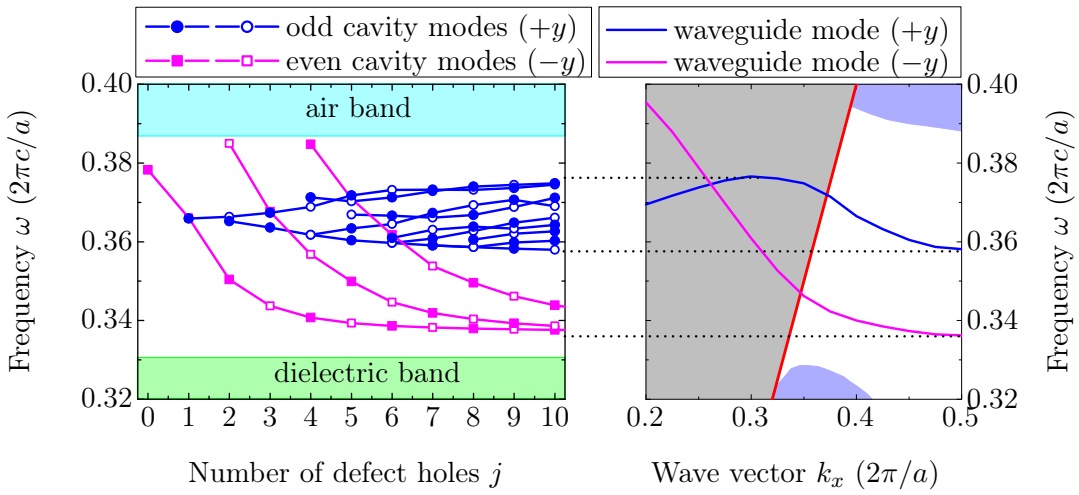

(a) several missing hole cavity (b) linear waveguide

Figure 5.23: Resonant states within the band gap as a function of the number j of missing holes forming the photonic crystal cavity in comparison to the waveguide dispersion curve: (a) The frequency of the cavity modes lie within the frequency range of (b) the corresponding waveguide mode of same y-mirror symmetry. (a) The modes are separated in $-y$ (□, ■) and $+y$ modes (○, ●) according to their reflection symmetry at $y = 0$. The open symbols (□, ○) correspond to $+x$ modes, whereas filled symbols (■, ●) represent $-x$-modes. The solid lines are a guide to the eye.

cavity modes are formed. The dispersion relation as well as the field distribution of the cavity modes strongly resemble the original waveguide mode. The cavity modes with $+y$ ($-y$) reflection symmetry originate from the $+y$- ($-y$-) waveguide mode. The dispersion curve of the $-y$ waveguide mode covers a frequency range of $\omega = [0.3375, 0.3985] \times 2\pi c/a$ coinciding with the spectral limits of $-y$ cavity modes, whereas the frequencies of the $+y$ waveguide mode lie in the interval $\omega = [0.3568, 0.3765] \times 2\pi c/a$ matching the spread in frequency of the cavity modes with equal symmetry (Fig. 5.23). The spectral range of the waveguide modes puts an upper and lower limit to the resonant frequencies of the resulting cavity modes when restricting the linear defect region. As the spectral width of both waveguide modes strongly differ, the same is true for the $+y$ and $-y$ cavity modes.

We analyze the correlation between waveguide and cavity modes in more detail for the case of a seven-missing hole cavity. In figure 5.24, a comparison is made between the calculated resonant frequencies of the higher-order TE-like M7-cavity modes and the TE-like dispersion curves of the photonic crystal waveguide presented in the previous section 5.5.1. Both the cavity and waveguide modes have been simulated for a triangular lattice of air holes with a radius of $R = 0.28\,a$ and a slab thickness of $H = 0.91\,a$. The M7-cavity modes, represented by pink and blue points in figure 5.24, coincide with the waveguide dispersion curve (solid line). Thereby, the wave vector component k_x, associated with

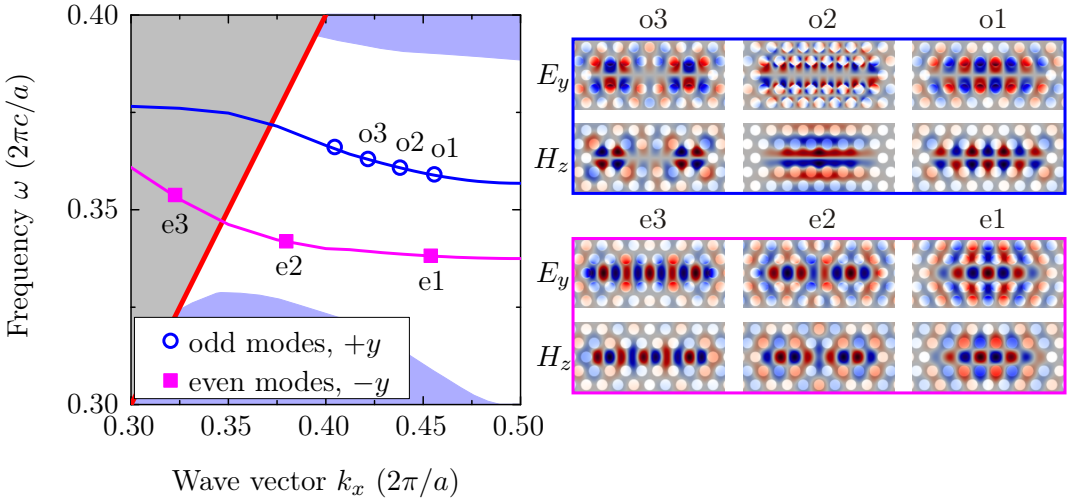

Figure 5.24: Resonant frequencies and field distribution of TE-like M7-cavity modes: The frequencies of the lowest order M7-cavity modes are plotted on the dispersion curves of a linear photonic crystal waveguide. According to their symmetry upon reflection in the (x, z)-plane, the cavity modes are classified as even (pink squares ■) and odd modes (blue open circles ○). The E_y and H_z field distributions of the $e1$, $e2$, $e3$ and $o1$, $o2$, $o3$ cavity modes are shown on the right. The E_y fields of all odd modes "o" change their sign upon reflection in the (x, z)-plane whereas the E_y patterns of the even modes "e" are unchanged upon reflection.

the M7-cavity mode, is determined by the intersection point of the cavity frequency ω with the waveguide dispersion curve. Alternatively, k_x can be determined via the one-dimensional Fourier transform of the cavity field calculated along the x-axis. The central position k_c of the main Fourier component determines $k_x = k_c - \pi/a$ [323]. Displayed on the waveguide dispersion curve, the wave vectors k_x of the cavity resonances are almost equally spaced. This strongly resembles to Fabry-Pérot resonances fulfilling the condition: [261, 262]:

$$\pi p = k_x L \tag{5.71}$$

with $p \in \mathbb{N}$ and L being the cavity length. For the cavity modes (pink squares in Fig. 5.24) plotted on the low-frequency waveguide dispersion curve (pink solid line in Fig. 5.24), the average wave vector interval is $\Delta k_x = 0.066 \times 2\pi/a$. Using equation (5.71), we find an effective M7-cavity length of $L = 7.6\,a$. Alternatively, from the Fourier transform of the E_y component along the x-axis, we obtain $\Delta k = 0.073 \times 2\pi/a$, which results in an effective cavity length of $L = 6.8\,a$.

In figure 5.24, we only consider TE-like cavity and waveguide modes whose electromagnetic fields have an even symmetry upon reflection in the (x, y)-plane (c.f. page 77 in section 5.2). Furthermore, the waveguide states and cavity modes can be classified in even and odd modes with respect to their mirror reflection symmetry in the (x, z)-plane. This separation has major consequences: In section 5.7.3, we will see that even and odd modes exhibit mutually orthogonal polarization. In the far field, even modes are polar-

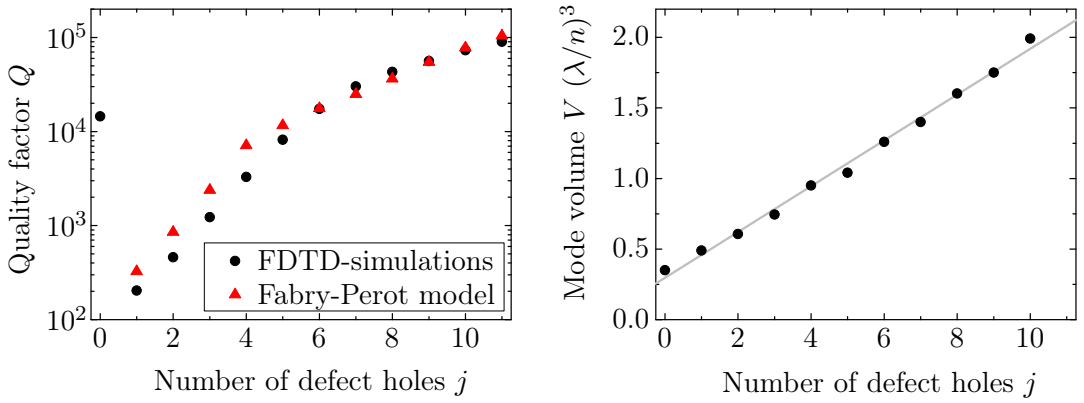

Figure 5.25: Dependence of the quality factor and mode volume as a function of the number j of missing holes forming the photonic crystal cavity: (a) The quality factor Q has been either calculated via FDTD-simulations (•) or via equation (5.72) based on a simple Fabry-Pérot model (▲). For small cavity sizes ($j \leq 5$) the Fabry-Pérot model overestimates the Q-factor. (b) The mode volume enlarges linearly as a function of the hole-defect number. The gray solid line is a linear fit to the data.

ized along the y-direction, whereas odd modes are polarized along the x-direction. This property allows for the identification of even and odd modes in the experiment using polarization-resolved spectroscopy. In the following, we will refer to even modes as "e" states and odd modes as "o" states. The simulated E_y and H_z field distributions of the three lowest-frequency modes $e1$, $e2$, $e3$ and $o1$, $o2$, $o3$ of each symmetry class are plotted in figure 5.24. The E_y component of the "o" modes has a node at $y = 0$ whereas the E_y field of the "e" modes shows an antinode.

With increasing wave vector k_x the field distribution of the M7-cavity modes (Fig. 5.24) is significantly modified. This is similar to the continuous change of the waveguide field distribution (Fig. 5.14(b-e)) with increasing wave vector due to the anti-crossing effect (c.f. section 5.5.1). The H_z distributions of the e1 and o1 mode have substantial similarity with the H_z waveguide pattern calculated for wave vectors at the edge of the Brillouin zone (Fig. 5.14(b),(d), respectively). Furthermore, the H_z field of the $e3$ and $o3$ M7-cavity modes strongly resemble to the H_z distributions of the waveguide modes taken near the light line (Fig. 5.14(c),(e), respectively). The field distributions of the $e2$ and $o2$ modes represent an intermediate state between the two waveguide patterns. The similarity in the dispersion curve and the field distribution clearly shows that the M7-cavity modes are decomposed of guided modes of a linear waveguide ended on both sides by photonic crystal lattices. For given frequencies and propagation wave vectors (ω, k_x), the waveguide modes fulfill the Fabry Pérot resonant condition (eq. (5.71)) and discrete cavity modes are formed via interference. The field pattern of the original waveguide mode is transferred to the resulting cavity mode confined to the defect region.

Figure 5.25 shows the quality factor and the mode volume of the fundamental mode $e1$ as a function of the number j of missing holes at the center of the photonic lattice. The mode volume increases linearly with the number j of defect holes with a slope of

$0.162 \pm 0.004\,(\lambda/n)^3$ per missing hole. According to the linear fit of the data indicated by the gray solid line in figure 5.25(b) a minimal mode volume of $V = 0.30 \pm 0.02\,(\lambda/n)^3$ can be obtained for a zero-hole defect. This value is close to the simulated mode volume $V = 0.35\,(\lambda/n)^3$ of the M0-cavity (see section above). From the linear fit, the mode volume of any defect size can be extracted without the need of time-consuming FDTD simulations. In contrast to the mode volume, there seems to be no simple relation between Q and j. For small cavity structures ($j < 6$), the quality factor dependence can be approximated as $Q \propto 2.5^j$, whereas for large defects ($j > 6$) the Q-factor seems to rise linearly and reaches $Q = 90,000$ for an eleven-hole defect. What is striking in figure 5.25(a), is the high quality factor of the M0-cavity mode compared to the values of the M1-M5-structures. The reason is that the M0-defect is not introduced by removing holes but by shifting two holes apart. This leads to modified distributed Bragg reflections at the edges of the surrounding air holes and a gentle decay of the cavity field resulting in minimized out-of-plane radiation losses and a high Q-factor. In subsequent section 5.5.3, we approximate the M1-M11-cavity by a one-dimensional Fabry-Pérot model to predict the quality factors for various defect sizes.

5.5.3 Fabry-Pérot model

A one-dimensional Fabry-Pérot cavity consists of two planar mirrors with reflectivity r positioned at a distance L along the x-axis. The space between the mirrors is filled with a medium of refractive index n_g. The quality factor of a linear Fabry-Pérot cavity is given by $Q = \nu/\delta\nu = \mathcal{F}\nu/\nu_{\mathrm{FSR}}$, where ν is the resonant frequency, $\delta\nu$ is the resonant linewidth (full width at half maximum), $\mathcal{F} \approx \pi/(1-|r|)$ denotes the finesse in the limit of $1 - |r| \ll 1$ and $\nu_{\mathrm{FSR}} = c/(2n_gL)$ is the free spectral range defining the frequency difference between two adjacent modes [324]. For a given mirror reflectivity r and cavity length L, the quality factor of a resonant mode with wavelength λ_0 ($k_0 = 2\pi/\lambda_0$) is then given by [325]:

$$Q = \frac{k_0}{1-|r|}\, n_g\, L. \tag{5.72}$$

For a one-dimensional linear resonator, the parameter n_g denotes the refractive index of the medium filled between the mirrors. In the case of a photonic crystal waveguide mode, that bounces between two planar mirrors, n_g must be replaced by the group index $n_g = c|dk_x/d\omega|$ of the waveguide mode [325]. The group index n_g of the fundamental waveguide mode is plotted in figure 5.26 as a function of the resonant frequency. At the edge of the Brillouin zone, the slope of the waveguide dispersion curve $\omega(k_x)$ almost vanishes (pink curve in Figs. 5.23(b) and 5.24 at $k_x = 0.5 \times 2\pi/a$) and hence the group index strongly increases near the resonant frequency of $\omega = 0.3375 \times 2\pi c/a$.

In a standard Fabry-Pérot resonator, the cavity length L is well defined by the distance between the mirrors. However, the light fields in a photonic crystal cavity do not vanish at the edge of the first hole but penetrate deeper into the crystal. The effective cavity length L can be determined via equation (5.71). Okano et al. [323] found a linear relation $L = ja$ between the effective cavity length L and the number j of missing holes. For the M7-cavity, we confirme that the cavity length $L = 7.0\,a$ predicted

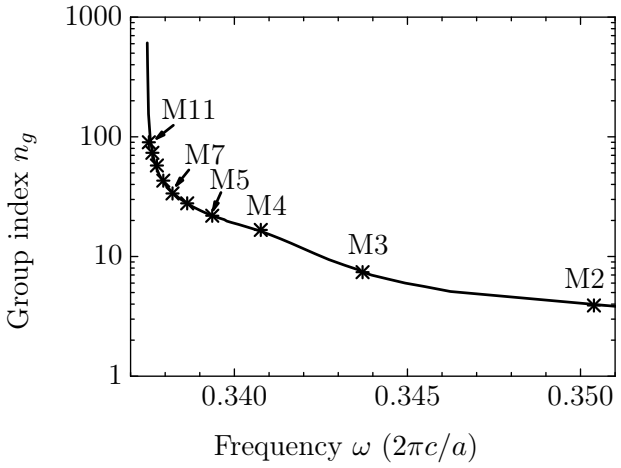

Figure 5.26: Group index n_g of the fundamental waveguide mode used to determine the quality factors of large size photonic crystal cavities. The group index calculated at the resonant frequencies of the $e1$ modes for the M2-M11-cavities are indicated by crosses ⁕.

by this simple linear relation is in reasonable agreement with the effective cavity lengths of the M7-cavity of $L = 7.6\,a$ determined via equation (5.71) and $L = 6.8\,a$ deduced from Fourier analysis (c.f. page 116). Therefore as a first approximation, we assume an effective cavity length $L = ja$ in the following.

FDTD simulations reveal a constant reflectivity of the waveguide mode at the position of the photonic crystal for frequencies inside the band gap. This means that we can assume the same reflectivity for every cavity structure independent of its defect size. We choose the M6-cavity to calculate the reflectivity, as its defect geometry is large enough such that corrections required for small size defects [326] become negligible. At the same time, the M6-defect is small enough such that the group index associated to its fundamental resonance frequency is outside the regime of high n_g in figure 5.26. From the quality factor $Q = 17,400$ of the fundamental M6-cavity mode $e1$, calculated via FDTD simulations, we determine the reflectivity $r = 0.9968$ of the photonic crystal lattice. Here, we take into account the effective cavity length $L = 6.0\,a$ and the group index $n_g = 28$. Once the reflectivity is specified, the quality factors of all other defect structures can be deduced from the group index n_g and the effective cavity length L using equation (5.72). Figure 5.25 displays the quality factors of the fundamental cavity modes $e1$ extracted from the simple Fabry-Pérot model as a function of the number j of missing holes forming the defect. For comparison, the quality factors determined via FDTD simulations are additionally shown. A very good agreement between the Fabry-Pérot model and the FDTD results is observed for large lattice defects with $j \geq 6$. However, for defect structures comprising more than 10 holes, the determination of the Q-factor gets error-prone due to the steep slope and large uncertainty of the group index n_g for frequencies near $\omega = 0.3375 \times 2\pi c/a$ (Fig. 5.26) corresponding to wave vectors at the edge of the Brillouin zone. For smaller cavities ($j < 6$), the simple model overestimates the quality factor by approximately a factor of two. The calculation of

the Q-factor is solely based on the dispersion curve of the fundamental waveguide mode and totally ignores contributions from other Bloch modes. Especially in the case of ultra-small cavity structures, higher order modes have a strong impact on the cavity performance and can not be neglected [327, 328].

The one-dimensional Fabry-Pérot model allows us to easily predict the resonant frequency and the quality factor for unoptimized defects. The results are in good agreement with three-dimensional FDTD simulations. Moreover, the mode volume can be extracted from the linear fit in figure 5.25. The only input data required for the model are the waveguide dispersion curve to determine the group index n_g as a function of the frequency and the quality factor of one single defect geometry calculated via FDTD simulations to extract the reflectivity of the photonic lattice. Once these data are obtained, the resonant frequency and quality factors of all other defect sizes can be easily determined. However, the situation is totally different for modified structures, where some holes are displaced or reduced in size. When the waveguide mode undergoes distributed Bragg reflections at the edges of the hole forming the surrounding photonic crystal, it acquires a phase shift ϕ and its amplitude is changed by $|r|e^{-i\phi}$. In the model above, we assumed a constant reflectivity r and a constant phase shift ϕ for all defect structures independent on the number of missing holes. However, for a modified photonic lattice the reflectivity and acquired phase are changed [325,327]. The modified Bragg condition results in a frequency shift and a changed effective length L, as the cavity mode might penetrate deeper into the photonic crystal. Hence, for every defect geometry the exact resonant frequency, the mode profile and the reflectivity of the photonic lattice have to be simulated via three-dimensional FDTD methods.

To summarize, we investigated the realization of waveguide and cavity structures by introducing line or point defects in the photonic crystal. The intentional break of the periodicity leads to the formation of localized waveguide or cavity modes within the band gap of the surrounding crystal. In this work, we will fabricate both small cavity structures such as M0- and M1-cavities with small mode volumes as well as large defect structures such as M7-cavities enabling high Q-factors without the need for sophisticated cavity design but with the expense of larger mode volumes.

5.6 Cavity quality factor

In the previous section, we discussed different point-defects in the photonic lattice that trap electromagnetic modes and hence form tiny optical cavities. The storage time of light in an optical resonator is characterized by the quality factor Q. There exist various equivalent definitions of the theoretical quality factor, whereof one includes the calculation of the dissipated power and the energy stored in the cavity. This definition allows for the discrimination between in-plane and out-off-plane radiation losses. We investigate the dependence of the in-plane losses and hence the Q-factor on the number of surrounding air hole periods. By transforming the near field components to Fourier space and by integrating over all wave vector components inside the light cone, we de-

termine the vertically radiated power in the far field. Together with the stored energy, this opens an alternative way to compute the Q-factor. We compare this alternative method with standard FDTD results by calculating the Q-factors for various M0-cavity geometries. Moreover, the intensity profile in the far field opens the way for an effective optimization procedure. A smooth decay of the cavity field into the surrounding crystal minimizes the wave vector components inside the light cone. We use the method of *gentle confinement* [300, 329] to boost the quality factor of M0- and M1-cavities by one order of magnitude.

The quality factor can be interpreted in many ways. Commonly, the quality factor denotes the dimensionless lifetime of the cavity mode describing the number of optical periods that pass before the energy decays by $e^{-2\pi}$ [256]. In the experiment, the quality factor is determined by the inverse of the bandwidth of the cavity resonance in the spectrum. The Fourier transform of a time-varying field confined to a cavity has a squared amplitude that is given by a Lorentzian peak, proportional to $((\omega - \omega_0)^2 + (\omega_0/2Q)^2)^{-1}$, and $1/Q$ is the peak's width at half maximum [256]. In FDTD simulations, the quality factor is computed via the real ω and imaginary part ω_i of the complex resonant frequency $\omega_c = \omega + i\omega_i$ of the cavity mode (see also section 5.7.2). Due to cavity losses, the square amplitude of the field exponentially decays with $e^{-\omega_i t/2}$. The imaginary part ω_i of the frequency hence determines the losses out of the cavity. The quality factor is calculated by $Q = -\omega/(2\omega_i)$. Alternatively, the cavity quality factor can be calculated via the mode energy U stored in the cavity divided by the radiated power P [304, 322]:

$$Q = \omega \frac{U}{P} \tag{5.73}$$

Here, ω denotes the resonant frequency. In the case of an ideal photonic crystal cavity, e.g. without material absorption, fabrication tolerances or surface roughness, the quality factor is limited by the radiated power P out of the cavity. In two-dimensional photonic crystals with a finite depth, we distinguish between in-plane $P_{||}$ and out-of-plane $P_{\perp}$ losses that determine the total radiation loss $P = P_{||} + P_{\perp}$. Similarly, the quality factor can be separated in horizontal $Q_{||}$ and vertical $Q_{\perp}$ contributions [304, 322]:

$$\frac{1}{Q} = \frac{1}{Q_{||}} + \frac{1}{Q_{\perp}} \tag{5.74}$$

The confinement in the horizontal photonic crystal plane is induced by distributed Bragg reflections at the edges of the air holes surrounding the missing hole defect. The confinement is similar to distributed Bragg reflections in a one-dimensional multilayer system consisting of alternating layers of material with different dielectric constants and optical thicknesses of $\lambda/4$ surrounding a central much wider defect layer with a resonant wavelength λ. Light waves originating from the central defect layer are reflected at the interfaces of the multilayer system, interfere constructively and are tightly localized in the defect region. Hence, the photonic multilayer films on both sides of the defect act as a frequency-specific mirror. Once the cavity modes enter the unperturbed layer structure they decay. Theses losses can be minimized by adding more layers to the

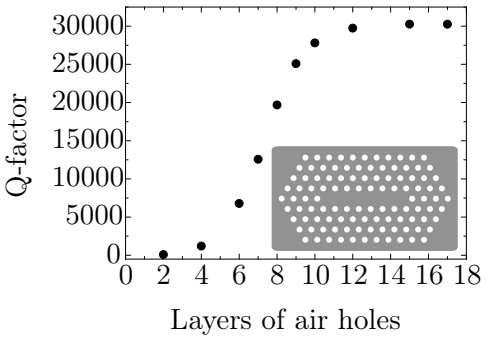

Figure 5.27: Dependence of the M7-cavity Q-factor on the number of air hole layers surrounding the defect: In the case of few surrounding holes, the cavity quality factor is limited by in-plane losses. With increasing number of photonic layers, in-plane losses are significantly reduced and vertical radiation losses become dominant. For large numbers of surrounding holes, Q saturates at a constant value limited by vertical radiation losses. The inset shows a M7-cavity with four layers of surrounding holes.

Bragg mirror system. By this, the reflectivity of the multilayer film is enhanced and the light is confined much longer in the cavity structure.

Impact of lattice size

The in-plane light confinement in a two-dimensional photonic crystal cavity, consisting of layers of air holes around a dielectric defect, is based on the same principle of distributed Bragg reflections at dielectric interfaces. As the number q of periods of air holes around the defect is increased, the in-plane losses can be significantly reduced and hence $Q_{||}$ raises. In contrast, $Q_{\perp}$ stays relatively constant, because adding more crystal layers is ineffective in capturing radiation losses in the vertical direction. Thus, for small numbers of surrounding air holes, the total quality factor is limited by in-plane losses, but as the number of layers increases, Q asymptotically approaches $Q_{\perp}$ [304,305]. Figure 5.27 shows the total quality factor of the fundamental $e1$ mode of the M7-cavity ($R = 0.28\,a$, $H = 0.91\,a$) as a function of the photonic crystal periods. For small numbers ($q < 4$) of hole periods, the total quality factor does not exceed $Q = 1,500$. With increasing number of layers, the Q-factor raises as the in-plane losses are reduced until Q saturates at a constant level of $Q = 30,200$ for $q > 10$. In our simulations of optimized cavity structures, we use nine to 13 surrounding hole layers to guarantee that in-plane losses are sufficiently reduced and Q is only limited by vertical radiation losses. In the experiment, the patterning time of photonic crystal structures significantly increases with the number of hole periods. For long fabrication times the probability of considerable device degradation increases due to sample drift during the milling process. Therefore, in practice, we chose cavity designs with six to eight hole periods to guarantee a sufficient in-plane confinement and reasonable patterning times. When comparing the experimental Q-factors to theoretical predictions, the actual number of surrounding

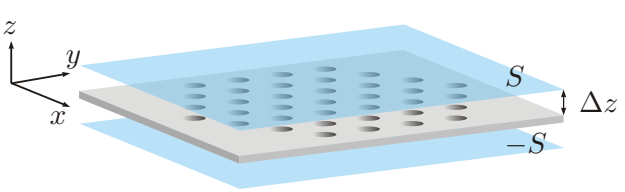

Figure 5.28: Schematic of the planes S at a distance Δz above and below the photonic crystal slab to compute the two-dimensional Fourier transforms of the cavity near fields.

holes is taken into account in our simulation.

The vertical quality factor $Q_\perp$ is limited by the out-of-plane losses due to non perfect index guiding of the cavity modes in the photonic slab. As discussed in section 5.4.2, light components with in-plane wave vectors $|\vec{k}_{||}| > \omega/c$ are guided in the slab, whereas all modes with $|\vec{k}_{||}| < \omega/c$ escape from the slab in the vertical direction and are radiated into the surrounding medium. The leaky components within the light cone hence determine $Q_\perp$. From the band structure of a photonic crystal slab, shown in figure 5.16, we can deduce that the lower the frequency of the cavity mode the smaller are the radiation losses in the light cone. Hence, high quality factors are expected for cavity modes localized deeply in the band gap. Indeed, the fundamental mode of the here simulated photonic crystal cavities with the lowest frequencies exhibit the highest quality factors. More detailed analysis shows, that the wave vector distribution of the cavity mode in Fourier space has a strong impact on radiation losses. By systematically tailoring the field distribution, the lossy Fourier components in the light cone can be minimized and $Q_\perp$ and hence the total quality factor can be enhanced significantly. We will present the basic design principles to minimize out-of-plane losses and to boost the cavity Q-factor in section 5.6.2.

5.6.1 Radiation Q-factor versus FDTD results

In this work the Q-factor is typically computed via finite-difference time-domain algorithm. However, FDTD results might vary with the chosen resolution. To confirm the numerical results, we apply an alternative method to calculate the quality factor via the stored energy U in the cavity and the radiated power P using $Q = \omega U/P$ (eq. 5.73), where ω denotes the resonant frequency. The stored energy U within the cavity is given by [322]:

$$U = \frac{1}{2}\int_{\text{cell}} (\varepsilon_0 \varepsilon(\vec{r})|\vec{E}(\vec{r})|^2 + \mu_0 |\vec{H}(\vec{r})|^2) d^3r, \tag{5.75}$$

where the volume integral is taken between two planes S and $-S$ parallel to the (x, y)-plane positioned at Δz below and above the crystal slab (Fig. 5.28). The total radiated power P is computed using two methods. In the first approach, the radiated power is calculated via the surface integral of the Poynting vector $\mathfrak{Re}(\vec{E}^* \times \vec{H})$ in all three directions through planes at the edge of the simulation cell:

$$P = \int_{\partial\,\text{cell}} \mathfrak{Re}(\vec{E}^* \times \vec{H}) d^2r. \tag{5.76}$$

The second method is based on momentum space analysis of the near field components. As discussed above, when the defect is surrounded by a sufficiently large number of

hole periods, in-plane losses are minimized and the quality factor is mainly limited by vertical radiation losses. To identify out-of-plane radiation losses, we calculated the two-dimensional Fourier transform FT_2 of the cavity near fields $f(x, y)$ taken in a plane S parallel to the (x, y)-plane at a distance Δz above the photonic crystal slab (Fig. 5.28):

$$\mathrm{FT}_2(f(x,y)) = \int_S f(x,y)\, e^{-i(k_x x + k_y y)}\, dxdy. \tag{5.77}$$

The radiated power in the far field is then given by the two-dimensional Fourier transform of the in-plane near field components E_x, E_y, H_x and H_y [330–332]:

$$P = \int\limits_{|\vec{k}_\parallel| \le k} I(k_x, k_y)\, dk_x\, dk_y, \quad \text{with} \tag{5.78}$$

$$I(k_x, k_y) = \frac{\eta}{8\lambda^2 k^2} \left| \mathrm{FT}_2(H_y) + \frac{1}{\eta}\, \mathrm{FT}_2(E_x) \right|^2 + \left| \mathrm{FT}_2(H_x) - \frac{1}{\eta}\, \mathrm{FT}_2(E_y) \right|^2,$$

where η is $\sqrt{\mu_0/\varepsilon_0}$ and I is the radiated intensity. The integral runs over all $\vec{k}$-vectors inside the light cone $|\vec{k}_\parallel| \le k$. Besides the qualitative computation of leaky components, the radiated intensity I distribution can be used to successively optimize the cavity structure. In the next section 5.6.2, we present a design recipe relying on the Fourier analysis to boost the quality factor. The optimal position of the plane S above the slab to separate the near- from the far-field is under debate. The distance Δz, given in literature, ranges from $\Delta z = 0$ [332], $\lambda/4$ [322], $\lambda/2$ [304, 332] to $H/4$ [332]. Balanis [330] claimed that the distance depends on the largest dimension D of the scatterer: $\Delta z \ge 2D^2/\lambda$. From the field distributions, we deduce a largest dimension of the M0-cavity field of $D \approx 0.5\lambda$. This would result in an optimal distance of $\Delta z = \lambda/2$ which will be applied in the following. The cavity near field is computed using FDTD simulations after 400 time-steps. After that time transient effects, resulting from a cutoff of our excitation pulse, have died away. Finally the stored energy U and the radiated power P are averaged over one period. This final time-averaging can be avoided by calculating the imaginary part as well as the real part of the fields instead of the real part only. It is sufficient to evaluate the complex fields at one instant in time, since the energy of complex fields does not change over one period.

We exemplary calculate the quality factor of modified M0-cavities via the radiated power and the stored energy and compare them to FDTD results. For three different background radii $R = 0.27\,a$, $R = 0.28\,a$ and $R = 0.29\,a$ and a fixed slab thickness of $H = 0.91\,a$, the size of the holes surrounding the M0 defect are varied. The structural parameters of the modified M0-cavities $\mathrm{M0}^A$-$\mathrm{M0}^D$ and $\mathrm{M0}^{h1}$-$\mathrm{M0}^{h4}$ and the used nomenclature can be found in section 5.6.2 and in annexe A. Figure 5.29 shows a very good agreement between the FDTD results and the Q-factor calculated via the radiated power and stored energy. Thereby, the radiated power has been either computed via the pointing vector using equation (5.76) or via integration of the leaky components in the light cone according to equation (5.78). A resolution of 32 points per lattice constant has been applied in the FDTD calculations. The errorbars in figure 5.29 (exemplary

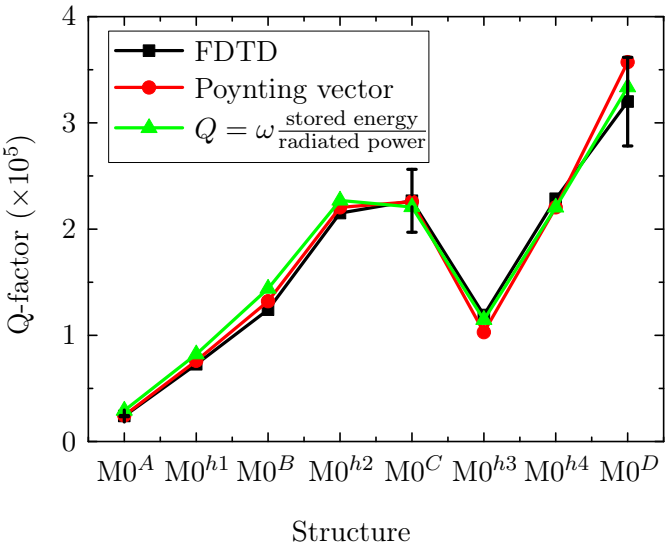

Figure 5.29: Comparison between the Q-factors of M0-cavities calculated via FDTD simulations and via the radiated power and stored energy. The radiated power is determined either via computation of the poynting vector (eq. (5.76)) or by integration over the leaky components inside the light cone (eq. (5.78)) calculated via the two-dimensional Fourier transform the in-plane components E_x, E_y, H_x, H_y. The stored energy is given by equation (5.75). The errorbars indicate the variation in Q when increasing the resolution from 32 to 50 points per lattice constant in the FDTD simulations. The design parameters of the M0^A-M0^C and M0^{h1}-M0^{h4} are given in annexe A and on page 129ff.

calculated for structures M0^A, M0^C and M0^D) indicate the variation in the Q-factor when increasing the resolution from 32 to 50 points per lattice constant. Within the error $< 13\%$, the FDTD results are very well reproduced by the Q-factor determined via the radiated power and stored energy.

5.6.2 Boosting the quality factor: gentle confinement

The definition of the Q-factor via the stored energy and the radiated power opens the way for an efficient optimization of the cavity design, that is referred as the method of gentle confinement. The basic goal of optimizing a photonic crystal cavity design is to increase the quality factor without delocalizing the mode, i.e. without enlarging the mode volume. The design principle is based on the modification of selected air holes surrounding the defect such that the field envelope retains a Gaussian function that smoothly decays into the surrounding crystal. This gentle localization comes along with reduced dissipation components inside the light cone of the radiated intensity profile (c.f. eq. (5.78)).

Above we have seen that the total quality factor can be decomposed into in-plane and out-of-plane contributions. To guarantee for minimal in-plane losses, we apply in our

simulations 13 layers of air holes around the defect. In this case, the total quality factor is limited by the out-of-plane losses, determined by the Fourier components inside the light cone. According to section 5.4.2, the in-plane wave vector $\vec{k}_{||}$ determines whether a plane wave is guided within the photonic slab or is radiated in the surrounding medium. All leaky components have in-plane wave vectors $|\vec{k}_{||}| < \omega/c = 2\pi/\lambda_{\text{air}}$ inside the light cone, whereas the in-plane wave vectors of guided modes $|\vec{k}_{||}| > \omega/c = 2\pi/\lambda_{\text{air}}$ lie outside the light cone and fulfill the condition of total internal reflection. Here, λ_{air} denotes the wavelength in air. In order to determine which components are guided or radiated, we calculate the spatial Fourier transform $\text{FT}(f)$ of the simulated cavity field f as a function of the wave vector $\vec{k}_{||}$. Fourier analysis reveals that abrupt changes in the cavity in-plane field distribution f lead to significant lossy components inside the light cone. For these plane wave components the condition of total internal reflection can not be fulfilled at the diamond-air interface and light is radiated in the vertical direction. In contrast, a gentle decay of the cavity fields into the photonic lattice suppresses radiation losses within the light cone and significantly increases $Q_{\perp}$ while retaining a small mode volume. In this section, we present the basic idea of *gentle confinement* [300,329] using the example of a one-dimensional Fabry-Pérot cavity. In the case of two-dimensional photonic crystal slabs, a gentle variation of the field distribution is achieved by modifying the geometry of the next-neighbor air holes surrounding the defect. Using the principle of gentle confinement, the quality factors of the M0- and M1-cavity are significantly enhanced.

Principle of gentle confinement in one dimension

In the following, we illustrate the basic idea of the gentle confinement method using the example of a linear Fabry-Pérot cavity consisting of two planar mirrors separated by a distance L along the x-axis. The gap between the mirror is filled with a dielectric medium with a refractive index $n = 2.4$ and a thickness H. Light waves in the medium are reflected by the mirrors, interfere with each other and form a standing wave. The electromagnetic field profile in the cavity can be expressed as a product of the fundamental sinusoidal wave $\sin(xk_0)$ of wavelength λ_{dia} ($k_0 = 2\pi/\lambda_{\text{dia}}$) and an envelope function determined by the cavity structure. The fundamental wave gives two delta functions in the Fourier spectrum centered at $\pm 2\pi/\lambda_{\text{dia}}$, while the envelope function modifies the spectrum. In the case of ideal mirrors, the electromagnetic fields vanish at the mirror surface. The Fourier transform of this rectangular field envelope is described by two sinc functions $\sin(L/2(k_x \pm k_0))/(k_x \pm k_0)$ centered at $k_x = \pm k_0$ (Figs. 5.30(a,b)). The abrupt change of the cavity field in real space results in pronounced Fourier components inside the light cone (light line is indicated by red lines at $2\pi/\lambda_{\text{air}} = 2\pi/(n\lambda_{\text{dia}})$ in Fig. 5.30(b)). The smaller the cavity length L the stronger are the leaky components in the light cone. However, according to Akahane et al. [300,329], radiation losses are strongly reduced by tailoring the field envelope to approach a Gaussian function that smoothly decays at the mirrors' positions. The field distribution with a Gaussian envelope and its associated Fourier transform, given as well by a Gaussian, are displayed in figures 5.30(c,d). The gentle confinement of the cavity modes leads to strongly reduced leaky

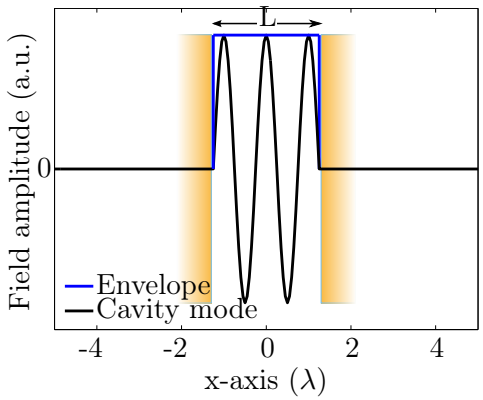

(a) Linear cavity mode

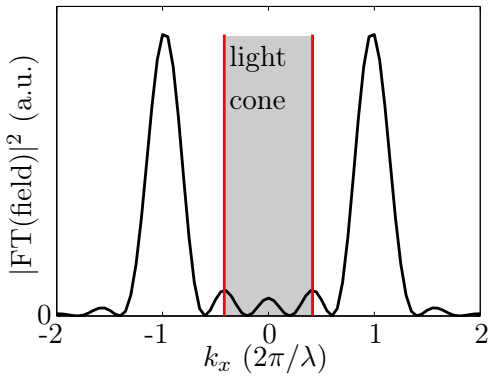

(b) FT of linear cavity mode

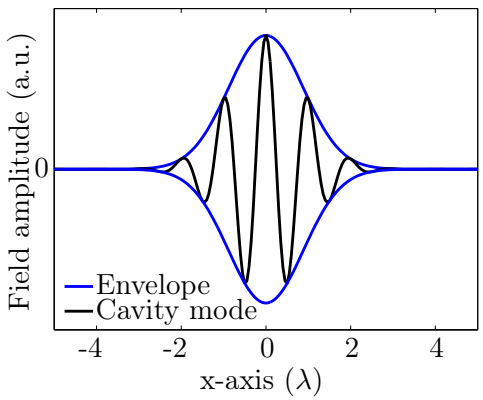

(c) Gently confined mode

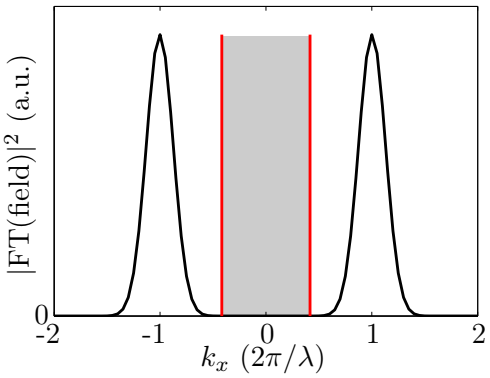

(d) FT of gently confined mode

Figure 5.30: Principle of gentle confinement in one dimension: (a) The standing wave confined in a linear Fabry Pérot cavity vanishes at the mirrors' positions. The abrupt change of the rectangular field envelope results in a Fourier spectrum (b) with important leaky components in the light cone (gray shaded region). The red line indicates the light line. (c) If the cavity field decays gently given by a Gaussian envelope (d) the radiation losses inside the light cone are significantly minimized. In (b,d) the squares of the absolute values of the Fourier transforms are displayed.

components inside the light cone and hence to a high cavity quality factor. The widths of the cavity field σ_x and of its Fourier transforms σ_{k_x} are inversely proportional. Hence, one can conclude that the more delocalized a cavity field is in space, the more localized its Fourier transform can be. This allows most of the Fourier components to lie outside the light cone and not radiate resulting in high Q-factors for gently confined modes. In the case of a linear Fabry Pérot cavity, a smooth decay of the standing wave at the mirror's positions is hard to realize. However, in the case of photonic crystal cavities, gentle confinement of the cavity mode is an effective method to significantly enhance the quality factor while retaining small mode volumes.

Gentle confinement in two-dimensional photonic crystal slabs

In the case of two-dimensional photonic crystal cavities, a gentle decay of the cavity field can be achieved by tailoring the photonic crystal structure around the defect region. The cavity field with frequencies inside the band gap is confined in the defect region via distributed Bragg reflections at the air holes forming the surrounding photonic lattice. By reducing the radius or shifting nearest neighbor holes outwards, the Bragg condition is locally modified leading to a phase shift upon reflection. The cavity field penetrates deeper into the crystal and its envelope decays much smoother at the edge of the defect. In fact, the delocalization of the cavity mode comes along with a slight increase in the mode volume. However, the detriment of a slightly larger mode volume is small compared to the boost in the Q-factor such that the ratio Q/V and the related theoretical Purcell factor can be significantly increased. In the ideal case, the main Fourier components would be tightly localized at the edge of the first Brillouin zone with no leakage inside the light cone [333]. Such ideal spatial Fourier spectrum is obtained for a Gaussian envelope function of the cavity field in real space [322]. In the following, the M0-cavity design is optimized according to the principles of gentle confinement to resume a Gaussian envelope and minimal Fourier components inside the light cone.

Optimization of the M0-cavity

The unoptimized M0-cavity is created by shifting two adjacent holes by a distance d apart along the x-axis of the photonic crystal lattice. The resulting donor type defect supports only one single resonant mode whose quality factor depends on the radius of the surrounding air holes R, the slab thickness H and the shift d. By successively modifying these three parameters in steps of $0.01\,a$ (c.f. Fig. 5.20 in section 5.5.2), a high quality factor of 24,500 and a small mode volume of 0.39 $(\lambda/n)^3$ of the unoptimized M0-cavity in diamond has been found for the parameter set $\mathrm{M0}^A$ summarized in table 5.2. By optimizing the radii of the surrounding lattice as well as the shift d and the back ground radius R, the M0-cavity quality factor can be significantly enhanced by one order of magnitude. Figure 5.31 shows the geometry of the improved M0-cavity design together with the used nomenclature. Thereby, we apply the following procedure: The radii of the surrounding air holes are varied and the corresponding Q-factor as well as

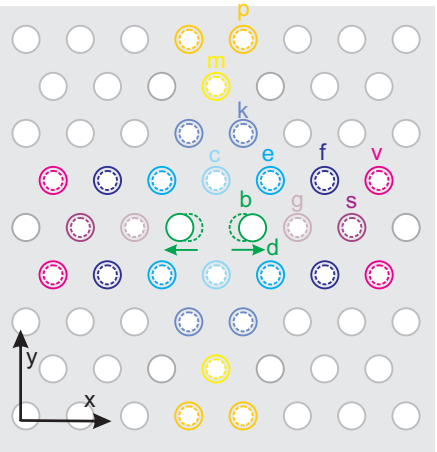

Figure 5.31: Modified M0-cavity design: By optimizing the surrounding air holes the quality factor is significantly improved.

the in-plane near-field components E_x, E_y, H_x and H_y are simulated for each parameter set. We start with the nearest neighbor holes along the y- and x-axis and further proceed with the holes at larger distances from the defect. The field components are taken in a two-dimensional plane at $\Delta z = \lambda/2$ [304, 332] above the photonic crystal slab. Via two-dimensional Fourier transform of the in-plane near-field distributions, we determine the radiated intensity I and normalize it to the stored energy U within the cavity. By integrating the intensity over all leaky components inside the light cone, the radiated power P is evaluated (c.f. eq. (5.78) in section 5.6). As the cavity quality factor is given by $Q = \omega U/P$ (c.f. eq. (5.73) in section 5.6), the normalized radiation losses are a direct measure of the inverse of the cavity quality factor. The smaller the leaky components inside the light cone the higher the cavity Q-factor.

As a first optimization step, the radii of the nearest neighbor air holes b, c, e and the shift d as well as the size of the holes f, g, k in the second and third row of the crystal are varied. The background radius $R = 0.26\,a$ and the slab thickness $H = 0.91\,a$ are

M0^A	$R(a)$	$h(a)$	$d(a)$	Q	$\omega(2\pi c/a)$	$V(\lambda/n)^3$
	0.26	0.91	0.15	24,500	0.3652	0.390

M0^B	$R(a)$	$d(a)$	$R_c(a)$	$R_e(a)$	$R_k(a)$	$R_f(a)$	Q	$\omega(2\pi c/a)$	$V(\lambda/n)^3$
	0.26	0.16	0.23	0.24	0.25	0.25	124,000	0.3606	0.388

Table 5.2: Starting point (parameter set M0^A) and M0-cavity design (parameter set M0^B) optimized along the x- and y-axis for background radius $R = 0.26\,a$. The radii not listed here correspond to the background radius R.

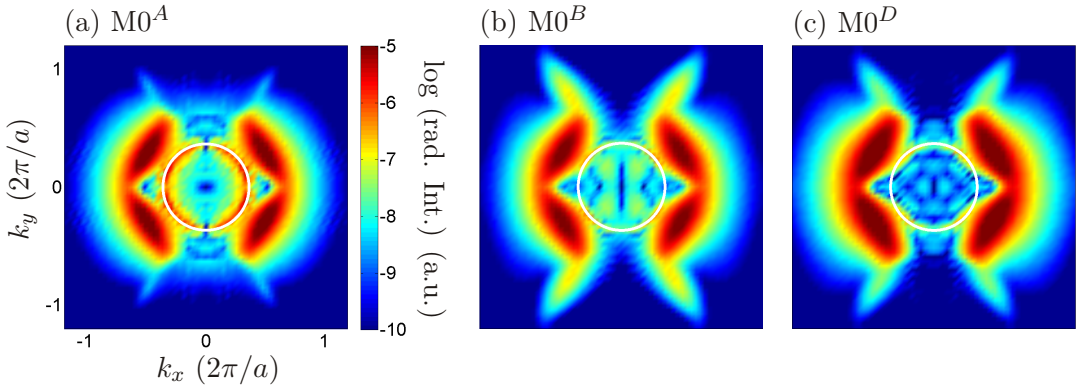

Figure 5.32: Comparison between the radiated intensity normalized to the stored energy of (a) the M0^A mode and (b) M0^B mode where the holes both along the x- and y-axis are optimized for background radius $R = 0.26\,a$. (c) Radiated normalized intensity of the optimized M0^D structure with background radius $R = 0.28\,a$.

fixed. A slight size reduction of the holes c, e, k leads to gentle confinement of the mode along the y-axis and to an improved quality factor up to $Q = 71,400$ while keeping the mode volume small. After subsequent tuning of the holes b, g, f along the x-axis, we yield a quality factor of $Q = 124,000$ and a mode volume of $V = 0.388\,(\lambda/n)^3$ for parameter set $M0^B$, summarized in table 5.2.

The reason for the raise in the Q-factor by one order of magnitude can be understood by comparing the normalized radiated intensity of the M0^A cavity (Fig. 5.32(a)) to the one of the optimized M0^B structure (Fig. 5.32(b)). The light cone is marked by the white circle. The Fourier components for both cavity structures are primarily localized at the edge of the first Brillouin zone. As the M0-defect creates donor type states that are pulled from the M-point of the upper air band into the band gap, the spatial Fourier transform is centered around the four M-points $(k_x, k_y) = 2\pi/a\,(\pm 0.5, \pm 0.5/\sqrt{3})$ in momentum space. Besides the confined wave vector components at the edge of the Brillouin zone, significant Fourier contributions inside the light cone are identified in the case of the unmodified M0^A cavity. On the other hand, in the case of the M0^B cavity,

M0^C	d (a)	R_c (a)	R_e (a)	R_k (a)	R_f (a)	ω $(2\pi c/a)$	Q	V $((\lambda/n)^3)$
	0.16	0.22	0.24	0.26	0.26	0.3673	226,600	0.35

M0^D	R_m (a)	R_p (a)	R_s (a)	R_v (a)	ω $(2\pi c/a)$	Q	V $((\lambda/n)^3)$
	0.31	0.34	0.29	0.27	0.3672	320,000	0.35

Table 5.3: Parameter sets M0^C and M0^D of improved M0-cavity in diamond with background radius $R = 0.28\,a$ and thickness $H = 0.91\,a$. The other parameters of structure M0^D are the same as in set M0^C.

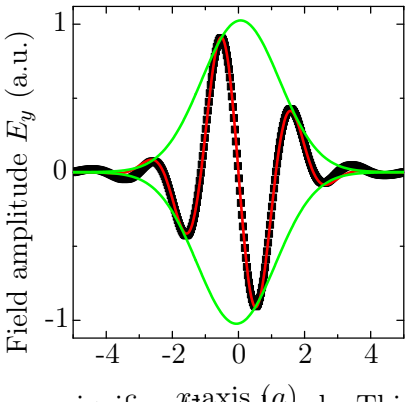

Figure 5.33: E_y field component of the optimized M0^D-cavity mode along the x-axis. The field envelope fits very well to a Gaussian distribution, which accounts for a gentle decay in the surrounding crystal.

the leaky components inside the light cone are significantly reduced. This results in minimized out-of-plane losses and in a strongly enhanced quality factor. However, when considering figure 5.32(b), there are still wave vector contributions left inside the light cone. This suggests further improvement by optimizing the holes at larger distances from the cavity center.

During the optimization process of the M0-cavity, it turns out, that higher Q-factors can be reached for slightly larger background radii $R = 0.28\,a$. By repeating the optimization procedure for the holes c, e, k and b, g, f for larger background radii $R = 0.28\,a$, the quality factor is almost doubled up to $Q = 226,600$ compared to smaller lattice holes $R = 0.26\,a$. Moreover, the mode volume slightly decreases to $V = 0.35\,(\lambda/n)^3$. For details see parameter set M0^C in table 5.3. As suggested by Fourier analysis, further improvement can be achieved by optimizing the holes at larger distances from the cavity center. Therefore, in a second step, we modify the radii of the remote air holes m, p along the y-axis and subsequently the size of the holes s, v along the x-axis while keeping the other parameters fixed. The parameter set M0^D, that yields the highest Q-factor of $Q = 320,000$ with a mode volume of $V = 0.35\,(\lambda/n)^3$, is summarized in table 5.3. The variation of remote air holes leads to further strong reduction of the leaky components inside the light cone (Fig. 5.32(c)) and hence to an improvement in Q while retaining a constant tiny mode volume.

The minimization of leaky wave vector components in Fourier space is closely related to gentle confinement of the cavity field in real space. Figure 5.33 shows the E_y cavity component simulated along the x-axis. The solid red line is a fit to the data composed of a sinusoidal fundamental mode multiplied by a Gaussian function (green solid line). The field distribution perfectly matches the Gaussian envelope function which reveals a gentle decay of the cavity mode into the surrounding crystal. Further details on the optimization procedure are given in annexe A and in our publication [274].

Optimization of the M1-cavity

The very same design procedure as described above has been used to optimize the M1-cavity in diamond [275] in order to boost the quality factor of the $-x-y$ quadrupole mode (c.f. section 5.5.2). The starting point is a modified M1-cavity shown in figure

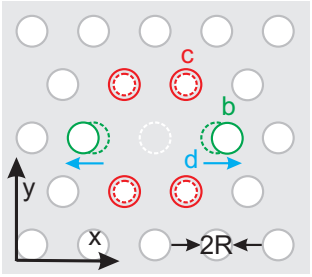

Figure 5.34: Modified M1-cavity design: By optimizing the surrounding air holes b, c and the shift d the quality factor is significantly improved.

5.34 with a background radius $R = 0.29\,a$ and a slab thickness $H = 0.91\,a$. In order to pull the pair of quadrupole modes inside the band gap and to lift its degeneracy, the radius of the next neighbor holes c is reduced to $R_c = 0.22\,a$ and the holes b are shifted by a distance $d = 0.21\,a$ along the x-axis. The $-x-y$ quadrupole mode of the initial M1-cavity has a resonant frequency of $\omega = 0.384 \times (2\pi c/a)$, a quality factor of $Q = 27,000$ and mode volume of $V = 1.23\,(\lambda/n)^3$ [275]. By analyzing the lossy Fourier components inside the light cone, the holes b, c and the shift d are systematically optimized. For a slightly enlarged slab thickness $H = 0.93\,a$, the optimized design yields a high cavity Q-factor of the quadrupole mode of $Q = 66,300$ and a mode volume of $V = 1.11\,(\lambda/n)^3$ [275]. The optimal parameter set of the M1-cavity is summarized in table 5.4. Compared to the initial structure, the Q-factor of the $-x-y$ quadrupole mode has been enhanced by more than a factor of 2.5, while the mode volume has been even slightly reduced. Although the design procedure was focused on the Q-factor boost of the quadrupole mode, the optimized M1-cavity supports additional modes in the band gap. The resonant frequencies, quality factors and mode volumes of dipole, quadrupole and hexapole modes are summarized in table 5.5. A monopole mode is not observed within the band gap. By shifting the holes b along the x-axis and by reducing the holes c in size, the original sixfold symmetry of the pure M1-cavity is broken, which lifts the degeneracy of the dipole and quadrupole modes (c.f. section 5.5.2). The highest quality factor is obtained for the $-x-y$ quadrupole mode on which we focused our design procedure. In contrast, all other modes retain modest Q-factors. The quality factor of the $-x+y$ dipole mode hardly exceeds $Q = 500$, whereas the Q-factor of its orthogonal analog is five times larger. From these data, we can conclude that the response of the modes on the modified cavity structure is very diverse due to their different symmetries. The modification of the surrounding air holes yields a gentle confinement for one specific cavity mode, but simultaneously the out-of-plane losses of a second resonant mode might be increased and hence degrade its Q-factor. Therefore, gentle confinement is a powerful tool to boost the quality factor of a single selected mode localized in a

$R\ (a)$	$H\ (a)$	$d\ (a)$	$R_b\ (a)$	$R_c\ (a)$	$\omega\ (2\pi c/a)$	Q	$V\ ((\lambda/n)^3)$
0.29	0.93	0.19	0.25	0.23	0.3821	66,300	1.11

Table 5.4: Parameter set $\mathrm{M1^{opt}}$ of optimized M1-cavity in diamond for a background radius $R = 0.29\,a$ and a slab thickness $H = 0.93\,a$. [275]

Mode	ω $(2\pi c/a)$	Q	V $((\lambda/n)^3)$	symmetry
Dipole	0.3451	2,400	0.64	$+x-y$
Dipole	0.3556	520	0.50	$-x+y$
Hexapole	0.3722	3,300	1.21	$-x+y$
Quadrupole	0.3821	66,300	1.11	$-x-y$
Quadrupole	0.3818	1,760	1.26	$+x+y$

Table 5.5: Resonant frequencies, quality factors and mode volumes of higher order modes confined in the $M1^{opt}$ cavity.

photonic crystal defect structure but is not capable of equally boosting the lifetime of all supported resonances.

To conclude, using the design principle of gentle confinement, we improved the M0-cavity yielding an extraordinary high theoretical quality factor of $Q = 320,000$ while retaining a tiny mode volume of $V = 0.35\,(\lambda/n)^3$. The boost in the Q-factor by more than one order of magnitude is unprecedented for a two-dimensional photonic crystal cavities in diamond. Furthermore, we increased the quality factor of one selected M1-cavity mode by a factor of 2.5 up to $Q = 66,300$ by varying the nearest-neighboring holes. During optimization of the M0-cavity, we have seen that the holes at larger distance from the defect might have a strong impact on the Q-factor. Therefore, we would expect further increase in the M1 quality factor by additionally optimizing remote holes.

5.7 Simulations methods

In this section, we present the numerical algorithms used in paragraphs 5.4 and 5.5 to simulate the photonic band structures as well as the field distributions, resonant frequencies, quality factors and mode volumes of the cavity modes. The computational techniques to solve electromagnetic problems can be separated in two classes: Frequency- and time-domain algorithms. The frequency approach directly calculates the eigenstates and eigenvalues of Maxwell's equations using a plane wave basis. Frequency codes are well suited to compute photonic band diagrams, as each computed field has a definite frequency. In contrast, time-domain algorithms, such as *finite-difference time-domain* (*FDTD*) codes, iterate Maxwell's equations in time on a finite discretized spatial mesh. Temporal approaches are well suited to simulated electromagnetic field distributions, transmission spectra, radiated power and resonance decay times, i.e. cavity quality factors. We use the freely available software program *MIT Photonic-Bands* (*mpb*) [259], that solves Maxwell's equations in the frequency-domain by expanding the fields in a plane wave basis. In section 5.7.1, we will present the principle ideas to compute the eigenfrequencies and eigenstates in the frequency-domain. To simulate the

electromagnetic modes confined within photonic crystal cavities and to compute their resonant frequencies and quality factors, we use the equally freely available software package *MIT Electromagnetic Equation Propagation* (*meep*) [334] and the commercial program *Lumerical FDTD Solutions* [335]. Both programs implement finite-difference time-domain codes. In section 5.7.2, we discuss the spatial and temporal discretization, present the applied boundary conditions and explain the analysis of the resonant modes. Plane wave expansion and FDTD algorithms both allow for computation of the near field components of the photonic crystal modes. However, in our experimental setup, the fields are collected and detected at large distances from the light source. To efficiently compute the far field pattern, we introduce in the last section 5.7.3 the concept of near-to-far-field transformation that is based on Fourier transforming the near field components. Using this transformation technique, we compute the far field pattern and polarization properties of M1- and M7-cavity modes and evaluate the collection efficiency of the radiated emission by our microscope objective.

5.7.1 Plane-wave expansion method

Here, we introduce the basic idea to solve Maxwell's equations in the frequency domain and to calculate the photonic band structure. The method relies on plane wave expansion of the electromagnetic fields to iteratively solve a generalized Maxwell's eigenvalue problem. The description follows references [256, 259, 336]. As shown in section 5.2, due to the discrete translational symmetry of the photonic lattice, the electromagnetic fields can be written as Bloch modes $\vec{H}_{\vec{k}}(\vec{r}) = e^{i\vec{r}\cdot\vec{k}}\vec{u}_{\vec{k}}(\vec{r})$. These are composed of a plane wave multiplied by a periodic function $\vec{u}_{\vec{k}}(\vec{r})$ that shares the periodicity of the dielectric function $\varepsilon(\vec{r})$. Substituted into the master equation (5.3), an eigenvalue equation for the periodic function $\vec{u}_{\vec{k}}(\vec{r})$ to the eigenvalue $(\omega(\vec{k})/c)^2$ was found in section 5.2:

$$\hat{\Theta}_{\vec{k}}\vec{u}_{\vec{k}}(\vec{r}) = (i\vec{k} + \vec{\nabla}) \times \frac{1}{\varepsilon(\vec{r})}(i\vec{k} + \vec{\nabla}) \times \vec{u}_{\vec{k}}(\vec{r}) = \left(\frac{\omega(\vec{k})}{c}\right)^2 \vec{u}_{\vec{k}}(\vec{r}). \tag{5.79}$$

Due to the periodicity of the function $\vec{u}_{\vec{k}}(\vec{r})$, the computation only needs to consider a single unit cell with periodic boundary conditions. Here, $\hat{\Theta}_{\vec{k}}$ defines the Hermitian operator derived from Maxwell's equations to wave vectors $\vec{k}$ within the first Brillouin zone. Furthermore, the function $\vec{u}_{\vec{k}}(\vec{r})$ has to satisfy the transversality constrain:

$$(i\vec{k} + \vec{\nabla} \cdot \vec{u}_{\vec{k}}(\vec{r})) = 0. \tag{5.80}$$

The smallest eigenvalue $(\omega_0/c)^2$ minimizes the energy functional for all given eigenvectors $\vec{u}_{\vec{k}}(\vec{r})$:

$$\left(\frac{\omega_0}{c}\right)^2 = \min_{\vec{u}_{\vec{k}}(\vec{r})} \frac{(\vec{u}_{\vec{k}}(\vec{r}), \hat{\Theta}_{\vec{k}}\vec{u}_{\vec{k}}(\vec{r}))}{(\vec{u}_{\vec{k}}(\vec{r}), \vec{u}_{\vec{k}}(\vec{r}))}. \tag{5.81}$$

This approach is known as *Rayleigh-quotient minimization*. The eigenvalues associated to higher order modes are obtained by minimizing the same Rayleigh-quotient under

the constrain that the eigenvectors are orthogonal to the previously calculated ones. In practice, the minimization of the energy functional (5.81) is performed using iterative methods. The program *mpb* uses a preconditioned nonlinear conjugate-gradient algorithm [259]. To calculate the matrix-vector product $\hat{\Theta}_{\vec{k}}\vec{u}_{\vec{k}}$, we develop the periodic function $\vec{u}_{\vec{k}}$ in a series of plane waves:

$$\vec{u}_{\vec{k}}(\vec{r}) = \sum_{\{\vec{G}\}} \vec{c}_{\vec{G}}(\vec{k}) e^{i\vec{G}\cdot\vec{r}}. \tag{5.82}$$

The sum in equation (5.82) is taken over all reciprocal lattice vectors $\vec{G}$. The coefficients $\vec{c}_{\vec{G}}$ are determined by the Fourier integral over the unit cell volume V: $\vec{c}_{\vec{G}} = \frac{1}{V}\int e^{-i\vec{G}\cdot\vec{r}}\vec{u}_{\vec{k}}(\vec{r})d^3r$. If we apply equation (5.82) to the transversality constrain (5.80), we obtain the simple relation: $(\vec{k}+\vec{G})\cdot\vec{c}_{\vec{G}} = 0$. The $\vec{c}_{\vec{G}}$ automatically obey this constrain as for every reciprocal lattice vector $\vec{G}$, we can find two primitive vectors that are orthogonal to $\vec{k}+\vec{G}$. Substituting the Fourier series (5.82) into the eigenvalue equation (5.79), and Fourier transforming both sides, we obtain [256]:

$$\sum_{\{\vec{G}\}} \left[-\varepsilon^{-1}_{\vec{G}'-\vec{G}} \cdot (\vec{k}+\vec{G}') \times (\vec{k}+\vec{G}')\times\right] \vec{c}_{\vec{G}} = \frac{\omega^2(\vec{k})}{c^2}\vec{c}_{\vec{G}'}. \tag{5.83}$$

The factor $\varepsilon^{-1}_{\vec{G}}$ is the Fourier coefficient to the inverse dielectric function $\varepsilon^{-1}(\vec{r})$. To numerically determine the coefficients $\vec{c}_{\vec{G}}$, we need to truncate the sum (5.82) for large $|\vec{G}|$ to a finite number of terms. The computation could be simplified even further by approximating $\varepsilon^{-1}_{\vec{G}}$ using discrete Fourier transform and omitting the terms involving large $|\vec{G}|$. By developing $\vec{u}_{\vec{k}}$ and $\varepsilon^{-1}_{\vec{G}}$ in truncated Fourier series, we have transformed the problem for finding $\vec{u}_{\vec{k}}$ to solving a set of linear equations: $\tilde{\Theta}_{\vec{G}}\vec{c}_{\vec{G}} = (\omega/c)^2\vec{c}_{\vec{G}}$, where $\tilde{\Theta}_{\vec{G}}\vec{c}_{\vec{G}}$ denotes the right-hand-side of equation (5.83). The matrix-vector product $\tilde{\Theta}_{\vec{G}}\vec{c}_{\vec{G}}$ can efficiently be calculated in three steps using fast Fourier transform (FFT) algorithms [256]:

1. At first, we calculate the vector product $(\vec{k}+\vec{G})\times\vec{c}_{\vec{G}}$
2. Secondly, as the multiplication by $\varepsilon^{-1}_{\vec{G}'-\vec{G}}$ is very time consuming, we compute the (inverse) FFT to transform into real space, where we multiply with $\varepsilon^{-1}(\vec{r})$.
3. Finally, the eigenequation (5.83) is transformed back to reciprocal space to perform the second cross product $(\vec{k}+\vec{G}')\times$.

This numerical approach is well suited for iterative methods. Once the matrix-vector product $\hat{\Theta}_{\vec{k}}\vec{u}_{\vec{k}}$ has been calculated, the Rayleigh-quotient can be minimized and the eigenvalues can be determined using iterative methods, such as preconditioned nonlinear conjugate-gradient algorithms.

5.7.2 Finite-difference time-domain (FDTD) algorithm

To simulate the electromagnetic field distributions confined in the photonic crystal cavity structure and to extract the resonance frequencies as well as the quality factors, we perform finite-difference time-domain (FDTD) simulations [337,338], using the freely available software package *MIT Electromagnetic Equation Propagation* (*meep*) [334] and the commercial program *Lumerical FDTD Solutions* [335]. The essence of FDTD algorithm is the direct computational implementation of Maxwell's equations by approximating all derivatives, both spatial and temporal, as finite differences. The computational space is subdivided into intervals much smaller than the wavelength. At each mesh point, the dielectric structure is specified and the electromagnetic fields are calculated for successive time steps. At the beginning of the simulation, a short light pulse, injected at the center of the structure, excites the electromagnetic fields. Once the light source is turned off, both FDTD software packages allow for the extraction of the resonant frequencies, the quality factors and the mode volumes of the computed cavity modes. In the following, we will briefly introduce the spatial and temporal, finite meshing, referred as the Yee grid, that is widely used in FDTD simulations. We discuss boundary conditions such as *perfectly matching layers* to restrict the simulation cell to a finite volume or mirror boundaries to reduce the computational costs. Finally, we give the basic ideas to extract the resonant frequency and quality factor. For that purpose, the additional package *harminv* is implemented in *meep*.

Spatial and temporal discretization: Yee grid

The finite-difference time-domain (FDTD) algorithm is one of the widely used numerical techniques to solve electromagnetic problems. The method directly implements Maxwell's equations by approximating all temporal and spatial derivatives as finite differences of the electromagnetic fields [338, 339]:

$$\frac{df}{dx}(x_0) \cong \frac{f(x_0+\Delta x)-f(x_0-\Delta x)}{2\Delta x}. \tag{5.84}$$

The computational cell is sampled at intervals defined by the spatial resolution. For successive time steps, the field components are calculated at different mesh positions. The spatial discretization of the computational cell is know as the *Yee grid* [340]. Figure 5.35 displays the cubic unit cell of the Yee grid with the edge length Δx. Let us consider an arbitrary vector $\vec{r} = (i\,\vec{e}_x + j\,\vec{e}_y + k\,\vec{e}_z)\,\Delta x$, that will in the following be referred as (i, j, k), with $\vec{e}_x$, $\vec{e}_y$, $\vec{e}_z$ being Cartesian unit vectors. The three components of the electric field $\vec{E}$ are calculated at the edge of the cubic unit cell, whereas the magnetic components are stored on the faces of the cube. According to figure 5.35, the v^{th} component, $(v \in \{x, y, z\})$, of the electric field E_v is stored at the location $(i, j, k) + \frac{1}{2}\,\vec{e}_v\,\Delta x$ of the Yee grid, whereas the H_v-field is computed at $(i + \frac{1}{2}, j + \frac{1}{2}, k + \frac{1}{2}) - \frac{1}{2}\,\vec{e}_v\,\Delta x$ [341]. By storing the electric and magnetic field components at different positions within the unit cell, the accuracy of the algorithm is improved without additional computational steps. One consequence of the Yee grid is that, whenever we need to compare or combine different field components, e.g. when computing the energy

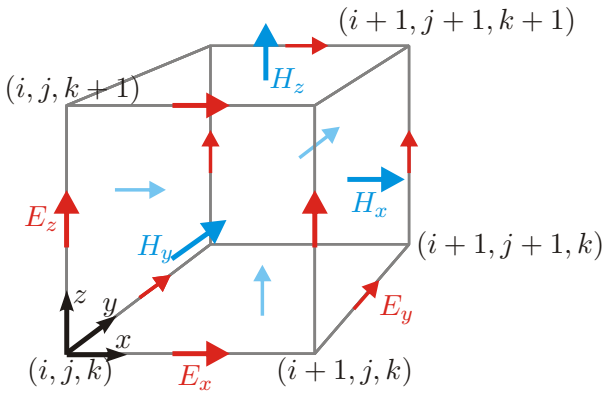

Figure 5.35: Yee grid used in FDTD simulations for spatial discretizations: The electric field components are calculated at the edge of the cubic unit cell, whereas the magnetic fields are simulated at the center of the faces.

density $(\vec{E}^*\vec{D}+|\vec{H}|^2)/2$ or radiated power $\mathfrak{Re}(\vec{E}^* \times \vec{H})$, the fields have to be interpolated to the center of the Yee unit. To improve the accuracy of the algorithm, *meep* uses subpixel smoothing of the dielectric function, where ε is averaged over several pixels at discontinuities of the dielectric material [342]. In contrast, *Lumerial FDTD solutions* enables to define a higher spatial resolution in parts of the computational cell.

Besides the spatial discretization Δx, the temporal derivations in Maxwell's equations are approximated by finite differences. Hence, the electromagnetic field at a time step t is determined by the electric field at $t - \Delta t$ and the magnetic field at $t - \Delta t/2$ on every spatial point of the Yee-grid. The relationship between the spatial and temporal discretization is determined by the Courant factor S. To guarantee the convergence of the FDTD-algorithm, the relation $S < n_{min}\sqrt{dimension}$ [341] has to be satisfied. In our simulations, the minimal refractive index n_{min} is typically 1. By default, *meep* applies a Courant factor $S = 0.5$ for one-, two- and three-dimensional systems [341]. Hence, doubling the spatial resolution requires a doubling of the time steps. In three dimensions, the doubling in spatial resolution, results in an eight-fold increased storage amount and in a more than 16-fold increase in the computational time.

Perfectly matching layers and boundary conditions

In order to truncated the simulation cell to a finite volume for simulating wave equations, we apply *perfectly matching layers* (PML) adjacent to the grid boundaries. This artificial absorbing medium was first introduced by Berenger [343]. When waves enter the artificial medium, they are attenuated by absorption and exponentially damped. To avoid reflections at the interface between the PML and photonic crystal, the solutions to Maxwell's equations are analytically continued in the PML by introducing complex coordinates. Behind the artificial absorbing layer, with a sufficient thickness to damp the fields, the computational cell is truncated using reflecting boundary conditions. Figure

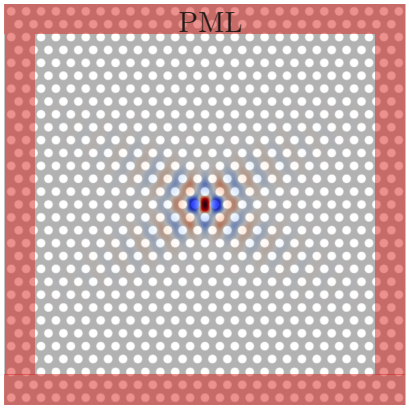

Figure 5.36: Schematic of perfectly matching layers surrounding the photonic lattice to exponentially damp the electromagnetic fields at the edge of the computational cell without reflections at the PML-photonic crystal interface.

5.36 schematically shows a PML layers with a thickness of $2\,a$ used in our simulations of photonic crystal cavities.

Besides the specification of the boundary conditions at the edge of the computational cell, *meep* and *Lumerical* also allows us to exploit mirror symmetries of the structure. If the material and the field sources are mirror symmetric upon reflection in the (x, y), (x, z) or (y, z) plane, the computational costs can be cut in two, by solving Maxwell's equations only in half of the computational cell and applying mirror boundary conditions to obtain the non-owed pixels adjacent to the mirror plane. Exploiting the mirror symmetries of the photonic cavity structures in all three spatial directions, the memory costs can be reduced to one eighth. Thereby, it is important that not only the photonic structure but also the electromagnetic fields are invariant under mirror reflections. In section 5.2 on page 77, we have seen that the electric and magnetic fields are classified in either even or odd modes depending whether they acquire an additional phase factor upon mirror reflection. The additional phase factor can be specified in FDTD simulations: even modes are multiplied by $+1$, whereas the factor is -1 for odd modes. We made sure, that the application of mirror boundaries has a negligible influence on the Q-factor or the resonant frequencies of the cavity modes. By successively adding one, two or three mirror boundaries, we verified that the relative error in Q is smaller than 4% [336].

Q-factor and resonance frequency computation: harminv

A point-dipole source with a temporal Gaussian profile is injected at the center of the structure and excites the electromagnetic fields in the photonic crystal. After the source is turned off, we analyze the resonant frequencies and the quality factor of the cavity modes using the built-in program *harminv*, which relies on a *filter-diagonalization method* introduced by Mandelshtam and Taylor [344, 345]. This computational method allows for the determination of the resonant frequencies and quality

factors with high precision and within short times, much faster than conventional Fourier analysis. Harminv registers the fields for sampling time steps t_n ($n = 1, 2, \ldots, N$) at given points in the crystal and expresses the fields as a sum of harmonic modes:

$$f(t_n) = \sum_{j=1}^{J} d_j e^{-i\omega_{j,c} t_n}. \tag{5.85}$$

The unknown complex frequencies $\omega_{j,c}$ and the associated amplitudes d_j are extracted from the signal by recasting the *harmonic inversion* problem as the one of a small matrix diagonalization. The real part $\omega_{j,r}$ of the complex frequency $\omega_{j,c} = \omega_{j,r} + i\omega_{j,i}$ denotes the dimensionless resonant frequency of the j^{th} mode expressed in units of $2\pi c/a$, with c being the speed of light and a being the lattice constant. The imaginary part $\omega_{j,i}$ characterizes the exponential decay of the fields' square amplitude. From these quantities, the cavity quality factor can be calculated as

$$Q = -\frac{\omega_r}{2\,\omega_i}. \tag{5.86}$$

The quality factor is the dimensionless lifetime of the cavity mode equal to the number of optical periods before the energy decays by $\exp(-2\pi)$. Alternatively, $1/Q$ is the fractional bandwidth at half-maximum of the resonance peak in Fourier domain. Please note that the calculated Q-factor might depend on the chosen resolution of the Yee grid. By applying different resolutions from 4 to 32 points per lattice constant in steps of 2, we verified that reliable and stable Q-factors are obtained for resolutions of 18 points or higher [336]. In the cavity simulations presented in this work, we typically applied a resolution of 20 grid points per lattice constant a. For one structure, a relative error in Q up to 20% has been detected when changing the resolution, but typically the error is smaller than 7% [336].

5.7.3 Near-to-far-field transformation

FDTD simulations allow for the computation of the near field components of the confined cavity modes. The spatial near field at the position of a single emitter enters the Purcell formula (5.63) and hence determines the coupling strength of a given cavity mode. In contrast, the experimentally accessible emission properties, e.g. the polarization or collection efficiency by the microscope objective, are defined by the radiation vectors at larger distances ($r \gg \lambda$) from the light emitter, in the so called far field. Direct application of the FDTD method to far field problems would be difficult because of the limited computer memory size and time. Here, we introduce the concept of near-to-far-field transformations that allows for efficient and accurate computation of the far field radiation patterns from the near field distributions obtained via FDTD simulations. Let us assume we know the near fields at the virtual surface S parallel to the (x, y)-plane at a distance Δz above the photonic crystal slab. Our goal is to deduce the far field at the observation point O on the hemisphere above the photonic crystal from the near field components at S. The tangential electromagnetic fields $\vec{E}_s$, $\vec{H}_s$ in the plane S give rise

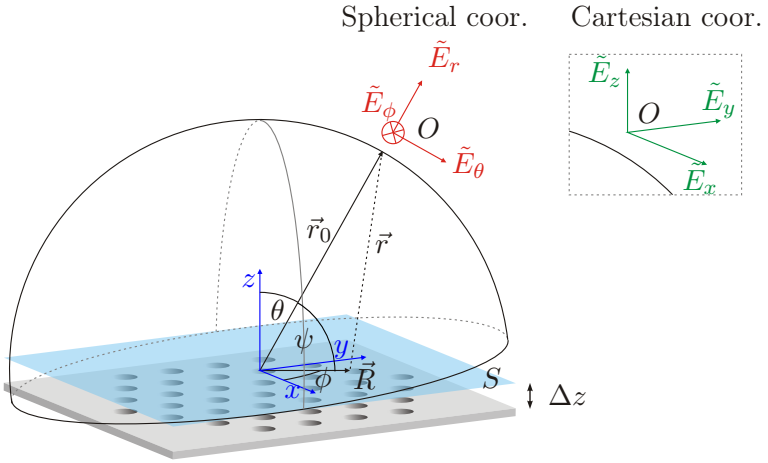

Figure 5.37: Schematic to calculate the far field at the observation point O by Fourier transforming the tangential near field components simulated at the virtual surface S above the photonic slab via FDTD simulations. The far field components are either given in spherical coordinates $\tilde{E}_r$, $\tilde{E}_\theta$, $\tilde{E}_\phi$ or in Cartesian $\tilde{E}_x$, $\tilde{E}_y$, $\tilde{E}_z$.

to electric and magnetic surface currents $\vec{J}_s$, $\vec{M}_s$ [330, 332]:

$$\vec{J}_s = \vec{e}_n \times \vec{H}_s \qquad \vec{M}_s = -\vec{e}_n \times \vec{E}_s, \tag{5.87}$$

where $\vec{e}_n$ is the vector normal to S. According to the surface equivalence theorem in electrodynamics, the electromagnetic fields in the far-zone can be obtained by integrating the equivalent surface currents $\vec{J}_s$, $\vec{M}_s$ over S [338]. To this end, we define the retarded vector potentials $\vec{A}$ and $\vec{F}$ that are related to the surface currents as follows [330, 332]:

$$\begin{aligned} \vec{A} &= \frac{\mu_0}{4\pi}\int_S \vec{J}_s \frac{e^{-ikr}}{r} dS \cong \mu_0 \frac{e^{-ikr_0}}{4\pi r_0}\vec{N}, \quad \text{with } \vec{N} = FT_2(\vec{J}_s)|_{\vec{k}_{||}} \\ \vec{F} &= \frac{\varepsilon_0}{4\pi}\int_S \vec{M}_s \frac{e^{-ikr}}{r} dS \cong \varepsilon_0 \frac{e^{-ikr_0}}{4\pi r_0}\vec{L}, \quad \text{with } \vec{L} = FT_2(\vec{M}_s)|_{\vec{k}_{||}} \end{aligned} \tag{5.88}$$

with r being the radial distance between the surface element dS and the observation point O. For the right hand side of equations (5.88), we used the approximation $r \cong r_0 - R\cos\psi$ in the far-zone, where ψ is the angle between the vector $\vec{r}$ and the in-plane vector $\vec{R}$ on the surface S. Using this approximation, $\vec{A}$ and $\vec{F}$ are expressed as the two-dimensional Fourier transforms FT_2 (c.f. eq. (5.77) in section 5.6) of the equivalent currents. The index $\vec{k}_{||}$ denotes the in-plane wave vector at S. It is important to note that for any observation point O, the in-plane wave vector lies within the light cone, i.e. $\vec{k}_{||} < \omega/c$. Thus, the radiation field is purely determined by the Fourier components inside the light cone [332]. From the retarded vector potentials, we derive the electromagnetic fields $\tilde{\vec{E}}$, $\tilde{\vec{H}}$ in the far-zone [330, 332]: $\tilde{\vec{E}} = -i\omega\vec{A} - 1/\varepsilon_0\vec{\nabla}\times\vec{F}$, and $\tilde{\vec{H}} = -i\omega\vec{F} + 1/\mu_0\vec{\nabla}\times\vec{A}$. By neglecting all terms that decay faster than $1/r_0$, the

electromagnetic fields at the observation point O can be derived. In spherical coordinates $(r,\, \theta,\, \phi)$, we obtain [330, 332]:

$$\begin{aligned} \tilde{E}_r &\cong 0 & \tilde{H}_r &\cong 0 \\ \tilde{E}_\theta &\cong -\frac{ike^{-ikr_0}}{4\pi r_0}[L_\phi + \eta N_\theta] & \tilde{H}_\theta &= -\frac{1}{\eta}\tilde{E}_\phi \\ \tilde{E}_\phi &\cong \frac{ike^{-ikr_0}}{4\pi r_0}[L_\theta - \eta N_\phi] & \tilde{H}_\phi &= \frac{1}{\eta}\tilde{E}_\theta, \end{aligned} \tag{5.89}$$

with $\eta = \sqrt{\mu_0/\varepsilon_0}$ and

$$\begin{aligned} N_\theta &= -FT_2(H_y)|_{\vec{k}_{||}} \cdot \cos\theta\cos\phi + FT_2(H_x)|_{\vec{k}_{||}} \cdot \cos\theta\sin\phi \\ N_\phi &= FT_2(H_y)|_{\vec{k}_{||}} \cdot \sin\phi + FT_2(H_x)|_{\vec{k}_{||}} \cdot \cos\phi \\ L_\theta &= FT_2(E_y)|_{\vec{k}_{||}} \cdot \cos\theta\cos\phi - FT_2(E_x)|_{\vec{k}_{||}} \cdot \cos\theta\sin\phi \\ L_\phi &= -FT_2(E_y)|_{\vec{k}_{||}} \cdot \sin\phi - FT_2(E_x)|_{\vec{k}_{||}} \cdot \cos\phi \end{aligned} \tag{5.90}$$

In the far zone, the θ and ϕ components of the $\tilde{\vec{E}}$ and $\tilde{\vec{H}}$ fields are dominant compared to the radial component. Hence, just by knowing the two-dimensional Fourier transform of the tangential near-field components E_x, E_y, H_x, H_y calculated via FDTD at the surface S, we can evaluate the far field distributions.

Moreover, from the electromagnetic fields given in the far zone, the radiation intensity $I(\theta, \phi)$ passing through the hemisphere above the photonic crystal slab can be evaluated [332]:

$$I(\theta,\phi) = \frac{\eta}{8\lambda^2}\left(\left|N_\theta + \frac{L_\phi}{\eta}\right|^2 + \left|N_\phi - \frac{L_\theta}{\eta}\right|^2\right). \tag{5.91}$$

The total power radiated into half-space $(z + \Delta z) > 0$ is then obtained via integration:

$$P = \int_0^{\pi/2}\int_0^{2\pi} I(\theta,\phi)\sin\theta\, d\phi\, d\theta. \tag{5.92}$$

In the case when most of the power is collected at vertical incidence (i.e. for small θ), formula (5.91) can be simplified [332]:

$$I(k_x,k_y) = \frac{\eta}{8\lambda^2 k^2}\left(\left|FT_2(H_y) + \frac{1}{\eta}FT_2(E_x)\right|^2 + \left|FT_2(H_x) - \frac{1}{\eta}FT_2(E_y)\right|^2\right). \tag{5.93}$$

This expression is equivalent to equation (5.78) presented in section (5.6) used to calculate vertical radiation losses. In the following, we present several applications of near-to-far-field transformations including far field distributions, polarization characteristics of cavity modes as well as their collection efficiency by the microscope objective in our confocal setup.

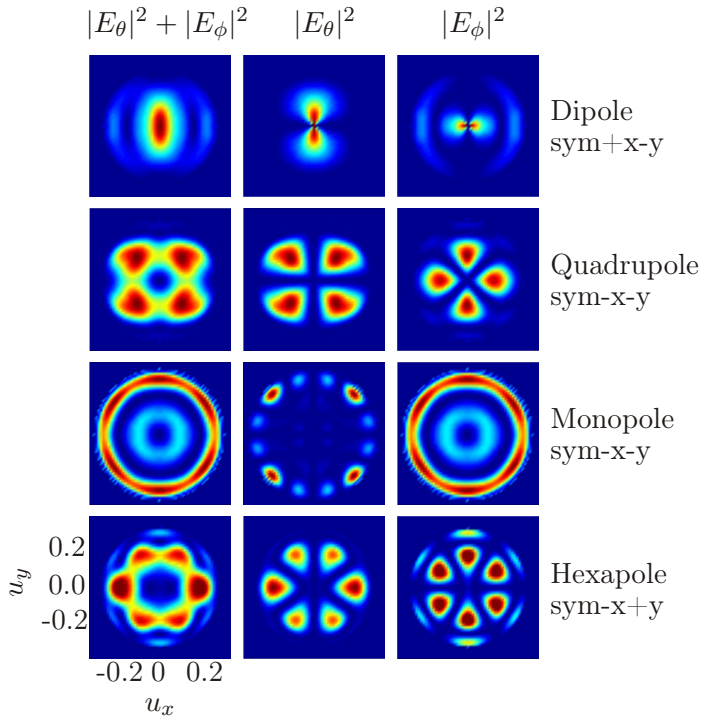

Figure 5.38: Far field pattern of the dipole, quadrupole, monopole and hexapole modes of the modified M1-cavity (c.f. Fig. 5.22, page 113) calculated in a plane S above the photonic crystal slab. The abscissa and ordinate are given by $u_x = \sin\theta\cos\phi$, $u_y = \sin\theta\sin\phi$.

Far field pattern of the M1-cavity modes

As an example of near-to-far-field transformation, we here compute the far field distributions for various M1-cavity modes and discuss their polarization properties. Figure 5.38 shows the far field components $|\tilde{E}_\theta|^2$, $|\tilde{E}_\phi|^2$ of the dipole, quadrupole, monopole and hexapole modes of the modified M1-cavity deduced from the near field components (c.f. Fig. 5.22, page 113) taken in a plane S above the photonic crystal slab. The data in figure 5.38 is plotted as a function of the direction unit vectors u_x, u_y given by the coordinate transformation from spherical coordinates to $u_x = \sin\theta\cos\phi$, $u_y = \sin\theta\sin\phi$. Depending on the rotational symmetry of the M1-cavity modes, the far field pattern shows several lobes, which determines the labeling of the modes, introduced in section 5.5 on page 112. For example, the intensity of the quadrupole mode has four maximum, whereas the hexapole mode shows six wings. The monopole mode exhibits a concentric ring shape emission profile. The 2$^{\text{nd}}$, 3$^{\text{rd}}$ row in figure 5.38 display the θ- and ϕ-polarized intensities $|\tilde{E}_\theta|^2$, $|\tilde{E}_\phi|^2$. In practice, these angle resolved quantities can be obtained in real measurements, by placing a polarizer in front of a detector which scans the whole hemisphere as a function of (θ, ϕ) [310, 321].

Polarization of M7-cavity modes

Our confocal setup described in chapter 4 does not allow for scanning of the whole hemisphere, but the position of the collection optics is fixed to vertical incidence. For our setup, it is more convenient to express the far field distributions in Cartesian coordinates. The $\tilde{E}_x$, $\tilde{E}_y$ and $\tilde{E}_z$ field components as well as $\tilde{H}_x$, $\tilde{H}_y$ and $\tilde{H}_z$ in the far zone are obtained

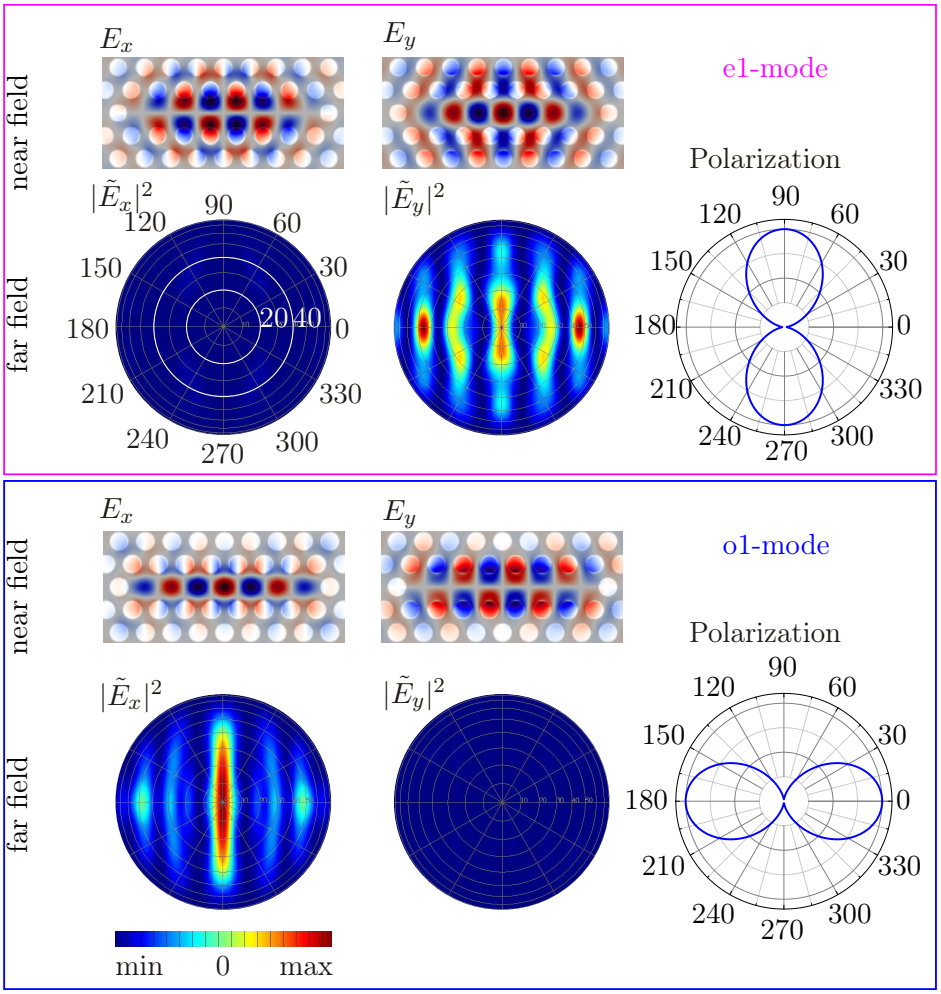

Figure 5.39: Simulated near-field components E_x, E_y and far field pattern $|\tilde{E}_x|^2$, $|\tilde{E}_y|^2$ and angular polarization of the o1 and e1 M7-cavity modes. In the case of the e1-mode, $|\tilde{E}_y|^2$ is dominant in the far field, resulting in a linear polarization along the y-axis. In contrast, $|\tilde{E}_x|^2$ is important for the o1-mode, yielding x-polarized far field emission.

by simply taking the two-dimensional Fourier transform of the associated in-plane field components simulated via FDTD in a plane above the photonic crystal slab. Thereby, only wave vectors inside the light cone contribute to the far field radiation. Figure 5.39 shows the near field components E_x and E_y as well as the normalized $|\tilde{E}_x|^2$ and

$|\tilde{E}_y|^2$ far field distributions of the e1- and o1-mode of the M7-cavity calculated using *Lumerical FDTD Solutions* [335]. The azimuthal angle ϕ in the far zone varies from 0° to 360°, whereas the polar angle θ is shown by concentric rings ranging from 0° (vertical incidence) to 90° (grazing incidence). In the case of the e1-mode, $|\tilde{E}_x|^2$ is very weak and $|\tilde{E}_y|^2$ is dominant in the far zone. For the o1-mode, it is vice versa; $|\tilde{E}_x|^2$ is prominent, whereas $|\tilde{E}_y|^2$ almost vanishes. In the experiment, the emitted light is collected by the microscope objective within the solid angle of 53.1° determined by the numerical aperture (NA = 0.8) of the objective. By integrating $|\tilde{E}_x|^2$ and $|\tilde{E}_y|^2$ within the collection angle, the polarization state of the M7-cavity modes can be obtained. As shown in figure 5.39, the e1-mode is linearly polarized along the y-axis, whereas the o1-mode is polarized along the x-direction. The linear polarization characteristic arises from the fact, that either $|\tilde{E}_x|^2$ or $|\tilde{E}_y|^2$ almost vanishes in the far field and the remaining component determines the polarization state. We account the cancellation of one vector field component in the far field by considering the near field distributions E_x, E_y of the e1- and o1-mode in figure 5.39. The E_x field of the e1-mode has a node in the (x, z)-plane (center line of the cavity defect). We consider the E_x pattern as a line of two identical oscillators separated by the (x, z)-mirror plane. As these two oscillators are out of phase, the radiation of the oscillator pair tends to cancel out in the far zone [132, 262]. In contrast, the E_y field of the e1-mode exhibits an anti-node at the cavity center line. In that case, both oscillators are in phase yielding to constructive interference in the far field. For the o1-mode, the situation is vice versa; the E_x near field has an anti-node in the (x, z)-plane and is dominant in the far field, whereas the E_y near field has a node along the cavity center line and hence vanishes at large distances from the photonic crystal slab. The polarization properties derived here, using the example of the e1- and o1-mode of the M7-cavity, are valid for all large-size cavity structures (c.f. section 5.5.2). In summary, all even modes of large size cavities are expected to show a linear polarization along the y-axis, whereas all odd modes are polarized along the x-axis. In chapters 7, 8 and 9 in this work, we will see, that the here presented theoretical predictions are in very good agreement with experimental polarization measurements. In the experiment, the linear polarization of the cavity modes helps to identify even and odd modes in the spectra.

Collection efficiency

In the experiment, we are interested in the photon count rate collected by our optics relative to the overall emission rate. The collected power normalized to the overall power emitted by the dipole source is defined as the collection efficiency η_{coll}. As already mentioned above, in our confocal setup (c.f. chapter 4), the microscope objective is positioned in z-direction above the photonic crystal slab and collects the emitted light within a solid angle of $\theta = 53.1°$, defined by the numerical aperture (NA = 0.8). The computation of the collection efficiency includes two steps: First, the transmitted power P_z passing in z-direction through the plane S above the photonic crystal slab is calculated via FDTD. The quantity is normalized to the total power P_{tot}, passing through all six faces of the virtual box surrounding the structure. However, due to

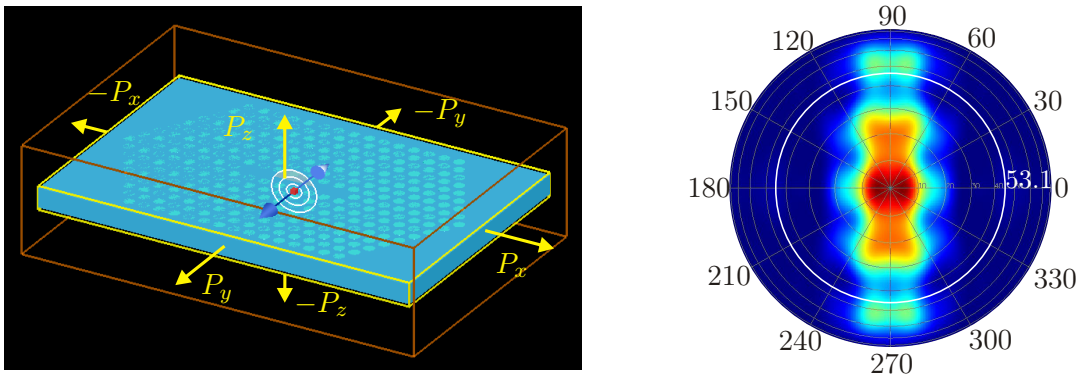

(a) Simulation cell (b) Radiated intensity

Figure 5.40: Layout of the simulation cell to compute the radiated power in all three spatial directions. (a) The Poynting vectors are calculated at the six faces of the yellow box surrounding the photonic crystal structure and the dipole source. The orange box marks the edges of the simulation cell. (b) Computed radiated intensity of the o2-mode of the M7-cavity. The white circle indicates the maximum collection angle $\theta = 53.1°$ for a microscope objective with a numerical aperture NA = 0.8.

the finite numerical aperture, the objective collects only the fraction $\eta_{NA} P_z$ of the out-of-plane emission P_z. To determine the ratio η_{NA}, we calculate in a second step the intensity radiated in the far field using equation (5.91). The spatial distribution of the radiated intensity is exemplary shown in figure 5.40(b) for the o2-mode of the M7-cavity ($R = 0.31\,a$, $H = 1.11\,a$). The white circle indicates the maximum collection angle $\theta = 53.1°$. By integrating the intensity over $\phi \in [0°, 360°]$ and $\theta \in [0°, 53.1°]$ and normalizing it to the total power determined by equation (5.92), we obtain the ratio η_{NA} collected by the microscope objective. The overall collection efficiency of the microscope objective is then given by:

$$\eta_{\text{coll}} = \eta_{NA}\, P_z / P_{tot} \tag{5.94}$$

For a point-dipole source placed at the center of the M7-cavity ($R = 0.31\,a$, $H = 1.11\,a$) and coupled to the o2-mode, we obtain a collection efficiency of $\eta_{\text{coll,cav}} = 0.23 \pm 0.06$. The collection efficiency is composed of $P_z/P_{tot} = 0.34$ of the power radiated in the vertical direction, whereof $\eta_{NA} = 0.67$ are collected by the microscope objective. In contrast, if the emitter is placed in an unperturbed photonic crystal lattice ($R = 0.31\,a$, $H = 1.11\,a$), we obtain a collection efficiency of $\eta_{\text{coll,PhC}} = 0.26 \pm 0.02$. For increased air hole radii $R = 0.34\,a$ and slab thicknesses $H = 1.61\,a$, the collection efficiencies are slightly increased to $\eta_{\text{coll,cav}} \approx 0.30$ and $\eta_{\text{coll,PhC}} \approx 0.30$. The collection efficiency determined here via FDTD simulations and near-to-far-field transformations, will become important in the experimental chapters 7 and 9. Together with the overall transmission through our confocal setup and the detection efficiency of the avalanche photo diodes used as single photon counters, the knowledge of the collection efficiency is essential in the experiment to predict for example the intensity enhancement of an

optical transition when coupled to a cavity mode or to estimate the quantum efficiency of a single emitter.

Summary

This chapter provides the theoretical background for the propagation and confinement of light in photonic crystal structures. The periodic variation of the refractive index leads to the formation of frequency bands and band gaps for electromagnetic fields in the crystal. By breaking the periodicity of the lattice, waveguides or cavities integrated in the photonic lattice are realized with resonance frequencies inside the band gap. In our analysis, we focused on two-dimensional photonic crystals consisting of a triangular lattice of air holes in diamond with a refractive index of $n = 2.4$. We considered purely two-dimensional systems as well as slab structures with a finite height.

Starting from Maxwell's equations, we derived an Hermitian eigenvalue equation for the electric and magnetic fields. Taken into account the discrete translational symmetry of the photonic lattice, the problem could be restricted to a single unit cell and to wave vectors within the first Brillouin zone. The solutions were separated in TE- and TM-polarization according to their mirror reflection symmetry. By numerically solving the restricted eigenvalue problem for a given dielectric function, we obtained the photonic band structure, i.e. the discrete spectrum of eigenfrequencies plotted as a function of the wave vector. As a first measure, we derived essential properties, like the appearance of a frequency gap between the first (dielectric) and second (air) TE-band from a purely two-dimensional system with no extend in the vertical direction. The physical origin of the band gap was explained by the variational theorem, i.e. the preferential localization of the first and second order modes in high- and low-dielectric material, respectively, resulting in a significant frequency difference. In a second step, we investigated photonic crystal slabs with a two-dimensional in-plane periodicity and a finite height. These structures are of inherent practical importance due to the relative ease of fabrication compared to three-dimensional crystals and the ability for compact chip-level integration. Photonic crystal slabs enable three-dimensional localization of light by a combination of the band gap effect in the horizontal plane and index guiding, a generalized form of total internal reflection, in the vertical direction. As the confinement via total internal reflection is not perfect, we introduced the light cone in the projected band diagram comprising all wave vector components $|\vec{k}_{||}| < \omega/c$ that are radiated into the surrounding medium, whereas all components $|\vec{k}_{||}| \geq \omega/c$ are guided in the slab. Including a finite slab thickness requires a modified classification of modes in TE- and TM-like modes according to their mirror symmetry. Analogous to purely two-dimensional structures, we observed a frequency gap in the band diagram for TE-like modes. We investigated the impact of the air hole radius as well as of the slab thickness on the gap width and the central frequency.

The appearance of a frequency gap comes along with a vanishing or reduced local density of states. We derived a compact relationship between the local density of states of the host material and the spontaneous emission rate and the radiated power of a

single dipole source within the material. This simple connection, allows us to derive the Purcell factor for emitter-cavity coupling involving spectral and spatial mismatch as well as misalignment of the dipole moment with respect to the cavity electric field. These contributions will become important in the experiment, when evaluating the enhancement or inhibition of spontaneous emission rates. We evaluated the Purcell factor and the local density of states for the photonic crystal lattice by computing the radiated power via FDTD simulations. For a purely two-dimensional photonic lattice, the local density of states vanishes at each lattice position for frequencies inside the band gap. This means that the spontaneous emission rate of a single emitter hosted in the photonic crystal is prohibited, as there are no states to which it can couple. In the case of photonic crystal slabs with a finite height, the local density of states as well as the spontaneous emission rate are strongly reduced inside the frequency gap. But in contrast to infinite structures, the two quantities do not vanish and depend on the polarization and position of the dipole source within the unit cell. For our geometries, we evaluated an averaged Purcell inhibition factor of $F_{\mathrm{PhC}} = 0.23 - 0.25$ of the photonic lattice compared to the emission rate in a homogeneous diamond slab.

The photonic band gap is the most important property of photonic crystals and has major consequences for light waves traveling through the periodic structure. The photonic crystal can be considered as a frequency- and polarization-specific mirror. Light waves with frequencies inside the band gap undergo distributed Bragg reflections at the edges of the air holes and the propagation through the material is hence prohibited, while the propagation of other modes outside the band gap is allowed. This property is essential for the realization of waveguides and cavities integrated in the photonic crystal. By introducing a defect in the periodic lattice, discrete states inside the band gap are formed with field distributions tightly localized in the defect region. The localization of light relies on distributed Bragg reflections in the horizontal plane and on index guiding in the vertical direction. In this work, we focused on waveguides created by the removal of one line of holes and cavities with zero, one or several missing holes. We characterized the localization of the cavity modes by its frequency, its symmetry, its quality factor and its mode volume. The smallest M0-cavity is a single mode resonator, whereas the M1-cavity supports multiple resonances referred as dipole, quadrupole, hexapole and monopole modes. Waveguide and large-size cavity modes were classified in even and odd modes according to their mirror reflection symmetry with respect to the waveguide or cavity center line at $y = 0$. We demonstrated that several-missing-hole cavities could be approximated as a line defect ended on both sides by a photonic lattice. Using this simple Fabry-Pérot model, we could derive essential properties, e.g. the mode profiles, resonant frequencies and cavity quality factors from the original waveguide mode.

The cavity quality factor can be separated in in- and out-off-plane contributions. We demonstrated that in-plane losses decrease with larger numbers of surrounding lattice periods. For sufficient in-plane confinement, the cavity Q-factor is limited by dissipative losses in the vertical direction. Based on Fourier transform of the tangential cavity near fields, we determined the power radiated in the far field by integrating over all Fourier components inside the light cone. Together with the stored energy, this provides an alternative method to calculate the Q-factor. For various M0-cavity designs, we con-

firmed that the Q-factors are in very good agreement with conventional FDTD results. Moreover, we introduced an efficient design procedure, referred as gentle confinement, to boost the cavity Q-factor without enlarging the mode volume. The goal was to modify the holes' radii around the defect such that the field envelope retains a Gaussian profile and smoothly decays in the surrounding crystal. In Fourier space, the gentle confinement of the cavity mode leads to minimal components inside the light cone and hence to a high quality factor. Using this design principle, we improved the M0-cavity yielding an extraordinary high quality factor of $Q = 320,000$ while retaining a tiny mode volume of $V = 0.35(\lambda/n)^3$. The boost in the Q-factor by more than one order of magnitude is unprecedented for two-dimensional photonic crystal cavities in diamond. Furthermore, we increased the quality factor of one selected M1-cavity mode by a factor of 2.5 up to $Q = 66,300$.

In the last section of this chapter, we presented the computational tools used in this work for band structure or cavity mode simulations. We distinguished between algorithms that solve Maxwell's equations in frequency- or time-domain. We applied a frequency-domain code based on plane wave expansion to simulate the photonic band structures. In contrast, finite-difference time-domain programs were used to numerically calculate the cavity field profiles, resonant frequencies and quality factors. This time-domain technique iterates Maxwell's equations on a discrete mesh. As both methods only allow for the computation of the near field components, we presented a supplementary near-to-far-field transformation, that enables to derive the far field distribution via Fourier transform of the near fields. Based on this transformation, we evaluated the far field pattern and polarization of various cavity modes and calculated the collection efficiency of the cavity emission by our microscope objective.

This chapter provides the theoretical background for the realization of photonic crystal cavities as well as Purcell enhancement and inhibition of the spontaneous transition rate of single emitters coupled to a cavity. In the next chapter, we present the fabrication of small cavities such as M0- and M1-cavities as well as large-size structures, e.g. M7-cavities, in diamond membranes. Exploiting the difference in the far field distributions, the cavity modes are identified in the spectra using polarization analysis. We compare the experimental Q-factor with the theoretical predictions simulated in this chapter. The frequency dependence on the lattice parameters will enables us to tune the cavity modes over a large spectral range into resonance with an ensemble as well as with single SiV centers. In chapter 9, we will experimentally demonstrate the inhibition and enhancement of the emission rate by structuring a photonic crystal around a pre-characterized single SiV center. Based on the computed collection efficiency together with the transmission through our setup and the detection efficiency of our single photon counters, the quantum efficiency of the single emitters can be deduced in and off resonance with the cavity mode.

Chapter 6

Realization of photonic crystal cavities in diamond

This chapter presents the fabrication of photonic crystal cavities in suspended single crystal diamond membranes. The first diamond-based photonic crystal cavities have been realized in nano-crystalline diamond films grown on a sacrificial substrate [132]. However, nano-crystalline diamond films suffer from strong material absorption and intrinsic scattering that limits the quality factors of resonant modes. Hence, for the realization of high-Q resonators, single-crystal diamond is the material of choice with best optical [346], excellent spin coherence properties [36] and narrow optical emission linewidths [173, 195] of incorporated color centers. The processing of single crystal diamond is challenging due to its extreme chemical inertness and mechanical stability. At the beginning of this thesis, no advanced nanofabrication technology was available for diamond. In this work, I developed a complete manufacturing process of diamond-based photonic crystal cavities. It includes the preparation of a free-standing single crystal diamond membrane, nano-size patterning of the desired structures and extensive post-processing.

The first step is the preparation of single crystal diamond membranes involving reactive ion etching to thin the membranes to a desired thickness of 300 nm. To precisely pattern the diamond films, we use a focused ion beam milling technique. The ion bombardment during the structuring causes lattice damages and amorphization of the diamond. The good material quality can be restored by an extensive annealing and cleaning procedure. We fabricate various optimized and unoptimized designs introduced and simulated in the previous chapter 5, ranging from small geometries, e.g. M0- and M1-cavities to large size structures, e.g. M3- and M7-cavities. By adjusting the lattice constant of the photonic crystal, the design wavelength is matched either to the zero-phonon line of SiV or NV centers. Resonant modes of the fabricated structures are identified in photoluminescence spectra using confocal spectroscopy. We analyze the quality factors of the modes and discuss possible limitations due to fabrication tolerances including non-perfect milling of air holes or material absorption.

6.1 Thin, free-standing diamond membranes

In this work, we investigate two different types of artificial diamond samples grown by chemical vapor deposition (CVD): The first type are heteroepitaxial diamond films deposited by a microwave assisted CVD process on a (001) silicon substrate via buffer layers. During the growth process a small amount of silicon is incorporated into the diamond film yielding optically active SiV centers. By adjusting the growth conditions, diamond layers with high concentrations of SiV centers as well as low density films with typically 2 single SiV centers per $20 \times 20\,\mu\text{m}^2$ are deposited. These samples are the basis for cavity-coupling experiments to SiV ensembles and for deterministic fabrication of photonic crystal cavities around a single SiV center.

The second class of samples are commercial ultra-pure (100) single crystal diamond membranes (electronic grade, Element Six N.V.) with a nitrogen concentration below 5 ppb and a thickness of $10\,\mu$m. These diamond membranes are well suited for targeted implantation of single NV centers into photonic crystal cavities in diamond. To handle and further process the fragile diamond films, we bond them via a spin-on glass adhesion layer onto a silicon substrate. In this section, we briefly present the characteristic CVD conditions to grow heteroepitaxial diamond films on silicon and we introduce the bonding procedure to glue diamond membranes onto silicon substrates. Furthermore, we present the dry etching processes to partially remove the silicon substrate in small areas to obtain suspended membranes and to thin down the diamond film to a desired thickness of 300 nm using oxygen plasma. We investigate the roughness of the as-grown and etched surface of the diamond films using atomic force microscopy. In addition, Raman spectroscopy is used to reveal intrinsic material strain both in the heteroepitaxial and ultra-pure bonded diamond films.

6.1.1 Heteroepitaxial diamond films

In general, artificial diamond can be grown via chemical vapor deposition in a hydrogen-methane plasma. Starting from small nucleation grains, hydrogen initiates free "dangling bonds" at the seed's surface where methyl radicals can adsorb [347]. The repetition of the scheme yields a closed diamond film. For cavity-coupling experiments to SiV centers, we use heteroepitaxial diamond films that are grown by chemical vapor deposition on a (001) silicon substrate via iridium/yttria-stabilized zirconia (Ir/YSZ) buffer layers [348]. The samples are provided by the group of Dr. Matthias Schreck from the University of Augsburg. The diamond films are deposited in a microwave-assisted CVD process using hydrogen and methane (1%) as precursor gases. A highly dense nucleation layer (typical areal density of $3 \times 10^{11}\,\text{cm}^{-2}$) on the iridium surface is achieved via bias enhanced nucleation (BEN) [142] by applying a voltage to the substrate, while injecting CH_4 and H_2 into the chamber. The diamond grains formed by BEN procedure exhibit an unmatched degree of initial alignment which enables preferential growth of the diamond layer. Together with the Ir/YSZ buffer layers that accommodate the lattice misfit between diamond and the silicon substrate the process allows for quasi single crystal diamond growth on a non-diamond substrate [348]. At the beginning of the diamond

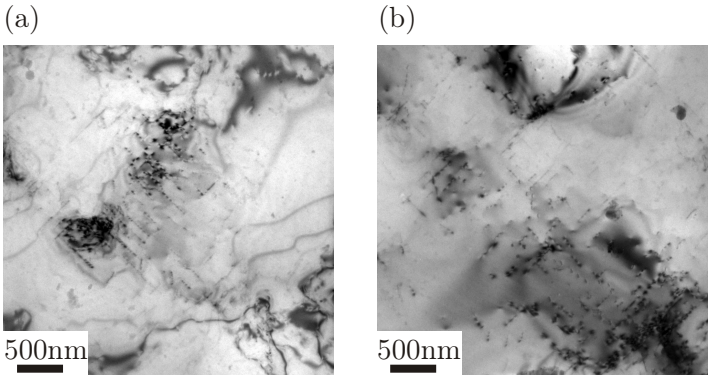

Figure 6.1: Transmission electron microscopy images of the topmost 250 nm layer of a 10 μm thick diamond sample grown on Ir/YSZ/Si(001) substrate. Large monocrystalline regions are observed that are interspersed with defects. The images are taken in two different sample regions.

growth, within the first few hundred nanometers, the diamond film shows a polycrystalline texture of crystallites with a marginal misorientation $< 1°$ [142]. With increasing slab thickness, the spread in the misorientation angles drops down to a few tenths of a degree until the network of small-angle grain boundaries disintegrate, adjacent grains merge and a dislocation-rich single crystalline diamond film is formed. Figure 6.1 shows a transmission electron microscopy (TEM) image of a 10 μm thick diamond layer near the growth surface. For the TEM images, the diamond film has been thinned down to 250 nm leaving only the topmost layer. The grains have merged into large monocrystalline regions that are partially interspersed with defects with typical distances and lengths of $2 - 5\,\mu$m [142]. For comparison, the photonic crystal cavities realized in this work have a typical size of $5 \times 4\,\mu$m, which is the same order of magnitude as the size of the monocrystalline diamond regions. Defects in diamond can be dislocations, grain boundaries or stacking faults [142]. The disappearance of grain boundaries with increasing growth thickness comes along with strong strain fields [142]. We analyze intrinsic material strain in section 6.1.5. After the growth, the diamond surface is mechanically polished.

In the CVD process, etching of the silicon substrate by the hydrogen plasma releases Si atoms into gas phase and allows them to be incorporated into the diamond film during growth [349]. Together with an adjacent vacancy, the incorporated silicon atoms form optically active SiV centers. With increasing microwave power and pressure, the plasma-induced etching of the silicon substrate is strongly enhanced yielding higher concentrations of SiV centers. Hence by adjusting the growth conditions, we are able to deposit diamond films containing large SiV ensembles down to 2 single SiV centers per $20 \times 20\,\mu\text{m}^2$ in the final membrane. The growth parameters are summarized in table 6.1. The growth gases are purified to yield a low concentration of nitrogen of about 1 ppm in the gas phase. Studies [350] on the incorporation of nitrogen into diamond have found that the nitrogen concentration in diamond is four orders of magnitude smaller

SiV content	Pressure (mbar)	MW-power (W)	Temp. (°C)	CH_4 in H_2 (%)
2 SiVs/$20 \times 20\,\mu m^2$	50	1,600	750	2
SiV ensemble	180	3,500	1,100	10

Table 6.1: CVD growth conditions of heteroepitaxial diamond films on Ir/YSZ/Si(001) yielding different concentrations of SiV centers.

than in gas phase. Assuming the same ratio for our diamond growth conditions, this would imply a nitrogen concentration below 1 ppb, which is even smaller than ultra-pure commercially available electronic grade diamond samples [151]. In the heteroepitaxial diamond films, no NV centers are observed.

After growth, the diamond films are prepared for further processing to obtain a free-standing membrane and the subsequent etching process. To this end, we remove the silicon substrate beneath the heteroepitaxial diamond film in small windows of $150 \times 150\,\mu m^2$ in size by a deep reactive ion etching process using SF_6 as an etching gas and C_4F_8 as passivation gas. The Ir/YSZ buffer layers beneath the diamond film are sputtered away via ion beam etching with argon ions.

6.1.2 Adhesion bonding of diamond

For targeted implantation of single NV centers at the center of a photonic crystal cavity, we use ultra-pure diamond films that are bonded onto a silicon substrate. The starting material is a $10\,\mu m$ thick (100) single crystal diamond membrane (electronic grade, Element Six N.V.) with a nitrogen concentration of < 5 ppb (specified by manufacturer). Both sides of the diamond film are polished to a root-mean-square roughness < 2 nm measured on an area of $1\,mm^2$ (specified by manufacturer). To facilitate the handling, we bond the diamond membrane via a spin-on glass adhesion layer (thickness $100-150$ nm) of hydrogen silsesquioxane (HSQ, chemical composition: $(HSiO_{3/2})_n$, Dow corning XR-1541-2%) onto a window etched in a polished silicon substrate. To achieve a free-standing diamond film, the silicon substrate has been removed over small areas of $150 \times 150\,\mu m^2$ by a deep reactive ion etching process using an alternation of SF_6 and C_8F_4 plasma etching steps. To promote a good adhesion, the diamond and silicon substrates are thoroughly cleaned prior to bonding in acetone and isopropyl alcohol for 5 min in an ultra-sonic bath and for 15 min in a 1:1 mixture of H_2O_2:H_2SO_4. The diamond film is carefully dried before it is attached to the spin-coated HSQ layer on the silicon substrate. Heating on two hot plates at 120°C and 210°C for 2 min each evaporates the solvents within the HSQ layer. After that, the adhesion layer is cured at 400°C in vacuum for 10 h. Under these annealing conditions, the Si-H bonds in the HSQ dissociate and a network structure forms with a chemical composition similar to silica [351]. The bond between the diamond and the silicon substrate via the cured HSQ layer is very strong, sustaining even high temperature annealing up to 1,000°C for several hours in vacuum as well as acid treatment in H_2O_2:H_2SO_4 or HNO_3:H_2SO_4:$HClO_4$ boiling mixtures.

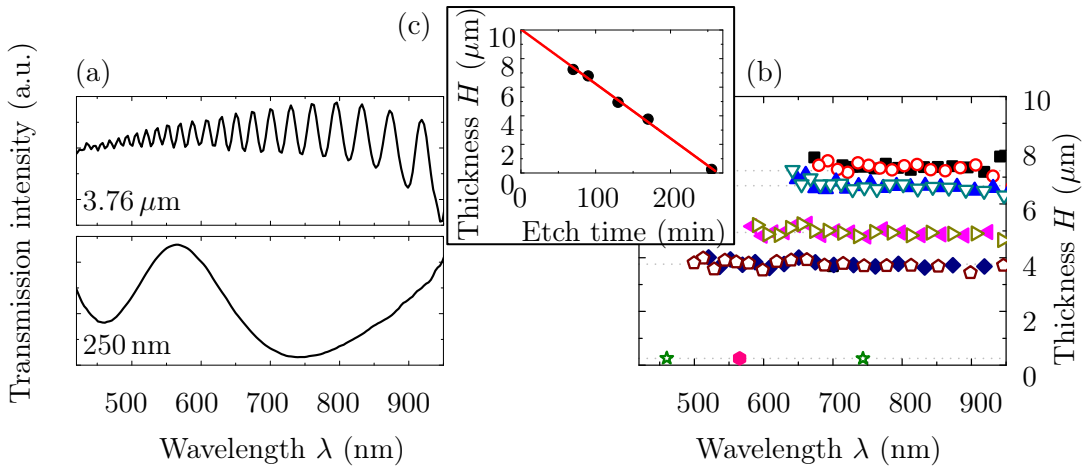

Figure 6.2: Measurement of the membrane's thickness using white light transmission spectroscopy: (a) White light transmission spectra through the diamond membrane with a thickness of $H = 3.76\,\mu$m and 250 nm. (b) We extract the membrane thickness using equation (6.1), from the transmission maxima (closed markers) and minima (open markers). (c) Slab thickness as a function of etching time. From the linear fit (red line), we determine an etch rate of 40 nm/min.

6.1.3 Reactive ion etching to thin the diamond

The heteroepitaxial diamond films and the bonded ultra-pure diamond membranes have an initial thickness of $10\,\mu$m that have to be thinned down to approximately 300 nm for the fabrication of photonic crystals. For the thinning, we use reactive ion etching (RIE) under the following conditions: 15 sccm of oxygen gas, 10 sccm of argon gas, 5 sccm of SF_6 at a chamber pressure of 1 Pa. Here, the gas flow is given in standard cubic centimeters per minute (sccm). During the etching, the sample holder is cooled from the bottom side via a helium gas flow of 5 sccm. A microwave power of 800 W is applied and 100 W of the high frequency generator are used. Under these conditions, the diamond is thinned from originally $\sim 10\,\mu$m to a desired thickness of 300 nm. The heteroepitaxial diamond films are thinned from the bottom side to remove the nucleation layer, while using the non-released silicon substrate as an etch mask. The bonded ultra-pure diamond membranes are homogeneously thinned from the top side.

We deduce the thickness H of the diamond membrane using white light transmission spectroscopy. Due to reflections at the bottom and top side of the diamond membrane, inference maxima and minima are observed in the transmission spectrum. Let λ_m denote the wavelength of the m^{th} minimum or maximum in the transmission spectrum, then the thickness is given by:

$$H = \frac{\lambda_{m-1} \cdot \lambda_m}{2n \cdot (\lambda_{m-1} - \lambda_m)}, \tag{6.1}$$

where $n = 2.4$ is the refractive index of diamond. Exemplarily, figure 6.2(a) shows the transmission spectra for a thinned membrane with a thickness of $H = 3.76\,\mu$m after an etching time of 170 min and $H = 250$ nm after 255 min. From the maximum and minimum, we extract the slab thickness using equation (6.1) (Fig. 6.2(b)). Plotting

the thickness as a function of the process times (Fig. 6.2(c)), we evaluate an etch rate of 40 nm/min for diamond films containing single SiV centers. For samples with large ensembles of SiV centers, we obtain slightly higher etch rates of $60 - 110$ nm/min. The ultra-pure diamond membranes (electronic grade) are thinned at a rate of 60 nm/min. The difference in the etch rates might be attributed to diverse concentrations of impurity atoms and to unequal growth conditions of the diamond films as well as to structural alteration of the RIE chamber. The thickness determined via white light interferometry is averaged over the whole membrane, which is well suited to evaluate overall etch rates and film thicknesses. However, due to polishing-induced wedges or inhomogeneous etching of the diamond membrane, the thickness can vary across the membrane. To locally determine the membrane thickness, we produce a cut through the diamond membrane via focused ion beam milling and deduce the thickness from SEM images (c.f. Fig. 6.11). Based on these local thickness measurements, we find a tapered profile of the ultra-pure diamond membranes with a wedge-angle of 0.022° (c.f. page 171). This means that the thickness varies by 4 nm over a length scale of 10 μm. The wedged profile probably results from mechanical polishing of the diamond surfaces. For the heteroepitaxial diamond films, we measure much larger thickness variations of ~ 30 nm over a length of 10 μm. The strong alternation is probably related to an inhomogeneous etch rate during reactive ion etching. In contrast to the ultra-pure diamond membranes that are thinned from the front side, heteroepitaxial diamond films are etched from the bottom side to remove the nucleation layer. In this etching process, the 500 μm-thick silicon substrate with small windows (size: $150 \times 150\,\mu\text{m}^2$) serves as an etch mask. It is suggested that the thick silicon substrate leads to a non-uniform etch plasma at the diamond layer and hence to an inhomogeneous etch rate.

The combination of heteroepitaxial growth or adhesion bonding of diamond to sacrificial substrates together with reactive ion etching to thin the films to a desired thickness, allows us to fabricate high-quality single crystal diamond membranes with sizes of $150 \times 150\,\mu\text{m}^2$, that can easily be handled and further processed, including e.g. structuring, high temperature annealing or acid cleaning. The membrane fabrication do not induce any damages or quality-degradation to the diamond material. Moreover, by using white light transmission spectroscopy, the membrane thickness can be very well controlled after each etching step in a non-destructive way.

In recent years, several alternative methods to fabricate thin diamond membranes and free-standing photonic crystal cavities have been proposed. One of these approaches involves the implantation of high-energy helium [352–354] or carbon [355] ions to create a damage layer at a well defined depth in the diamond substrate. The buried amorphous layer can be dissolved using high-temperature annealing and chemical etching to obtain an air gap beneath the membrane. However, this technique suffers from severe radiation damages upon helium implantation [356, 357] which prevents observation of cavity modes. Recent studies improved the procedure by subsequent reactive ion etching of the diamond surfaces to remove the topmost damaged layers [358, 359] and epitaxial overgrowth [85,359,360]. Another method is to etch thin trenches with a depth of 10 μm into bulk diamond using reactive ion etching in an oxygen plasma and a chromium etch mask [361, 362]. Subsequently, the 200 nm-thick diamond slices are exfoliated using a

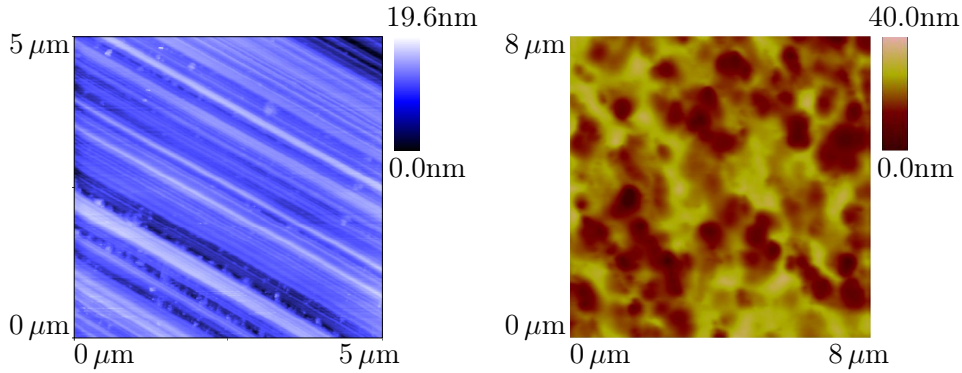

(a) Polished surface (b) Thinned nucleation side

Figure 6.3: Surface roughness determined via atomic force microscopy scans: (a) Mechanically polished diamond surface with a rms roughness of 2.6 nm. Measurement performed by Dr. Stefan Gsell (Experimentalphysik IV, Universität Augsburg), reproduced with permission. (b) Diamond nucleation side thinned to 250 nm using reactive ion etching exhibits a rms roughness of 5.4 nm.

syringe to fracture the slab near the base and are transferred to a glass substrate using a polydimethylsiloxane (PDMS) stamping technique [361, 362]. The NV centers in the exfoliated membranes show excellent optical and spin coherence properties. The huge drawback of this technique is the small size of the membranes limited to $10 \times 10\,\mu m^2$. An alternative method, that supersedes the fabrication of a free-standing membrane, is based on angled-under-cutting of photonic structures. Using either FIB milling [363] or anisotropic plasma etching via a Faraday cage [364] at an oblique angle to the sample surface, photonic structures are under-etched yielding a triangular cross section and released from the diamond substrate. This technique is limited to waveguide-like geometries with a small width in one direction, such as nanobeam cavities or cantilevers and can hardly be applied to large-size two-dimensional structures. Moreover, the theoretically predicted quality factors for triangular shaped waveguide cavities are moderate [363] compared to optimized rectangular nanobeams in diamond [255].

6.1.4 Surface roughness

After growth and mechanical polishing of the heteroepitaxial diamond films, we measure the surface roughness using atomic force microscopy. Scanning over an area of $5 \times 5\,\mu m^2$, we obtain a root-mean-square (rms) roughness of 2.6 nm. The roughness is mainly limited by grooves induced by the mechanical polishing, that are observable in figure 6.3(a) by inclined straight lines. Polishing defects could be minimized by removing the first few micrometers of the diamond surface using RIE [365]. However, the surfaces of the heteroepitaxial diamond samples, used in this work, are not further processed.

After thinning the diamond film from the nucleation side via RIE, we measure the surface roughness of the thinned bottom side. From the AFM-scan on an area

of $8 \times 8\,\mu m^2$ shown in figure 6.3(b), we obtain a root-mean-square roughness of 5.4 nm. The roughness is mainly limited by circular etching pits, that originate from a rough nucleation layer starting to grow as small crystallites. The smoothness could possibly be improved by applying argon-chlorine plasma etching instead of SF_6 and oxygen plasma. Very recently, extremely high surface quality has been reported for diamonds that have been exposed to argon-chlorine etching [366]. However, the rms roughness of both the surface and the bottom side is sufficiently small for the realization of photonic crystal cavities.

6.1.5 Strain analysis

Material strain might have a significant impact of the spectral properties of color center incorporated or implanted in diamond. In chapters 8 and 9, we will see that the zero-phonon lines of single NV^- and SiV centers might shift in the presence of strain. Material strain in the diamond films can be revealed using Raman spectroscopy. For high-purity strain-free single crystal diamond, the diamond Raman line has been found at $1332.5\,cm^{-1}$ [134]. However, it is well known, that tensile strain induces a shift of the diamond Raman line to smaller wavenumbers, whereas compressive stress leads to a shift in the opposite direction [367]. In this section, we investigate the presence of strain in the heteroepitaxial membranes as well as in the bonded ultra-pure diamond films using Raman spectroscopy and discuss possible origins of material strain. For that purpose, a 532 nm-excitation laser is focused onto the sample and the Raman signal with respect to the laser line is detected by the confocal setup and analyzed by a grating spectrometer (c.f. chapter 4).

Strain in heteroepitaxial diamond

We start our analysis with heteroepitaxial diamond films grown on Ir/YSZ/Si(001) substrates. Figure 6.4(a) shows the Raman spectra taken on the as-grown 10 μm-thick film, on the thinned diamond membrane and on a photonic crystal cavity patterned using focused ion beam milling (FIB, c.f. section 6.2). The sample has been annealed in vacuum at 1,000°C for 2 h and thoroughly cleaned in acid and thermally oxidized in air. The luminescence background has been subtracted in the spectra. The peak at zero wavenumber is associated to the excitation laser at 532 nm. The diamond Raman peak appears at $\sim 1326\,cm^{-1}$ and seems to be independent of the location on the sample. For a more general overview, figure 6.4(b) shows a statistic of the central Raman positions deduced from 35 spectra taken on different samples with high and low densities of SiV centers as well as on various locations including as-grown, thinned and structured regions. In all spectra, the diamond Raman line is shifted to smaller wavenumbers with respect to the bulk value at $1332.5\,cm^{-1}$ [134]. In more than half of the investigated spectra, the peak occurs at $1326\,cm^{-1}$. This significant deviation from the ideal value is attributed to material strain, that might have various reasons.

One origin of strain might be the patterning or reactive ion etching process to structure and thin out the diamond membrane, respectively. However, as the Raman shifts

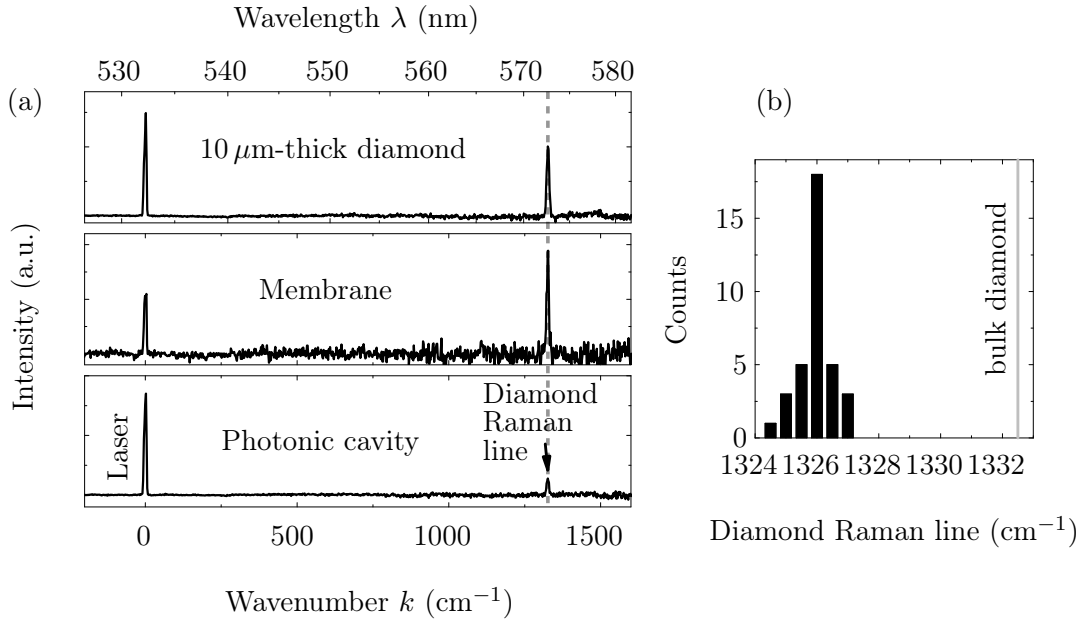

Figure 6.4: Raman spectra of heteroepitaxial diamond films: (a) The Raman lines recorded on the 10 μm-thick diamond film, the thinned membrane and the photonic crystal cavity are shifted to 1326 cm^{-1} with respect to the bulk value at 1332.5 cm^{-1}. (b) Statistic of the central position of the diamond Raman line evaluated from 35 spectra taken on different samples and locations, including as-grown diamond films, membranes and cavity structures.

measured on the photonic crystal cavity, the unstructured diamond membrane and the 10 μm-thick diamond film are similar, we do not expect FIB milling or RIE to be responsible for material strain.

The fact that the diamond Raman line of the as-grown diamond layer reveals the same significant shift, suggests that the CVD growth process on the Ir/YSZ/Si(001) substrate might be the source of strain. In general, one distinguishes several sources of strain [368]: thermal stress, which appears during the cooling, lattice misfit stress and intrinsic stress which is built up during growth and is possibly related to vacancies, dislocations and grain boundaries [368]. Fischer et al. [369] could show that the formation of intrinsic stress in heteroepitaxial diamond films is attributed to dislocations and the merging of grains during the first few microns of growth. As discussed above, with increasing growth thickness, small-angle grain boundaries disintegrate until a quasi single crystal diamond film is formed. The disappearance of grain boundaries comes along with a high strain field [142]. In contrast, the lattice misfit between diamond and the Ir/YSZ/Si(001) substrate as well as the mismatch in the thermal expansion coefficients play only a minor role. Moreover, they found a strong impact of the deposition temperature on the stress formation. By varying the temperature between 800°C and 1,100°C, the measured stress values covered a range of more than 3 GPa and changed from compressive to tensile stress [369].

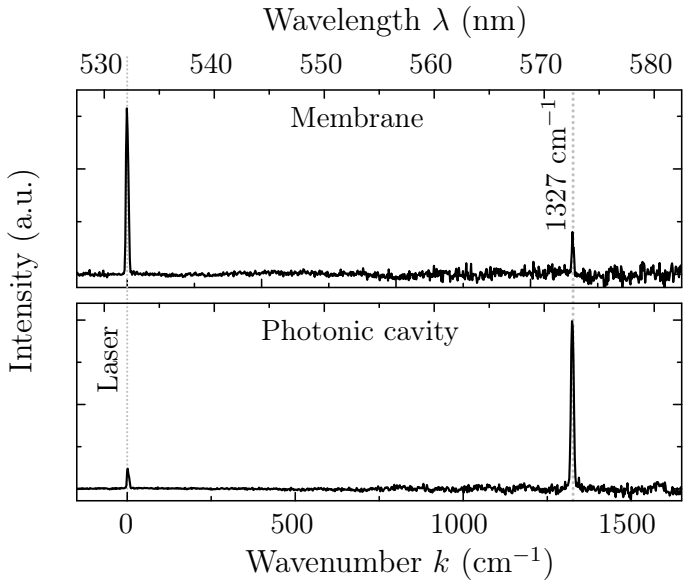

Figure 6.5: Raman spectra of the bonded, ultra-pure diamond membrane and a photonic crystal cavity patterned into it: The diamond Raman line is shifted down to $1327\,\mathrm{cm}^{-1}$ with respect to the bulk value, possibly resulting from material strain.

The observed Raman shift in figure 6.4 allows us to estimate the strain present in the diamond films deposited on Ir/YSZ/Si(001). In accordance with literature [368–370], we assume that the heteroepitaxial grown layer undergoes biaxial stress in the plane of the film. Based on group theory, von Kaenel et al. [368] deduced a linear dependency of $-0.61\,\mathrm{GPa/cm}^{-1}$ between biaxial stress in the (001) lattice plane and the offset of the diamond Raman line. Based on these data, the mean peak shift of $-6.5\,\mathrm{cm}^{-1}$ measured for the heteroepitaxial diamond films would correspond to tensile strain of 3.96 GPa.

Strain in ultra-pure bonded diamond

In a second step, we investigate the Raman spectra and the formation of strain in ultra-pure diamond membranes bonded on a silicon substrate. Figure 6.5 shows the Raman spectra recorded on the thinned unstructured membrane and on a photonic crystal cavity. The sample has been post-processed involving high temperature annealing in vacuum at 800°C, acid treatment and thermal oxidation in air.

The diamond Raman lines recorded on the membrane and the cavity are shifted down to $1327\,\mathrm{cm}^{-1}$. For comparison, we measure the diamond Raman line on an unprocessed reference membrane provided by the same manufacturer (Element Six) yielding $1329\,\mathrm{cm}^{-1}$. Both values deviate from the ideal bulk Raman line at $1332.5\,\mathrm{cm}^{-1}$ [134]. In the case of the as-received diamond membranes, the shift of the Raman line to smaller wavenumbers might result from mechanical polishing of the diamond surfaces inducing mechanical strain in the membrane that leads to a shift of the diamond Raman line with respect to the bulk value. The intrinsic strain seems to be further increased by our processing method (adhesion bonding and thinning) presented above, as indicated by

an additional shift of $2\,\mathrm{cm}^{-1}$ of the Raman line to $1327\,\mathrm{cm}^{-1}$. One possible origin of increased tensile strain in the membrane might be the mismatch in the thermal expansion coefficients of the diamond and the HSQ adhesion layer that transforms to a silica-like layer upon annealing (c.f. section 6.1.2). At 400°C, the thermal expansion coefficient of the HSQ layer of $\alpha_{\mathrm{HSQ}} = 15 \times 10^{-6}\,\mathrm{K}^{-1}$ [351] is approximately five times larger than the one of diamond ($\alpha_{\mathrm{dia}} = 3 \times 10^{-6}\,\mathrm{K}^{-1}$). With increasing temperature the HSQ layer expands and cures at elevated temperatures. When the sample is again cooled down to room temperature, thermal stress σ_{th} remains at the diamond/HSQ interface. The thermal stress can be estimated by [134]:

$$\sigma_{th}[GPa] = \frac{E_{\mathrm{dia}}}{1-\nu_{\mathrm{dia}}}(T[K] - T_{\mathrm{RT}}[K])(\alpha_{\mathrm{dia}}[K^{-1}] - \alpha_{\mathrm{HSQ}}[K^{-1}]), \tag{6.2}$$

where $E_{\mathrm{dia}} = 1{,}000\,\mathrm{GPa}$ and $\nu_{\mathrm{dia}} = 0.1$ are the Young's modulus and Poisson's ratio of diamond [371]. Using equation (6.2), we estimate an upper bound of the induced thermal stress of 5 GPa at the diamond/HSQ interface. As the diamond film is thinned down in a second step from the top side using reactive ion etching, the remaining 300 nm-thick membrane might be strongly affected by the thermally induced strain, leading to a theoretical Raman shift of $5.85\,\mathrm{cm}^{-1}$ [134]. Although this rough estimate slightly overestimates the induced Raman shift, it predicts the correct order of magnitude.

A second source of strain might be the high temperature annealing at 800°C in vacuum after the fabrication of the diamond membrane. However, the thermal expansion coefficient of the HSQ adhesion layer significantly decreases at elevated temperatures [351] and becomes comparable to the expansion coefficient of diamond at 800°C. Therefore, we conclude that thermal stress is mainly induced by the HSQ hard bake at 400°C. Once the HSQ layer is cured, the high temperature annealing of the sample does not cause additional material strain.

Finally, the patterning and thinning procedures of the diamond membrane might induce stress. However, FIB milling can be ruled out as the same Raman shift on the cavity structure and on the membrane is observed. Moreover, as the same etching technique to thin the membranes is applied for heteroepitaxial and ultra-pure diamond films, we conclude that, similar to the results above, the impact of the RIE process on stress formation in the bonded membrane is negligible.

To conclude, we identified the CVD growth process as the main source of material strain in heteroepitaxial diamond films, whereas mechanical polishing and the thermal expansion mismatch between diamond and the spin-on glass adhesion layer upon low-temperature annealing is responsible for stress formation in ultra-pure diamond membranes bonded on a silicon substrate.

6.2 Focused ion beam milling

Focused ion beam (FIB) milling is widely used in contemporary nanofabrication as it enables small feature resolution for arbitrary geometries and processing of a variety of materials without masks. Here, a beam of high-energetic ions locally sputters away

atoms of the target material and thereby allows for direct writing or milling of patterns into hard materials. In the following, we briefly introduce the FIB system used to pattern photonic crystal cavities in diamond. The FIB instrument is located at the department of materials science at the Universität des Saarlandes. Ion bombardment might cause FIB-induced damages and graphitization of the diamond material. We deposit a metal layer on the diamond film to protect the unstructured areas from ion irradiation. Moreover, thorough post-processing allows us to restore the pristine diamond quality and reliably remove all non-diamond phases what we confirm via Raman spectroscopy.

6.2.1 FIB instrument

To pattern the diamond membranes, we use a dual beam platform instrument (Helios NanoLab 600, FEI company) that is equipped with a scanning electron microscope for sample imaging and a focused ion beam system for structuring. The ion beam system includes an evacuated ion column with a liquid-metal ion source, providing a beam of gallium ions that are focused onto the sample by electrostatic lenses (Fig. 6.6). The description follows references [372,373]. Gallium is the most commonly used ion species for commercial FIB systems, due to its low melting point (29.8°C) that minimizes any reaction or interdiffusion with the source material, its low vapor pressure that allows Ga to be used in its pure form instead of an alloy and its low volatility at the melting point conserving the supply of metal and yielding a long lifetime source [372]. The liquid-metal ion source consists of a tungsten needle connected to a gallium metal reservoir and an extraction electrode. The heated gallium wets the tip and is ionized and extracted at the apex via a high electric field ($> 10^8\,\mathrm{V/cm}$) [372]. The extracted Ga^+ ions are accelerated by a fixed voltage of 30 kV and are collimated into a parallel beam by the (upper) condenser lens and focused onto the sample by the (lower) objective lens. A set of apertures of various sizes defines the beam diameter and allows for selection of the current in the range from 1 pA to 20 nA. For the photonic crystals presented in this work, we typically apply a current of 10 pA with a beam diameter of 13 nm, determined by the full-width at half-maximum of the Gaussian beam profile. To instantaneously switch the ion irradiation on and off, e.g. while milling a line of holes, a beam blanker interrupts the Ga^+ beam and hence avoids unwanted erosion of the diamond between the holes. The electrostatic beam deflector controls the final trajectory and impinging location of the ions on the substrate. The sample is mounted on a five-axis positioning stage for translation in the x-, y- and z-direction, as well as for rotation and tilt. The automated stage allows for control and for correction of possible sample drifts. To this end, next to the planned photonic structure, a cross marker is milled whose position is checked and eventually adjusted every 30 s during the crystal patterning. To minimize drifts, the sample is mechanically clamped on the sample holder instead of gluing it via copper tape, as widely-used. Moreover, to avoid drifts due to sample charging, a metal protection layer is sputtered prior to FIB milling onto the sample (c.f. section 6.2.3).

The desired pattern with specified hole positions and radii is imported into the FIB software that allows for automated serial structuring of the holes. Hereby, the milling is

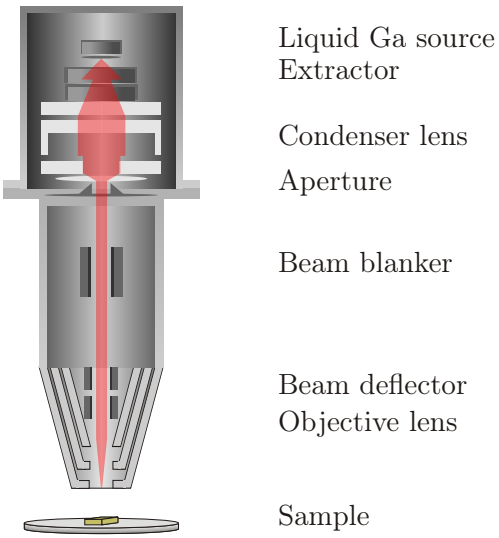

Figure 6.6: The FIB column includes a liquid-metal ion source providing a beam of Ga^+ ions, that are focused by the condenser and objective lens on the sample. A set of apertures defines the beam spot size and current. The beam blanker allows for instantaneous switching of the ion irradiation on and off and the beam deflector determines the final trajectory of the ions.

performed by a precise pixel-by-pixel movement [373]. The distance between adjacent pixels is chosen to be half the beam diameter such that the milled profiles of adjacent pixels overlap and guarantee for a smooth uniform pattern. The duration of time that the beam remains on a given pixel, referred to as the dwell time, is chosen to be 1 μs.

6.2.2 FIB damages

Depending on the ion species, the kinetic energy, the angle of incidence as well as the target material, an energetic ion can interact with the target in various ways. The interaction processes range from swelling, sputtering, redeposition, implantation, backscattering to nuclear reactions [373]. In the case of FIB milling, sputtering of the target surface by the impinging ion beam is the primary effect. Besides the desired material abrasion, secondary effects like redeposition, implantation of gallium and damages to the diamond lattice play a non-negligible role.

When the energetic gallium ions penetrate the target material, they undergo elastic collisions with the carbon atoms of the diamond lattice. For adequate acceleration voltages, the collision transfers sufficient energy to the target atoms to recoil them from their lattice positions. The latter can cause on his part a cascade of recoiled carbon atoms yielding significant lattice damages. To gain further insight into the ion-matter interaction, we performed Monte Carlo simulations using the freely available software package SRIM (Stopping and Range of Ions in Matter) [374]. Figure 6.7(a) shows the trajectories of 30 keV-gallium ions in diamond and the cascade of recoil C-atoms leaving a large amount of lattice vacancies. At an energy of 30 keV, the mean penetration depth

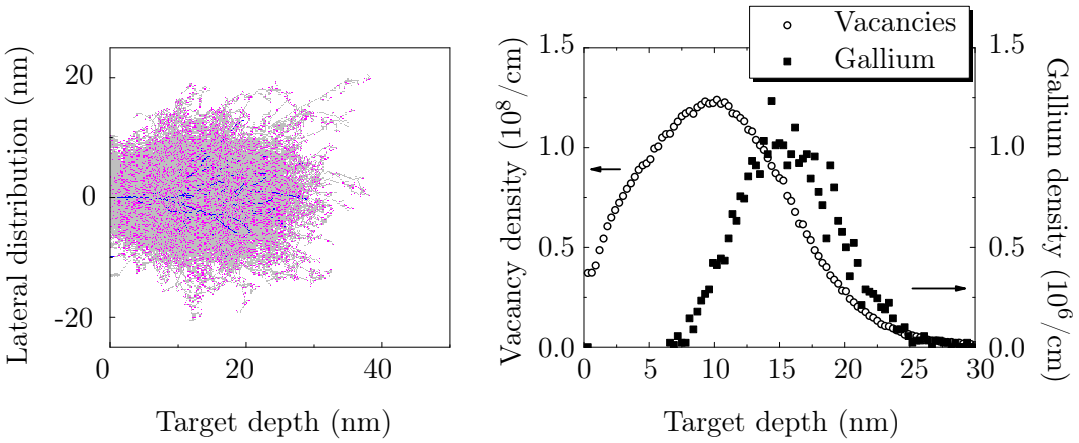

Figure 6.7: Stopping range simulations of gallium ions in diamond: (a) SRIM simulation of 30 keV-Ga^+ ions in diamond. The Ga^+ trajectories are shown in blue, whereas the created vacancies in the diamond lattice are shown in gray and the stopped atoms are shown in pink, respectively. (b) The mean penetration depth of 30 keV-Ga^+ ions is at 15 nm, whereas the maximum of the vacancies distribution is found at 10 nm below the diamond surface.

of the gallium ions is 15 nm (Fig. 6.7(b)). Remarkably, the location of maximum lattice damage at 10 nm does not coincide with the mean penetration depth of the gallium ions. The reason is that most of the vacancies are induced by recoiled C-atoms rather than by the original Ga^+ ions. Besides the recoil of carbon atoms, the impinging gallium ions lead to significant abrasion of the diamond surface. At 30 keV, the gallium ions transfer sufficient energy to the carbon atoms to overcome their surface binding energy and eject the atom from the substrate. According to SRIM simulations, on average two C-atoms per Ga-ion are ejected from the substrate. The number of ablated atoms per incident ion is defined as the sputtering yield. For single crystal diamond, sputtering yields of 2.3, 2.55 [375] and 2.73 [376] C-atoms per gallium ions at an energy of 30 keV and sputter rates of 0.08, 0.09 [375] and 0.18 μm^3/nC [376] have been reported. The low sputter rate is attributed to the high C-C surface binding energy of diamond ranging from 6.7 to 7.4 eV [377, 378], depending on the crystal quality. For comparison, the surface binding energy of silicon is 4.73 eV [379].

Since the ion beam profile resembles a Gaussian beam profile, the intensity at the fringe (tail) of the beam is much smaller than at the core (center region). The tail intensity is not strong enough to sputter material, but it is sufficient to cause amorphization. For single crystal diamond bombarded with gallium ions at an energy of 30 keV, the dose that causes amorphization has been determined to be 2×10^{14} Ga/cm^2, while significant sputtering requires doses that are at least two orders of magnitude higher [380]. The non-vanishing intensity of the beam tails causes a damaged, amorphous carbon layer, implanted with gallium ions, near the surface of the sputtered diamond material. The measured widths of the damaged zones vary between 11 nm [362] and 35 nm [380] are in agreement with the vacancy distribution simulated via SRIM (Fig. 6.7(b)). Based

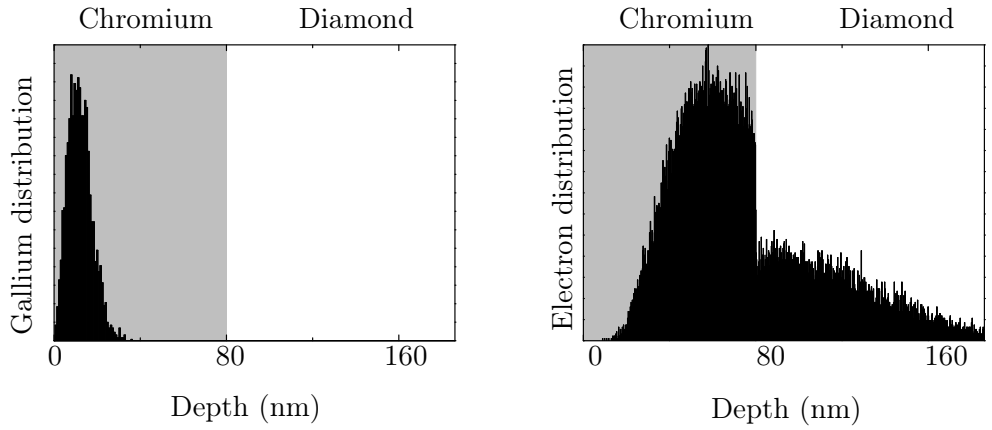

(a) Stopping range of 30 keV-Ga^+ ions in 80 nm-chromium

(b) Stopping range of 5 keV-electrons in 80 nm-chromium

Figure 6.8: Stopping range of gallium ions and electrons in chromium: (a) All impinging gallium ions with an energy of 30 keV are blocked within the 80 nm-thick chromium layer and do not irradiate the diamond beneath. (b) During SEM imaging, 70% of the electrons with an energy of 5 keV are stopped in the chromium protection layer.

on these data, we would expect a thin damaged layer of sp^2 bonded carbon and implanted gallium surrounding the holes' sidewalls after FIB milling of the photonic crystal structures in diamond. In the next sections, we present two measures to overcome the FIB-induced damages. A metal protection mask on top of the diamond avoids amorphization by the Gaussian beam tail, whereas an extensive post-process cleaning procedure removes the implanted gallium ions and the amorphous carbon layer.

6.2.3 Protection metal mask

Prior to the FIB milling, we sputter a metal protection mask with a thickness of $80 - 120$ nm on top of the diamond surface. In this work, we tested titanium and chromium as suitable protection layers that are removed after the FIB milling in hydrofluoric acid or chromium etchant, respectively. The metal masks offer a variety of advantages:

Prevent charging of the diamond membrane: As diamond is an insulating material, ion- or electron-irradiation might cause sample charging, which prohibits precise structuring or high resolution imaging of the diamond film. The charging can be overcome by depositing a thin conductive metal layer.

Protection of the non-irradiated regions: The metal film prohibits unwanted damaging and ion bombardment of the diamond material by the Gaussian tail of the ion beam. Monte Carlo simulations, using SRIM [374], illustrate that none of the 30 keV-

gallium ions penetrate the 80 nm-thick chromium protection layer and irradiate the diamond film beneath (Fig. 6.8(b)). The same result is obtained for a titanium mask. SEM images (Fig. 6.12) taken after the FIB milling of photonic crystals certify the pertinacity of the metal layer upon scattered ion bombardment.

Protection of single color centers: It has been shown that color centers bleach or completely switch off upon electron irradiation during SEM imaging [381]. This effect is probably associated to charge state switching of the color center due to electron-induced variation of the center's local electrostatic surrounding, e.g. charging of trapping states. Emission bleaching is especially harmful for imaging and target structuring of photonic crystal cavities around single color centers. A metal layer allows for the protection of the pre-localized single emitters. We use Monte Carlo simulations (CASINO, "monte CArlo SImulation of electroN trajectory in sOlids") [382, 383] to compute the penetration depth of electrons in chromium. In the simulation, we use an electron acceleration voltage of 5 kV, typically applied for SEM imaging. Figure 6.12(a) shows that 70% of the impinging electrons stop within the 80 nm-tick chromium layer and do not irradiate the diamond. If the mask thickness is enlarged to 120 nm, more than 97% of the electrons are blocked within the metal layer. Similar results are obtained for titanium.

Overmilling of air holes: Without a protection mask, the milled air holes of the photonic crystal exhibit an important inclination angle. To increase the sidewall steepness, we overmill the holes, which means that the target milling depth is raised beyond the membrane thickness. Thereby, the metal layer prevents abrasion of the diamond material and prevents a merging of the neighboring holes due to the Gaussian profile of the ion beam at the upper surface.

6.2.4 Post-processing

As discussed above, besides desired material abrasion, the FIB milling process causes possible amorphization of the lattice and implantation of gallium ions, that both strongly degrade the optical quality of the diamond film. In this section, we present an extensive post-process cleaning procedure of the diamond sample including high temperature annealing in vacuum as well as wet chemical etching and thermal oxidation in air. These measures allow for the recovery of the pristine diamond lattice, as well as for the removal of any sp^2 hybridized carbon phases, and for reduction of the concentration of implanted gallium ions near the surface.

High temperature annealing

The Ga^+ ion bombardment causes severe damages to the diamond crystal by breaking the sp^3 bonds and introducing lattice vacancies. If the concentration of vacancies is below the amorphization threshold of 10^{22} vacancies/cm^3 [384], the diamond lattice can be recovered via high temperature annealing in vacuum at $900 - 1200°C$ [384–386]. In contrast, if the defect density exceeds the amorphization threshold, the damage can

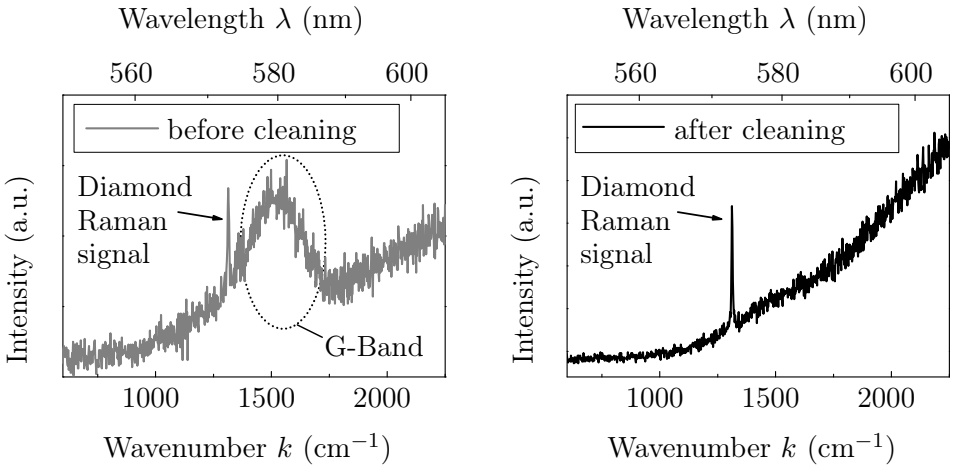

Figure 6.9: Raman spectroscopy of the photonic crystal cavities: (a) Raman spectrum taken on the photonic crystal cavity after the high temperature annealing and prior to the oxidation cleaning. Besides the narrow diamond Raman line at 572.8 nm ($\sim 1326 \pm 2\,\mathrm{cm}^{-1}$), the broad peak at $\sim$ 580 nm ($\sim 1554 \pm 7\,\mathrm{cm}^{-1}$) is attributed to the G-band of graphite-like inclusions induced by the FIB milling and annealing [134]. (b) After the extensive post-processing, there is no indication of non-diamond phases in the spectrum.

no longer be eliminated. Instead, the heavily damaged material transforms to stable sp^2 bonds such as amorphous carbon or graphite [384]. The graphite-like residuals can be removed subsequently using oxidation. In order to graphitize the heavily irradiated volume and recover the weakly damaged lattice, the samples are annealed in vacuum (10^{-4} Pa) after FIB milling for 2 h at 1,000°C (heteroepitaxial diamond films) or at 800°C (bonded ultra-pure diamond films). The recovery of the diamond quality is confirmed via Raman spectroscopy. To this end, we focus a 532 nm-excitation laser onto the photonic crystal cavities and detect the Raman signal by the confocal setup described in chapter 4. The Raman spectrum in figure 6.9(a), taken on the fabricated photonic crystal cavities after high temperature annealing, reveals a clear narrow diamond Raman line at 572.8 nm ($\sim 1326 \pm 2\,\mathrm{cm}^{-1}$) and broad peak around 580 nm ($\sim 1554 \pm 7\,\mathrm{cm}^{-1}$) attributed to the G-band of graphite-like inclusions and sp^2 hybridized carbon [134]. The Raman signal clearly indicates the transformation of heavily damaged lattice regions to graphite and amorphous carbon as well as the successful partial recovery of the lightly damaged diamond upon vacuum annealing 1,000°C for 2 h.

Removal of gallium ions

The high temperature annealing has a positive side effect. The gallium ions, implanted into the diamond lattice, diffuse out of the lattice and vaporize at the diamond surface at temperatures above 700°C [387]. Several groups have studied the diffusion of FIB-induced gallium ions in diamond [388], diamond like carbon films [389] and amorphous carbon pillars [387]. We investigated the incorporation of gallium using energy-dispersive

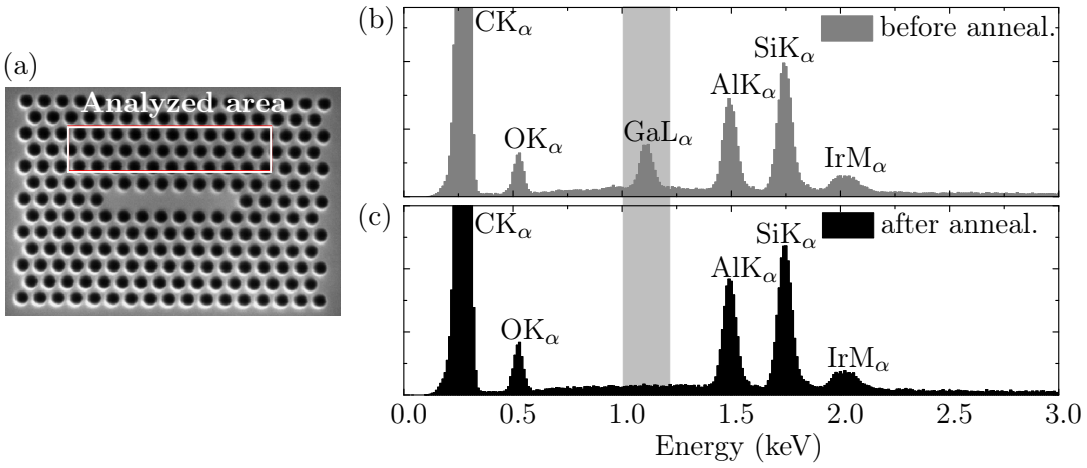

Figure 6.10: Energy-dispersive X-ray spectroscopy of the photonic crystal cavity before and after high temperature annealing. (a) SEM image of the photonic crystal cavity under investigation. The white rectangle marks the analyzed area. (b) EDX spectrum taken directly after the FIB milling. A pronounced peak at 1.1 keV indicates the presence of incorporated gallium. (c) After high temperature annealing, the GaL$_\alpha$ line disappeared.

X-ray (EDX) spectroscopy before and after high temperature annealing. Figure 6.10(a) shows the photonic crystal cavity under investigation with the analyzed area marked by a white rectangle. Directly after the FIB milling, a significant peak at 1.1 keV, attributed to the GaL$_\alpha$ line, reveals the presence of incorporated gallium at the photonic crystal structure (Fig. 6.10 (b)). This peak completely disappears after high temperature annealing of the diamond sample (Fig. 6.10 (c)). Hence, within the detection limit of the EDX method of $\sim 1\%$, we confirmed the efficient removal of incorporated gallium ions.

Removal of amorphous carbon and graphite

As discussed above, if the defect concentration of the diamond lattice surpasses the amorphization threshold, the damaged layer is transformed into sp^2 bonded carbon, namely graphite or amorphous carbon upon high temperature annealing. The sp^2 hybridized layer results in significant absorption losses and hence strongly limits the performance of our fabricated cavities. In order to remove non-diamond material, the sample is thoroughly cleaned in strongly oxidizing acids using either a 1:1 mixture of H_2O_2:H_2SO_4 for 30 min or a 1:1:1 boiling mixture of HNO_3:H_2SO_4:$HClO_4$ for up to 4 h. Moreover, the sample is annealed in air for 2 h at 420°C. For nanodiamonds it has been demonstrated, that annealing in oxygen atmosphere below 450°C selectively removes graphite-like residuals while leaving the diamond crystal intact [390, 391]. If necessary, the measures are repeated several times. To confirm successful oxidation of the non-diamond material, we use Raman spectroscopy with a 532 nm-excitation laser. Figure 6.9 shows a comparison between the Raman spectra taken before and after the

cleaning procedure. Prior to cleaning but after high temperature vacuum annealing, the G-band around 580 nm ($\sim 1554 \pm 7\,\mathrm{cm}^{-1}$) clearly reveals the presence of sp^2 bonded carbon and graphite-like inclusions [134] (Fig. 6.9(a)). In contrast, after the extensive post-processing, the Raman signal between $1400 - 1600\,\mathrm{cm}^{-1}$ completely disappears and solely the diamond Raman line at 572.8 nm ($\sim 1326 \pm 2\,\mathrm{cm}^{-1}$) is still visible (Fig. 6.9(b)). Therefore, we conclude that non-diamond phases are completely removed upon acid treatment and annealing in air.

By the here presented process, graphite-like phases are oxidized and selectively removed, while leaving the diamond intact. Alternatively, the sample could be exposed to a hydrogen plasma to remove the damaged layer [385, 392]. However, especially for NV centers, it is well known that the negative charge state is favored for oxygen terminated surfaces, whereas it is converted to NV^0 in the case of hydrogen terminated surfaces [393, 394]. To stabilize the NV^- emission at 637 nm and the SiV signal around 738 nm, equally attributed to the negative charge state [395], we exclusively apply strongly oxidizing treatments. A detailed discussion on charge state switching and stabilization of NV centers can be found in chapter 8.

6.3 Fabricated photonic crystal cavities

In this work we fabricate both small size photonic crystal cavities such as optimized M0 and M1 structures as well as large size cavity structures with several missing holes, e.g. M3- and M7-cavities. The lattice constants and air hole radii are chosen such that the resonant modes match the zero-phonon line of either the NV^- center at 637 nm or the SiV center at 738 nm. In the following, we present the cavities fabricated in ultra-pure and heteroepitaxial diamond films intended for cavity-coupling to NV or SiV centers, respectively.

6.3.1 Structures for coupling to SiV centers

We fabricate in total 42 photonic crystal cavities via FIB milling in heteroepitaxial diamond films. The photonic structures are designed for coupling to SiV centers incorporated during the CVD growth into the diamond films. The lattice constant and air hole radius are chosen between $a = 260 - 285$ nm and $R = 80 - 90$ nm to match the design wavelength of 738 nm. Figure 6.11 exemplarily shows the SEM pictures of a seven and one missing hole defect in a heteroepitaxial diamond membrane fabricated using focused ion beam milling. The M7-cavity has a lattice constant of $a = 275$ nm and a uniform air hole radius of $R = 85$ nm. The defect structure is surrounded by six hole periods to guarantee for sufficient in-plane confinement of the mode (c.f. simulation, Fig. 5.27 in section 5.6). The patterning time of the overall structure is ~ 30 min at a beam current of 10 pA. The holes exhibit a perfect circular shape with a standard variation in diameter below 4 nm (Fig. 6.11(a,b)).

For the M1-cavity, we chose a design that has been optimized according to the principle of gentle confinement (c.f. section 5.6.2). By reducing the hole sizes and

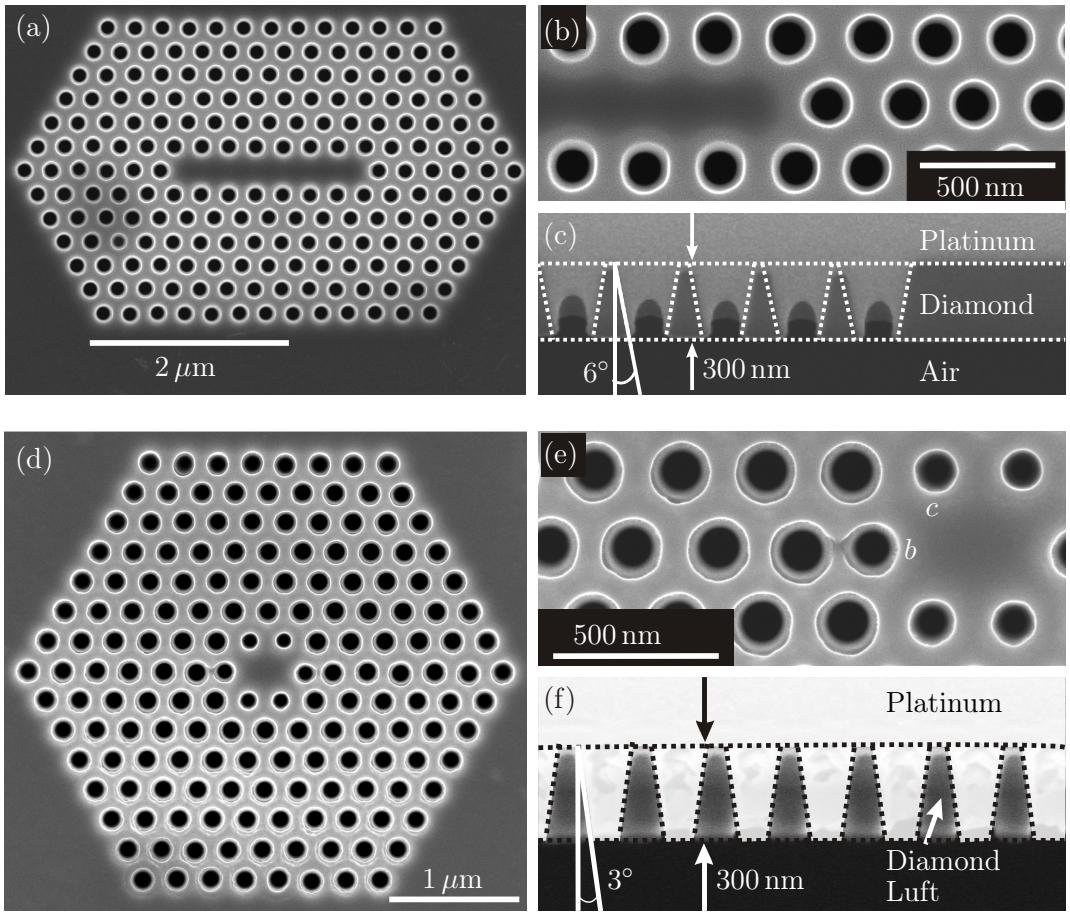

Figure 6.11: SEM images of fabricated (a-c) M7- and (d-f) M1-cavity in diamond: (a,d) Top view of the seven and one missing hole cavity with M7: $a = 275\,\text{nm}$ and $R = 85\,\text{nm}$ and M1: $a = 260\,\text{nm}$, $R = 85\,\text{nm}$, $R_c = 68\,\text{nm}$ and $R_b = 74\,\text{nm}$. Prior to milling of the M1-cavity, a chromium protection layer was deposited on the diamond surface. (b,e) Close-up of the cavity centers. (c,f) Cross-sectional images (tilt angle 52°). A thin platinum layer was deposited to allow for a straight cut through the structure. The image reveals a thickness of the diamond membrane of 300 nm and hole sidewalls inclined by an angle of $\sim 6°$ in the case of the M7-cavity and $\sim 3°$ for the metal-protected M1-structure.

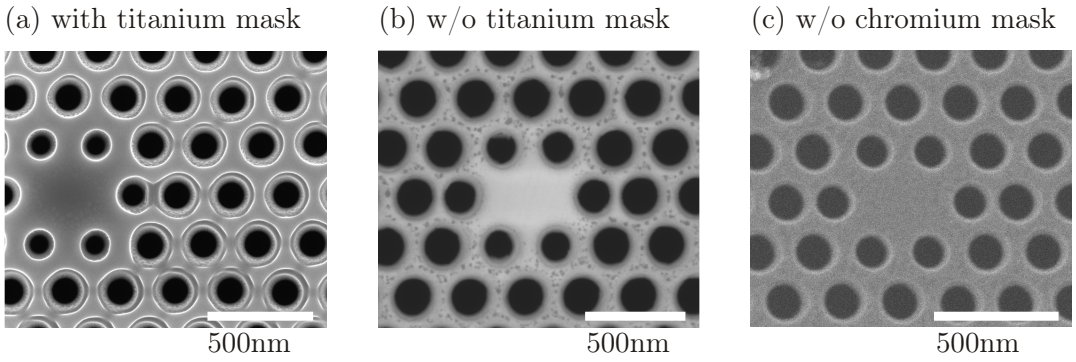

Figure 6.12: Titanium and chromium protection metal masks: (a) Optimized M1-cavity directly after FIB milling with titanium mask on top. (b) Same M1-cavity without titanium mask, after annealing and post-processing. (c) M1-cavity structured using a chromium mask after mask removal and post-processing.

shifting the nearest neighbor air holes by a distance d along the x-axis, the theoretical Q-factor is significantly increased. The structural parameters are chosen according to table 5.4 in section 5.6.2 and to reference [275]. The one missing hole cavity displayed in figure 6.11(d,e) has a lattice constant of $a = 260\,\text{nm}$, a background radius of $R = 85\,\text{nm}$. The radii of the nearest neighbor air holes c and b are reduced to $R_c = 68\,\text{nm}$ and $R_b = 74\,\text{nm}$ and the holes b are shifted by a distance $d = 50\,\text{nm}$ outwards. A close-up of the fabricated M1-cavity clearly reveals the smaller size and shift of the holes in close vicinity to the defect (Fig. 6.11(e)). The undisturbed lattice holes around the defect exhibit a standard deviation in diameter below 6 nm.

The M7-cavity was directly milled into the diamond membrane, whereas in the case of the M1-cavity, a thin chromium layer was sputtered on the sample surface prior to structuring in order to protect the non-patterned areas from unwanted ion-irradiation and to improve sidewall steepness. To deduce the film thickness and the steepness of the hole sidewalls, cross-sectional images are taken from reference structures. To this end, a thin platinum layer is deposited to allow for a straight cut through the patterns via FIB milling. The cross-sectional SEM images (Fig. 6.11(c,f)) reveal a slab thickness of $H = 300\,\text{nm}$ as well as non-vertical hole sidewalls. Without a metal protection mask, we obtain an inclination angle of the sidewalls of 6° for the M7-cavity. This angle is reduced to 3° in the case of the M1-cavity by overmilling the air holes. Upon overmilling, the 80 nm-thick chromium mask protects the non-structured regions and hence prevents a merging of the air holes due to the Gaussian profile of the ion beam. Figure 6.11(f) reveals a clear separation of the air holes in the presence of a metal layer during patterning.

Besides chromium, we also tested titanium as suitable protection layer during the FIB patterning. The key criteria for choosing the mask material are the pertinacity of the metal mask upon ion irradiation and its residual-free removal after the structuring process. SEM images taken after the FIB milling of photonic crystals certify that the metal layers sustain the bombardment by scattered ions. Figures 6.11(d,e) and 6.12(a)

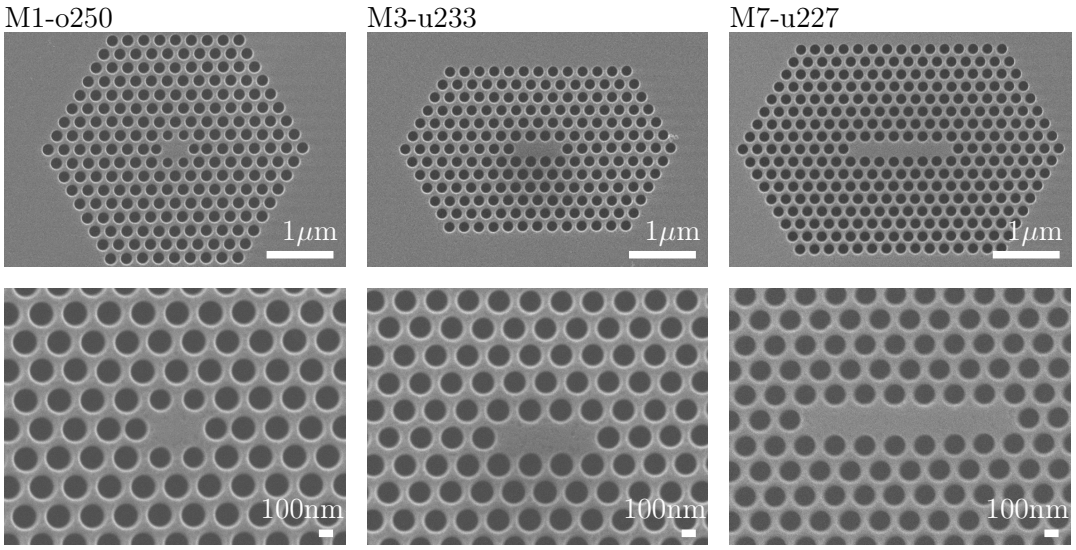

Figure 6.13: Scanning electron microscope images of the fabricated M1-o250, M3-u233 and M7-u227 photonic crystal cavities for target nitrogen implantation. The upper row shows the whole structure whereas the lower row displays a zoom of the cavity center. The pictures are taken after all post-processing steps.

reveal intact chromium and titanium layers, respectively, between the milled air holes of two M1-cavities. After milling, the titanium and chromium masks are dissolved in hydrofluoric acid and chromium etchant, respectively, and the samples are annealed and oxidized. Figures 6.12(b,c) reveal an excellent removal of the titanium and chromium layers without any residuals neither from the mask nor the subsequent acid treatment. For some individual structures, that were patterned using a titanium mask, a slight swelling at the air hole edges has been observed, probably due to redeposition during FIB milling. Together with the fact that titanium removal requires chemical treatment in hazardous hydrofluoric acid, we prefer to use chromium as metal protection layer in the following.

6.3.2 Structures for implantation of NV centers

For targeted nitrogen implantation and deterministic coupling to single NV centers, we fabricated 15 photonic crystal cavities with a design wavelength of 637 nm in two different ultra-pure diamond membranes bonded on a silicon substrate. The lattice constants and background hole radii of the realized M0-, M1-, M3- and M7-cavities are chosen between $a = 220 - 255\,\mathrm{nm}$ and $R = 80 - 83\,\mathrm{nm}$, such that the resonant modes match the NV^- zero-phonon line. Every defect is surrounded by eight periods of air holes. Prior to FIB milling, a chromium protection mask is deposited on the sample. We fabricated one optimized M0-cavity, as well as optimized and unoptimized one- and three-missing hole structures and unoptimized M7-cavities. The structures' names first mention the number of missing holes at the center termed either M1, M3 or M7 followed

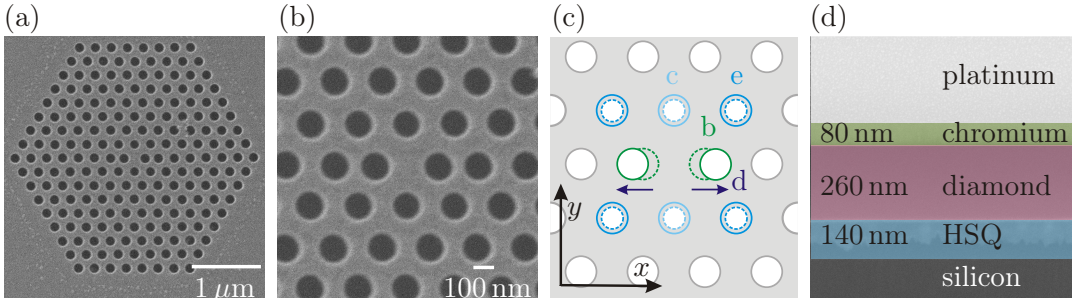

Figure 6.14: SEM images and cavity design of the fabricated M0-o250 cavity: (a) SEM image and (b) close-up of the M0-cavity. Images are taken after all post-processing steps. (c) M0 design with the nearest neighbor holes optimized. (d) False color cross-sectional SEM image of the bonded diamond film next to the free-standing structures, taken at an tilt angle of 52°. The thickness of the chromium:diamond:HSQ layers are (80:260:140) nm.

by the letter 'u' or 'o' for unoptimized or optimized designs. The final number indicates the lattice constant in nanometers. Scanning electron microscope images of the M1-o250, M3-u233 and M7-u227 cavity are exemplarily shown in figure 6.13. Figure 6.14 displays the SEM image of an optimized M0-o250 structure together with the corresponding design layout. All images are taken after the complete post-processing procedure. At the center of the M1-o240 and M0-o250 cavities the optimized nearest-neighbor air holes can clearly be seen. The hole patterns look very regularly with a perfect circular shape. No residuals of the chromium mask or acid treatment are visible. The geometry of the other photonic crystal cavities fabricated in ultra-pure diamond look equally perfect (SEM pictures not shown).

We measure the thickness of the diamond film at two points of the bonded material next to the free-standing, structured membrane by local deposition of platinum and cut through the sample via FIB milling. The cross-sectional SEM image (Fig. 6.14(d)) reveals a multilayer system with the chromium protection layer on top and the HSQ-layer beneath the diamond to promote the adhesion to the silicon substrate. Considering that the image was taken at a tilt angle of 52°, we evaluate the thickness of the chromium:diamond:HSQ-layer system to be 80:260:140 nm. From a second height measurement at a different sample position, we find a tapered profile of the diamond film with a wedge-angle of 0.022°, probably due to mechanical polishing. Taking the wedge shape into account, we evaluate the thickness of the diamond membrane at the position of the photonic crystal structures to be $200 - 220$ nm.

6.4 Photonic crystal cavity modes

Photonic crystal cavity modes resonantly enhance the emission of color centers and spectrally filter the broadband luminescence of the diamond material. This allows for the identification of the modes as distinct peaks in photoluminescence spectra. We measure the photoluminescence spectra at the center of the fabricated structures using confocal

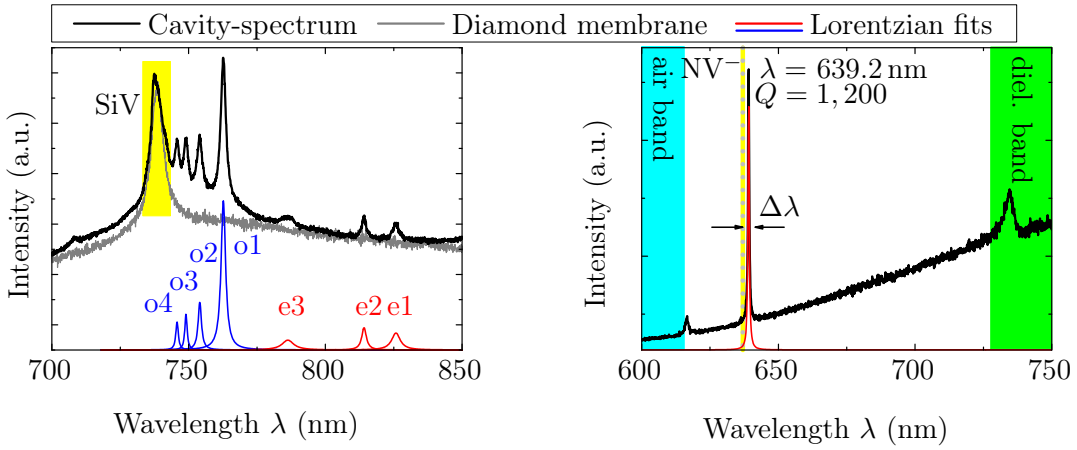

(a) M7-cavity spectrum

(b) M0-o250 cavity spectrum

Figure 6.15: Cavity spectra of the M7- and M0-cavity fabricated in heteroepitaxial or ultra-pure diamond, respectively: (a) The spectra taken on the M7-cavity and unstructured diamond membrane reveal a peak at 738 nm attributed to the zero-phonon line of an ensemble of SiV centers. At longer wavelengths $745-825$ nm, multiple resonant peaks are observed in the M7-cavity spectrum that are attributed to cavity modes. The peaks are fitted with Lorentzian profiles to extract the resonant wavelengths and Q-factors. The M7-cavity modes are referred to $e1-e3$ and $o1-o4$. (b) The M0-o250-cavity spectrum reveals one single resonance at 639.2 nm with a quality factor of $Q = 1,200$, almost matching the design wavelength of 637 nm. The two peaks to the left and right are attributed to the air and dielectric band limiting the band gap. The blue and green region mark the simulated band edges. Yellow-gray dotted line: target NV^- ZPL.

microscopy. For excitation, either continuous green or red laser light at wavelengths of 532 nm or 660 nm, is focused onto the sample using a microscope objective with a numerical aperture of 0.8. The fluorescence is coupled into an optical fiber and analyzed by a spectrometer. Details on the confocal setup are given in chapter 4.

Figure 6.15 exemplary shows the spectra taken at the M7-cavity with a design wavelength of 738 nm milled in a heteroepitaxial diamond film (SEM image shown in Fig. 6.11(a-b)) and at the M0-o250 cavity realized in ultra-pure diamond (SEM image shown in Fig. 6.14(a,b)) intended for coupling to NV^- centers. For comparison, a reference spectrum taken on the bare unstructured heteroepitaxial diamond membrane is displayed in figure 6.15(a). The M7-cavity and reference spectrum exhibit both a distinguished peak at 738 nm that is attributed to the zero-phonon line of a large ensemble of SiV centers incorporated into the diamond during the CVD growth. At longer wavelengths between $745-825$ nm, several cavity modes appear in the M7-spectrum that are not present in the reference spectrum. The experiment is in good agreement with FDTD simulations, predicting multiple higher order modes for the M7-cavity. As discussed in section 5.5.2, M7-cavity modes are classified in even "e" and odd "o" modes according

Modes	e1	e2	e3	o1	o2
Q_{exp}	300 ± 50	450 ± 40	180 ± 20	380 ± 40	400 ± 50
Q_{theory}	7,900	1,350	255	450	110
Q_{SEM}	3,700	1,100	250	600	590
Q_{tilt}	900	770	250	570	115

Table 6.2: Comparison between measured quality factors Q_{exp} and theoretical predictions: Q_{theory}: calculated Q-factors for an ideal M7-cavity. Q_{SEM}: simulated Q-factors for a M7-cavity with a dielectric structure based on the imported SEM image of the actual fabricated M7 structure (assuming vertical sidewalls of the air holes). Q_{tilt}: modeled Q-factor for an ideal M7-cavity with sidewalls inclined by an angle of 6°.

to their mirror reflection symmetry. A detailed comparison between measurement and theory involving polarization analysis is given in chapter 7.

The M0-o250 spectrum reveals three distinct peaks. The central peak at 639.2 nm is associated to the resonant mode of the M0-cavity in close vicinity to the design wavelength at 637 nm. The two distinct peaks on either side of the mode are attributed to the edges of the band gap, namely the dielectric and air band. Both dielectric and air band are visible in the spectrum, as the local density of states exhibits strong maximum at the edge of the band gap (c.f. section 5.4). Our observation is confirmed via FDTD simulations. The green and blue areas in figure 6.15(b) mark the simulated dielectric and air band, respectively. Please note that in the M7-cavity spectrum, the band edges are outside the spectral region plotted in figure 6.15(a).

Besides the resonant wavelength, the cavity quality factor can be extracted from the spectra by subtracting the background and fitting the resonant peaks with a Lorentzian profile. The quality factor is then given by the fitted central wavelength λ divided by the full-width at half-maximum $\Delta\lambda$:

$$Q = \frac{\lambda}{\Delta\lambda} \tag{6.3}$$

Figure 6.15 shows the Lorentzian fits to the M7- and M0-o250 cavity modes. For the M7-cavity, the evaluated Q-factors range from $Q = 180$ to 450 (c.f. Q_{exp} in table 6.2). With $Q = 1,200$, the M0-o250-cavity exhibits the highest quality factor of all photonic crystal cavities realized in this work.

In the following, we give a brief statistical overview over all fabricated photonic crystal cavities realized in heteroepitaxial or ultra-pure diamond. Similarly to the M7- and M0-o250 cavities presented above, the central wavelengths and Q-factors have been extracted from Lorentzian fits to all measured cavity resonances. In the case of the photonic crystal cavities realized in heteroepitaxial diamond films, 33 of the 42 fabricated structures reveal resonant modes, corresponding to a success rate of 79% . Figure 6.16 shows the measured resonant wavelengths and quality factors, evaluated for 15 cavities, including M1, M3 and M7 point defects. The resonant modes show a large spread in wavelength between $700 - 840$ nm. However, 80% of the 15 structures reveal multiple

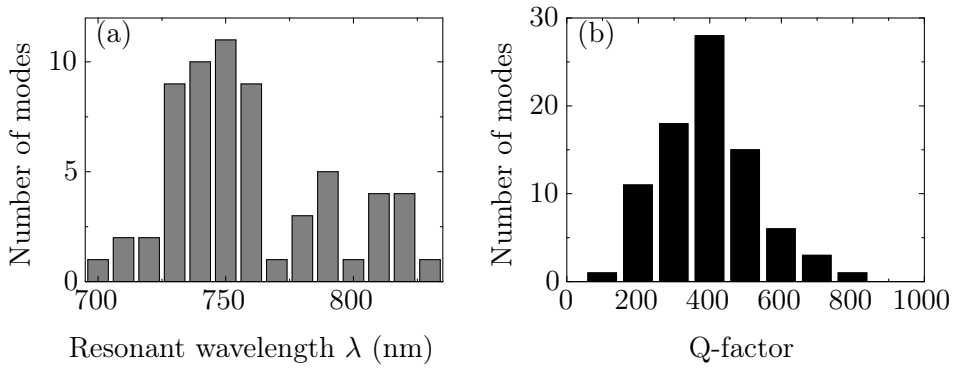

Figure 6.16: Measured resonant wavelengths and quality factors of various photonic crystal cavities realized in heteroepitaxial diamond films designed for coupling to SiV centers. (a) Most of the structures reveal resonant modes in the wavelength range between $730 - 760\,\text{nm}$. The resonances beyond 760 nm are attributed to low-order M7-cavity modes, namely $e1$, $e2$ and $e3$. (b) The mean quality factor is 383 with a standard deviation of 122. For the histograms, 15 cavities have been analyzed.

resonances in the range between $730 - 760\,\text{nm}$ near the SiV ZPL. The cavity modes beyond 760 nm are attributed to lower order M3- and M7-cavity modes, namely $e1$, $e2$ and $e3$. Hence, the broad distribution of mode wavelengths is not due to a lack of fabrication accuracy but is rather associated to the intrinsic wide wavelength range of M3- and M7-cavity spectra. From the cavity linewidth, we deduce quality factors that range from 100 to 800 with a maximum at $Q = 400$. For the 15 analyzed structures, we obtain a mean Q-factor of 383 with a standard deviation of 122.

In the case of photonic crystal cavities realized in ultra-pure diamond, 12 of the 15 structures reveal resonant modes in the wavelength range between $590 - 730\,\text{nm}$ (success rate: 80%). Figure 6.17 displays the resonant wavelengths and quality factors analyzed for 12 different cavity structures, including M0, M1, M3 and M7 designs. Wavelengths around 650 nm occur most frequently, almost matching the design wavelength of 637 nm. The quality factors show a large spread between $Q = 200 - 1,200$. The highest Q-factor of 1,200 has been detected for the single mode M0-o250 cavity. Similarly, large Q-factors up to $Q = 900$ have been found for the fundamental M3- and M7-cavity modes. Apart from these high values, 70% of the analyzed cavity modes exhibit Q-factors in the range between 200 and 300.

The measured cavity Q-factors realized in heteroepitaxial and ultra-pure diamond membranes are moderate compared to theoretical predictions presented in chapter 5. In the next section 6.5, we will discuss in detail the limitations of the experimental Q-factor due to fabrication tolerances using the example of the M7-cavity fabricated in heteroepitaxial diamond.

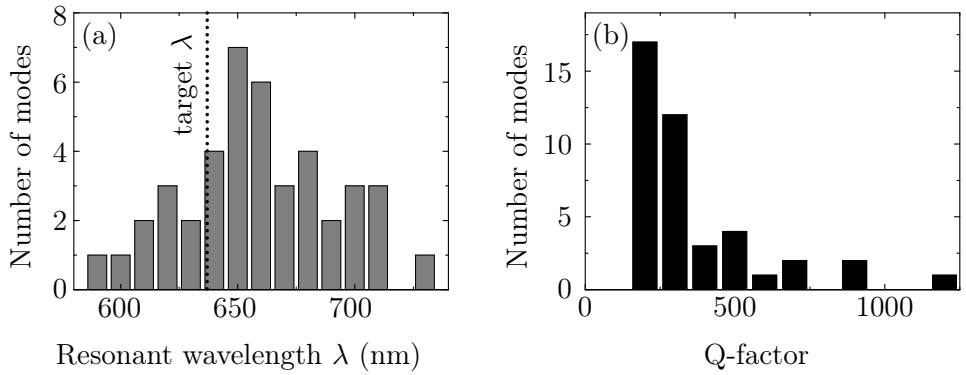

Figure 6.17: Measured resonant wavelengths and quality factors of various photonic crystal cavities realized in ultra-pure diamond films designed for coupling to single NV centers. (a) The wavelength range of the resonant modes extends between $590 - 730\,\mathrm{nm}$. The dotted line marks the design wavelength $\lambda = 637\,\mathrm{nm}$. (b) Quality factors up to 1,200 have been measured. However, 70% of the cavities show Q-factors between 200 and 300. For the histograms, 12 cavities have been analyzed.

6.5 Fabrication tolerances

At first sight, the fabricated photonic crystal structures seem to be almost perfect. The holes are well circular, uniform in size and milled through the membrane with the targeted thickness. However, a comparison between the experimental Q-factors realized for the M7-cavity modes and the simulated values reveals a discrepancy by more than one order of magnitude (c.f. table 6.2). The limitation of the measured Q-factors can have various origins. The dominant sources of losses can be categorized as either (A) imperfections in the cavity geometry, or (B) imperfections in the cavity material. As imperfections of the cavity geometry induced by fabrication tolerances, we consider (A1) variation of the air hole positions and radii and (A2) tilt of the air hole sidewalls. As imperfection of the cavity material, we investigate (B) material absorption. In the following, we analyze the main sources of loss using the example of the M7-cavity fabricated in heteroepitaxial diamond and evaluate the impact on the cavity Q-factor using numerical simulations.

Variation of hole positions and radii

The main discrepancy between an ideal M7-cavity and the actual fabricated structure is the variation in the hole positions. During the FIB milling, a drift control is used, which compares the actual position to the ideal pattern after every third hole and compensates for a possible drift. Figure 6.18 displays the actual hole positions (yellow circles) of a fabricated M7-cavity and the ideal pattern (red circles). The comparison reveals a rather random variation of the hole positions from ideal values which is measured to be $\sim 13\,\mathrm{nm}$ on average.

Besides the position, the air hole size has a major impact on the resonant wavelength

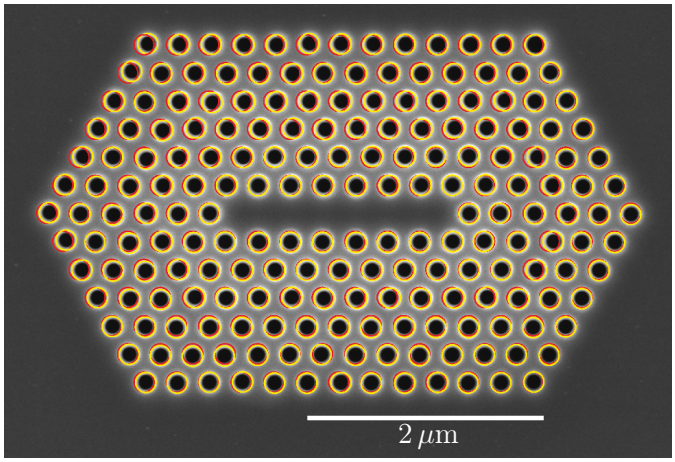

Figure 6.18: Variation in the hole positions and radii of the M7-cavity: red circles: air holes of the ideal pattern, yellow: air holes of the fabricated structure.

and quality factor as discussed in chapter 5. A comparison between the SEM pictures taken directly after FIB milling and taken after the extensive sample post-processing including high temperature annealing and oxidation treatment (c.f. Fig. 6.12(a,b)), reveals an increase in the hole radii by $25 \pm 5\%$. The reason for this increase is attributed to highly damaged diamond material at the hole edges that transforms to graphite-like carbon upon high temperature annealing and is subsequently removed by heat oxidation in air and acid treatment. As this uniformly affects all holes, we compensate for the size modification by intentionally reducing the radius by 25% during the FIB milling. This adaptation allows us to efficiently overcome the increase in hole size upon post-processing and to closely match the desired geometry specifications. Please note that all radii specified in this work refer to the hole size after all annealing and cleaning steps.

The variation of the radii between different holes is small. From SEM images of the cavity structures taken after all treatments, the fabrication tolerance is deduced to be $\sim 6\,\mathrm{nm}$ on average. The inaccuracy is mainly due to the fact that air holes, which are milled first, are slightly larger than air holes, which are patterned last. This is due to ion irradiation upon image acquisition during the drift control process. Every 30 s an image is taken using the ion beam that allows for the correction of a possible sample drift. This leads unwanted ion irradiation and a slight degradation of the structure and to an enlargement of the holes, particularly of the holes that are milled first.

To further quantify the impact of the fabrication tolerances, we calculate the Q-factors of the actual realized M7-cavity using FDTD simulations. For this purpose, the SEM image of the fabricated structure, taken after all post-processing steps, is directly imported into the simulation software *Lumerical FDTD Solutions* [335] and converted into a meshed dielectric structure. Note that only the top view of the cavity geometry can be considered. As the software *Lumerical FDTD Solutions* does not allow for the simulation of tilted sidewalls for structures generated via imported SEM images, we here assume vertical hole sidewalls. The quality factors Q_{SEM} of the five lowest M7-cavity

modes calculated for the dielectric structure based on the imported SEM image are summarized in table 6.2. The quality factor of the fundamental mode $e1$ drops by a factor of ~ 3 to $Q_{\mathrm{SEM}} = 3,700$ whereas the Q-factors of the $e2$ and $e3$ modes are almost unaffected. The quality factors Q_{SEM} of the odd cavity modes $o1$ and $o2$ calculated from the imported SEM image are comparable to each other and are even higher than the Q-factors of the ideal M7-cavity. As the fields of the $o1$ and $o2$ mode (c.f. Fig. 5.24 in chapter 5) are mainly localized in the defect region and in its near vicinity, the radii and positions of the first upper and lower rows of the air holes surrounding the defect have a major impact on the Q-factor of the odd modes. Thus, the incidental variation of the air holes surrounding the cavity center lead to the high experimental Q-factors of the odd cavity modes. In summary, we find that the incidental departure of the fabricated structure from the ideal in-plane geometry reduces the high Q-factor of the $e1$ mode by a factor of ~ 3, leaves the quality factors of the $e2$ and $e3$ modes almost unaffected and enhances the Q-factors of the odd modes $o1$ and $o2$. However, the geometrical imperfections due to size variation and non-perfect hole-positioning do not thoroughly explain the discrepancy between the measured Q-factors and theoretical predictions. Therefore, in a second step, we investigate the losses induced by non-vertical sidewalls.

Inclined side walls

From the cross-sectional SEM images (Fig. 6.11 (c,f)) of the fabricated M7- and M1-cavity structures, we deduce a tilt angle of the air hole sidewalls of $\sim 6°$ and $\sim 3°$, respectively. To investigate the impact of non-vertical hole walls, we perform FDTD simulations to model the quality factors of the M7-cavity modes as a function of the sidewall inclination angle ϕ. The hole radius at the center of the slab is kept fixed to $R = 0.31\,a$ and a slab thickness of $H = 1.1\,a$ is assumed. We take into account six hole periods surrounding the defect as in the fabricated M7-cavity structure. In figure 6.19, the simulated quality factors of the $e1$ and $o1$ mode are plotted in dependence of the tilt angle ϕ. The Q-factor of the $e1$ mode strongly decreases with increasing tilt angle. At $\phi = 3°$, the quality factor drops from originally 7,900 to 2,200. At $\phi = 6°$, Q is reduced to even below 900. The reason for the strong degradation in Q is a coupling between confined TE-like modes and freely propagating TM-like modes. Due to the vertical asymmetry, the polarization can no longer be classified in purely TE- and TM-like, but the tapering of the air holes causes a perturbation in the dielectric constant that breaks the orthogonality relation between the two modes [396]. As there is only a band gap for TE- but not for TM-like modes, the hybrid modes are no longer sufficiently localized in the photonic crystal plane, resulting in increased in-plane losses and reduced Q-factors. Due to the small group velocity of the fundamental $e1$ state, the interaction with lossy modes is strong. In contrast, higher order modes are less affected. The quality factor of the $e2$ mode is reduced by a factor of two when increasing the tilt angle to $6°$, whereas the confinement of the $e3$ and $o2$ modes is hardly modified (c.f. $\mathrm{Q}_{\mathrm{tilt}}$ in table 6.2). Surprisingly, the quality factor of the $o1$ mode increases from 450 to ~ 570, when tilting the hole sidewalls to $6°$ (Fig. 6.19(b)). This raise in Q has been attributed to a reduced coupling strength of the $o1$ mode with non-localized TM-like modes of the

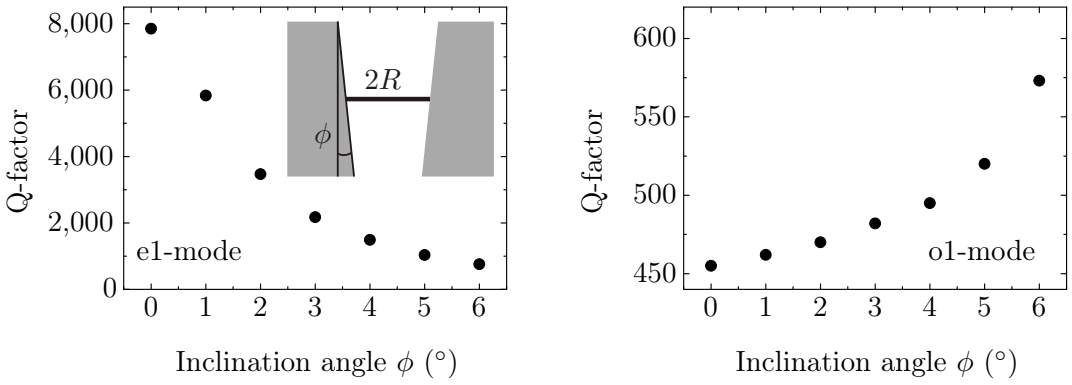

Figure 6.19: Impact of non-vertical hole sidewalls on the Q-factor: The quality factors of the M7-cavity modes $e1$ and $o1$ are plotted as a function of the sidewall inclination angle ϕ. The radius at the slab center is kept fixed.

photonic lattice [397]. For vertical sidewalls, simulations reveal that the cavity mode is energetically close to TM-like modes favoring coupling between the modes. With increasing tilt angle of the holes, the $o1$ mode shifts to smaller frequencies and losses to TM-like mode are strongly reduced, resulting in a higher Q-factor. The quality factors Q_{tilt} of the five lowest-order M7-cavity modes calculated for an inclination angle of 6° are summarized in table 6.2.

Material absorption

In order to study the influence of material absorption on the M7-cavity Q-factor, we include a complex dielectric function ε in our simulation, such that the imaginary part ε_i is proportional to the absorption coefficient α of the diamond material, whereas the real part ε_r is almost constant. The dependence of Q on α can be approximated by a very simple model of a linear cavity with a homogeneous diamond slab placed between two planar mirrors [274, 275, 398]:

$$\frac{1}{Q} = \frac{1}{Q_0} + \frac{1}{Q_{\text{abs}}}. \tag{6.4}$$

Here, Q_0 denotes the Q-factor of an ideal lossless cavity and Q_{abs} the Q-factor including material absorption. The absorption quality factor can be written as $Q_{\text{abs}} = k/\alpha$, with the wave vector $k = 2\pi\sqrt{\varepsilon_r}/\lambda$ [274, 275, 398]. Figure 6.20 shows the dependence of the M7 quality factor on the absorption coefficient α, calculated by FDTD simulations and using equation (6.4). For nanocrystalline diamond films, absorption coefficients can reach values as high as $\alpha \approx 4{,}000\,\text{cm}^{-1}$ [399]. This would strongly decrease the M7 cavity Q-factor to only ~ 100. For the heteroepitaxial diamond films used to fabricate the photonic cavities, the absorption coefficient α depends on the height of the film used to fabricate the membrane: For the first hundred nanometers of the diamond nucleation layer, an absorption coefficient of $\alpha \approx 200\,\text{cm}^{-1}$ has been determined using

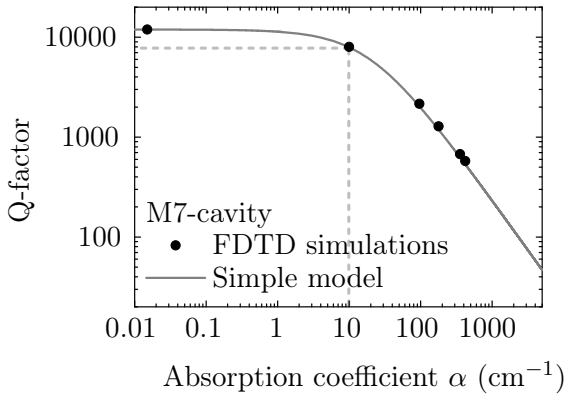

Figure 6.20: Influence of material absorption on the Q-factor of the fundamental M7-cavity mode: The dots denote the FDTD simulation results of a M7-cavity including lossy material and the line is the calculated Q-factor using equation (6.4). For an absorption coefficient α <10 cm^{-1} of the diamond membrane the quality factor is limited to $Q > 8,000$.

ellipsometry measurements[1]. Compared to nanocrystalline diamond films this is already an improvement by more than one order of magnitude. Such an absorption coefficient would limit the Q-factor to $Q \sim 1,000$, which is on the order of the limitation caused by fabrication tolerances. However, with increasing film thickness the absorption coefficient of the heteroepitaxial diamond films is drastically reduced: For very large thicknesses (500-800 μm), the absorption coefficient of the film was measured via ellipsometry[1] to be $\alpha \sim$2.5 cm^{-1} (the nucleation layer had been removed). For the fabrication of photonic crystals, we thin the heteroepitaxial diamond films from 10 μm to 300 nm starting from the backside, thus removing the nucleation layer and leaving a thin diamond membrane with low absorption coefficient. Based on these measurements, we estimate an upper boundary of the absorption coefficient of our thinned heteroepitaxial diamond membranes to be $\alpha < 10$ cm^{-1}. The manufacturer of the ultra-pure diamond films specifies the absorption coefficient of their single crystal diamond samples with comparable optical quality to be 0.003 cm^{-1} at 1.064 μm [346]. Considering an upper boundary of $\alpha < 10$ cm^{-1} for all of the diamond membranes realized in this work, the cavity quality factor of the fundamental $e1$ mode is limited to $Q > 8,000$. Compared to fabrication tolerances, material absorption has a significantly smaller impact on the cavity Q-factor.

By analyzing geometry and material imperfections, we clarified the discrepancy by more than one order of magnitude between the measured and theoretical Q-factors. We demonstrated, that fabrication tolerances such as the variation of the air hole positions, radii and tilt of the air hole sidewalls have a strong impact on the lowest-order modes $e1$, $e2$, whereas higher order modes $e3$, $o1$, $o2$ are much less affected. The strong degradation in Q of the fundamental $e1$ mode is mainly due to non-vertical sidewalls of the air holes, reducing Q by one order of magnitude. Moreover, the incidental variation of

[1] Ellipsometry measurements were performed by Dr. M. Fischer (Experimentalphysik IV, Universität Augsburg).

the hole positions and radii has a non-negligible impact, decreasing Q of the $e1$ mode by a factor of 3 and increasing Q of the $o1$ and $o2$ mode. In contrast, the impact of the material absorption plays only a minor role in the case of the high-quality heteroepitaxial and ultra-pure diamond membranes realized in this work.

In this chapter, we presented the realization of photonic crystal cavities in single crystal diamond using either heteroepitaxial diamond films grown on Ir/YSZ/Si as starting material or ultra-pure diamond membranes bonded via an adhesion layer on a silicon substrate. The substrate was partially removed and the suspended diamond films were subsequently thinned by reactive ion etching in an oxygen plasma. Photonic crystal cavities were patterned into the diamond membrane via focused ion beam milling. FIB is a maskless technique well suited for hard materials like diamond, that relies on precise sputtering of the target atoms by highly energetic gallium ions. Besides the desired material abrasion, the method entails possible lattice amorphization and implantation of gallium in the diamond film. To overcome these damages, we investigated the deposition of a metal protection layer and presented an extensive post-processing treatment involving high temperature annealing in vacuum, acid treatment and oxidation in air. This allows for successful removal of amorphous carbon and incorporated gallium ions and for recovery of the excellent diamond quality. We fabricated small cavity structures, e.g. M0- and M1-cavities as well as large size defects such as M3- and M7-structures with design wavelengths near the ZPL of NV^- or SiV centers. In general, 80% of the realized photonic cavities reveal resonant modes in the photoluminescence spectra with quality factors up to 1,200. When comparing the experimental Q-factors to theoretical predictions, a discrepancy by one to two orders of magnitude was revealed. By analyzing various fabrication tolerances, we could identify imperfections of the cavity geometry, i.e. variation of the air hole positions, radii and non-vertical sidewalls, as the main limiting factors of the measured Q-factors, whereas the impact of material absorption of the single crystal diamond film plays only a minor role.

Chapter 7

Coupling of a photonic crystal cavity to an ensemble of SiV centers

In this chapter, we demonstrate coupling of a photonic crystal cavity to an ensemble of SiV centers in single crystal diamond. The SiV centers are homogeneously incorporated into the heteroepitaxial diamond membrane during CVD growth providing intrinsic optically active sources. Ensemble experiments are an ideal test bed to study light-matter interaction without requiring precise positioning and alignment techniques. We here develop essential tools for the realization of weakly coupled atom-photon interfaces in solid-state systems that can easily be transferred to single emitter-cavity coupling experiments in the subsequent chapters. One important prerequisite for the demonstration of Purcell enhancement is the ability to tune cavity modes across the emission spectrum. At the beginning of this work, tuning of photonic crystal cavities in diamond has not yet been demonstrated but past experiments relied on random chance. In the framework of this thesis, I developed a digital tuning technique based on repetitive oxidation of diamond material that enables to successively blue shift the cavity modes and tune them into resonance with the color centers ZPL. On resonance, we observe a clear intensity enhancement of the SiV ZPL. This increase in the photoluminescence signal is attributed to a spectrally resolved Purcell enhancement of the spontaneous emission of the SiV centers. We investigate cavity-mediated enhancement of the spontaneous decay rate by measuring the excited state lifetime on- and off-resonance. Using a thorough analysis, we deduce the cavity Purcell factor perfectly describing the experimental observations. Our analysis includes experimental quality factors and mode volumes of the cavity modes as well as spatial and spectral averaging over the SiV ensemble and the associated dipole moments, on- and off-resonance collection efficiencies and the quantum efficency of the SiV centers. The here developed methods are pivotal for the deterministic cavity-coupling experiments in the following chapters.

7.1 Cavity modes: Polarization analysis

For cavity-coupling experiments to ensembles of SiV centers, we use heteroepitaxial diamond films grown on Ir/YSZ/Si(001) substrates. The growth conditions are chosen such that a large amount of silicon is incorporated from the substrate into the diamond film to form, together with adjacent vacancies, large ensembles of SiV centers homogeneously distributed within the diamond. The substrate has been partially removed to yield free-standing diamond membranes and the membranes are thinned to $H = 300\,\mathrm{nm}$ using reactive ion etching and patterned via focused ion beam milling. After the fabrication, the sample is annealed at 1,000°C in vacuum and extensively cleaned in oxidizing acids and thermally oxidized in air. For details on the fabrication process, the reader is referred to chapter 6.

We fabricate several M7-cavities with a design wavelength of 738 nm corresponding to the ZPL of SiV centers. The radii of the structures are $R = 85\,\mathrm{nm}$ for the M7^A-cavity, $R = 88\,\mathrm{nm}$ for the M7^B-cavity and $R = 86\,\mathrm{nm}$ for the M7^C-geometry. An unoptimized seven missing hole geometry is chosen as it provides several cavity modes facilitating the comparison between theory and experiment. The defect modes exhibit theoretical quality factors up to $Q = 7,900$ and mode volumes of $V = 1.5\,(\lambda/n)^3$.

We use confocal microscopy to investigate the cavity spectral properties. To this end, we focus a 532 nm continuous wave laser onto the sample to excite the structures. The photoluminescence signal is collected from the top by a microscope objective (numerical aperture of 0.8), coupled into a multi-mode fiber and directed to a spectrometer. All measurements are performed at room-temperature. Details on the confocal setup are given in chapter 4.

Figure 7.1(a) exemplarily shows the spectrum taken on the M7^A-cavity (SEM see Fig. 6.11(a-b)) and a reference spectrum taken on the bare unstructured heteroepitaxial diamond membrane. The photoluminescence signal measured on the M7-cavity is six times larger compared to the intensity detected on the bare membrane (reference spectrum in Fig. 7.1(a) is scaled up by a factor of six), which is attributed to a pure photonic band gap effect. In section 5.4.2 on page 100, we have seen that the local density of states is strongly reduced for frequencies inside the photonic stop band. This means that the propagation of modes in the crystal plane is forbidden. Light, originally distributed within a homogeneous diamond slab, is channeled in the vertical direction, when the membrane is patterned with a photonic lattice of air holes. This channeling effect results in a strongly enhanced extraction efficiency by a factor of $2.5 - 4.0$ in the vertical direction (c.f. Fig. 5.13 and related discussion). The higher out-coupling ratio due to the band gap effect is considered as the main reason for the increased photoluminescence signal registered on the photonic structures compared to the bare unpatterned diamond membrane. Another reason for the increase in the fluorescence signal might be defects induced by the FIB milling. However, thanks to our thorough cleaning process of the sample after FIB patterning, this background contribution is reduced to a minimum.

In figure 7.1(a), both spectra of the M7-cavity and the membrane exhibit a distinguished peak at 738 nm that is attributed to the zero-phonon line of a broad ensemble

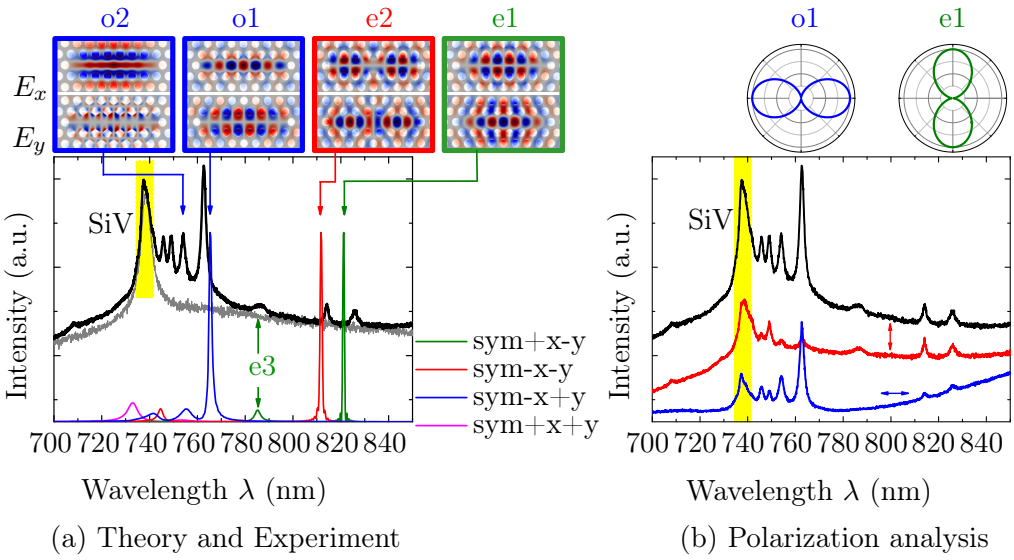

Figure 7.1: M7-cavity spectrum and polarization analysis: (a) Comparison between measured spectrum and simulation data. The peaks between $745 - 830\,\text{nm}$ are attributed to M7-cavity modes $e1 - e3$, $o1 - o2$ with $Q = 200 - 500$, whereas the maximum at 738 nm is associated to emission of an SiV ensemble incorporated in the heteroepitaxial diamond film. The colored lines show the simulated spectrum of the ideal M7-cavity with $R = 85\,\text{nm}$, $H = 300\,\text{nm}$ and $a = 275\,\text{nm}$ for different mirror symmetries. At the top, the theoretical E_x and E_y field distributions are displayed. (b) Polarization analysis of the M7-spectrum. The even modes $e1 - e3$ are linearly polarized along the y-axis, whereas the odd modes $o1 - o3$ reveal x-polarized emission. At the top, the theoretical polarization of the $e1$ and $o1$ mode are shown confirming the experimental results.

of SiV centers incorporated into the diamond during the CVD growth. At longer wavelengths between $745 - 825\,\text{nm}$, several cavity modes appear in the M7-spectrum that are not present in the reference spectrum. To identify the cavity modes, we perform FDTD simulations, assuming an ideal M7-cavity with a lattice constant of 275 nm, an air hole radius of 85 nm and a slab thickness of 300 nm. The computed cavity modes for different applied mirror symmetries are shown in figure 7.1(a) by the colored solid lines. The modes are classified in even (e, $-y$) and odd (o, $+y$) modes according to their mirror reflection symmetry in the plane at $y = 0$ and are consecutively numbered starting with the highest wavelength (c.f section 5.7.3 on page 143). The theoretical predictions are in very good agreement with the experimental spectrum. The small discrepancy between the simulation and measurement arises from imperfect fabrication accuracies (c.f. section 6.5). The resonant modes observed in the $M7^B$- and $M7^C$-cavity spectra coincide equally well with simulation results (data not shown). Fitting the resonant peaks with Lorentzian functions, we deduce the experimental quality factors of the five lowest-order modes of the $M7^A$-, $M7^B$- and $M7^C$-cavity (table 7.1). All three structures

Cavity	R (nm)	$Q_{exp,e1}$	$Q_{exp,e2}$	$Q_{exp,e3}$	$Q_{exp,o1}$	$Q_{exp,o2}$
$M7^A$	85	300 ± 50	450 ± 40	180 ± 20	380 ± 40	400 ± 50
$M7^B$	88	230 ± 60	240 ± 10	130 ± 10	590 ± 20	460 ± 70
$M7^C$	86	280 ± 40	450 ± 70	220 ± 10	740 ± 90	430 ± 40

Table 7.1: Experimental quality factors Q_{exp} of the five lowest-order modes $e1$, $e2$, $e3$, $o1$, $o2$ of the fabricated $M7^A$-, $M7^B$- and $M7^C$-cavity with different radii R and identical lattice constant $a = 275\,\text{nm}$ and slab thickness $H = 300\,\text{nm}$.

exhibit moderate Q-factors ranging from 130 to 740. Compared to theoretical Q-factors, the measured values are more than one order of magnitude smaller, which is attributed to imperfect fabrication accuracy, i.e. non-vertical hole sidewalls (c.f. section 6.5).

Besides the resonant wavelengths, FDTD simulations also allow us to predict the polarization of the cavity modes starting with the near field patterns and using near-to-far field transformations (c.f. section 5.7.3). Exemplarily, the E_x and E_y fields of the even modes $e1$, $e2$ and the odd states $o1$, and $o2$ are shown at the top of figure 7.1(a). The E_x field of the even modes has a node at $y = 0$ and the E_y mode exhibits an anti-node, whereas it is vice versa for odd states. As discussed in section 5.7.3 on page 143, this symmetry relation results in a linear polarization of even modes along the y-axis, whereas the odd modes are expected to show x-polarization (c.f. Fig. 5.39). To confirm the theoretical predictions, we place a polarization analyzer in the detection path of our confocal setup either aligned along the x- or y-axis of the $M7^A$-cavity structure. The polarization resolved $M7^A$ spectra, presented in figure 7.1(b), reveal that the even modes are pronounced if the analyzer is aligned along the y-axis, whereas they are hardly visible in the x-polarized spectrum. The behavior of the odd modes is vice versa: Here, the peaks are prominent for the polarization analyzer aligned along the x-axis and almost vanish for an orientation in y-direction. The polarization measurements clearly indicate a linear polarization of the even (odd) modes along the y- (x)-direction, which is in excellent agreement with the theoretical predictions. Together with the simulated spectrum, the polarization analysis unambiguously proves that the observed spectral features are true cavity modes. In the following, we investigate emitter-cavity coupling by actively tuning the M7-cavity modes into resonance with the SiV center emission line.

7.2 Tuning photonic crystal cavities

The resonant modes identified in the $M7^A$-cavity spectrum are shifted to longer wavelengths with respect to the zero-phonon line of the SiV ensemble at 738 nm. In chapter 6, we have seen that due to fabrication tolerances it is challenging to fabricate cavity structures that exactly match the emission line of incorporated or implanted color centers. Therefore, it is essential to actively tune the cavity modes after the manufacturing process. Here, we make use of the fact that the resonant wavelengths are extremely sen-

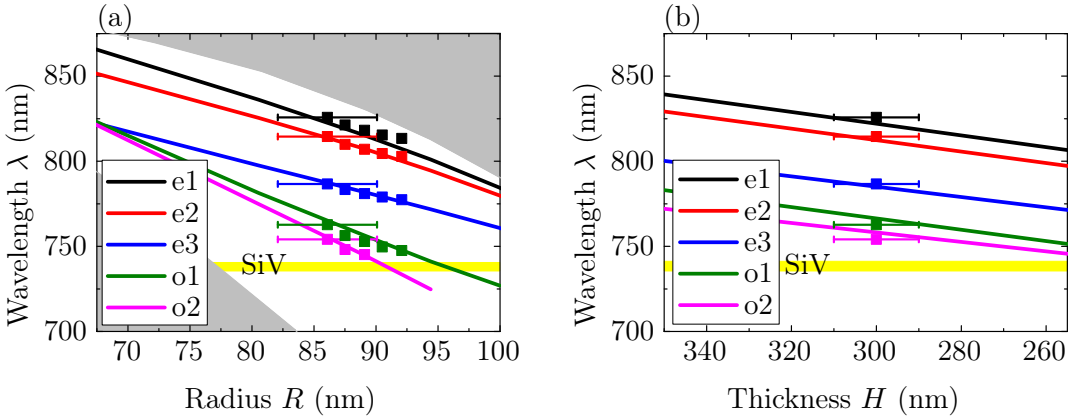

Figure 7.2: Theoretical and experimental tuning curve of the M7^A-cavity: The resonant modes $e1 - e3$ and $o1$, $o2$ shift to smaller wavelengths with (a) increasing air hole radius R and (b) decreasing slab thickness H.

sitive to geometrical parameters. In section 5.5.2 using the example of the M0-cavity, we have seen that the resonant wavelengths of two-dimensional photonic crystal cavity modes shift to smaller values with increasing radii and with decreasing slab thickness. Figure 7.2 displays the theoretical tuning curves of the M7-cavity simulated using FDTD methods as a function of either the hole radii R or the slab thickness H, while keeping the other non-varied parameter $H = 300\,\text{nm}$ or $R = 85\,\text{nm}$ fixed. Notably, the radius has a strong impact on the resonant wavelength. Increasing R by 1 nm would blue tune the M7-cavity modes $e1 - e3$ and $o1$, $o2$ on average by 2.3 nm, whereas decreasing the slab thickness H by 2 nm (1 nm on both sides) would result in blue shift of only 0.6 nm.

The enlargement of the holes and thinning of the slab thickness can be accomplished by slightly etching away diamond material. This approach is motivated by the digital etching technique developed for semiconductor materials. Hennessy et al. [400] shifted the resonant modes of a photonic crystal cavity in GaAs up to 80 nm in steps of $2-3\,\text{nm}$ and tuned them in resonance with the emission of a single quantum dot via successive wet chemical etching steps. As diamond is chemically inert to almost all wet chemical etchants, we use thermal oxidation at 480°C for 10 min in air to slightly remove diamond material. For diamond nanopowder, it has been shown that diamond starts to oxidize in air for temperatures above 450°C [390]. Figures 7.3(a) and 7.4 show the M7^A-M7^C-cavity spectra taken after successive annealing steps for 10 min each. All resonant modes clearly blue shift by $\sim 3\,\text{nm}$, on average, per oxidation step. The central positions and measured quality factors of the M7^A-cavity resonances are plotted in figure 7.3(b,c) as a function of the annealing steps. In total, the cavity modes are tuned up to 15 nm without significant degradation of the Q-factor. The variation in Q upon tuning is within the previously determined errorbar of ± 50 (c.f. table 7.1). Figure 7.2 presents a comparison between the simulated (solid lines) and experimental (dots) tuning curves of the M7^A-cavity. The graph reveals that the measured blue shift by $\sim 3\,\text{nm}$ of the modes corresponds very well with the theoretical prediction for an increase in the radius

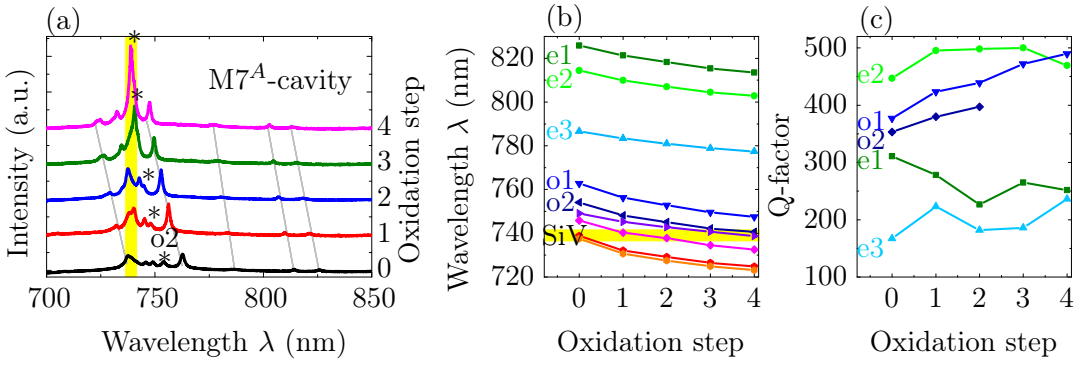

Figure 7.3: Cavity tuning: (a) M7^A-cavity spectrum taken before the first oxidation step (black) and after one, two, three and four oxidation steps (colored curves). When the cavity mode $o2$ (marked by *) is tuned into resonance with the emission line of incorporated SiV centers, the intensity of the zero-phonon line (the peak in the yellow region) is clearly enhanced. (b) Wavelengths for various cavity modes are blue shifted by 3 nm on average per oxidation step. The four lines at the bottom show higher-order modes ($e4$, $o3$, $o4$, $o5$; not labeled for clarity). In total, the cavity modes are tuned up to 15 nm. (c) Quality factors of the fundamental cavity modes show no significant degradation following tuning.

of 1.5 nm per oxidation step and an almost constant film thickness.

The tuning technique developed in the framework of this thesis allows for frequency matching of the cavity modes via air oxidation over an extremely wide tuning range up to 50 nm (c.f. chapter 9) without inducing damages to the diamond lattice or significant degradation of the cavity Q-factor. The tuning step size can be adjusted by changing the oxidation time or temperature. The method has been reproduced by other groups [88] to match the frequency of a diamond-based nanobeam cavity to the NV^- emission line.

However, there is one drawback to the oxidation approach: The wavelength shift is irreversible. Once the diamond material has been slightly oxidized, the modes can not be red shifted back to their original wavelength. A complementary method, that allows for tuning of the mode to longer wavelengths, involves gas condensation (e.g. xenon or nitrogen) on the photonic crystal structure that is cooled down to cryogenic temperatures. The thin condensed gas layer induces a change in the refractive index contrast and shifts the cavity modes to larger wavelengths or equivalently to smaller frequencies. This technique has been widely used for photonic crystals and micro-ring cavities in diamond [83, 87, 88, 90] as well as in gallium arsenide [401–403] with a tuning range of 5 nm. The huge advantage of the gas condensation method is its reversibility. By heating the sample to room temperature, the gas dissolves from the photonic crystal and the original structure and resonant frequencies are restored.

For some semiconductor materials, e.g. gallium phosphide or silicon, the refractive index can furthermore be changed by focusing intense laser light onto the structure. Induced by pulsed laser light, free carriers are generated in silicon which reduce the refractive index by the carrier plasma effect and lead to a wavelength shift [404]. Sim-

ilarly, the refractive index of gallium phosphide or gallium arsenide can be changed by laser irradiation that locally oxidizes the material and blue tunes the photonic crystal wavelengths by $2.5 - 3.4\,\mathrm{nm}$ [75, 405]. The drawback of this method is the relative small tuning range, its irreversibility and a degradation in the quality factor reported by references [74, 75]. We tried to transfer this technique to diamond material. However, no wavelength shift for our photonic crystal cavities was observed when focusing either a 532 nm or a 404 nm continuous wave laser with powers of 30 mW and 7 mW, respectively, onto the structures during 40 min. Local oxidation of gallium phosphide can also be achieved using an atomic force microscope with a conductive negatively bias metal tip to grow an anodic oxide [406, 407] at the cavity center. The nano-oxidation leads to a blue shift up to 3-4 nm of the resonances with a step size comparable to the cavity linewidth enabling virtually continuous tuning of the modes [406]. For dielectric materials whose refractive index cannot be changed by laser irradiation, thin photochromic layers [408] or chalcogenide glasses [409] on top the photonic structure have been applied. By local optical excitation the refractive index of the cladding layer can be modified leading to a frequency shift up to 3 nm [408, 409] of the photonic structure. Besides the refractive index change of the dielectric material, it is also possible to modify the index of the holes. This can be achieved by selectively infiltrating the holes with fluid [410] or liquid crystals [411] using a glass micro-tip. In the case of three-dimensional photonic crystals, it has been shown that the orientation of the infiltrated liquid crystals can be rearranged by an external electric field, enabling the appearance or disappearance of a complete photonic band gap [412]. Within this work, we tested the infiltration-tuning ability of our diamond-based photonic crystal cavities by wetting the surface with water, isopropyl or methyl alcohol. The cavity modes shifted by $44 - 57\,\mathrm{nm}$ to longer wavelengths. Unfortunately, the step size could not be fine-tuned and moreover a significant drop in the quality factor down to $Q \approx 100$ was observed, due to the significant degradation of the refractive index contrast. Details can be found in [397].

7.3 Purcell enhancement of SiV ensemble emission

Frequency tuning of photonic crystal cavity modes is an essential prerequisite for the demonstration of light-matter interaction. By comparing the on/off resonance spectra, we find a significant intensity increase of the SiV emission line for zero detuning. Moreover, we investigate cavity-meditated modification of the spontaneous emission rate. To this end, we measure the excited state lifetime of SiV centers in and off resonance with the cavity mode and compare it to the value determined on the unstructured diamond membrane. The experimental observations are attributed to a spectrally resolved Purcell enhancement of spontaneous emission. By taking into account spatial and orientational averaging of the emitter-mode overlap; spectral mismatch of SiV zero phonon line width and cavity linewidth; modification of the local density of states by the photonic crystal; and different collection efficiencies for cavity mode and uncoupled emission, we evaluate the cavity Purcell factor as well as the theoretically expected increase in the photolumi-

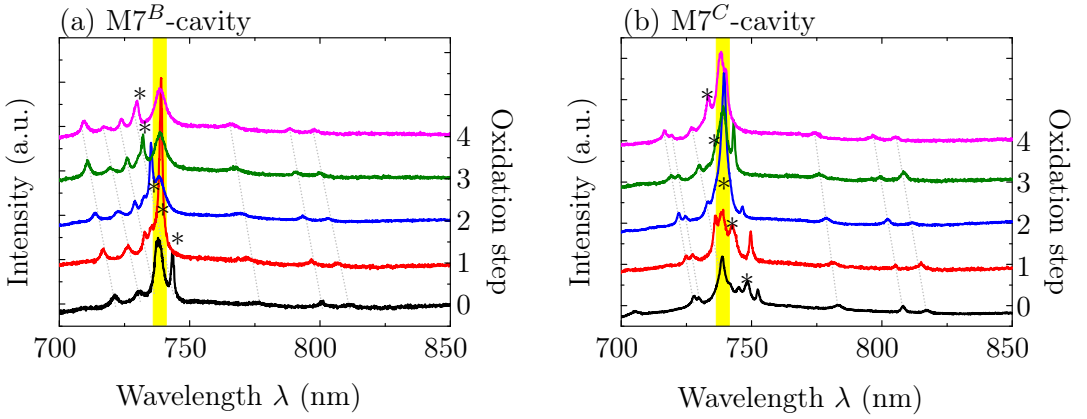

Figure 7.4: Tuning spectra of the (a) M7^B- and (b) M7^C-cavity: M7^B- and M7^C-cavity spectra taken before the first oxidation step (black) and after one, two, three and four oxidation steps (colored). When the $o1$ ($o2$) mode of the M7^B- (M7^C-) cavity is tuned into resonance with the SiV emission line after one (two) oxidation steps, a clear enhancement of the ZPL intensity by a factor of 2.8 (2.1) is observed. The photoluminescence signal drops back to its original value when the modes are tuned again out off resonance.

nescence (PL) signal and the reduction of the spontaneous emission rates. The thorough analysis perfectly describes the experimental observations.

7.3.1 Experimental intensity enhancement

The digital oxidation technique allows us to actively tune the M7-cavity modes in resonance with the zero-phonon line of the ensemble of SiV centers. In figure 7.3(a), the M7^A-cavity mode $o2$ marked with a star is successively blue shifted toward the SiV emission line at 738 nm. On resonance, we observe a significant enhancement of the ZPL intensity by a factor of 2.8, compared to the off-resonant spectrum (Fig. 7.5(a)). The phenomena is reproduced for the M7^B- and M7^C-cavity: Tuning the $o1$ ($o2$) mode of the M7^B (M7^C)-cavity after one (two) oxidation steps into resonance with the ZPL of the SiV ensemble yields an increase in the PL signal by a factor of 2.8 (2.1) (Figs. 7.4 and 7.5). When the cavity modes are shifted again out off resonance, the intensity of the SiV ZPL drops back to its original value (oxidation steps $2-4$ in Fig. 7.4(a) and oxidation steps 3, 4 in Fig. 7.4(b)). The observed intensity increase is attributed to a spectrally resolved Purcell enhancement of the spontaneous emission rate of the SiV centers.

In literature, similar intensity enhancements of the ZPL have been reported for single or several NV centers when coupled to all-diamond photonic crystal cavities [87, 88] or diamond micro-disk resonators [83] as well as to GaP photonic crystal cavities [75, 76] or GaP micro-rings [74].

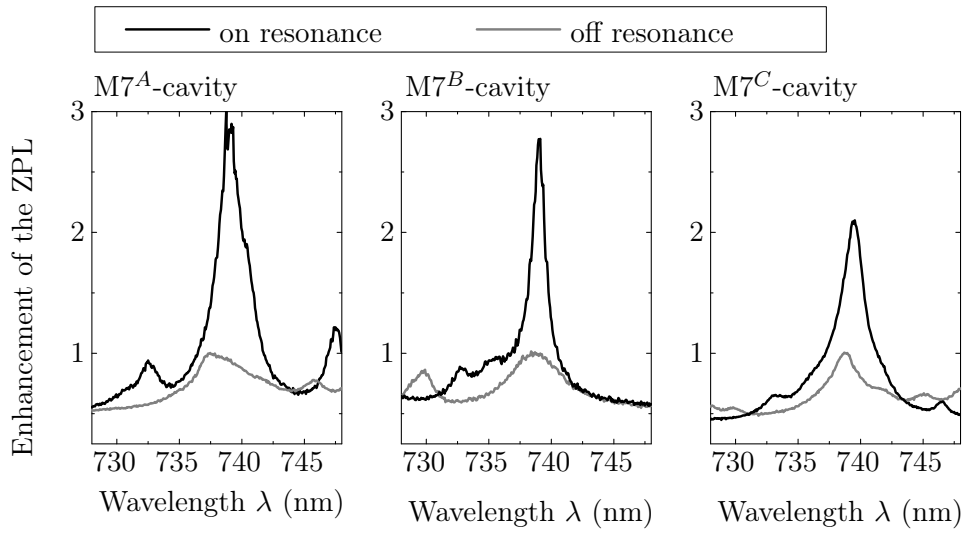

Figure 7.5: Enhancement of the SiV ZPL intensity $I^{exp}_{\mathrm{cav}}/I^{exp}_{\mathrm{PhC}}$ due to resonant coupling: By tuning the cavity mode of the (a) M7^A- (b) M7^B- or (c) M7^C-cavity into resonance with the emission line of the SiV centers, the ZPL is enhanced by a factor of (a,b) 2.8 or (c) 2.1, respectively. The gray (black) curves are the cavity spectra off (on) resonance.

7.3.2 Lifetime in and off resonance with cavity

As a next step, we investigate the modification in the spontaneous emission rate. To this end, we perform lifetime measurements under pulsed excitation with a repetition rate of 80 MHz at a wavelength of 700 nm. The photons emitted by the repetitively excited SiV ensemble are filtered in the spectral window between $730-750$ nm and their arrival times are registered by the TCSPC electronics with respect to the excitation pulse. The number of photons detected per time interval after a certain time delay are plotted in a histogram. Details on time correlated single photon counting experiments are given in chapter 4. We measure the lifetime on three different sample regions: (a) At the center of the M7^A-cavity, when the $o2$ mode is tuned in resonance with the ZPL of the SiV ensemble; (b) at the center of the M7^B-cavity, with the SiV ensemble off resonance with any cavity mode and (c) on the bare unstructured membrane. The three time-correlated histograms are displayed in figure 7.6. The peak centered at zero time delay represents the excitation pulse with an exponential decay for $t > 0$. The smaller peak centered at 12.5 ns is the following excitation pulse of the 80 MHz-pulse train but with a strongly diminished amplitude due to the use of a pulse picker [242]. The experimental data are fitted using equation (4.7). The fit function is a convolution of a mono-exponential decay with the instrument response function of our detection device approximated by a Gaussian function with a FWHM of 864 ps (c.f. section 4.4). From the fit, we extract the lifetime of the ensemble of SiV centers $T_{1,\mathrm{cav}} = 1.18 \pm 0.02$ ns and $T_{1,\mathrm{PhC}} = 1.20 \pm 0.02$ ns in- and off-resonance with a cavity mode and $T_{1,\mathrm{bulk}} = 1.19 \pm 0.02$ ns on the unpatterned diamond membrane. The measured T_1-

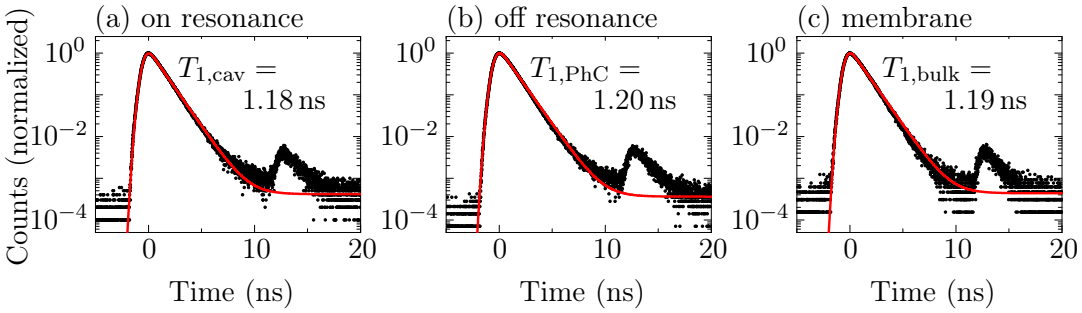

Figure 7.6: Lifetime measurements of the ensemble of SiV centers: (a) In resonance with the $o2$ mode of the M7^A-cavity, the theoretical fit yields a lifetime of $T_{1,\mathrm{cav}} = 1.18\,\mathrm{ns}$. (b) Off resonance with any cavity mode, we find $T_{1,\mathrm{PhC}} = 1.20\,\mathrm{ns}$. (c) On the unstructured diamond membrane, the lifetime is $T_{1,\mathrm{bulk}} = 1.19\,\mathrm{ns}$.

times do not differ much. The change in the spontaneous emission rate (inverse of the excited state lifetime) is approximately 1% when coupling the SiV ensemble to a cavity mode: $\gamma_{\mathrm{cav}}/\gamma_{\mathrm{bulk}} = T_{1,\mathrm{bulk}}/T_{1,\mathrm{cav}} \approx 1.01$. Similarly, the spontaneous emission rate is inhibited by $\sim 1\%$ for the ensemble of SiV centers located in a photonic crystal lattice but off-resonance with any cavity mode: $\gamma_{\mathrm{PhC}}/\gamma_{\mathrm{bulk}} = T_{1,\mathrm{bulk}}/T_{1,\mathrm{PhC}} \approx 0.99$. Please note that the T_1-times measured on various positions of the diamond membrane differ already by 0.7%, which is on the order of the experimental lifetime change. Moreover, the error induced by the fitting routine is about 0.02 ns, corresponding to a relative error in lifetime of 2%. Due to the measurement uncertainties, it is not possible to deduce a lifetime reduction (increase) for the ensemble of SiV centers in- (off-) resonance with the M7-cavity modes compared to the unstructured situation.

In a related work, Lee et al. [85] demonstrated a lifetime reduction by a factor ~ 1.3 for SiV centers resonantly coupled to a higher-order mode of a micro-disk cavity in diamond with $Q = 2,200$ and $V = 9.6\,(\lambda/n)^3$. Although the ideal Purcell factor $F_P = 17.4$ of the whispering gallery mode is comparable to the figure of merit determined for our photonic crystal cavities (see below), they observed a decreased lifetime $T_{1,\mathrm{cav}} = 1.48\,\mathrm{ns}$ for a SiV ensemble located within the micro-disk resonator compared to the decay time $T_{1,\mathrm{bulk}} = 1.83\,\mathrm{ns}$ of SiV centers hosted in the unstructured diamond film with a SiO_2 substrate beneath. The difference to our experiment is not yet clear. Unfortunately, the authors do not comment on the emitters' quantum efficiency or on possible lifetime variations across the membrane although they are using highly strained, inhomogeneous material. To unambiguously prove Purcell enhancement of an ensemble, it would be desirable to apply cavity tuning techniques and to compare the lifetime of one SiV ensemble on- and off-resonance with a cavity mode.

In literature, unfortunately, there is no consistent definition of the experimental Purcell factor. In some publications, the Purcell factor is associated to the intensity ratio [75, 88], to the lifetime change [74, 83, 87] or to a change in both quantities [76] measured on- and off-resonance. To clarify the relation between the Purcell factor, the intensity enhancement and the lifetime change, we present a thorough analysis in

the following, which includes spatial, spectral and orientational averaging over the SiV centers and their dipole moments coupled to a photonic crystal cavity mode, as well as radiative and non-radiative decay rates of the emitters. The derived Purcell factor perfectly describes the observed intensity enhancement and the lifetime measurements of the SiV ensemble.

7.3.3 Theoretical Purcell enhancement of ensemble emission

In general, the photonic crystal can both enhance and reduce the spontaneous emission rate of a color center. The modification of the spontaneous emission rate is referred to as the Purcell factor. In a homogeneous diamond slab the excited state of the color center decays through three channels with a total rate

$$\gamma_{\mathrm{bulk}} = \gamma_{\mathrm{ZPL}} + \gamma_{\mathrm{PSB}} + \gamma_{\mathrm{nr}}, \tag{7.1}$$

where γ_{ZPL} and γ_{PSB} are the radiative recombination rates into the zero-phonon line (ZPL) and the phonon side bands (PSB), respectively, and γ_{nr} denotes the sum of non-radiative decay rates. For single SiV centers, a ratio of $\gamma_{\mathrm{ZPL}} : \gamma_{\mathrm{PSB}} = 4 : 1$ [25] has been found. The ratio of the radiative transitions $\gamma_{\mathrm{rad}} = \gamma_{\mathrm{ZPL}} + \gamma_{\mathrm{PSB}}$ to the total decay rate $\gamma_{\mathrm{rad}} + \gamma_{\mathrm{nr}}$ is defined as the quantum efficiency η_{qe} of the emitter: $\eta_{\mathrm{qe}} = \gamma_{\mathrm{rad}}/(\gamma_{\mathrm{rad}} + \gamma_{\mathrm{nr}})$. There exist only few studies on the quantum efficiency of SiV centers: For ensembles of SiV centers in polycrystalline diamond, an average radiative quantum efficiency of 0.05 [413] was found. Similar values of 0.003-0.09 have been reported for single SiV centers in nanodiamonds grown on iridium [55]. Our own experiments on single SiV centers in heteroepitaxial diamond membranes reveal much larger quantum efficiencies up to 0.6 (c.f. chapter 9). Here, one has to take into account that the quantum efficiency strongly depends on the local density of states. Moreover, the presence of non-diamond carbon phases, such as grain boundaries or dislocations, might increase non-radiative recombination rates [233] that would explain reduced quantum efficiencies for SiV centers in polycrystalline diamond films compared to bulk material. In chapter 9, different effects on the quantum efficiency will be discussed in more detail for single SiV centers. As the analysis in this chapter is focused on large SiV ensembles, we here consider a range of quantum efficiencies with a lower and upper boundary of 0.05 and 0.6 reported in literature and determined by our own measurements.

By coupling an emitter to a cavity, solely the radiative transition rates γ_{ZPL} and γ_{PSB} are either Purcell-enhanced by the cavity mode or suppressed by the photonic band gap effect, whereas the non-radiative decay rate γ_{nr} is unaffected. If the zero-phonon line of the color centers is resonantly enhanced by the photonic crystal cavity mode and the phonon side bands are off-resonance, the total decay rate is given by:

$$\gamma_{\mathrm{cav}} = F_{\mathrm{cav}}\ \gamma_{\mathrm{ZPL}} + F_{\mathrm{PhC}}\ \gamma_{\mathrm{PSB}} + \gamma_{\mathrm{nr}}. \tag{7.2}$$

Here, F_{cav} denotes the Purcell enhancement factor associated to the cavity mode given by equation (5.63) in section 5.3 and F_{PhC} represents the Purcell inhibition factor associated to the photonic band gap effect introduced in section 5.4.2 on page 100. For

simplicity, we assume in equation (7.2) a constant inhibition factor F_{PhC} independent on the wavelength. Moreover, we expect the spectral range of the phonon-side band to coincide with the photonic band gap; which is the case for the SiV centers investigated here. The Purcell factor $F_{\mathrm{cav}} = F_{\mathrm{P}} R_r R_d R_\lambda$ is decomposed of the ideal Purcell factor F_{P} and the terms R_λ and R_r accounting for the spectral and spatial misalignment of the emitter-cavity field and the factor R_d considering the orientation of the emitter dipole moment with respect to the polarization of the resonant electric field. In the off resonance case, both decay channels through the zero-phonon line and phonon side bands are suppressed by the band gap effect and the total decay rate is given by:

$$\gamma_{\mathrm{PhC}} = F_{\mathrm{PhC}} \left(\gamma_{\mathrm{ZPL}} + \gamma_{\mathrm{PSB}}\right) + \gamma_{\mathrm{nr}}. \tag{7.3}$$

The change in the spontaneous emission rate comes along with a modification of the PL signal collected by the spectrometer. For on-resonance emitters, the total intensity I_{cav} is given by the emission rate γ_{cav} integrated over the spectral and spatial density $\rho(\vec{r}, \vec{d}, \lambda) = \rho(\vec{r})\rho(\vec{d})\rho(\lambda)$ of an ensemble of emitters and the orientation of their dipole moments [273]:

$$I_{\mathrm{cav}} = \iiint d\vec{r}\, d\vec{d}\, d\lambda\; \rho(\vec{r})\rho(\vec{d})\rho(\lambda)\; \left(\eta_{\mathrm{cav}}\, F_{\mathrm{cav}}\, \gamma_{\mathrm{ZPL}} + \eta_{\mathrm{PhC}}\, F_{\mathrm{PhC}}\, \gamma_{\mathrm{PSB}}\right). \tag{7.4}$$

Here η_{cav} and η_{PhC} are the collection efficiencies of the objective lens for the on- and off-resonant emission, respectively. The total intensity for emitters spectrally detuned from the cavity mode is given by:

$$I_{\mathrm{PhC}} = \iiint d\vec{r}\, d\vec{d}\, d\lambda\; \rho(\vec{r})\rho(\vec{d})\rho(\lambda)\, \eta_{\mathrm{PhC}}\, F_{\mathrm{PhC}}\; (\gamma_{\mathrm{ZPL}} + \gamma_{\mathrm{PSB}}). \tag{7.5}$$

This situation corresponds to the spectra taken at oxidation step "0" in figures 7.3(a) and 7.4. The ratio of the integrated intensities $I_{\mathrm{cav}}/I_{\mathrm{PhC}}$ describes the enhancement of the ZPL when the cavity is tuned in resonance with the emission line of the color centers.

Spectrally resolved Purcell enhancement

In this section, we evaluate the experimental Purcell factor and estimate the spectrally resolved intensity enhancement of the SiV zero-phonon line, when a cavity mode is tuned into resonance. As the measured quality factors and observed increase in the PL signals are very similar for the three fabricated M7-cavities, we here restrict our analysis to the $o2$ mode of the M7^A-cavity. Starting from the ideal Purcell factors associated to cavity mode and the photonic crystal lattice, we include random dipole orientation, spectral and spatial emitter-mode overlap and the collection efficiency of the on- and off resonant SiV emission in our calculation. To solve the integrals (7.4)-(7.5), we make use of the fact, that the distribution function $\rho(\vec{r}, \vec{d}, \lambda) = \rho(\vec{r})\rho(\vec{d})\rho(\lambda)$ is separable [414], enabling independent integration over position r, dipole orientation d and wavelength λ. The individual contributions are evaluated in the following.

Ideal Purcell factors: From the measured quality factor $Q = 400$ and the simulated mode volume $V = 1.5(\lambda/n)^3$, we deduce the ideal Purcell factor $F_P = \frac{3}{4\pi^2}\frac{Q}{V}\left(\frac{\lambda}{n}\right)^3 \approx 20$ of a single hypothetical emitter coupled to the $o2$ mode of the M7^A-cavity. This ideal enhancement factor assumes a single atomic-like transition of the emitter spectrally and spatially perfectly aligned with the cavity mode and with its dipole moment oriented parallel to the cavity electric field. The Purcell inhibition factor F_{PhC} of the photonic crystal lattice has been simulated in section 5.4.2 on page 100. Averaged over various positions in the photonic crystal unit cell and polarization directions, we obtain $F_{\mathrm{PhC}} = 0.23$ at $\lambda = 738\,\mathrm{nm}$ ($\omega = 0.375 \times 2\pi c/a$) (c.f. Fig. 5.12 in section 5.4.2). Hence, due to the photonic band gap effect, the spontaneous emission rate of a SiV ensemble with unity quantum efficiency would be suppressed by an average factor of ~ 4 compared to its bulk decay rate.

Dipole orientation: The factor $R_d = |\langle \vec{e}_d \cdot \vec{e}_E \rangle|^2$ accounts for the orientation of the individual dipole moments $\vec{d}$ of the SiV centers with respect to the cavity electric field $\vec{E}$. In general, the SiV complex is incorporated along the $\langle 111 \rangle$ crystallographic axes into the diamond lattice (c.f. section 3.4). This corresponds to four equivalent sites [111], [$\bar{1}\bar{1}$1], [$\bar{1}$1$\bar{1}$] and [1$\bar{1}\bar{1}$], that are inclined by an angle of 35.3° with respect to the (001)-oriented facet of the diamond membrane. The projection of the dipole into the (001) diamond plane, results in a degradation of the coupling strength by a factor of 2/3. Moreover, as there are two equivalent projections into the (001) plane, an additional factor of 1/2 have to be considered when averaging over the SiV ensemble. Consequently, the integral $\langle R_d \rangle = \int \rho(\vec{d})\, R_d\, d\vec{d}$ in equation (7.4) yields 1/3.

Spectral overlap: The factor $R_\lambda = (1 + 4Q^2(\frac{\lambda}{\lambda_{\mathrm{cav}}} - 1)^2)^{-1}$ accounts for different bandwidths and spectral detuning of the cavity mode λ_{cav} with respect to the central position λ of the SiV ZPL governed by the spectral density $\rho(\lambda)$. From the spectrum 7.1, we deduce the Lorentzian distribution $\rho(\lambda)$ of the SiV centers with a FWHM of $\Delta\lambda \approx 4.0\,\mathrm{nm}$ being significant broader than the cavity linewidth $\Delta\lambda_{\mathrm{cav}} = 1.85\,\mathrm{nm}$. Owing to our tuning technique, we can assume perfect matching of the central wavelengths $\lambda_{\mathrm{cav}} = \lambda_{\mathrm{SiV}}$ and only have to account for the different linewidths. With this, the spectral overlap integral $\langle R_\lambda \rangle = \int \rho(\lambda)\, R_\lambda\, d\lambda$ yields $\Delta\lambda_{\mathrm{cav}}/\Delta\lambda_{\mathrm{SiV}} = 0.46$.

Spatial overlap: The term $R_r = |\vec{E}(\vec{r}_0)|^2/\max|\vec{E}(\vec{r})|^2$ accounts for the spatial overlap of the SiV centers with the electric field of the cavity mode. We assume that the spatial extend of the SiV ensemble within the lattice defect is determined by the spot size of the excitation laser described by a Gaussian beam with a FWHM of 480 nm in the (x, y) plane (c.f. Fig. 4.2 in chapter 4) and uniform in z-direction. By numerically integrating the Gaussian distribution of the SiV ensemble with the simulated electric field intensity of the cavity mode $o2$, we obtain the spatial overlap $\langle R_r \rangle = \int \rho(\vec{r})\, R_r\, d\vec{r} \approx 0.35$ for the $o2$ mode.

Collection efficiencies: Finally, we calculate the collection efficiency of the dipole emission coupled to the $o2$ cavity mode, i.e. η_{cav}, and to the periodic photonic crystal

Cavity	F_{P}	$\langle R_d \rangle$	$\langle R_r \rangle$	$\langle R_\lambda \rangle$	F_{cav}	$I_{\mathrm{cav}}/I_{\mathrm{PhC}}$	$I^{exp}_{\mathrm{cav}}/I^{exp}_{\mathrm{PhC}}$
$M7^A$	20	0.33	0.35	0.46	1.07	3.5	2.8
$M7^B$	30	0.33	0.36	0.32	1.15	3.7	2.8
$M7^C$	22	0.33	0.35	0.43	1.10	3.6	2.1

Table 7.2: Calculated cavity Purcell factor F_{cav} and expected intensity enhancement $I_{\mathrm{cav}}/I_{\mathrm{PhC}}$ of the $M7^A$-, $M7^B$- and $M7^C$-cavity deduced from the ideal Purcell factor F_{P}, the averaged dipole orientation $\langle R_d \rangle$, the spatial and spectral overlap integrals $\langle R_r \rangle$ and $\langle R_\lambda \rangle$ as well as the on-off-resonance collection efficiencies and the branching ratio $\gamma_{\mathrm{ZPL}} : \gamma_{\mathrm{PSB}} = 4 : 1$. The theoretical intensity increase $I_{\mathrm{cav}}/I_{\mathrm{PhC}}$ is in very good agreement with the experimental data $I^{exp}_{\mathrm{cav}}/I^{exp}_{\mathrm{PhC}}$ observed in figure 7.5.

lattice, i.e. η_{PhC}. By numerically integrating the far-field intensity distribution radiated in the vertical direction over the collection angle defined by the objective lens (numerical aperture of 0.8), we obtain $\eta_{\mathrm{cav}} \approx 0.23 \pm 0.06$ and $\eta_{\mathrm{PhC}} \approx 0.26 \pm 0.02$ (c.f. section 5.7.3 on page 144). The error in the collection efficiencies accounts for a variation of the air hole radii within the fabrication tolerances and tilt of the air hole sidewalls by an angle of 6° in the simulation (c.f. section 6.5).

Taking into account the average dipole orientation and the spectral and spatial mismatch, the experimental Purcell factor $F_{\mathrm{cav}} = F_{\mathrm{P}} \langle R_r \rangle \langle R_d \rangle \langle R_\lambda \rangle \approx 1.07$ can be evaluated. Together with the simulated collection efficiencies and assuming a branching ratio $\gamma_{\mathrm{ZPL}} : \gamma_{\mathrm{PSB}} = 4 : 1$ [25], we calculate the resonant enhancement of the ZPL intensity compared to the off resonant situation $I_{\mathrm{cav}}/I_{\mathrm{PhC}} = 3.5 \pm 1$. In the experiment, we measure an enhancement of the intensity $I^{exp}_{\mathrm{cav}}/I^{exp}_{\mathrm{PhC}} = 2.8$ (Fig. 7.5), which is in excellent agreement with the theoretical predictions. The large error of the intensity enhancement is mainly due to the uncertainty of the collection efficiency when including variations of the air hole radii and tilted hole sidewalls in the simulation. We equivalently calculate the cavity Purcell factor and the expected intensity enhancement of the SiV emission line, when the $o1$ mode of the $M7^B$-cavity or the $o2$ mode of the $M7^C$-cavity are tuned into resonance. Table 7.2 reveals very good agreement between the evaluated PL enhancement $I_{\mathrm{cav}}/I_{\mathrm{PhC}}$ and the experimental increase $I^{exp}_{\mathrm{cav}}/I^{exp}_{\mathrm{PhC}}$ deduced from figure 7.5.

Purcell enhancement of the spontaneous emission rate

Analogous to the enhancement of the spectrally resolved intensity of the ZPL, we can estimate the enhancement of the spontaneous emission rate when the photonic crystal cavity is tuned into resonance with the color centers in the diamond film. Using the cavity Purcell factor F_{cav} evaluated above and the inhibition factor F_{PhC}, the modification of the spontaneous emission rate can be determined via equations (7.2) and (7.3). However, there is a subtlety: The estimation of the spontaneous decay rate presumes

detailed knowledge of the emitter quantum efficiency η_{qe}. As cavity-coupling only affects radiative decay rates, a quantum efficiency smaller than one would imply a significant degradation of the experimental Purcell factor. Here, we consider a lower and upper bound of the SiV quantum efficiency of $\eta_{qe} = 0.05$ [413] and $\eta_{qe} = 0.6$ (c.f. chapter 9), respectively. Taking into account these specific quantum efficiencies, we estimate the spontaneous emission rate of a SiV ensemble in and off resonance with the M7^A-cavity mode $o2$.

The modification of the spontaneous decay rate γ_{cav} averaged over the ensemble of SiV centers coupled to the cavity mode compared to its emission rate in a homogeneous medium γ_{bulk} is given by (c.f. [76])

$$\frac{\gamma_{\mathrm{cav}}}{\gamma_{\mathrm{bulk}}} = \frac{F_{\mathrm{P}} \langle R_r \rangle \langle R_d \rangle \langle R_\lambda \rangle \gamma_{\mathrm{ZPL}} + F_{\mathrm{PhC}} \gamma_{\mathrm{PSB}} + \gamma_{\mathrm{nr}}}{\gamma_{\mathrm{ZPL}} + \gamma_{\mathrm{PSB}} + \gamma_{\mathrm{nr}}}. \tag{7.6}$$

Considering $F_{\mathrm{cav}} = 1.07$ and $F_{\mathrm{PhC}} = 0.23$, we find a theoretical change in the spontaneous emission rate $\gamma_{\mathrm{cav}}/\gamma_{\mathrm{bulk}}$ that deviates from unity by 0.005 for quantum efficiencies between $0.05 - 0.6$ and a branching ratio $\gamma_{\mathrm{ZPL}} : \gamma_{\mathrm{PSB}} = 4 : 1$ [25]. As this predicted change in the spontaneous emission rate is much smaller than our detection precision (c.f. discussion on page 190), we conclude that the spontaneous emission rate is essentially unchanged $\gamma_{\mathrm{cav}} \approx \gamma_{\mathrm{bulk}}$. This theoretical prediction is conform with our lifetime measurements on SiV ensembles in resonance with the M7^A-cavity mode and on the unstructured diamond membrane. Due to the spatial, spectral and orientational averaging, a modification in the spontaneous emission rate is not detected.

Similarly, the inhibition of the spontaneous emission rate due to the photonic band gap effect could in principle be evaluated:

$$\frac{\gamma_{\mathrm{PhC}}}{\gamma_{\mathrm{bulk}}} = \frac{F_{\mathrm{PhC}}(\gamma_{\mathrm{ZPL}} + \gamma_{\mathrm{PSB}}) + \gamma_{\mathrm{nr}}}{\gamma_{\mathrm{ZPL}} + \gamma_{\mathrm{PSB}} + \gamma_{\mathrm{nr}}}. \tag{7.7}$$

If the SiV centers exhibit an average quantum efficiency of $\eta_{qe} = 0.05$, the spontaneous emission rate would be almost unaffected yielding $\gamma_{\mathrm{PhC}}/\gamma_{\mathrm{bulk}} = 0.96$. In contrast, if we assume a SiV quantum yield of $\eta_{qe} = 0.6$, the spontaneous emission rate would be inhibited by approximately a factor of 2 leading to $\gamma_{\mathrm{PhC}}/\gamma_{\mathrm{bulk}} = 0.54$. These simple calculations show that detailed knowledge of the SiV quantum efficiency as well as the impact of ensemble averaging is required in order to correctly relate our experimental data with these theoretical predictions. Moreover, measurements on other photonic crystals or other samples would be desirable to gain deeper insight into the inhibition processes of SiV ensembles when placed in a periodic lattice.

Summary

In this chapter, we studied the coupling of a photonic crystal cavity mode to an ensemble of SiV centers incorporated into the diamond membrane. In order to spectrally overlap the cavity resonances with the SiV ZPL, we developed a tuning method that relies on successive thermal oxidation in air. Using this digital oxidation technique, the cavity

modes could be shifted by up to 15 nm with an average increment of 3 nm per oxidation step. Tuning a cavity mode into resonance with the ZPL of the SiV ensemble, we observed a clear intensity enhancement by a factor of $2.8-3$ compared to the off-resonant spectrum. We associated the raise in the PL signal to a spectrally resolved Purcell enhancement of the spontaneous emission rate of the SiV centers. Via detailed analysis, we could relate the measured intensity enhancement to an ideal Purcell factor of $F_P \approx 20$ deduced from the measured quality factor of $Q = 400$ and the simulated mode volume $V = 1.5(\lambda/n)^3$. The thorough analysis takes into account spatial and oriental averaging of the emitter-mode overlap; spectral mismatch of SiV zero-phonon line width and cavity linewidth; modification of the local density of states by the photonic crystal; and different collection efficiencies for cavity mode and uncoupled emission. Furthermore, one has to account for the branching ratio of SiV emission into the zero-phonon line and phonon side bands of $4 : 1$. The thorough analysis reveals a cavity Purcell factor of $F_{\text{cav}} = 1.07$ of the SiV ensemble emission coming along with an enhancement of the ZPL intensity of 3.5 ± 1, which is in good agreement with experimental measurements.

For a single emitter with perfect spatial and spectral matching to the cavity mode, an ideal Purcell factor of $F_P \approx 20$ results in an approximately twofold emission rate enhancement and a fraction of 50% of total emission into the zero phonon line, thereby increasing the radiative quantum efficiency by a factor of 10. Such an experiment would require deterministic placement of a single SiV center relative to the cavity mode, which will be demonstrated in chapter 9.

Chapter 8

Nanoimplantation of NV centers into photonic crystal cavities

In the previous chapter, we demonstrated the coupling of a large ensemble of SiV centers to a photonic crystal cavity mode and observed a large intensity enhancement due to the Purcell effect. The following two chapters are dedicated to the controlled coupling of one single color center to a photonic crystal cavity mode. The coupling of single color centers to all-diamond nanocavities with very small modal volume, i.e. photonic crystal cavities, has been demonstrated for single NV centers [87, 88] at cryogenic temperatures necessary to reduce the zero-phonon line broadening. Using thermal oxidation and gas condensation, the cavity modes were tuned into resonance with the NV zero-phonon line. On resonance, a lifetime reduction up to 3.4, attributed to a Purcell enhancement of the zero-phonon line by a factor of 69 has been demonstrated [87]. The photonic crystal structures were etched in pure diamond membranes with single color centers incorporated during the CVD growth. Hence, the color centers' positions within the photonic crystal cavities were completely random and the cavity-emitter systems were selected for optimum coupling after fabrication. In the case of low densities of color centers, the probability for a single color center placed inside the photonic crystal cavity is fairly low due to the small cavity mode volume. Assuming a density of 2 single color centers per $20 \times 20\,\mu\mathrm{m}^2$, which is a typical density of single SiV centers incorporated in CVD diamond membranes (c.f. chapter 9), and a defect area of a one-missing hole cavity of $300 \times 300\,\mathrm{nm}^2$, the probability to obtain a single optically active center in the cavity is 4.5×10^{-4}. In other words, more than 2,200 photonic crystal cavities have to be fabricated and characterized to end up with one single emitter placed inside the cavity defect region. The approach relying on random positioning is extremely material and time consuming and lacks of reproducibility. An attractive alternative to achieve coupling with a single color center is to actively position the emitter in the cavity. Such an approach, although technically challenging, would be incredibly useful in the realization of single color center devices and would offer a level of reproducibility not available using random positioning techniques. In this work, we present two approaches to actively

position a single color center at the center of a photonic crystal cavity fabricated in diamond. The first strategy is based on high resolution creation of single color centers via ion implantation into a photonic crystal cavity. The second method involves the fabrication of a photonic crystal around a pre-characterized single color center localized in a diamond membrane.

For the first approach, we use an ultra-pure diamond membrane as starting material to fabricate photonic structures. Subsequently single NV centers are created at the cavity center using a combined system of a nitrogen ion beam and a pierced atomic force microscopy tip as a beam collimator. This strategy is focused on NV centers, as they can be very well created via nitrogen implantation and subsequent capture of a diffusing lattice vacancy upon high temperature annealing. In this chapter, we will present in detail the targeted creation of single NV centers in photonic crystal cavities.

The second method starts with a diamond membrane that already contains single SiV centers that are incorporated into the diamond membrane during CVD growth. Once a single optical center is identified and its emission properties, e.g. central wavelength, linewidth, dipole orientation, are determined, we fabricate a photonic crystal structure around the emitter via focused ion beam milling using alignment markers. Here, we concentrate on single SiV centers, as they can be incorporated at low density into the diamond during CVD growth and furthermore they show bright and spectrally narrow emission lines well suited for cavity coupling. The next chapter 9 is dedicated to the deterministic positioning and coupling of a single SiV center to a photonic crystal cavity.

This chapter is divided into two parts: The first part demonstrates the successful creation of a small number of NV centers in photonic crystal cavities via ion implantation whereas the second part presents a generalized Purcell theory to model the coupling of a broad-band NV center to a narrow cavity mode. The experimental sections introduce the basic physical principle of ion implantation and the limitation of the spatial resolution. We present the nanoimplanter setup consisting of a nitrogen ion beam combined with an atomic force microscopy (AFM) system to image the photonic structures. Moreover, a hole in the AFM tip simultaneously serves as a beam collimator to implant nitrogen ions with high resolution. We discuss the impact of the implantation energy and dose on the creation efficiency of single color centers. The photonic crystal cavities are fabricated in ultra-pure diamond membranes with resonant design wavelengths near the NV^- zero-phonon line. The cavity defect region can clearly be identified in the AFM scans. Once the collimation hole is positioned above the cavity center, we implant nitrogen ions under different implantation parameters into the photonic structures. Using confocal spectroscopy at cryogenic temperatures, we identify single implanted NV centers at the center of the photonic crystal cavities. From the spectra, we can estimate the number of implanted NV centers and the experimental creation yield.

The second part is dedicated to the theoretical description of coupling a broad-band emitter to a narrow cavity line. Beyond the standard description of light-matter interaction, a generalized Purcell factor has been derived recently by Auffèves et al. [91, 92] and successfully adapted and expanded by Albrecht et al. [80] to describe coupling of a single NV center to a Fabry Pérot cavity. Within this framework, they approximate

the NV center as a multi-level system undergoing pure dephasing as a source of spectral broadening. We adopt this model to calculate the expected Purcell enhancement when tuning a photonic crystal cavity mode on resonance with the NV zero-phonon line or phonon side band. Thereby, we take into account the moderate experimental cavity quality factor and mode volumes of the fabricated cavity structures. The input parameters for the multi-level scheme of a broad-band emitter are obtained by fitting the measured spectrum of shallow implanted NV centers. Moreover, we discuss the implementation of a non-unity quantum efficiency of the emitter in our model as well as the impact of the positioning accuracy and dipole orientation on the coupling strength.

8.1 Physical background of ion implantation

The first section of this chapter provides the basic principles of ion implantation into matter. We discuss the physical and technical limitations of the spatial resolution and present different implantation techniques to create single color centers in diamond with a resolution near the physical limit. We introduce the nanoimplanter setup used in this work for targeted creation of single NV centers in diamond-based photonic crystal cavities. We discuss the impact of the ion's kinetic energy and implantation dose on the number of created NV centers and present different strategies to boost the NV production yield.

8.1.1 Spatial resolution of ion implantation

The spatial resolution of the ion implantation process is defined as the position accuracy of the implanted ion in the target material. In the case of many implanted ions, the spatial resolution is given by the volume distribution in which the implanted ions will end up. For single ions, the spatial resolution can be considered as the position uncertainty around the most probable final position. In most cases, technical limitations of the focusing optics of the implantation setup are the major source of positing inaccuracy. However, there are also intrinsic physical limitations due to ion-matter interaction that restrict the implantation accuracy. In this section, we will discuss the main physical limitations of the spatial resolution before we present in detail the nano-implantation technique for creating NV centers in diamond with high spatial resolution. The following sections are based on references [415–417].

Ion straggle

No matter how good the focusing capabilities of the implantation setup are, the ion displacement in matter sets a physical limit to the spatial resolution of the position and size of the implantation spot within the implanted substrate. Straggling (deviation of ions from their mean straight line of propagation) occurs due to multiple collisions by the moving ion with the atoms of the target material. The ion-matter interaction depends on several parameters such as the ion's kinetic energy, the nature of the target material,

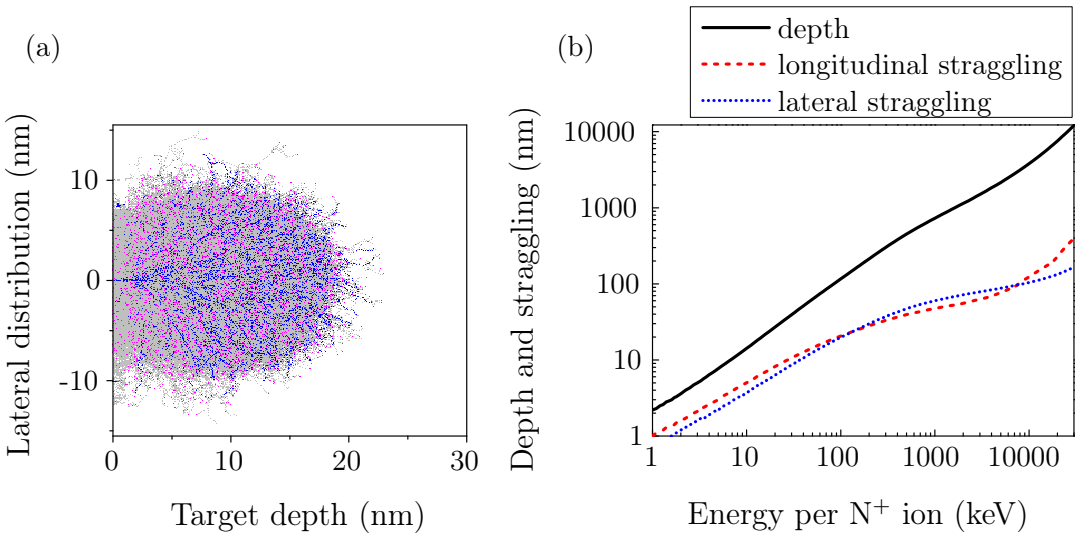

Figure 8.1: Stopping range simulations of nitrogen ions implanted into diamond: (a) SRIM simulation of 5 keV N^+ ions implanted in diamond. The ion trajectories are shown in blue, whereas the moving and stopping atoms are shown in gray and pink, respectively. (b) Implantation depth and ion straggle (longitudinal and lateral) as a function of the N^+ energy.

the temperature, the crystallographic orientation, etc. It results in a broadened implantation volume that can be seen as an increased uncertainty in position of each individual implanted ion. Qualitatively, ion straggling is defined as the standard deviation of the ion distribution [416]. We distinguish between longitudinal (parallel to implantation direction) and lateral straggling (perpendicular to implantation direction). Both contributions have comparable magnitudes and therefore, we refer to just one "straggling" as a measure of broadening of the implantation volume. To calculate the penetration and straggling of energetic ions into matter, we perform Monte Carlo simulations using the free software package SRIM (Stopping and Range of Ions in Matter) [374]. As an example, figure 8.1(a) shows the simulated trajectories of nitrogen ions implanted into diamond with an energy of 5 keV. At this energy, the nitrogen ions stop at an average depth of 8 nm in the target material with a lateral and longitudinal straggle of 3 nm. Figure 8.1(b) displays the implantation depth and straggling of nitrogen implanted into diamond as a function of the ions' kinetic energy. Both the ion range and straggle strongly increase with the ion energy. Assuming a target implantation depth of 150 nm at the center of a 300 nm-thick diamond slab, an implantation energy of 135 keV would be required coming along with an ion straggle of 24 nm. For implantation energies in the MeV range, the ion straggle is even larger than 50 nm. As straggling is an intrinsic effect of the ion-implantation process, high-energy impurity doping cannot be used to achieve a position accuracy in the nanometer range. Therefore, aiming at nanometer spatial resolution, a low ion energy of a few keV has to be used in order to assure a small ion displacement in matter. However, in this case, the ion implantation depth is very

shallow. The presence and the termination of the surface may have a considerable impact on the creation yield, the emission and the spin coherence properties of implanted NV centers. The impact of the surface is discussed in more detail in section 8.1.5.

Ion channeling

Ion channeling is another effect that might have an impact on the longitudinal accuracy when implanting ions into crystal substrates. Ions propagating along low-index crystallographic axes and planes of the target material penetrate much deeper and produce less vacancies. Recently, secondary ion mass spectroscopy has been used to detect penetration depths as twice as deep than predicted by SRIM simulations for nitrogen ions implanted at 10 keV, 20 keV and 30 keV in (100) single crystal diamond [49]. Ion channeling leads to a loss of spatial resolution in the implantation direction. In practice, ion channeling occurs within a critical angle around a given crystallographic axis and crucially depends on many parameters including ion nature, ion energy and sample temperature [417–419]. The impact of various factors makes the effect hardly predictable. Simulations by Ofori-Okai et al. [419] predict that $64-70\%$ of nitrogen ions implanted at 5 keV under normal incident in (100) or (111) single crystal diamond undergo channeling. Under these implantation conditions, the critical angle is calculated to be $\sim 10^\circ$. However, for very low ion energies < 0.6 keV, the effect of ion channeling should be strongly minimized [419]. In contrast, more recent simulations by Antonov et al. [420] take into account the crystal structure of the diamond lattice. For nitrogen irradiation at normal incident with an energy of 4 keV into a (100) diamond substrate, they found that only 32% of the nitrogen ions undergo channeling and stop at 21.0 ± 17.7 nm below the surface. Consequently, the majority of nitrogen ions (68%) are not affected by ion channeling and come to rest at a depth of 7.5 ± 7.7 nm which is in good agreement with SRIM simulations. In practice, for implantation into cubic crystals (e.g. diamond), it has been found, that tilting the substrate normal by an angle of $7^\circ - 10^\circ$ with respect to the incident ion beam, avoids extensive channeling in the implantation direction [49, 416, 421]. Alternatively, one could deposit a thin amorphous layer, e.g. SiO_2, on top of the diamond surface to mitigate channeling [49]. In our experiments, ion implantation is performed at vertical incidence without using an amorphous cap layer. As outlined above, this might result in a larger penetration depth of single implanted nitrogen ions and in a decreased positioning accuracy in the longitudinal direction.

Diffusion of impurity atoms

Ion implantation always induces damages within the crystal lattice. For diamond, the damages are mainly vacancies, interstitial carbon atoms and simple defects [416]. In order to restore the diamond lattice, the samples are typically annealed in vacuum. The heating process might lead to an increased mobility of the implanted species which would affect the spatial resolution. However, diffusion of nitrogen atoms in diamond is extremely small because of the high activation energy of 6 eV [419, 422]. The diffusion coefficient of nitrogen in diamond has been measured at high temperatures in the con-

text of geology [422]: At 800°C, the diffusion coefficient is $D = 3 \times 10^{-35}\,\mathrm{m}^2/\mathrm{s}$. The corresponding diffusion length after 2 h annealing is $L = \sqrt{D\,t} = 5 \times 10^{-16}\,\mathrm{m}$, which is much smaller than the interatomic distances ($\sim 10^{-10}\,\mathrm{m}$). Hence, under the high-temperature treatment we use (800°C to 1,000°C, 2 hours), the nitrogen atoms do not migrate to a measurable extend. This is a crucial point since the spatial resolution of the ion implantation will be examined in annealed diamond samples. However, at elevated temperatures above 600°C vacancies become mobile and diffuse towards implanted nitrogen atoms to form optically active NV centers.

8.1.2 High resolution implantation schemes

As mentioned before, straggling of implanted ion species within the target material represents a lower bound of the spatial resolution. In practice, the spatial accuracy is mainly restricted by the technical limitations of the focusing optics of the implantation setup. In recent years, several schemes have been realized, that allow for implantation of single NV centers with high spatial resolution near the fundamental physical limit of ion straggling in diamond. The smallest lateral resolution down to 20 nm has been achieved by using a low energetic nitrogen beam in combination with a pierced atomic force microscopy (AFM) tip as a collimator (c.f. section 8.1.3). This technique allows for implantation of single NV centers at positions into structures within the diamond. The details of this method are discussed in this chapter. Another scheme that even allows for deterministic implantation of single ions with high spatial resolution is pursued by the group of F. Schmidt-Kaler at the University of Mainz. The basic idea of this approach is to use single ions trapped in a Paul trap for implantation. This would allow for precise control of the number of doping ions and for deterministic implantation of a single ion [423]. As most of the ions that would be interesting for doping into diamond, e.g. nitrogen, cannot be trapped or laser cooled, sympathetic laser cooling is used by including the doping ions in a string of $^{40}Ca^{+}$ ions that can be laser cooled [423]. Finally, the doping ions are extracted from the trap and focused on the diamond sample. However, up to now, no experimental data on the deterministic implantation of nitrogen into diamond using this scheme are available. Recently, a third maskless method relying on focused ion beam (FIB) technique equipped with a novel developed plasma source has been presented [424]. The setup is combined with a scanning electron microscope to image the sample and to focus the nitrogen beam at well defined positions. The resolution of this new FIB technique is limited by the spot size of 100 nm of the $^{14}N_2^{+}$ molecular nitrogen beam accelerated at a fixed voltage of 30 kV. Assuming the nitrogen molecules split into two nitrogen ions when they hit the diamond surface with a kinetic energy of 15 keV per atom, a penetration depth of 20 nm can be reached. An alternative method, that allows for parallel implantation of large arrays of single NV centers, involves a structured electron beam lithography resist as a mask on top of the diamond target material [49, 417, 421]. Small apertures with diameters of $60 - 80\,\mathrm{nm}$ are defined via electron beam lithography in the positive resist with a thickness of $200 - 300\,\mathrm{nm}$. The resist thickness is chosen such that nitrogen ions implanted with an energy of 20 keV [49, 421] or 55 keV [417] stop within the mask material and are solely

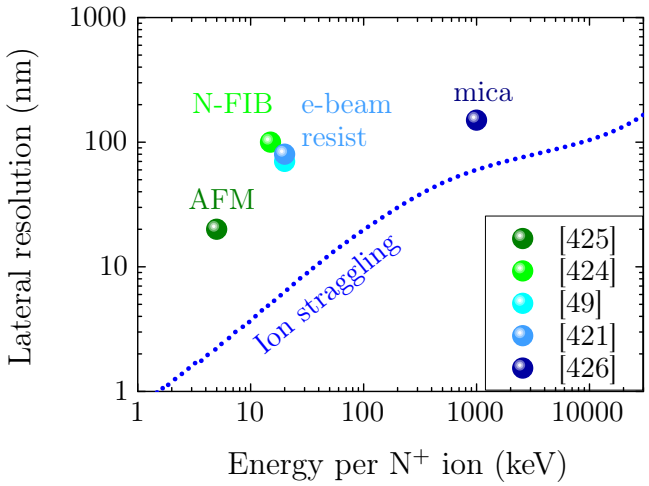

Figure 8.2: Comparison between realized implantation schemes operating at different kinetic ion energies. All techniques aim at high spatial resolution near the fundamental limit defined by ion straggling within the diamond target material.

implanted in the uncovered regions of the diamond with a spatial resolution defined by the size of the aperture. The resolution could even be increased using smaller aperture sizes which, however, would require smaller thicknesses of the electron beam resist and hence lower kinetic ion energies to make sure that the impinging ions stop within the mask material [49, 421]. Another parallel technique to produce large arrays of NV centers at much larger depths relies on the implantation of high energetic nitrogen ions through nano-channels in mica foils [426]. The straight nano-channels with cross sections of only 30 nm are produced in mica foils with thicknesses of several micrometers by irradiation with heavy ions and subsequent chemical etching. Nitrogen ions with 1-2 MeV kinetic energy pass the nano-channels and are implanted into the diamond with a spatial resolution approaching the ion straggling limit [426]. Figure 8.2 displays the lateral resolution achieved by each technique as a function of the applied kinetic energy of the implanted nitrogen ions. As a reference, the physical limit of the spatial resolution determined by ion straggling is shown by the dotted line. The implantation parameters of the different techniques such as the ions' kinetic energy and the penetration depth as well as the experimentally achieved spatial resolution and NV creation yield are summarized in table 8.1.

A kinetic ion energy of 135 keV would be required to reach an ideal depth of the stopping ions of 150 nm at the center of a 300 nm-thick photonic crystal slab. However, for the required energy no high resolution implantation scheme is available at this moment. The techniques involving a collimating mask can hardly be applied for target implantation into photonic crystal structures. The positioning of a mica mask with respect to the center of a photonic structure is extremely challenging, as the pores in the mask have a diameter of only 30 nm and as they are completely randomly positioned within the mica foil. Equally, using a structured PMMA layer as a mask for target implanta-

method	energy/N^+ (keV)	depth (nm)	resolution (nm)	yield (%)	ion species used in exp.	Ref.
AFM-tip	5	8 ± 3	25	0.8	$^{15}N^+$	[425]
N-FIB	15	20 ± 7	100	1	$^{14}N_2^+$	[424]
e-beam	20	30 ± 8	60	5	$^{15}N^+$	[49]
e-beam	20	30 ± 8	80	7	CN^-	[421]
mica mask	1,000	700 ± 50	150	15	$^{15}N^+$	[426]

Table 8.1: Implantation techniques allowing for creation of single NV centers with high spatial resolution. The kinetic energy per ion, the penetration depth as well as the measured spatial resolution and NV creation yield are summarized for the different methods. In some experiments other ion species than atomic nitrogen have been used.

tion in predefined patterns is not well suited. The challenge is to uniformly illuminate and develop small apertures in the resist. After the ion implantation the resist has to be completely removed particularly from the air holes defining the photonic crystal lattice. Very recently, the use of a silicon hard mask with a small hole at the center was proposed in a conference contribution [133]. In this paper [133], the silicon mask simultaneously serves as an etch mask for patterning the photonic crystal cavities and as an aperture upon N^+ implantation at the center of a cavity structure. This scheme would allow for overcoming of difficulties in positioning, aligning and defining a mask. In the present work, we apply a maskless technique allowing for a high flexibility and for quick modification of the doping structure. As the recently developed nitrogen FIB technique is limited by a spot size of 100 nm [424], which is to large for the implantation at the center of photonic crystal cavities, we use a high-resolution technique involving a pierced AFM tip as a collimator. In the following, we briefly describe the nanoimplanter setup.

8.1.3 Nanoimplanter setup

In order to aim at the highest position accuracy, the implantation energy has to be reduced to a few keV. In this energy range, the ion straggle is less than several nanometers. However, focusing a low-energy ion beam of a few keV or less to a nanometer spot size is almost impossible due to chromatic aberration. The solution to this problem is to use a small aperture within the beam path such that the implantation spot becomes independent of the ion-beam focus. The 5 keV-nanoimplanter built at the RUBION in Bochum combines a low-energy ion gun with a pierced atomic force microscopy (AFM) tip. On the one hand, the nano-hole drilled in the hollow AFM tip serves as an aperture to collimate the ion beam. On the other hand, the AFM tip is used to scan over the sample and to previously image a structure (e.g. photonic crystal cavity) in which ions have to be implanted.

The setup in Bochum is equipped with a gas-source ion gun (5 kV, SPECS IQE

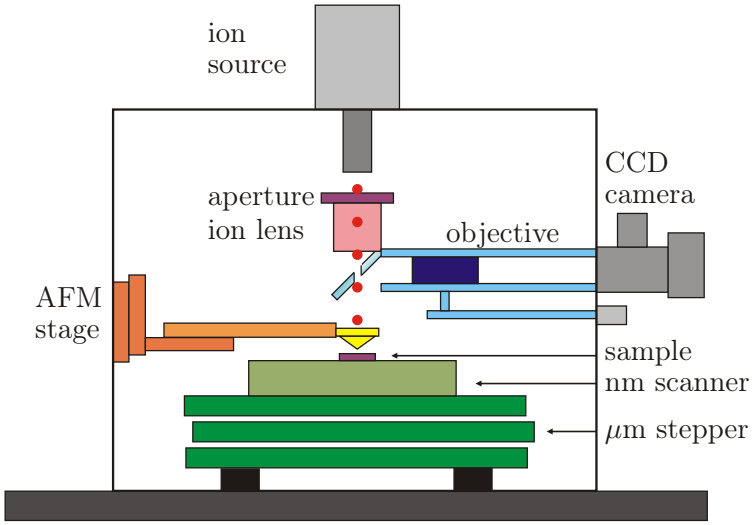

Figure 8.3: Nanoimplanter setup (after [415]): The ion beam extracted from the ion source is focused by an aperture and electrostatic lens on a pierced AFM tip positioned directly above the target substrate. The sample is mounted on a scanner with sub-nm position accuracy and a stepper motor table providing a large moving range. For in-situ observation and alignment of the tip with respect to the ion beam, the setup is equipped with a microscope objective, which focuses the white light image of the sample, deflected by a mirror, on a CCD camera. The whole setup is placed in a vacuum chamber mounted on an optical table. Dimensions of the chamber are 40 cm × 40 cm × 50 cm.

12/38) combined with a Wien mass filter [417] and an electrostatic lens to pre-focus the beam. The ion gun system provides positive species of any inert gas (He, Ar, Ne, Xe, Kr, N_2) as well as reactive ions by use of O_2 or H_2. The acceleration voltage can be varied from 0.2 kV to 5 kV. In the present work, we apply a fixed voltage of 5 kV. The ion beam current can be chosen from 10 μA to less than 1 pA. To further reduce the spot size of the ion beam, an additional electrostatic lens close to the AFM cantilever is used. The ion lens demagnifies the image of an aperture with a diameter between 1 and 20 μm to the surface of the AFM tip [415]. To facilitate the alignment, an aperture of 20 μm is used in the following. The AFM (Alpha contact) works in contact mode and uses piezoresistive cantilevers with a hollow tip. The cantilevers and tips are made of silicon nitride with a thickness of 150 nm (Witec). Close to the apex of the hollow tip, a nanometer-sized hole is drilled using FIB milling with gallium ions. The AFM stage is mounted on a three-axis table (Physik Instrumente PI) with a resolution of 200 nm. The AFM device is based on a piezoresistive positioning sensor system with a resolution of 1 nm. The sample holder is mounted on a piezo-electric scanner with a resolution of 0.1 nm and a moving range of 150 μm in the horizontal and 20 μm in the vertical direction [415]. To extend the moving rage, the piezo-translation stage is placed on a second long-range stepper motor table providing micrometer positioning over several centimeters. In order to measure the ion current, the setup is equipped with

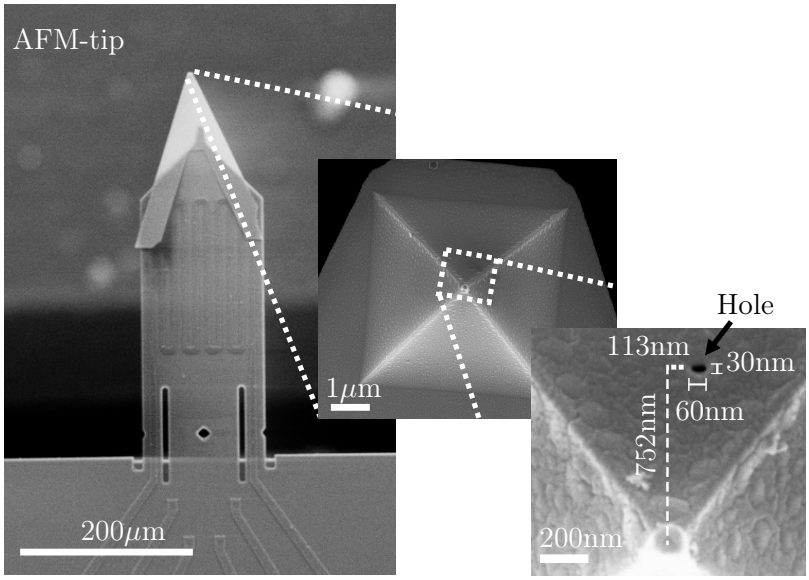

Figure 8.4: Scanning electron microscope image of the atomic force microscopy tip: The hollow silicon nitride AFM tip is glued on a piezoresistive cantilever. Using focused ion beam milling, a hole is drilled in the tip at position $(x, y) = (113, 752)\,\mathrm{nm}$ with respect to the apex. The hole has an elliptical shape with a size of $60\,\mathrm{nm} \times 30\,\mathrm{nm}$.

a Faraday cup directly fabricated on the sample holder and a picoampermeter. In the case of very low currents, an additional electron multiplier (detection efficiency $> 90\%$) allows for the detection of single ions. A long working distance microscope objective ($10\times$) and a white light source integrated in the chamber enable live observation and adjustment of the AFM tip with respect to the ion beam. The white light image is deflected by a 45° pierced mirror towards the objective connected to a high resolution and high sensitivity CCD camera. The whole setup is placed in a vacuum chamber equipped with a turbo pump and an ion pump reaching pressures of $10^{-4}\,\mathrm{Pa}$. To avoid vibrations, the nanoimplanter is installed on an optical table and the turbo pump is turned off during implantation. A schematic of the nanoimplanter setup is shown in figure 8.3.

Pierced AFM tip

The AFM device is based on a piezoresistive cantilever with an integrated Wheatstone bridge [415, 427]. Compared to conventional optical beam deflection methods, the piezoresistive technique allows for very compact high-resolution AFM systems that can be integrated in ultra-high vacuum setups. The interaction of the AFM probe with the sample causes a change of the cantilever bending, its resonance frequency or a phase shift. When the cantilever is deflected by a force acting on the tip located at the beam end, mechanical stress occurs in the lever volume, being proportional to the applied force [428]. Using complementary metal-oxide-semiconductor (CMOS) tech-

nology, piezoresistors are integrated in the cantilever made of silicon [427]. Silicon is known to change its electrical resistance under applied mechanical strain (piezoresistive effect) [429]. The change of the resistance with respect to stress is detected by a Wheatstone bridge integrated in this area. Figure 8.4 shows the AFM cantilever with four integrated active piezoresistors connected to form a Wheatstone bridge. At the end of the silicon lever a hollow pyramidal tip made of silicon nitride with a thickness of 150 nm is attached. In the combined nanoimplanter setup, the AFM is used to image the sample and collimate the ion beam for implantation into predefined structures. For imaging, the tip is scanned in direct contact over the target. In contact mode, the piezoresistive Wheatstone bridge is biased directly and the output voltage of the bridge is read out and amplified to drive the feedback loop of the AFM.

To reach a spatial nanometer resolution, a small hole in the AFM tip works as a last beam limiting aperture defining the beam spot size. The nano-hole is drilled in the tip using focused ion beam milling with 30 keV Ga^+ ions and a current of 10 pA. When milling the hole, the AFM cantilever is inclined by an angle of 17° with respect to the substrate, which is equal to the tilting angle during the implantation. In general, it is not desirable to mill the nano-hole directly at the apex of the tip as it will possibly be congested or damaged when working in contact mode. Therefore, in our experiments, the hole is shifted by 113 nm in x-direction and 752 nm along the y-axis with respect to the apex of the tip. The milled nano-hole has an elliptical shape with a transverse diameter of 60 nm and a conjugate diameter of 30 nm, which results in a hole cross section of 1,413 nm^2. A labeled scanning electron microscope image of the tip taken after FIB milling of the hole is shown in figure 8.4. The image is taken at an angle of 17°. Ion beam irradiation can lead to reduction or even closing of the nano-hole. This effect is often desired to reach extremely small collimation of the ion beam to perform implantation at very high spatial resolution [425]. After the ion implantation of our samples, we check by SEM images that the nano-hole in the used AFM tip is still open to make sure that all structures have been implanted with nitrogen.

8.1.4 Post processing

After the ion implantation process the samples are annealed in vacuum. There are basically two reasons for the high-temperature treatment: The first reason is the increased mobility of vacancies. At elevated temperatures above 600°C [416], vacancies can diffuse within the crystal lattice towards implanted impurity atoms. This is especially important as most of the color centers (e.g. NV and SiV centers) involve lattice vacancies to form active emitters. Second, ion bombardment causes damages to the diamond lattice that can be recover via high-temperature annealing [416] (c.f. chapter 6), if the lattice damage is below a certain threshold. As ion bombardment damages lead to significant non-radiative recombination channels [430, 431], it is impertinent to repair the crystal lattice in order to achieve bright luminescence of the implanted color centers.

High-temperature annealing after ion radiation is crucial for bright and efficient color center emission with low background contribution of the diamond lattice. However, there is one side effect that has to be tackled: surface graphitization. Annealing in

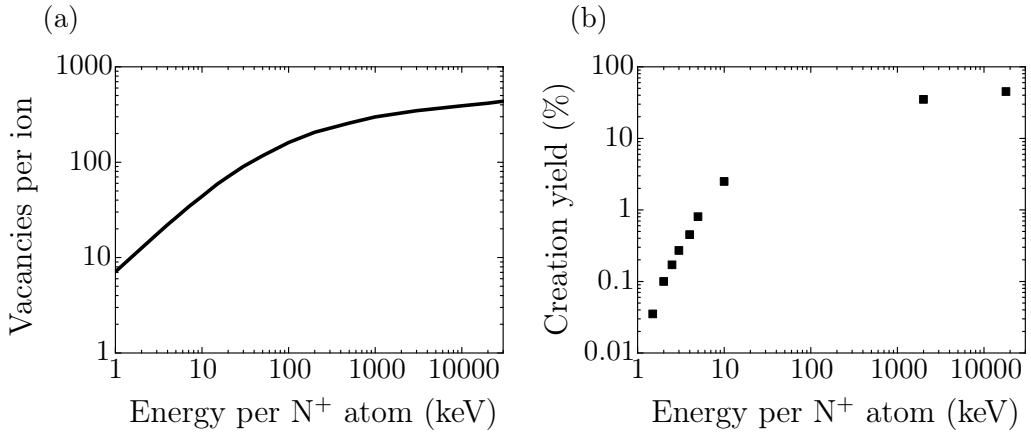

Figure 8.5: (a) Number of vacancies created per implanted N^+ ion simulated using SRIM. (b) Creation yield measured by Pezzagna et al. [432] as a function of the N^+ ion's kinetic energy implanted in diamond.

vacuum for several hours at temperatures above 900°C might cause a nanometer-thick graphitic layer at the diamond surface. The rate of graphitization and the thickness of the graphite layer strongly depend on the heating conditions. Using Raman spectroscopy, the presence of sp^2 bonded carbon such as graphite or amorphous carbon can be revealed. Especially for low-energy implantation, surface graphitization becomes a serious problem, as in this case the ion penetration depth is very shallow. To remove the graphitic residues, the sample is cleaned in a 1:1:1 mixture of boiling nitric, sulfuric, perchloric acid for several hours after ion irradiation. Furthermore, annealing in air at 420°C for several hours selectively oxidizes sp^2 carbon while leaving the diamond intact [390].

8.1.5 Theoretical creation yield

Not every implanted substitutional nitrogen atom is transformed into an optically active NV center. The ratio of the number of created NV centers divided by the amount of implanted substitutional nitrogen ions is defined as the creation yield. As the NV center complex involves an adjacent lattice vacancy next to the substitutional nitrogen atom, the production efficiency strongly depends on the amount of vacancies created by ion bombardment. In the following, we will discuss the dependence of the NV creation efficiency on the ion kinetic energy and the implantation dose.

Ion kinetic energy

Figure 8.5(a) displays the number of vacancies created per implanted nitrogen ion simulated by SRIM [374]. The higher the implantation energy, the more vacancies are created in the vicinity the implanted substitutional nitrogen atoms, leading to an enhanced probability of NV center creation, as long as the damage of the diamond lattice is not too strong. To qualitatively determine the production efficiency, Pezzagna et

al. [432] measured the number of created NV centers as a function of the $^{15}N^{+}$ ion energy. Their results, that are shown in figure 8.5(b) taken from reference [432], suggest a strong correlation between the number of vacancies and the NV production yield. For low energetic ion implantation of a few keV, the slope is very steep and saturates in the MeV range. At 18 MeV, a high yield of 45% is reached, while in the case of low energetic ion implantation of 5 keV the creation efficiency of single NVs is significantly reduced to only 0.8% [432]. The creation yield at high energetic ion irradiation is physically limited by the amount of substitutional nitrogen atoms that stop or diffuse upon annealing to an on lattice site. Simulations [420] suggest that only half of the implanted nitrogen ions are placed on-site and hence can be transformed into optically active NV centers defining an upper bound for the creation yield. In contrast, for small ion energies lower than 10 keV, the NV production efficiency is limited by the number of vacancies that can diffuse towards the implanted substitutional nitrogen atoms to form NV centers [432]. Depending on the ion energy and hence the implantation depth, the lack of vacancies is mainly attributed to either recombination with interstitial carbon atoms or migration towards the diamond surface. The impact of the surface is dominant in the case of very shallow implantation, whereas for higher ion energies the recombination process is critical. For low-energetic implantation at 5 keV, Antonov at al. [420] predict that 44% of the created vacancies recombine with interstitial carbon atoms during high temperature annealing and 49% of the vacancies are lost at the surface. The amount of vacancies migrated towards the surface reduces to 26% when the implantation energy is increased to 50 keV and the recombination with carbon atoms becomes important, annihilating 62% of the vacancies. Hence, the presence of a nearby surface significantly reduces the amount of vacancies available to form single NV centers. Moreover, the proximity to the surface has a strong impact on the charge state of the NV center [393]. The decrease in the NV production yield with decreasing ion energy has been investigated by Ofori-Okai et al. [419] for very low nitrogen implantation energies of $0.4 - 5$ keV. They attribute the decrease in the photoluminescence signal to a reduced formation of NV^{-} centers at energies below 3 keV. This suggests the presence of a possible depth threshold below which the NV^{-} charge state becomes unstable [394]. Later in this section, we will present strategies to boost the creation efficiency by increasing the amount of vacancies via co-implantation and by controlling the NV charge state via surface termination.

Ion fluence

As seen in the previous section, the creation yield of NV centers strongly depends on the kinetic energy of the implanted nitrogen ions. In this section, we discuss the impact of the ion fluence on the creation yield for constant implantation energy of 5 keV and compare our considerations with experimental data obtained for very low fluences [420] and for moderate and high ion doses [432]. For very low fluences of 3×10^{8} ions/cm^{2}, Antonov et al. [420] measured a creation efficiency of $23 - 29\%$ of single NV centers that is found to be independent of the implantation energy of 2.5 keV, 5 keV and 20 keV. Their experimental findings have been supported by sophisticated simulations including the amount of available vacancies after high temperature annealing

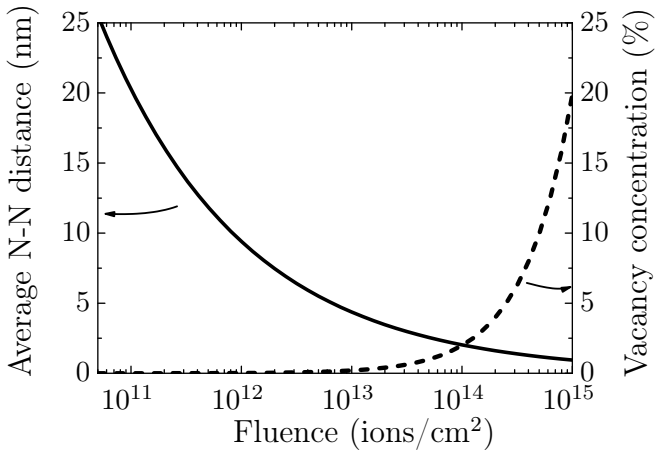

Figure 8.6: Solid line: Average distance between two adjacent nitrogen atoms implanted into diamond with an energy of 5 keV as a function of the ion fluence. Dotted line: Volume concentration of vacancies created by 5 keV nitrogen irradiation in the diamond lattice.

as well as the number of nitrogen atoms on-lattice sites. The simulations predict a creation yield of 25% that is claimed to be independent of the implantation energy in the range of $4 - 50$ keV. Their experimental findings for extreme low ion doses exceed previous efficiencies of $< 1.5\%$ [432] obtained for an implantation energy 5 keV and high fluences of $10^{11} - 10^{14}$ ions/cm^2 by one order of magnitude. The significant difference in production yield is attributed to the extreme low ion dose used in Ref. [420]. In fact, when increasing the fluence to $\sim 10^9$ ions/cm^2 the creation yield is reduced by more than a factor of 3 and decreased even further when lowering the ion energy or increasing the implantation dose [420]. These results suggest that even slight damages in the vicinity of implanted nitrogen ions induced by ion fluences $< 10^9$ ions/cm^2 inhibit the photoluminescence of single NV centers and lower the creation yield [420].

Apart from very low ion doses, the creation yield of single NV centers induced by 5 keV-ion implantation is typically $< 1.5\%$ [432]. In order to produce at least one single NV center at the center of a photonic crystal cavity by ion implantation through the pierced AFM tip, ion fluences exceeding 10^{11} ions/cm^2 are required (assuming unity creation efficiency). As in practice the yield is smaller than unity, the nitrogen implantation into photonic crystal structures presented in section 8.3 has been performed at ion doses between $10^{13} - 5 \times 10^{14}$ ions/cm^2. In the following, we will discuss the expected NV production yield for moderate fluences. The solid curve in figure 8.6 shows the simulated average distance between two adjacent implanted substitutional nitrogen atoms as a function of the ion dose: the stronger the fluence the smaller the N-N-distance. For very large distances between adjacent nitrogen ions, the vacancies created by one implanted nitrogen ion cannot be trapped by a second nitrogen ion. Therefore, we would expect a constant NV creation yield as long as the vacancies clouds around the nitrogen atoms do not overlap. This has been confirmed by Pezzagna et al. [432]: Over a wide range of fluences between $6.9 \times 10^{10} - 2 \times 10^{12}$ ions/cm^2, they found a constant yield of

$0.7\% - 0.8\%$. However, at higher fluences, the measured production yield raises up to 1.3% [432]. At fluences above 4×10^{12} ions/cm^2 the N-N-distance is reduced to < 6 nm such that the shells of vacancies around implanted ions start to overlap, if we consider the lateral extend of the implantation spot shown in figure 8.1. For small N-N-distances, the created vacancies can additionally be trapped by a second adjacent substitutional nitrogen atoms, which would result in an increased probability of NV center production. However, the boost in the creation yield with higher fluences has a physical limit: If the ion irradiation exceeds the amorphization threshold, the damages within the material become too strong and the diamond lattice cannot be recovered by thermal annealing. Amorphization of the diamond would heavily suppress the color centers fluorescence. Pezzagna et al. [432] found a maximum fluorescence intensity for an implantation dose of 1.2×10^{14} ions/cm^2. At higher fluences, the intensity strongly drops. Considering a vacancy density of 0.35 vacancies/Å/ion calculated using SRIM [374] for $^{15}N^+$ ion implantation at an energy of 5 keV, the dose yielding maximal fluorescence intensity would correspond to a threshold of 4×10^{21} vacancies/cm^3 or a vacancy volume concentration of 2.3% in the diamond (dotted line in Fig. 8.6). For fluences exceeding the damage threshold, the diamond lattice is irreparable destroyed and graphitization occurs upon annealing. The here derived critical value is comparable to the damage density threshold of 10^{22} vacancies/cm^3 determined by Uzan-Saguy et al. [384]. They claimed the graphitization threshold to be independent of the ion species and implantation energy. To summarize, for shallow $^{15}N^+$ implantation at 5 keV the NV creation yield of 0.8% is constant for fluences $< 4 \times 10^{12}$ ions/cm^2 and increases up to 1.3% for ion fluences between $4 \times 10^{12} - 5 \times 10^{13}$ ions/cm^2 before it significantly drops at large ion doses. In the case of low ion doses, the creation yield is limited by the amount of vacancies, whereas for large fluences graphitization of the diamond lattice, that inhibits the NV photoluminescence, becomes important.

Increasing the creation yield

As discussed above, nanometer spatial resolution can only be achieved for ion energies of a few keV that comes along with an implantation depth close to the diamond surface. However, the close proximity to the surface leads to a reduced production yield of single NV centers that has to be tackled. First of all, for very shallow implantation depths, the NV creation yield is significantly limited by the amount of vacancies. During high temperature annealing, a major part of the vacancies diffuses towards the diamond surface instead of recombining with a substitutional nitrogen atom to form an optically active NV center. Secondary, the surface termination of the diamond has a strong impact on the charge state of the NV center as well as on its photostability. In the following, we will discuss in detail different strategies to enhance the creation yield of NV^- centers via co-implantation of other ion species to increase the amount of vacancies or via controlled surface treatments to stabilize the NV^- charge state and suppress photochromism.

To overcome the lack of vacancies in the case of low energetic ion implantation, subsequent irradiation with other ion species could enrich the N implanted region with vacancies and facilitate the NV formation. Schwartz et al. [433] studied the co-implantation

of 7.7 keV hydrogen, helium and carbon atoms into high purity (100) single crystal diamond implanted with 7.7 keV $^{14}N^+$ ions. During the ion bombardment, the sample was heated to 780°C. At the depth of the implanted nitrogen ions, additional vacancies are induced by the subsequent ion irradiation yielding an enhanced NV photoluminescence intensity by 7%, 10% and even 25% for hydrogen, helium or carbon co-implantation, respectively. Similarly, subsequent irradiation of inert 28 keV-argon atoms after the implantation of 14 keV $^{15}N^{2+}$ nitrogen ions into ultra pure diamond leads to an increase by $5 - 130\%$ in the NV photoluminescence intensity depending on the nitrogen and argon ion doses [434]. However, detailed further studies on the optimal annealing conditions as well as the argon and nitrogen doses are needed, as not only a strong variation in the intensity enhancement but also a decrease of the yield for low fluences has been observed. The co-implantation of carbon atoms to enhance the NV production yield has been studied by several groups. Using a two step implantation process, which involves the implantation of molecular nitrogen ions $^{15}N_2^+$ with an energy of 30 keV per atom into single crystal diamond followed by a high dose ^{12}C irradiation at 40 keV, the NV creation efficiency has been more than doubled reaching yields of 33% [435]. Similar raise in the creation efficiency up to $36 \pm 9\%$ have been achieved for $^{15}N_2^+$ molecular nitrogen accelerated with an energy of 10 keV per atom and co-implanted with ^{12}C atoms at 20 keV into (100) single crystal diamond [436]. The same effect can be achieved, by implanting CN^- molecules instead of nitrogen ions [421]. When the CN^- molecule hits the surface, it splits into a nitrogen and a carbon atom leading to additional vacancies around the implanted nitrogen atom. Doping a single crystal ultra-pure diamond with CN^- molecules at an energy of 40 keV, produces single NV centers with a yield of 7% [421]. However, very high ^{12}C fluences favor the formation of vacancy complexes and vacancy related defects that compete and hinder the creation of NV centers [433, 435].

Besides the effect of vacancy capture, the close proximity to the surface has also a strong impact on the charge state of the NV center. In order to convert the NV^0 center, that is formed by recombination of a substitutional nitrogen atom and a vacancy [394], into its negatively charged state NV^-, an additional electron donor located in the vicinity of the defect is required. It is widely expected that substitutional nitrogen atoms are the main electron donor [394, 437]. However, it has been shown that the amount of NV^- centers is significantly reduced near the surface compared to bulk material [437]. This suggest the presence of an electron depletion layer induced by surface acceptor states leading to ionization of the nitrogen donors within the first ten to hundred nanometers [393, 437]. Possible acceptor species are graphite defects [394, 437], polishing damages, implanted gallium ions during FIB milling [437] or a hydrogen surface termination [393]. By removing graphitic shells and amorphous carbon via acid treatment or annealing in air [391, 394] as well as by changing a hydrogenated surface to an oxygen-termination via O_2 plasma treatment [393], the NV center can be switched from its neutral to the negative charge state and the NV^- photoluminescence intensity can be strongly increased. The impact of controlled surface termination on the production yield of single NV^- centers created by ion implantation has been studied by several groups. For an ensemble of NV centers that were created by 10 keV $^{14}N^+$ ion implantation at a depth of 15 nm, Cui at al. [438] observed a stabilization of the

NV^- charge state in the case of fluorine- and oxygen-terminated diamond surfaces. The impact of CF_4 or O_2 plasma treatment on the creation yield of NV centers has equally been studied by Osterkamp et al. [439]. Using plasma treatment, they observe a four fold increase in the production yield of single NV centers that were implanted at a depth of 5 nm with an implantation energy of 2.5 keV. Surface treatment not only increases the production yield but also suppresses photochromism. Before plasma treatment, 86% of very shallow NV centers implanted with 1.25 keV at a depth of 3 nm below the surface showed blinking. This blinking can totally be suppressed and the charge state is completely converted to NV^- by fluorination of the diamond surface [439]. In the present work, we assure a well defined oxygen surface termination by thorough acid treatment and oxidation in air. The overall conversion to the negative charge state is confirmed by fluorescence spectroscopy.

Another way to stabilize the NV^- charge state and to significantly enhance its spin coherence times, is to epitaxially overgrow shallow (< 10 nm) implanted NV^- centers with a nominally undoped 30 nm-thick diamond layer [440]. This approach combines the high spatial positioning accuracy via low energetic nitrogen implantation with good optical and spin properties of stable NV^- centers by keeping the color centers sufficiently away from the diamond surface. After the re-growth, most of the NV centers are converted to the negative charge state and only $5 - 10\%$ reside in the neutral state.

8.2 Photonic crystal cavities in ultra-pure diamond

After having discussed the physical basis of ion implantation into matter and having presented the implantation setup, we will focus in this section on the fabrication of photonic crystal cavities in ultra-pure diamond membranes intended for targeted creation of single NV centers via ion implantation. Using confocal spectroscopy, we identify cavity modes near the design wavelength of 637 nm in the spectra and analyze the quality factors.

Sample preparation

The starting material is a 10 μm thick (100) single crystal diamond membrane (electronic grade, Element Six N.V.) with a specified nitrogen concentration of < 5 ppb that is bonded via a spin-on glass adhesion layer onto a silicon substrate with partially removed areas. The free-standing diamond membrane is thinned from the top side to a thickness of $200 - 220$ nm using reactive ion etching and patterned via focused ion beam milling using a chromium protection layer during milling. As a final step, the sample is annealed at 800°C for 2 h in vacuum and is thoroughly cleaned in hot acid (HNO_3:H_2SO_4:$HClO_4$ = 1:1:1) for 45 min and annealed in air for 6 h at 420°C to oxidize any graphite residuals. For details on the sample preparation, please see chapter 6.

structure	a (nm)	R (nm)	R_b (nm)	R_c (nm)	d (nm)
M1-o240	240	82	75	71	46
M1-o250	250	83	75	72	48
M3-u220	220	80	unoptimized		
M3-u227	227	83	unoptimized		
M3-u233	233	81	unoptimized		
M7-u227	227	83	unoptimized		

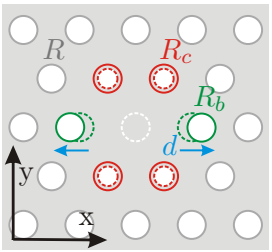

Table 8.2: Design parameters of the six fabricated photonic crystal cavities and optimized M1-layout: The lattice constant a and the hole radius R are summarized for every structure. For the optimized M1-cavities, the reduced hole radii R_c, R_b and the lateral hole shift d are given with the corresponding layout on the right.

Cavity designs

As already presented in section 6.3.2, we fabricate 15 photonic crystal structures with different cavity sizes ranging from one-, three- to seven-hole defects at the center. Six of the 15 photonic cavities are used in this chapter for ion implantation. Two optimized M1-cavities with lattice constants of $a = 240\,\text{nm}$ and 250 nm are fabricated, referred to as M1-o240 and M1-o250 (M1-layout see table 8.2). The lateral shift d and the radii R_b, R_c of the nearest-neighbor air holes have been optimized according to the principle of gentle confinement to increase the quality factor. The design parameters are chosen according to table 5.4 in section 5.6.2 and to reference [275]. Besides the small M1-cavities, we fabricate large-size defect structures: Three unoptimized M3-cavities with different lattice constants of 220, 227 and 233 nm and one unoptimized M7-cavity with $a = 227\,\text{nm}$, referred to as M3-u220, M3-u227, M3-u233 and M7-u227. The design parameters of the six photonic crystal structures are summarized in table 8.2. Scanning electron microscope images of the M1-o250, M3-u233 and M7-u227 cavity are exemplary shown in figure 6.13 in section 6.3.2. The images are taken after all post-processing steps. A distance of $\sim 40\,\mu\text{m}$ between the cavity patterns is chosen to avoid unintentional irradiation of adjacent structures during the nitrogen implantation.

Cavity Modes

To determine the resonant wavelengths and the experimental quality factors, we measure the photoluminescence spectra under continuous wave 532 nm-excitation at the center of the fabricated structures using confocal microscopy. For details on the confocal setup designed for room temperature spectroscopy, the reader is referred to chapter 4. Figure 8.7 shows the photoluminescence spectra taken at room temperature of the M1-

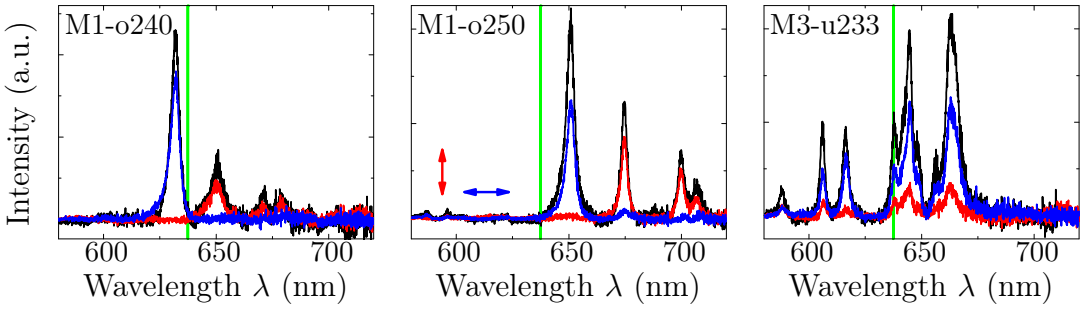

Figure 8.7: Photoluminescence spectra of the M1-o240, M1-o250 and M3-u233 photonic crystal cavity: Several cavity modes close to the design wavelength of 637 nm (marked by green line) of the NV^- zero-phonon line are observed in the spectra. Polarization analysis shows that odd modes are pronounced for horizontal oriented polarizer (blue line), whereas even modes are prominent for vertical orientation (red line).

o240, M1-o250 and M3-u233 cavity structures. Several cavity modes near the design wavelength of 637 nm, corresponding to the NV^- zero-phonon line, are observed. To determine the polarization of the cavity modes, a polarization analyzer is placed in the detection path either aligned to the x- or y-axis of the structure. The polarization resolved spectra are displayed by colored curves in figure 8.7. The M1-cavities show four distinct modes. Three M1-modes reveal a linear polarization along the y-axis, whereas the mode at shortest wavelength is polarized along the x-direction. From the width of the resonant peaks, we deduce quality factors between 130 and 210. Based on the polarization measurements and FDTD simulations, we identify the higher order modes as dipole, quadrupole and hexapole modes. For the theoretical description of cavity modes supported by one-missing hole defects, the reader is referred to section 5.5.2. We attribute the peak centered at the shortest wavelength in the spectrum to the hexapole mode. FDTD simulations reveal a linear polarization along the x-axis of the hexapole mode confined in the optimized M1-cavity [316]. Moreover, a highly directive emission in the vertical direction is expected for the deformed hexapole mode [316], resulting in

	M1-o240		M1-o250	
mode	λ (nm)	Q	λ (nm)	Q
hexapole	634 ± 2	130 ± 30	653 ± 2	161 ± 6
quadrupole	653 ± 2	160 ± 20	676 ± 2	206 ± 34
dipole	670 ± 3	170 ± 40	700 ± 2	210 ± 26
dipole	681 ± 2	180 ± 70	708 ± 3	148 ± 20

Table 8.3: Cavity modes of the fabricated M1-o240 and M1-o250 cavities, their resonant wavelengths and Q-factors. The error denotes the standard deviation averaged over eight measurements.

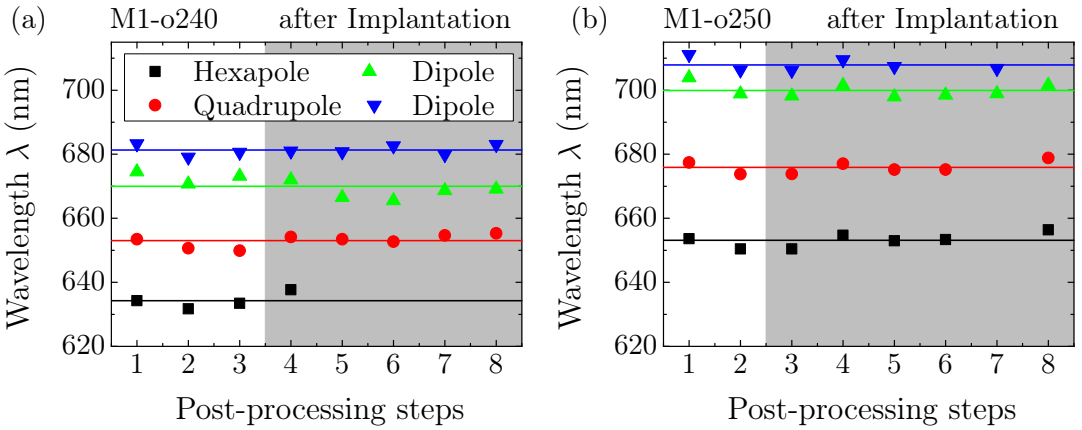

Figure 8.8: Central position of the M1-o240 and M1-o250 cavity modes as a function of the number of post-processing steps. The post-processing steps include high-temperature annealing, acid treatment and nitrogen implantation (gray shaded region indicates measurements after ion implantation). Despite small fluctuations, the resonant wavelengths are unaffected by the processing steps. Please note that the treatment does explicitly not imply oxidation of the sample to tune the cavity modes.

a high collection efficiency by the microscope objective. The predictions are conform with the linear x-polarization and the strong intensity of the lowest-wavelength peak in the spectrum. We assign the next peak at longer wavelengths to the $-x-y$ quadrupole mode. Due to the asymmetry of the defect structure, the degeneracy of the dipole and quadrupole modes is lifted and the ordering of the modes might change. According to FDTD calculations, the resonant wavelength of the $-x-y$ quadrupole should be longer than the one of the hexapole mode and shorter than the dipole modes. Moreover, the $-x-y$ quadrupole mode is expected to be mainly polarized along the y-direction, which is conform with our polarization analysis. The modes at longest wavelength are identified as dipole modes. For an ideal cavity structure, we expect an orthogonal linear polarization of the dipole modes. However, due to the asymmetry of the defect design or due to fabrication tolerances, the linear polarization of x-dipole mode might be switched. Table 8.3 summarizes the resonant wavelengths and the quality factors of the M1-o240 and M1-o250 cavity.

The values given in table 8.3 are averaged over eight measurements, where the error indicates the standard deviation of the resonant wavelengths and quality factors. The eight spectra are taken after different processing steps including high-temperature annealing and acid treatment. It is crucial that the resonant wavelengths are not affected by the post-processing steps. The fitted central wavelengths of the M1-o240 and M1-o250 cavity modes are plotted in figure 8.8 as a function of the number of processing steps. The gray shaded region in figure 8.8 indicates the measurements performed after ion implantation. Despite small fluctuations, we confirm the resonant wavelengths of the cavity modes to be constant upon acid treatment, high temperature annealing and nitrogen implantation. We emphasize that the diamond sample is not oxidized in

M3-u233					
mode	λ (nm)	Q	mode	λ (nm)	Q
o8	588	170	o4	644	160
o7	605	280	o3	648	250
o6	616	210	o2	655	320
o5	638	240	o1	663	100

Table 8.4: Cavity modes of the fabricated M3-u233 cavity, their resonant wavelengths and Q-factors.

order to tune the cavity modes. Here, we only focus on the post-processing steps to restore the diamond lattice after FIB milling or ion implantation or to remove graphite residuals. These measures should leave the spectral positions of the modes unchanged, which is confirmed in figure 8.8. However, strikingly, the hexapole mode of the M1-o240 cavity at a wavelength of 634 nm disappears after the fourth cleaning step. This is unexpected. We can exclude extensive contamination of the structure as residuals from acid treatments would equally affect other cavity modes.

The M3-u233 cavity spectrum reveals several modes, all polarized along the x-direction. The moderate quality factors of the cavity modes range from 100 to 300. According to the classification of the modes with respect to their mirror reflection symmetry at $y = 0$, we refer to these modes as odd modes, abbreviated by "o" (c.f. section 5.5.2). The odd modes are numbered consecutively starting with the lowest-order mode at the longest wavelength. The resonant wavelengths and the quality factors are summarized in table 8.4. The presented M1-o240, M1-o250 and M3-u233 are the only cavities which show modes. As the membrane is slightly wedged due to non-ideal polishing, the thickness at the positions of the three other fabricated structures M3-u220, M3-u227 and M7-u227 is too high favoring the formation of higher-order resonant modes with low quality factors. Due to the broad cavity linewidth, low-Q cavity modes can hardly be identified in the spectrum.

8.3 Ion Implantation into photonic crystal cavities

For high-resolution implantation of nitrogen ions at the center of the fabricated photonic crystal cavities, we use a pierced AFM tip as a beam collimator. Integrated in the nanoimplanter setup, the AFM is used to image the photonic crystals by scanning the tip in immediate contact over the sample. Once the nano-hole in the AFM tip is positioned above the cavity center the 5 keV-ion beam is focused on the tip and nitrogen ions are implanted through the hole into the predefined diamond structures. In this section, we present the AFM scans of the photonic crystal structures used to identify the cavity center and to precisely position the pierced tip. In our experiments, we aim at a low number of implanted NV centers and ideally one single optically active defect.

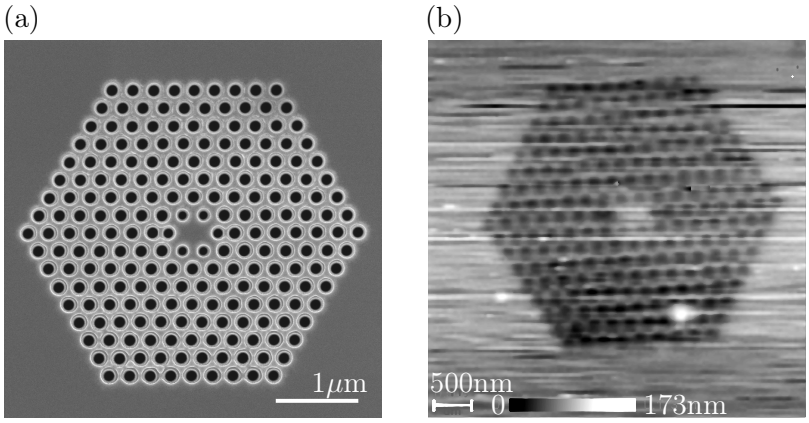

Figure 8.9: (a) Scanning electron microscope image and corresponding (b) surface topography detected via atomic force microscopy of M1-o240 cavity structure. AFM scan area: $5 \times 5\,\mu\text{m}^2$

The chosen implantation parameters are given in this section.

8.3.1 Atomic force microscopy scans

To align the AFM tip with respect to the ion beam, we use a silicon test sample coated with an electron beam resist polymethyl methacrylate (PMMA) which is sensitive to ion irradiation. The position and the size of the ion beam can be observed as a dark spot in the PMMA layer using the microscope objective integrated in the nanoimplanter setup. The AFM tip is subsequently aligned to the imprint of the ion beam. The tip is optimally positioned, when only a dark halo of the ion spot is still visible around a blank center that was covered by the AFM tip during irradiation. For large beam diameters ($\sim 20\,\mu$m) the alignment is easy, but becomes more delicate for smaller beam focuses. From the spot size in the PMMA layer, we deduce a beam diameter of $13\,\mu$m for our experimental parameters.

In the combined nanoimplanter setup, the AFM is used to image the sample and to position the tip such that ions are implanted through the nano-hole into predefined structures. To image the surface topography, the tip is scanned in immediate contact over the sample. In figure 8.9 the scanning electron microscope image and associated surface topography detected via atomic force microscopy of the M1-o240 structure are displayed. The milled air holes and the center of the photonic crystal cavity are clearly visible in the AFM scan. With the piezoresistive AFM system a resolution of 1 nm [415] can be achieved. Prior to implantation, several AFM scans of every cavity center are performed. As an example, detail scans of the M1-o240, M3-u233 and M7-u227 cavities are shown in figure 8.10. The center of the cavity structures can clearly be identified. However, with increasing number of scans the resolution of the AFM images gets worse. The image of cavity M1-o240 (Fig. 8.10(a)) is the third scan performed with the AFM tip. The air holes of the photonic lattice and the cavity center can clearly be identified. After eleven scans, the resolution of the AFM picture is still sufficiently good, as can be

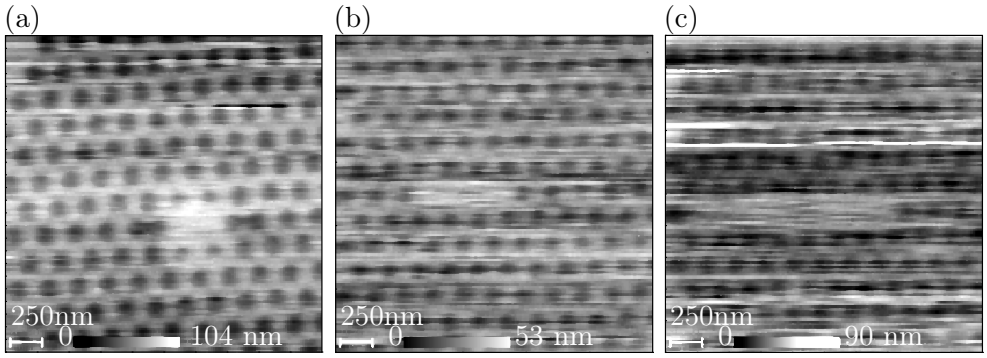

Figure 8.10: Detail AFM scans of the (a) M1-o240, (b) M3-u233 and (c) M7-u227 cavities. Scan area: $2.5 \times 2.5\,\mu\text{m}^2$

seen in the figure 8.10(b) of the M3-u233 cavity. However, the resolution significantly degrades after 18 scans: In the AFM image of the M7-u227 structure (Fig. 8.10(c)), the cavity center and the air holes can hardly be identified. The deterioration in resolution originates from the degradation of the AFM probe. Scanning the tip in contact mode over the sample leads to an abrasion of the tip material, as the diamond substrate is much harder than the silicon nitride tip. As the resolution of AFM images are mainly determined by the radius of curvature of the tip, its material abrasion results in a loss of precision with increasing scan number.

In order to implant nitrogen ions with high precision at the cavity center, the nano-hole drilled in the tip has to be placed directly above the center of the structure. To this end, we have to take into account that the hole is not positioned at the apex of the tip but shifted by 113 nm in x-direction and 752 nm along the y-axis (c.f. Fig. 8.4) to avoid a degradation or closing of the hole while scanning the tip in contact mode over the sample. In the experiment, the position of the tip is corrected for this shift.

8.3.2 Implantation parameters

We implant $^{15}\text{N}^+$ ions at a fixed kinetic energy of 5 keV at the center of six photonic crystal structures of different cavity sizes ranging from one-, three-, to seven-missing holes: M1-o240, M1-o250, M3-u220, M3-u227, M3-u233 and M7-u227. To precisely determine the dose, the ion beam current is measured prior to each implantation using a Faraday cup fabricated directly on the sample holder and using a picoamperemeter. From the measured beam currents between $0.24 - 0.33$ pA, the ion flux of $1.13 - 1.55 \times 10^{12}$ ions/(cm^2 s) can be determined when taking into account one elementary charge of the $^{15}\text{N}^+$ ions and the beam diameter of 13 μm deduced by irradiation of the PMMA test sample. Multiplying the flux with the irradiation time gives the applied ion fluences, also called dose. Fluences between $0.2 - 4.4 \times 10^{14}$ ions/cm^2 are chosen such that only a small number of NV centers would be created. To estimate the theoretical number of created NV centers, we assume a NV creation yield of 0.8% [432] and an area of 1,413 nm^2 of the nano-hole drilled in the AFM tip. The hole size has been determined by scanning electron microscope images of the tip taken prior to implantation (c.f. Fig. 8.4 in section

structure	fluence (ions/cm^2)	theo. NV	created NV$^-$	yield (%)
M1-o240	2.65×10^{13}	3	3 ± 1	0.8 ± 0.3
M3-u220	4.40×10^{13}	5	5 ± 2	0.8 ± 0.3
M3-u233	1.77×10^{14}	20 (9)	11 ± 3	0.4 ± 0.1 (0.9 ± 0.2)
M1-o250	1.77×10^{14}	20 (9)	7 ± 2	0.3 ± 0.1 (0.6 ± 0.1)
M7-u227	4.42×10^{14}	50 (23)	21 ± 8	0.3 ± 0.1 (0.7 ± 0.3)
M3-u227	1.00×10^{13}	112	84 ± 20	0.6 ± 0.1

Table 8.5: Implantation parameters: Six photonic crystal structures are implanted with $^{15}N^+$ ions at a fixed kinetic energy of 5 keV. The fluences and the aimed number of NV centers assuming a hole area of 1,413 nm^2 and a yield of 0.8% are given as well as the actual number of created NV$^-$ centers and the associated production yield. The numbers in brackets take into account a hole area reduction down to 657 nm^2 upon ion irradiation. The ion beam is directly focused on structure M3-u227 without collimation via the pierced AFM tip.

8.1.3). However, in the course of ion irradiation, the nano-hole size might be reduced, resulting in a smaller expected number of NV centers and in a modified creation yield (see discussion below). In the case of the M3-u227 photonic crystal cavity, the AFM tip is removed and the ion beam is focused on the structure without collimation of the nano-hole. To calculate the expected number of NV centers, we take into account the three-missing holes area of 0.14 μm^2 at the center of the M3-u227 cavity. Assuming a theoretical yield of 0.8%, we would expect 112 implanted NV centers at the applied dose of 1×10^{13} ions/cm^2. Table 8.5 summarizes the applied fluences and the aimed number of created NV centers for each photonic crystal cavity. The numbers given in brackets take into account a size reduction of the nano-hole in the AFM tip upon ion irradiation.

After the implantation, the diamond sample is annealed at 800°C for 2 h in vacuum (1×10^{-4} Pa). Subsequently, the diamond is cleaned in a boiling 1:1:1 mixture of nitric, sulfuric, perchloric acids for 8 h and annealed three times in air at 420°C for 2 h to remove possible graphitic residuals after the high temperature annealing and to prepare a well defined oxygen-terminated surface [394, 441] that favors the conversion to the negatively charge state of implanted NV centers.

8.4 NV centers implanted in photonic crystals

Using confocal spectroscopy at ambient and cryogenic temperatures, we check the success of the ion implantation into the photonic crystal cavities. As a first step, we assure that up to 70% of the NV centers are converted to the negative charge state after the oxidizing post-processing steps. Detailed fluorescence scans provide the first evidence that the pierced AFM tip was optimally positioned above the cavity structure during implantation. Photoluminescence spectra at cryogenic temperature unambiguously prove the creation of NV centers at the center of every photonic crystal defect. The spectra reveal

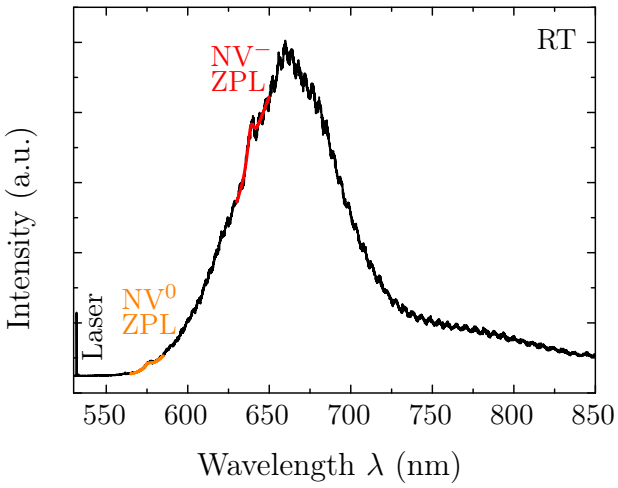

Figure 8.11: Room temperature photoluminescence spectrum of a NV ensemble created by 5 keV $^{15}N^-$ ion implantation with high dose $> 5 \times 10^{14}$ ion/cm^2. The zero-phonon lines of the NV^0 at 575 nm and NV^- center at 637 nm are visible. The ripples in the spectrum are associated to the transmission curve of the utilized stop-band filters.

several distinct zero-phonon lines around 637 nm that are attributed to single implanted NV^- centers. We investigate the spectral properties such as the central peak positions and linewidths of the created optically active defects. From the normalized peak intensity of the zero-phonon lines, we deduce the production yield of single NV centers. Taking into account the size reduction of the nano-hole in the tip upon ion irradiation, we find a yield of $0.8\% \pm 0.1\%$ which is almost independent on the implantation dose.

8.4.1 Ratio of NV^0 and NV^- emission

After the first 6 h of acid treatment, we determine the ratio of remaining NV^0 centers compared to the overall NV emission. To this end, we measure the photoluminescence spectra at room temperature in a wide spectral range of $530 - 900$ nm at different test spots on the sample implanted with high doses $> 5 \times 10^{14}$ ions/cm^2. In the NV ensemble spectrum in figure 8.11, the zero-phonon lines of the NV^0 and NV^- center at 575 nm and 637 nm can be observed, respectively. The ripples in the spectrum are due to the transmission curve of the utilized stop-band filter (Notch 532, Semrock) to suppress the excitation laser. We assure that the deviation in transmission of the applied filters is smaller than 2% at wavelengths 575 nm and 637 nm. From the photoluminescence signal integrated in a spectral range of 20 nm around the NV^0 and NV^- ZPLs, we find an intensity ratio of $I_{NV^-}/I_{NV^0} = 16 \pm 3$. To infer from this intensity ratio the number of created NV^0 centers compared to the total number of NV centers, several factors have to be included in the analysis. First of all, we take into account different detection efficiencies of our spectrometer at wavelengths 575 nm and 637 nm: $\eta_{det,NV^-}/\eta_{det,NV^0} = 1.8 \pm 0.2$. Second, different absorption efficiencies for the NV^- and NV^0 center under

532 nm excitation need to be considered: $\eta_{\mathrm{abs,NV^-}}/\eta_{\mathrm{abs,NV^0}} = 2.5 \pm 0.5$ [442] as well as different quantum efficiencies of the two charge states: $\eta_{\mathrm{qe,NV^-}}/\eta_{\mathrm{qe,NV^0}} = 2.0 \pm 0.3$ [431]. Including all these factors as well as the measured intensity ratio in our analysis, we evaluate the ratio of NV^0 centers to be $NV^0/(NV^0+NV^-) = 0.36 \pm 0.15$. To further reduce the number of NV^0 centers, the sample is boiled for another 2 h in oxidizing acid mixture and beyond that, it is heated in air three times at 420°C for 10 min. After the thorough surface treatment, it is assumed that the ratio of remaining NV^0 centers is well below 30% and most of the NV centers are converted to their negative charge state.

In the photoluminescence spectra, no Raman signal attributed to sp^2-hybridized carbon (graphite and disordered carbon) could be observed after the acid treatment. Hence, beside the effect of preparing a well defined oxygen-terminated diamond surface, the acid treatment reliably removes any graphitic residuals that might be induced during ion bombardment and subsequent high temperature annealing in vacuum.

8.4.2 Spectroscopy at cryogenic temperatures

We confirm the creation of single NV centers via ion implantation using confocal spectroscopy at cryogenic temperatures. Cooling the sample to liquid helium temperatures has one reason: At room temperature, the linewidth of the zero-phonon line is broadened due to spectral diffusion as well as due to phonon interaction with the diamond lattice. Phonon interactions are temperature dependent and can be significantly reduced by cooling the diamond to liquid helium temperatures. Hence, at low temperatures, the ZPL linewidth is solely limited by spectral diffusion. This results in a much narrower ZPL emission line that can be very well distinguished from background luminescence. The identification of the ZPL in the spectrum clearly indicates the successful creation of single NV centers via ion implantation. To perform measurements down to liquid helium temperatures, the sample is mounted on the cold finger of a continuous flow cryostat that is integrated in a confocal microscopy setup (c.f. chapter 4). Figure 8.12 shows the fluorescence scans of the implanted cavity structures at 10 K excited at 532 nm and detected in the spectral range of 650-750 nm. The bright implantation spots of large ensembles of NV centers created by the focused nitrogen beam are clearly visible. From the fluorescence scans, we deduce a beam diameter of 15 μm that is slightly larger than the diameter of 13 μm estimated by ion irradiation of the PMMA test sample prior to implantation. The center of the bright spots appear dark in the scans. This region has been shielded during ion implantation by the pierced AFM tip and was not implanted except at the position of the nano-hole. In the middle of the dark area, the contours of the photonic crystal cavities are visible. To estimate the position of the pierced tip upon ion irradiation, the edges of the tip and the nano-hole are indicated in the scans by dashed lines and a red dot, respectively. Within the resolution of the fluorescence scans, we confirm that the nano-hole was well placed above the center of each cavity structures. No fluorescence scan of the M3-u227 structure is shown in figure 8.12, because the ion beam was directly focused on this structure without the AFM tip collimator. Hence, a large spot around the M3-u227 cavity has been implanted.

To gain more insight into the spectral properties of the implanted NV centers, we

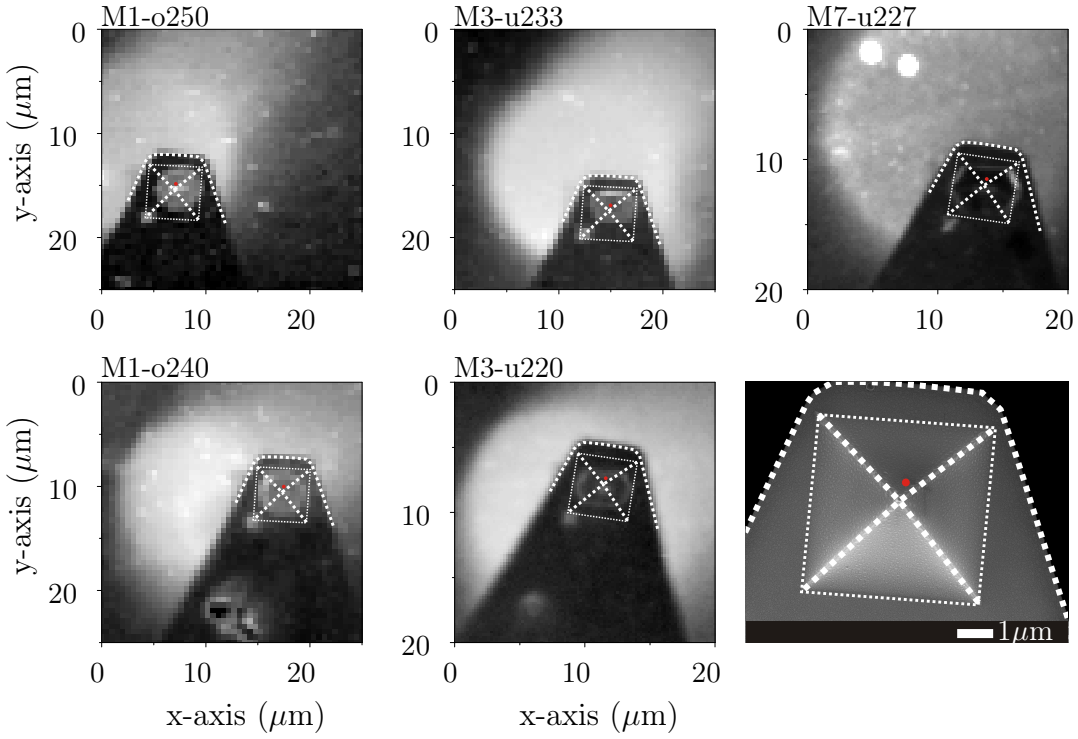

Figure 8.12: Fluorescence scans of the implanted photonic crystal structures and scanning electron microscope image of the pierced AFM tip. The red dot marks the position of the nanohole and the dotted white line the edge of the AFM tip. White/ black: high/ low fluorescence intensity.

perform detailed fluorescence scans and measure the spectra at the center of the photonic crystal cavities. Figure 8.13 shows the fluorescence scans and spectra of the M1-o240, M3-u220 and M7-u227 cavities at 10 K. The spectra taken at the cavity center (position marked by red dot in the scan) show NV^- emission around 637 nm. In the M1-o240 spectrum, four cavity modes at longer wavelengths $650-690$ nm with low quality factors between $160-230$ are visible (c.f. Fig. 8.7 in section 8.2). The M3-u220 and M7-u227 spectra do not reveal any cavity modes. The ion implantation is restricted exclusively to the cavity center. In the reference spectra taken 1 μm apart from the cavity center (position marked by yellow dot in the scan), neither NV^- emission nor any cavity modes are observed. We emphasize that the spectra of all cavities doped with nitrogen show clearly NV^- emission when cooled down to cryogenic temperatures. For clarity, only three of the six implanted structures are presented exemplary in figure 8.13.

In the case of the structures M1-o240 and M3-u220, which were implanted using low ion doses, a zoom into the spectral range around 637 nm reveals several distinct lines that can be attributed to single implanted NV^- centers (Fig. 8.13(b,d)). At the center of the M1-o240 structure, four distinct zero-phonon lines appear in the spectrum. The central spectral positions and linewidths of the four peaks are summarized in table 8.6. The intensity of the peak observed at $\lambda = 636.28$ nm is very weak. In some

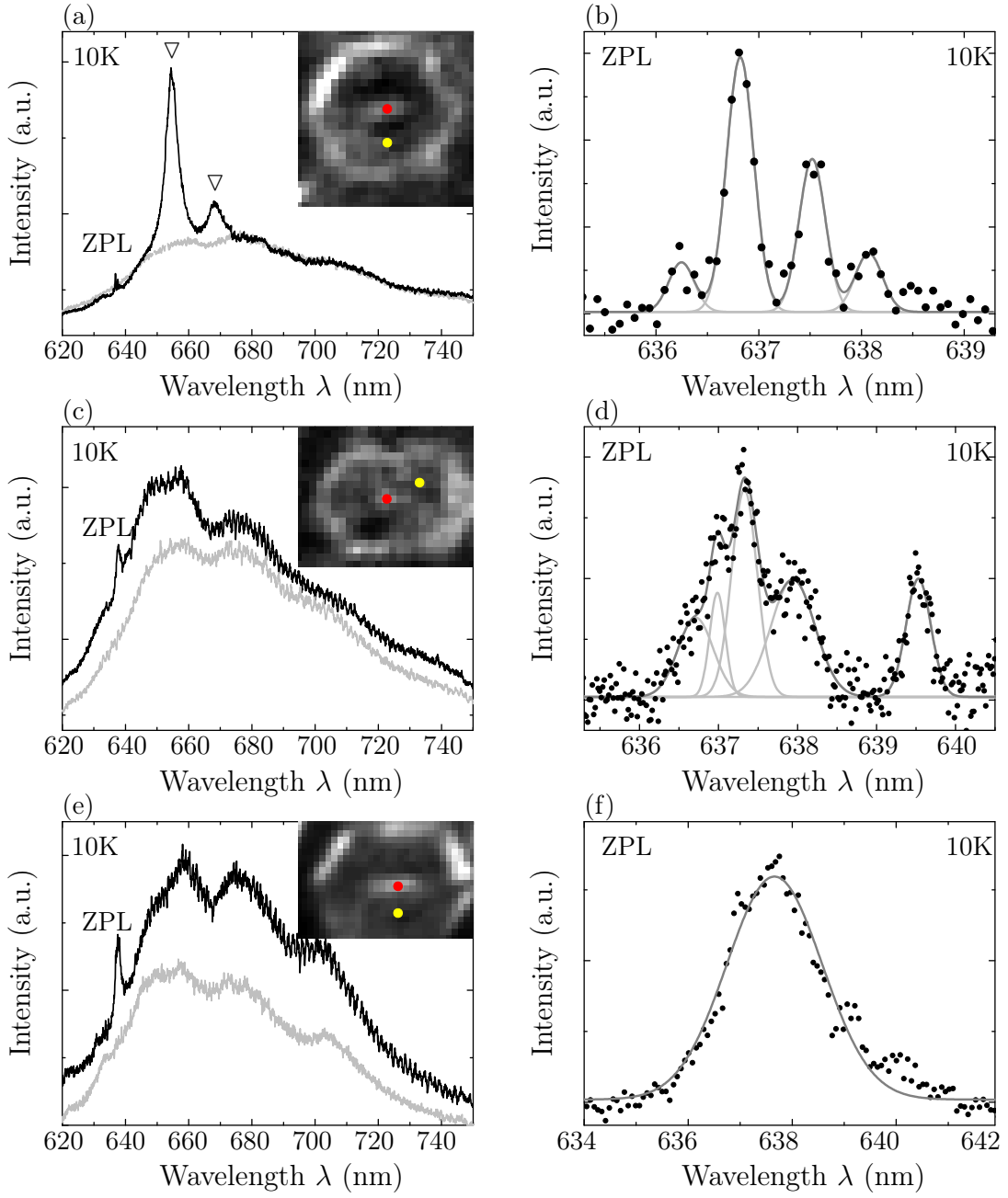

Figure 8.13: Photoluminescence spectra and scans of the (a,b) M1-o240, (c,d) M3-u220 and (e,f) M7-u227 structure at 10 K: (a,c,e) Insets: PL scans of area (a) $5 \times 5\,\mu\text{m}^2$, (c) $5 \times 4\,\mu\text{m}^2$, (e) $6 \times 4\,\mu\text{m}^2$. In the spectra taken at the center of the photonic crystal (black line, position marked by red dot in the scan) zero-phonon lines of NV^- centers around 637 nm are visible. In the M1-o240 spectrum, cavity modes ($\triangledown$) at longer wavelengths are identified. The reference spectra taken 1 μm apart from the center (gray line, position marked by yellow dot in the scan) do neither show NV^- ZPL nor cavity mode signals. (b,d,f) Zoom into the background corrected zero-phonon lines. (b,d) Several distinct lines are attributed to single NV^- centers implanted at the cavity center. Results from the Gaussian fits are given in table 8.6. (f) Zero-phonon line of a large NV ensemble. Dots: measured data, gray lines: Gaussian fits.

M1-o240	λ (nm)	$\Delta\lambda$ (nm)	$\Delta\nu$ (GHz)
NV 1	636.28 ± 0.06	0.33 ± 0.03	244 ± 20
NV 2	636.87 ± 0.06	0.36 ± 0.04	266 ± 30
NV 3	637.57 ± 0.06	0.31 ± 0.02	229 ± 15
NV 4	638.17 ± 0.1	0.36 ± 0.07	265 ± 50
M3-u220	λ (nm)	$\Delta\lambda$ (nm)	$\Delta\nu$ (GHz)
NV 1	636.71	0.53	392
NV 2	636.99	0.23	170
NV 3	637.33	0.38	280
NV 4	637.94	0.66	486
NV 5	639.53	0.37	271

Table 8.6: Central spectral positions and linewidths (FWHM) of zero-phonon lines associated to several single NV^- centers identified in the M1-o240 cavity spectrum (Fig. 8.13(b)) and M3-u220 cavity spectrum (Fig. 8.13(d)). The peaks have been fitted with Gaussians. The data of the M1-o240 cavity are averaged over four measurements. The error indicates the standard deviation.

spectra (not shown), this peak is hardly visible. To not overestimate the number of implanted color centers in the following, we refer to 3 ± 1 NV^- centers implanted at the M1-o240 structure. This number is reasonable: Assuming a theoretical NV creation yield of 0.8% [432], we would have expected three NV centers produced by 5 keV-ion doping for the utilized fluence (see table 8.5). Equally, the M3-u220 spectrum reveals several NV^- zero-phonon lines. However, these lines are not well separated and partially overlap. From Gaussian fits, we extract the central wavelengths and linewidths that are summarized in table 8.6. It is possible that some of the lines originate from two implanted centers, as their linewidths are twice as broad as the width of the other peaks. From the spectrum, we estimate 5 ± 2 single NV centers. The experimental findings are conform with the targeted number of five implanted NV centers (see table 8.5). In contrast, the M7-u227 cavity spectrum, that has been implanted at a high ion fluence, shows a broad zero-phonon line at a center wavelength of 637.66 nm with a linewidth of $\Delta\lambda = 1.84$ nm indicating a large ensemble of NV centers. Normalizing the background corrected ZPL intensity to the averaged intensity of a single NV center (extracted from M1-o240 spectrum), we estimate a number of 21 ± 8 implanted NV^- centers within the M7-u227 cavity. The NV production number and yield for each implanted structure are discussed in section 8.4.3.

On the cavity structures, a significant background is measured at the reference positions (positions marked by yellow dots in the scans in Fig. 8.13). For implantation at low fluences, the background is strong compared to the NV emission. When higher doses are applied, the zero-phonon line and phonon side bands become more and more pronounced. Due to this significant background, it is not possible to identify the im-

planted NV centers as bright spots in the fluorescence scans. The presence of single NV centers is only revealed in the spectra. Moreover, we are not able to confirm the number of implanted NV centers by intensity auto-correlation measurements. Because of the poor signal to background ratio, no anti-bunching dip is observed at zero time delay.

We observe a clear signature of NV^- emission in the spectra taken at the center of every photonic crystal cavity. This unambiguously proves the successful implantation of nitrogen into every irradiated structure. The number of created NV centers is in good agreement with the expected quantity, assuming a theoretical creation yield of 0.8%. Even in the case of the smallest implanted M1-o240 cavity, single NV^- centers are identified. From these results, we can deduce the spatial resolution of the ion implantation process to be much smaller than 300 nm which corresponds to the dimensions of the smallest M1-o240 defect structure. A more precise specification is not possible due to the limited resolution of our confocal microscopy setup. In literature, the spatial resolution of the nanoimplanter setup used in this work has been specified to be 25 nm [425]. Pezzagna et al. [425] used high resolution spectroscopy based on stimulated emission depletion to resolve single NV centers implanted at a distance of 16 nm.

In the following, we will discuss in detail the spectral positions and linewidths of the observed zero-phonon lines. The zero-phonon line of an ideal NV center would have a Lorentzian shape with a Fourier-transform limited linewidth $\Delta\nu_{\mathrm{FT}}$ that is determined via the Heisenberg time-energy uncertainty relation $\Delta\nu_{\mathrm{FT}}\ T_1 \geq 2\pi$ by the lifetime of the excited state T_1 [443]. Taking into account a lifetime of 11.6 ns [23] of the excited state, a transform-limited linewidth of 13 MHz is expected. This has been measured for a single NV^- center in bulk diamond at cryogenic temperatures under resonant excitation [173,195]. However, in many cases, the emission line is broader than the Fourier-transform of the time-profile of the emitted photon. The broadening arises from fluctuations of the optical frequency that can be attributed to either dephasing or spectral diffusion processes depending on the amplitude and rate of the fluctuations [443]. Dephasing processes are related to fast fluctuations with a weak amplitude that arise from interaction with phonons in the crystalline matrix. Dephasing leads to homogeneous line broadening which follows a Lorentzian profile [444]. In contrast, slow and large-amplitude fluctuations of the optical resonance frequency (termed spectral diffusion) result in an inhomogeneous spectral broadening described by a Gaussian distribution [444].

Pure dephasing of the optical transition is attributed to a dynamic Jahn-Teller effect [217, 218] in the excited state of the NV^- center (c.f. chapter 3). Phonon scattering and electron-phonon interaction with the diamond lattice results in a homogeneously broadened zero-phonon linewidth with a Lorentzian line shape. The ZPL linewidth was found to follow a T^5 temperature dependence for temperatures $T < 100$ K [217]. Hence, with decreasing temperature, the dynamic Jahn-Teller effect can be suppressed and the linewidth becomes narrower.

In contrast, spectral diffusion is associated to electrostatic fluctuations induced by photo-ionized impurities like isolated substitutional nitrogen (electron donor) in the diamond or defects near an etched surface. Charge fluctuations at a distance of several nanometers can shift the excited state of the NV center via DC Stark effect by several

hundred GHz [219]. This results in random spectral jumps of the NV emission line resulting in an inhomogeneously broadened zero-phonon line with a Gaussian profile. Further details are given in chapter 3.

The shapes of the zero-phonon lines observed in M1-o240 and M3-u220 spectra (Fig. 8.13) are very well described by Gaussian profiles with a full-width at half-maximum around 250 GHz. In contrast, a Lorentzian curve does not at all fit the spectral distribution. The linewidth is not limited by the resolution of the spectrometer. The results from the Gaussian fits including the central spectral positions and linewidths are summarized in table 8.6. Owing to the measured Gaussian profile, we conclude that spectral diffusion is the major broadening mechanism of the NV^- zero-phonon line at 10 K. Our findings are conform with literature. In various experiments on shallow implanted NV centers in single crystal diamond or hosted in nano-diamonds, inhomogeneous broadening due to spectral diffusion is dominant at cryogenic temperatures. Previously, spectral diffusion up to 10 GHz has been observed under 532 nm-illumination for shallow implanted NV centers in single crystal diamond [391]. The authors of [391] claimed that the random spectral jumps are attributed to charge traps near the implanted NV centers. In contrast, for NV centers incorporated during CVD growth in high-quality diamond at a depth of 60 μm, little spectral diffusion $<$ 200 MHz [391] has been measured. This suggest a strong impact of the concentration of charge impurities in the center's direct environment on its spectral jump rate [220]. In diamond nano-crystals, spectral jump widths ranging from 20 to 260 GHz upon green excitation has been detected by correlation interferometry [219]. The measured linewidths summarized in table 8.6 are comparable to spectral diffusion widths measured for NV centers in nano-diamonds [219] and are slightly larger than previously reported data for shallow implanted NV centers [391]. The presence of the thinned, patterned and post-processed photonic crystal surface with a roughness of approximately 3 nm is expected to contribute to spectral diffusion, particularly for NV centers close to the holes of the photonic lattice. This might explain a slightly broader spectral linewidth measured in this work compared to previously reported results for shallow implanted NV centers [391]. Another explanation for the slightly broader linewidths is related to an uncertainty in the temperature measurement. In our experimental setup, the temperature is measured on the cold finger of the continuous flow cryostat, which might deviate from the actual sample temperature. Hence, it might be possible that the sample temperature is higher than 10 K which would explain the slightly broader linewidths. One measure to overcome this uncertainty in temperature measurement is to use the temperature-dependent shift of the diamond Raman line for calibration [445].

It is remarkable that all peaks in table 8.6 exhibit comparable linewidths of around 250 GHz, except two lines in the M3-u220 spectrum that might originate from two single NV centers. Hence, we conclude that the influence of spectral diffusion is similar for all individual NV centers within the cavities. In contrast, the zero-phonon lines of the NV^- centers observed in the M1-o240 and M3-u220 spectra do not appear at the same central wavelength but differ by up to $\sim$2 nm from the ideal NV transition. This suggest the presence of strain in the single crystal diamond membrane although its high-quality. Davies and Hamer [168] measured the wavelength shift of the zero-

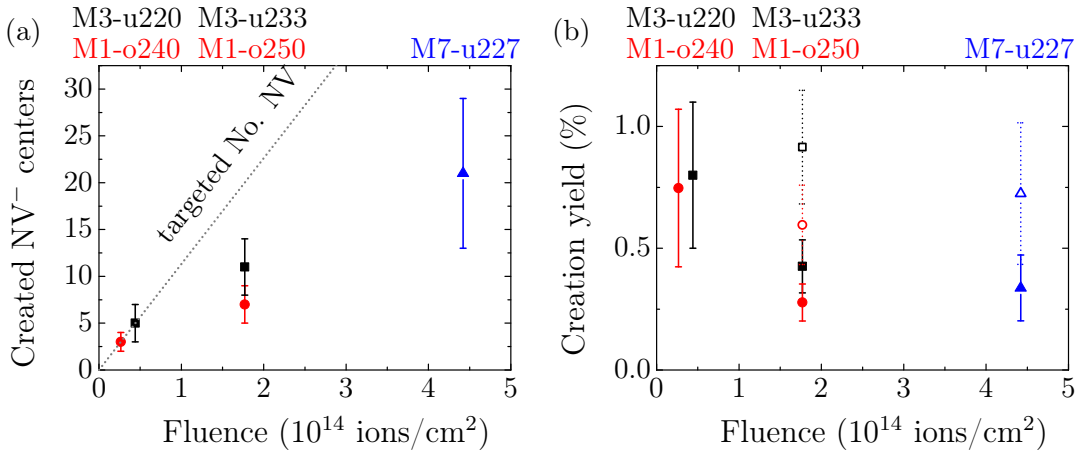

Figure 8.14: (a) Number of created NV^- centers and their associated (b) production yield as a function of the applied dose upon $^{15}N^+$ ion implantation at 5 keV into photonic crystal cavities M1-o240, M1-o250, M3-u220, M3-u233 and M7-u227. (a) The dotted line indicates the targeted number of NV^- centers assuming a theoretical production yield of 0.8%. (b) The filled markers show the yield assuming a hole area of 1,413 nm^2 whereas the open markers indicate the yield corrected for a reduced hole size of 657 nm^2.

phonon transition at cryogenic temperatures when uniaxial stress is applied to the ⟨111⟩, ⟨110⟩ and ⟨001⟩ crystal axes. Based on their shift rate, the discrepancy in wavelength suggests present strain up to several GPa within the diamond membrane depending on the crystallographic direction. The presence of strain in the membrane has already been revealed using Raman spectroscopy. As discussed in section 6.1.5, material strain might be induced by the mismatch of thermal expansion coefficient of the diamond and the spin-on-glass adhesion layer used to promote the bonding to the silicon substrate.

8.4.3 Experimental creation yield

From the photoluminescence spectra taken at cryogenic temperatures (10 K, Fig. 8.13 in section 8.4.2), we determine the number of NV^- centers created via ion implantation. We integrate the background corrected fluorescence signal of the NV^- zero-phonon line in the spectral range of $630 - 645$ nm and normalize it to the mean intensity of a single NV^- center. The mean intensity of a single NV^- center is extracted from the photoluminescence spectra taken at the center of the M1-o240 structure (Fig. 8.13(b)). Figure 8.14(a) shows the number of created NV^- defects measured at the center of each structure as a function of the implantation dose. For comparison, the expected number of created single emitters is shown as a dotted line assuming a creation yield of 0.8%. By dividing the number of created NV^- centers by the amount of implanted nitrogen atoms, we obtain the NV^- production yield shown in figure 8.14(b).

At low doses $< 5 \times 10^{13}$ ions/cm^2 applied for ion implantation into structures M1-o240 and M3-u220, the NV creation efficiency reaches 0.8 ± 0.3%, whereas for higher

doses $> 10^{14}$ ions/cm^2, the NV production yield does not exceed $0.4 \pm 0.1\%$ as observed for structures M1-o250, M3-u233 and M7-u227. The NV creation yield determined for every implanted structure is given in table 8.5. The limited creation efficiency for high fluences might have two reasons. First of all, as discussed in section 8.1.5, the creation yield of single NV centers depends on the ion dose. As shown by Pezzagna et al. [432] for a fixed $^{15}N^+$ kinetic energy of 5 keV, creation efficiencies of $0.8\% - 1.3\%$ are obtained for ion fluences $< 5 \times 10^{13}$ ions/cm^2. Their experimental findings are in very good agreement with the production yield of single NV centers that have been implanted at structures M1-o240 and M3-u220 with low fluences. At high implantation doses $> 1.2 \times 10^{14}$ ions/cm^2, according to reference [432], the amorphization threshold of the diamond lattice is reached and the NV yield drops below 0.4%. The same behavior can be observed in figure 8.14(b): For fluences $\geq 1.77 \times 10^{14}$ ions/cm^2 the NV production efficiency does not exceed $0.4 \pm 0.1\%$. However, in contrast to the data obtained by Pezzagna et al. [432], the creation yield measured in this work does not further decrease with increasing dose but rather remains at a constant low level.

The second reason for the small number of created NV centers in structures M1-o250, M3-u233 and M7-u227 might be a reduction of the nano-hole in the AFM tip upon ion bombardment [425], leading to fewer implanted nitrogen ions. Indeed, the low dose implantation into the M1-o240 and M3-u220 structures, that reaches the highest production yield, have been performed at first. Afterwards, two reference pattern (not shown) at an overall implantation dose of 1.22×10^{15} ions/cm^2 have been written that might have caused a size reduction of the nano-hole used to collimate the ion beam. According to reference [425], the hole closing rate is estimated to be 62 nm^2/(ions/nm^2). Taking into account the total implantation dose of the two reference pattern, the hole area diminishes from 1,413 nm^2 by factor of two to 657 nm^2. Thereby, the number of implanted nitrogen ions is only half as big as suggested assuming a constant hole area. Normalizing the measured number of NV centers to the reduced amount of implanted nitrogen ions results in a doubled production yield. For the ion implantation into structures M1-o250, M3-u233 and M7-u227, the recalculated expected number of NV centers, assuming a theoretical yield of 0.8%, and the actual measured production yield, taking into account a hole size reduction to 657 nm^2, are given in brackets in table 8.5. Furthermore, the corrected yield is plotted as open markers in figure 8.14(b). Taking into account the hole closing rate upon ion irradiation, an almost constant NV creation efficiency of $0.8 \pm 0.1\%$ over a wide range of ion doses is achieved for the implantation of nitrogen ions at 5 keV into photonic crystal cavities.

To summarize, high resolution creation of NV centers at the center of photonic crystal cavities in diamond was achieved using a combined system of a 5 keV-nitrogen ion beam and a pierced AFM tip as beam collimator. After subsequent high temperature annealing and cleaning steps, optically active NV^- centers were formed with a creation yield of $0.8\% \pm 0.1\%$. The production efficiency was found to be almost independent of the implantation dose when taking into account the size reduction of the collimation hole in the AFM tip upon ion irradiation. For the lowest applied implantation dose 2.65×10^{13} ions/cm^2, 3 ± 1 single NV^- centers were created at the center of a M1-cavity. Reducing the dose by a factor of three, the deterministic generation of one single

optically active NV center in the middle of a photonic crystal cavity would be possible.

8.5 Theory of cavity-coupling to a broad-band NV center

What Purcell factors can we expect, when coupling a single implanted NV center to a photonic crystal cavity mode with moderate Q-factors of 100-300 and mode volumes of around one or two cubic wavelengths? Due to its broad emission bandwidth, the standard Purcell theory fails to appropriately describe cavity-coupling to a single NV center. The standard theoretical description of light-matter interaction assumes a single two-level atom with a narrow linewidth that is coupled to a single mode of the cavity electric field. However, in the case of solid state emitters, that are embedded in a host matrix, decoherence and phase relaxation unavoidably broaden any transition. These conditions open a new regime of cavity coupling, where the emitter linewidth is on the same order of magnitude or even broader than the cavity mode. For quantum dots coupled to a photonic crystal cavity, a generalized Purcell factor has recently been defined by Auffèves et al. [91, 92] that includes a two-level emitter undergoing pure dephasing as a source of broadening. Solving the master equation, they calculated the temporal evolution of the emitter and the cavity-mode population and showed that in the incoherent regime the system can be described by classical rate equations. More recently, the model has been adapted by Albrecht et al. [80] to the case of a NV center and expanded to include higher vibrational levels of the ground state. Within this framework, the coupling of a single NV center to a Fabry Pérot fiber cavity could be well described.

In the following, we review the generalized Purcell factor for cavity coupling to a broad-band emitter described by a multi-level system, involving an excited state and a ground state with several vibrational levels. The mathematical description is based on references [80, 81, 91, 92, 174]. Starting from the master equation including pure dephasing, the temporal evolution of the atomic and cavity decay are derived. In the incoherent regime, when the cavity loss rate exceeds the coupling constant between the cavity field and the emitter, the dynamic evolution of the system can be described by classical rate equations. Using this theoretical framework, the experimentally achievable Purcell factor for a single NV center implanted and coupled to a photonic crystal cavity is estimated.

8.5.1 Effective atom-cavity coupling

To appropriately describe the broad-band spectrum, we introduce a multi-level scheme of the NV center including an excited and a ground state as well as higher vibrational levels of the ground state. Pure dephasing and inter-level transition rates are included in the theoretical description to model the homogenous broadening of the zero-phonon line and phonon side bands. The presented multi-level system of the NV center and the expended master-equation model for emitter-cavity coupling are taken from references [80,81,174].

In the framework of cavity quantum electrodynamics, the interaction of a two-

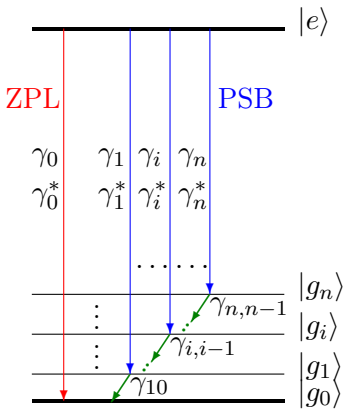

Figure 8.15: Model of the NV center including a single excited state $|e\rangle$ and a ground state $|g_0\rangle$ with n higher vibrational sublevels $|g_1\rangle, \ldots |g_n\rangle$. The spontaneous decay rates between the excited state and the vibrational ground states are $\gamma_0, \ldots, \gamma_n$, whereof γ_0 corresponds to the zero-phonon line transition. All optical transitions are homogeneously broadened due to pure dephasing at rate γ^*. Phonon side bands are additionally subject to fast relaxation between vibrational sublevels $|g_i\rangle \longrightarrow |g_{i-1}\rangle$ at rates $\gamma_{i,i-1}$.

level atom with a single mode radiation field was first described by Jaynes and Cummings [116] (c.f. chapter 2). To apply the same mathematical description to the NV center, we neglect the intermediate metastable singulett-states of the NV center. We treat the center as an atomic system with a single excited state $|e\rangle$ and a ground state $|g_0\rangle$ with n higher vibrational sublevels $|g_i\rangle$, $(i = 1, \ldots, n)$ (Fig. 8.15). The spontaneous decay rate of the zero-phonon line transition ($|e\rangle \longrightarrow |g_0\rangle$) is denoted by γ_0 with the associated energy $\hbar\omega_{\mathrm{ZPL}}$, whereas the excited state decays with rates $\gamma_1 \ldots \gamma_n$ into the higher vibrational sublevels $|g_i\rangle$. The non-radiative phononic relaxation between vibronic side bands $|g_i\rangle$ and $|g_{i-1}\rangle$ are considered to be very fast at a rate $\gamma_{i,i-1}$. At room temperature, the optical transitions are subject to different line broadening mechanisms: First, electron-phonon coupling of the NV transitions lead to homogeneous broadening of the lines that can be described by a pure dephasing rate γ^*. Second, the phonon side bands exhibit additional non-radiative broadening due to the inter-sublevel decay rates $\gamma_{i,i-1}$ [80].

All optical transitions of the NV center are coupled to a cavity mode with coupling constants g_i with $(i = 1, \ldots, n)$. Mathematically, the coupling is described by the Jaynes-Cummings Hamiltonian:

$$\hat{\mathcal{H}}^{JC} = \sum_{i=0}^{n} \hbar\omega_i \hat{\sigma}_{ii} + \hbar\omega_{\mathrm{ZPL}} \hat{\sigma}_{ee} + \hbar\omega_c \hat{a}^\dagger \hat{a} + \hbar \sum_{i=0}^{n} g_i (\hat{a}^\dagger \hat{\sigma}_{ie} + \hat{\sigma}_{ie}^\dagger \hat{a}), \tag{8.1}$$

where $\hat{a}(\hat{a}^\dagger)$ are the cavity photon annihilation (creation) operator and σ_{ij} are the transition $(i \neq j)$ and population $(i = j)$ operators. The level energies are denoted $\hbar\omega_i$, $(i = 0, \ldots, n)$ with $\omega_0 = \omega_{\mathrm{ZPL}}$ being the frequency of the zero-phonon line transition. Furthermore, ω_c is the frequency of the cavity mode and $g_0 \ldots g_n$ are the cavity coupling constants.

The time evolution of the coupled system can be derived from the master equation:

$$\dot{\rho} = -\frac{i}{\hbar}\left[\hat{\mathcal{H}}^{JC}, \rho\right] + \mathcal{L}^{\mathrm{cav}}_{\mathrm{damp}} + \mathcal{L}^{\mathrm{at}}_{\mathrm{damp}} + \mathcal{L}^{\mathrm{at}}_{\mathrm{deph}} + \mathcal{L}^{\mathrm{at}}_{\mathrm{GS-Relax}}, \tag{8.2}$$

where ρ denotes the density matrix. We assume a Markovian approximation, i.e. the coupling of the system to the environment is a memoryless process solely depending on the present state but independent on the future and the past. Besides the coherent

Jaynes-Cummings interaction $-\frac{i}{\hbar}\left[\hat{\mathcal{H}}^{JC},\rho\right]$, the master equation includes damping due to cavity loss at a rate κ

$$\mathcal{L}^{\text{cav}}_{\text{damp}} = \kappa\,\mathcal{L}[\hat{a},\rho] \tag{8.3}$$

as well as loss of polarization

$$\mathcal{L}^{\text{at}}_{\text{damp}} = \sum_{i=0}^{n}\gamma_i\,\mathcal{L}[\hat{\sigma}_{ie},\rho]. \tag{8.4}$$

All transitions are homogeneously broadened due to pure dephasing

$$\mathcal{L}^{\text{at}}_{\text{deph}} = -\frac{\gamma^*}{4}(\hat{\tilde{\sigma}}_z\rho\hat{\tilde{\sigma}}_z-\rho), \qquad \hat{\tilde{\sigma}}_z \equiv \hat{\sigma}_{ee}-\sum_{i=0}^{n}\hat{\sigma}_{ii}, \tag{8.5}$$

whereas the phonon side bands are additionally subject to fast relaxations within the vibrational ground states

$$\mathcal{L}^{\text{at}}_{\text{GS-Relax}} = \sum_{i=0}^{n}\gamma_{i+1,i}\,\mathcal{L}[\hat{\sigma}_{i,i+1},\rho]. \tag{8.6}$$

In the above equations, $\mathcal{L}[\hat{A},\rho]$ denotes the standard Lindblad relation for any operator $\hat{A}$:

$$\mathcal{L}[\hat{A},\rho] := \hat{A}\rho\hat{A}^\dagger - \frac{1}{2}(\hat{A}^\dagger\hat{A}\rho+\rho\hat{A}^\dagger\hat{A}) \tag{8.7}$$

Considering the relation:

$$\frac{d}{dt}\langle\hat{A}\rangle = tr(\dot{\rho}\hat{A}), \tag{8.8}$$

as well as the invariance of the trace tr under cyclic permutation of operators $\hat{A}$,$\hat{B}$ and $\hat{C}$

$$tr(\hat{A}\hat{B}\hat{C}) = tr(\hat{B}\hat{C}\hat{A}) = tr(\hat{C}\hat{A}\hat{B}), \tag{8.9}$$

we can derive a set of coupled differential equations governing the temporal evolution of all coherences $\langle\sigma_{ij}\rangle$, $(i\neq j)$ and populations $(i=j)$ of the atom as well as the cavity photon number $\langle\hat{a}^\dagger\hat{a}\rangle$. For details on the calculation see references [81, 174]. In the following, we restrict the Hilbert-space to one single photon within the cavity. This assumption is justified due to the high cavity loss rate κ compared to the coupling constant g and the atomic decay γ. The high κ guarantees that the photon exits the cavity as soon as it is released from the emitter. Furthermore, in the weak coupling regime at room temperature, when the incoherent atom decay rate γ, the cavity decay rate κ and the pure dephasing rate γ^* are much larger than the coherent coupling rates $g_0,\ldots,g_n$ to the cavity, the coherences $\langle\hat{\sigma}^\dagger_{ij}\hat{a}\rangle$ and their complex conjugates can adiabatically be eliminated. This means that the time derivatives of the coherence terms are set to zero. Under these assumptions, the following rate equations of the excited state population $\langle\hat{\sigma}_{ee}\rangle$ and the cavity photon number $\langle\hat{a}^\dagger\hat{a}\rangle$ are obtained [80]:

$$\frac{d}{dt}\langle\hat{a}^\dagger\hat{a}\rangle = -(\kappa+R_0)\langle\hat{a}^\dagger\hat{a}\rangle + \sum_{i=0}^{n}R_i\langle\hat{\sigma}_{ee}\rangle \tag{8.10}$$

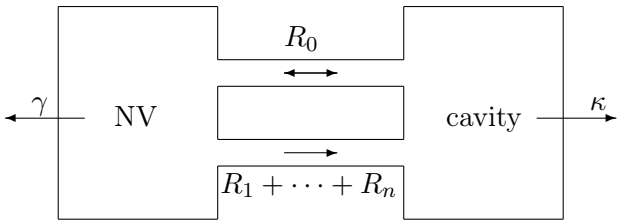

Figure 8.16: Schematic of two connected boxes describing the coupling of a single NV center to a cavity: The "NV center box" and "cavity box" are coupled at rates R_i, $i = 0, \ldots n$, whereof only the rate R_0 is bidirectional. Incoherent rates γ and κ describe the loss of photons out of the emitter and cavity box in the environment, respectively.

$$\frac{d}{dt}\langle\hat{\sigma}_{ee}\rangle = R_0\langle\hat{a}^\dagger\hat{a}\rangle - \left(\gamma + \sum_{i=0}^{n} R_i\right)\langle\hat{\sigma}_{ee}\rangle, \tag{8.11}$$

The effective coupling rates R_i are given by [80]

$$R_0 = \frac{4\,g_0^2}{\kappa + \gamma + \gamma^*}\,\frac{1}{1 + \left(\frac{2\,\delta_0}{\kappa+\gamma+\gamma^*}\right)^2} \tag{8.12}$$

$$R_i = \frac{4\,g_i^2}{\kappa + \gamma + \gamma_{i,i-1} + \gamma^*}\,\frac{1}{1 + \left(\frac{2\,\delta_i}{\kappa+\gamma+\gamma_{i,i-1}+\gamma^*}\right)^2}, \tag{8.13}$$

with $i = 1, \ldots, n$. The total decay rate γ is defined as the sum over all optical transitions $\gamma = \sum_{i=0}^{n} \gamma_i$ and $\delta_i = \omega_i - \omega_c$ denotes the detuning of the i^{th} optical transition from the cavity mode frequency ω_c. The quantities R_i can be interpreted as effective coupling rates between the color center and the cavity. This system theoretically described by equations (8.10)-(8.11) is formally equivalent to two coupled boxes involving a "NV center box" and a "cavity box" (see Fig. 8.16) [92]. Here, the NV center box symbolizes the excited state population $\langle\hat{\sigma}_{ee}\rangle$, whereas the cavity box represents the cavity photon number $\langle\hat{a}^\dagger\hat{a}\rangle$. Initially excited, the atom decays at a rate γ to the environment or it couples at rates $\sum_{i=0}^{n} R_i$ to the cavity box. In return, the atom is feeded by the cavity at a rate R_0. The photons in the cavity exit at a rate κ to the environment or they are reabsorbed by the atom with a probability R_0 per unit time [92]. The rate R_0, which is associated to the NV zero-phonon line, is bidirectional. This means that photons can both be emitted into the cavity mode and be absorbed from the cavity mode via this transition. In contrast, all other rates R_i, $i = 1, \ldots, n$, which are related to the vibronic side transitions are one directional. Photons with wavelengths in the side band regime can indeed be emitted into the cavity but they are not absorbed by the NV center, as the excitation of a color center obligatory involves the ground state level.

8.5.2 Generalized Purcell factor

The effective coupling rates R_i given by equations (8.12)-(8.13) allow for the definition of a generalized Purcell factor. In the Purcell regime $\kappa \gg R_i$, the atomic relaxation can be derived from the set of rate equations (8.10)-(8.11) with $\gamma + \sum_{i=0}^{n} R_i$. Coupling a cavity mode to the emitter can be considered as additional loss channels for the atom with rates R_i. To quantify the enhancement of the spontaneous emission rate, we define a generalized Purcell factor $F_i^* = R_i/\gamma$ [92] of the i^{th} optical transition that simultaneously takes into account the influence of pure dephasing. The generalized Purcell factor of the zero-phonon line F_0^* and the phonon side bands F_i^*, $i = 1, \ldots, n$ are expressed by:

$$F_0^* = \frac{4\,g_0^2}{\gamma \cdot (\kappa + \gamma + \gamma^*)} \frac{1}{1 + \left(\frac{2\,\delta_0}{\kappa+\gamma+\gamma^*}\right)^2} \tag{8.14}$$

$$F_i^* = \frac{4\,g_i^2}{\gamma \cdot (\kappa + \gamma + \gamma_{i,i-1} + \gamma^*)} \frac{1}{1 + \left(\frac{2\,\delta_i}{\kappa+\gamma+\gamma_{i,i-1}+\gamma^*}\right)^2}. \tag{8.15}$$

In the resonant case for a vanishing pure dephasing rate $\gamma^* = 0$ and instantaneous relaxation $\gamma_{i,i-1} = 0$ of the vibronic side bands to the ground state, the usual expression of the Purcell factor $F = 4g^2/(\kappa\,\gamma)$ recovers. With respect to the standard expression of the Purcell factor, F_i^*, $i = 0, \ldots, n$ are obtained by replacing the cavity loss rate κ by the sum over κ and the total emitter's linewidth $\gamma+\gamma^*$or $\gamma+\gamma^*+\gamma_{i,i-1}$, respectively [92]. The total Purcell enhancement F_{tot}^* at a given cavity resonance wavelength λ_c is determined by the sum over all contributions of the n atomic transitions:

$$F_{\text{tot}}^*(\lambda_c) = \sum_{i=0}^{n} F_i^*(\lambda_c) = \frac{1}{\gamma} \sum_{i=0}^{n} R_i(\lambda_c) \tag{8.16}$$

Similarly to the generalized Purcell factor, the emission efficiency β into the cavity mode can be calculated from the effective coupling rates R_i. The ratio β_i of each transition i coupled to the cavity compared to the overall NV emission rate, is determined by:

$$\beta_i = \frac{R_i}{\gamma + \sum_{j=0}^{n} R_j} = \frac{F_i^*}{1 + \sum_{j=0}^{n} F_j^*}, \qquad i = 0, \ldots, n \tag{8.17}$$

The right hand side of the above equation relates the efficiency β_i to the generalized Purcell factor F_i^* defined by equation (8.15). When the cavity mode is tuned to any given wavelength λ_c, the total emission efficiency β_{tot} into the cavity mode is given by the sum over all β_i associated to $n+1$ optical transitions.

$$\beta_{\text{tot}}(\lambda_c) = \sum_{i=0}^{n} P_i(\lambda_c) = \frac{\sum_{i=0}^{n} R_i(\lambda_c)}{\gamma + \sum_{j=0}^{n} R_j(\lambda_c)} = \frac{F_{\text{tot}}^*(\lambda_c)}{1 + F_{\text{tot}}^*(\lambda_c)}. \tag{8.18}$$

The right hand side of the above equation reproduces the well known relation between the β-factor and the Purcell factor F (c.f. chapter 2).

8.5.3 Experimental achievable Purcell factors

In this section, we calculate the expected Purcell enhancement for shallow implanted NV centers when coupled to a photonic crystal cavity mode with moderate Q-factor and small mode volume. All required input parameters to describe the contributions of the individual transitions to the cavity coupling are extracted from the measured NV spectrum taken at cryogenic temperatures. Fitting the broad emission spectrum of the implanted NV centers with Lorentzians, we deduce the transition frequencies, the experimental pure dephasing rate, inter-level relaxation rates as well as relative strengths and coupling constants of the individual transitions that are included in the master-equation model. To estimate the impact of the cavity mode, we take into account the measured moderate quality factor $Q = 160$ and a simulated mode volume of $V = 1.1\,(\lambda/n)^3$ of the fabricated M1-o240 cavity in diamond. Based on these data, we calculate the experimental achievable Purcell factor, the lifetime reduction as well as the emission efficiency into the cavity mode when the M1-o240 cavity mode is either tuned into resonance with the NV zero-phonon line or the side band transitions. Furthermore, we discuss the impact of the cavity Q-factor and the linewidth of the NV zero-phonon line on the coupling strength as well as the influence of the emitter's quantum efficiency, dipole orientation and position with respect to the cavity field.

Model parameters

To be able to estimate the achievable Purcell enhancement and the coupling efficiency of the NV centers to the cavity, we first have to gain more insight into the spectral properties of the phonon side bands. We fit the NV spectrum with $n+1$ Lorentzians [80], one zero-phonon line and n phonon side bands, of the form

$$y = \frac{2A_i}{\pi} \cdot \frac{\Delta\nu_i}{4(\nu_i - \Delta\nu_i)^2 + \Delta\nu_i^2}. \tag{8.19}$$

From the fit, we determine the transition frequencies ν_i of each ground state sublevel i as well as its full-width at half-maximum $\Delta\nu_i$ and the relative transition strength e_i. The relative strength e_i of each transition can be deduced by the area ratio [80]:

$$e_i = \frac{A_i}{\sum_{i=0}^{n} A_i}, \qquad i = 0, \ldots, n \tag{8.20}$$

The decay rate γ_i of each single transition i is determined by the product of the relative strength and the total decay [81]:

$$\gamma_i = e_i \cdot \gamma, \qquad i = 0, \ldots, n \tag{8.21}$$

The pure dephasing γ^* and the vibronic ground states relaxation rate $\gamma_{i,i-1}$ are related to the widths $\Delta\nu_i$ of the fitted Lorentzians [81]:

$$\gamma^* = 2\pi \cdot \Delta\nu_0 \tag{8.22}$$

$$\gamma^* + \gamma_{i,i-1} = 2\pi \cdot \Delta\nu_i, \qquad i = 1, \ldots, n \tag{8.23}$$

Here we assume that the zero-phonon line is solely broadened due to pure dephasing, whereas the phonon side bands are additionally subject to ground state relaxation. The cavity coupling constants g_i of each transition i are given by [81]:

$$g_i = \sqrt{e_i} \cdot g, \qquad i = 0, \ldots, n \tag{8.24}$$

The overall coupling constant g is governed by the total atomic decay rate $\gamma = \sum_{i=0}^{n} \gamma_i$ and the mode volume V of the cavity mode:

$$g = \sqrt{\frac{3}{16\pi^2} \frac{\gamma\, \omega_c}{V} \left(\frac{\lambda}{n}\right)^3}, \tag{8.25}$$

where V is given in units of $(\lambda/n)^3$. Using the relation $F = 4g^2/(\kappa\,\gamma)$, we obtain the well known equation of the standard Purcell factor $F = \frac{3}{4\pi^2} \frac{Q}{V} \left(\frac{\lambda}{n}\right)^3$ [56]. The cavity loss rate κ is determined by the resonance frequency ω_c and the cavity quality factor Q:

$$\kappa = \frac{\omega_c}{Q}. \tag{8.26}$$

Modeling the experimental NV spectrum

In the following, we focus on the 3 ± 1 NV centers that have been implanted at the center of the M1-o240 cavity structure. Figure 8.17(a) shows the spectrum of the M1-o240 cavity taken at 10 K after ion implantation. At the resonance wavelengths of the quadrupole and dipole modes at 653 nm and 670 nm, the intensity of the phonon side band is strongly enhanced compared to the off-resonance NV side band emission. In order to model coupling of the NV centers to the photonic crystal cavity modes and to deduce a generalized Purcell factor, we first have to gain deeper insight into the emission of the centers under investigation. Usually this done by measuring the NV spectrum prior to cavity coupling and fitting the zero-phonon line and phonon side band emission with eight Lorentzians [80]. From the fit parameters, the pure dephasing rate γ^*, the ground state relaxation rates $\gamma_{i,i-1}$ and the relative strengths e_i of each transition i are deduced, needed to evaluate the rate equations or to solve the full master equation (8.2). However, in our experiment, we cannot proceed like this. As the NV centers are directly created at the center of the photonic crystal cavity no reference spectrum prior to coupling exists. Therefore, we have to extract the relevant information from the spectrum shown in figure 8.17(a). To this end, several assumptions have to be made.

First of all, figure 8.17(a) displays a combined spectrum of the M1-o240 cavity and 3 ± 1 implanted NV centers. Therefore, care has to be taken to distinguish between NV^- emission and cavity modes. As the resonance wavelengths and linewidths are known from the bare M1-o240 cavity spectrum (Fig. 8.7), we can estimate the bare NV^- spectrum, shown by the orange line in figure 8.17(a) without the cavity modes.

Please note that the estimated orange spectrum does not displays the spectrum of one single center but the broad-band emission averaged over 3 ± 1 NV^- centers. In a first approach, we assume the same side band spectrum for every of the three implanted

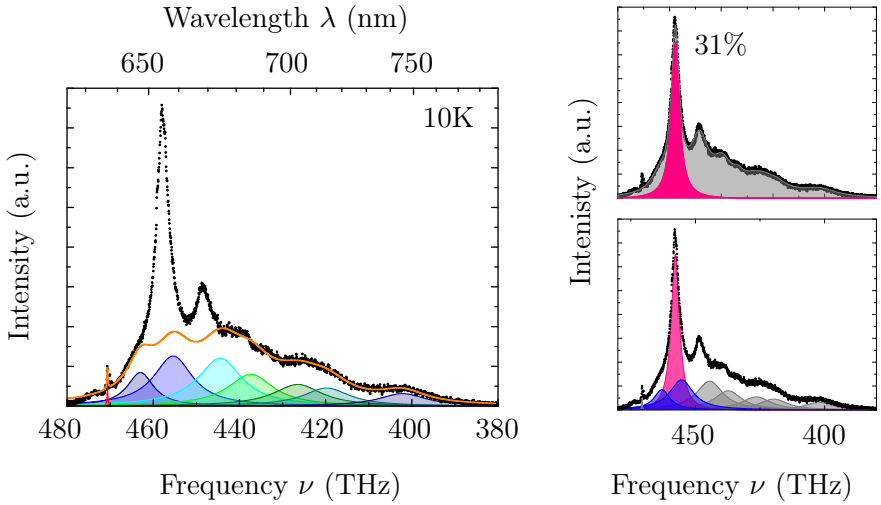

Figure 8.17: Spectrally resolved Purcell enhancement of the NV^- emission via coupling to the M1-o240 cavity: (a) Spectrum taken at 10 K, at the center of the M1-o240 cavity after implantation of 3 ± 1 NV^- centers (black dots). The orange line indicates the estimates spectrum of the bare NV^- emission without cavity modes. The bare NV^- spectrum is fitted with eight Lorentzians (colored curves). The resulting fit parameters are summarized in table 8.7. (b) Relative integrated intensity of the NV^- emission radiated into the cavity mode (pink) compared to the total emission (pink + gray) yielding $I_{\mathrm{cav}}/I_{\mathrm{tot}} = 31\%$. (c) The cavity mode (pink) significantly overlaps with the first and second phonon side band (blue) of the NV^- emission.

NV^- centers and use the average spectrum to extract the input parameters for the cavity-coupling model.

The third remark concerns the high background luminescence signal (c.f. Fig. 8.13(a)) probably due to defects near the diamond surface that might be induced by the mechanical polishing or the reactive ion etching process to thin the membrane. Because of the high background, we can hardly separate the actual NV signal from parasitic fluorescence. This might lead to a large error in the relative strength of the zero-phonon line compared to the phonon side band contributions.

Based on these assumptions, we fit the estimated bare NV^- spectrum (orange line) with eight Lorentzians, as shown in figure 8.17(a). The obtained transition frequencies and linewidths together with the relative strengths e_i of each transition i extracted from the areas below the Lorentzian curves (shaded regions) are summarized in table 8.7.

Apart from a slight blue shift of the 3^{rd}-5^{th} side bands, the transition frequencies and linewidths deduced from the fit to the averaged NV^- spectrum are in good agreement with previous data reported for single NV centers hosted in nanodiamonds [80, 81]. These studies [81] observed a variation in the side band features between different single NV^- centers.

Remarkably, the relative strength e_0 of the zero-phonon line compared to the overall emission is fairly low, i.e. $< 1\%$ for the implanted NV centers. In literature, a large

i	ν_i THz	$\Delta\nu_i$ THz	e_i %	γ_i MHz	$\gamma_{i,i-1}$ THz	g_i GHz
0	470.6	0.25	0.7%	0.6	0.0	5.4
1	463.0	7.40	8.9%	7.4	44.9	19.1
2	455.4	10.9	20.3%	16.8	67.2	28.8
3	444.5	12.4	23.1%	19.2	76.3	30.8
4	437.3	12.8	16.3%	13.5	78.6	25.8
5	426.5	13.6	12.5%	10.4	84.1	22.6
6	419.8	13.1	10.3%	8.5	80.5	20.5
7	402.1	13.3	7.9%	6.6	81.9	18.0

Table 8.7: Parameters obtained by fitting the NV spectrum with eight Lorentzians. The spectrum is taken at the center of the implanted M1-o240 cavity measured at 10 K (c.f. Fig. 8.17).

spread in the NV branching ratio can be found. In some experiments, branching ratios into the ZPL of $e_0 = 2\%$ [80], 2.4% [170](determined by absorption measurements), 3% [83] and 4% [125] were observed. In contrast, other studies reported small branching ratios, i.e. $< 1\%$, for single NV^- centers hosted in nanodiamonds that were placed on various substrates [446]. In our experiment, the small branching ratio is related to a large uncertainty in fitting the spectrum due to significant background contributions.

Based on the fitted transition frequencies, linewidths and relative transition strengths, we evaluate in a next step the pure dephasing rate γ^*, the relaxation rates $\gamma_{i,i-1}$, the spontaneous decay rates γ_i, as well as the coupling constants associated to the individual transitions i between the excited state and vibrational ground state levels and the cavity loss rate κ.

Pure dephasing rate γ^* and relaxation rates $\gamma_{i,i-1}$: Considering the NV zero-phonon linewidth of $\Delta\nu_0 = 250\,\text{GHz}$ measured at 10 K, we obtain the pure dephasing rate γ^*

$$\gamma^* = 2\pi \times 250\,\text{GHz}. \tag{8.27}$$

Here, we assume that the broadening due to spectral diffusion happens on a time scale much shorter than the typical spontaneous emission decay time. In this case, spectral diffusion can be modeled by a pure dephasing term in the master equation [92]. Moreover, according to equation (8.23), the relaxation rates $\gamma_{i,i-1}$ between the vibronic ground state sublevels i can be calculated from the fit parameters summarized in table 8.7.

Spontaneous emission rate γ: Unfortunately, the exact spontaneous decay rate γ of the NV^- centers incorporated in the photonic crystal cavity is unknown, due to the lack of a pulsed green excitation laser to perform lifetime measurements similar to the

experiments on SiV centers. For single NV centers hosted in bulk diamond an excited state lifetime of 12 ns has been reported [23]. However, as we know from our simulations (c.f. section 5.4.2) and our experiments on ensemble and single SiV centers presented in chapters 7 and 9, the spontaneous decay rate might be strongly suppressed by the lattice Purcell factor F_{PhC} for frequencies inside the photonic band gap. From our simulations we deduced an averaged inhibition factor of $F_{\mathrm{PhC}} = 0.23 - 0.25$ (c.f. Fig. 5.12). This means that the actual decay rate γ_{PhC} might be inhibited by the lattice Purcell factor yielding $\gamma_{\mathrm{PhC}} = F_{\mathrm{PhC}}\,\gamma_{\mathrm{rad}} + \gamma_{\mathrm{nr}}$, where the ratio of the radiative and non-radiative decay rates γ_{rad} and γ_{nr}, respectively, is determined by the quantum efficiency. However, these simulations assume that the phonon side band spectrum completely coincides with the frequency range of the photonic band gap. This is a valid assumption for narrow-band SiV centers with weak phonon side band contributions. For SiV centers, we could assure from the spectrum, that the phonon side band lies completely within the band gap of the photonic lattice. For the NV emission extending over 100 nm, this conclusion is much more difficult. In literature, lifetimes of 13.7 ns [87] and 18.4 ns [90] have been reported for single NV centers hosted in diamond-based photonic crystal cavities. These lifetimes are slightly larger compared to the value in bulk diamond, suggesting that the NV center is weakly subjected to inhibition by the photonic band gap effect. As comparable lifetime measurements on the 3 ± 1 NV^- centers implanted within the M1-o240 cavity are missing, we are not able to deduce a possible inhibition of the spontaneous decay rate. Therefore, we disregard a possible photonic band gap effect in our experiment and assume a spontaneous decay rate reported for NV^- centers in bulk diamond [23]:

$$\gamma = 83\,\mathrm{MHz} = (12\,\mathrm{ns})^{-1}. \tag{8.28}$$

Cavity loss rate κ and coupling constant g: In order to determine the cavity loss rate κ and the coupling constant g, we take into account a cavity quality factor of $Q = 160$, reported for the quadrupole mode of the M1-o240 cavity at a resonance wavelength of $\lambda_c = 653\,\mathrm{nm}$ (c.f. table 8.3) and a simulated modal volume of the quadrupole mode of $V = 1.1\,(\lambda/n)^3$ (c.f. table 5.1 on page 112), where $n = 2.4$ is the refractive index of diamond. Based on these data, we calculate the loss rate of $\kappa = \omega_c/Q$ of the photonic crystal cavity and the coupling constant g via equation (8.25):

$$\kappa = 18\,\mathrm{THz}, \qquad g = 64\,\mathrm{GHz}. \tag{8.29}$$

Once the total coupling constant g and decay rate γ are determined, the rates g_i and γ_i of the individual transitions i can be evaluated as summarized in table 8.7.

According to equations (8.28) and (8.29), the emitter-cavity interaction is in the weak coupling limit, as $\kappa \gg g > \gamma$. In this regime, the atom-cavity coupling is incoherent. As the cavity decay rate κ exceeds g and γ by two orders of magnitude, we assure that photons exit the cavity as soon as they are released from the emitter. Hence, the assumption used to derive the rate equations is valid claiming that at maximum one photon being present in the cavity.

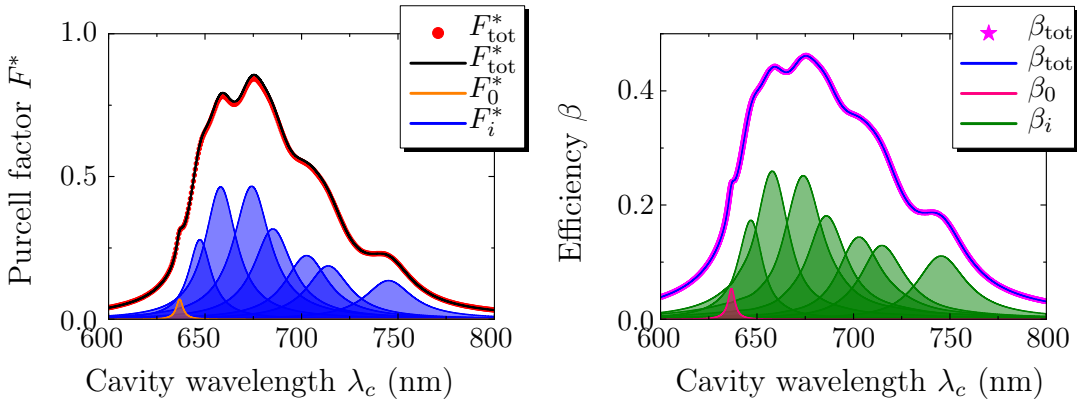

Figure 8.18: Generalized Purcell factor F^* and emission efficiency β as a function of the cavity wavelength λ_c: (a) The generalized Purcell factor of the zero-phonon line F_0^*, of the phonon side bands F_i^*, $(i \geq 1)$ and the total Purcell factor $F_{\rm tot}^*$ are calculated using the rate equations (8.14)-(8.16) (solid lines) and solving the full master equation (8.2) (red dots). (b) Emission efficiency of the zero-phonon line β_0 and phonon side bands β_i, $(i \geq 1)$ into the cavity mode as well as the total efficiency $\beta_{\rm tot}$ are determined using the rate equations (8.17)-(8.18) (solid lines) and by solving the master equation (8.2) (pink stars). Parameters used in the calculation: $Q = 160$, $V = 1.1\,(\lambda/n)^3$, $\kappa = 18\,\text{THz}$, $g = 64\,\text{GHz}$, $\gamma^* = 2\pi \times 250\,\text{GHz}$, $\gamma = 83\,\text{MHz}$, $e_0 < 1\%$.

Generalized Purcell factor of the NV$^-$ spectrum

Based on the deduced cavity and atomic decay rates κ, γ, the coupling rate g and pure dephasing rate γ^* at cryogenic temperatures (c.f. eqs. (8.27)-(8.29) and table 8.7), the generalized Purcell enhancement of the NV emission in resonance with the photonic crystal cavity mode can now be calculated. According to the model of two coupled boxes, discussed on page 233, the coupling to the cavity introduces additional decay channels of the NV center. These additional decays to the cavity are given by the effective coupling rates R_i. Equivalently, the coupling rates can be interpreted as generalized Purcell factors $F_i^* = R_i/\gamma$ associated to the individual transitions between the excited state and the different vibrational levels of the ground state. The total decay rate of the NV center placed in the cavity is then given by:

$$\gamma_{\rm cav} = \gamma + \sum_i^n R_i = \gamma\,(1 + \sum_i^n F_i^*). \tag{8.30}$$

The effective coupling rates R_i, $i = 0, \ldots, n$, the associated generalized Purcell factors F_i^* and the emission efficiencies β_i for each transition i are calculated via the rate equations (8.12)-(8.18) and by solving the full master equation (8.2). For the NV centers implanted within the M1-o240 photonic crystal with $Q = 160$ and $V = 1.1\,(\lambda/n)^3$, figure 8.18 displays the generalized Purcell factors F_0^*, F_i^*, $i = 1, \ldots, n$ and the emission efficiencies β_0, β_i of the zero-phonon line and phonon side bands. Furthermore, the total Purcell factor $F_{\rm tot}^*$ and the total efficiency $\beta_{\rm tot}$ are plotted as a function of the cavity

resonance wavelength λ_c. As the relative strength $e_0 < 1\%$ of the zero-phonon line is fairly small, the overall Purcell enhancement is only $1 + F^*_{\text{tot}}(\lambda_c = 637\,\text{nm}) = 1.32$ when the cavity mode is tuned to $\lambda_c = 637\,\text{nm}$. At this wavelength, up to 24% of the released photons are emitted into the cavity mode, whereof $\beta_0(637\,\text{nm}) = 5\%$ are emitted by the zero-phonon line and $\sum_{i=1}^{7} \beta_i(637\,\text{nm}) = 19\%$ are contributed by the phonon side bands.

Significantly larger Purcell factors can be obtained when the cavity mode with $Q = 160$ and $V = 1.1\,(\lambda/n)^3$ is tuned into resonance with the NV phonon side band. At a resonance wavelength of $\lambda_c = 653\,\text{nm}$ (corresponding to the measured M1-o240 spectrum), a high Purcell factor of $1 + F^*_{\text{tot}}(\lambda_c = 653\,\text{nm}) = 1.70$ is achieved coming along with an emission efficiency of 42% into the cavity mode. This means that the total decay rate of the NV center would be enhanced or equivalently its lifetime would be reduced by a factor of 1.7 via coupling to the M1-o240 cavity. This enhancement is already quite impressive, bearing in mind that only a small fraction of the broad-band phonon side band is spectrally overlapped with the cavity mode exhibiting a low Q-factor. However, due to the extremely small mode volume, the interaction between the NV center and the cavity field is sufficiently strong to achieve a Purcell enhancement.

Please note that in the above analysis we neglect the fact that not one but 3 ± 1 NV centers were implanted at the M1-o240 cavity center. Hence, the experimental achievable Purcell factor would be an average value over all spatial positions and dipole orientations of the small ensemble, which we here assumed to be perfectly aligned with the cavity mode.

Purcell factor extracted from the intensity enhancement

To show that the rate equation model gives reliable predictions on the Purcell factor, we consider a second analysis method based on the pronounced intensity of the NV side band emission in resonance with the M1-o240-cavity mode (Fig. 8.17). By comparing the integrated intensity of the NV^- phonon side band on-resonance with the quadrupole mode, i.e. I_{cav}, to the overall integrated intensity, i.e. I_{tot}, we can determine the NV^- spontaneous emission efficiency into the cavity mode, $\tilde{\beta} = I_{\text{cav}}/I_{\text{tot}}$ [90]. Figure 8.17(b) shows the integrated intensity of the NV^- emission radiated into the quadrupole mode (pink area) compared to the overall integrated intensity (pink + gray areas) yielding an emission efficiency into the cavity mode of $\tilde{\beta} = I_{\text{cav}}/I_{\text{tot}} = 0.31$. This result is slightly smaller than the emission efficiency of 0.42 predicted by the rate equation model for a resonant wavelength of 653 nm. The reason for the smaller experimental value might be that in this rough estimate, we assume that the emission preferentially emitted into the cavity mode is redirected into the vertical direction and collected by the microscope objective. In the experiment, this redirection of emission in the vertical direction might be less efficient, than it is assumed here.

As a next step, we consider the intensity enhancement in the presence of the cavity mode. By comparing the integrated intensity of the measured emitter-cavity spectrum to the integrated intensity of the estimated bare NV spectrum (orange line in Fig. 8.17(a)), we deduce an overall intensity enhancement of the NV emission by a factor 1.24 induced

by cavity coupling. This value will now be compared to the intensity enhancement predicted by the generalized Purcell factor. The on resonance intensity enhancement is given by equation (7.4) deduced for SiV ensemble coupling experiments to photonic crystal cavities. As the exact positions of the NV centers within the cavity are unknown, we here assume perfect overlap of the NV centers with the cavity field. Hence the integral over $\rho(r)$ is assumed to yield one. Moreover, we assume perfect overlap of the XY dipoles with the cavity field. Such that the integral over $\rho(d)$ equals one. The impact of the spatial and orientational overlap, will be addressed in section 8.5.4. The spectral overlap of the cavity mode and the NV emission can be estimated using the fitted NV spectrum. Figure 8.17(c) reveals that the quadrupole mode preferentially overlaps with the first and second phonon side band of the NV^- spectrum. Taking into account the relative strengths e_1 and e_2 of the two side bands, we find the spectral overlap integral over $\rho(\lambda)$ to be $e_1 + e_2 = 29.2\%$. This allows now to estimate the intensity enhancement

$$I_{\mathrm{cav}}/I_0 = [\gamma\,(1 + F^*_{\mathrm{tot}})\,(e_1 + e_2) + \gamma(1 - e_1 - e_2)]/\gamma = 1.2, \tag{8.31}$$

where we used $1 + F^*_{\mathrm{tot}} = 1.7$. This rough estimate is in reasonable agreement with the intensity enhancement observed in the experiment of 1.24. The reason for the slightly larger experimental value might be, that in the above analysis, we assumed equal collection efficiencies for on and off resonant emission. This assumption might lead to slightly overestimated experimental intensity enhancements.

Based on our analysis, we conclude that the observed pronounced intensity signal at the resonance wavelength of the M1-o240 cavity mode is attributed to a spectrally resolved Purcell enhancement of the NV emission. Using the rate equation model and relating the theoretical Purcell factor of 1.7 to the ratio of the on resonance integrated intensity and the integrated intensity of the bare NV spectrum, we find reasonable agreement between theoretical predictions and the experimental intensity enhancement observed, when coupling a photonic crystal cavity mode with $Q = 160$ and $V = 1.1\,(\lambda/n)^3$ to the NV phonon side band.

In summary, the measured photoluminescence signal is well described by the rate equation model that includes higher vibrational levels of the NV ground state to mimic cavity coupling to a broad-band emitter. Please note that the above analysis assumes unity quantum efficiency and perfect spatial and orientational overlap of the cavity field with the dipoles of the NV center. In a more rigorous calculation these contributions needs to be considered as well as the actual lifetime of the NV centers. On page 244, we discuss the impact of non-unity quantum efficiencies and the limitations of the generalized Purcell model.

Impact of the cavity quality factor

As already mentioned above, the measured relative strength $e_0 < 1\%$ of the zero-phonon line for the NV centers implanted in the M1-o240 structure is much less than typical branching ratios of 2-4% [80,83,125,170] obtained for single NV centers. In the following, we give a short outlook on Purcell factors, excited state lifetimes and emission efficiencies that can be reached when coupling a single NV center with a ZPL relative strength of

$e_0 = 3\%$ to either a cavity mode with $Q = 160$, e.g. the M1-o240 structure or to a cavity mode with quality factors up to $Q = 1,000$, as presented in chapter 6. Hereby, we consider a constant mode volume of $V = 1.1\,(\lambda/n)^3$. In addition, the impact of the pure dephasing rate γ^* on the Purcell enhancement and efficiency are discussed.

Figure 8.19(a,c) displays the generalized total Purcell factor as a function of the cavity resonance wavelength λ_c for a quality factor of $Q = 160$ and $Q = 1,000$, respectively. Here, we assume a constant pure dephasing rate $\gamma^* = 2\pi \times 250\,\mathrm{GHz}$, when the NV center is cooled down to cryogenic temperatures. The impact of the Q-factor on the zero-phonon line enhancement is striking. Raising the quality factor from $Q = 160$ to $Q = 1,000$ almost doubles the total Purcell enhancement from $1 + F^*_{\mathrm{tot}}(\lambda_c = 637\,\mathrm{nm}) = 1.55$ up to $1 + F^*_{\mathrm{tot}}(\lambda_c = 637\,\mathrm{nm}) = 2.60$. This means, that the excited state lifetime would be shortened to 4.6 ns when the ZPL is resonantly enhanced by the high-Q cavity mode compared to 12 ns for the off-resonant decay time. The increase in the Purcell factor F^*_{tot}, comes along with an enhanced total efficiency into the zero-phonon line from $\beta_{\mathrm{tot}}(\lambda_c = 637\,\mathrm{nm}) = 35\%$ for $Q = 160$ to 61% for $Q = 1,000$ (inset in Fig. 8.19(e)). In contrast to the ZPL, the quality factor has only a minor effect on the phonon side band transitions: Improving the quality factor by a factor of six leads to an increases in F^*_{tot} by less than 7%. Equivalently, the change in emission efficiency into the vibronic side bands is less than 1% for enhanced cavity Q-factors.

Impact of the pure dephasing rate γ^*

We have already seen that the cavity linewidth determined by the Q-factor has a major impact on the Purcell enhancement of the NV zero-phonon line, whereas the impact on the phonon side band transitions is small. Now, we investigate the Purcell factor and the NV excited state lifetime as a function of the zero-phonon linewidth while keeping the Q-factor fixed to either $Q = 160$ or $Q = 1,000$. Furthermore, we assume a branching ratio into the ZPL of $e_0 = 3\%$. When cooling the diamond sample to cryogenic temperatures, the broadening of the ZPL due to the dynamic Jahn-Teller effect is reduced and the linewidth narrows. In the master equation, the linewidth of the zero-phonon transition is modeled by the pure dephasing rate γ^*, whereas the phonon side bands are additionally broadened by the ground state relaxation rates $\gamma_{i,i-1}$. Hence, decreasing the pure dephasing rate γ^* only affects the ZPL linewidth and has no impact on the vibronic transitions. Using the rate equations (8.12)-(8.13) as well as by solving the full master equation (8.2), we calculate the generalized Purcell factor F^*_0 of the zero-phonon transition for various pure dephasing rates γ^*. The associated lifetime of the exited state is determined by fitting the time evolution of the atomic population with an exponential function, extracting the decay time. In figure 8.19(b,d), the Purcell factor F^*_0 and the excited state lifetime of the ZPL are displayed as a function of γ^* when coupled to a cavity mode with $Q = 160$ or $Q = 1,000$. When the pure dephasing rate is decreased below $\gamma^* = 200\,\mathrm{GHz}$, maximum Purcell factors of $1 + F^*_0 = 1.57$ for $Q = 160$ and even $1 + F^*_0 = 3.3$ for $Q = 1,000$ are reached that result in excited state lifetimes of $T_1 = 7.64\,\mathrm{ns}$ and $T_1 = 3.64\,\mathrm{ns}$, respectively. Associated to the Purcell factor, emission efficiencies of 36% and 69% at a pure dephasing rate below $\gamma^* = 200\,\mathrm{GHz}$ are obtained

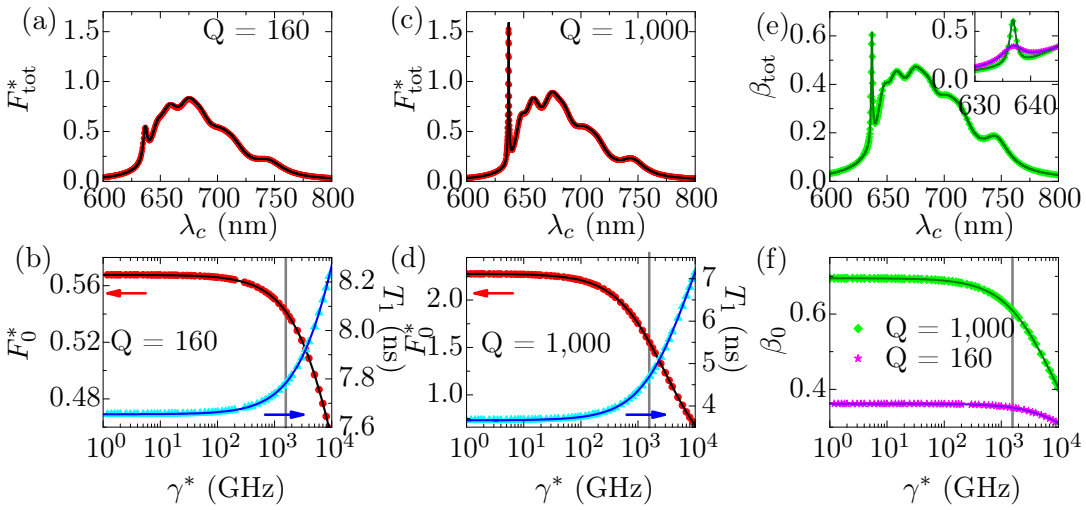

Figure 8.19: Generalized Purcell factor F^*, excited state lifetime T_1 and emission efficiency β as a function of the cavity wavelength λ_c and pure dephasing rate γ^*: (a,c) Total generalized Purcell factor F^*_{tot} as a function of the cavity wavelength λ_c for constant $\gamma^* = 2\pi \times 250\,\text{GHz}$ as well as (b,d) Purcell factor F^*_0 (red) of the ZPL and excited state lifetime T_1 (blue) as a function of the pure dephasing rate γ^* for cavity quality factors (a,b) $Q = 160$ and (c,d) $Q = 1,000$. (e) Total emission efficiency β_{tot} as a function of the cavity wavelength λ_c with $Q = 1,000$ and $\gamma^* = 2\pi \times 250\,\text{GHz}$. The inset shows a zoom into the ZPL for $Q = 160$ (pink) and $Q = 1,000$ (green). (f) Emission efficiency β_0 into the ZPL as a function of the pure dephasing rate γ^* for $Q = 160$ (pink) $Q = 1,000$ (green). (b,d,f) The gray vertical line marks $\gamma^* = 2\pi \times 250\,\text{GHz}$. Solid lines: calculation via rate equations, (●, ▲, ♦, ⋆): solution of master equation. Calculation parameters: $\kappa = 18\,\text{THz}$ for $Q = 160$, $\kappa = 3\,\text{THz}$ for $Q = 1,000$, $V = 1.1\,(\lambda/n)^3$, $g = 64\,\text{GHz}$, $\gamma^* = 2\pi \times 250\,\text{GHz}$ (if not varied), $\gamma = 83\,\text{MHz}$, $e_0 = 3\%$.

for $Q = 160$ and $Q = 1,000$, respectively. A pure dephasing rate of $\gamma^* = 200\,\text{GHz}$ is experimentally achievable. For shallow implanted NV center in bulk diamond, spectral linewidths down to 10 GHz have previously been measured [391]. The linewidth would correspond to a pure dephasing rate $\gamma^* = 2\pi \cdot \Delta\nu = 63\,\text{GHz}$, that should enable high Purcell factors and extremely low excited state lifetimes calculated in figure 8.19(b,d). In the experiments presented in this work, an inhomogeneously broadened ZPL linewidth due to spectral diffusion has been measured that is limited to 250 GHz even at cryogenic temperatures. The experimentally limited linewidth is marked by a vertical gray line in figure 8.19(b,d,f) at $\gamma^* = 2\pi \times 250\,\text{GHz}$.

Impact of the emitter's quantum efficiency

In the formalism of the generalized Purcell factor, we take into account radiative decay rates through the zero-phonon line and phonon side band transitions to model the broadband emission of the NV center. However, possible non-radiative decay rates have been

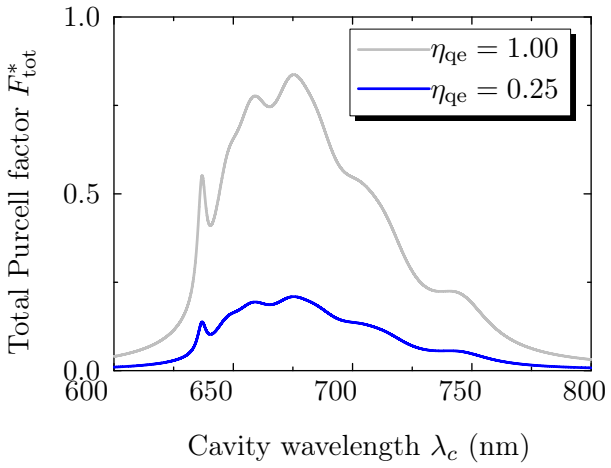

Figure 8.20: Impact of the emitter's quantum efficiency η_{qe} on the total Purcell factor ${F^*}_{\mathrm{tot}}$ as a function of the cavity wavelength λ_c: The Purcell factor scales proportional to the quantum efficiency: Decreasing η_{qe} from 1.00 to 0.25 reduces the Purcell factor by a factor of four.

totally neglected so far. In general, the excited state population of a single NV center can decay through various channels including radiative transitions γ_{rad}, e.g. the zero-phonon line and phonon side bands, and non-radiative decays γ_{nr}. The quantum efficiency is defined as the ratio of the radiative decay rates to the overall transition rates: $\eta_{\mathrm{qe}} = \gamma_{\mathrm{rad}}/(\gamma_{\mathrm{rad}} + \gamma_{\mathrm{nr}})$. For vanishing non-radiative decay rates, we obtain a unity quantum efficiency. Cavity-coupling solely enhances the radiative emitter's decay rates whereas the non-radiative transition rates are unaffected. A quantum efficiency smaller than one would result in a significantly reduced Purcell enhancement when coupling the emitter to a photonic crystal cavity. In literature [447, 448], quantum efficiencies of single NV centers hosted in diamond nanocrystals have been reported as low as 0.25 that strongly differ from unity. The technique applied by Frimmer and Mohtashami et al. [447, 448] relies on the modification of the local density of optical states at the emitter's position by approaching a mirror to the nanocrystal. By measuring the excited state lifetime of the NV center as a function of the emitter-mirror distance, the quantum efficiency can be extracted. Their measurements reveal a large spread in the quantum efficiency from center to center, which they attributed to varying distances to the nanocrystal surface that might induce non-radiative recombination rates. Based on their findings, it might be probable that the quantum efficiency of shallow implanted NV centers also strongly differs from unity and varies between the emitters. Therefore in practice, it is indispensable to characterize the quantum efficiency of individual implanted NV centers to be able to correctly predict their Purcell enhancement via cavity-coupling.

In the rate equation model non-unity quantum efficiencies can be implemented. For a finite quantum efficiency η_{qe}, the relative transition strengths e_i of the zero-phonon line and phonon side bands are modified:

$$e'_i = e_i \cdot \eta_{\mathrm{qe}}, \qquad i = 0, \ldots, n \tag{8.32}$$

Similar to the relative strengths, the decay rates γ_i for each individual transition i have to be corrected for the finite quantum efficiency:

$$\gamma_i' = \eta_{\mathrm{qe}}\, e_i\, \gamma, \qquad i = 0, \ldots, n \tag{8.33}$$

Summing over the all individual decay rates γ_i' gives the radiative decay rate $\sum_{i=0}^{n} \gamma_i' = \eta_{\mathrm{qe}}\, \gamma = \gamma_{\mathrm{rad}}$. Please note that the total excited state decay rate γ, comprising both radiative and non-radiative transition rates, does not depend on the quantum efficiency. The quantum efficiency affects as well the coupling constants g_i of the individual transitions i:

$$g_i' = \sqrt{\eta_{\mathrm{qe}}\, e_i}\, g, \qquad i = 0, \ldots, n \tag{8.34}$$

Including non-radiative decay rates in the rate equation model, decreases the total coupling constant g by the square root of the quantum efficiency: $g' = \sqrt{\eta_{\mathrm{qe}}}\, g$. In contrast, the total exited state decay rate γ as well as the pure dephasing rate γ^* and the vibronic ground state relaxation rates $\gamma_{i,i-1}$ are independent on the emitter's quantum efficiency. According to equations (8.14)-(8.15), the resulting generalized Purcell factors F_i^*, which are proportional to the square of the coupling constants g_i^2, scales with the emitter's quantum efficiency η_{qe}:

$$F_i^{*\prime} = \eta_{\mathrm{qe}} F_i^*, \qquad i = 0, \ldots, n \tag{8.35}$$

The same relation holds for the total Purcell factor

$$F_{\mathrm{tot}}^{*\ \prime} = \eta_{\mathrm{qe}} F_{\mathrm{tot}}^* \tag{8.36}$$

To illustrate the impact of the emitter's quantum efficiency, figure 8.20 displays the total Purcell factor F_{tot}^* calculated for $\eta_{\mathrm{qe}} = 1.00$ and $\eta_{\mathrm{qe}} = 0.25$ as a function of the cavity wavelength λ_c. Over the whole wavelength range, the generalized Purcell factor is reduced by a factor of four assuming $\eta_{\mathrm{qe}} = 0.25$ compared to unity quantum efficiency.

8.5.4 Limitation of the generalized Purcell model

By modeling the NV center as a multi-level system its broad-band emission and the spectral overlap with a narrow cavity mode can be very well described. Furthermore, a non-unity quantum efficiency of the single emitter can be implemented in the scheme. Although the spectral properties of the emitter and cavity mode are very well describes, the model neglects the spatial overlap and the orientation of the NV dipole moments with respect to the cavity field. In practice, both contributions have a strong impact on the coupling strength and have to be taken into account.

Orientation of the dipole moment

For optimal cavity-coupling, the dipole moment of the emitter has to be aligned parallel to the electric field of the cavity mode. The NV center has two XY-emission dipole moments [171] that are oriented in the plane perpendicular to the nitrogen-vacancy axis

aligned along ⟨111⟩ crystal directions [168] (c.f. chapter 2). The expression ⟨111⟩ symbolizes the four equivalent sites of the NV axis: [111], [$\bar{1}\bar{1}$1], [$\bar{1}$1$\bar{1}$] and [1$\bar{1}\bar{1}$]. In order to optimally align the NV dipole moments with the cavity in-plane electric fields, it would be optimal to fabricate the photonic crystal cavities in the (111)-facet of a diamond membrane and to use NV centers oriented perpendicularly to this facet. Recently, the nearly perfect preferential alignment of the NV center along the [111] diamond axis has been demonstrated by several groups [449–451]. The formation of NV centers in one out of four possible configurations is attributed to particular dynamics in the CVD diamond growth process on a (111) diamond substrate. (111) oriented diamond membranes with thicknesses of 10-30 μm would be well suited for efficient coupling of single NV centers placed into a photonic crystal cavity.

In this work, we use (001) oriented diamond membrane for the fabrication the photonic crystal cavities and subsequent implantation of nitrogen ions. For all four possible nitrogen-vacancy orientations, the plane defined by the XY dipole moments of the NV center would be inclined by an angle of 54.74° with respect to the cavity fields in the (001) diamond plane. In that case, the projection of the dipole moments $\vec{d}$ onto the $\vec{E}$ cavity electric field reduces the effective Purcell enhancement by:

$$F^*_{\text{tot,dipole}} = \frac{|\vec{d}\cdot\vec{E}|^2}{|\vec{d}|^2\,|\vec{E}|^2}\,F^*_{\text{tot}}, \tag{8.37}$$

where $F^*_{\text{tot,dipole}}$ denotes the generalized Purcell factor corrected for the orientation mismatch. To illustrate the effect of the dipole moment, let us assume an orientation of the nitrogen-vacancy center along the [111] direction and an alignment of its X and Y dipole moments along the [11$\bar{2}$] and [1$\bar{1}$0] axes, respectively. In that case, the Y dipole moment would lie in the (x, y) photonic crystal plane and optimal coupling to the cavity electric field would be possible. However, the X dipole moment is inclined by an angle of 54.7° with respect to the cavity electric fields in the (001) diamond plane. This reduces the coupling strength of the X dipole moment to the cavity mode to one third. The maximal achievable Purcell factor $F^*{}_{\text{tot,dipole}}$ is reduced to at least 2/3 of the ideal F^*_{tot} assuming optimal alignment. For the calculation, we assumed the cavity x- and y-axis to be aligned along the [1$\bar{1}$0] and [110] diamond direction. The exact enhancement factor might be even lower, depending on the spatial distribution of the E_x and E_y field components of the cavity mode.

Spatial alignment

In the model of the generalized Purcell factor, it is assumed that the NV center is placed at the maximum of the cavity electric field to achieve optimum coupling. In practice, the position of the implanted NV centers might deviate from the ideal placement. In that case, the Purcell factor is reduced by the cavity electric field $\vec{E}(\vec{r})$ at the emitter's position $\vec{r}$ normalized to the field maximum max$\vec{E}(\vec{r})$:

$$F^*_{\text{tot,pos}} = \frac{|\vec{E}(\vec{r})|^2}{|\max\limits_{\vec{r}}\vec{E}(\vec{r})|^2}\cdot F^*_{\text{tot}} \tag{8.38}$$

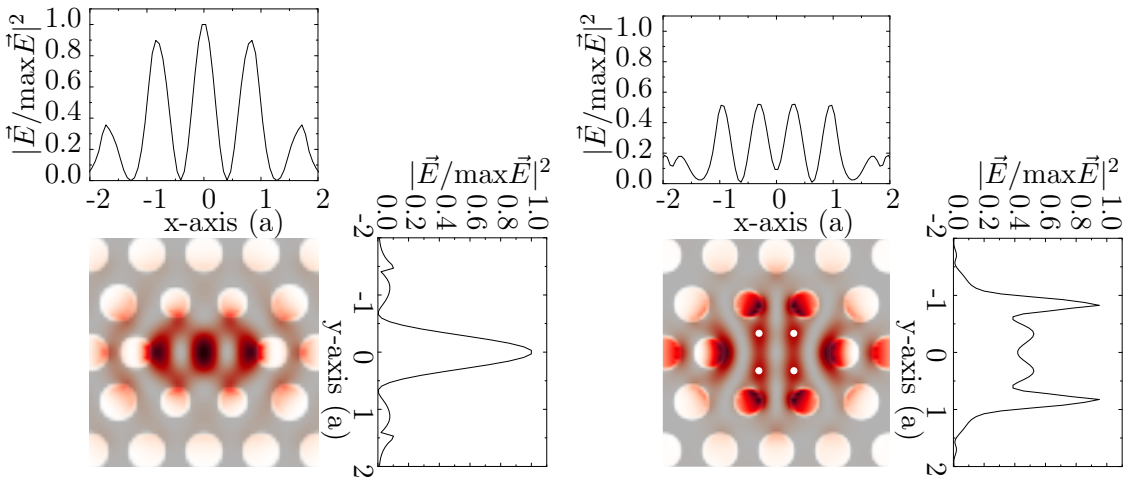

(a) Dipole-mode (b) Quadrupole-mode

Figure 8.21: Normalized electric field distribution $|\vec{E}(\vec{r})|^2/|\max\vec{E}(\vec{r})|^2$ and their cross section parallel to the x- and y-axis of the (a) $+x-y$ dipole and (b) $-x-y$ quadrupole mode of the M1-cavity: (a) The dipole mode is maximum at the center of the structure. (b) For the quadrupole mode, $|\vec{E}(\vec{r})|^2/|\max\vec{E}(\vec{r})|^2 > 50\%$ is obtained at four equivalent points marked by white dots within the defect region.

Here, $F^*_{\mathrm{tot,pos}}$ symbolizes the generalized Purcell factor that takes into account the emitter's position with respect to the cavity field. Figure 8.21 shows the square amplitude of the electric field $|\vec{E}(\vec{r})|^2$ of the $+x-y$ dipole and $-x-y$ quadrupole mode of the optimized M1-cavity. In the case of the dipole mode, the electric field maximum is concentrated at the structure's center. Displacing the emitter by 50 nm from the origin of the lattice, we still retain $|\vec{E}(\vec{r})|^2/|\max\vec{E}(\vec{r})|^2 > 90\%$. In contrast, the electric field of the quadrupole mode vanishes at its center and is maximum at the edge of the four nearest-neighbor air holes. Within the defect structure, $|\vec{E}(\vec{r})|^2/|\max\vec{E}(\vec{r})|^2 > 50\%$ is reached at four equivalent points marked by white points in figure 8.21(b). Efficient coupling to the quadrupole mode would be achieved if the emitter's position is at one of the four field maxima. The required implantation accuracy is 35 nm in x-direction and 70 nm in y-direction. The spatial resolution of the nanoimplanter setup used in this work for nitrogen doping is specified to be 25 nm [425]. This high accuracy is sufficient to implant NV centers at the field maximum of photonic crystal cavity modes.

8.6 Summary

In the first part of this chapter, high resolution creation of a few numbers of the NV centers at the center of a photonic crystal cavity has been demonstrated. The NV centers were deterministically generated using a combined system of a nitrogen ion beam and a pierced atomic force microscopy tip as a beam collimator. The atomic force mi-

croscopy tip was used as a beam collimator as well as to position the beam aperture above the photonic crystal cavity center. The photonic crystal cavities were fabricated via focused ion beam milling in a high-quality ultra-pure (001) diamond membrane that was glued via an adhesion layer on a silicon substrate. Six different cavity geometries of one, three or seven missing holes have been produced with moderate experimental Q-factors up to 320 and mode volumes around one cubic wavelength. Three of the six fabricated photonic structures showed cavity modes near the design wavelength of 637 nm corresponding to the NV^- zero-phonon line. Using confocal spectroscopy, we verify the successful formation of NV centers at the center of every implanted cavity structure. The implantation of the nitrogen ions was restricted to the cavity center. The narrow zero-phonon lines of several single NV centers were identified in spectra taken at cryogenic temperatures. The central wavelengths deviate by up to 2 nm from the ideal value of 637 nm. This variation is attributed to strain in the diamond membrane. At 10 K, we measure a linewidth of 250 GHz of the zero-phonon lines that are inhomogeneously broadened due to spectral diffusion. From the spectra, we deduce the number of implanted NV centers and the NV production yield for every doped structure. We find an overall creation yield of single NV centers of $0.8 \pm 0.1\%$ that is almost independent on the implantation dose. Here, we took into account the size reduction of the aperture hole in the AFM tip upon ion bombardment. For the lowest applied implantation dose of $2.65 \times 10^{13}\,\mathrm{ions/cm^2}$, we created 3 ± 1 single NV centers at the center of a one-missing hole cavity. Reducing the implantation dose by a factor of three, the deterministic creation of one single NV center at the center of a photonic crystal cavity can be achieved.

In the second part of this chapter, we calculated the expected Purcell enhancement of a single shallow implanted NV center when coupled to a photonic crystal cavity mode. To appropriately describe the coupling of the broad-band NV spectrum to a narrow cavity mode, we adopt an extended master-equation model that was recently developed to describe the coupling of a single NV center to a Fabry Pérot fiber cavity [80]. Within this framework, the NV center is approximated as a multi-level system undergoing pure dephasing as a source of broadening. In the incoherent weak coupling regime, the solution to master-equation could be approximated by two coupled rate equations governing the temporal evolution of the emitter and cavity-mode population. From the rate equations, we derive a generalized Purcell factor. Supposing a single implanted NV center coupled to a one-missing hole cavity, we estimate a Purcell enhancement of the zero-phonon line by a factor of 1.32 and of the phonon side band by a factor of 1.7. We deduced the model's input parameters from Lorentzian fits to the measured NV spectrum. Furthermore, we took into account the experimental M1-cavity Q-factor of 160 and a modal volume of $1.1\,(\lambda/n)^3$. Assuming a realistic branching ratio of 3% into the ZPL and a quality factor of $Q = 1,000$, already achieved in this thesis (c.f. section 6), a ZPL Purcell factor of 2.6 is within reach that comes along with a reduced excited state lifetime 4.6 ns compared to 12 ns reported for NV centers in bulk diamond [23]. Beyond the presented model, we discussed the impact of the emitter's quantum efficiency as well as the orientation of the NV dipole moments and its position with respect to the cavity field.

In the near future, we will repeat the implantation of nitrogen ions into photonic crystal structures with a reduced dose. The thorough studies presented in this work on the number of created NV centers and the experimental production yield provide all required information for the successful deterministic formation of one single NV center at the center of a photonic cavity. From our analysis, we infer an optimal implantation dose of $1 \times 10^{13}\,\mathrm{ions/cm^2}$ for the creation of one single NV center. Once a single NV center is identified in the spectrum, the photonic crystal cavity modes can be tuned across the NV emission spectrum using either thermal oxidation (c.f. chapters 7 and 9) to blue tune the cavity modes or gas condensation [87, 88, 401, 402] to red shift the modes. The Purcell enhancement can be deduced from the lifetime change of the NV transition in and off resonance with the cavity mode. To this end, we propose to perform time correlated single photon counting experiments under 532 nm pulsed excitation to deduce the excited state lifetime. Just recently, a green pulsed laser system has been integrated in our optical setup. From an exponential fit to the data, the excited state lifetime can be extracted (c.f. section 4.4). Using time correlated photon counting, we can discriminate very well between the fast decaying background signal of $< 1\,\mathrm{ns}$ [413] and the slower NV decay time. For single NV centers in bulk diamond an excited state lifetime of $\sim 12\,\mathrm{ns}$ [23] has been measured, which can be significantly reduced by cavity coupling. From the lifetime reduction the experimental generalized Purcell factor can be evaluated.

To unambiguously prove the existence of one single optical center after nitrogen implantation, several challenges have to be tackled. The first one is the reduction of the important fluorescent background of the diamond membrane. One source of background could be defects induced by the polishing of the diamond membrane's surfaces. By removing the first few micrometers from both diamond surfaces by reactive ion etching in an oxygen plasma, most of the polishing defects should be eliminated [365]. Furthermore, using an argon-chlorine plasma instead of oxygen and SF_6 plasma to thin out the diamond membrane might reduce background luminescence and allow for much smoother surface roughness [366]. The high background measured on the photonic crystal structures is probably related to the focused ion beam milling process, which might be overcome by using reactive ion etching techniques instead of FIB milling to fabricate the photonic crystals. Various etching recipes based on oxygen plasma involving spin-on glass [84, 88, 452–454], silica [132], silicon nitride [83, 87] or metal masks [358] have been successfully applied for the fabrication of photonic structures in diamond.

The second measure concerns the exact position of the implanted NV center within the cavity. Based on the photoluminescence spectra taken at the center of the doped cavity structures, we could verify the successful implantation and the number of created NV centers. However, to deduce their exact position, the optical resolution of our confocal microscope setup is not sufficient. More elaborated techniques based on stimulated emission depletion (STED) [455] would be well suited to determine the NV centers' positions in the photonic crystal cavity with a precision of several nanometers [456, 457] and to deduce the spatial resolution of our implantation setup.

In order to efficiently enhance the emission rate, the XY dipole moments of the NV^- center have to be aligned in the plane of the cavity electric fields. To achieve better

in-plane orientation, it would be favorable to fabricate the photonic crystal structures in the (111)-facet of a single crystal diamond membrane. Furthermore, recent theoretical studies [458] suggested a preferential reorientation of the NV complex in diamond under the presence of high temperature (970°C) and strain. By post-processing the diamond sample, this would allow for optimal alignment and coupling of the NV^- dipoles after ion implantation to the cavity in-plane fields.

Besides the orientation of its dipole moments, the quantum efficiency of a single emitter has a strong impact on the Purcell enhancement. Recently, the quantum efficiencies of single NV centers in nanodiamonds have been successfully deduced using fluorescence lifetime measurements of the emitter as a function of the its distance to a high-reflective silver mirror [447, 448]. As the presence of the mirror changes the local density of states at the emitter's position and hence its lifetime, the quantum efficiency of the NV center can be deduced from the fit to the data. In literature [447, 448], quantum efficiencies of single NV centers hosted in nanodiamonds have been reported that strongly differ from unity and vary from nanocrystal to nanocrystal. Therefore, to correctly estimate the Purcell enhancement of a single NV center, resonantly enhanced by the cavity, it is indispensable to determine the quantum efficiency of the individual emitter.

Chapter 9

Deterministic coupling of a single SiV center to a photonic crystal cavity in diamond

In the previous chapter, we demonstrated the targeted implantation of single NV centers at the center of photonic crystal nanocavities realized in ultra-pure diamond membranes. In this chapter, we pursue a complementary approach starting with a diamond membrane containing single color centers and subsequent alignment and patterning of photonic crystal structures around them. Using active alignment techniques, we here demonstrate for the first time deterministic coupling of a single SiV center to an all-diamond photonic crystal cavity. The extraordinarily narrow emission line of the SiV center allows for the study of cavity quantum electrodynamics effects even at room temperature. Both inhibition and Purcell enhancement of spontaneous emission are presented in this chapter.

As a first step, we identify single SiV centers incorporated during CVD growth in the heteroepitaxial diamond membrane. Using confocal spectroscopy, we locate the SiV position with respect to alignment markers and investigate the emission properties into the zero-phonon line, phonon side bands and near-infrared transitions and determine the orientation of the dipole moment via polarization analysis. Moreover, we prove the single emitter character, deduce the internal population dynamics and evaluate the radiative quantum efficiency of single SiV centers hosted in the diamond membrane. Cross markers next to the SiV centers are subsequently used to pattern a photonic crystal structure with one, three or seven missing holes around the single emitters using focused ion beam milling. This technique allows us to deterministically achieve coupling between a single color center and a photonic crystal cavity. We study the persistence of the SiV spectral properties upon FIB milling and demonstrate the inhibition of spontaneous emission via the photonic band gap effect for single emitters placed in a periodic photonic lattice. From the measured data, we deduce the experimental Purcell factor F_{PhC} of the photonic crystal lattice. As a next step, we demonstrate controlled cavity-coupling of

single SiV centers to a photonic crystal cavity mode. The cavity modes are tuned across the entire SiV emission spectrum using the digital etching technique already applied in chapter 7. The controlled room temperature coupling gives rise to a Purcell enhancement of spontaneous emission coming along with a significant increase in the intensity and a modification of the internal population dynamics of the single SiV centers. We analyze in detail the emitter-cavity coupling Purcell factor F_{cav}, for which all parameters are deduced from independent measurements confirming a perfect agreement of the experimental observations with theoretical predictions. From the measured internal population dynamics, we evaluate the change in the radiative quantum efficiency of the emitter via inhibition due to the photonic band gap effect or via Purcell enhancement in resonance with a cavity mode. Moreover, we show precise polarization control of the SiV emission angle by tuning a photonic crystal cavity mode into resonance.

9.1 Single SiV centers in heteroepitaxial diamond membranes

In this section, we identify and characterize single SiV centers in heteroepitaxial diamond membranes. We investigate the spectral properties including the central position and linewidth of the zero-phonon line, phonon side bands and near infrared transitions. Polarization analysis in emission and absorption allows us to determine the orientation of the SiV dipole moment, which is essential to achieve efficient emitter cavity coupling. We detect the maximum single photon count rate at saturation and verify the single emitter character using intensity auto-correlation measurements. From power-dependent $g^{(2)}$ functions, we extract internal population dynamics as well as the spontaneous emission rate, the excited state lifetime and the radiative quantum efficiency of single SiV centers in the diamond membrane. The thorough analysis of the SiV emission properties is the basis to quantify modification of spontaneous decay due to cavity-coupling.

As a starting material, we use a heteroepitaxial diamond films with a thickness of $10\,\mu$m, grown on a silicon (001) substrate via iridium/yttria-stabilized zirconia buffer layers in between [348] (c.f. chapter 6). During the growth process a small amount of silicon is incorporated into the diamond film forming, together with an adjacent vacancy, optically active single SiV centers. To obtain a freestanding diamond membrane, the silicon substrate and buffer layers are removed from beneath (c.f. chapter 6) and the diamond film is thinned out from $10\,\mu$m to $270 - 400\,$nm using reactive ion etching in an oxygen plasma. To locate single emitters, cross markers are milled into the diamond membrane via focused ion beam milling. During the patterning, the color centers in the diamond membrane are protected by a 80 nm-chromium layer that is wet-chemically removed afterward. As a final step, the sample is annealed at 1,000°C and cleaned in H_2O_2:H_2SO_4.

We use confocal microscopy scans to locate and identify single SiV centers within the diamond membrane as bright spots. To this end, a continuous wave laser at a wavelength of 660 nm is focused by a microscope objective (numerical aperture 0.8) onto the sample whose position is scanned with respect to the excitation beam. During the scanning, the

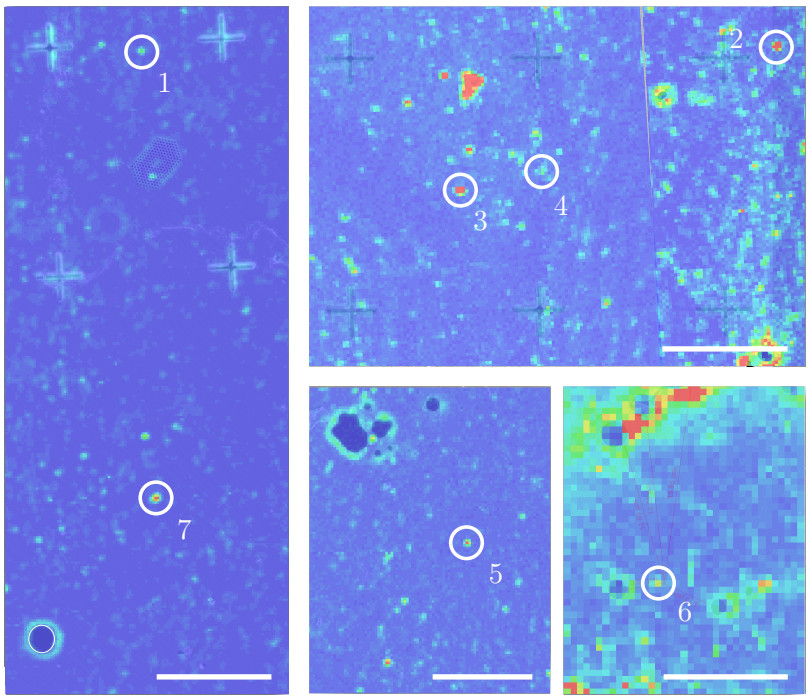

Figure 9.1: Confocal fluorescence scans of the diamond membrane with excitation 660 nm: Single emitters are stick up as bright, localized spots. The numbered fluorescence spots are identified as single SiV centers and are investigated further. From the scans, we deduce an average density of 2 single SiV centers per $20 \times 20\,\mu\text{m}^2$. Cross markers or holes in the membrane are used subsequently as positioning markers. Scale bars: 10 μm.

fluorescence is collected by the microscope objective, separated from the excitation light, and coupled into a single mode fiber and detected by single photon counters. As SiV centers exhibit a narrow emission line around 738 nm, we apply band pass filters in front of the detectors with high transmission in the range 700 to 720 nm or between 730 and 750 nm. For details on the optical setup see chapter 4. Figure 9.1 shows an example of fluorescence maps collected on the thinned diamond membrane. Several localized bright spots (numbered 1-7) are observed in the fluorescence scans that are investigated further and are identified later in this chapter as single SiV centers. From the scans, we deduce an average density of 2 single SiV centers per $20 \times 20\,\mu\text{m}^2$. To identify the bright spots as SiV centers, the spectrum is recorded at these points using a grating spectrometer combined with a nitrogen-cooled CCD camera. Figure 9.2 displays the room-temperature spectra recorded at positions $1-5$ marked in the fluorescence scans (Fig. 9.1). All spectra reveal an intense zero-phonon line with low phonon side band emission and low fluorescence background contributions of the diamond membrane. In the following, we will analyze in more detail the ZPL position and linewidth as well as the narrow phonon sideband features.

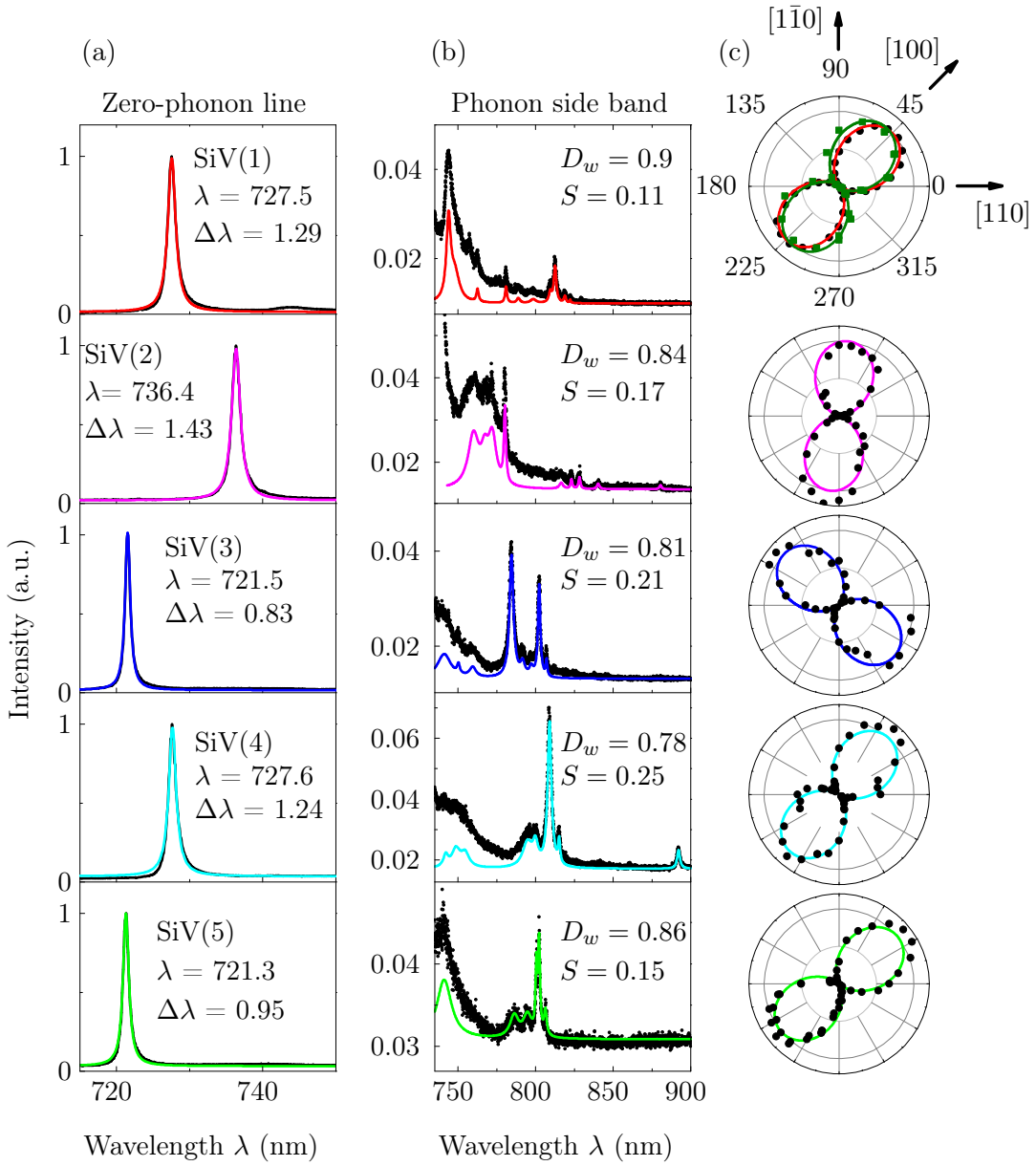

Figure 9.2: Spectra and polarization analysis of selected single SiV centers in the diamond membrane: (a) Zero-phonon lines and (b) phonon side bands of the SiV centers. The central position λ and linewidth $\Delta\lambda$ of the SiV ZPL are given in nm. The spectra are normalized to the ZPL maximum. Black: recorded spectra, Color: Lorentzian fits to the ZPL or multipeak fits to the PSB after baseline subtraction. (c) Polar plots of the ZPL emission. All SiV centers show a preferential polarization along the $\langle 100 \rangle$ or $\langle 110 \rangle$ crystallographic axis of the diamond lattice. For the SiV(1) center, polarization-dependent absorption measurements are additionally shown in green. Dots: data, solid lines: fits.

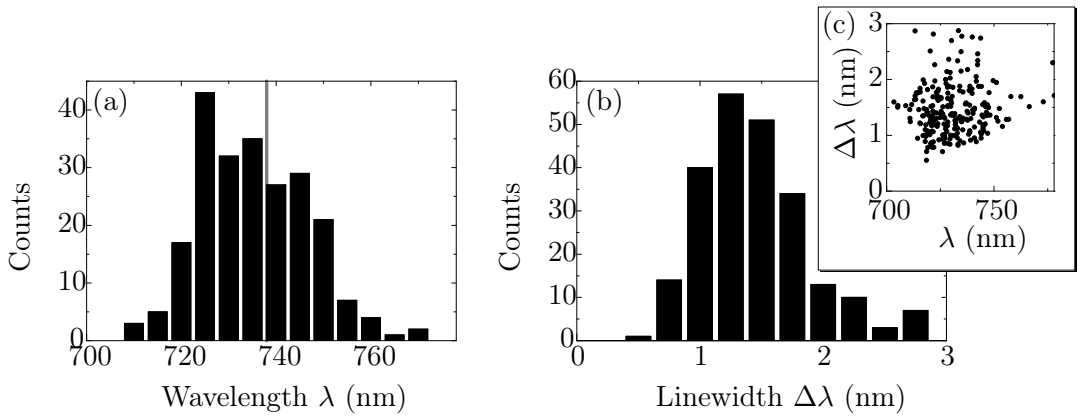

Figure 9.3: Central wavelengths and linewidths of SiV centers incorporated in the diamond membrane: (a) Histogram of the observed ZPL positions with a mean value of 734 nm and a standard deviation of 12 nm. The dark gray line marks the ideal ZPL position at 738 nm. (b) Histogram of the ZPL widths ranging from 0.55 to 3 nm with the most frequent width of 1.35 nm and a standard deviation of 0.4 nm. (c) Linewidth as a function of the spectral position. No correlation is found between the two quantities.

Zero-phonon line

The central position of the SiV zero-phonon lines observed in figure 9.2(a) varies between 720 and 740 nm with linewidths of $\Delta\lambda = 0.8 - 1.4$ nm. More comprehensive statistics on the ZPL positions and linewidths evaluated from 236 spectra are shown in figure 9.3. We find ZPLs in the spectral range between $710 - 770$ nm with a mean value in position at 734 nm and a standard deviation of 12 nm. The spectral interval is slightly blue shifted and broadened compared to data reported for single SiV centers hosted in nanodiamonds [227]. Neu et al. [227] found a mean value in position of 742.5 nm with a standard deviation of 5.1 nm. The reason for the narrower bandwidth might be attributed to the fact that they restricted their analysis to the spectral window of $730-750$ nm by using appropriate band pass filters in front of the single photon counters. Anyway, our reference measurements on single SiV centers in nanodiamonds on iridium comparable to those samples used by Neu et al. [227] equally reveal ZPL wavelengths down to 710 nm and up to 760 nm coinciding with the spectral range plotted in figure 9.3(a) for SiV centers in the thinned diamond membrane. The ZPL linewidths of the investigated SiV centers extends from 0.55 to 3 nm with a mean value at 1.35 nm and a standard deviation of 0.4 nm (Fig. 9.3(b)). The data are in good agreement with the widths found by Neu et al. [227]. Figure 9.3(c) displays the measured linewidths as a function of the spectral position. We do not find any correlation between the two quantities. Narrow and broad ZPL linewidths are observed across the whole spectral range.

The large spread in the central ZPL position is probably related to material strain. The presence of tensile strain in the heteroepitaxial diamond membrane was already indicated by Raman spectroscopy in chapter 6. Sternschulte et al. [233] studied the

impact of uniaxial stress on the SiV fine structure. To this end, the sample was cooled to cryogenic temperatures and stress was applied along the ⟨100⟩ diamond direction. Under stress, the four lines of the SiV fine structure exhibit different wavelength shifts ranging from -3.3 nm/GPa to 4.4 nm/GPa [233]. These stress measurements demonstrate the high sensitivity of the SiV ZPL to material strain and strongly suggest that tensile strain locally experienced by the color center is indeed responsible for the observed broad distribution of the ZPL positions observed for our diamond membranes. Unfortunately, comparable stress measurements at room-temperature or along other crystallographic directions are missing, precluding qualitative correlation between of the magnitude of the local strain field and the individual SiV line shifts. The significant sensitivity of the SiV electronic transitions to the surroundings potentially enables coupling to mechanical resonators and allow for the study of energy level shifts induced by the motion of a macroscopic cantilever as it has been recently demonstrated for NV centers [459, 460].

Phonon sidebands

Even at room-temperature, the SiV center exhibits weak vibronic side band emission. Figure 9.2(b) shows the side band spectra of the five selected SiV centers. The spectra are normalized to the ZPL maximum. On top of the broad sideband background in the one-phonon region ($0 - 1326\,\mathrm{cm}^{-1} \cong 790\,\mathrm{nm}$), several narrow peaks with a width down to 1.25 nm are observed whose positions and linewidths strongly vary between different spectra. In general, electronic transitions of a color center can couple to the vibrations of the undisturbed diamond lattice or to (quasi)local modes of the defect atom and its neighboring carbon atoms [227]. For the SiV center, sideband features with energies at 42, 64, 80, 100, 125, 148, 155, 165 and 183 meV with respect to the SiV ZPL have been reported in literature. For a summary see publication [227] and references herein. Lattice vibrations are restricted to the energy range between 70 and 165 meV [227, 461–463], determined by the phonon density of states of diamond at high symmetry points of the Brillouin zone. Hence, sidebands outside this interval have been attributed to (quasi)local modes of the defect center [227]. In recent experiments, the sideband peak at 64 meV has been assigned to a local vibrational mode of the Si atom oscillating along the ⟨111⟩ symmetry axis [226, 464]. Figure 9.4 shows a detailed view of the vibronic sidebands plotted as a function of their energy shift with respect to the individual ZPL of five selected single SiV(1)-SiV(5) centers. The peak energies coincide well with vibronic energies reported in literature (indicated as gray lines in Fig. 9.4) and the spectral range of phonon sidebands discovered for single SiV centers in nanodiamonds [227]. Moreover, except for the SiV(5) center, all spectra in figure 9.2(b) reveal a distinct peak at energies between $63 - 70$ meV (indicated by purple line in Fig. 9.4), probably attributed to the local vibrational mode of the SiV atom.

A measure of the electron-phonon coupling strength is the Debye-Waller factor or the Huang-Rhys factor. The Debye-Waller factor D_w is defined as the ratio of the integrated intensity I_{ZPL} of the ZPL to the overall intensity I_{tot} including phonon side bands [162]: $D_w = I_{\mathrm{ZPL}}/I_{\mathrm{tot}}$. The Huang-Rhys factor is defined as $S = -\ln(I_{\mathrm{ZPL}}/I_{\mathrm{tot}})$ [214, 465]. The Debye-Waller (Huang-Rhys) factor varies between 0 (∞) and 1 (0),

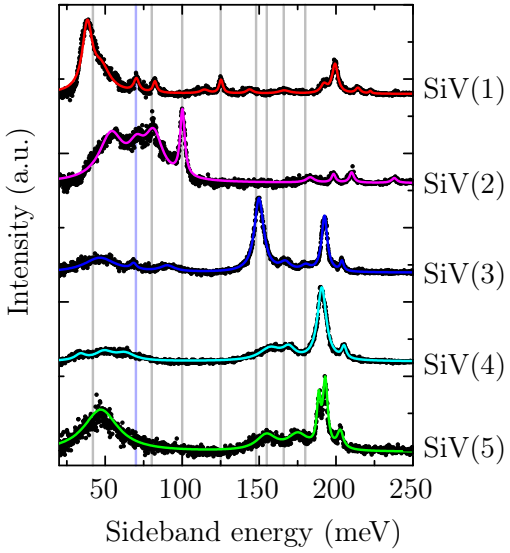

Figure 9.4: Phonon sidebands of five SiV centers plotted as a function of their energy shift with respect to the zero-phonon line. The narrow peaks observed in the sideband regime coincide well with the vibronic energies at 42, 64, 80, 100, 125, 148, 155, 165 and 183 meV reported in literature [227], which are indicated by gray solid lines. The sideband at 64 meV (purple line) has recently been attributed to a local vibrational mode of the Si atom.

where a unity Debye-Waller or equivalently a vanishing Huang-Rhys factor indicate no coupling to vibronic modes. By fitting the spectra with multiple Lorentzians after careful background subtraction, we extract the intensity emitted into the zero-phonon line and phonon sidebands. As displayed in figure 9.2(b), the selected SiV centers incorporated in the thinned diamond membrane show Debye-Waller factors of $D_w = 0.77 - 0.9$ corresponding to Huang-Rhys factors of $S = 0.25 - 0.11$. A Debye-Waller factor of 0.9 symbolizes that up to 90% of the photons released by the SiV center are emitted into the ZPL. In contrast, the emission into the phonon side bands is very weak. The intensity of the one-phonon side band amounts to 11% relative to the ZPL intensity (with $S = 0.11$). Comparable large branching ratios into the zero-phonon line have been found for single SiV centers located in nanodiamonds [25, 227] and in single crystal diamond [26] as well as for SiV ensembles in polycrystalline diamond films [464]. Due to its bright and narrow emission into the ZPL and the weak phonon side band contribution, the SiV center is an ideal candidate for coupling to narrow cavity modes.

Near-infrared transition

Beyond the phonon sidebands, the spectra of all SiV centers in figure 9.2(b) exhibit remarkably narrow lines down to $\Delta\lambda = 1.1$ nm in the wavelength range between 802 and 840 nm (corresponding to $183 - 238$ meV in Fig. 9.4). Moreover, for the SiV(2) and SiV(4) centers narrow peaks at 880 nm and 892 nm are observed in the spectra (Fig. 9.2(b)). Recent studies show strong evidence that the lines at $820 - 845$ nm are

attributed to additional purely electronic transitions of the SiV center [228, 229]. Using intensity cross-correlation measurements between the zero-phonon line and the line at 822.7 nm, Neu et al. [228] could show that both peaks originate from the same single SiV center. They proposed an extended SiV level scheme involving a second excited state and the same ground state as the ZPL to model the near-infrared transitions. Based on internal population dynamics, they exclude that the near-infrared transition is a vibronic side band or that it arises due to a transition from/to the metastable (shelving) state [228]. The assumption of purely electronic transitions is supported by a previous work by Sittas et al. [466]. They discovered significant spectral narrowing upon cooling of three lines at 776, 797 and 812 nm of an SiV ensemble. Owing to the spectral change, Sittas et al. interpreted these features as electronic transitions. Moreover, recent absorption measurements on single crystal diamond containing large ensembles of SiV centers revealed absorptions lines in the range of $830 - 860$ nm [224], which indicates that a ground state is involved in this transition. As only purely electronic transitions can be observed both in absorption and emission, all these studies strongly suggest that the near-infrared lines are electronic rather than vibronic transitions. Based on these studies, we tentatively attribute the lines in the near-infrared range observed in spectra 9.2(b) to additional electronic transitions of the SiV centers. Although, the absolute central peak positions are slightly shifted to smaller values compared to the range $820 - 845$ nm assigned to the near-infrared transition [227, 228], the energies of $183 - 238$ meV with respect to the zero-phonon line perfectly accord with literature [227]. In addition, the measured linewidths of $1.1 - 2.9$ nm deduced from the multipeak fits in figure 9.2(b) are conform with stated data [227]. Due to limitations in the detection efficiency of their setup, Neu et al. [227] did not discover lines beyond 860 nm. Hence, it is unclear if the lines at 880 and 892 nm detected for the SiV(2) and SiV(4) are equally attributed to electronic transitions. Further investigations are required to support this assumption.

Polarization characteristics

For future coupling experiments to a photonic crystal cavity, the orientation of the color center's dipole moment plays a substantial role. In principle, the dipole orientation can be deduced from polarization characteristics of the fluorescence light [467]. Lethiec at al. [467] developed a complex analysis requiring detailed knowledge of the objective numerical aperture, the 1D or 2D nature of the emitting dipole, and the environment close to the dipole, to the deduce the orientation of CdSe/CdS nanocrystals. For chromium related defect centers, the dipole orientation in three dimensions has been determined using defocused imaging in the back focal plane of the microscope objective and comparing the experimental results with numerical simulations [158]. Unfortunately, our experimental settings do not allow for a direct three-dimensional analysis of the dipole moment. Here, we investigate the polarization characteristics of the emitted fluorescence light as well as the polarization-dependent absorption of the single SiV centers in the (001) plane of the diamond membrane. Together with previous results reported in literature, this allows us to draw essential conclusions on the dipole orientation of the

SiV	$\phi_{\max}$	Visibility (%)	
1	52.5°	97	Absorption
1	45.0°	97	
2	82.7°	96	
3	137.7°	94	Emission
4	49.7°	94	
5	38.5°	95	

Table 9.1: Polarization characteristics of the five investigated single SiV centers in absorption and emission: The angle $\phi_{\max}$ at maximum intensity and the visibility are deduced from the sine-square fits to the raw data in figure 9.2(c).

single SiV centers.

The polarization of the emitted light is measured by placing a linear polarization analyzer in the detection path of our confocal setup and detecting the count rate of the filtered ZPL via the APDs as a function of the azimuthal angle ϕ. Bandpass filters in front of the APDs filter the ZPL signal in a spectral window of 10 nm. Moreover, in the case of the SiV(1) center, we measure the polarization in absorption. To this end, the polarization angle of the excitation laser light is rotated via a half-wave-plate while registering the count rate in dependence of the polarization angle ϕ. Again, the ZPL signal is filtered in a spectral window of 10 nm. The polar plots of the single SiV(1)-SiV(5) centers in figure 9.2(c) clearly reveal linearly polarized emission with a preferential orientation along 0°, 45°, 90° or 135°. Similarly, the absorption characteristic of the SiV(1) center shows a sinusoidal variation. Within the detection precision of 10°, the angle at maximum absorption coincides with the angle at maximum emission intensity. The large error of 10° is related to the fact that between the measurements, the sample is removed and mounted again on the sample holder resulting in a relative angle discrepancy of a few degrees. The raw data are fitted by a sine-square function. Please note that we do not subtract any background contributions or dark counts of the APDs. From the maximum $I_{\max}$ and minimum intensity $I_{\min}$, we extract the visibility:

$$\text{Visibility} = \frac{I_{\max} - I_{\min}}{I_{\max} + I_{\min}} \tag{9.1}$$

The visibilities for each polarization measurement together with the angles $\phi_{\max}$ at which the intensity is maximum are listed in table 9.1. The linear polarization characteristics of all single SiV centers exhibit high visibilities of $94-97\%$ in emission. The fit to the polarization-dependent absorption of the SiV(1) center shows a visibility of 97%. The high visibility suggest that the absorption and emission process are dominated by a single dipole transition of the SiV center. Furthermore, from the almost identical angles $\phi_{\max}$ in absorption and emission, we conclude absorption and emission dipole moments to be aligned parallel to each other within the experimental error. Similar results have been found for single SiV centers at room-temperature hosted in nanodiamonds grown

on iridium [227]. Moreover, parallel orientation of emission and absorption dipole moments have been found for chromium related defect centers [155] and single color centers emitting in the near infrared observed after nickel implantation and annealing [444].

As a next step, we would like to investigate the orientation of the SiV dipole moment with respect to the crystallographic axis of the diamond lattice. As the emission in our experiment is collected from the top, we are only able to determine the projection of the SiV dipole into the (001) diamond plane oriented perpendicular to the excitation laser beam. The crystallographic directions of the diamond membrane have been determined using electron back scattering. For our experimental settings, an angle of $\phi = 0°$ ($45°$) corresponds to an orientation along the [110] ([100]) crystallographic direction in the (001)-diamond plane. In figure 9.2(c), the projected dipole moment of the SiV center is preferentially alined either along the $\langle 100 \rangle$ or $\langle 110 \rangle$ diamond axis. This is conform with experimental findings on single SiV centers hosted in nanodiamonds on iridium [227] and with SiV ensemble measurements in diamond films [468]. However, all these host materials exhibit important material strain. Group theoretical calculation predict an alignment of the SiV dipole moment along the $\langle 111 \rangle$ axis [222]. Recent polarization analysis of single SiV centers in low-strain (001) single crystal diamond support this prediction [26, 223, 225]. At room-temperature, the SiV ZPL is linearly polarized along the $\langle 110 \rangle$ crystal axis corresponding to the projection of the $\langle 111 \rangle$ direction in the (001) diamond plane [26]. At cryogenic temperatures, the four fine structure lines can be grouped in two subsets. The inner lines are polarized parallel to each other and perpendicular to the outer ones. All polarization axes appear along the $\langle 110 \rangle$ direction in the (001) diamond plane [223, 225]. The inner lines have been attributed to a dipole moment $d_{\parallel}$ aligned along the $\langle 111 \rangle$ axis, whereas the outer lines have been assigned to a dipole moment $d_{\perp}$ perpendicular to the $\langle 111 \rangle$ direction [223, 225]. From the intensity ratio, Rogers et al. [223, 225] concluded, $d_{\parallel}$ being the dominant dipole moment four times stronger than $d_{\perp}$. Under the influence of strain, theoretical simulations of the SiV center electronic transitions [223] predict that the polarization orientation rotates away from $\langle 110 \rangle$ toward $\langle 100 \rangle$. Both polarization directions have been found for the here investigated single SiV centers suggesting severe material strain present in the diamond membrane. The presence of material strain has already been identified using Raman spectroscopy (c.f. section 6.1.5). Remarkably, the ZPL of the SiV(2) center whose central position is close to 738 nm, suggesting low material strain, is the only center exhibiting a linear polarization along the $\langle 110 \rangle$ axis. The other single SiV centers in figure 9.2(c) with ZPLs strongly blue shifted probably by the presence of strain show linear polarizations along $\langle 100 \rangle$. However, more reliable statistics are required to confirm a possible correlation between the spectral position and the linear polarization of the SiV ZPL.

Saturation measurements

After having discussed the spectral properties and polarization characteristics, we would like to study the suitability of the SiV centers as single photon sources. An essential figure of merit of a single photon source is the maximum count rate obtained at sat-

uration. To this end, we detect the photon count rate via the APDs as a function of the excitation power measured in front of the microscope objective. As shown in figure 9.5(a), the count rate of all five SiV centers saturates for high excitation powers. In figure 9.5(a), the count rate detected on the diamond membrane next to the single SiV centers is shown for reference by the gray dots. All measurements reveal high signal to noise ratios of $20-120$. To extract the maximum SiV count rate I^{∞} at saturation and the saturation power P_{sat}, we fit the measured data using the following equation:

$$I = I^{\infty}\frac{P}{P+P_{\mathrm{sat}}}. \tag{9.2}$$

The obtained fit parameters are given for each SiV center in figure 9.5(a) in units $[I^{\infty}] = \mathrm{k\,counts/s}$ and $[P_{\mathrm{sat}}] = \mathrm{mW}$. The highest count rate of all investigated centers is detected for the single SiV(1) center yielding $I^{\infty} = 360{,}000\,\mathrm{counts/s}$ with a saturation power of 1 mW. The other four SiV centers selected in figure 9.5(a) exhibit maximum count rates of $I^{\infty} = 70{,}000 - 220{,}000\,\mathrm{counts/s}$ with saturation powers of $P_{\mathrm{sat}} = 0.42 - 0.8\,\mathrm{mW}$. The saturation powers are comparable to literature data on single SiV centers in nanodiamonds [25, 232]. However, the measured count rates are approximately a factor of 20 smaller than the record value of $6.2 \times 10^6\,\mathrm{counts/s}$ reached for a single SiV center hosted in a nanodiamond grown on an iridium substrate [55]. The reason for the lower count rate is partially attributed to the smaller collection efficiency by the microscope objective, when the emitter is hosted in bulk compared to a nano-size particle. For dipoles oriented parallel to the sample surface, simulations predict up to 20-times higher collection efficiencies of the SiV emission in nanodiamond on iridium compared to bulk [55]. Beside the collection efficiency, the actual count rate of a single color center depends on its internal population dynamics and especially on its quantum efficiency. The quantum efficiency in its turn significantly depends on the emitter's surroundings as will be discussed on page 269. In the following, we deduce the internal population dynamics and the quantum efficiency exemplarily for the single SiV(2) and SiV(3) centers hosted in the thin diamond membrane.

Intensity correlation measurements

To prove the single emitter character of the identified SiV centers and to deduce the internal population dynamics, we perform intensity correlation measurements, i.e. $g^{(2)}$ measurements, using a Hanbury Brown and Twiss interferometer with two avalanche photo diodes (APDs). For details on the setup, see chapter 4. The excitation power applied during the individual intensity correlation measurement is well below saturation as marked in the saturation curve by the yellow star. The $g^{(2)}$-functions of the five SiV centers SiV(1), SiV(2), SiV(3), SiV(4) and SiV(5) are displayed in figure 9.5(b,c). For long decay times τ, all experimental $g^{(2)}$-functions exceed one. This bunching behavior can be explained by a three level model of the SiV center involving a ground state, an excited state and one metastable (shelving) state (c.f. section 3.5). At small times τ, an antibunching dip with $g^{(2)}(0) < 0.5$ unambiguously proves that the investigated SiV centers are indeed single emitters. The fact that the correlation function does not completely vanish at zero time delay, is mainly attributed to the limited temporal resolution

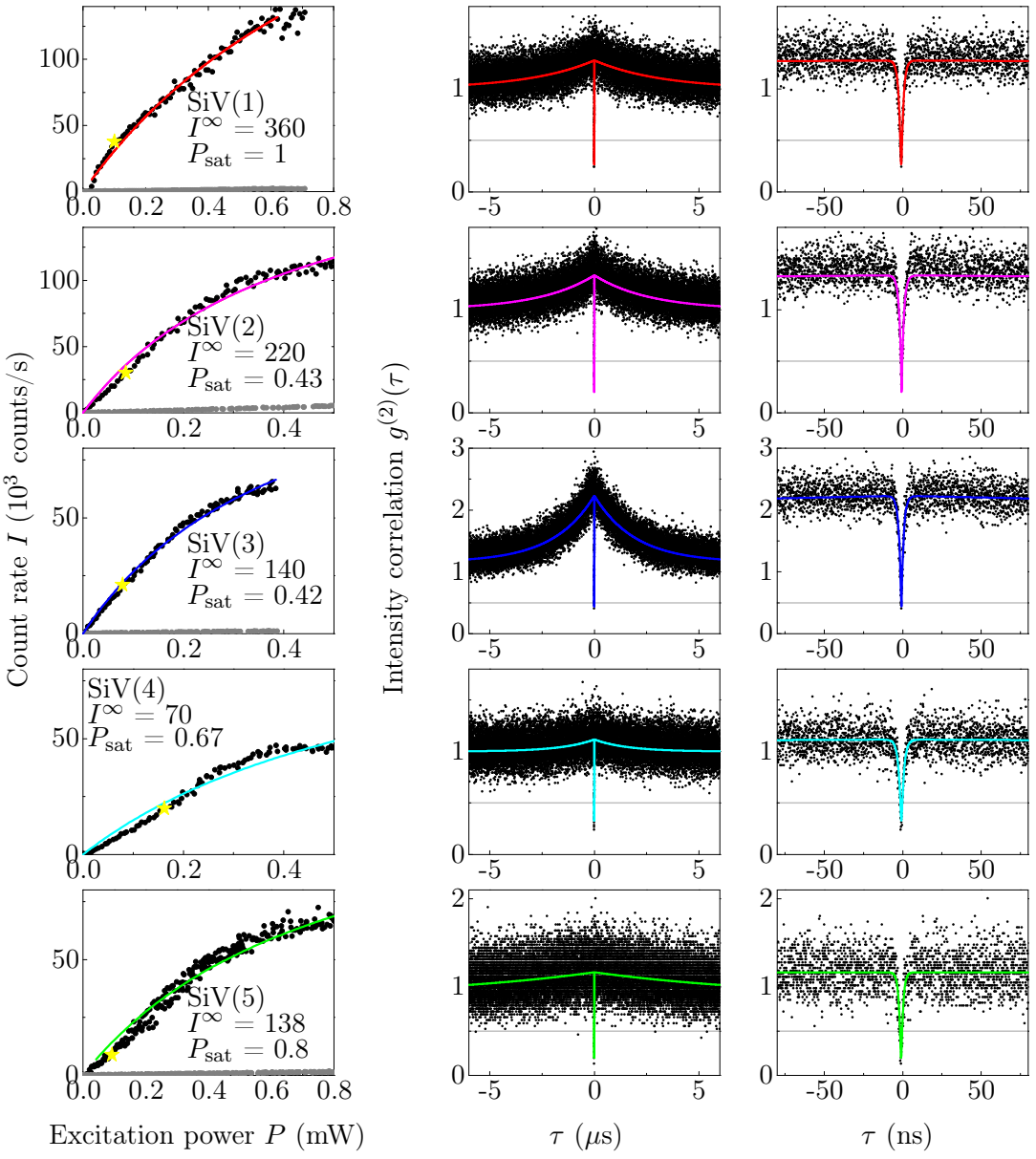

Figure 9.5: Saturation measurements and intensity correlation functions of selected single SiV centers: (a) Photon count rate as a function of the excitation power P. For reference, background contributions are shown in gray. For high powers, the SiV count rates saturate. From the fit (solid line) using equation (3.20), we obtain the saturation count rates I^∞ given in k counts/s and the saturation powers P_{sat} in mW. The yellow star indicates the power applied for the $g^{(2)}$ measurements in (b,c). (b) For large times τ, the $g^{(2)}$ functions show a bunching behavior. (c) Detailed view of the antibunching dip at small delay times with $g^{(2)}(0) < 0.5$ revealing single emitter character of the investigated color centers. (b,c) Dots: measured data, solid line: fit according to equation (3.7) convoluted with the setup instrument response function.

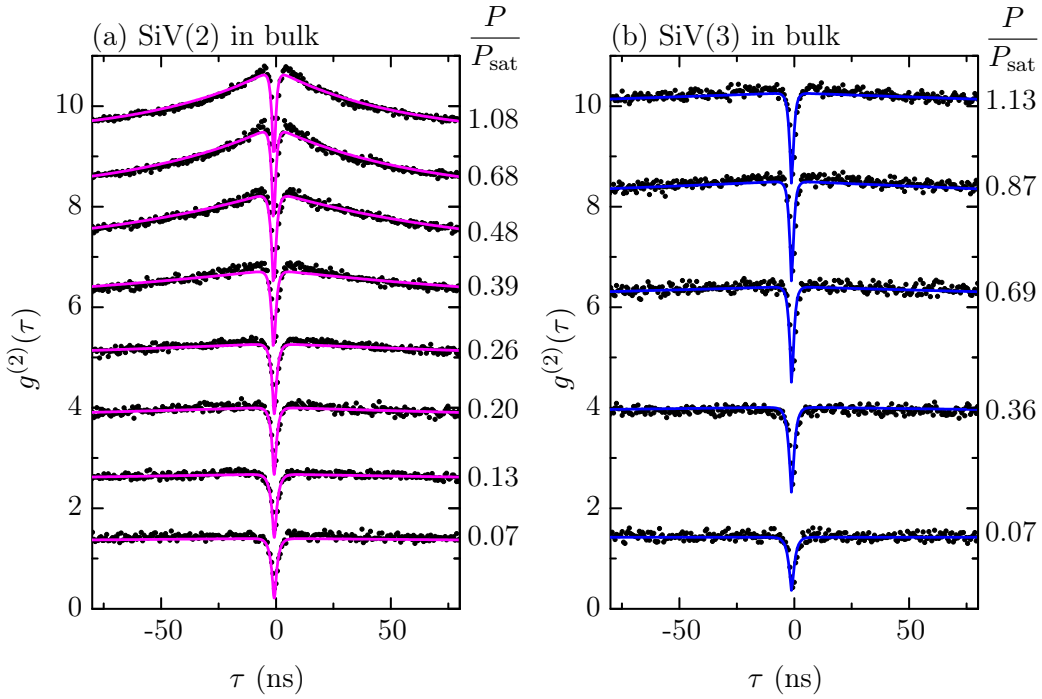

Figure 9.6: Intensity correlation measurements of the single (a) SiV(2) and (b) SiV(3) center for various excitation powers P/P_{sat}. For clarity, the curves have been shifted by 1.2 points in (a) and by 2 in (b). Dots: measured data, solid lines: fit according to equation (3.7) convoluted with the setup instrument response function.

of the APDs with a timing jitter of 296 ps (c.f. chapter 4). Background contributions of the diamond membrane play only a minor role as already seen in the saturation measurements. Based on the three level model, we fit the measured $g^{(2)}$-functions with two exponentials according to equation (3.7) including background contributions, convoluted with the instrument response function of our setup to account for the timing jitter of the APDs. The theoretical fits are shown in figure 9.5(b,c) by solid lines. From the fits, we extract the times τ_1 and τ_2 governing the antibunching and bunching time scales as well as the parameter a. We obtain $\tau_1 = 1.2-1.56$ ns for the antibunching time of the SiV(1)-SiV(5) centers. In contrast, the parameters τ_2 and a governing the bunching dynamics strongly vary between the centers. The $g^{(2)}$ functions of the SiV(2) and SiV(3) centers both performed at similar excitation powers with respect to P_{sat} reveal significantly different bunching dynamics. In the following, we measure the intensity correlation function for various powers and investigate the power-dependence of the fit parameters τ_1, τ_2 and a exemplarily for the SiV(2) and SiV(3) centers. The power-dependent parameters enable deeper insight into the internal population dynamics of the single color centers.

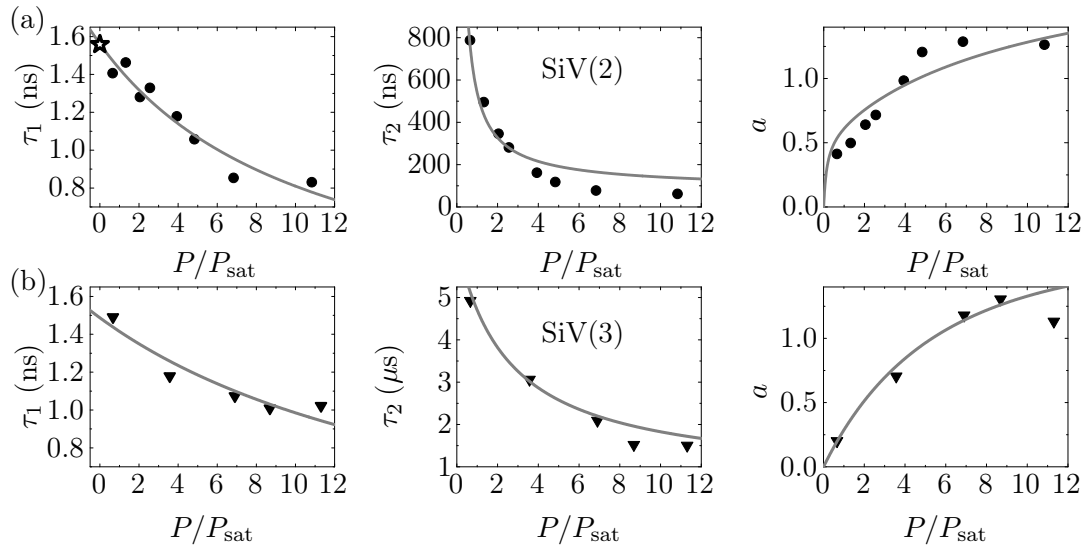

Figure 9.7: Population dynamics of the single SiV(2) and SiV(3) centers in the diamond membrane: Power-dependent model parameters τ_1, τ_2 and a of (a) the SiV(2) center and of (b) the SiV(3) center extracted from the fits to the measured $g^{(2)}$-functions for various excitation powers P/P_{sat}. Dots: extracted parameters, solid lines: theoretical power-dependence of the model parameters.

Internal population dynamics

To deduce the internal population dynamics of the single SiV(2) and SiV(3) centers, we measure the $g^{(2)}$-functions for various excitation powers P/P_{sat} as shown in figure 9.6. With increasing power, the bunching becomes strongly pronounced. From the fit to the data using equation (3.7) convoluted with the instrument response function, we extract the parameters τ_1, τ_2 and a that are plotted in figure 9.7 as a function of the normalized excitation power P/P_{sat} applied during the individual correlation measurements. With increasing power, the τ_1 and τ_2 times diminish, whereas a raises. While the parameters τ_1 and a are comparable for both SiV centers, the τ_2 times significantly differ. For low powers, τ_2 of the SiV(2) center reaches 800 ns, whereas for the SiV(3) center, this parameter is 6-times larger. Fitting the power dependent parameters τ_1, τ_2 and a in figure 9.7 according to equations (3.14), we extract the limiting values τ_1^0, τ_2^0, τ_2^∞, a^∞ as well as the parameters σ, c and d. The fit results are summarized in table 9.2. Here, the superscripts ^{0} and $^\infty$ denote the limits for vanishing and high power, respectively. The theoretical fit curves, displayed as solid lines in figure 9.7, match the experimental data sufficiently well. The slight oscillatory behavior of the measured parameters is mainly attributed to an uncertainty in the signal to noise ratio included in the fit routine of the $g^{(2)}$ function and in a slight drift in the alignment of the optical setup. This drift is hardly noticed during the experiment especially for high powers, as the SiV count rate does not significantly change for powers well above saturation. Once the fit parameters are obtained, we can calculate the decay rates k_{12}, k_{21}, k_{23} and k_{31} using equation (3.19).

SiV	τ_1^0 (ns)	τ_2^0 (μs)	τ_2^∞ (ns)	a^∞	σ $\left(\frac{\text{MHz}}{P_{\text{sat}}}\right)$	k_{21} (MHz)	k_{23} (MHz)	k_{31}^0 (MHz)	d (MHz)	c (P_{sat})
2	1.56	2.5	62	2.0	60	630	11.0	0.40	4.9	3
3	1.49	6.3	640	1.4	34	671	0.9	0.16	0.5	50

Table 9.2: Limiting values and decay rates governing the population dynamics of the SiV(2) and SiV(3) centers in the diamond membrane. The limiting values and rate coefficients are deduced from figure 9.7 using a three level model including a power-dependent deshelving rate $k_{31} = dP/(P+c) + k_{31}^0$ and a pump rate $k_{12} = \sigma P$.

Here, we assume a pump rate $k_{12} = \sigma P$ increasing linearly with the excitation power P, a constant spontaneous decay rate k_{21} from the excited state $|2\rangle$ to the ground state $|1\rangle$, a constant rate k_{23} into the shelving state $|3\rangle$ and a power-dependent deshelving rate $k_{31} = dP/(P+c) + k_{31}^0$. For the SiV(2) and SiV(3) centers, the rates are listed in table 9.2. Both color centers exhibit comparable decay rates k_{21}, significantly exceeding the other transition rates at low excitation power. In contrast, the rates k_{23} and k_{31} involving the shelving state strongly differ for the two SiV centers by one order of magnitude. This discrepancy is reflected in the different bunching dynamics of the $g^{(2)}$ functions shown in figure 9.6.

In the limit of vanishing excitation power, the τ_1 time approaches the lifetime of the excited state T_1 [21, 209, 236]. According to limiting times τ_1^0 listed in table 9.2, we obtain for the SiV(2) center a lifetime of 1.56 ns and for the SiV(3) center a lifetime of the excited state of 1.49 ns. In the next section, we confirm the excited state lifetime deduced from the internal population dynamics by measuring the lifetime of the SiV(2) center under pulsed excitation. Moreover, we give a brief overview of excited state lifetimes reported in literature for SiV centers.

Lifetime measurement

To confirm the excited state lifetime deduced from the population dynamics in the limit for vanishing excitation power, we perform time correlated single photon counting experiments (c.f. chapter 4). To this end, the SiV(2) center is excited by a pulsed laser with a repetition rate of 80 MHz at a wavelength of 700 nm. The number of photons arriving per time interval $t \pm \Delta t/2$ ($\Delta t = 4$ ps) after the time t with respect to the excitation pulse is detected by an avalanche photon diode and plotted in a histogram shown in figure 9.8. For times $t > 0$ the signal reveals an exponential decay with the decay time equal to the emitter's excited state lifetime. We fit the data by an exponential function convoluted with a Gaussian with a FWHM of 864 ps to account for the instrument response function of our setup (c.f. chapter 4) according to equation (4.7) in section 4.4. From the fit, we obtain an excited state lifetime of the SiV(2) center of $T_1 = 1.56$ ns which is in perfect agreement with the limit τ_1^0 extracted from the population dynamics (c.f. table 9.2). The result from the time correlated single photon

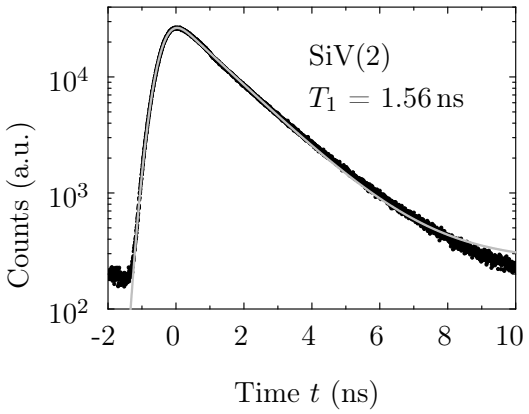

Figure 9.8: Lifetime measurement of the excited state of the single SiV(2) center: Under pulsed excitation, the number of photons arriving after a certain time t in the interval $t \pm \Delta t/2$ ($\Delta t = 4\,\mathrm{ps}$) with respect to the laser pulse are registered and plotted in a histogram. The data are fitted using equation (4.7). From the fit, we extract an excited state lifetime of $T_1 = 1.56\,\mathrm{ns}$ of the SiV(2) center.

counting experiment is shown by a star in τ_1-plot in figure 9.7(a). Hence, the limiting values of the internal dynamics deliver reliable results on the excited state lifetime of single SiV centers.

The excited state lifetime of 1.56 ns for the SiV(2) center and 1.49 ns for the SiV(3) center is slightly larger than the excited state lifetimes determine in chapter 7 for SiV ensembles hosted in heteroepitaxial diamond membranes. The data reported in literature show a significant variation. For single SiV centers in low strain single crystal diamond, an excited state lifetime of 1.28 ns has been determined recently at room temperature that increases to 1.72 ns at 4 K [26]. Ensemble experiments revealed lifetimes of $1-1.3\,\mathrm{ns}$ for SiV centers hosted in polycrystalline diamond films [233] and $2.7-4.0\,\mathrm{ns}$ in homoepitaxial grown diamond [233]. The reduced excited state lifetime of SiV centers in polycrystalline diamond films was attributed to the existence of competitive, non-radiative decay channels associated to grain boundaries or to the presence of strain [233]. In these experiments [233], the lifetime decreased with increasing temperature. For SiV ensembles in a 500 nm-thick diamond membrane placed on a silica substrate, a lifetime of 1.83 ns has been detected [85]. Other ensemble experiments [242] revealed lifetimes of $1.04-1.17\,\mathrm{ns}$ for polycrystalline diamond films on silicon, heteroepitaxial diamond films (comparable to our high-density samples used in chapter 7) and single crystal diamond implanted with SiV centers. Lifetime measurements on polycrystalline diamond films on silica and high-density nanocrystals exhibit slightly smaller times constant of 0.74 and 0.93 ns, respectively [242]. Even smaller lifetimes and an extremely large spread in lifetime have been deduced for single SiV centers hosted in nanodiamonds grown on iridium. Based on the population dynamics summarized by Neu [469], we find four single SiV centers with lifetimes smaller than 0.5 ns, six centers with $\tau_1^0 = 0.5 - 1\,\mathrm{ns}$, three emitters with $\tau_1^0 = 1 - 1.3\,\mathrm{ns}$ and even one center exceeding 5 ns. The results of

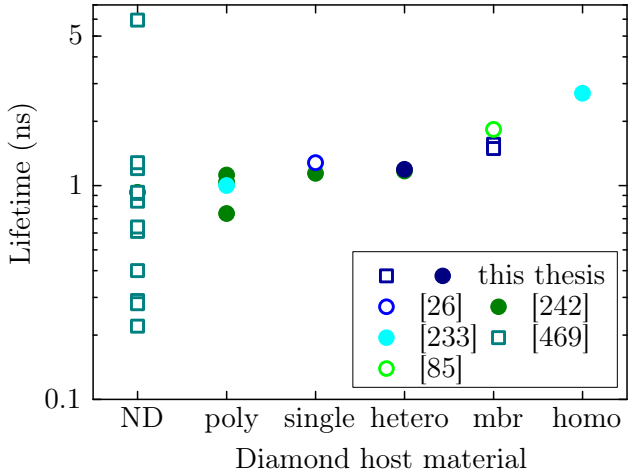

Figure 9.9: Review of excited state lifetimes of SiV centers at room temperature reported in literature for different host materials: ND: nanodiamonds, poly: polycrystalline diamond films, single: single crystal diamond, hetero: heteroepitaxial diamond films, mbr: single crystal diamond membrane, homo: homoepitaxial diamond films. The open (closed) markers indicate measurements on single (ensembles of) SiV centers. Circles (○): Lifetime detected via time correlated single photon counting experiments. Squares (□): Lifetime deduce from internal population dynamics.

the cited literature data are summarized in figure 9.9. All values determined via time correlated single photon counting experiment are show by circles, whereas all lifetimes deduce from internal population dynamics in the limit of vanishing excitation power are symbolized by squares.

The comparison between the data reported in literature reveal that the excited state lifetime is not an intrinsic property of the color center but strongly depends on the diamond host material, i.e. on the distance to the diamond-air interface in bulk [157] and the size of the nanodiamonds [158] as well as on the presence of grain boundaries or material strain [233]. These contributions give rise either to modified radiative or to competing non-radiative recombination rates. Beside the excited state lifetime, the quantum efficiency of the individual emitter is strongly effected by the change of the emitters surrounding as will be explained in the following.

Quantum efficiency of single SiV centers

The quantum efficiency η_{qe} of a single emitter is defined as the ratio of the radiative transitions $\gamma_{\mathrm{rad}} = \gamma_{\mathrm{ZPL}} + \gamma_{\mathrm{PSB}}$ to the total decay rate:

$$\eta_{\mathrm{qe}} = \frac{\gamma_{\mathrm{rad}}}{\gamma_{\mathrm{rad}} + \gamma_{\mathrm{nr}}}, \tag{9.3}$$

where γ_{nr} are non-radiative transition rates. The knowledge of the quantum efficiency is vital for applications requiring single photons on demand [470] as well as for light-matter

interaction in solid-state systems based on the integration of single emitters in microcavities [83, 87, 89] or optical antenna structures [126, 471, 472]. The quantification of the coupling strength, the enhancement in the collection efficiency and the modification of radiative and non-radiative decay rates strongly depend on the emitter's quantum efficiency.

The quantum efficiencies of the most prominent single color centers in diamond have been investigated. Depending on the host material, the quantum efficiency ranges from a few percent up to 0.9. Here, we give a brief overview of the data reported in literature. Recent studies [447, 448] on single NV centers hosted in nanodiamonds reveal quantum efficiencies between 0.25 and 0.9 strongly differing between individual centers. For NV centers in single crystal diamond a quantum efficiency of 0.7 has been deduced from the stimulated-emission cross section in super-resolution microscopy [456]. The quantum efficiency has equally been determined for nickel-related defects, notably for the NE8 center, which has been investigated as single photon source [162–164, 473] and is most probably composed of a nickel atom, two vacancies and four nitrogen atoms. For the NE8 center hosted in single crystal diamond, quantum efficiencies of 0.52 ± 0.2 [163], 0.57 [473] and 0.7 [162] has been found. For chromium-related defect centers in bulk, a quantum efficiency of 0.3 was reported [157], whereas the estimated quantum yields in nanodiamonds strongly vary between different chromium emitters ranging from a few percent to 0.9 [158]. For SiV centers, we are aware of only two studies on the quantum efficiency [55, 413]. Turukhin et al. [413] deduced a quantum efficiency of 0.05 for SiV centers hosted in polycrystalline diamond films. Neu et al. [55] estimated quantum efficiencies between 0.003 and 0.09 for single SiV centers in nanodiamonds grown on an iridium substrate.

In this section, we evaluate the quantum yield of single SiV centers incorporated in the thinned diamond membrane. The analysis is based on internal population dynamics and saturation measurements of the individual color centers, provided that the overall detection efficiency of the setup is known. Under continuous wave laser excitation, the quantum efficiency η_{qe} is given by:

$$\eta_{\mathrm{qe}}^{\mathrm{exp}} = \frac{I^{\infty}}{\eta_{\mathrm{det}} k_{21} n_2^{\infty}}. \tag{9.4}$$

Thereby, we take into account the saturation photon count rate I^{∞} measured with an overall detection efficiency of our setup η_{det} and the maximum steady state population of the excited state [25]:

$$n_2^{\infty} = \frac{1}{1 + \dfrac{k_{23}}{k_{31}^0 + d}}. \tag{9.5}$$

The rates k_{21}, k_{23}, k_{31}^0, d are determined by the population dynamics of the SiV center. In the following, we calculate the quantum efficiencies of the SiV(2) and SiV(3) centers from the saturation count rate and population dynamics determined above.

The overall detection efficiency η_{det} of our setup is a product of the collection efficiency η_{obj} of the emitted photons by the microscope objective, the transmission through

the confocal setup η_{setup} including the detection efficiency of the APDs and the transmission η_{filter} through the applied band pass filters. Considering the limiting case of a dipole emitter placed at the diamond-air interface with parallel orientation, the collection efficiency by a microscope objective (numerical aperture 0.8) has been calculated numerically yielding $\eta_{\text{obj,bulk}} = 3.5 \pm 0.5\%$ [474]. The overall transmission through our confocal setup including the detection efficiency of the APDs has been measured in chapter 4 to be $\eta_{\text{setup}} = 0.14 \pm 0.02$. When performing intensity correlation measurements, the SiV ZPL is filtered via band pass filters in front of each APD. The bandpass filters have a transmission specified by the manufacturer of $\eta_{\text{filter}} = 0.65$ in the wavelength range of $725-735\,\text{nm}$ (for SiV(2)) and $715-725\,\text{nm}$ (for SiV(3)). Based on these factors, the overall collection efficiency of our setup amounts $\eta_{\text{det,bulk}} = (3.3 \pm 0.8) \times 10^{-3}$.

For the SiV(2) center, the saturation measurement yields a count rate of $I^{\infty}_{\text{SiV(2)}} = 220{,}000\,\text{counts/s}$. Taking into account the decay rate $k_{21,\text{SiV(2)}} = 630\,\text{MHz}$ and the excited state population $n^{\infty}_{2,\text{SiV(2)}} = 0.325$, we determine the quantum efficiency of the SiV(2) center in the diamond membrane to be $\eta^{\text{exp}}_{\text{qe,SiV(2)}} = 0.32 \pm 0.08$.

Equivalently, we can evaluate the quantum efficiency of the single SiV(3) center. Considering the saturation photon count rate $I^{\infty}_{\text{SiV(3)}} = 140{,}000\,\text{counts/s}$, the decay rate $k_{21,\text{SiV(3)}} = 671\,\text{MHz}$ and the excited state population $n^{\infty}_{2,\text{SiV(3)}} = 0.42$, the quantum efficiency of the SiV(3) center is determined to be $\eta^{\text{exp}}_{\text{qe,SiV(3)}} = 0.15 \pm 0.04$. To summarize, the experimental quantum efficiencies of the SiV(2) and SiV(3) center are

$$\eta^{\text{exp}}_{\text{qe,SiV(2)}} = 0.32 \pm 0.08, \qquad \eta^{\text{exp}}_{\text{qe,SiV(3)}} = 0.15 \pm 0.04. \tag{9.6}$$

At first sight, the here deduced quantum efficiencies of single SiV centers incorporated in the thin diamond membrane are considerably larger than the quantum efficiencies reported for single SiV centers hosted in nanodiamonds on iridium [55] or for SiV ensembles in polycrystalline diamond film [413]. However, care has to be taken as the available studies on the SiV quantum efficiency cannot directly be applied to our experiments. The reason is that the radiative quantum yield is not solely an intrinsic property of the color center but critically depends on the crystal quality and the geometry of the surrounding host medium, i.e. on the local density of states. For polycrystalline diamond films, quenching of radiative transitions have been reported [475]. Hence, the data reported by Turukhin et al. [413] might underestimate the quantum efficiency for SiV centers hosted in single crystal diamond membranes as it is the case for our samples. Moreover, if the size of the host crystal approaches the emission wavelengths, the local density of states might be strongly reduced, resulting likewise in a quenching of radiative transitions. This is the case for single SiV center hosted in nanodiamonds reported by Neu et al. [55]. It is well known, that in the case of sub-wavelength nanodiamond, the emission rate γ_{nano} is drastically suppressed due to the strong reduction of the local density of states within the nanoparticle compared to the emission rate in bulk material γ_{bulk} [476]:

$$\gamma_{\text{nano}} = \gamma_{\text{bulk}} \frac{1}{n} \left(\frac{3}{n^2 + 2} \right)^2 . \tag{9.7}$$

Here, a spherical shape of the nanoparticle with a refractive index of n is assumed. For

diamond with $n = 2.4$, the reduction factor amounts 0.06. Hence, if the environment of single SiV centers would change from bulk to a nanoparticle, the quantum efficiency would decrease to

$$\eta_{\mathrm{qe,nano}}^{-1} = 1 + n\left(\frac{n^2+2}{3}\right)^2\left(\eta_{\mathrm{qe,bulk}}^{-1} - 1\right). \tag{9.8}$$

If the single SiV(2) and SiV(3) centers were hosted in a nanodiamond, the quantum efficiency would reduce to $\eta_{\mathrm{qe,nano}} = 0.04\pm0.01$ and 0.009 ± 0.005, respectively, coinciding perfectly with the range determined in earlier experiments [55].

The placement of a single emitter inside a thin dielectric slab might equally induce changes of the spontaneous emission rate. Calculations based on quantum electrodynamics reveal a suppression of the spontaneous emission rate by a factor of 0.65 for a suspended dielectric slab with a refractive index of $n = 2.0$ and a thickness of $H/\lambda = 0.1$, which is surrounded by air, compared to the decay rate in bulk material [477,478]. With increasing slab thickness ($H/\lambda = 1$) the transition rate within a suspended membrane approaches the one of bulk material. Based on these calculation, we would expect only very small effects [477–479] for our parameters $H/\lambda \approx 0.54$, such that we can treat the thin diamond membrane as bulk material.

To summarize, the single SiV centers incorporated in the thinned diamond membrane show excellent spectral properties with bright and narrow zero-phonon lines down to 0.8 nm and low phonon side band contributions at room-temperature. The zero-phonon line shows linear polarization characteristics in emission and absorption with a preferential orientation along the $\langle 110\rangle$ or $\langle 100\rangle$ diamond direction. At saturation, single photon count rates up to 360 k counts/s have been detected. Using intensity auto-correlation measurements, we verified the single emitter character of the investigated SiV centers and deduced the internal population dynamics. These measurements allow us to extract the excited state lifetime, the spontaneous emission rate and the quantum efficiency reaching 0.32 for single SiV centers located in the diamond membrane. These figures of merit are not intrinsic properties of the emitter but strongly depend on the local density of states of the surrounding material. We subsequently demonstrate the controlled modification of the spontaneous emission rate as well as the quantum efficiency by targeted positioning of a photonic crystal around a single pre-selected SiV center. To this end, we apply an active alignment technique using positioning markers as will be presented in the following.

9.2 Active alignment of photonic crystal cavities to single SiV centers

Two groups [87, 88] have already demonstrated coupling of a single color center, i.e. a NV center, to a photonic crystal cavity in single crystal diamond. In these experiments, the color centers are distributed randomly throughout the cavity. For low densities of color centers within the membrane, the probability of achieving coupling can become

very small considering the extremely small mode volumes of the cavity mode. Hence, this random positioning approach requires fabrication and characterization of hundreds or even thousands of cavity structures [88] to ensure that several NV centers possess both the correct position and alignment with a defect mode. An attractive alternative to achieve coupling with a single emitter is to actively position a color center in the cavity. Such an approach, although technically difficult, would be incredibly useful in the construction of single color center devices and would offer a level of reproducibility not available using random positioning techniques [312]. The primary focus of this section is to present a technique for actively positioning single color centers in photonic crystal cavities.

The photonic crystal cavities consist of a triangular lattice of air holes with a lattice constant of $a = 283 - 285\,\mathrm{nm}$ and air hole radii of $R = 85 - 90\,\mathrm{nm}$ that are milled into the suspended (001) diamond membrane with a thickness of $H = 250 - 400\,\mathrm{nm}$. A cavity is introduced at the center of the photonic lattice by omitting one, three or seven missing holes. For the M1-cavity, we choose an optimized design presented in table 5.4 on page 132 with the nearest neighbor holes reduced in size. In contrast, the air holes of the M3- and M7-cavity are uniform in size.

To align the photonic structures with respect to the pre-characterized single SiV centers, cross markers with a distance of $15\,\mu\mathrm{m}$ and $20\,\mu\mathrm{m}$ along the x- and y-axis are milled into the diamond membrane via FIB. To protect the non-processed areas from damages induced by the FIB, the diamond film was covered by a 80 nm thick chromium layer prior to the milling process. The protection layer is chemically removed afterward with a chromium etchant. Figure 9.10(a) shows a photoluminescence scan of the final thinned diamond membrane: the single SiV(1) center is identified as a bright localized spot with cross markers next to it. For emitter-cavity alignment, we determine the distance in x and y between the SiV center and the origin of the alignment mark in the fluorescence scan. The FIB system is equipped with a high-resolution SEM to image the cross markers (Fig. 9.10(b)). As the fluorescence mapping and cavity structuring are performed with different techniques, it is important to calibrate the distances of these two systems using the regular spacing of the alignment markers. Once the relative position of the SiV center with respect to the cross markers in the SEM image is determined, we use focused ion beam milling to pattern a photonic crystal cavity around the single emitter. Figure 9.10(b,c) shows SEM images before and after structuring a photonic crystal M1-cavity around the pre-selected SiV(1) center. In the SEM pictures, an additional M3-cavity is observed that has been patterned prior to the M1-cavity around of the SiV(3) center. With this alignment technique, we achieve a positioning accuracy of about 280 nm, which is comparable to the lattice constant a of the fabricated photonic crystals.

Our positioning technique not only allows for accurate positioning of photonic crystal cavities relative to single SiV centers, but also enables the alignment of the cavity field with the in-plane SiV dipole moment. The polarization orientation together with the spectrum, the saturation count rate and the $g^{(2)}$ function of the SiV(1)-SiV(5) centers has been presented in section 9.1. As shown in figure 9.2(c), the emission of the SiV(1) center is polarized along the [100] crystallographic direction within the (001) diamond

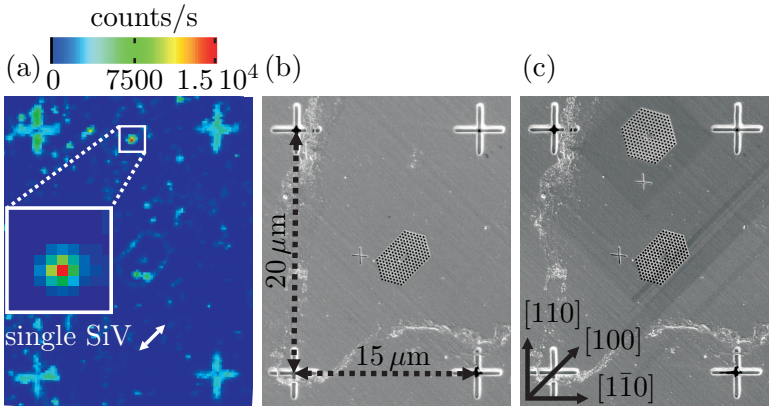

Figure 9.10: Deterministic positioning of a photonic crystal cavity relative to a pre-characterized single color center: (a) PL scan of the diamond membrane containing single SiV centers and cross markers with horizontal and vertical distances of 15 μm and 20 μm next to it, respectively. Inset: 4 μm $\times$ 4 μm detail scan of the SiV(1) center. Its polarization direction is indicated by the white arrow. SEM images (b) before and (c) after structuring a M1-cavity around the single SiV(1) center using FIB milling (same sample region as in (a)). The M1-cavity is oriented such that its x-axis coincides with the polarization direction of the single emitter along [100] crystallographic axis in diamond.

plane, indicated by the small white arrow in figure 9.10(a). To achieve optimal emitter-cavity coupling, the cavity electric field has to be aligned with the color center emission direction. As either the E_x- or E_y-field are the dominant cavity near field components, it is desirable to orient the emitter's dipole polarization along the cavity x- or y-axis, respectively. Therefore, the fabricated M1-cavity is tilted by 45° with respect to the lower edge of the SEM picture 9.10(c) such that the cavity x-axis coincide with the emitter's [100] polarization axis. Similarly, when structuring M3-cavities around the SiV(3) (Fig. 9.10) or SiV(5) center, the pattern is fabricated at an angle of 45° in order to align the three missing hole defect with the SiV(3) and SiV(5) polarization along the [100] axis.

After high temperature annealing at 1,000 °C in vacuum and acid cleaning steps as well as oxidation in air (c.f. section 6.2.4), photoluminescence scans clearly reveal the presence of single SiV centers within the photonic crystal structures. Figure 9.11 shows SEM images of fabricated M1-, M3- and M7-cavities overlapped with their fluorescence scans. The SiV(1) center within the M1-cavity as well as the SiV(2) and SiV(5) centers within M3-cavities are displaced from the cavity center but still residing in the photonic crystal lattice (Fig. 9.11(a-c)). Due to the displacement and the small mode volume of the structures, the emitters do not couple to cavity modes. Therefore, we expect the emission of SiV(1), SiV(2) and SiV(5) centers to be rather modified by the band gap effect of the periodic photonic crystal lattice than by cavity modes. The polarization of the SiV(1) and SiV(5) centers is perfectly aligned with the cavity x-axis, whereas the polarization of the SiV(2) center is parallel to the y-axis of the M3-cavity. In the case of

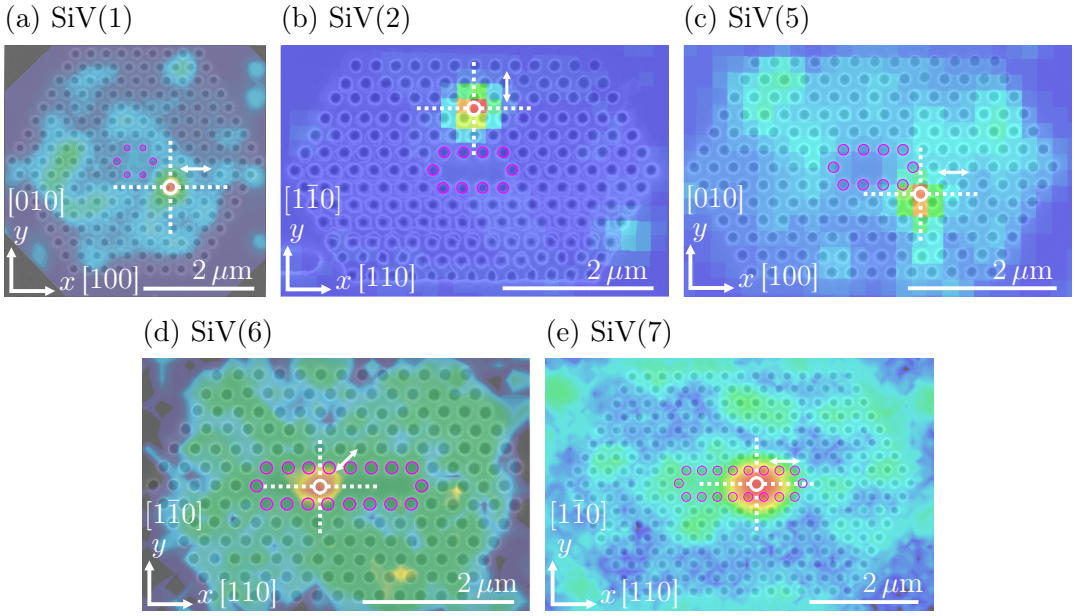

Figure 9.11: SEM images of fabricated photonic crystal cavities overlapped with fluorescence scans: (a) M1-cavity with single SiV(1) center and M3-cavities with single (b) SiV(2) and (c) SiV(5) center within the photonic lattice. (d,e) The SiV(6) and SiV(7) center are placed at the center of M7-cavities. Positions of SiV centers are marked by white circles. Polarization directions are indicated by white arrows. The nearest-neighbor holes surrounding the defect are indicated by pink circles. (a,c) The M1- and M3-cavity have been fabricated at an angle of 45°, such that the cavity x-axis coincide with the polarization of the SiV(1) and SiV(5) center along the [100] crystallographic direction.

the larger M7-cavities, the single SiV(6) and SiV(7) centers are perfectly placed on the cavities' center lines with distances of one lattice constant ($a \approx 280\,\mathrm{nm}$) from the origin. To distinguish both M7-cavities, we refer in the following to the structure around the SiV(6) center as M7(A)-cavity and to the photonic crystal around the SiV(7) center as M7(B)-cavity. In figure 9.10(b), the SiV(6) polarization is tilted by 45° with respect to the x-axis of the M7(A)-cavity. In contrast, the M7(B)-cavity in figure 9.10(c) contains the SiV(7) center with its emission perfectly aligned with the x-axis. The difference in polarization allows us to study the impact of the emitter's dipole orientation on the Purcell enhancement when tuning cavity modes into resonance with the emission lines. In the case of the SiV(3) and SiV(4) center, the patterning is not successful. The SiV(4) center photo bleaches before patterning, whereas the SiV(3) center is not retrieved after structuring a M3-cavity around it.

To conclude, with the deterministic positioning and alignment technique, we are able to solve one major obstacle placing a single color center within a photonic crystal structure and to adjust the cavity electric field with the emitter's polarization. On average, we achieve efficient cavity coupling of single SiV centers for 2 out of 7 fabricated photonic crystal structures. Moreover, 3 out of 7 emitters were displaced from the cavity

center but sill residing in the photonic crystal lattice.

Comparable methods have been successfully applied to accurately align quantum dots to photonic crystal cavities in GaAs. Hennessy et al. [312] and Badolato et al. [109] grew a stack of tracer dots on top of a buried light emitting InAs quantum dot to visualize its position as a small hill at the slab surface. The tracer dot can be imaged using SEM [109, 312] or AFM [110]. Ruler markers next to the quantum dot allow for exactly aligned electron-beam lithography of a photonic crystal cavity with the quantum dot at the center as well as for calibration correction yielding a final positioning error of 25 nm [312]. Kojima et al. [480] identified single quantum dots in the fluorescence scan with a sub-pixel resolution using image analysis techniques. Cross markers and reference points next to the quantum dots are used as alignment markers in the electron-beam lithography process to define the photonic crystal cavities with a positioning error of 48 nm [480]. Thon et al. [481] located self-assembled InAs quantum dots relative to an array of gold markers using fluorescence scans. Although the wavelength of the scanning laser was much larger than the required positioning accuracy, they managed to locate the center of the quantum dot emission very precisely by fitting the emission peak and averaging over many scans. After the quantum dot positions are extracted, they fabricated photonic crystal cavities around the quantum dot locations with sub-10 nm accuracy using electron beam lithography.

To achieve comparable positioning accuracies in our experiments, the resolution of our fluorescence scans have to be improved. One possibility is to perform multiple scans and build up statistics on the emitter-marker distance. The error in the mean distance decreases with $1/\sqrt{N}$ where N is the number of fluorescence scans [481]. Another way would be to detect the color centers with nanometer precision using stimulated emission depletion (STED) microscopy [455, 482]. STED microscopy allows for overcoming of the diffraction limit by overlapping the outer regions of the excitation beam with a second donut-shaped laser beam that stimulates emission and depletes the excited state of the emitter before fluorescence takes place. Although successfully established for NV centers [456, 457], STED microscopy has not yet been successfully applied to SiV centers up to now.

9.3 Emission properties upon structuring

After successful alignment and patterning of a photonic crystal cavity around a single SiV center, we investigate the persistence of the color centers' spectral position and linewidth as well as the polarization properties upon FIB structuring. This is essential for frequency matching the cavity modes to the SiV emission line in order to achieve efficient cavity-coupling. Using the example of the single SiV(1), SiV(2), SiV(5) and SiV(6) centers, we will study in the following a possible modification of the ZPL spectral position and linewidth when structuring a photonic crystal lattice around the emitters. Furthermore, the polarization properties of the single SiV centers placed in a photonic crystal lattice after structuring are compared to their characteristics in a homogeneous diamond membrane before the FIB milling.

SiV	λ_{before} (nm)	λ_{after} (nm)	λ_{after}-λ_{before} (nm)	$\Delta\lambda_{\text{before}}$ (nm)	$\Delta\lambda_{\text{after}}$ (nm)	$\phi_{\text{max}}^{\text{before}}$ (°)	$\phi_{\text{max}}^{\text{after}}$ (°)
1	727.5	726.5	-1.1	1.29	1.29	45.0	33.8
2	736.4	728.9	-7.5	1.43	1.18	82.7	76.7
5	721.3	732.7	+11.4	0.95	1.10	38.5	32.2
6	726.0	728.6	+2.6	0.70	0.77	-	40.8

Table 9.3: Central positions λ, linewidths $\Delta\lambda$ and polarization angle ϕ_{max} of the zero-phonon lines of four single SiV(1), SiV(2), SiV(5), SiV(6) centers before and after structuring a photonic crystal around them.

Spectral position and linewidth of the zero-phonon line

Figures 9.12 and 9.13 show the fluorescence spectra taken before and after the FIB milling of photonic crystal structures around the single SiV(1), SiV(2), SiV(5) and SiV(6) centers. All spectra reveal pronounced zero-phonon lines in the wavelength range of $720 - 740$ nm and weak phonon side band contributions before and after the structuring. In addition to the SiV emission lines, the SiV(6) spectrum taken at the center of the M7(A)-cavity (Fig. 9.11(d)) reveals several cavity modes between 750 and 840 nm. The resonant modes will be identified and discussed in detail in section 9.5.1. In contrast, the spectra of the SiV(1), SiV(2) and SiV(5) centers do not exhibit any cavity modes as the single emitters are displaced from the photonic crystal center (Fig. 9.11(a-c)). Here, we first consider the spectral position of the ZPL upon patterning. A detailed view of the ZPL, as displayed in the insets of figures 9.12(a,c) and 9.13, reveals a wavelength shift of the ZPL by several nanometers after the milling of the photonic air hole patterns. Although, the spectral positions of the four SiV centers are comparable, the wavelength shift is different: The SiV(1) and SiV(2) centers exhibit a red shift by 1 and 7.5 nm (Figs 9.13(a) and 9.12(a)), respectively, whereas the SiV(5) and SiV(6) ZPL position blue shifts by 11.4 and 2.6 nm (Figs 9.12(b) and 9.13(b)), respectively. The spectral positions of the four SiV ZPLs before and after the milling are summarized in table 9.3. The significant wavelength shifts are attributed to a change in the emitters' environment. In section 9.1, we have seen that the emission wavelengths of the single SiV centers hosted in the diamond membrane range from 710 to 770 nm, depending on local material strain [227]. Milling of air holes locally alternates the emitters' environment and most probably the local strain field experienced by the single color centers. This change results in a wavelength shift by several nanometers. In the experiment, the wavelength shift of the SiV ZPL can be compensated by actively tuning the cavity modes after the fabrication of the photonic crystal cavity. The cavity modes can be shifted up to 50 nm to smaller wavelengths via air oxidation (c.f. sections 7.2, 9.5.2). In return, the cavity modes can equally be red tuned via gas condensation, e.g. Xe gas, on top of the photonic crystal cooled down to cryogenic temperatures [87, 88]. Possible tuning mechanisms are presented in more detail in section 7.2.

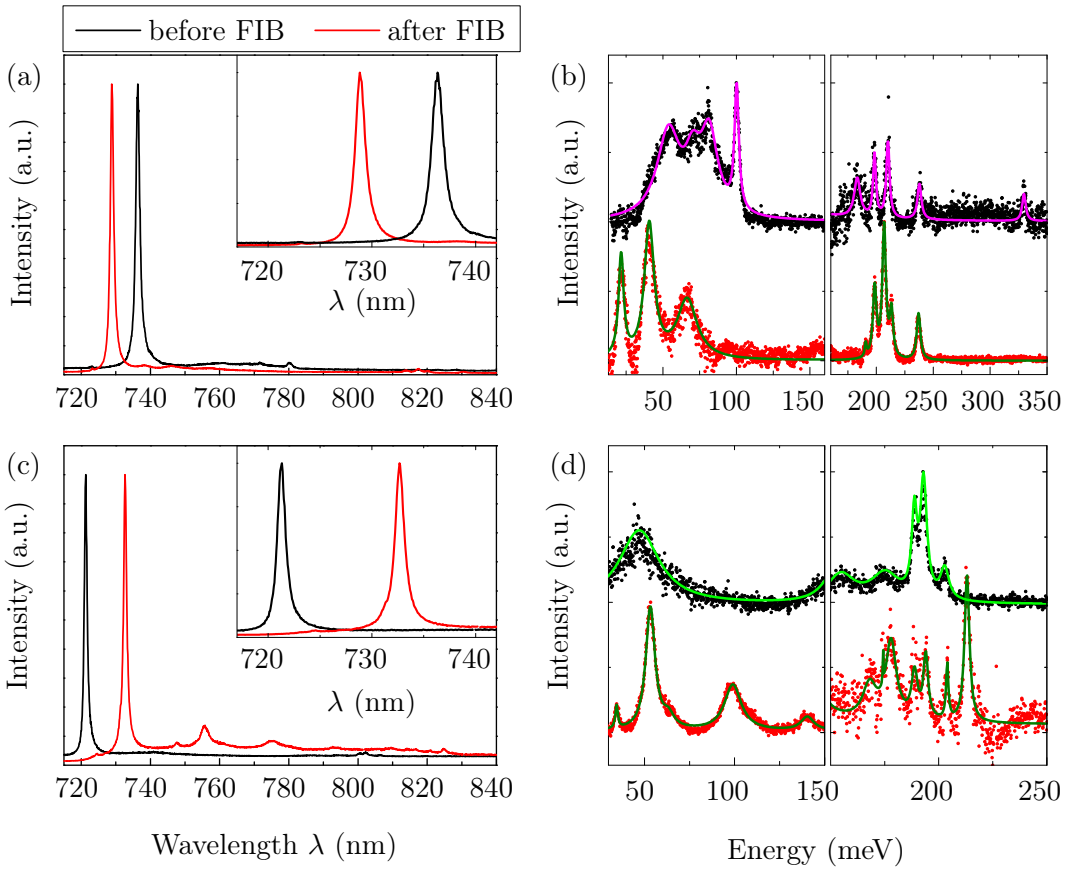

Figure 9.12: Zero-phonon line and phonon side band spectrum of the single (a,b) SiV(2) and (c,d) SiV(5) centers upon structuring: (a,c) Spectra taken before (black) and after (red) FIB milling. The insets show a detailed view of the ZPL (a) blue shifting upon structuring by 7.5 nm or (c) red shifting by 11.4 nm. (b,d) Detailed view of the phonon side bands as a function of their energy with respect to the ZPL. The one-phonon side band features ($0-165$ meV) significantly change, whereas most of the narrow lines at $165-250$ meV attributed to the near-infrared transitions persist upon structuring. Each section of the phonon side band has been normalized to its maximum and the curves have been shifted by 1 for clarity.

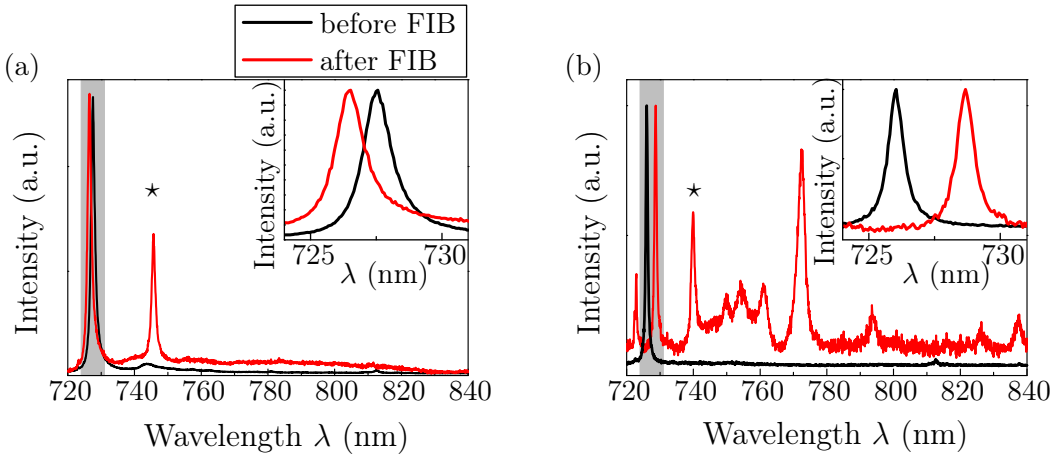

Figure 9.13: Spectral position and linewidth upon structuring: Spectra of the single (a) SiV(1) and (b) SiV(6) centers taken before (black) and after (red) FIB milling of a (a) M1- and (b) M7-cavity. The insets show a close-up of the zero-phonon line (gray shaded region). Besides the original emission lines at $\lambda_{\mathrm{SiV(1)}} = 727.5\,\mathrm{nm}$ and $\lambda_{\mathrm{SiV(6)}} = 726.0\,\mathrm{nm}$ additional ZPLs at 745.7 nm and 739.9 nm (marked by stars $\star$) of new created SiV centers appear in the (a) M1- and (b) M7-spectrum, respectively. The peaks at wavelengths 750-840 nm in spectrum (b) are attributed to phonon side bands and M7(A)-cavity modes.

In addition to the spectral position, the ZPL linewidth slightly changes due to the modification of the color centers' immediate environment upon structuring. However, the variation of the ZPL linewidth induced by the FIB etching is small: The linewidth of the SiV(1) center is essentially unaffected, whereas the linewidths of the SiV(5) and SiV(6) centers increase by 13% and 10%, respectively. Remarkably, the linewidth of the SiV(2) center becomes narrower upon FIB milling. Hence, the alteration of the local emitter surrounding can both increase and decrease the linewidth. The spectral positions and linewidths summarized in table 9.3 suggest the tendency that the larger the ZPL wavelength shift the stronger the modification in linewidth. Indeed, the SiV(2) and SiV(5) centers, which exhibit the larges ZPL shifts, show the strongest change in linewidths. However, to certify a possible correlation between the spectral position and linewidth variation, more comprehensive statistics are needed. Besides these details, for every SiV center, we find the linewidth alternation to be smaller 20%, which indicates that almost no additional broadening mechanisms are induced by the photonic crystal structuring.

Phonon side bands

As a next step, we investigate the spectral properties of the phonon side bands upon FIB milling. Figure 9.12 displays a detailed view of the phonon side band of the single SiV(2) and SiV(5) centers as a function of the energy with respect to the zero-phonon line. The side band spectra in the one-phonon region ($0 - 165\,\mathrm{meV}$) show substantial

modification. We observe the appearance and disappearance of several spectral features, which indicates that the electron-phonon coupling to diamond lattice modes or to (quasi)local defect modes is significantly altered by structuring photonic crystals around the emitters. Some of the new lines are probably related to zero-phonon lines of newly created SiV centers (see discussion below).

Near-infrared transition

Beyond the phonon side bands, both spectra of the SiV(2) and SiV(5) center before and after structuring exhibit narrow lines with energies of $170 - 250$ meV with respect to the ZPL. These lines have been attributed to additional purely electronic transitions of the SiV center in the near-infrared spectral range involving the same ground state as the ZPL and additional excited levels (c.f. section 9.1 on page 259). Figure 9.12 reveals that most of the near-infrared lines are persistent upon FIB milling, although some of the peaks disappear. The modification of the relative intensities might be attributed to varying alignment and focusing of the confocal setup between the different measurements. Remarkably, the near-infrared lines appear at the same energies with respect to the ZPL before and after the structuring. As the ZPL wavelength shifts upon FIB milling by several nanometers, the near-infrared transitions exhibit the same shift while keeping the energetic distance to the ZPL constant. The presumption that the near-infrared transitions are strongly related to the ZPL transition is consolidated by photo-bleaching experiments. The intensity of the excitation laser is ramped up to intentionally bleach the SiV(5) center. With disappearance of the SiV(5) ZPL in the spectrum, the near-infrared lines between 165 and 250 meV equally fade away, whereas the side band features at $0 - 165$ meV are still present in the spectrum. This reveals that the near-infrared transitions are closely related to the SiV zero-phonon line.

Creation of new SiV centers

After the photonic crystal structuring, we observe additional SiV ZPLs in the fluorescence spectra besides the original emission lines: In the SiV(1) and SiV(6) spectra (Fig. 9.13), ZPLs at 745.7 nm and 739.9 nm of newly created SiV centers appear after FIB milling. Moreover, the peaks at 747.5 and 755.8 nm in the SiV(5) spectrum (Fig. 9.12(c,d)) are probably related to ZPLs of new SiV centers. The line at 747.5 nm becomes much more pronounced, when the polarization of the excitation laser light is rotated by 45°. We attribute the formation of new SiV centers to additional vacancies introduced in the diamond film by milling of the air hole patterns. By subsequent annealing the sample at 1,000°C in vacuum, these vacancies become mobile and combine with substitutional silicon atoms to form new SiV centers in the diamond film. We observe the creation of new SiV centers in every fabricated photonic crystal structure.

Polarization

To achieve efficient cavity-coupling to the SiV ZPL, the wavelength of the cavity mode do not only have to match the SiV emission line but also the polarizations need to

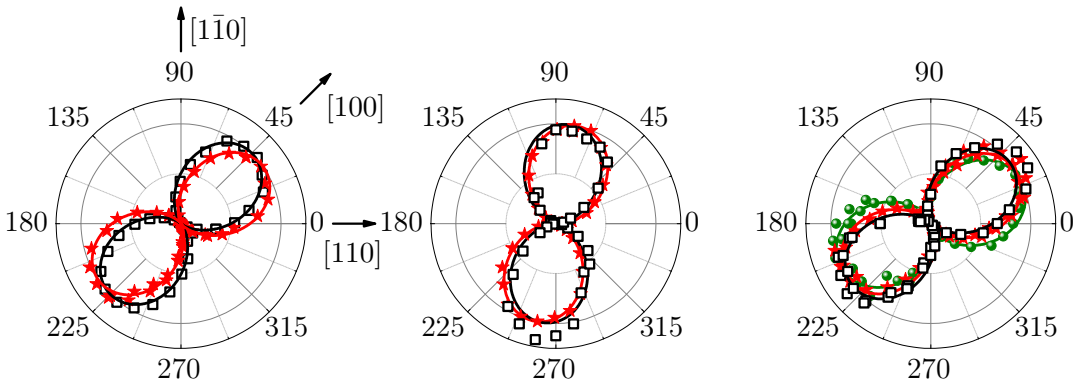

Figure 9.14: Polarization upon structuring: Polarization polar plot of ZPL of the single (a) SiV(1), (b) SiV(2) and (c) SiV(5) center before (□) and after (⋆) milling photonic crystal cavity structures around the color centers. For the SiV(5) center, the polarization-dependent absorption is additionally shown (●). The slight variation in polarization is mainly due to the limited detection precision of 10°.

coincide. Fabrication of the photonic crystal cavity around a pre-characterized single color center allows us to align the cavity field with the SiV dipole emission. However, it is crucial that the emitter's orientation is persistent upon structuring. To confirm this, we measure the ZPL polarization characteristics in emission and absorption of single SiV centers before and after milling photonic crystals around the emitters. Figure 9.14 shows the polarization polar plot of the spectrally filtered SiV(1), SiV(2) and SiV(5) ZPL emission (detection window $730 \pm 10\,\mathrm{nm}$) before and after the structuring process. For the SiV(5) center, the polarization-dependent absorption is additionally displayed by green dots. As in figure 9.2, an azimuthal angle of $\phi = 0°$ (45°) corresponds to an polarization alignment along the [110] ([100]) crystallographic axis of the diamond lattice. Before and after structuring, the SiV(1) and SiV(5) emission is polarized along the [100] diamond axis, whereas the SiV(2) emission is polarized preferentially along the [110] direction. The angles ϕ_{max} at maximum intensity are summarized for the individual SiV centers in table 9.3. All polar plots confirm that the SiV polarization and hence the associated dipole moment of the SiV center are persistent upon FIB milling. The slight variation in ϕ_{max} is rather attributed to the detection uncertainty of $\sim 10°$ than to a real modification of the SiV dipole orientation. Hence, the SiV dipole orientation is basically unaffected by the photonic crystal structuring process. Please note that the large error of 10° is related to the fact that the sample is not fixed on the sample holder but (un-)mounted between the measurements that leads to an error of several degrees.

Our measurements confirm that we are dealing with the same SiV centers before and after patterning photonic crystals around them. The FIB milling process slightly changes the local environment of the emitters leading to a possible blue or red shift in

the ZPL central position and to a possible increase or decrease in the linewidth. The phonon side bands are modified, whereas the near-infrared spectral lines appear at the same energy shift with respect to the ZPL. Polarization studies reveal that the orientation of the SiV dipole moment is unaffected by the structuring process. Moreover, the gallium ion bombardment during FIB milling creates additional vacancies in the diamond, that form after high temperature annealing, new single SiV centers incorporated in the photonic crystal cavities. As a next step, we investigate a possible change in the internal population dynamics and the excited state lifetime when the single SiV centers are located in the photonic crystal lattice compared to the homogeneous diamond membrane.

9.4 Inhibition of spontaneous emission via photonic band gap effect

Spontaneous emission is not an intrinsic property of the quantum emitter itself but crucially depends on the density of states of the surrounding environment. If the local density of states is greater than the one of free space, the spontaneous emission will be enhanced, if it is less, it will be inhibited. Photonic crystals can significantly alter the local density of states. In his milestone paper [247], Yablonovitch suggested that if a light emitter is introduced into a three-dimensional photonic crystal, its emission can be fundamentally eliminated by the perfect photonic band gap with vanishing photon local density of states. Indeed, the suppression of spontaneous decay has already been demonstrated for quantum emitters embedded in three-dimensional photonic crystals [250]. As discussed in section 5.4.2, the partial band gap of a two-dimensional photonic crystal slab equally gives rise to a reduced local density of states. Based on FDTD simulations, we quantified the averaged Purcell factor of the photonic crystal slab to be $F_{\mathrm{PhC}} = 0.23 - 0.25$.

In the following, we investigate the effect of a two-dimensionally periodic photonic crystal on the spontaneous emission of a single SiV centers. Here, we focus on the SiV(1) and SiV(2) centers located in the M1- and M3-cavity but displaced from the cavity center (Fig. 9.11(a,b)). From $g^{(2)}$ measurements, we determine the population dynamics of the color centers in the periodic structure and compare it to the emission properties in the bulk membrane. From the measured decay rates and excited state lifetimes, we finally evaluate the experimental Purcell factor F_{PhC} of the photonic lattice and compare it to FDTD simulations.

9.4.1 Inhibition of the spontaneous emission rate

To prove the single emitter character and to determine the population dynamics of the SiV centers after structuring, we perform intensity auto-correlation measurements of the filtered ZPL signal. The $g^{(2)}$ functions are compared to the data prior to FIB milling (Figs. 9.5 and 9.6). In figure 9.15, the $g^{(2)}$ functions for various excitation powers P/P_{sat} are exemplarily shown for the SiV(1) and SiV(2) centers hosted in the photonic crystal

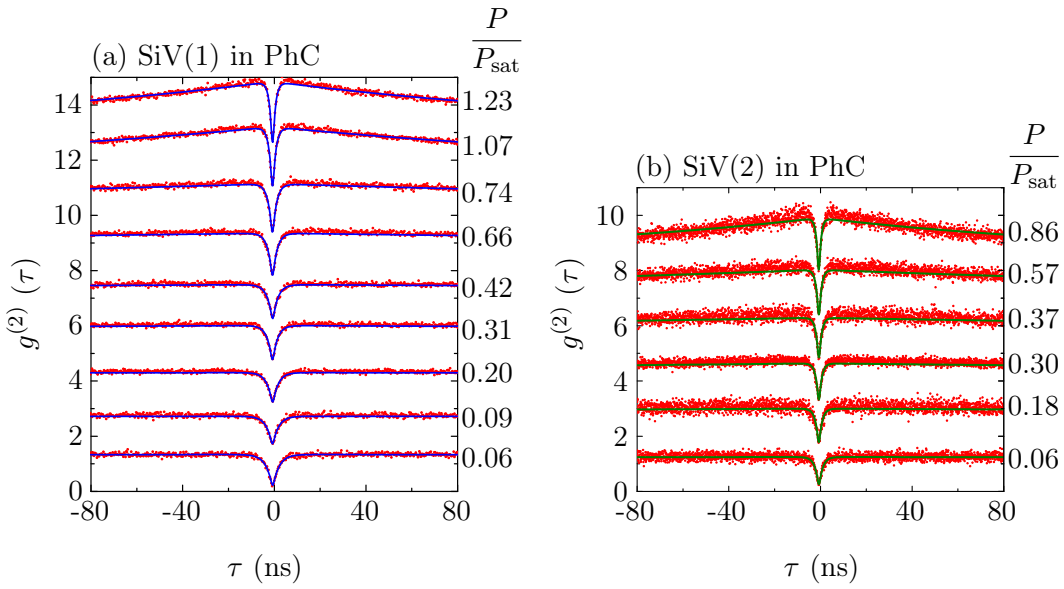

Figure 9.15: Intensity correlation $g^{(2)}$ measurements at various excitation powers of the (a) SiV(1) and (b) SiV(2) center placed in a photonic crystal lattice after FIB milling: The excitation power P is normalized to the saturation power (a) $P_{\text{sat}} = 0.76\,\text{mW}$, (b) $P_{\text{sat}} = 0.30\,\text{mW}$. The $g^{(2)}$ functions have been displaced by 1.5 for clarity. Dots: measured data, solid lines: least square fits according to equation (3.7) convoluted with the instrument response function.

lattice. Before and after the structuring process, the intensity correlation functions clearly exhibit an antibunching dip $g^{(2)}(0) < 0.5$ at zero time delay, proving the single emitter character of the SiV centers. For intermediate delay times, $g^{(2)}(\tau)$ exceeds values of one before it converges to one at long time scales, giving rise to bunching. The $g^{(2)}$ functions of the SiV(1) and SiV(2) centers are fitted using equation (3.7) convoluted with the instrument response function of the setup. The extracted fit parameters τ_1, τ_2 and a are displayed in figure 9.16 as a function of the pump power P/P_{sat} applied during the correlation measurements. The black squares (red stars) indicate measurements before (after) the structuring of the photonic crystals. From the power-dependent model parameters τ_1, τ_2 and a, we deduce in the following the internal decay rates as well as the excited state lifetime of the SiV(1) and SiV(2) center located either in the photonic crystal or in the unpatterned diamond membrane.

Spontaneous emission rate of the SiV(1) center

First, we consider the population dynamics of the SiV(1) center located in the M1-cavity and compare them to the unstructured case before the milling. Fitting the experimental parameters τ_1, τ_2 and a in figure 9.16(a) via equations (3.11)-(3.14), we obtain the constants σ_{PhC}, c_{PhC} and d_{PhC} listed in table 9.4, together with the limiting values $\tau^0_{1,\text{PhC}} = 2.6\,\text{ns}$, $\tau^0_{2,\text{PhC}} = 20\,\mu\text{s}$, $\tau^\infty_{2,\text{PhC}} = 0.3\,\mu\text{s}$ and $a^\infty_{\text{PhC}} = 3.5$ for the SiV(1) center placed in a photonic crystal lattice. From these data and via relations (3.19), we

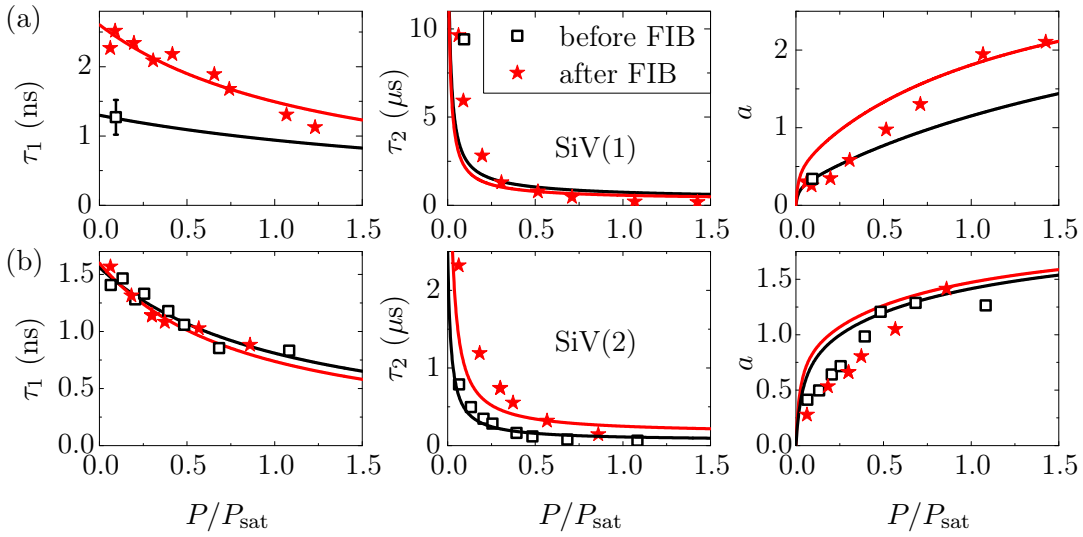

Figure 9.16: Population dynamics of the (a) SiV(1) and (b) SiV(2) centers before and after FIB milling: The power dependent model parameters τ_1, τ_2, a are extracted from $g^{(2)}$ fits measured for various excitation powers P/P_{sat} (e.g. Fig. 9.15). Black hollow squares: after FIB milling, SiV centers placed in a photonic crystal. Red stars: before FIB structuring, SiV centers in a homogeneous diamond slab. Solid lines: Theoretical power dependence of τ_1, τ_2, a used to determine the population dynamics before (red) and after (black) FIB. Dashed lines in (c) are a guide to the eye.

deduce the pump rate $k_{12}^{\mathrm{PhC}} = \sigma_{\mathrm{PhC}} P$, the spontaneous decay rate k_{21}^{PhC}, and the rates k_{23}^{PhC} and $k_{31}^{\mathrm{PhC}} = d_{\mathrm{PhC}} P/(P + c_{\mathrm{PhC}}) + k_{31}^{0,\mathrm{PhC}}$ listed in table 9.4. Here, the excitation power P is given in units of the saturation power $P_{\mathrm{sat}} = 0.76\,\mathrm{meV}$ measured after the structuring process. From the τ_1 time in the limit at vanishing pump power, we can extract the excited state lifetime of $\tau_{1,\mathrm{PhC}}^{0} = 2.6\,\mathrm{ns}$ of the SiV(1) center in the photonic crystal.

As a reference, we equally determine the parameters τ_1, τ_2 and a (black square in Fig. 9.16(a)) from the $g^{(2)}$ measurement of the SiV(1) center before FIB patterning (Fig. 9.5). While the parameters τ_2 and a are almost unaffected, the time τ_1 significantly changes for the SiV(1) center in a homogeneous diamond slab compared to the same color center placed in a photonic crystal lattice. Fitting the model parameters, assuming constant decay rates k_{23} and k_{31} and an invariant pump rate k_{12}, we deduce a spontaneous decay rate $k_{21}^{\mathrm{bulk}} = 767\,\mathrm{MHz}$ and a τ_1 time for vanishing pump powers of $\tau_{1,\mathrm{bulk}}^{0} = 1.3 \pm 0.25\,\mathrm{ns}$ of the SiV(1) center in the unpatterned diamond film. Hence, by patterning a photonic crystal lattice around the SiV(1) center, its spontaneous emission rate is inhibited by a factor of 2 from 767 to 382 MHz due to the photonic band gap effect. The decrease of the spontaneous emission rate comes along with a two-fold increase of the excited state lifetime from 1.3 to 2.6 ns.

	τ_1^0 (ns)	τ_2^0 (μs)	τ_2^∞ (μs)	a^∞	σ $\left(\frac{\text{MHz}}{P_{\text{sat}}}\right)$	k_{21} (MHz)	k_{23} (MHz)	k_{31}^0 (MHz)	d (MHz)	c (P_{sat})
SiV(1)										
bulk	1.3	20	0.3	3.5	0.3	766.6	2.6	0.05	0.69	0.2
PhC	2.6	20	0.3	3.5	0.3	382.0	2.6	0.05	0.69	0.2
SiV(2)										
bulk	1.6	2.5	0.06	2	0.6	630.3	10.8	0.40	4.98	0.5
PhC	1.6	8	0.15	2	0.7	620.6	4.4	0.13	2.10	0.4

Table 9.4: Decay rates governing the population dynamics of the SiV(1) and SiV(2) centers before (bulk) and after (PhC) structuring a photonic crystal lattice around them. The limiting values and rate coefficients are deduced from figure 9.16 using a three level model including a power-dependent deshelving rate $k_{31} = dP/(P+c) + k_{31}^0$ and a pump rate $k_{12} = \sigma P$.

Spontaneous emission rate of the SiV(2) center

As a next step, we investigate the population dynamics of the SiV(2) center located in the M3-cavity and compare them to the dynamics before structuring. Figure 9.16(b) displays the experimental times τ_1, τ_2 and the parameter a extracted from $g^{(2)}$ measurements on the SiV(2) center in bulk (Fig. 9.6(a)) and in the photonic lattice (Fig. 9.15). Upon structuring, the τ_1 and a curves are almost unaffected, whereas τ_2 is modified. Similar to the procedure described above, we extract the constants σ_{PhC}, c_{PhC} and d_{PhC} and the limiting values $\tau_{1,\text{PhC}}^0$, $\tau_{2,\text{PhC}}^0$, $\tau_{2,\text{PhC}}^\infty$ and a_{PhC}^∞ from the fits to the power-dependent parameters τ_1, τ_2 and a (red stars and red solid lines in Fig. 9.16(b)). Together with the resulting decay rates $k_{12}^{\text{PhC}} = \sigma_{\text{PhC}} P$, k_{21}^{PhC}, k_{23}^{PhC} and $k_{31}^{\text{PhC}} = d_{\text{PhC}} P/(P+c_{\text{PhC}}) + k_{31}^{0,\text{PhC}}$, the data are listed in table 9.4. For reference, the decay rates obtained in section 9.1 on page 267 for the single SiV(2) center in the unstructured diamond membrane are reproduced in table 9.4. For the SiV(2) center, the spontaneous emission rate k_{21} from the excited to the ground state as well as the excited state population $n_2^\infty = 0.33$, determined via equation (9.5), are essentially unaffected by the photonic crystal lattice. In contrast, the recombination rates k_{23} and k_{31} involving the metastable shelving state are modified.

One possible explanation for the unchanged spontaneous decay rate might be that the SiV(2) emission line does not coincide with the frequency range of the photonic band gap of the surrounding M3-cavity. Indeed, spectra taken at the center of the M3-cavity reveal cavity modes and a photonic band gap ranging from 640 to 700 nm. As the SiV(2) ZPL at 728.9 nm is beyond the stop band of the photonic lattice, its spontaneous decay rate is unaffected. The same phenomena has been observed for quantum wells located in a two-dimensional photonic crystal lattice fabricated in GaInAsP [267, 268]. The spontaneous emission rate of quantum wells with emission lines in the photonic band gap was strongly suppressed, whereas outside the stop band the bulk value of the unstructured slab was resumed [267, 268].

The change of the decay rates k_{23} and k_{31} from and to the shelving state is attributed to a variation in the τ_2 curve upon structuring especially for low excitation powers (Fig. 9.16(b)). As the exact nature of the shelving state as well as its energy level with respect to the SiV ground and excited state are unknown, we are at the moment not able to explain the increase in lifetime τ_2^0 of the metastable shelving state. Further investigations are needed here.

To summarize, we deduced the population dynamics of the SiV(1) and SiV(2) centers by fitting the intensity correlation functions measured at various excitation powers. For the SiV(1) center, we detect an inhibition of the spontaneous emission rate when structuring a photonic crystal lattice around it. This inhibition comes along with a two-fold increase of the excited state lifetime from $\tau_{1,\mathrm{bulk}}^0 = 1.3\,\mathrm{ns}$ prior FIB milling to $\tau_{1,\mathrm{PhC}}^0 = 2.6\,\mathrm{ns}$ after structuring. In contrast, the emission line of the SiV(2) center outside the photonic band gap region is essentially unchanged. These results clearly demonstrate that if the emission wavelength is within the photonic band gap region, the spontaneous decay rate decreases compared to the decay rate in bulk. By contrast, when the emission wavelength lies outside the photonic band gap, the spontaneous transition rate is comparable to the one observed in the unstructured diamond membrane. Hence, the change in the decay rate is a real effect of the reduced local density of states within the photonic band gap rather than a result of the patterning process itself.

9.4.2 Experimental Purcell factor F_{PhC} of the photonic crystal lattice

The detailed analysis of the internal population dynamics of the single SiV(1) center allows us to deduce the experimental inhibition factor F_{PhC} of the spontaneous emission rate caused by the photonic band gap effect. As already outlined in section 7.3, the excited state of a SiV center located in the diamond membrane undergos radiative transitions at a recombination rate γ_{rad} and non-radiative decays at a rate γ_{nr}:

$$\gamma_{\mathrm{bulk}} = \gamma_{\mathrm{rad}} + \gamma_{\mathrm{nr}}. \tag{9.9}$$

By fabricating a photonic crystal around the emitter, the radiative decay rates would be suppressed by a factor F_{PhC} due to the photonic band gap, whereas all non-radiative transitions are unaffected:

$$\gamma_{\mathrm{PhC}} = F_{\mathrm{PhC}}\gamma_{\mathrm{rad}} + \gamma_{\mathrm{nr}}. \tag{9.10}$$

From the measured internal populations dynamics, we deduce the recombination rates $\gamma_{\mathrm{bulk}} = k_{21}^{\mathrm{bulk}} = 766.6\,\mathrm{MHz}$ and $\gamma_{\mathrm{PhC}} = k_{21}^{\mathrm{PhC}} = 382.0\,\mathrm{MHz}$ of the SiV(1) center located in the unstructured diamond membrane and in the photonic crystal lattice, respectively. Taking into account the SiV(1) quantum efficiency $\eta_{\mathrm{qe,bulk}} = 0.63 \pm 0.13$ determined via independent saturation measurements (c.f. eq. (9.20) in section 9.6), the radiative and non-radiative decay rates are evaluated: $\gamma_{\mathrm{rad}} = \eta_{\mathrm{qe,bulk}}\,\gamma_{\mathrm{bulk}} = 485 \pm 100\,\mathrm{MHz}$ and $\gamma_{\mathrm{nr}} = (1 - \eta_{\mathrm{qe,bulk}})\gamma_{\mathrm{bulk}} = 285 \pm 100\,\mathrm{MHz}$. Substituting the decay rates into equation (9.10), we obtain the experimental Purcell factor

$$F_{\mathrm{PhC}}^{\mathrm{exp}} = 0.21 \pm 0.16. \tag{9.11}$$

The measured Purcell factor is in excellent agreement with the averaged inhibition factor of $F_{\mathrm{PhC}} = 0.25$ determined via FDTD simulations in chapter 5 on page 101. The large error in $F_{\mathrm{PhC}}^{\mathrm{exp}}$ is related to the uncertainty of the experimental quantum efficiency. For an ideal emitter with unity quantum efficiency, a Purcell factor of $F_{\mathrm{PhC}} = 0.21$ would induce a decrease in the spontaneous emission rate by a factor of 4.8. The difference to the experimental inhibition factor of 2 is completely explained by the non-unity quantum efficiency of the SiV(1) center. The thorough analysis of the inhibition factor including internal population dynamics and the actual measured quantum efficiency is unprecedented for single color centers in diamond. Although a slight increase in lifetime has been reported for single NV centers located in photonic crystals compared to bulk [87], precise measurements before and after structuring and a rigorous analysis of the inhibition of spontaneous emission was missing to date.

9.5 Purcell enhancement of spontaneous emission via cavity-coupling

In this section, we demonstrate deterministic coupling of an all-diamond photonic crystal cavity to a single pre-selected SiV center. The outstanding emission properties of the SiV center enable the demonstration of cavity quantum electrodynamic effects even at room temperature. First, we identify the SiV emission lines and resonant modes in the cavity spectra. In a second step, the cavity modes are tuned across the entire SiV emission spectrum. On resonance, we study the spectral intensity increase and Purcell enhancement of the spontaneous emission rate and we deduce the modification of the internal population dynamics of the single SiV center. We analyze the cavity Purcell factor including the experimental quality factor and mode volume of the cavity mode as well as the spectral overlap, the actual emitter position and dipole orientation with respect to the cavity field. The theoretical predictions are compared to the experimental observations. The measured internal population dynamics are essential to evaluate a possible modification in the quantum efficiency when the SiV center is couple to a cavity mode.

9.5.1 Single SiV centers in photonic crystal cavities

Prior to cavity-coupling, we have a detailed look at the spectral properties of the single SiV(6) and SiV(7) centers located at the center the M7(A)- and M7(B)-cavity, respectively (Fig. 9.11(d,e)). The photoluminescence spectra taken at the center of both fabricated M7-cavities (Fig. 9.17) show several distinct peaks that are attributed either to SiV emission lines or cavity modes. The color centers' emission is colored in blue, whereas all cavity modes are highlighted by red Lorentzians.

The SiV(6)/M7(A)-spectrum deviates from the spectrum shown in figure 9.13(b). Unfortunately, after some annealing steps, the original SiV(6) center with a ZPL at 728.6 nm irrecoverably photo bleached. The spectrum in figure 9.17(a), taken after bleaching of the 728.6 nm-SiV center, reveals four lines at 739.9, 746.3, 769.0 and

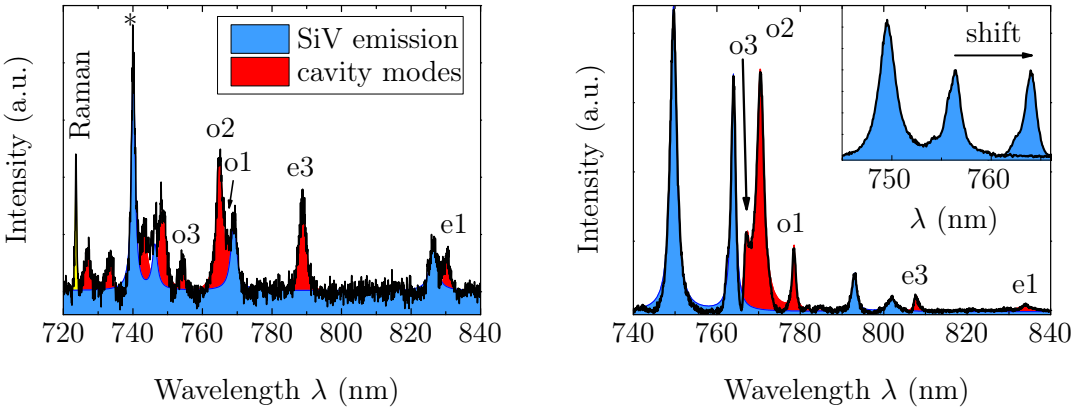

Figure 9.17: Photoluminescence spectra of the (a) M7(A)- and (b) M7(B)-cavity: Multiple distinct peaks are observed in the cavity spectra, that are either attributed to SiV emission lines (blue) or cavity modes (red). (a) The SiV(6*) center in the M7(A)-cavity shows a ZPL at 739.9 nm. The peaks associated to the lowest order cavity modes $e1$, $e3$, $o1$, $o2$ and $o3$ are indicated. (b) In the M7(B)-cavity spectrum, two single SiV centers are observed with a ZPLs at 749.6 nm and at 756.4 nm. The 756.4 nm-line abruptly shifts to 764.1 nm following tuning. The spectrum is taken after the jump in wavelength. The inset in (b) shows a close up of the zero-phonon lines before and after the spectral displacement. The background in the spectra has been subtracted.

828.6 nm that are attributed to emission lines of new SiV centers created upon FIB milling and high temperature annealing. The peak at 722.85 nm ($\hat{=}$ 1326 cm^{-1}) corresponds to the diamond Raman line. The deviation of the diamond Raman line with respect to the ideal value of 1332.5 cm^{-1} indicates the presence of tensile strain in the diamond membrane (c.f. section 6.1.5). The peaks at 739.9 and 746.3 nm are attributed to zero-phonon lines of the new SiV centers. In the following, we will refer to the single SiV center with a ZPL at 739.9 nm as SiV(6) center. The prominent phonon side band at 769.0 nm, corresponding to an energy shift of 66 meV with respect to the 739.9 nm-ZPL, is attributed to a local mode of the Si atom oscillating along the ⟨111⟩ of the diamond lattice [226]. In contrast, the peak at 828.6 nm, shifted by 201 meV with respect to the 739.9 nm-ZPL is assigned to a purely electronic transition in the near-infrared spectral range of the SiV center [228, 466]. For a detailed discussion on the SiV phonon side bands see page 258. Phonon side bands related to the 746.3 nm-ZPL are not resolved in the spectrum. The spectral positions and linewidths of the ZPLs and the phonon side bands as well as the energy shift of the phonon side bands with respect to the SiV(6) ZPL are summarized in table 9.5.

Similarly, we identify two single SiV centers in the SiV(7)/M7(B)-cavity spectrum (Fig. 9.17(b)) with zero-phonon lines at 749.6 and 756.4 nm. As will be discussed in the following section, the spectral position of the ZPL at 756.4 nm is not stable upon tuning but suddenly shifts in wavelength to 764.1 nm before it irrecoverably bleaches (inset in Fig. 9.17(b)). The abrupt change in spectral position comes along with a

	ZPL_1	1^{rst} PSB_1	2^{nd} PSB_1	ZPL_2
λ (nm)	740.0 ± 0.2	769.0 ± 0.5	828.6 ± 0.3	746.3 ± 0.3
$\Delta\lambda$ (nm)	1.50 ± 0.2	2.06 ± 0.3	2.16 ± 0.3	1.76 ± 0.5
energy (meV)			66	201

Table 9.5: Spectral position λ and linewidth $\Delta\lambda$ of the two zero-phonon lines and associated phonon side bands as well as the phonon side band energy of the SiV(6) center within the M7(A)-cavity. The values are averaged over 18 measurements. The error reflects the standard deviation.

	ZPL_1	1^{rst} PSB_1	2^{nd} PSB_1	ZPL_2	ZPL_2
λ (nm)	749.6 ± 0.1	793.1 ± 0.2	801.8 ± 0.4	756.4 ± 0.2	764.1 ± 0.1
$\Delta\lambda$ (nm)	1.92 ± 0.2	1.45 ± 0.4	1.52 ± 0.7	1.51 ± 0.4	1.25 ± 0.1
energy (meV)		96	115		

Table 9.6: Spectral position λ and linewidth $\Delta\lambda$ of the zero-phonon lines and phonon side bands as well as the phonon side band energy of the SiV(7) center within the M7(B)-cavity. The values are averaged over 60 measurements. The error reflects the standard deviation.

narrowing of the linewidth from 1.51 ± 0.4 to 1.25 ± 0.1 nm. Both effects might be attributed to a significant variation of the emitters environment following tuning. Table 9.6 summarizes the spectral positions and linewidths of the zero-phonon lines and the associated phonon side bands. In the phonon side band regime, two peaks at 793.1 and 801.8 nm are observed corresponding to energy shifts of 96 meV and 115 meV with respect to the ZPL at 749.6 nm. The peak at 96 meV coincide with a vibrational mode of the diamond lattice at 100 meV reported in literature, whereas the peak at 801.8 nm might be probably related to an electronic near-infrared transition of the SiV center. It is assumed, that due to presence of material strain, the here observed phonon energies slightly differ from literature data. In the SiV(7)/M7(B)-cavity spectrum, no phonon side band related to the SiV ZPL at 756.4/764.1 nm can be identified.

Beside the SiV emission lines, cavity modes are clearly observed in the M7(A)- and M7(B)-spectra. As discussed in chapters 5 and 7, the cavity modes are classified in even "e" and odd "o" modes according to their mirror symmetry upon reflection at the cavity center line in simulation and according to their polarization in experiment. We number the modes consecutively starting with the lowest frequency. In figure 9.17, the lowest order modes $e1$, $e3$, $o1$, $o2$ and $o3$ are indicated in the spectrum. In the subsequent section, we apply the digital oxidation technique to tune the cavity modes into resonance with the SiV emission lines.

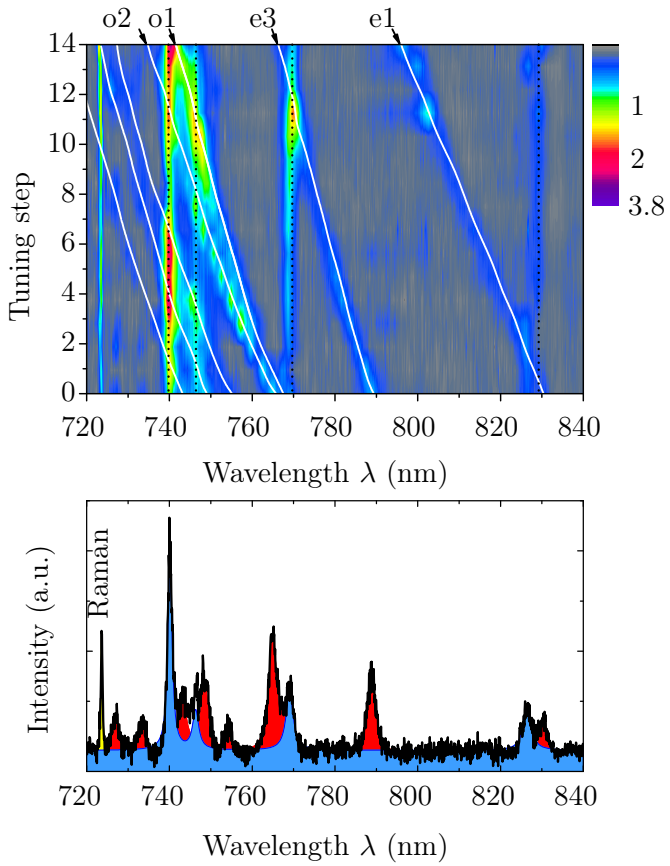

Figure 9.18: Spectral tuning of photonic crystal M7(A)-cavity modes: (a) Color plot showing the PL spectra obtained while tuning the cavity modes $e1$, $e3$, $o1$ and $o2$ over the SiV(6) ZPL and PSBs. On resonance a clear intensity enhancement is observed. The intensity is normalized to the off-resonant intensity of the SiV(6) ZPL. Note the logarithmic color scale. (b) M7(A)-cavity spectra before cavity tuning. The diamond Raman line at 722.85 nm as well as the SiV(6) emission lines (blue peaks) are fixed, whereas the cavity modes blue shift on average by 1.8 nm per oxidation step.

9.5.2 Cavity tuning of M7-cavities

Efficient resonant enhancement of SiV spontaneous emission rate requires spectral overlap of the cavity modes with the narrow-band transitions of the emitter, e.g. the ZPL. However, due to fabrication imperfections the frequency of the cavity modes does not match the emission lines but is red detuned (Fig. 9.17). To overcome this spectral mismatch, we employ the digital etching technique already presented in chapter 7. Thermal oxidation at 480 °C for 10 min in air slightly etches away diamond material. By this, the photonic crystal air holes are enlarged and the slab thickness is decreased, resulting in a blue shift of the cavity modes. Figures 9.18 and 9.19 show color plots of photoluminescence spectra upon tuning of the M7(A)- and M7(B)-cavity modes. The spectra are

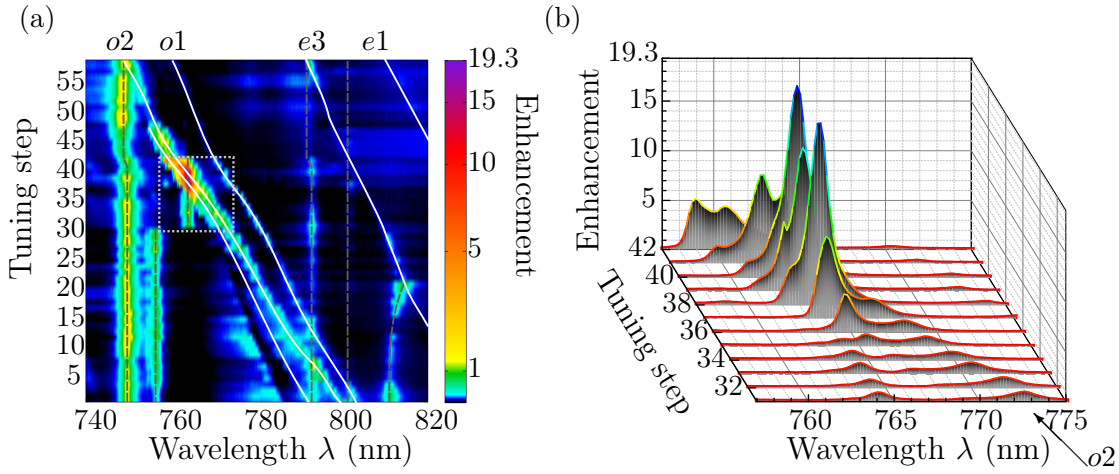

Figure 9.19: Spectral tuning of photonic crystal M7(B)-cavity modes: (a) Color plot showing the PL spectra obtained while tuning the cavity modes $e1$, $e3$, $o1$ and $o2$ over the SiV(7) ZPL at 764 nm and PSBs. The intensity is normalized to the off-resonant intensity of the SiV(7) ZPL. Note the logarithmic color scale. (b) Detailed view of the 764 nm-ZPL at tuning steps 31-42 (Region marked by rectangle in (a)). Shifting the $o2$ mode into resonance results in a large intensity enhancement by a factor of 19.3.

normalized to the off-resonant intensity of the incorporated SiV(6) or SiV(7) ZPL. As expected, the spectral positions of the zero-phonon line and phonon side bands as well as the diamond Raman line are fixed, while the cavity modes blue shift as a function of the oxidation steps. When the cavity modes are tuned into resonance with the ZPL or PSB of the SiV centers, the intensity significantly increases. We observe a maximal intensity enhancement of the SiV(6) ZPL by a factor of 3.8 when the $o1$ mode of the M7(A)-cavity is shifted into resonance (Fig. 9.18(c)). Even more impressive enhancement by a factor of 19.3 is observed for the SiV(7) ZPL when the $o2$ mode of the M7(B)-cavity is tuned into resonance. The ZPL intensity enhancement will be analyzed and discussed in detail in section 9.5.3. Similarly, when the cavity modes are tuned into resonance with the phonon side band transitions of the SiV(6) center at 828.6, 769.0 and 746.3 nm additional resonances are detected. The same phenomena is observed for the 793.1 and 801.8 nm lines in the SiV(7) side band region. As cavity enhancement is only effective for narrowband transitions comparable to the cavity bandwidth ($1.7 - 2.3$ nm), this observation supports the assumption that most of the coupled transitions are electronic transitions additional to the ZPL or a narrow local vibrational mode of the silicon atom in the case of the 769.0 nm line (c.f. page 258 ff.).

From the cavity tuning spectra, we deduce the tuning range and the dependence of the cavity Q-factors upon tuning (c.f. page 295). The central spectral positions of the M7(A)- and M7(B)-cavity modes $e1$, $e3$, $o1$, $o2$, $o3$ and the SiV zero-phonon lines and phonon side bands are plotted in figure 9.20 as a function of the oxidation step. Applying the digital oxidation technique, the M7(A)-cavity modes shift in total up to 45.6 nm with a mean tuning rate of 1.8 nm per tuning step. For oxidation steps

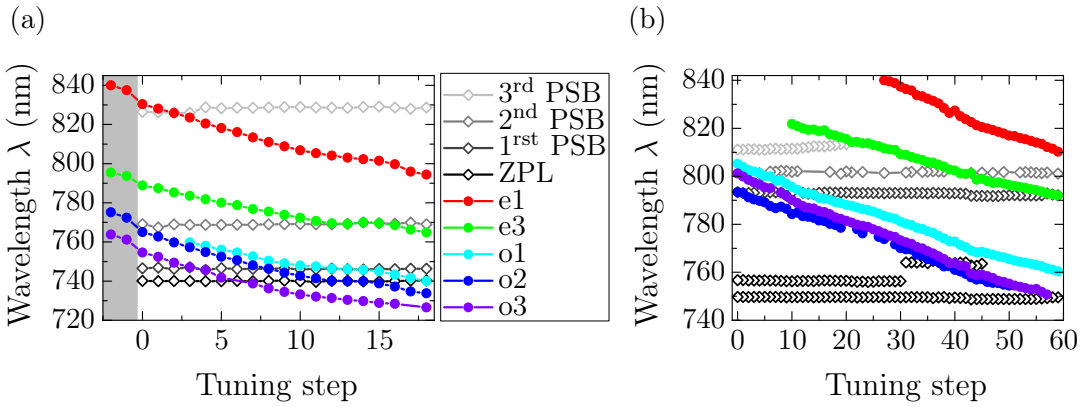

Figure 9.20: Central spectral positions of the (a) M7(A)- and (b) M7(B)-cavity modes, the zero-phonon lines (ZPL) and phonon side bands (PSB) of single SiV centers within the cavities as a function of the tuning steps.

$12-16$, the tuning rate is reduced to 1 nm per annealing step to study in more detail the coupling of the M7(A)-cavity modes to the SiV(6) center. For the M7(B)-cavity, we achieve a similar large total tuning range of 50.5 nm with a mean tuning rate of 0.8 nm. For comparison, we measured a mean tuning rate of 3 nm per oxidation step for the photonic crystal cavities used for coupling experiments to SiV ensembles (c.f. section 7.2). Although all three samples are oxidized under the same thermal conditions (annealing in air at 480 °C for 10 min), the tuning rates strongly differ. For the cavities realized in diamond with a high SiV density, the tuning rate is twice as big as the one of the M7(A)-cavity and four times larger than for the M7(B)-cavity. This reveals the strong dependence of the oxidation rate on the diamond quality and the CVD growth conditions.

Cavity tuning: comparison between experiment and theory

When tuning the cavity modes by the digital etching technique, we make use of the fact that the photonic crystal cavity modes are very sensitive to structural parameters, e.g. the air hole radius R or the thickness H of the diamond membrane. By slightly oxidizing diamond material, we increase the air holes and decrease the slab thickness, which both leads to a blue shift of the cavity modes. In order to relate the oxidation of the sample to structural changes of the photonic crystal and to assign the peaks in the spectra with the correct cavity modes, we numerically model the M7(A)- and M7(B)-cavity using FDTD simulations and compare them to experimental data. First, we have a detailed look at the M7(A)-cavity. Figure 9.20 shows the simulated resonance wavelengths of an ideal M7-cavity as a function of the air hole radius R and the slab thickness H. The constant slab thickness $H = 0.91a = 258\,\text{nm}$ (Fig. 9.20(a)) and the hole radius $R = 0.32a = 90.6\,\text{nm}$ (Fig. 9.20(b)) correspond to the parameters of the fabricated M7(A)-cavity, where $a = 283\,\text{nm}$ is the lattice constant. Comparing the experimental data to simulations, we confirm that the peaks in the tuning spectra

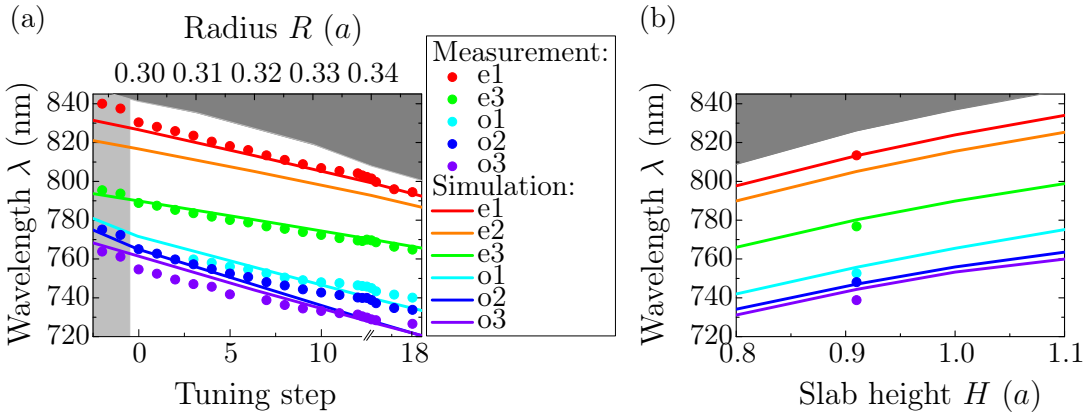

Figure 9.21: Comparison between experimental data of the M7(A)-cavity and simulated cavity modes: (a) Measured central spectral position of the M7(A)-cavity modes $e1$, $e3$, $o1$, $o2$ and $o3$ in dependence of the number of tuning steps. For comparison, calculated cavity modes as a function of the air hole radius R of an ideal M7-cavity are shown. In the simulation the slab thickness of $H = 0.91\,a = 258\,\text{nm}$ is kept constant, where $a = 283\,\text{nm}$ being the lattice constant. (b) Calculated cavity modes as a function of the slab thickness H. For comparison the measured mode wavelengths at tuning step seven are given. In the simulation the air hole radius $R = 0.32\,a = 90.6\,\text{nm}$ is kept constant. Dark gray shaded region: edge of the band gap, lines: simulated cavity modes, dots: measured data.

(Fig. 9.18) are attributed to the $e1$, $e3$, $o1$, $o2$ and $o3$ modes of the M7(A)-cavity. The $e2$ mode predicted by theory is not observed in the measured spectra. By comparing the experimental tuning spectra to theoretical simulations (Fig. 9.21), we deduce that successive oxidization of the diamond sample leads to an enlargement of hole radius of the M7(A)-cavity from $R = 0.30a = 84\,\text{nm}$ to $R = 0.35a = 100\,\text{nm}$ with a mean etch rate of the diamond material of 0.9 nm per oxidation step. The radius enlargement induces a theoretical tuning rate of 1.88 nm per annealing step (Fig. 9.21), which is in very good agreement with our experimental findings. Only for higher numbers of oxidation steps, the measured wavelengths of the odd cavity modes $o1$, $o2$ slightly differ from the theoretical predictions.

The disagreement between the measured and simulated resonant wavelengths is more pronounced for the M7(B)-cavity modes $e1$, $e3$, $o1$, and $o2$, which are displayed in figure 9.22(a) as a function of the air hole radius. At the beginning of the cavity tuning, the measured data follow perfectly the numerical predictions. However, the experimental tuning rate of the modes seems to slow down after several tuning steps and differs from theory. The discrepancy can not be explained by the fact that we neglected the change of the slab thickness in our simulations. Including a thickness decrease would predict even larger tuning rates coming along a steeper slope of the theoretical curves and the deviation from the experimental data would be even worse than plotted in figure 9.22(a).

We rather attribute the diminished tuning rate with increasing number of oxidation steps to anisotropic etch rates of the single crystal diamond membrane depending on

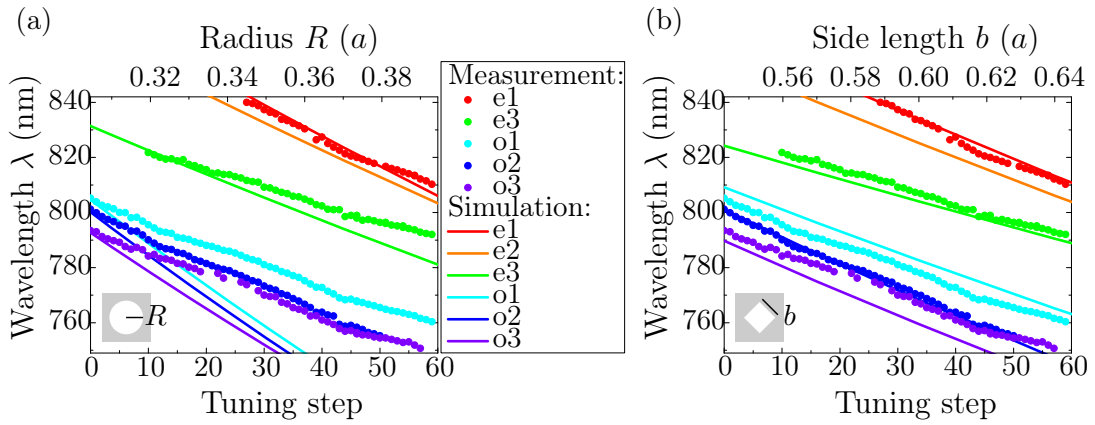

Figure 9.22: Comparison between measured wavelengths of the M7(B)-cavity modes as a function of oxidation steps and simulated modes of an ideal M7-cavity as a function of (a) the radius R assuming round air holes and of (b) the side length b assuming rectangular air holes. In the FDTD simulations the diamond slab thickness of $H = 1.41\,a = 400\,\text{nm}$ is kept constant. Here $a = 285\,\text{nm}$ is the lattice constant. Lines: simulated cavity modes, dots: measured spectral positions of M7(B)-cavity modes.

the crystallographic direction. Etch rates of natural diamond are known to exhibit strong orientation dependence with the (111) surface exhibiting the highest oxidation rate, followed by (110) with (100) being the lowest [483, 484]. During the oxidation process the diamond is preferentially removed along the fast etching crystallographic planes. Once reached a (100) diamond facet the etch rate significantly slows down and the (100) surfaces remain. The crystal orientation dependence of the etch rate results in a deformation of the air holes from the original round shape to a rectangular shape with side walls defined by (100) faces. To confirm this assumption, we check the air hole shape after 20 oxidation steps of the photonic crystal cavities that has been oriented 45° with respect to each other. The x-axis of the M3-cavity at the SiV(2) position has been aligned along the [110] diamond crystal axis, whereas the M3-cavity around the SiV(3) center is oriented along the [100] direction. After 20 oxidation steps, SEM images (Fig. 9.23) of both M3-cavities clearly reveal rectangular air holes with (100) oriented facets confirming anisotropic etch rate of the single crystal diamond membrane upon oxidation in air.

Interestingly, the appearance of a photonic band gap is not prohibited by the structural change of the air hole shape. Our simulations of triangular photonic crystal slabs reveal similar band gap widths both for rectangular and circular holes with the same filling factor $f = \pi R^2/A_u = b^2/A_u$, where $A_u = \sqrt{3}a^2$ being the area of the triangular unit cell and b the edge length of the rectangular holes. Figure 9.22(b) shows a comparison between the experimental resonant wavelengths and the numerical M7-cavity modes assuming rectangular air holes with varying edge length b. Even for large tuning steps, the theoretical curves almost perfectly model the measured data.

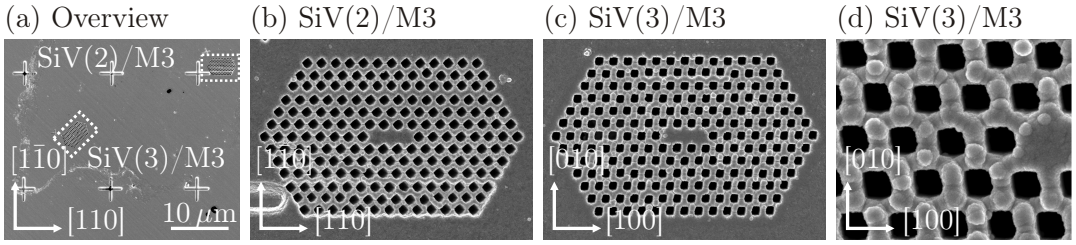

Figure 9.23: Structural change of the photonic crystal air holes due to anisotropic etch rates of diamond: (a) Overview of the M3-cavities fabricated around the SiV(2) and SiV(3) centers in the diamond membrane. The M3-cavity at the SiV(3) position is inclined by an angle of 45°. (b,c) SEM pictures of the M3-cavities at the (b) SiV(2) and (c) SiV(3) position reveal rectangular air holes with (100) oriented facets after 20 oxidation steps. (d) Detailed view of the SiV(3)/M3-cavity center.

Q-factor upon tuning

As a final step, we want to investigate the change of the experimental quality factors of the cavity modes following tuning. Fitting the cavity peaks in the photoluminescence spectra with Lorentzians, we determine the quality factor $Q = \lambda/\Delta\lambda$ via the spectral position λ and the linewidth $\Delta\lambda$. The dependence of the Q-factors as a function of the oxidation steps is depicted in figure 9.24 for the M7(A)- and M7(B)-cavity. Generally speaking, the cavity Q-factor is not degraded upon tuning. Disregarding small fluctuations the quality factors of the M7(A)-cavity modes are constant over a large number of oxidation steps (Fig. 9.24(a)). The same is true for the $e1$, $o1$ and $o2$ cavity modes of the M7(B) structure (Fig. 9.24(b)). Only the M7(B)-cavity mode $e3$ randomly fluctuates over the whole tuning range. These fluctuations are attributed to the weak signal to noise ratio of the $e3$ mode in the spectrum, which leads to large errors in the fitting procedure and hence to a large uncertainty in Q. Besides the fluctuations in Q due to the fitting routine, we observe at certain oxidation steps an apparent raise in Q decreasing after a few steps back to its original value. At these specific tuning steps, the cavity modes are shifted into resonance with an emission line of a single SiV center. In resonance, the lines of the cavity mode and SiV center can not be spectrally resolved and appear as one peak in the spectrum with its linewidth determined

Cavity	$Q_{exp,e1}$	$Q_{exp,e3}$	$Q_{exp,o1}$	$Q_{exp,o2}$	$Q_{exp,o3}$
M7(A)	300 ± 95	300 ± 60	320 ± 75	440 ± 75	
M7(B)	330 ± 50	600 ± 210	680 ± 130	430 ± 110	420 ± 180

Table 9.7: Experimental quality factors Q_{exp} of the lowest-order modes $e1$, $e3$, $o1$, $o2$, $o3$ of the of the M7(A)- and M7(B)-cavity. The M7(A) values are averaged over 18 measurements, whereas the M7(B) data are averaged over 60 measurements. The error reflects the standard deviation.

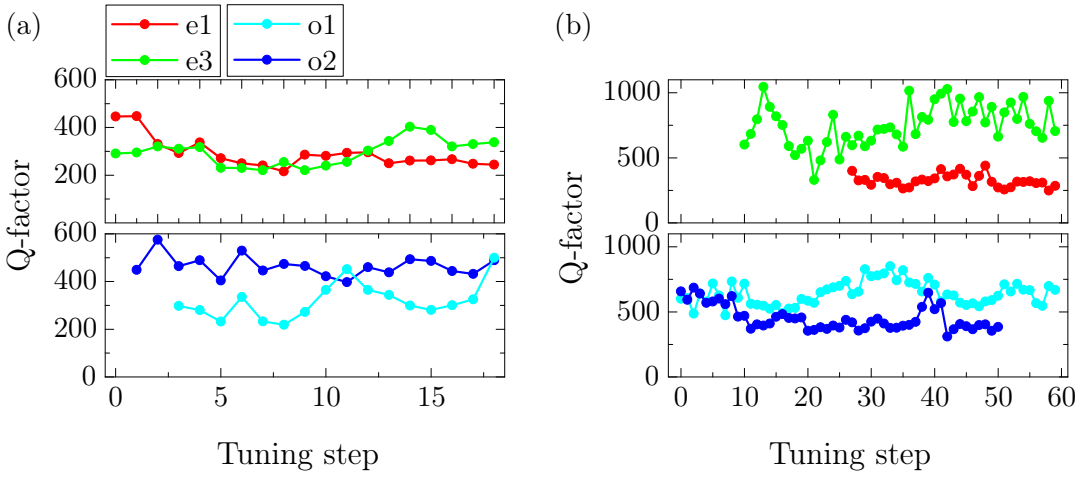

Figure 9.24: Dependence of the quality factor of the even modes $e1$, $e3$ and odd modes $o1$, $o2$ of the (a) M7(A)- and (b) M7(B)-cavity as a function of tuning steps.

by the linewidth of the color center's emission. To illustrate this, we consider the increase in the quality factor of the M7(A)-cavity mode $o1$ at tuning steps 11 and 18 (Fig. 9.24(a)). At these steps, the $o1$ mode resonantly couples to the side band at 746.3 nm and to the ZPL of the SiV(6) center, respectively. In resonance, the linewidth of the coupled emitter-cavity peak is dominated by the linewidth $\Delta\lambda_{\mathrm{PSB}} = 1.76\,\mathrm{nm}$ of the first PSB and $\Delta\lambda_{\mathrm{ZPL}} = 1.49\,\mathrm{nm}$ of the SiV(6) ZPL resulting in an apparent increase of the $o1$ Q-factor from 300 to $Q = (\lambda/\Delta\lambda)_{\mathrm{PSB}} = 746.3/1.76 \approx 450$ and $Q = (\lambda/\Delta\lambda)_{\mathrm{ZPL}} = 739.9/1.49 \approx 500$. The same effect can be observed at oxidation step 14, when the M7(A)-cavity mode $e3$ is tuned into resonance with the local defect mode of the SiV(6) center at 769.0 nm (Fig. 9.24 (a)) leading to an increase in the quality factor from 300 to $Q = (\lambda/\Delta\lambda)_{\mathrm{PSB}} = 769.0/2.0 \approx 400$. The measured Q-factors for the M7(B)-cavity modes are equally affected by the linewidth of the SiV emission peaks, when tuned into resonance. At oxidation step 39, the $o2$ mode is shifted in resonance with the SiV(7) ZPL with a linewidth of $\Delta\lambda_{\mathrm{ZPL}} = 1.25\,\mathrm{nm}$ raising the Q-factor from ~ 430 to $Q = (\lambda/\Delta\lambda)_{\mathrm{ZPL}} = 764.1/1.25 \approx 650$.

When calculating the average quality factors of the M7(A)-cavity, we neglect the resonant increase in linewidth, as the change in Q is rather attributed to a temporal effect of the emitter-cavity coupling than to permanent structural changes of the photonic crystal cavity. Table 9.7 specifies the quality factors of the M7(A)- and M7(B)-cavity modes that have been averaged over 18 and 60 measurements, respectively. The quality factors of the M7(A)-cavity modes are rather low ranging from 300 to 440. The same is true for the Q-factors of the $e1$, $o2$, $o3$ modes of the M7(B) structure. In contrast, the quality factors of the M7(B)-cavity modes $e3$ and $o1$ are significantly higher achieving averaged values of 600 and 680, respectively. The high $e3$ Q-factor comes along with a large error due to its weak signal to noise ratio in the spectrum due to uncertainties in the fitting procedure.

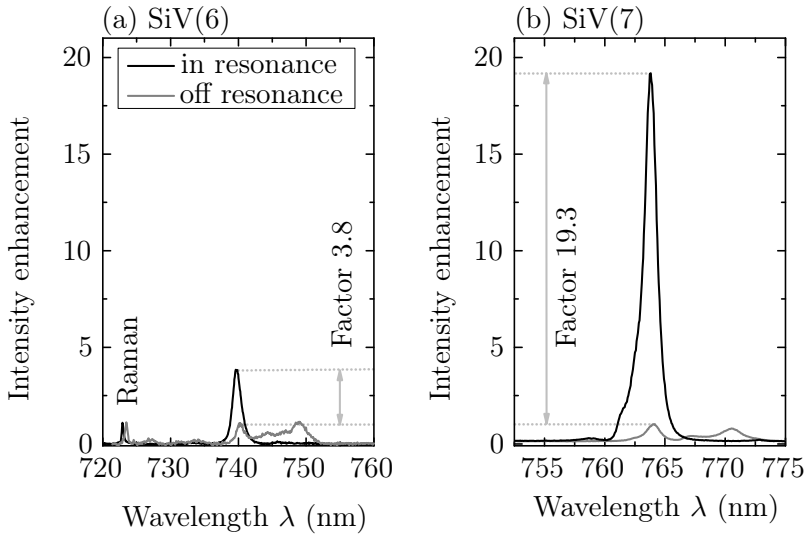

Figure 9.25: Spectrally resolved intensity enhancement of single SiV centers: (a) In resonance with the $o1$ mode of the M7(A)-cavity, the SiV(6) emission line is enhanced by a factor of 3.8 compared to the off resonant situation. (b) The SiV(7) ZPL signal increases by a factor of 19.3 when tuning the $o2$ mode of the M7(B)-cavity into resonance. The gray (black) curves are the cavity spectra off (on) resonance.

9.5.3 Resonant intensity enhancement

The digital oxidation technique allows us to tune the M7-cavity modes across the whole spectral range of the SiV center. In resonance with the SiV ZPL or PSBs, a clear intensity enhancement is detected. To extract the correct increase in the PL signal, we subtract the background in the in and off resonance spectra and normalize the data to the off-resonance maximum of ZPL signal (Fig. 9.25). When the $o1$ mode of the M7(A)-cavity is tuned into resonance, the intensity of the SiV(6) ZPL is increased by a factor of 3.8 (Fig. 9.25(a)). For reference, the intensity of the diamond Raman line is the same revealing correct normalization. The enhancement factor of the single SiV(6) ZPL is comparable to ensemble measurements presented in chapter 7. Significantly stronger raise in the PL signal by a factor of 19.3 is registered when the $o2$ mode of the M7(B)-cavity is tuned into resonance with the SiV(7) ZPL (Fig. 9.25(b)). In section 9.5.5, we will analyze the different coupling strengths to the SiV(6) and SiV(7) centers including the actual emitter position and dipole orientation with respect to the cavity field.

9.5.4 Enhancement of the spontaneous emission rate

As a next step, we investigate a possible change in the spontaneous emission rate of the SiV(7) center when tuning the $o2$ mode of the M7(B)-cavity into resonance. To this end, we deduce the internal population dynamics of the SiV(7) center by performing

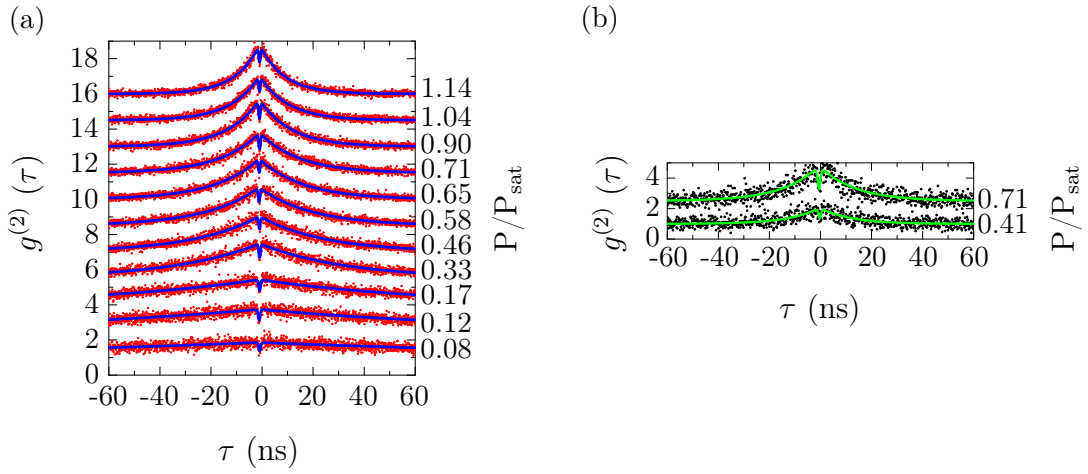

Figure 9.26: Intensity correlation measurement of the SiV(7) ZPL (a) in and (b) off resonance with the *o*2 M7-cavity mode taken for various excitation powers P. P is given in terms of the saturation power $P_{\mathrm{sat,cav}} = 0.89\,\mathrm{mW}$ and $P_{\mathrm{sat,PhC}} = 0.98\,\mathrm{mW}$ of the SiV(7) center on- and off-resonant with the cavity, respectively. The $g^{(2)}$ functions have been displaced by 1.5 for clarity. Dots: measured data, solid lines: fit according to equation (3.7) convoluted with the instrument response function of the setup.

intensity auto-correlation measurements at different excitation powers in and off resonance with the cavity mode. Moreover, the excited state lifetime is determined from the τ_1 time in the limit for vanishing excitation powers. Figure 9.26 displays the experimental $g^{(2)}$ functions of the SiV(7) center in and off resonance with the *o*2 M7(B)-cavity mode. Fitting the correlation measurements with equation (3.7) convoluted with the instrument response function of the setup, we determine the parameters τ_1, τ_2, a as a function of the excitation power P (Fig. 9.27), with the following limiting values at vanishing and high excitation powers: $\tau^0_{1,\mathrm{cav}} = 180 \pm 50\,\mathrm{ps}$, $\tau^0_{2,\mathrm{cav}} = 1\,\mu\mathrm{s}$, $\tau^\infty_{2,\mathrm{cav}} = 3\,\mathrm{ns}$ and $a^\infty_{\mathrm{cav}} = 29$. Here the excitation power P is given in terms of the saturation power $P_{\mathrm{sat,cav}} = 0.89\,\mathrm{mW}$. Using the theoretical three level model described in section 3.5, we extract the decay rates $k^{\mathrm{cav}}_{12} = \sigma P$, k^{cav}_{21}, k^{cav}_{23}, $k^{\mathrm{cav}}_{31} = dP/(P+c) + k^{0,\mathrm{cav}}_{31}$ listed in table 9.8 for the SiV(7) on resonance with the *o*2 mode.

For the same SiV(7) center off-resonant with M7(B)-cavity modes, we find the decay constants $k^{\mathrm{PhC}}_{12} = \sigma P$, k^{PhC}_{21}, k^{PhC}_{23}, $k^{\mathrm{PhC}}_{31} = dP/(P+c) + k^{0,\mathrm{PhC}}_{31}$ listed in table 9.8, with the limiting values $\tau^0_{1,\mathrm{PhC}} = 445 \pm 20\,\mathrm{ps}$, $\tau^0_{2,\mathrm{PhC}} = 1\,\mu\mathrm{s}$, $\tau^\infty_{2,\mathrm{PhC}} = 3\,\mathrm{ns}$ and $a^\infty_{\mathrm{PhC}} = 29$. The excitation power P is given in terms of the saturation power $P_{\mathrm{sat,PhC}} = 0.98\,\mathrm{mW}$. From the τ_1 curve in the limit of vanishing pump powers, we deduce the excited state lifetime of the SiV(7) center. The lifetime reduces by a factor of 2.4 from $\tau^0_{1,\mathrm{PhC}} = 450\,\mathrm{ps}$ off resonance to $\tau^0_{1,\mathrm{cav}} = 180\,\mathrm{ps}$ on resonance with the *o*2 cavity mode. As a consequence, the spontaneous decay rate k_{21} is 2.7 times faster in resonance compared to the off-resonant situation, whereas all other radiative decay rates are unchanged.

The here demonstrated controlled Purcell enhancement of the spontaneous emission

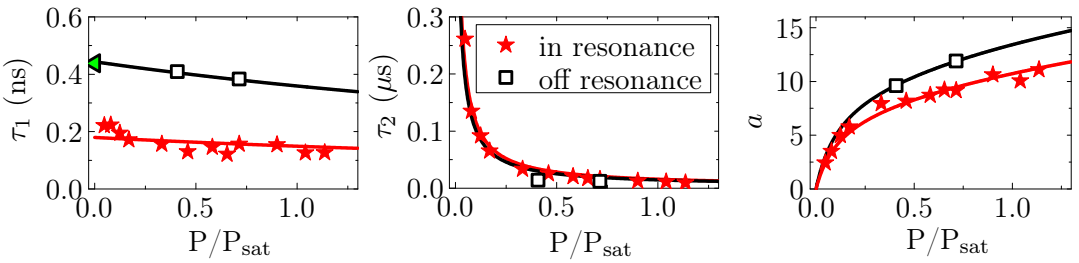

Figure 9.27: Population dynamics of the SiV(7) in and off resonance with the cavity mode: Power dependent model parameters τ_1, τ_2, a obtained from $g^{(2)}$ fits (Fig. 9.26). Black hollow squares: measured parameters off resonance, red stars: measured parameters in resonance, solid lines: theoretical power dependence of τ_1, τ_2, a used to determine the population dynamics of the SiV(7) center in (red) and off (black) resonance with the cavity mode. The green triangle in the τ_1 curve at $P = 0$ indicates the excited state lifetime $T_1 = 440 \pm 10$ ns deduced from time correlated single photon counting experiments under pulsed excitation.

SiV(7)	τ_1^0 (ps)	σ $\left(\frac{\text{MHz}}{P_{\text{sat}}}\right)$	k_{21} (MHz)	k_{23} (MHz)	k_{31}^0 (MHz)	d (MHz)	c (P_{sat})
cav	180 ± 50	1.2	5,238	322	1	10.1	1.3
PhC	445 ± 20	0.6	1,932	322	1	10.1	1.3

Table 9.8: Decay rates governing the population dynamics of the SiV(7) center on and off resonance with the M7(B)-cavity mode $o2$. The rate coefficients are evaluated from the limiting values τ_1, τ_2 and a shown in figure 9.27 using a three level model including a power-dependent deshelving rate $k_{31} = dP/(P+c) + k_{31}^0$ and a pump rate $k_{12} = \sigma P$. From figure 9.27, we deduce constant limiting values $\tau_{2,\text{cav}}^0 = \tau_{2,\text{PhC}}^0 = 1\,\mu$s, $\tau_{2,\text{cav}}^\infty = \tau_{2,\text{PhC}}^\infty = 3$ ns and $a_{\text{cav}}^\infty = a_{\text{PhC}}^\infty = 29$ upon tuning.

rate k_{21} of a single color center is one of the major results of this thesis. Via precise alignment and patterning a photonic nanocavity around the single SiV center and tuning the cavity modes across the entire emission spectrum, we here demonstrate for the first time deterministic coupling of a single color center at room temperature to an all-diamond photonic crystal cavity. The controlled cavity coupling is a major improvement compared to past schemes relying on completely random chance. Moreover, all previous cavity-coupling experiments to single color centers were performed at cryogenic temperatures where the NV ZPL features narrow emission lines.

Lifetime measurement of SiV(7) center

To confirm the lifetime $\tau_{1,\text{PhC}}^0$ deduced from $g^{(2)}$ measurements, we additionally perform lifetime measurements of the SiV(7) ZPL when it is detuned from the cavity mode. For this purpose, a fs Ti:sapphire laser (Spectra Physics Tsunami, 703 nm, 80 MHz repetition

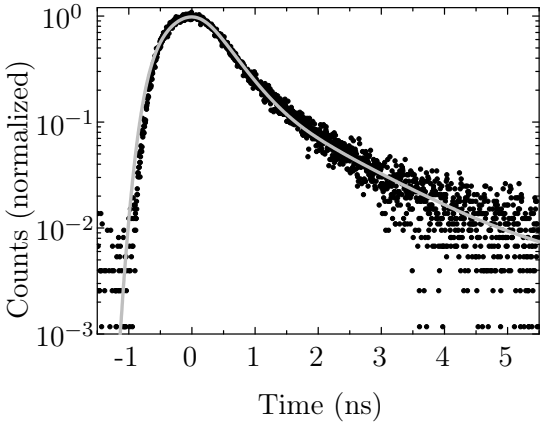

Figure 9.28: Lifetime measurement (black dots) of the SiV(7) center off-resonant with the cavity mode. The data is fitted with a bi-exponential decay convoluted with the instrument response function. The fit (red line) yields a lifetime of 440 ± 10 ps of the excited state.

rate, 400 mW average power) is used to excite the SiV(7) center. The spectrally filtered ZPL signal is detected by an APD with a timing jitter of 354 ps. Figure 9.28 shows the measured histogram taken on the SiV(7) ZPL. The data is fitted with a bi-exponential decay function convoluted with the instrument response function. From the fit, we determine an off-resonant lifetime of the excited state of 440 ± 10 ps, which is in very good agreement with the lifetime extracted from $g^{(2)}$ measurements for vanishing pump powers. The result of the lifetime measurement is plotted as a green triangle at $P = 0$ in the τ_1 curve of figure 9.27. The second, longer exponential decay time of $\sim$1.4 ns is attributed to background fluorescence of a second SiV center next to the SiV(7) center within the cavity.

9.5.5 Theoretical analysis of the Purcell factor

Our experiments demonstrate the considerable alternation of the spontaneous decay rate of a single color center via coupling to a photonic crystal cavity mode coming along with a significant intensity increase. In this section, we theoretically analyze the measured lifetime decrease and the associated intensity enhancement. To this end, we calculate the cavity Purcell factor $F_{\mathrm{cav}} = F_{\mathrm{P}}\, R_r\, R_d\, R_\lambda$ considering the ideal Purcell factor F_P of the M7(A)- and M(B)-cavity modes as well as the terms R_λ and R_r accounting for the spectral and spatial misalignment of the emitter-cavity field and the factor R_d considering the orientation of the SiV(6) and SiV(7) dipole moments with respect to the cavity electric field. From the theoretical cavity Purcell factor, we evaluate the expected enhancement of the spontaneous emission rate and the related rise in the PL signal and compare the predictions to the measured data.

As outlined already in chapter 7, coupling a photonic crystal cavity mode to the ZPL of a single color center, e.g. its ZPL, enhances the decay rate γ_{ZPL} by the cavity Purcell factor F_{cav}, whereas other radiative transitions into the phonon side bands γ_{PSB} are

inhibited by a factor $F_{\mathrm{PhC}} < 1$ due to the reduced local density of states in the photonic band gap [267]. Non-radiative transitions are completely unaffected by cavity-coupling. According to equations (7.2) and (7.3), γ_{cav} and γ_{PhC} are given by:

$$\gamma_{\mathrm{cav}} = F_{\mathrm{cav}}\,\gamma_{\mathrm{ZPL}} + F_{\mathrm{PhC}}\,\gamma_{\mathrm{PSB}} + \gamma_{\mathrm{nr}} \tag{9.12}$$

$$\gamma_{\mathrm{PhC}} = F_{\mathrm{PhC}}\,(\gamma_{\mathrm{ZPL}} + \gamma_{\mathrm{PSB}}) + \gamma_{\mathrm{nr}}. \tag{9.13}$$

The associated intensity enhancement $I_{\mathrm{cav}}/I_{\mathrm{PhC}}$ of the SiV ZPL is given as the ratio of the radiative rates on (off) resonance with the cavity mode, which are enhanced (inhibited) by Purcell coupling (photonic bandgap effect):

$$I_{\mathrm{cav}} = \eta_{\mathrm{cav}}\,F_{\mathrm{cav}}\,\gamma_{\mathrm{ZPL}} + \eta_{\mathrm{PhC}}\,F_{\mathrm{PhC}}\,\gamma_{\mathrm{PSB}} \tag{9.14}$$

$$I_{\mathrm{PhC}} = \eta_{\mathrm{PhC}}\,F_{\mathrm{PhC}}\,(\gamma_{\mathrm{ZPL}} + \gamma_{\mathrm{PSB}}), \tag{9.15}$$

where, η_{cav} and η_{PhC} denote the calculated collection efficiencies by the microscope objective (numerical aperture 0.8) of a dipole emitter in a photonic crystal in and off resonant with the cavity mode. Due to the weak phonon side band contributions of the SiV centers, the decay rate γ_{ZPL} into the ZPL is significantly larger than the rate γ_{PSB} into the PSB, yielding a simplified expression for the intensity enhancement:

$$\frac{I_{\mathrm{cav}}}{I_{\mathrm{PhC}}} \approx \frac{\eta_{\mathrm{cav}}}{\eta_{\mathrm{PhC}}}\frac{F_{\mathrm{cav}}}{F_{\mathrm{PhC}}}, \tag{9.16}$$

solely determined by the ratio of the collection efficiencies as well as the cavity and lattice Purcell factors.

In the following analysis, we deduce the cavity Purcell factor of the single SiV(6) and SiV(7) centers when coupled to the $o1$ and $o2$ mode of the M7(A)- and M7(B)-cavities. The resulting theoretical enhancement in the spontaneous emission rate and in the intensity are subsequently compared to the experimental data. First, we consider the coupling of the M7(A)-cavity to the SiV(6) center. From the quality factor $Q = 320 \pm 75$ and the mode volume $V = 1.3(\lambda/n)^3$ of the $o1$ mode, we calculate an ideal Purcell factor of $F_P = 18.7$, which would provoke an ideal intensity raise of $I_{\mathrm{cav}}/I_{\mathrm{PhC}} = 75$. In the case of the $o2$ mode of the M7(B)-cavity with $Q = 430 \pm 150$ and $V = 1.7(\lambda/n)^3$, we obtain a similar ideal Purcell factor of $F_P = 19.2$, resulting in an increase in the PL signal of $I_{\mathrm{cav}}/I_{\mathrm{PhC}} = 77$. Although both structures yield comparable figure of merits, the experimental intensity enhancement strongly differs by a factor of 5 (Fig. 9.25). The reasons are non-optimal dipole orientation and non-ideal position of the SiV centers within the cavity defect region. In the following, we determine the factors R_r, R_d and R_λ for the single SiV(6) and SiV(7) centers taking into account the actual emitter position in the M7(A) and M7(B)-cavity, the dipole orientation deduced from polarization measurements as well as the spectral emitter-cavity overlap. Moreover, we determine the in and off resonant collection efficiencies. From these individual contributions, the experimental cavity Purcell factors are evaluated.

Spatial overlap: For efficient coupling of a single SiV center to a photonic crystal cavity, the emitter should be placed at the maximum of the electric field. However,

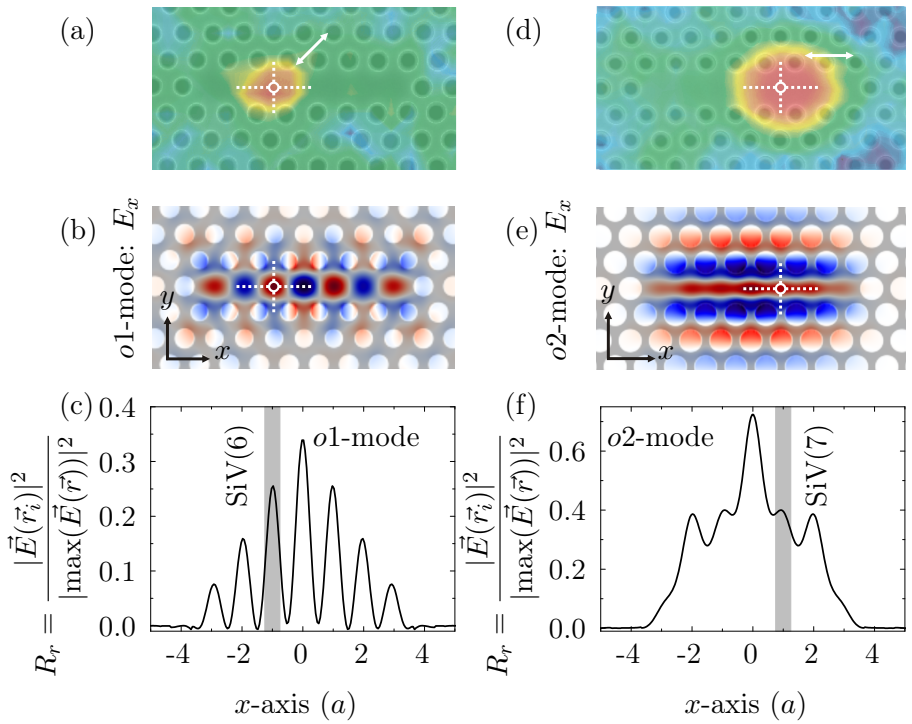

Figure 9.29: Positions of the SiV(6) and SiV(7) centers with respect to the electric cavity fields: (a,d) Fluorescence scans of the SiV(6) and SiV(7) centers within the M7-cavities overlapped with the SEM images. The emitters' positions are marked by white circles. (b,e) E_x component of the electric fields of the $o1$ and $o2$ modes of a M7-cavity. (c,f) Simulated normalized electric fields $|\vec{E}(\vec{r})|^2/|\max(\vec{E}(\vec{r}))|^2$ along the x-axis. The emitters' positions are marked by gray areas.

due to non-perfect positioning accuracy the ideal Purcell factor will be reduced by $R_r = |\vec{E}(\vec{r}_i)|^2/|\max(\vec{E}(\vec{r}))|^2$. By overlapping the fluorescence scans with the scanning electron microscope images of the fabricated cavity structures (Fig. 9.29(a,d)), the positions of the SiV(6) and SiV(7) center within the M7-cavities are estimated to be $(x, y) = (-a, 0)$ and $(a, 0)$, respectively, where a denotes the lattice constant. The E_x field distributions of the $o1$- and $o2$ modes that are tuned into resonance with the SiV(6) and SiV(7) center, respectively, are shown in figures 9.29 (b,e). The emitters' positions are marked by white circles. The factor R_r is determined by calculating the square of the absolute value of the cavity electric fields $|\vec{E}(\vec{r}_i)|^2$normalized to the field maximum. For the $o1$ and $o2$ modes, $|\vec{E}(\vec{r})|^2/|\max(\vec{E}(\vec{r}))|^2$ along the x-axis is displayed in figure 9.29(c,f). The emitters' positions are marked by the gray areas. For the SiV(6) center we obtain $R_r \approx 0.25$ and for the SiV(7) center we deduce $R_r \approx 0.4$. Note that deviations along the z-axis have a minor impact: Displacing the emitter by 150 nm out of the slab center changes R_r by less than 10%.

Dipole orientation: In the ideal case, the dipole moment of the emitter should be aligned parallel to the cavity electric field. For non-optimal dipole orientation, the Pur-

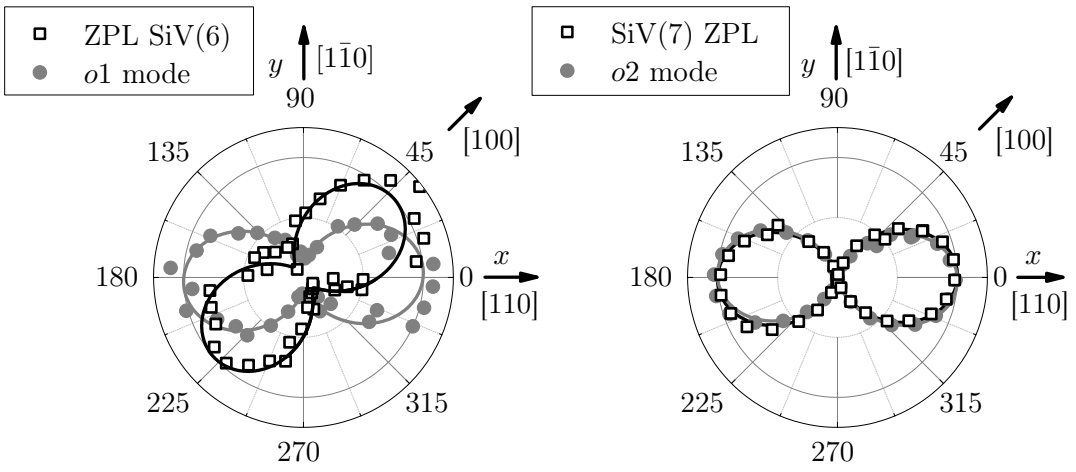

(a) SiV(6)/M7(A) (b) SiV(7)/M7(B)

Figure 9.30: Polarization polar plots of the SiV(6) and SiV(7) centers as well as of the M7(A)-cavity mode $o1$ and of the M7(B)-cavity mode $o2$. The cavity modes are linearly polarized along the cavity x-axis.

cell factor is lowered by $R_d = |\langle \vec{e}_d \cdot \vec{e}_E \rangle|^2$, where $\vec{e}_d$ and $\vec{e}_E$ are unit vectors pointing along the SiV dipole moment and the cavity electric field, respectively. Simulation of the odd cavity modes $o1$ and $o2$ predict that the E_x-field being the dominant field component giving rise to a linear polarization along the cavity x-axis (c.f. Fig. 5.39 on page 143). In the experiment, this prediction is confirmed via polarization analysis. As the x-axis of the M7(A)-cavity and M7(B)-cavities coincide with the [110] direction of the diamond membrane, we obtain $\vec{e}_E = (110)/\sqrt{2}$. For the SiV center in low-strain diamond, we would expect an orientation along the $\langle 111 \rangle$ crystallographic direction (c.f. page 262). Projected into the (001) diamond plane, this would correspond to an expected linear polarization along the $\langle 110 \rangle$ diamond direction. However, in the presence of material strain, the SiV dipole might rotate away from this ideal orientation. For the SiV(6) ZPL emission, we find a linear polarization along the [100] diamond axis (Fig. 9.30). Taking into account the z-component of the dipole, we obtain $\vec{e}_d = (101)/\sqrt{2}$. The out-off-plane tilt together with the angle discrepancy of 45° of the SiV(6) emission with respect to the cavity E_x-field results in a reduction of the Purcell factor by $R_d = 0.25$. In contrast, the polarization of the SiV(7) center projected into the (001) diamond plane seems to be perfectly aligned with the cavity E_x-field. Considering an orientation of the SiV dipole moment along the $\langle 111 \rangle$ crystallographic direction, i.e. $\vec{e}_d = (111)/\sqrt{3}$, we find an inclination angle of 35.3° with respect to the cavity in-plane fields, yielding $R_d = 0.67$ for the SiV(7) center coupled to the M7(B)-cavity mode.

Spectral overlap: Using the digital etching technique, the spectral mismatch between the cavity modes and the SiV(6) and SiV(7) ZPL is minimized yielding $R_\lambda = 1$. This assumption is valid as the $o1$ and $o2$ cavity modes have much wider linewidths of 2.3 nm

SiV/Cavity	F_{P}	R_d	R_r	R_λ	F_{cav}	$\frac{I_{\mathrm{cav}}}{I_{\mathrm{PhC}}}$	$\frac{I_{\mathrm{cav}}^{exp}}{I_{\mathrm{PhC}}^{exp}}$	$\frac{\gamma_{\mathrm{cav}}}{\gamma_{\mathrm{PhC}}}$	$\frac{\gamma_{\mathrm{cav}}^{exp}}{\gamma_{\mathrm{PhC}}^{exp}}$
SiV(6)/M7(A)	18.7	0.25	0.25	1	1.17	4.7	3.8	-	-
SiV(7)/M7(B)	19.2	0.67	0.40	1	5	20	19.3	2.66	2.7

Table 9.9: Calculated cavity Purcell factor F_{cav} and expected intensity enhancement $I_{\mathrm{cav}}/I_{\mathrm{PhC}}$ of the M7^A- and M7^B-cavity deduced from the ideal Purcell factor F_{P}, the non-optimal dipole orientation R_d, the spatial and spectral mismatch R_r and R_λ as well as the on-off-resonance collection efficiencies. The theoretical intensity increase $I_{\mathrm{cav}}/I_{\mathrm{PhC}}$ and enhancement of the spontaneous emission rate $\gamma_{\mathrm{cav}}/\gamma_{\mathrm{PhC}}$ are in very good agreement with the experimental data $I_{\mathrm{cav}}^{exp}/I_{\mathrm{PhC}}^{exp}$ and $\gamma_{\mathrm{cav}}^{exp}/\gamma_{\mathrm{PhC}}^{exp}$.

(1.7 nm) than the narrow SiV(6) (SiV(7)) zero-phonon line with $\Delta\lambda = 1.5$ nm (1.25 nm).

Collection efficiencies: As outlined in section 5.7.3 on page 144, we calculate the collection efficiencies by numerically integrating the far-field intensity distribution radiated in the vertical direction over the collection angle defined by the microscope objective (numerical aperture of 0.8). The simulations for the $o1$ and $o2$ field distributions confined to the M7(A) and M7(B)-cavity, reveal almost identical collection efficiencies $\eta_{\mathrm{cav}} \approx 30\%$ and $\eta_{\mathrm{PhC}} \approx 30\%$ for a dipole emitter in and off resonance with the cavity modes.

Due to non-ideal emitter positioning and non-optimal orientation of the emitter dipole moment with the cavity electric field, we obtain an effective Purcell factor of $F_{\mathrm{cav}} = F_P\, R_r\, R_d\, R_\lambda = 1.17$ for the $o1$ mode of the M7(A)-cavity. Together with the calculated collection efficiencies and the average Purcell factor $F_{\mathrm{PhC}} = 0.25$ of the photonic lattice, we obtain a theoretical intensity enhancement of $I_{\mathrm{ZPL}}/I_{\mathrm{PSB}} \approx 1.17/0.25 = 4.7$, which is in very good agreement with the experimental increase in the PL signal of 3.8. The Purcell factor of the $o2$ mode of the M7(B)-cavity yields $F_{\mathrm{cav}} = 5$, resulting in a theoretical intensity increase of $I_{\mathrm{ZPL}}/I_{\mathrm{PSB}} \approx 5/0.25 = 20$, which almost perfectly reflects the measured enhancement by a factor of 19.3. Moreover, taking into account the measured quantum efficiencies $\eta_{\mathrm{qe,cav}}^{\mathrm{exp}} = 0.49 \pm 0.04$ and $\eta_{\mathrm{qe,PhC}}^{\mathrm{exp}} = 0.08 \pm 0.01$ of the single SiV(7) center in- and off-resonant with the $o2$ cavity mode (c.f. section 9.6), we calculate a theoretical enhancement of the spontaneous emission rate of $\gamma_{\mathrm{cav}}/\gamma_{\mathrm{PhC}} = 2.66 \pm 0.09$. This prediction is in excellent agreement with the enhancement by 2.7 of the spontaneous decay rate k_{21} deduced from internal population dynamics. All correction factors of both cavity modes as well as the deduced cavity Purcell factors together with the theoretical and experimental intensity enhancement and modification in the spontaneous decay rate are summarized in table 9.9. Our detailed analysis of emitter-cavity coupling, whereof all parameters are deduced from independent measurements, allows us identity the limitations of our coupling scheme and to deduce the experimental cavity Purcell factor perfectly describing the impact of light-matter interaction on the internal population dynamics of a single emitter.

9.6 Modification of the SiV quantum efficiency

As seen in the previous sections, by coupling an emitter to a cavity, solely the radiative decay rates $\gamma_{\mathrm{rad}} = \gamma_{\mathrm{ZPL}} + \gamma_{\mathrm{ZPL}}$ is either Purcell-enhanced by the cavity mode or suppressed by the photonic bandgap whereas the non-radiative transition rates γ_{nr} are unaffected. The modification of the radiative transitions rates induces a change in the emitter's quantum efficiency compared to bulk when structuring a photonic crystal pattern around it. We expect an increase/decrease in the quantum yield when the SiV center is on/off resonance with a photonic crystal cavity mode. In this section, we deduce the quantum efficiencies of the single SiV(1) and SiV(7) centers located in the photonic crystal and compare them to the efficiencies in the unstructured membrane. The calculation is based on two independent measurements: The first approach involves the theoretical Purcell factors of the photonic lattice F_{PhC} and the cavity modes F_{cav}, whereas the second method is based on independent saturation measurements and internal population dynamics of the individual SiV centers.

Theory (inferred from Purcell measurements) The quantum efficiency of a single SiV center can be deduced from the Purcell enhancement factor F_{cav}, the photonic lattice inhibition factor F_{PhC} and the population dynamics of the emitter on/off resonance with a cavity mode of the photonic crystal. When the emitter is placed in a photonic lattice off resonance with any cavity mode, the radiative decay rates are suppressed by a factor F_{PhC} due to the photonic bandgap, resulting in a quantum efficiency of

$$\eta_{\mathrm{qe,PhC}}^{\mathrm{th}} = \frac{F_{\mathrm{PhC}}\gamma_{\mathrm{rad}}}{F_{\mathrm{PhC}}\gamma_{\mathrm{rad}} + \gamma_{\mathrm{nr}}} \tag{9.17}$$

When a photonic crystal cavity mode is tuned into resonance with the ZPL, γ_{ZPL} is enhanced by the Purcell factor F_{cav} whereas the phonon side bands are suppressed by the inhibition factor F_{PhC}. On resonance, the quantum efficiency is given by

$$\eta_{\mathrm{qe,cav}}^{\mathrm{th}} = \frac{F_{\mathrm{cav}}\gamma_{\mathrm{ZPL}} + F_{\mathrm{PhC}}\gamma_{\mathrm{PSB}}}{F_{\mathrm{cav}}\gamma_{\mathrm{ZPL}} + F_{\mathrm{PhC}}\gamma_{\mathrm{PSB}} + \gamma_{\mathrm{nr}}} \tag{9.18}$$

From the measured population dynamics, the decay rates from the excited state $|2\rangle$ to the ground state $|1\rangle$ $\gamma_{\mathrm{bulk}} = k_{21}^{\mathrm{bulk}}$, $\gamma_{\mathrm{cav}} = k_{21}^{\mathrm{cav}}$ and $\gamma_{\mathrm{PhC}} = k_{21}^{\mathrm{PhC}}$ of a single SiV center placed either in bulk or in a photonic lattice on/off resonance with a cavity mode are determined. In combination with the Purcell factors F_{cav} and F_{PhC}, the quantum efficiencies on/off resonance can be evaluated.

Experiment (measured from saturation count rates) The alternative method to deduce the quantum efficiency at the single quantum level is based on independent saturation measurements and the internal population dynamics of the single SiV center. As presented on page 269, under continuous wave laser excitation, the quantum efficiency $\eta_{\mathrm{qe}}^{\mathrm{exp}}$ can be deduced via equation (9.4) from the saturation photon count rate

I^{∞} normalized to the overall detection efficiency of our setup η_{det}, the spontaneous decay rate k_{21} and the maximum steady state population of the excited state n_2^{∞}. The population n_2^{∞} is evaluated via equation (9.5) from the rates k_{23}, k_{31}^0 and d governing the population dynamics of the SiV center. In the following, we calculate the quantum efficiencies of the SiV(1) and SiV(7) centers using both approaches.

Quantum efficiency of the SiV(1) center

First, we calculate the quantum efficiency of the SiV(1) center when it is either placed in the bare unstructured membrane or located in a periodic photonic lattice.

Theory Taking into account the population dynamics (table 9.4) deduced from the $g^{(2)}$ measurements, the decay rates on the transition $|2\rangle$ to $|1\rangle$ of the SiV(1) center placed in the bare membrane and in the photonic lattice are given by: $\gamma_{\mathrm{bulk}} = k_{21}^{\mathrm{bulk}} = 766.6\,\mathrm{MHz}$ and $\gamma_{\mathrm{PhC}} = k_{21}^{\mathrm{PhC}} = 382.0\,\mathrm{MHz}$, respectively. Considering the inhibition Purcell factor $F_{\mathrm{PhC}} = 0.25$ calculated by FDTD simulations (c.f. section 5.4.2 on page 100), we obtain the radiative and non-radiative decay rates $\gamma_{\mathrm{rad}} = (1.95\,\mathrm{ns})^{-1}$ and $\gamma_{\mathrm{nr}} = (3.94\,\mathrm{ns})^{-1}$, respectively. With these values, the theoretical quantum efficiencies of the SiV(1) in bulk and in the photonic crystal lattice are deduced:

$$\eta_{\mathrm{qe,bulk}}^{\mathrm{th}} = \frac{\gamma_{\mathrm{rad}}}{\gamma_{\mathrm{rad}} + \gamma_{\mathrm{nr}}} = 0.66, \qquad \eta_{\mathrm{qe,PhC}}^{\mathrm{th}} = \frac{F_{\mathrm{PhC}}\gamma_{\mathrm{rad}}}{F_{\mathrm{PhC}}\gamma_{\mathrm{rad}} + \gamma_{\mathrm{nr}}} = 0.33 \tag{9.19}$$

Experiment To confirm the theoretical quantum efficiency determined by the Purcell inhibition factor, we alternatively calculate the quantum efficiency using independent saturation measurements. For the SiV(1) center located in the bare unstructured membrane, the saturation measurement yields a count rate of $I_{\mathrm{bulk}}^{\infty} = 360{,}000\,\mathrm{counts/s}$. The overall detection efficiency of our setup is estimated to be $\eta_{\mathrm{det,bulk}} = (3.3 \pm 0.8) \times 10^{-3}$. Thereby, we suppose a collection efficiency of $3.5 \pm 0.5\%$ [474] of an emitting dipole by a microscope objective (numerical aperture 0.8) when the dipole is placed at the diamond-air interface and oriented parallel to the interface. Taking into account the decay rate $k_{21}^{\mathrm{bulk}} = 766.6\,\mathrm{MHz}$ and the excited state population $n_{2,\mathrm{bulk}}^{\infty} = 0.22$ evaluated using equation (9.5), we determine the quantum efficiency of the SiV(1) center in the unstructured diamond membrane to be $\eta_{\mathrm{qe,bulk}}^{\mathrm{exp}} = 0.63 \pm 0.13$. In contrast, when the SiV(1) center is placed in a photonic crystal lattice, a saturation photon count rate of $I_{\mathrm{PhC}}^{\infty} = 270{,}000\,\mathrm{counts/s}$ is measured with an overall detection efficiency of $\eta_{\mathrm{det,PhC}}^{\mathrm{exp}} = (23 \pm 5) \times 10^{-3}$. Considering the decay rate $k_{21}^{\mathrm{PhC}} = 382.0\,\mathrm{MHz}$ and the excited state population $n_{2,\mathrm{PhC}}^{\infty} = 0.22$, the quantum efficiency of the SiV(1) center is reduced to $\eta_{\mathrm{qe,PhC}}^{\mathrm{exp}} = 0.18 \pm 0.04$. Due to the photonic bandgap effect coming along with an inhibition of the radiative decay rates, the quantum efficiency strongly decreases. To summarize, the experimental quantum efficiencies

$$\eta_{\mathrm{qe,bulk}}^{\mathrm{exp}} = 0.63 \pm 0.13, \qquad \eta_{\mathrm{qe,PhC}}^{\mathrm{exp}} = 0.18 \pm 0.04 \tag{9.20}$$

are in very good agreement with the theoretical values estimated from the Purcell inhibition factor.

Quantum efficiency of the SiV(7) center

Second, we determine the quantum efficiency of the SiV(7) center in and off resonance with the $o2$ mode of the M7(B)-cavity.

Theory To calculate the quantum efficiency of the SiV(7) center when its ZPL is in and off resonance with the $o2$ mode, we take into account the Purcell factor $F_{\mathrm{cav}} = 5$ (table 9.9 in section 9.5.5) and the simulated inhibition factor $F_{\mathrm{cav}} = 0.25$ due to the photonic bandgap effect. From the population dynamics (table 9.8 in section 9.5.4), the on resonance decay rate $\gamma_{\mathrm{cav}} = k_{21}^{\mathrm{cav}} = 5{,}238\,\mathrm{MHz}$ and off resonance transition rate $\gamma_{\mathrm{PhC}} = k_{21}^{\mathrm{PhC}} = 1{,}932\,\mathrm{MHz}$ are deduced. Assuming a branching ratio $\gamma_{\mathrm{ZPL}} : \gamma_{\mathrm{PSB}}$ of 4:1 [25], we extract the zero-phonon emission rate $\gamma_{\mathrm{ZPL}} = (1.44\,\mathrm{ns})^{-1}$, the phonon side band rate $\gamma_{\mathrm{PSB}} = (5.75\,\mathrm{ns})^{-1}$ and the non-radiative decay rate $\gamma_{\mathrm{nr}} = (583\,\mathrm{ps})^{-1}$. Based on these transition rates the on/off resonance quantum efficiency as well as a hypothetical quantum efficiency for the SiV(7) center in the unpatterned diamond membrane can be evaluated using equations (9.17) and (9.18):

$$\eta_{\mathrm{qe,cav}}^{\mathrm{th}} = 0.67, \qquad \eta_{\mathrm{qe,PhC}}^{\mathrm{th}} = 0.11, \qquad \eta_{\mathrm{qe,bulk}}^{\mathrm{th}} = 0.34. \tag{9.21}$$

Experiment To verify the theoretical values determined above from the Purcell factors, we additional deduce the quantum efficiency of the SiV(7) center from independent saturation measurements. When the SiV(7) center is off resonance with the $o2$ mode, we obtain a quantum efficiency of $\eta_{\mathrm{qe,PhC}}^{\mathrm{exp}} = 0.08 \pm 0.01$, with $I_{\mathrm{PhC}}^{\infty} = 8.2\,\mathrm{k\,counts/s}$, $\eta_{\mathrm{det}} = (1.6 \pm 0.2) \times 10^{-3}$, $n_2^{\infty} = 3.3\%$ and $k_{21}^{\mathrm{PhC}} = 1{,}932\,\mathrm{MHz}$. For the SiV(7) ZPL in resonance with the $o2$ cavity mode, we estimate a quantum efficiency of $\eta_{\mathrm{qe,cav}}^{\mathrm{exp}} = 0.47 \pm 0.04$, with $I_{\mathrm{cav}}^{\infty} = 428\,\mathrm{k\,counts/s}$, $\eta_{\mathrm{det}} = (5.3 \pm 0.7) \times 10^{-3}$, $n_2^{\infty} = 3.3\%$ and $k_{21}^{\mathrm{cav}} = 5{,}238\,\mathrm{MHz}$. To summarize, the experimental quantum efficiencies

$$\eta_{\mathrm{qe,cav}}^{\mathrm{exp}} = 0.47 \pm 0.04, \qquad \eta_{\mathrm{qe,PhC}}^{\mathrm{exp}} = 0.08 \pm 0.01 \tag{9.22}$$

of the SiV(7) center on/off resonance with the $o2$ mode are in good agreement with the theoretical predictions calculated via the Purcell enhancement and inhibition factors.

The increase and decrease in the quantum efficiency unambiguously proves the impact of the cavity coupling and photonic band gap effect on the emission properties of the single emitter. On resonance with the SiV(7) center, a fraction of $F_{\mathrm{cav}}\gamma_{\mathrm{ZPL}}/\gamma_{\mathrm{cav}} = 63\%$ of the total decay rate γ_{cav} and $F_{\mathrm{cav}}\gamma_{\mathrm{ZPL}}/\gamma_{\mathrm{rad}} = 98.8\%$ of the radiative emission γ_{rad} are channeled into the cavity mode. However, the bulk quantum efficiency of single SiV centers investigated in this section and in section 9.1 differ a lot, ranging from 0.11 (SiV(3)) over $0.32 - 0.34$ (SiV(2) and SiV(7)) to 0.66 (SiV(1)). It is well-known that the radiative decay rates scatter largely for emitters in strained diamond material. Differences in the quantum efficiencies have also been detected for single SiV centers [55], NV

centers [447,448,476] and chromium-related defects [158] in nanodiamonds. Besides this variation due to material strain, our measurements demonstrate the suitability of single SiV centers as bright and efficient single photon sources with radiative quantum yields up to 0.66 that can be even enhanced via cavity-coupling. The quantum efficiency in bulk is definitely competitive with $\eta_{\mathrm{qe}} = 0.3$ [157] reported for single chromium-related centers in bulk diamond, with $\eta_{\mathrm{qe}} = 0.52 - 0.7$ [162, 163, 473] found for single NE8 centers in single crystal diamond and with 0.7 [456] deduced for single NV centers in bulk, respectively.

9.7 Polarization control

Beyond the change of the spontaneous emission, the emitter's polarization can be controlled by cavity-coupling, as shown previously e.g. for quantum dots weakly coupled to photonic crystal cavities [485, 486] or to micropillars [487]. Here, we consider the transition at 793.1 nm in the side band region of the SiV(7) center linearly polarized along the azimuthal angle $\phi = 60°$. By progressively tuning two cavity modes $m_{0°}$ and $m_{-45°}$ with polarization angles $\phi = 0°$ and $\phi = -45°$ into resonance with the SiV phonon side band, we continuously rotate its polarization emission angle ϕ from $+60°$ to $-45°$ (Fig. 9.31(a)). At zero detuning, the SiV polarization is oriented parallel to the cavity mode. For large detunings the original polarization state of the SiV center is restored. The polarization visibility of the emitted light remains high for all detunings as can be seen in the polar plots at the center of figure 9.31 measured at different tuning steps. In contrast to emission, the angle of maximum absorption is unchanged upon tuning and remains at 60° (Fig. 9.31(b)).

In the case of quantum dots weakly coupled to a photonic crystal cavity, Gallardo et al. [485] associated the observed polarization rotation of the emitted light to (1) a preferential enhancement of the emission parallel to the cavity mode via Purcell coupling as the detuning decreases and to (2) a detuning-dependent hybridization of the emitter cavity states. For the first explanation, the total emission can be considered as a superposition of cavity-enhanced photons and uncoupled photons. The linear combination of the two virtually inclined dipoles results in a change of the polarization state as the detuning decreases. However, in the case of large difference in the polarization degree, the visibility is expected to strongly diminish. In our experiments (Fig. 9.31) and in reference [485], no important degradation in visibility was observed. Hence, the preferential Purcell enhancement of the emitted photons with parallel orientation to the cavity mode is not considered as the major origin for polarization rotation. The second explanation implies the hybridization of emitter-cavity states. The concept of mixed emitter-cavity eigenstates is well established to mathematically describe coherent light-matter interaction in the strong coupling regime. Gallardo et al. [485] transfer the idea to the weak coupling regime. The coupled emitter-cavity system is presented by hybridized states as a linear combination of the bare color center and cavity states. With decreasing detuning, the combined system evolves from the emitter state to the cavity state coming along with a continuous rotation of the polarization. This concept

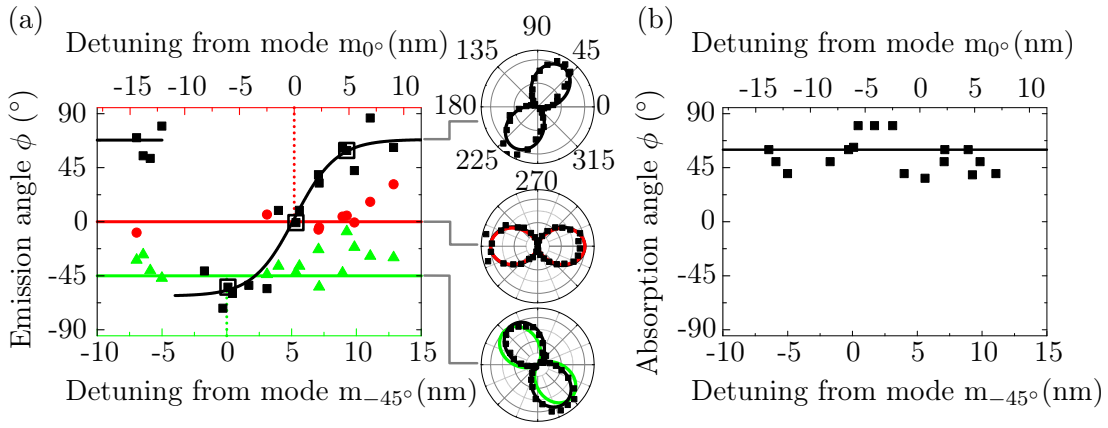

Figure 9.31: (Color) Continuous polarization control: (a) Polarization emission angle ϕ of the SiV(7) phonon side band (■) as a function of the detuning from the cavity modes $m_{0°}$ and $m_{-45°}$ with polarization angles $\phi = 0°$ (●) and $\phi = -45°$ (▲), respectively. The solid lines are a guide to the eye. At the center: Polar plots of SiV phonon side band (■) and of cavity modes (red/green solid line) for selected detunings (□). (b) In contrast to emission, the absorption angle is constant over the whole detuning range.

qualitatively explains our measured data.

To summarize, precise and almost continuous control of the linear polarization emission angle was achieved by changing the energy detuning between the SiV emission line and the cavity mode. Deterministic rotation of the linearly polarized emission is an essential prerequisite for polarization controlled single photon emitters.

9.8 Summary

In this chapter, we presented active alignment and deterministic coupling of an all-diamond photonic crystal cavity to a single pre-selected SiV center. Our active positioning technique offers major improvement in reproducibility and reliability compared to past schemes relying on completely random chance. The outstanding emission properties of the SiV center enabled the demonstration of cavity quantum electrodynamic effects even at room-temperature, whereas all previous cavity coupling experiments to single NV centers were performed at cryogenic temperatures where the NV ZPL exhibit narrow emission lines. We observed both inhibition and enhancement of the spontaneous emission rate due to the photonic band gap effect and due to cavity-coupling, respectively. From the measured internal population dynamics, we clearly deduced a change in the quantum efficiency of single color centers when coupled to the cavity.

As a first step, we investigated the spectral properties of single SiV centers incorporated in heteroepitaxial diamond membranes. The SiV centers exhibit extraordinarily narrow zero-phonon lines with linewidths down to 0.55 nm and weak contributions of phonon side bands. Single photon count rates up to 360 k counts/s were detected at

saturation. Using intensity correlation measurements, we verified the single emitter character of the investigated SiV centers and deduced the internal population dynamics as well as the excited state lifetime and the quantum efficiency. Due to the presence of material strain within the diamond membrane, the ZPL position ($710 - 770\,\mathrm{nm}$), linewidth ($0.55 - 3.0\,\mathrm{nm}$) and linear polarization angle as well as the excited state lifetime ($0.35 - 1.56\,\mathrm{ns}$) and quantum efficiency ($0.15 - 0.66$) varies between different centers located in the diamond membrane. It is well-known that these properties scatter largely for SiV centers in strained diamond material. Taking into account the different host material and local density of states, we made sure that the wavelengths and lifetimes observed here fall well into the range of previously determined values [25, 55, 227]. The outstanding narrow emission lines of the SiV centers allow us to study cavity coupling at room temperature using a tailored fabrication process: We structured monolithic photonic crystal cavities around pre-characterized single SiV centers in the diamond membrane using positioning markers and focused ion beam milling. The technique enables deterministic positioning of single color centers at the center of photonic crystal structures as well as the controlled alignment to the SiV dipole moment with respect to the cavity axis. Using active alignment, we achieved spatial positioning of a single SiV center within a photonic crystal with success rate of approximately 70%. Upon patterning of the material, the SiV dipole orientation was preserved, whereas release of local strain might slightly shift the ZPL and modify the linewidth. For SiV centers hosted in the periodic photonic crystal lattice, the spontaneous transition rate was suppressed for ZPLs coinciding with the photonic band gap, whereas beyond the stop band the bulk values of the unstructured membrane were resumed. Based on internal population dynamics, we demonstrated inhibition of the spontaneous emission rate of a single SiV center by a factor of two coming along with a two-fold increase in the excited state lifetime. From the recombination rates and the experimental quantum efficiency, we evaluated the Purcell factor $F_{\mathrm{PhC}}^{exp} = 0.21 \pm 0.16$ of the photonic crystal lattice. This value is in very good agreement with the averaged inhibition factor $F_{\mathrm{PhC}} = 0.25$ calculated via FDTD simulations. As a next step, we demonstrated deterministic cavity-coupling of two single SiV centers each located at the center of a photonic crystal M7-cavity. The spectrum taken at the center of the photonic structure clearly reveal both SiV emission lines and cavity modes. Using digital oxidation technique, the cavity modes were tuned across the entire SiV spectrum with a maximum tuning rage of 50 nm. In resonance with the SiV ZPL, a clear enhancement in the photoluminescence signal by a factor of 3.4 or 19.3 was observed for the two individual SiV centers. The 19-fold intensity increase came along with an increase in the spontaneous emission rate by a factor of 2.7, deduced from internal populations dynamics. By precisely determining all parameters contributing to cavity coupling, we evaluated the Purcell factors of $F_{\mathrm{cav}} = 1.17$ and 5 of the two SiV ZPLs coupled to the M7-cavities. The different enhancement factors could be attributed to different dipole orientations and position displacement with respect to the cavity fields. The theoretical intensity increase and enhancement of the spontaneous emission rate were in very good agreement with the experimental data. Our detailed analysis also allows for tracing back the modification of the radiative quantum efficiency. Based on the evaluated Purcell factors together with the internal population dynamics

and independent saturation measurements, we presented an enhancement in the quantum efficiency by a factor of > 6 for Purcell coupling on resonance and a reduction by a factor of > 2 in the case of inhibition of the spontaneous emission rate. The increase in the quantum efficiency unambiguously proved the impact of the cavity coupling on the emission properties of the single emitters. On resonance, a fraction of 63% of the total decay rate and 98.8% of the radiative emission were channeled into the cavity mode. Finally, we demonstrated precise and almost continuous polarization control of the SiV emission via cavity coupling. By changing the detuning of the cavity mode, the SiV emission angle was rotated over 100° while retaining a high visibility. Deterministic cavity coupling to single color centers paves the way for efficient, polarization-controlled single photon sources.

At the moment, the cavity coupling strength is mainly restricted by the limited positioning accuracy of the photonic crystal structures and the dipole misorientation with respect to the in-plane cavity field components. Therefore, we eventually propose the following measures tackling these problems. One possibility to increase the resolution of the fluorescence maps, and hence the positioning accuracy, is to perform multiple scans and to build up statistics on the emitter-marker distance. The error in the mean distance decreases with $1/\sqrt{N}$ where N is the number of fluorescence scans [481]. Another way would be to detect the color centers with nanometer precision using stimulated emission depletion (STED) microscopy [455, 482]. STED microscopy allows for overcoming of the diffraction limit by overlapping the outer regions of the excitation beam with a second donut-shaped laser beam that stimulates emission and depletes the excited state of the emitter before fluorescence takes place. Although successfully established for NV centers [456, 457], STED microscopy has not yet been applied to SiV centers up to now. To overcome the dipole misalignment with respect to the cavity electric fields, the SiV dipole moment pointing along the $\langle 111 \rangle$ diamond axis should be oriented in the plane of the photonic crystal slab. By using (110) faceted diamond membranes together with the preferential orientation of single color centers in the diamond lattice during growth, as recently demonstrated for single NV centers [449–451], perfect alignment of the dipole moment to the cavity electric field could in principle be achieved. Furthermore, we suggest to use low-strain diamond films, to overcome the large spread in the spectral properties especially in the dipole orientation of the single SiV centers as well as in the spontaneous decay rates and quantum efficiencies. Intrinsically identical SiV centers, as demonstrated recently [26], would enable much more predictable and reproducible coupling experiments. Finally, the cavity Q-factor should be increased. By using e.g. inductively coupled reactive ion etching, two-dimensional photonic crystal M3-cavities with quality factors of $Q = 3,000$ [87] as well as one-dimensional waveguide-cavity structures with $Q = 6,000 - 10,000$ have been realized in single crystal diamond [88, 90]. With such quality factors and modal volumes of $V = 1.5(\lambda/n)^3$ as deduced for our M7-cavity structures, it would be possible to enter the strong coupling regime and to study coherent light-matter interaction. This is reachable due to the narrow emission line and the short lifetime of approximately $T_1 = 1.5\,\mathrm{ns}$ measured in this chapter for single SiV centers in our diamond membranes. To guarantee for the SiV emission line to be narrower than the cavity linewidth, strong coupling experiments would require

cryogenic temperatures. At 10 K, the SiV ZPL splits into four emission lines with linewidths of 40 GHz detected for our heteroepitaxial diamond films. For low-strain diamond, linewidths of 230 MHz near the Fourier limit has recently been reported [26]. All these measures including improved positioning accuracy, perfect dipole orientation, high Q-factors, narrow linewidths and short lifetimes, would allow for coherent control of a single solid state quantum emitter, i.e. a color center in diamond, via deterministic strong coupling to a tiny photonic crystal cavity structure.

Chapter 10

Summary and future prospects

In this work, we fabricated for the first time photonic crystal cavities in single crystal diamond. The monolithic nanocavities were subsequently used for coupling experiments with ensembles of SiV centers and for deterministic coupling to single color centers in diamond. To frequency match the resonant modes with the color center emission line we developed a tuning mechanism to shift the cavity modes into resonance. For controlled positioning of the single emitters at the center of the cavity structure we pursued two approaches. The first approach was based on targeted implantation of nitrogen ions at the center of photonic crystal cavities fabricated in ultra-pure diamond films. In the second approach, we fabricated photonic crystal cavities around pre-characterized single SiV centers using positioning markers.

Summary

As solid-state emitters we used single color centers in diamond, i.e. the nitrogen-vacancy (NV) center and the silicon-vacancy (SiV) center that exhibit extraordinary properties, such as long spin-coherence times, and narrowband and bright single photon emission, respectively. In order to improve optical spin readout or enhance the emission of single photons, it is necessary to couple single color centers to a cavity with small mode volume and high quality factor. Photonic crystal cavities directly fabricated within a monocrystalline diamond membrane are well suited for this task, as they offer tiny mode volumes for efficient emitter-cavity coupling, as well as scalable architectures for integrated photonic devices.

Here, we focused on two-dimensional photonic crystals consisting of a triangular lattice of air holes etched in a thin diamond membrane. By introducing a defect in the periodic structure, integrated cavities are created that are well suited for coupling to single color centers in diamond. At the beginning of this thesis only a few studies on photonic crystal cavity designs in diamond existed. Therefore, we performed numerical simulations on photonic crystal cavities. Large size structures with three- or seven missing holes at the center, referred to as M3- and M7-cavities, are well suited for proof-of-principle studies on the far-field emission, collection efficiency, and polarization

properties as they exhibit multiple cavity modes of different symmetries, and yield moderate theoretical Q-factors of 10,000 and modal volumes of around $1.5\,(\lambda/n)^3$, without the need for extended optimization of the geometry. More sophisticated designs with ultra-small mode volumes and high Q-factors such as the M0-cavity and the M1-cavity are required for large Purcell enhancement. Both cavity structures yield extremely small modal volumes of $V_{\mathrm{M0}} = 0.35\,(\lambda/n)^3$ and $V_{\mathrm{M1}} = 1.11\,(\lambda/n)^3$, respectively. Using Fourier- and real-space analysis of the simulated cavity fields, we successively optimized the surrounding air holes such that out-of-plane radiation losses are minimized, which yielded cavity quality factors up to $Q_{\mathrm{M0}} = 320,000$ and $Q_{\mathrm{M1}} = 66,300$, respectively.

The realization of such cavity structures in diamond requires precise patterning techniques that were not well developed at the beginning of this work. The first challenge was to fabricate a 300 nm-thick, free-standing diamond membrane in high-quality single crystal diamond that can be easily handled and further processed. As starting materials, we used ultra-pure diamond membranes and hetero-epitaxial diamond films already containing SiV ensembles or single SiV centers. The hetero-epitaxial diamond films are deposited via chemical vapor deposition on a sacrificial substrate of Ir/YSZ/Si(001), that is subsequently removed in small areas using dry etching. For the ultra-pure diamond membranes, we developed a bonding procedure involving a spin-on glass adhesion layer to glue the diamond membranes on a structured silicon substrate. The diamond films were subsequently thinned to the desired thickness using reactive ion etching in an oxygen plasma, and patterned using focused ion beam milling. By adapting the lattice constant and air hole radii, we fabricated various photonic crystal cavities with design wavelengths at 637 nm and 738 nm, intended for coupling to NV and SiV centers, respectively. The fabricated cavities exhibited quality factors up to $Q = 1,100$. Compared to theoretical predictions, the experimental Q-factors were one to three orders of magnitude smaller. We analyzed possible limitations of the quality factor, including fabrication tolerances, such as non-optimal hole positions and sizes, as well as non-vertical sidewalls, and material absorption. For our structures fabricated in high-quality single crystal diamond we identified inclined sidewalls as the main limiting factor for the experimental Q-factor.

The fabricated structures are subsequently used for cavity-coupling experiments with color centers in diamond. As a first step, we focused on coupling to ensembles of SiV centers using hetero-epitaxial diamond films with a high, homogeneous SiV density. These diamond films are chosen for a "proof-of-principle" demonstration of cavity-coupling, without the need for sophisticated positioning techniques, and to develop and test essential methods, such as frequency tuning of photonic crystal cavity modes to spectrally match the SiV emission line. The tuning technique developed in the framework of this thesis was based on thermal oxidation of diamond material in air, and allowed for the demonstration, for the first time, of cavity tuning of an all-diamond photonic crystal cavity, with a tuning range up to 50 nm and a mean tuning rate down to 0.8 nm per oxidation step. Shifting the cavity modes onto resonance with the SiV ZPL, we observed a clear enhancement of the photoluminescence signal by a factor of ~ 3 compared to the off resonance spectrum. Taking into account the measured quality factor of 400 and the simulated mode volume of $V = 1.5\,(\lambda/n)^3$ of a M7-cavity mode that was

tuned into resonance, we deduced an ideal Purcell factor of 20 as a figure of merit. A more detailed analysis of the spectrally resolved Purcell enhancement included spatial and orientational averaging of the emitter-mode overlap, spectral mismatch of SiV zero phonon line width and cavity linewidth, modification of the local density of states by the photonic crystal cavity, and different collection efficiencies for cavity mode and uncoupled emission, as well as the branching ratio into the zero-phonon line and phonon side band. Due to ensemble averaging, no lifetime change induced by cavity-coupling could be detected.

The fabrication and tuning techniques developed and tested for SiV ensembles provide an excellent basis for subsequent controlled cavity-coupling to single color centers at room and cryogenic temperatures. In previous experiments [87, 88] on coupling of diamond-based photonic crystal cavities to single NV centers, the color center's position within the cavity was completely random and cavity-emitter systems were post-selected after fabrication for optimum coupling. On the contrary, in the framework of this thesis, we presented, for the first time, deterministic coupling of single color centers to all-diamond photonic crystals, which required high-resolution positioning and active alignment of the emitter with respect to the cavity electric field. For active emitter-cavity positioning and alignment, we pursued two approaches: The first approach involves targeted implantation of nitrogen ions at the center of a photonic crystal cavity fabricated in ultra-pure diamond. The second procedure is based on a tailored fabrication process of photonic crystal cavities around pre-characterized single SiV centers. Our active positioning techniques offer major improvements in reproducibility and reliability compared to past schemes relying on random chance.

High-resolution ion-implantation of single NV centers at the center of a photonic crystal cavity have been performed in collaboration with S. Pezzagna and J. Meijer at the RUBION in Bochum. The implantation setup consists of an ion gun, which provides nitrogen ions at an energy of 5 keV, and an atomic force microscope. The pierced atomic force microscopy tip was used as a beam collimator, as well as to position the beam aperture above the cavity structure, yielding lateral resolutions down to 25 nm [425]. We implanted nitrogen ions into various photonic crystal cavities using ion doses in the range of $0.2 - 4.4 \times 10^{14}\,\mathrm{ions/cm^2}$. After high temperature annealing, using confocal spectroscopy at 10 K we verified the successful formation of a few NV centers at the center of every implanted cavity. Due to the presence of strain, the ZPL of individual NV centers was shifted by 2 nm. At low temperatures, homogeneous broadening effects were minimized, resulting in a reduced linewidth of 250 GHz, which was limited by spectral diffusion, and a more pronounced ZPL signal. From the spectrum, we determined the number of single NV centers and the experimental creation yield of $0.8 \pm 0.1\%$. For the lowest dose of $2.56 \times 10^{13}\,\mathrm{ions/cm^2}$, we created 3 ± 1 NV centers in the middle of a M1-cavity. Based on our experimental findings, we deduced an optimal dose of $1 \times 10^{13}\,\mathrm{ions/cm^2}$ for the formation of one single NV center.

To describe cavity coupling to a broad-band emitter, we adopted a master-equation model that was recently derived by Auffève et al. [91, 92], and adapted by Albrecht et al. [80] to the case of NV centers, including higher vibrational levels of the NV ground state, as well as pure dephasing to account for homogenous broadening of the zero-

phonon line. The model input parameters were obtained by fitting the experimental spectrum of implanted NV centers with multiple Lorentzians. Taking into account the measured cavity quality factor of $Q = 160$ and a mode volume of the M1-cavity of $V = 1.1\,(\lambda/n)^3$, we deduced a generalized Purcell enhancement of the zero-phonon line by a factor of 1.32, and of the phonon side bands by a factor of 1.7, assuming one single implanted NV center at the photonic crystal cavity center. Larger Purcell enhancement of the ZPL up to 2.6 could be achieved in principle using cavity structures with Q-factors of $Q = 1,000$, as already realized in this work, and assuming a NV branching ratio of 3% into the ZPL. The high Purcell factor would come along with a reduced NV excited state lifetime of 4.6 ns, compared to 12 ns [23] reported in bulk diamond.

In a second approach, we presented active alignment and deterministic positioning of an all-diamond photonic crystal cavity around a pre-selected single SiV center. The single SiV centers in hetero-epitaxial diamond exhibited excellent spectral properties, such as narrow zero-phonon line emission, weak phonon side band contributions, and high quantum efficiencies. The outstanding properties of the single SiV centers allow for the study of cavity quantum electrodynamics effects, even at room-temperature. Deterministic coupling was achieved via a tailored fabrication process to structure photonic crystal cavities into the diamond membrane around pre-characterized single SiV centers, using positioning markers and focused ion beam milling. This approach allows for deterministic emitter-cavity positioning with a success rate of 70%, and controlled alignment of its dipole axis with the cavity electric field. Active alignment enabled the observation of both Purcell inhibition and enhancement of the spontaneous emission rate of single color centers in diamond. From the measured internal population dynamics and the experimental quantum efficiency, we deduced a Purcell inhibition factor of $F_{\mathrm{PhC}}^{exp} = 0.21 \pm 0.06$ for a single SiV center off resonance with any cavity mode. The measured value was in very good agreement with the simulated averaged Purcell factor $F_{\mathrm{PhC}} = 0.25$ of the photonic crystal lattice. By tuning an M7-cavity mode with $Q = 500$ and $V = 1.5\,(\lambda/n)^3$ into resonance with the ZPL, we observed Purcell enhancement of spontaneous emission by a factor of 2.7, along with a 19-fold intensity increase. By precisely determining all parameters contributing to cavity coupling, i.e. dipole orientation and spatial positioning, we evaluated a Purcell factor of $F_{\mathrm{cav}} = 5$ for a single SiV center coupled to a photonic crystal cavity mode. Based on the measured internal population dynamics, together with our detailed analysis, we deduced an enhancement in the emitters quantum efficiency by a factor of > 6 for Purcell coupling on resonance, and a reduction by a factor of > 2 for off resonance inhibition of the spontaneous emission rate. Finally, we demonstrated continuous polarization control varied over more than 100 degrees by tuning a cavity mode onto resonance with the ZPL of a single SiV center. Our findings pave the way for efficient polarization controlled single photon sources embedded in a photonic network, with applications in secure quantum communication, quantum information processing, and ultrasensitive magnetometry. Before we proceed with future prospects on single color centers coupled to photonic crystal cavities, we briefly discuss measures to further improve cavity coupling to solid-state emitters.

Suggestions for improvement

The presence of material strain within the diamond membrane has substantial impact on the emission properties of single color centers. We observed a variation in the ZPL wavelength of 2 nm for single NV centers implanted in the ultra-pure diamond membranes. Raman analysis suggested that material strain was induced by the mismatch between the thermal expansion coefficients of the diamond membrane and the spin-on glass adhesion layer. The impact of material strain is even more pronounced for single SiV centers in hetero-epitaxial diamond films, resulting in a strong variation of the ZPL position ($710 - 770$ nm), linewidth ($0.55 - 3.0$ nm) and linear polarization angle, as well as the excited state lifetime ($0.35 - 1.56$ ns), and quantum efficiency ($0.15 - 0.66$) between different emitters. By improving the bonding process, e.g. annealing at higher temperatures, and using low-strain diamond with single SiV centers as recently reported [26], much more reproducible and reliable spectral properties of single color centers can be expected.

Proving single emitter character of the implanted NV centers via intensity autocorrelation measurements was hindered in our experiments by the pronounced fluorescence background detected on the cavity structures. One source of background could be defects induced by the polishing of the diamond membrane. By removing the first few micrometers from both diamond surfaces via reactive ion etching in an oxygen plasma, most of the polishing defects should be eliminated [365]. Furthermore, using an argon-chlorine plasma, instead of an oxygen and SF_6 plasma, to thin out the diamond membrane might reduce background luminescence, and significantly minimize surface roughness. Extremely smooth surface roughness after long etching times has been reported for samples exposed to argon-chlorine plasma [366]. The high background measured on the photonic crystal structures might also be induced by the focused ion beam milling process. The incorporation of gallium ions (although most of them diffuse towards the surface upon high temperature annealing) and lattice damages due to ion bombardment are considered as the main sources of FIB induced background luminescence. These contributions might be overcome by using reactive ion etching techniques, instead of FIB milling, to fabricate photonic crystals. Various etching recipes based on oxygen plasma involving spin-on glass [84, 88, 452–454], silica [132], silicon nitride [83, 87], or metal masks [358], have been successfully applied for the fabrication of photonic structures in diamond. Besides the reduction of background fluorescence, reactive ion etching processes allow for parallel fabrication of hundreds of structures in one run. By optimizing the etching process to obtain vertical sidewalls, and by post-selecting the best structures, high quality factors of 6,000 [88], and even up to 10,000 [90], have been reported for one-dimensional photonic crystal cavities. In corporation with the IMTEK at the University of Freiburg, and the NSC at the University of Kaiserslautern, we developed a reactive ion etching process using oxygen as an etch gas and a silica etch mask. The first etching tests were performed in free-standing nanocrystalline diamond films. Figure 10.1 shows a SEM image of a M3-cavity fabricated using reactive ion etching. A detailed view and cross sectional image reveal slightly irregular shapes of the air holes, and inclined hole sidewalls. Moreover, significant intrinsic material absorption in the

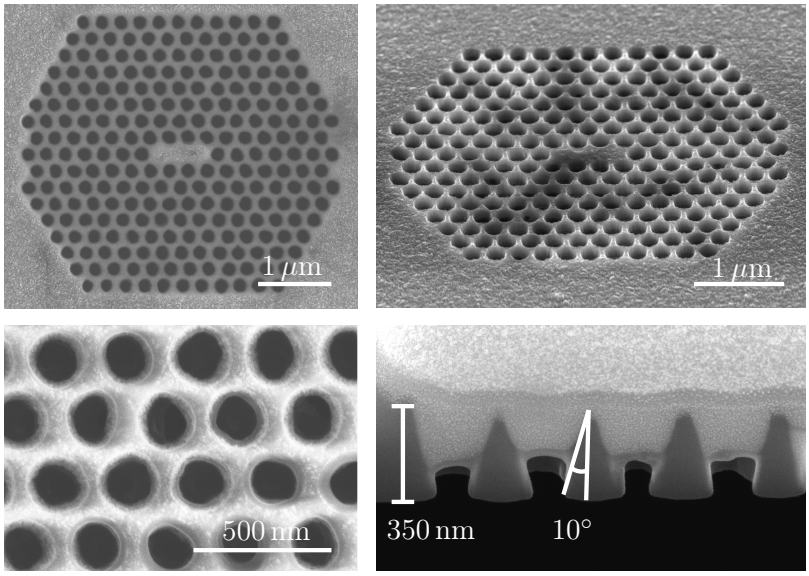

Figure 10.1: Reactive ion etching tests of photonic crystal cavity structures in nanocrystalline diamond films using a silica mask and oxygen as an etching gas. The detailed view and the cross sectional image reveal slightly irregular shape of the air holes and non-vertical sidewalls.

nanocrystalline diamond films prevented the observation of cavity modes. The development and optimization of a dry etching process, in order to obtain circular shaped holes and vertical sidewalls, is subject to current work in our group.

The identification of single NV centers implanted within the cavity structure, and the positioning accuracy of photonic crystal cavities around single pre-selected color centers, could be strongly improved using more elaborate, high-resolution spectroscopy techniques, such as simulated emission depletion (STED). The invention of STED was awarded this year with the Nobel Prize in chemistry of S. Hell, E. Betzig and W. Moerner. STED spectroscopy [455], with optical spatial resolutions down to 2.4 nm [482], has been applied to localize single NV centers in two [456] and three dimensions [457]. The diffraction limit is overcome by overlapping the outer regions of the excitation laser spot with a second laser beam that induces stimulated emission and depletes the emitter's excited state before fluorescence takes place. STED microscopy would be well suited to determine the NV centers' positions in the photonic crystal cavity with a precision of several nanometers, and to deduce the spatial resolution of our implantation setup. Although well established for the detection of single NV centers, STED microscopy has, up to now, not been successfully applied to single SiV centers. High-resolution detection of single SiV centers with respect to the positioning markers would greatly improve the positioning accuracy of photonic crystal cavities relative to single emitters.

In order to achieve efficient coupling, the emitter dipole must be oriented parallel to the cavity electric field confined in the diamond plane. The orientations of the NV and SiV dipole moments are well known. The two XY dipoles associated with the NV

center are oriented in the {111} plane perpendicular to the NV axis. In contrast, the dominant Z dipole of the SiV center is aligned along the ⟨111⟩ crystallographic axes of the diamond lattice. In this thesis, we use (001) oriented single-crystal diamond membranes for the realization of photonic crystal cavities. For this material, the NV and SiV dipoles were inclined with respect to the in-plane cavity fields, limiting the effective Purcell factor. The overlap between the NV dipole and the cavity field can be maximized by fabricating photonic crystal cavities in the (111)-facet of a diamond membrane, and using NV centers oriented perpendicularly to this facet. Recently, nearly perfect preferential alignment of NV centers along the [111] diamond axis has been demonstrated by several groups [449–451]. The formation of NV centers in one out of the four possible configurations is attributed to the particular reaction kinetics in the CVD diamond growth process on a (111) diamond substrate. In contrast, cavity-coupling to single SiV centers could be improved using (110)-oriented diamond films, and selecting SiV centers aligned in parallel to the growth plane. First investigations on preferential incorporation of single SiV centers in CVD diamond deposited on (110) diamond substrates have been performed [224]. However, in these studies [224], the SiV symmetry axis was oriented out of the growth-plane. Tailored CVD growth processes towards preferential alignment of single SiV and NV centers, together with improved polishing techniques of (110) and (111) oriented diamond membranes with thicknesses of 10-30 μm, would greatly improve coupling of single color centers to diamond-based photonic crystal cavities.

The interpretation of observed Purcell enhancement and inhibition of spontaneous emission via cavity-coupling requires detailed knowledge of the emitter's quantum efficiency. The reason for this is that cavity-coupling modifies only radiative decay rates, whereas non-radiative recombination rates are unaffected. In order to achieve effective Purcell enhancement, high emitter quantum efficiencies are desirable. Unfortunately, only a few studies of the quantum efficiency on single NV and SiV centers hosted in unstrained bulk diamond exist. For single NV centers in bulk diamond, quantum efficiencies up to 0.7 have been reported [456]. In contrast, for single NV centers located in nanodiamonds, quantum efficiencies much smaller than unity, and strong variations between different nanocrystals have been found [447,448]. For SiV centers, we are aware of only two studies, one on SiV ensembles in polycrystalline diamond films [413], and one on single SiV centers hosted in nanodiamonds grown on iridium [55]. Both studies [55,413] reveal SiV quantum efficiencies of only a few percent. However, the quantum efficiency strongly depends on the local density of states at the position of the single color center as well as on the quality of the host material, rendering a direct comparison difficult. In this work, we evaluated the quantum efficiency of single SiV centers that were used for cavity-coupling. Our analysis, based on internal population dynamics and independent saturation measurements, revealed a large spread in the SiV quantum efficiency, between $0.15 - 0.66$. If the here investigated single SiV centers were placed in a diamond nano-particle instead of bulk material, their quantum efficiency would be decreased to $0.009 - 0.10$, due to the reduced local density of states, perfectly coinciding with the range determined in earlier experiments on SiV centers in nanodiamonds [55]. However, our estimation of the quantum efficiency suffers from large errors due to un-

certainties in the collection efficiency of our setup, and by the microscope objective. In recent years, alternative methods to deduce the quantum efficiency of single color centers have been presented. The first method involves comparing numerical simulations with experimental results of measurements of the excited state lifetime under pulsed excitation and of the dipole orientation in three dimensions using defocused imaging in the back focal plane of the microscope objective [157, 158]. The second method relies on fluorescence lifetime measurements of the emitter as a function of its distance to a high-reflective silver mirror [447, 448]. As the presence of the mirror changes the local density of states at the emitter's position and hence its lifetime, the quantum efficiency of the NV center can be deduced from a fit to the data. Currently, the adaptation of the latter method to single SiV centers incorporated in diamond membranes is subject to current work in our group in collaboration with the group of S. Götzinger at the "Max-Planck-Institut für die Physik des Lichts" in Erlangen.

Future prospects

The results achieved in this work, including the targeted creation of single NV centers and deterministic placement of cavities to single SiV centers, pave the way for various applications, including cavity-enhanced single photon sources, cavity-enhanced spin-measurements, entanglement generation between two separate color centers, and cavity-enhanced ultrasensitive magnetometers.

One focus of future implementations of single color centers is efficient single photon sources. As demonstrated in this work, by coupling single emitters to photonic crystal cavities, the spontaneous emission rate, as well as the radiative quantum efficiency, can be greatly improved, and the emission polarization can be controlled. This offers significant improvements for quantum communication protocols, such as quantum key distribution based on color centers as single photon sources [28–30]. Recent theoretical proposals with single NV [57] and SiV centers [58] for quantum key distribution require quality factors of 10^4. By further improving the here presented nanofabrication techniques, using e.g. reactive ion etching instead of focused ion beam milling, as suggested above, cavity-enhanced single photon sources for quantum key distribution can be realized in the near future.

Another field of future investigations is cavity-enhanced spin measurement of the SiV and NV electronic spin state. The flexible design of solid-state devices allow for direct lithography of microwave striplines on the sample surface, which are used to manipulate the electronic spin, and direct incorporation of a feeding photonic crystal waveguide for in- and out-coupling of probe light, used to perform spin-selective reflectivity measurements [59]. This scheme requires much less intensity and fewer readout cycles, and hence minimizes the probability of unwanted spin-flip transitions upon optical illumination. Theoretical proposals [59] on cavity-enhanced spin measurements of single NV centers require cavity quality factors of $Q = 3,000$, which is feasible with the state-of-the-art nanofabrication techniques presented in this thesis.

Targeted, high-resolution implantation of single NV centers at the center of a photonic crystal cavity would allow for deterministic and robust entanglement generation

between the electronic ground states of the individual NV centers [61]. For this proposal [61], cavity designs with several missing holes, such as the M3- and M7-cavities realized in this work, would be ideal as they allow for sufficient separation of single NV centers within the defect structure, enabling independent optical initialization and readout of the spin states. Both NV centers would be in resonance with one photonic crystal cavity mode, which mediates the interaction between the spin states. Again, the required quality factor of $Q = 10^4$ is within reach of current fabrication technologies.

Besides the above proposal of NV-NV entanglement directly mediated by the cavity mode, large distance entanglement generation between single color centers would enormously profit from cavity-enhanced emission. In a recent experiment by Bernien et al. [53], long distance entanglement between two separate NV centers was achieved by two-photon interference on a beam splitter. This scheme requires indistinguishable single photons emitted by the individual NV centers. In the experiment, indistinguishability was achieved by tight filtering of the NV ZPL emission at the expense of poor success rates. By coupling NV centers to photonic crystal cavities, the spontaneous emission rate of single photons, the emission efficiency into the cavity mode, and the collection efficiency can be significantly increased, which would enable much larger success rates of entangled photon pairs.

For the generation of indistinguishable photons, the usual strategy is to reduce the linewidth, i.e. the pure dephasing rate, by lowering the temperature and using resonant excitation. However, a recent theoretical proposal [91] has identified pure dephasing as a source of indistinguishable photons by coupling the emitter to a cavity. By increasing the pure dephasing rate beyond the cavity linewidth, the frequency and linewidth of the emitted photons are imposed by the cavity allowing for tailored photon emission. However, this proposal requires cavity decay rates equal to the atomic transition rates, i.e. $\kappa = \gamma$, necessitating high Q-factors. For the realization of this scheme, Fabry-Pérot type cavities [80] that reach high Q-factors would probably be more appropriate than photonic crystal cavities.

Moreover, a scheme for distributed entanglement generation has been proposed that relies on two single emitters, each coupled to an optical cavity [4]. The basic idea is to create a Λ-scheme between two ground state levels and the excited state of the atom. Thereby, one optical transition of the Λ-scheme is driven by a classical laser field, while the other one is coupled to a mode of an optical cavity. When the classical control field is applied, the cavity-coupled optical transition quickly causes the excitation to coherently emit a photon into the cavity mode. Hence, the coherence between the ground state levels is transferred onto the emitted photon. For well chosen emitter-cavity coupling rates, and by slowly turning the classical drive field on and off, it can be achieved that the temporal wave function of the emitted photon follows the wave function of the classical laser field. This allows for the generation of photons with indistinguishable temporal wave functions. By simultaneously driving two emitters in two separate optical cavities, generating indistinguishable photons, followed by two-photon interference on a beam splitter, entanglement between the emitters can be achieved. This scheme has successfully been implemented for single atoms and ions [488–490]. For solid-state emitters, the realization of Λ transitions is more demanding. Using two classical laser

fields to drive a Λ transition between NV ground state sub levels, entanglement between a single NV spin and the emitted photons has been demonstrated [50]. Recently, Λ transitions have also been identified for the SiV center [16,27,223]. Moreover, the emission of indistinguishable photons by two separate SiV centers has been demonstrated via Hong-Ou-Mandel interference [27]. Combining the Λ type transitions identified for both color centers with cavity-coupling to an optical mode might allow for coherent spin-photon state transfer, distributed entanglement generation [4], and the implementation of long distance quantum computing schemes [491].

Beyond multiple applications in quantum information science, coupling of single NV centers to a photonic crystal cavity would allow for optical sensing of small magnetic fields with high resolution. Very recently, ultrasensitive room-temperature magnetometry based on the detection of the infrared absorption signal of NV centers has been demonstrated [492]. To enhance interaction length in the diamond sample, and to increase the absorption from the NV centers and the spin-state detection contrast, the color centers were placed in an external Fabry-Pérot cavity, leading to an improvement in sensitivity by two orders of magnitude. The sensitivity could be even further improved by using photonic crystal cavities instead of Fabry-Pérot cavities as external cavities to enhance the infrared absorption signal [493].

Similar to atom-photon interfaces, phonons might be used to mediate interaction between distant qubits. Placing a single color center into a mechanical resonator, its atomic transitions can be coupled to the mechanical motion of the device. Recently, this has been demonstrated for single NV centers hosted in a diamond-based cantilever, revealing strain-induced level shifts originating from the mechanical motion [459, 460]. This might allow for coherent spin-phonon interfaces, given the high mechanical resonator quality factors and low temperatures. Moreover, one could think of extending the scheme to different degrees of freedom. Combining the mechanical resonator with an optical cavity would enable coupling of mechanical motion to confined light fields. For such opto-mechanical coupling [252–254], photonic crystal cavities are well suited. Various geometries have been proposed that allow for simultaneous confinement of optical and mechanical modes. Here, diamond is of special interest due to its outstanding mechanical material stiffness, allowing for high mechanical frequencies, up to a few GHz, and high mechanical quality factors [494, 495].

Appendix A

Optimization of the M0-cavity

This annexe summarizes the parameters sets of the M0-cavity optimization using Fourier- and real-space analysis. The design procedure based on the principle of gentle confinement has been discussed in section 5.6.2 and has been published in our paper [274]. We start with a simple M0-cavity, where a defect is introduced in the photonic crystal lattice by shifting two holes outward along the x-axis. The starting design is summarized in table A.1. The M0-cavity design together with the used nomenclature is shown in figure A.1. By adjusting the neighboring holes around the introduced defect, e.g. by reducing the radii or shifting some holes outwards, the cavity mode can be tailored to resume a Gaussian envelope. According to the principle of gentle confinement, this leads to reduced radiation losses within the light cone and hence to an increase in the cavity quality factor without significant increase in the mode volume.

$R(a)$	$h(a)$	$d(a)$	Q	$\omega(2\pi c/a)$	$V(\lambda/n)^3$
0.26	0.91	0.15	24,500	0.3652	0.390

Table A.1: Starting point for the design optimization of the M0-cavity (Parameter Set M0^A)

Step 1: Optimization for background radius $R = 0.26\,a$

As a first optimization step, we fix the background radius to $R = 0.26\,a$ and fine tune the holes c, e, k in the vicinity of the defect such that the cavity mode profile along the y-axis can be approximated by a Gaussian envelope. This yields to parameter set M0^{h1} summarized in table A.2.

$R(a)$	$d(a)$	$R_c(a)$	$R_e(a)$	$R_k(a)$	Q	$\omega(2\pi c/a)$	$V(\lambda/n)^3$
0.26	0.15	0.23	0.24	0.25	72,700	0.3622	0.390

Table A.2: Optimization of first, second and third next-neighbor holes along the y-axis (Parameter Set M0^{h1}).

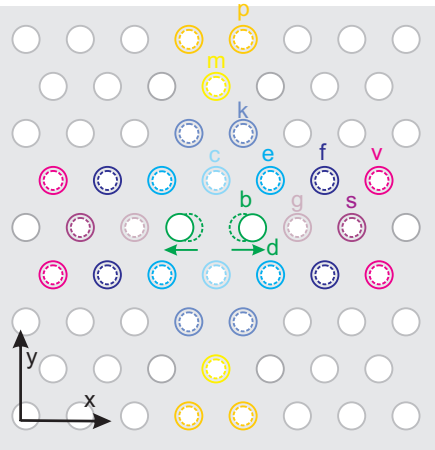

Figure A.1: Modified M0-cavity design: By optimizing the surrounding air holes the quality factor is significantly improved.

As a next step, we vary the radii of the holes b, g, and f aligned along the x-axis next to the defect, while keeping the other parameters and the background radius $R = 0.26\,a$ fixed. This results in parameters set M0^B given in table A.3.

$R(a)$	$d(a)$	$R_c(a)$	$R_e(a)$	$R_k(a)$	$R_f(a)$	Q	$\omega(2\pi c/a)$	$V(\lambda/n)^3$
0.26	0.16	0.23	0.24	0.25	0.25	124,000	0.3606	0.388

Table A.3: Optimization of the holes along the x- and y-axis for background radius $R = 0.26a$ (Parameter Set M0^B). The radii not listed here correspond to the background radius R.

Step 2: Optimization for background radii $R \in [0.27\,a, 0.29\,a]$

As a next step, we check, whether the choice of the background radius R and thus the in-plane localization of the modified mode are still optimal. Therefore, we repeat step 1 for changed background radii $R \in [0.27\,a, 0.29\,a]$. The optimal geometries M0^{h2}, M0^C, and M0^{h3} yielding the highest quality factors for each background radius are summarized in table A.4.

$R(a)$	$d(a)$	$R_c(a)$	$R_e(a)$	$R_k(a)$	$R_f(a)$	Q	$\omega(2\pi c/a)$	$V(\lambda/n)^3$
0.27	0.16	0.22	0.24	0.25	0.25	215,000	0.3634	0.351
0.28	0.16	0.22	0.24	0.26	0.26	226,600	0.3673	0.350
0.29	0.17	0.22	0.24	0.27	0.27	120,000	0.3695	0.342

Table A.4: Optimized M0-cavity for background radii $R = 0.27a$ (Parameter Set M0^{h2}), $R = 0.28a$ (Parameter Set M0^C) and $R = 0.29a$ (Parameter Set M0^{h3}).

From these optimization procedure, we conclude that a background radius of $R = 0.28\,a$ results in the best in-plane confinement of the mode. As a final step, we consider the holes m, p and s, v, and t at larger distances from the defect. We vary the radii of the holes m, and p along the y-axis yielding parameter set $M0^{h4}$ in table A.5.

$R_m(a)$	$R_p(a)$	Q	$\omega(2\pi c/a)$	$V(\lambda/n)^3$
0.31	0.34	228,500	0.3671	0.350

Table A.5: Optimization of the holes along the y-axis (Parameter Set $M0^{h4}$). The other parameters are the same as in Set $\mathrm{M0}^C$.

As a final step, we optimize the holes s, t, and v along the x-axis resulting in a further strong increase in the quality factor to $Q = 320,000$ while retaining a small mode volume of $V = 0.35\,(\lambda/n)^3$. Parameter set $M0^D$ in table A.6 together with set $\mathrm{M0}^C$ summarize the optimal design of the M0-cavity.

$R_m(a)$	$R_p(a)$	$R_s(a)$	$R_v(a)$	$R_t(a)$	Q	$\omega(2\pi c/a)$	$V(\lambda/n)^3$
0.31	0.34	0.29	0.27	0.28	320,000	0.3672	0.350

Table A.6: Optimization of the holes along the x-axis (Parameter Set $M0^D$). The other parameters are the same as in Set $\mathrm{M0}^C$.

Bibliography

[1] L. K. Grover, "A Fast Quantum Mechanical Algorithm for Database Search," in "Proceedings of the Twenty-eighth Annual ACM Symposium on Theory of Computing," (ACM, New York, NY, USA, 1996), STOC '96, pp. 212–219.

[2] P. W. Shor, "Polynomial time algorithms for prime factorization and discrete logarithms on a quantum computer," SIAM J. Comput. **26**, 1484–1509 (1997).

[3] R. P. Feynman, "Simulating physics with computers," Int. J. Theor. Phys. **21**, 467–488 (1982).

[4] J. I. Cirac, P. Zoller, H. J. Kimble, and H. Mabuchi, "Quantum State Transfer and Entanglement Distribution among Distant Nodes in a Quantum Network," Phys. Rev. Lett. **78**, 3221–3224 (1997).

[5] H. J. Kimble, "The quantum inernet," Nature **453**, 1023 (2008).

[6] D. P. DiVincenzo, "The physical implementation of quantum computation," Fortschr. Phys. **48**, 771–783 (2000).

[7] F. Schmidt-Kaler, H. Haffner, M. Riebe, S. Gulde, G. P. T. Lancaster, T. Deuschle, C. Becher, C. F. Roos, J. Eschner, and R. Blatt, "Realization of the Cirac-Zoller controlled-NOT quantum gate," Nature **422**, 408–411 (2003).

[8] J. I. Cirac and P. Zoller, "Quantum Computations with Cold Trapped Ions," Phys. Rev. Lett. **74**, 4091–4094 (1995).

[9] R. Blatt and C. F. Roos, "Quantum simulations with trapped ions," Nature Phys. **8**, 277–284 (2012).

[10] J. I. Cirac, A. K. Ekert, S. F. Huelga, and C. Macchiavello, "Distributed quantum computation over noisy channels," Phys. Rev. A **59**, 4249–4254 (1999).

[11] D. L. Moehring, P. Maunz, S. Olmschenk, K. C. Younge, D. N. Matsukevich, L.-M. Duan, and C. Monroe, "Entanglement of single-atom quantum bits at a distance," Nature **449**, 68–71 (2007).

[12] C. Bennett and G. Brassard, "Quantum cryptography: Public key distribution and coin tossing," in "IEEE International Conference on Computers, Systems and Signal Processing," , vol. 175 (1984), vol. 175, p. 8.

[13] F. Jelezko, T. Gaebel, I. Popa, A. Gruber, and J. Wrachtrup, "Observation of Coherent Oscillations in a Single Electron Spin," Phys. Rev. Lett. **92**, 076401 (2004).

[14] F. Jelezko, T. Gaebel, I. Popa, M. Domhan, A. Gruber, and J. Wrachtrup, "Observation of Coherent Oscillation of a Single Nuclear Spin and Realization of a Two-Qubit Conditional Quantum Gate," Phys. Rev. Lett. **93**, 130501 (2004).

[15] T. Müller, C. Hepp, B. Pingault, E. Neu, S. Gsell, M. Schreck, H. Sternschulte, D. Steinmüller-Nethl, C. Becher, and M. Atatüre, "Optical signatures of silicon-vacancy spins in diamond," Nat. Commun. **5**, 3328 (2014).

[16] B. Pingault, J. N. Becker, C. H. H. Schulte, C. Arend, C. Hepp, T. Godde, A. I. Tartakovskii, M. Markham, C. Becher, and M. Atature, "All-optical formation of coherent dark states of silicon-vacancy spins in diamond," (2014). ArXiv:1409.4069.

[17] L. J. Rogers, K. D. Jahnke, M. H. Metsch, A. Sipahigil, J. M. Binder, T. Teraji, H. Sumiya, J. Isoya, M. D. Lukin, P. Hemmer, and F. Jelezko, "All-optical initialization, readout, and coherent preparation of single silicon-vacancy spins in diamond," (2014). ArXiv:1410.1355.

[18] L. Childress, J. M. Taylor, A. S. Sørensen, and M. D. Lukin, "Fault-tolerant quantum communication based on solid-state photon emitters," Phys. Rev. Lett. **96**, 070504 (2006).

[19] Y. L. Lim, S. D. Barrett, A. Beige, P. Kok, and L. C. Kwek, "Repeat-until-success quantum computing using stationary and flying qubits," Phys. Rev. A **73**, 012304 (2006).

[20] P. Barclay, *Quantum information processing with diamond* (Woodhead publishing series in electronics and optical materials, 2014), chap. 1 Principles of quantum information processing (QIP) using diamond, pp. 3–20.

[21] C. Kurtsiefer, S. Mayer, P. Zarda, and H. Weinfurter, "Stable solid-state source of single photons," Phys. Rev. Lett. **85**, 290–293 (2000).

[22] R. Brouri, A. Beveratos, J. Poizat, and P. Grangier, "Photon antibunching in the fluorescence of individual color centers in diamond," Opt. Lett. **25**, 1294–1296 (2000).

[23] A. T. Collins, M. F. Thomaz, and M. I. B. Jorge, "Luminescence decay time of the 1.945 eV centre in type Ib diamond," J. Phys. C: Solid State Phys. **16**, 2177 (1983).

[24] C. Wang, C. Kurtsiefer, H. Weinfurter, and B. Burchard, "Single photon emission from SiV centres in diamond produced by ion implantation." J. Phys. B: At. Mol. Opt. Phys. **39**, 37–41 (2006).

[25] E. Neu, D. Steinmetz, J. Riedrich-Möller, S. Gsell, M. Fischer, M. Schreck, and C. Becher, "Single photon emission from silicon-vacancy colour centres in chemical vapour deposition nano-diamonds on iridium," New J. Phys. **13**, 025012 (2011).

[26] L. J. Rogers, K. D. Jahnke, L. Marseglia, C. Müller, B. Naydenov, H. Schauffert, C. Kranz, T. Teraji, J. Isoya, L. P. McGuinness, and F. Jelezko, "Multiple intrinsically identical single-photon emitters in the solid state," Nat. Commun. **5**, 4739 (2014).

[27] A. Sipahigil, K. D. Jahnke, L. J. Rogers, T. Teraji, J. Isoya, A. S. Zibrov, F. Jelezko, and M. D. Lukin, "Indistinguishable Photons from Separated Silicon-Vacancy Centers in Diamond," Phys. Rev. Lett. **113**, 113602 (2014).

[28] A. Beveratos, R. Brouri, T. Gacoin, A. Villing, J.-P. Poizat, and P. Grangier, "Single Photon Quantum Cryptography," Phys. Rev. Lett. **89**, 187901 (2002).

[29] R. Alléaume, F. Treussart, G. Messin, Y. Dumeige, J.-F. Roch, A. Beveratos, R. Brouri-Tualle, J.-P. Poizat, and P. Grangier, "Experimental open-air quantum key distribution with a single-photon source," New J. Phys. **6**, 92 (2004).

[30] M. Leifgen, T. Schröder, F. Gädeke, R. Riemann, V. Métillon, E. Neu, C. Hepp, C. Arend, C. Becher, K. Lauritsen, and O. Benson, "Evaluation of nitrogen- and silicon-vacancy defect centres as single photon sources in quantum key distribution," New J. Phys. **16**, 023021 (2014).

[31] D. Giggenbach, "Optimierung der optischen Freiraumkommunikation durch die turbulente Atomosphäre - Focal array receiver," Ph.D. thesis, Deutsches Luft- und

Raumfahrtzentrum, Institut für Kommunikation und Navigation, Digitale Netze (2005).

[32] A. Gruber, A. Dräbenstedt, C. Tietz, L. Fleury, J. Wrachtrup, and C. v. Borczyskowski, "Scanning Confocal Optical Microscopy and Magnetic Resonance on Single Defect Centers," Science **276**, 2012–2014 (1997).

[33] L. Robledo, L. Childress, H. Bernien, B. Hensen, P. F. A. Alkemade, and R. Hanson, "High-fidelity projective read-out of a solid-state spin quantum register," Nature **477**, 574–578 (2011).

[34] G. de Lange, Z. H. Wang, D. Risté, V. V. Dobrovitski, and R. Hanson, "Universal Dynamical Decoupling of a Single Solid-State Spin from a Spin Bath," Science **330**, 60–63 (2010).

[35] G. D. Fuchs, V. V. Dobrovitski, D. M. Toyli, F. J. Heremans, and D. D. Awschalom, "Gigahertz Dynamics of a Strongly Driven Single Quantum Spin," Science **326**, 1520–1522 (2009).

[36] G. Balasubramanian, P. Neumann, D. Twitchen, M. Markham, R. Kolesov, N. Mizuochi, J. Isoya, J. Achard, J. Beck, J. Tissler, V. Jacques, P. R. Hemmer, F. Jelezko, and J. Wrachtrup, "Ultralong spin coherence time in isotopically engineered diamond," Nature Mater. **8**, 383–387 (2009).

[37] C. A. Ryan, J. S. Hodges, and D. G. Cory, "Robust Decoupling Techniques to Extend Quantum Coherence in Diamond," Phys. Rev. Lett. **105**, 200402 (2010).

[38] B. Naydenov, F. Dolde, L. T. Hall, C. Shin, H. Fedder, L. C. L. Hollenberg, F. Jelezko, and J. Wrachtrup, "Dynamical decoupling of a single-electron spin at room temperature," Phys. Rev. B **83**, 081201 (2011).

[39] N. Bar-Gill, L. Pham, A. Jarmola, D. Budker, and R. Walsworth, "Solid-state electronic spin coherence time approaching one second," Nat. Commun. **4**, 1743 (2013).

[40] P. C. Maurer, G. Kucsko, C. Latta, L. Jiang, N. Y. Yao, S. D. Bennett, F. Pastawski, D. Hunger, N. Chisholm, M. Markham, D. J. Twitchen, J. I. Cirac, and M. D. Lukin, "Room-Temperature Quantum Bit Memory Exceeding One Second," Science **336**, 1283–1286 (2012).

[41] P. Neumann, J. Beck, M. Steiner, F. Rempp, H. Fedder, P. R. Hemmer, J. Wrachtrup, and F. Jelezko, "Single-Shot Readout of a Single Nuclear Spin," Science **329**, 542–544 (2010).

[42] A. Dréau, P. Spinicelli, J. R. Maze, J.-F. Roch, and V. Jacques, "Single-shot readout of multiple nuclear spin qubits in diamond under ambient conditions," Phys. Rev. Lett. **110**, 060502 (2013).

[43] G. D. Fuchs, G. Burkard, P. V. Klimov, and D. D. Awschalom, "A quantum memory intrinsic to single nitrogen-vacancy centres in diamond," Nature Phys. **7**, 789–793 (2011).

[44] T. van der Sar, Z. H. Wang, M. S. Blok, H. Bernien, T. H. Taminiau, D. M. Toyli, D. A. Lidar, D. D. Awschalom, R. Hanson, and V. V. Dobrovitski, "Decoherence-protected quantum gates for a hybrid solid-state spin register," Nature **484**, 82–86 (2012).

[45] G. Waldherr, Y. Wang, S. Zaiser, M. Jamali, T. Schulte-Herbruggen, H. Abe, T. Ohshima, J. Isoya, J. F. Du, P. Neumann, and J. Wrachtrup, "Quantum error correction in a solid-state hybrid spin register," Nature **506**, 204–207 (2014).

[46] T. Taminiau, J. Cramer, T. van der Sar, V. Dobrovitski, and R. Hanson, "Universal control and error correction in multi-qubit spin registers in diamond," Nature Nanotech. **9**, 171–176 (2014).

[47] P. Neumann, R. Kolesov, B. Naydenov, J. Beck, F. Rempp, M. Steiner, V. Jacques, G. Balasubramanian, M. Markham, D. Twitchen, S. Pezzagna, J. Meijer, J. Twamley, F. Jelezko, and J. Wrachtrup, "Quantum register based on coupled electron spins in a room-temperature solid," Nature Phys. **6**, 249–253 (2010).

[48] F. Dolde, I. Jakobi, B. Naydenov, N. Zhao, S. Pezzagna, C. Trautmann, J. Meijer, P. Neumann, F. Jelezko, and J. Wrachtrup, "Room-temperature entanglement between single defect spins in diamond," Nature Phys. **9**, 139–143 (2013).

[49] D. M. Toyli, C. D. Weis, G. D. Fuchs, T. Schenkel, and D. D. Awschalom, "Chip-Scale Nanofabrication of Single Spins and Spin Arrays in Diamond," Nano Lett. **10**, 3168–3172 (2010).

[50] E. Togan, Y. Chu, A. S. Trifonov, L. Jiang, J. Maze, L. Childress, M. V. G. Dutt, A. S. Sørensen, P. R. Hemmer, A. S. Zibrov, A. S. Zibrov, and M. D. Lukin, "Quantum entanglement between an optical photon and a solid-state spin qubit," Nature **466**, 730–734 (2010).

[51] H. Bernien, L. Childress, L. Robledo, M. Markham, D. Twitchen, and R. Hanson, "Two-Photon Quantum Interference from Separate Nitrogen Vacancy Centers in Diamond," Phys. Rev. Lett. **108**, 043604 (2012).

[52] A. Sipahigil, M. L. Goldman, E. Togan, Y. Chu, M. Markham, D. J. Twitchen, A. S. Zibrov, A. Kubanek, and M. D. Lukin, "Quantum Interference of Single Photons from Remote Nitrogen-Vacancy Centers in Diamond," Phys. Rev. Lett. **108**, 143601 (2012).

[53] H. Bernien, B. Hensen, W. Pfaff, G. Koolstra, M. Blok, L. Robledo, T. Taminiau, M. M. D. Twitchen, L. Childress, and R. Hanson, "Heralded entanglement between solid-state qubits separated by 3 meters," Nature **497**, 86–90 (2013).

[54] W. Pfaff, B. J. Hensen, H. Bernien, S. B. van Dam, M. S. Blok, T. H. Taminiau, M. J. Tiggelman, R. N. Schouten, M. Markham, D. J. Twitchen, and R. Hanson, "Unconditional quantum teleportation between distant solid-state quantum bits," Science **345**, 532–535 (2014).

[55] E. Neu, M. Agio, and C. Becher, "Photophysics of single silicon vacancy centers in diamond: implications for single photon emission," Opt. Express **20**, 19956–19971 (2012).

[56] E. Purcell, "Spontaneous emission probabilities at radio frequencies," Phys. Rev. Lett. **69**, 681 (1946).

[57] C.-H. Su, A. D. Greentree, and L. C. L. Hollenberg, "Towards a picosecond transform-limited nitrogen-vacancy based single photon source," Opt. Express **16**, 6240–6250 (2008).

[58] C.-H. Su, A. D. Greentree, and L. C. L. Hollenberg, "High-performance diamond-based single-photon sources for quantum communication," Phys. Rev. A **80**, 052308 (2009).

[59] A. Young, C. Y. Hu, L. Marseglia, J. P. Harrison, J. L. O'Brien, and J. G. Rarity, "Cavity enhanced spin measurement of the ground state spin of an NV center in diamond," New J. Phys. **11**, 013007 (2009).

[60] A. B. Young, C. Y. Hu, and J. G. Rarity, "Generating entanglement with low-Q-factor microcavities," Phys. Rev. A **87**, 012332 (2013).

[61] J. Wolters, J. Kabuss, A. Knorr, and O. Benson, "Deterministic and robust entanglement of nitrogen-vacancy centers using low-Q photonic-crystal cavities," Phys. Rev. A **89**, 060303 (2014).

[62] L. Childress, J. M. Taylor, A. S. Sørensen, and M. D. Lukin, "Fault-tolerant quantum repeaters with minimal physical resources and implementations based on single-photon emitters," Phys. Rev. A **72**, 052330 (2005).

[63] I. Aharonovich, A. D. Greentree, and S. Prawer, "Diamond photonics," Nature Photon. **5**, 397–405 (2011).

[64] I. Aharonovich and E. Neu, "Diamond Nanophotonics," Adv. Opt. Mater. **2**, 911–928 (2014).

[65] M. Lončar and A. Faraon, "Quantum photonic networks in diamond," MRS Bull. **38**, 144–148 (2013).

[66] O. Benson, "Assembly of hybrid photonic architectures from nanophotonic constituents," Nature **480**, 193–199 (2011).

[67] S. Schietinger, T. Schröder, and O. Benson, "One-by-One coupling of single defect centers in nanodiamonds to high-Q modes of an optical microresonator," Nano Lett. **8**, 3911–3915 (2008).

[68] S. Schietinger and O. Benson, "Coupling single NV-centres to high-Q whispering gallery modes of a preselected frequency-matched microresonator," J. Phys. B: At. Mol. Opt. Phys. **42**, 114001 (2009).

[69] M. Gregor, R. Henze, T. Schröder, and O. Benson, "On-demand positioning of a preselected quantum emitter on a fiber-coupled toroidal microresonator," Appl. Phys. Lett. **95**, 153110 (2009).

[70] M. Larsson, K. N. Dinyari, and H. Wang, "Composite optical microcavity of diamond nanopillar and silica microsphere," Nano Lett. **9**, 1447–1450 (2009).

[71] P. E. Barclay, C. Santori, K.-M. Fu, R. G. Beausoleil, and O. Painter, "Coherent interference effects in a nano-assembled diamond NV center cavity-QED system," Opt. Express **17**, 8081–8097 (2009).

[72] P. E. Barclay, K.-M. C. Fu, C. Santori, and R. G. Beausoleil, "Chip-based microcavities coupled to NV centers in single crystal diamond," Appl. Phys. Lett. **95**, 191115 (2009).

[73] K.-M. Fu, P. Barclay, C. Santori, A. Faraon, and R. Beausoleil, "Low-temperature tapered-fiber probing of diamond NV ensembles coupled to GaP microcavities," New J. Phys. **13**, 055023 (2011).

[74] P. E. Barclay, K.-M. C. Fu, C. Santori, A. Faraon, and R. G. Beausoleil, "Hybrid nanocavity resonant enhancement of color center emission in diamond," Phys. Rev. X **1**, 011007 (2011).

[75] J. Wolters, A. W. Schell, G. Kewes, N. Nüsse, M. Schoengen, H. Döscher, T. Hannappel, B. Löchel, M. Barth, and O. Benson, "Enhancement of the zero phonon line emission from a single nitrogen vacancy center in a nanodiamond via coupling to a photonic crystal cavity," Appl. Phys. Lett. **97**, 141108 (2010).

[76] D. Englund, B. Shields, K. Rivoire, F. Hatami, J. Vučković, H. Park, and M. D. Lukin, "Deterministic coupling of a single nitrogen vacancy center to a photonic crystal cavity," Nano Lett. **10**, 3922–3926 (2010).

[77] T. van der Sar, J. Hagemeier, W. Pfaff, E. C. Heeres, S. M. Thon, H. Kim, P. M. Petroff, T. H. Oosterkamp, D. Bouwmeester, and R. Hanson, "Deterministic nanoassembly of a coupled quantum emitter-photonic crystal cavity system," Appl. Phys. Lett. **98**, 193103 (2011).

[78] M. Barth, N. Nüsse, B. Löchel, and O. Benson, "Controlled coupling of a single-diamond nanocrystal to a photonic crystal cavity," Opt. Lett. **34**, 1108–1110 (2009).

[79] Y. Dumeige, R. Alléaume, P. Grangier, F. Treussart, and J.-F. Roch, "Controling the single-diamond nitrogen-vacancy color center photoluminescence spectrum with a Fabry-Perot microcavity," New J. Phys. **13**, 025015 (2011).

[80] R. Albrecht, A. Bommer, C. Deutsch, J. Reichel, and C. Becher, "Coupling of a single nitrogen-vacancy center in diamond to a fiber-based microcavity," Phys. Rev. Lett. **110**, 243602 (2013).

[81] R. Albrecht, "Coupling of a single Nitrogen-Vacancy center in diamond to a fiber-based microcavity," Ph.D. thesis, Universität des Saarlandes (2014).

[82] H. Kaupp, C. Deutsch, H.-C. Chang, J. Reichel, T. W. Hänsch, and D. Hunger, "Scaling laws of the cavity enhancement for nitrogen-vacancy centers in diamond," Phys. Rev. A **88**, 053812 (2013).

[83] A. Faraon, P. E. Barclay, C. Santori, K.-M. C. Fu, and R. G. Beausoleil, "Resonant enhancement of the zero-phonon emission from a colour centre in a diamond cavity," Nature Photon. **5**, 301–305 (2011).

[84] B. J. M. Hausmann, B. Shields, Q. Quan, P. Maletinsky, M. McCutcheon, J. T. Choy, T. M. Babinec, A. Kubanek, A. Yacoby, M. D. Lukin, and M. Lončar, "Integrated Diamond Networks for Quantum Nanophotonics," Nano Lett. **12**, 1578–1582 (2012).

[85] J. C. Lee, I. Aharonovich, A. P. Magyar, F. Rol, and E. L. Hu, "Coupling of silicon-vacancy centers to a single crystal diamond cavity," Opt. Express **20**, 8891–8897 (2012).

[86] J. Riedrich-Möller, L. Kipfstuhl, C. Hepp, E. Neu, C. Pauly, F. Mücklich, A. Baur, M. Wandt, S. Wolff, M. Fischer, S. Gsell, M. Schreck, and C. Becher, "One- and two-dimensional photonic crystal microcavities in single crystal diamond," Nature Nanotech. **7**, 69–74 (2012).

[87] A. Faraon, C. Santori, Z. Huang, V. M. Acosta, and R. G. Beausoleil, "Coupling of Nitrogen-Vacancy Centers to Photonic Crystal Cavities in Monocrystalline Diamond," Phys. Rev. Lett. **109**, 033604 (2012).

[88] B. J. M. Hausmann, B. J. Shields, Q. Quan, Y. Chu, N. P. de Leon, R. Evans, M. J. Burek, A. S. Zibrov, M. Markham, D. J. Twitchen, H. Park, M. D. Lukin, and M. Lončar, "Coupling of NV centers to photonic crystal nanobeams in diamond," Nano Lett. **13**, 5791–5796 (2013).

[89] J. Riedrich-Möller, C. Arend, C. Pauly, F. Mücklich, M. Fischer, S. Gsell, M. Schreck, and C. Becher, "Deterministic coupling of a single silicon-vacancy color center to a photonic crystal cavity in diamond," Nano Lett. **14**, 5281–5287 (2014).

[90] L. Li, T. Schröder, E. H. Chen, M. Walsh, I. Bayn, J. Goldstein, O. Gaathon, M. E. Trusheim, M. Lu, J. Mower, M. Cotlet, M. L. Markham, D. J. Twitchen, and D. Englund, "Coherent spin control of a nanocavity-enhanced qubit in diamond," (2014). Arxiv 1409.1602.

[91] A. Auffèves, J.-M. Gérard, and J.-P. Poizat, "Pure emitter dephasing: A resource for advanced solid-state single-photon sources," Phys. Rev. A **79**, 053838 (2009).

[92] A. Auffèves, D. Gerace, J.-M. Gérard, M. F. Santos, L. C. Andreani, and J.-P. Poizat, "Controlling the dynamics of a coupled atom-cavity system by pure dephasing," Phys. Rev. B **81**, 245419 (2010).

[93] H. Mabuchi and A. C. Doherty, "Cavity Quantum Electrodynamics: Coherence in Context," Science **298**, 1372–1377 (2002).

[94] S. Haroche and J.-M. Raimond, *Exploring the quantum: Atoms, Cavities and Photons* (Oxford University Press Inc., New York, 2006).

[95] R. J. Thompson, G. Rempe, and H. J. Kimble, "Observation of normal-mode splitting for an atom in an optical cavity," Phys. Rev. Lett. **68**, 1132–1135 (1992).

[96] A. Boca, R. Miller, K. M. Birnbaum, A. D. Boozer, J. McKeever, and H. J. Kimble, "Observation of the Vacuum Rabi Spectrum for One Trapped Atom," Phys. Rev. Lett. **93**, 233603 (2004).

[97] P. Maunz, T. Puppe, I. Schuster, N. Syassen, P. W. H. Pinkse, and G. Rempe, "Normal-Mode Spectroscopy of a Single-Bound-Atom-Cavity System," Phys. Rev. Lett. **94**, 033002 (2005).

[98] A. Kreuter, C. Becher, G. P. T. Lancaster, A. B. Mundt, C. Russo, H. Häffner, C. Roos, J. Eschner, F. Schmidt-Kaler, and R. Blatt, "Spontaneous Emission Lifetime of a Single Trapped Ca^+ Ion in a High Finesse Cavity," Phys. Rev. Lett. **92**, 203002 (2004).

[99] R. Miller, T. E. Northup, K. M. Birnbaum, A. Boca, A. D. Boozer, and H. J. Kimble, "Trapped atoms in cavity QED: coupling quantized light and matter," J. Phys. B: At. Mol. Opt. Phys. **38**, S551–S565 (2005).

[100] H. Walther, B. Varcoe, B.-G. Englert, and T. Becker, "Cavity quantum electrodynamics," Rep. Prog. Phys. **69**, 1325–1382 (2006).

[101] J. M. Gérard, B. Sermage, B. Gayral, B. Legrand, E. Costard, and V. Thierry-Mieg, "Enhanced Spontaneous Emission by Quantum Boxes in a Monolithic Optical Microcavity," Phys. Rev. Lett. **81**, 1110–1113 (1998).

[102] G. S. Solomon, M. Pelton, and Y. Yamamoto, "Single-mode Spontaneous Emission from a Single Quantum Dot in a Three-Dimensional Microcavity," Phys. Rev. Lett. **86**, 3903–3906 (2001).

[103] A. Kiraz, P. Michler, C. Becher, B. Gayral, A. Imamoglu, L. Zhang, E. Hu, W. V. Schoenfeld, and P. M. Petroff, "Cavity-quantum electrodynamics using a single InAs quantum dot in a microdisk structure," Appl. Phys. Lett. **78**, 3932–3934 (2001).

[104] D. Englund, D. Fattal, E. Waks, G. Solomon, B. Zhang, T. Nakaoka, Y. Arakawa, Y. Yamamoto, and J. Vučković, "Controlling the spontaneous emission rate of single quantum dots in a two-dimensional photonic crystal," Phys. Rev. Lett. **95**, 013904 (2005).

[105] J. P. Reithmaier, G. Sek, A. Löffler, C. Hofmann, S. Kuhn, S. Reitzenstein, L. V. Keldysh, V. D. Kulakovskii, T. L. Reinecke, and A. Forchel, "Strong coupling in a single quantum dot-semiconductor microcavity system," Nature **432**, 197 (2004).

[106] D. Press, S. Götzinger, S. Reitzenstein, C. Hofmann, A. Löffler, M. Kamp, A. Forchel, and Y. Yamamoto, "Photon Antibunching from a Single Quantum-Dot-Microcavity System in the Strong Coupling Regime," Phys. Rev. Lett. **98**, 117402 (2007).

[107] E. Peter, P. Senellart, D. Martrou, A. Lemaître, J. Hours, J. M. Gérard, and J. Bloch, "Exciton-Photon Strong-Coupling Regime for a Single Quantum Dot Embedded in a Microcavity," Phys. Rev. Lett. **95**, 067401 (2005).

[108] T. Yoshie, A. Scherer, J. Hendrickson, G. Khitrova, H. M. Gibbs, G. Rupper, O. B. Shchekin, and D. G. Deppe, "Vacuum Rabi splitting with a single quantum dot in a photonic crystal nanocavity," Nature **432**, 200 (2004).

[109] A. Badolato, K. Hennessy, M. Atatüre, J. Dreiser, E. Hu, P. M. Petroff, and A. Imamoğlu, "Deterministic Coupling of Single Quantum Dots to Single Nanocavity Modes," Science **308**, 1158–1161 (2005).

[110] K. Hennessy, A. Badolato, M. Winger, D. Gerace, M. Atatüre, S. Gulde, S. Fält, E. L. Hu, and A. Imamoğlu, "Quantum nature of a strongly coupled single quantum dot-cavity system," Nature **445**, 896–899 (2007).

[111] A. Wallraff, D. I. Schuster, A. Blais, L. Frunzio, R.-S. Huang, J. Majer, S. Kumar, S. M. Girvin, and R. J. Schoelkopf, "Strong coupling of a single photon to a superconducting qubit using circuit quantum electrodynamics," Nature **431**, 162–167 (2004).

[112] S. Haroche, "Nobel Lecture: Controlling photons in a box and exploring the quantum to classical boundary," Rev. Mod. Phys. **85**, 1083–1102 (2013).

[113] D. J. Wineland, "Nobel Lecture: Superposition, entanglement, and raising Schrödinger's cat," Rev. Mod. Phys. **85**, 1103–1114 (2013).

[114] R. Coccioli, M. Boroditsky, K. W. Kim, Y. Rahmat-Samii, and E. Yablonovitch, "Smallest possible electromagnetic mode volume in a dielectric cavity," IEE Proc. Optoelectron. **145**, 391–397 (1998).

[115] M. Fox, *Quantum Optics - An Introduction* (Oxford University Press Inc., New York, 2006).

[116] E. Jaynes and F. W. Cummings, "Comparison of quantum and semiclassical radiation theories with application to the beam maser," Proc. IEEE **51**, 89–109 (1963).

[117] M. O. Scully and M. S. Zubairy, *Quantum optics* (Cambridge University Press, Cambridge, 1997).

[118] C. M. da Silva Baptista Russo, "Photon statistics of a single ion coupled to a high-finesse cavity," Ph.D. thesis, Leopold-Franzens-Universität Innsbruck (2008).

[119] T. Steinmetz, "Resonator-Quantenelektrodynamik auf einem Mikrofallenchip," Ph.D. thesis, Ludwig-Maximilians-Universität München (2008).

[120] L. Novotny and B. Hecht, *Principles of Nano-Optics* (Cambridge University Press, Cambridge UK, 2006).

[121] J.-M. Gérard and B. Gayral, "Strong Purcell effect for InAs quantum boxes in three-dimensional solid-state microcavities," J. Lightw. Technol. **17**, 2089–2095 (1999).

[122] D. J. Heinzen, J. J. Childs, J. E. Thomas, and M. S. Feld, "Enhanced and inhibited visible spontaneous emission by atoms in a confocal resonator," Phys. Rev. Lett. **58**, 1320–1323 (1987).

[123] S. Noda, M. Fujita, and T. Asano, "Spontaneous-emission control by photonic crystals and nanocavities," Nature Photon. **1**, 449–458 (2007).

[124] J. Bleuse, J. Claudon, M. Creasey, N. S. Malik, J.-M. Gérard, I. Maksymov, J.-P. Hugonin, and P. Lalanne, "Inhibition, Enhancement, and Control of Spontaneous Emission in Photonic Nanowires," Phys. Rev. Lett. **106**, 103601 (2011).

[125] Y.-S. Park, A. K. Cook, and H. Wang, "Cavity QED with diamond nanocrystals and silica microspheres," Nano Lett. **6**, 2075–2079 (2006).

[126] J. Wolters, G. Kewes, A. W. Schell, N. Nüsse, M. Schoengen, B. Löchel, T. Hanke, R. Bratschitsch, A. Leitenstorfer, T. Aichele, and O. Benson, "Coupling of single nitrogen-vacancy defect centers in diamond nanocrystals to optical antennas and photonic crystal cavities," Phys. Status Solidi B **249**, 918–924 (2012).

[127] T. Schröder, A. W. Schell, G. Kewes, T. Aichele, and O. Benson, "Fiber-Integrated Diamond-Based Single Photon Source," Nano Lett. **11**, 198–202 (2011).

[128] A. W. Schell, G. Kewes, T. Schröder, J. Wolters, T. Aichele, and O. Benson, "A scanning probe-based pick-and-place procedure for assembly of integrated quantum optical hybrid devices," Rev. Sci. Instrum. **82**, 073709 (2011).

[129] L. Liebermeister, F. Petersen, A. v. Münchow, D. Burchardt, J. Hermelbracht, T. Tashima, A. W. Schell, O. Benson, T. Meinhardt, A. Krueger, A. Stiebeiner, A. Rauschenbeutel, H. Weinfurter, and M. Weber, "Tapered fiber coupling of single photons emitted by a deterministically positioned single nitrogen vacancy center," Appl. Phys. Lett. **104**, 031101 (2014).

[130] T. van der Sar, E. C. Heeres, G. M. Dmochowski, G. de Lange, L. Robledo, T. H. Oosterkamp, and R. Hanson, "Nanopositioning of a diamond nanocrystal containing a single nitrogen-vacancy defect center," Appl. Phys. Lett. **94**, 173104 (2009).

[131] L. A. Stewart, Y. Zhai, J. M. Dawes, M. J. Steel, J. R. Rabeau, and M. J. Withford, "Single photon emission from diamond nanocrystals in an opal photonic crystal," Opt. Express **17**, 18044–18053 (2009).

[132] C. F. Wang, R. Hanson, E. Hu, T. Feygelson, J. Yang, and J. E. Butler, "Fabrication and characterization of two-dimensional photonic crystal microcavities in nanocrystalline diamond," Appl. Phys. Lett. **91**, 201112 (2007).

[133] T. Schröder, E. Chen, L. Li, M. Walsh, M. E. Trusheim, I. Bayn, and D. Englund, "Targeted creation and Purcell enhancement of NV centers within photonic crystal cavities in single-crystal diamond," in "CLEO: 2014," (Optical Society of America, 2014), p. FW1B.6.

[134] A. M. Zaitsev, *Optical Properties of Diamond* (Springer-Verlag, Berlin, 2001).

[135] H. Liander and E. Lundblad, "Artificial diamonds," ASEA Journal **28**, 97 (1955).

[136] F. P. Bundy, H. T. Hall, H. M. Strong, and R. H. Wentorf, "Man-made diamond," Nature **176**, 51–55 (1955).

[137] H. P. Bovenkerk, F. P. Bundy, R. M. Chrenko, P. J. Codella, H. M. Strong, and R. H. Wentorf, "Errors of diamond synthesis," Nature **365**, 19 (1993).

[138] H. P. Bovenkerk, F. P. Bundy, H. T. Hall, H. M. Strong, and R. H. Wentorf, "Preparation of Diamond," Nature **184**, 1094–1098 (1959).

[139] R. C. Burns, A. I. Chumakov, S. H. Connell, D. Dube, H. P. Godfried, J. O. Hansen, J. Härtwig, J. Hoszowska, F. Masiello, L. Mkhonza, M. Rebak, A. Rommevaux, R. Setshedi, and P. V. Vaerenbergh, "HPHT growth and x-ray characterization of high-quality type IIa diamond," J. Phys.: Condens. Matter **21**, 364224 (2009).

[140] J. E. Butler, R. L. Woodin, L. M. Brown, and P. Fallon, "Thin Film Diamond Growth Mechanisms," Phil. Trans. R. Soc. Lond. A. **342**, 209–224 (1993).

[141] M. Schwander and K. Partes, "A review of diamond synthesis by CVD processes," Diamond Relat. Mater. **20**, 1287–1301 (2011).

[142] M. Schreck, F. Hörmann, H. Roll, J. K. N. Lindner, and B. Stritzker, "Diamond nucleation on iridium buffer layers and subsequent textured growth: A route for the realization of single-crystal diamond films," Appl. Phys. Lett. **78**, 192–194 (2001).

[143] T. Tachibana, Y. Yokota, K. Hayashi, and K. Kobashi, "Growth of 111-oriented diamond on Pt/Ir/Pt substrate deposited on sapphire," Diamond Relat. Mater. **10**, 1633 – 1636 (2001).

[144] N. Mohan, C.-S. Chen, H.-H. Hsieh, Y.-C. Wu, and H.-C. Chang, "In Vivo Imaging and Toxicity Assessments of Fluorescent Nanodiamonds in Caenorhabditis elegans," Nano Lett. **10**, 3692–3699 (2010).

[145] L. Hall, D. Simpson, and L. Hollenberg, "Nanoscale sensing and imaging in biology using nitrogen-vacancy center in diamond," MRS Bull. **38**, 162–167 (2013).

[146] N. R. Greiner, D. S. Phillips, J. D. Johnson, and F. Volk, "Diamonds in detonation soot," Nature **333**, 440–442 (1988).

[147] Y. Liang, M. Ozawa, and A. Krueger, "A General Procedure to Functionalize Agglomerating Nanoparticles Demonstrated on Nanodiamond," ACS Nano **3**, 2288–2296 (2009).

[148] W. Kaiser and W. L. Bond, "Nitrogen, A Major Impurity in Common Type I Diamond," Phys. Rev. **115**, 857–863 (1959).

[149] C. M. Breeding and J. E. Shigley, "The "Type" classification system of diamonds and its importance in gemology," Gems & Gemology **45**, 96–111 (2009).

[150] H. B. Dyer, F. A. Raal, L. Du Preez, and J. H. N. Loubser, "Optical absorption features associated with paramagnetic nitrogen in diamond," Philos. Mag. **11**, 763–774 (1965).

[151] "Element Six, Synthetic CVD diamond, Electronic grade diamond," www.e6cvd.com/cvd.

[152] M. Markham, J. Dodson, G. Scarsbrook, D. Twitchen, G. Balasubramanian, F. Jelezko, and J. Wrachtrup, "{CVD} diamond for spintronics," Diamond Relat. Mater. **20**, 134 – 139 (2011).

[153] S. Prawer and I. Aharonovich, eds., *Quantum information processing with diamond* (Woodhead publishing series in electronics and optical materials, 2014).

[154] I. Aharonovich, S. Castelletto, D. Simpson, A. Greentree, and S. Prawer, "Photophysics of chromium-related diamond single-photon emitters," Phys. Rev. A **81**, 043813 (2010).

[155] T. Müller, I. Aharonovich, L. Lombez, Y. Alaverdyan, A. N. Vamivakas, S. Castelletto, F. Jelezko, J. Wrachtrup, S. Prawer, and M. Atatüre, "Wide range electrical tunability of single photon emission from chromium-based colour centres in diamond," New J. Phys. **13**, 075001 (2011).

[156] I. Aharonovich, S. Castelletto, D. A. Simpson, A. Stacey, J. McCallum, A. D. Greentree, and S. Prawer, "Two-level ultrabright single photon emission from diamond nanocrystals," Nano Lett. **9**, 3191–3195 (2009).

[157] S. Castelletto, I. Aharonovich, B. Gibson, B. Johnson, and S. Prawer, "Imaging and quantum-efficiency measurement of chromium emitters in diamond," Phys. Rev. Lett. **105**, 217403 (2010).

[158] S. Castelletto and A. Boretti, "Radiative and nonradiative decay rates in chromium-related centers in nanodiamonds," Opt. Lett. **36**, 4224–4226 (2011).

[159] I. Aharonovich, S. Castelletto, B. C. Johnson, J. C. McCallum, and S. Prawer, "Engineering chromium-related single photon emitters in single crystal diamonds," New J. Phys. **13**, 045015 (2011).

[160] I. Aharonovich, C. Zhou, A. Stacey, J. Orwa, S. Castelletto, D. Simpson, A. D. Greentree, F. m. c. Treussart, J.-F. Roch, and S. Prawer, "Enhanced single-photon emission in the near infrared from a diamond color center," Phys. Rev. B **79**, 235316 (2009).

[161] D. Steinmetz, E. Neu, J. Meijer, W. Bolse, and C. Becher, "Single photon emitters based on Ni/Si related defects in single crystalline diamond," Appl. Phys. B **102**, 451–458 (2011).

[162] T. Gaebel, I. Popa, A. Gruber, M. Domhan, F. Jelezko, and J. Wrachtrup, "Stable single-photon source in the near infrared," New J. Phys. **6**, 98 (2004).

[163] E. Wu, V. Jacques, H. Zeng, P. Grangier, F. Treussart, and J.-F. Roch, "Narrow-band single-photon emission in the near infrared for quantum key distribution," Opt. Express **14**, 1296–1303 (2006).

[164] J. R. Rabeau, Y. L. Chin, S. Prawer, F. Jelezko, T. Gaebel, and J. Wrachtrup, "Fabrication of single nickel-nitrogen defects in diamond by chemical vapor deposition," Appl. Phys. Lett. **86**, 131926 (2005).

[165] N. B. Manson, J. P. Harrison, and M. J. Sellars, "Nitrogen-vacancy center in diamond: Model of the electronic structure and associated dynamics," Phys. Rev. B **74**, 104303 (2006).

[166] F. Jelezko, I. Popa, A. Gruber, C. Tietz, J. Wrachtrup, A. Nizovtsev, and S. Kilin, "Single spin states in a defect center resolved by optical spectroscopy," Appl. Phys. Lett. **81**, 2160–2162 (2002).

[167] C. Santori, D. Fattal, S. M. Spillane, M. Fiorentino, R. G. Beausoleil, A. D. Greentree, P. Olivero, M. Draganski, J. R. Rabeau, P. Reichart, B. C. Gibson, S. Rubanov, D. N. Jamieson, and S. Prawer, "Coherent population trapping in diamond N-V centers at zero magnetic field," Opt. Express **14**, 7986–7993 (2006).

[168] G. Davies and M. Hamer, "Optical studies of the 1.945 eV vibronic band in diamond," Proc. R. Soc. Lond. A. **348**, 285–298 (1976).

[169] L. J. Rogers, S. Armstrong, M. J. Sellars, and N. B. Manson, "Infrared emission of the NV centre in diamond: Zeeman and uniaxial stress studies," New J. Phys. **10**, 103024 (2008).

[170] G. Davies, "Vibronic spectra in diamond," J. Phys. C: Solid State Phys. **7**, 3797 (1974).

[171] C. Clark and C. Norris, "Photoluminescence associated with the 1.673, 1.944 and 2.498 eV centres in diamond," J. Phys. C: Solid State Phys. **4**, 2223–2229 (1971).

[172] R. J. Epstein, F. M. Mendoza, Y. K. Kato, and D. D. Awschalom, "Anisotropic interactions of a single spin and dark-spin spectroscopy in diamond," Nature Phys. **1**, 94–98 (2005).

[173] A. Batalov, C. Zierl, T. Gaebel, P. Neumann, I.-Y. Chan, G. Balasubramanian, P. R. Hemmer, F. Jelezko, and J. Wrachtrup, "Temporal Coherence of Photons Emitted by Single Nitrogen-Vacancy Defect Centers in Diamond Using Optical Rabi-Oscillations," Phys. Rev. Lett. **100**, 077401 (2008).

[174] A. Bommer, "Aufbau eines fasergekoppelten Mikroresonators zur Kopplung von Farbzentren in Diamant bei kryogenen Temperaturen," Master's thesis, Universität des Saarlandes (2013).

[175] F. Treussart, V. Jacques, E. Wu, T. Gacoin, P. Grangier, and J.-F. Roch, "Photoluminescence of single colour defects in 50nm diamond nanocrystals," Physica B **376–377**, 926 – 929 (2006).

[176] L. J. Rogers, M. W. Doherty, M. S. J. Barson, S. Onoda, T. Ohshima, and N. B. Manson, "Singlet levels of the NV^- centre in diamond," (2014). ArXiv:1407.6244.

[177] M. W. Doherty, N. B. Manson, P. Delaney, and L. C. L. Hollenberg, "The negatively charged nitrogen-vacancy centre in diamond: the electronic solution," New J. Phys. **13**, 025019 (2011).

[178] J. R. Maze, A. Gali, E. Togan, Y. Chu, A. Trifonov, E. Kaxiras, and M. D. Lukin, "Properties of nitrogen-vacancy centers in diamond: the group theoretic approach," New J. Phys. **13**, 025025 (2011).

[179] F. M. Hossain, M. W. Doherty, H. F. Wilson, and L. C. L. Hollenberg, "Ab Initio," Phys. Rev. Lett. **101**, 226403 (2008).

[180] N. Reddy, N. Manson, and E. Krausz, "Two-laser spectral hole burning in a colour centre in diamond," J. Lumin. **38**, 46 – 47 (1987).

[181] E. van Oort, N. B. Manson, and M. Glasbeek, "Optically detected spin coherence of the diamond N-V centre in its triplet ground state," J. Phys. C: Solid State Phys. **21**, 4385 (1988).

[182] E. van Oort and M. Glasbeek, "Optically detected adiabatic fast passage and cross-relaxation of the N-V center in diamond," Appl. Magn. Reson. **2**, 291–300 (1991).

[183] K. Holliday, N. B. Manson, M. Glasbeek, and E. van Oort, "Optical hole-bleaching by level anti-crossing and cross relaxation in the N-V centre in diamond," J. Phys.: Condens. Matter **1**, 7093 (1989).

[184] D. A. Redman, S. Brown, R. H. Sands, and S. C. Rand, "Spin dynamics and electronic states of N-V centers in diamond by EPR and four-wave-mixing spectroscopy," Phys. Rev. Lett. **67**, 3420–3423 (1991).

[185] L. Rogers, "How far into the infrared can a colour centre in diamond emit?" Phys. Proc. **3**, 1557–1561 (2010).

[186] V. M. Acosta, A. Jarmola, E. Bauch, and D. Budker, "Optical properties of the nitrogen-vacancy singlet levels in diamond," Phys. Rev. B **82**, 201202 (2010).

[187] N. Manson, L. Rogers, M. Doherty, and L. Hollenberg, "Optically induced spin polarisation of the NV^- centre in diamond: role of electron-vibration interaction," (2010). ArXiv:1011.2840.

[188] J. H. N. Loubser and J. A. van Wyk, "Electron spin resonance in the study of diamond," Rep. Prog. Phys. **41**, 1201 (1978).

[189] A. Nizovtsev, S. Kilin, F. Jelezko, I. Popa, A. Gruber, and J. Wrachtrup, "NV centers in diamond: spin-selective photokinetics, optical ground-state spin alignment and hole burning," Physica B **340**, 106–110 (2003).

[190] N. B. Manson, X.-F. He, and P. T. H. Fisk, "Raman heterodyne detected electron-nuclear-double-resonance measurements of the nitrogen-vacancy center in diamond," Opt. Lett. **15**, 1094–1096 (1990).

[191] X.-F. He, N. B. Manson, and P. T. H. Fisk, "Paramagnetic resonance of photoexcited N-V defects in diamond. I. Level anticrossing in the ^{3}A ground state," Phys. Rev. B **47**, 8809–8815 (1993).

[192] A. Lenef and S. C. Rand, "Electronic structure of the N-V center in diamond: Theory," Phys. Rev. B **53**, 13441–13455 (1996).

[193] G. D. Fuchs, V. V. Dobrovitski, R. Hanson, A. Batra, C. D. Weis, T. Schenkel, and D. D. Awschalom, "Excited-State Spectroscopy Using Single Spin Manipulation in Diamond," Phys. Rev. Lett. **101**, 117601 (2008).

[194] P. Neumann, R. Kolesov, V. Jacques, J. Beck, J. Tisler, A. Batalov, L. Rogers, N. B. Manson, G. Balasubramanian, F. Jelezko, and J. Wrachtrup, "Excited-state spectroscopy of single NV defects in diamond using optically detected magnetic resonance," New J. Phys. **11**, 013017 (2009).

[195] P. Tamarat, T. Gaebel, J. R. Rabeau, M. Khan, A. D. Greentree, H. Wilson, L. C. L. Hollenberg, S. Prawer, P. Hemmer, F. Jelezko, and J. Wrachtrup, "Stark shift control of single optical centers in diamond," Phys. Rev. Lett. **97**, 083002 (2006).

[196] E. van Oort and M. Glasbeek, "Electric-field-induced modulation of spin echoes of NV centers in diamond," Chem. Phys. Lett. **168**, 529–532 (1990).

[197] A. Batalov, V. Jacques, F. Kaiser, P. Siyushev, P. Neumann, L. J. Rogers, R. L. McMurtrie, N. B. Manson, F. Jelezko, and J. Wrachtrup, "Low Temperature Studies of the Excited-State Structure of Negatively Charged Nitrogen-Vacancy Color Centers in Diamond," Phys. Rev. Lett. **102**, 195506 (2009).

[198] P. Tamarat, N. B. Manson, J. P. Harrison, R. L. McMurtrie, A. Nizovtsev, C. Santori, R. G. Beausoleil, P. Neumann, T. Gaebel, F. Jelezko, P. Hemmer, and J. Wrachtrup, "Spin-flip and spin-conserving optical transitions of the nitrogen-vacancy centre in diamond," New J. Phys. **10**, 045004 (2008).

[199] L. J. Rogers, R. L. McMurtrie, M. J. Sellars, and N. B. Manson, "Time-averaging within the excited state of the nitrogen-vacancy centre in diamond," New J. Phys. **11**, 063007 (2009).

[200] T. P. M. Alegre, C. Santori, G. Medeiros-Ribeiro, and R. G. Beausoleil, "Polarization-selective excitation of nitrogen vacancy centers in diamond," Phys. Rev. B **76**, 165205 (2007).

[201] F. Grazioso, B. R. Patton, P. Delaney, M. L. Markham, D. J. Twitchen, and J. M. Smith, "Measurement of the full stress tensor in a crystal using photoluminescence from point defects: The example of nitrogen vacancy centers in diamond," Appl. Phys. Lett. **103**, 101905 (2013).

[202] P. R. Dolan, X. Li, J. Storteboom, and M. Gu, "Complete determination of the orientation of NV centers with radially polarized beams," Opt. Express **22**, 4379–4387 (2014).

[203] L. Childress, M. V. Gurudev Dutt, J. M. Taylor, A. S. Zibrov, F. Jelezko, J. Wrachtrup, P. R. Hemmer, and M. D. Lukin, "Coherent Dynamics of Coupled Electron and Nuclear Spin Qubits in Diamond," Science **314**, 281–285 (2006).

[204] M. V. G. Dutt, L. Childress, L. Jiang, E. Togan, J. Maze, F. Jelezko, A. S. Zibrov, P. R. Hemmer, and M. D. Lukin, "Quantum Register Based on Individual Electronic and Nuclear Spin Qubits in Diamond," Science **316**, 1312–1316 (2007).

[205] J. Harrison, M. Sellars, and N. Manson, "Optical spin polarisation of the N-V centre in diamond," J. Lumin. **107**, 245 – 248 (2004).

[206] N. Manson and R. McMurtrie, "Issues concerning the nitrogen-vacancy center in diamond," J. Lumin. **127**, 98 – 103 (2007).

[207] M. Steiner, P. Neumann, J. Beck, F. Jelezko, and J. Wrachtrup, "Universal enhancement of the optical readout fidelity of single electron spins at nitrogen-vacancy centers in diamond," Phys. Rev. B **81**, 035205 (2010).

[208] L. Robledo, H. Bernien, T. van der Sar, and R. Hanson, "Spin dynamics in the optical cycle of single nitrogen-vacancy centres in diamond," New J. Phys. **13**, 025013 (2011).

[209] A. Beveratos, R. Brouri, T. Gacoin, J.-P. Poizat, and P. Grangier, "Nonclassical radiation from diamond nanocrystals," Phys. Rev. A **64**, 061802 (2001).

[210] R. P. Mildren and J. R. Rabeau, eds., *Optical engineering of diamond* (Wiley-VCH, Weihnheim, 2013).

[211] P. Neumann, N. Mizuochi, F. Rempp, P. Hemmer, H. Watanabe, S. Yamasaki, V. Jacques, T. Gaebel, F. Jelezko, and J. Wrachtrup, "Multipartite entanglement among single spins in diamond," Science **320**, 1326–1329 (2008).

[212] R. Hanson, F. M. Mendoza, R. J. Epstein, and D. D. Awschalom, "Polarization and Readout of Coupled Single Spins in Diamond," Phys. Rev. Lett. **97**, 087601 (2006).

[213] M. W. Doherty, N. B. Manson, P. Delaney, F. Jelezko, J. Wrachtrup, and L. C. Hollenberg, "The nitrogen-vacancy colour centre in diamond," Phys. Rep. **528**, 1–45 (2013).

[214] G. Davies, "The Jahn-Teller effect and vibronic coupling at deep levels in diamond," Rep. Prog. Phys. **44**, 787 (1981).

[215] H. A. Jahn and E. Teller, "Stability of Polyatomic Molecules in Degenerate Electronic States. I. Orbital Degeneracy," Proc. R. Soc. Lond. A **161**, 220–235 (1937).

[216] J. Zhang, C.-Z. Wang, Z. Z. Zhu, and V. V. Dobrovitski, "Vibrational modes and lattice distortion of a nitrogen-vacancy center in diamond from first-principles calculations," Phys. Rev. B **84**, 035211 (2011).

[217] K.-M. C. Fu, C. Santori, P. E. Barclay, L. J. Rogers, N. B. Manson, and R. G. Beausoleil, "Observation of the Dynamic Jahn-Teller Effect in the Excited States of Nitrogen-Vacancy Centers in Diamond," Phys. Rev. Lett. **103**, 256404 (2009).

[218] T. A. Abtew, Y. Y. Sun, B.-C. Shih, P. Dev, S. B. Zhang, and P. Zhang, "Dynamic Jahn-Teller Effect in the NV- Center in Diamond," Phys. Rev. Lett. **107**, 146403 (2011).

[219] J. Wolters, N. Sadzak, A. W. Schell, T. Schröder, and O. Benson, "Measurement of the ultrafast spectral diffusion of the optical transition of nitrogen vacancy centers in nano-size diamond using correlation interferometry," Phys. Rev. Lett. **110**, 027401 (2013).

[220] L. Robledo, H. Bernien, I. van Weperen, and R. Hanson, "Control and Coherence of the Optical Transition of Single Nitrogen Vacancy Centers in Diamond," Phys. Rev. Lett. **105**, 177403 (2010).

[221] R. Farrer, "On the substitutional nitrogen donor in diamond," Solid State Commun. **7**, 685 – 688 (1969).

[222] J. P. Goss, P. R. Briddon, and M. J. Shaw, "Density functional simulations of silicon-containing point defects in diamond," Phys. Rev. B **76**, 075204 (2007).

[223] C. Hepp, T. Müller, V. Waselowski, J. N. Becker, B. Pingault, H. Sternschulte, D. Steinmüller-Nethl, A. Gali, J. R. Maze, M. Atatüre, and C. Becher, "Electronic Structure of the Silicon Vacancy Color Center in Diamond," Phys. Rev. Lett. **112**, 036405 (2014).

[224] U. F. S. D'Haenens-Johansson, A. M. Edmonds, B. L. Green, M. E. Newton, G. Davies, P. M. Martineau, R. U. A. Khan, and D. J. Twitchen, "Optical properties of the neutral silicon split-vacancy center in diamond," Phys. Rev. B **84**, 245208 (2011).

[225] L. J. Rogers, K. D. Jahnke, M. W. Doherty, A. Dietrich, L. McGuinness, C. Müller, T. Teraji, J. Isoya, N. B. Manson, and F. Jelezko, "Electronic structure of the

negatively-charged silicon-vacancy center in diamond," Phys. Rev. B **89**, 235101 (2014).

[226] A. Dietrich, K. D. Jahnke, J. M. Binder, T. Teraji, J. Isoya, L. J. Rogers, and F. Jelezko, "Isotopically varying spectral features of silicon vacancy in diamond," (2014). ArXiv:1407.7137.

[227] E. Neu, M. Fischer, S. Gsell, M. Schreck, and C. Becher, "Fluorescence and polarization spectroscopy of single silicon vacancy centers in heteroepitaxial nanodiamonds on iridium," Phys. Rev. B **84**, 205211 (2011).

[228] E. Neu, R. Albrecht, M. Fischer, S. Gsell, M. Schreck, and C. Becher, "Electronic transitions of single silicon vacancy centers in the near-infrared spectral region," Phys. Rev. B **85**, 245207 (2012).

[229] A. Gali and J. R. Maze, "Ab initio study of the split silicon-vacancy defect in diamond: Electronic structure and related properties," Phys. Rev. B **88**, 235205 (2013).

[230] C. Hepp, "Electronic Structure of the Silicon Vacancy Color Center in Diamond," Ph.D. thesis, Universität des Saarlandes (2014).

[231] C. D. Clark, H. Kanda, I. Kiflawi, and G. Sittas, "Silicon defects in diamond," Phys. Rev. B **51**, 16681–16688 (1995).

[232] E. Neu, C. Hepp, M. Hauschild, S. Gsell, M. Fischer, H. Sternschulte, D. Steinmüller-Nethl, M. Schreck, and C. Becher, "Low temperature investigations of single silicon vacancy colour centres in diamond," New J. Phys. **15**, 043005 (2013).

[233] H. Sternschulte, K. Thonke, R. Sauer, P. C. Münzinger, and P. Michler, "1.681-eV luminescence center in chemical-vapor-deposited homoepitaxial diamond films," Phys. Rev. B **50**, 14554–14560 (1994).

[234] R. Loudon, *The Quantum Theory Of Light* (Oxford University Press Inc., New York, 1997).

[235] S. C. Kitson, P. Jonsson, J. G. Rarity, and P. R. Tapster, "Intensity fluctuation spectroscopy of small numbers of dye molecules in a microcavity," Phys. Rev. A **58**, 620–627 (1998).

[236] A. Beveratos, S. Kühn, R. Brouri, T. G. andJ. P. Poizat, and P. Grangier, "Room temperature stable single-photon source," Eur. Phys. J. D **18**, 191–196 (2002).

[237] R. H. Webb, "Confocal optical microscopy," Rep. Prog. Phys. **59**, 427–471 (1996).

[238] E. Gross, "Spektroskopische Untersuchung von Farbzentren in Diamant im sichtbaren und infraroten Spektralbereich," Master's thesis, Universität des Saarlandes (2011).

[239] "PicoQuant," www.picoquant.com.

[240] R. H. Brown and R. Q. Twiss, "Correlation between photons in two coherent beams of light," Nature **177**, 27–29 (1956).

[241] R. H. Brown and R. Twiss, "A test of a new type of stellar interferometer on sirius," Nature **178**, 1046–1048 (1956).

[242] C. Arend, "Kontinuierliche und zeitabhängige Spektroskopie an Farbzentren in Diamant," Master's thesis, Universität des Saarlandes (2011).

[243] D. Steinmetz, "Ni/Si-basierte Farbzentren in Diamant als Einzelphotonenquellen," Ph.D. thesis, Universität des Saarlandes (2011).

[244] M. Wahl, "Time-correlated single photon counting," Tech. rep., PicoQuant GmbH (2009).

[245] V. P. Bykov, "Spontaneous Emission in a Periodic Structure," Sov. J. Exp. Theor. Phys. **35**, 269–273 (1972).

[246] V. P. Bykov, "Spontaneous emission from a medium with a band spectrum," Sov. J. Quantum Electron. **4**, 861 (1975).

[247] E. Yablonovitch, "Inhibited Spontaneous Emission in Solid-State Physics and Electronics," Phys. Rev. Lett. **58**, 2059–2062 (1987).

[248] S. John, "Strong localization of photons in certain disordered dielectric superlattices," Phys. Rev. Lett. **58**, 2486–2489 (1987).

[249] P. Lodahl, A. Floris van Driel, I. S. Nikolaev, A. Irman, K. Overgaag, D. Vanmaekelbergh, and W. L. Vos, "Controlling the dynamics of spontaneous emission from quantum dots by photonic crystals," Nature **430**, 654–657 (2004).

[250] S. Ogawa, M. Imada, S. Yoshimoto, M. Okano, and S. Noda, "Control of Light Emission by 3D Photonic Crystals," Science **305**, 227–229 (2004).

[251] M. D. Leistikow, A. P. Mosk, E. Yeganegi, S. R. Huisman, A. Lagendijk, and W. L. Vos, "Inhibited Spontaneous Emission of Quantum Dots Observed in a 3D Photonic Band Gap," Phys. Rev. Lett. **107**, 193903 (2011).

[252] M. Aspelmeyer, T. Kippenberg, and F. Marquardt, "Cavity Optomechanics," (2013). ArXiv:1303.0733.

[253] M. Eichenfield, J. Chan, R. M. Camacho, K. J. Vahala, and O. Painter, "Optomechanical crystals," Nature **462**, 78–82 (2009).

[254] M. Eichenfield, R. Camacho, J. Chan, K. J. Vahala, and O. Painter, "A picogram and nanometer scale photonic crystal opto-mechanical cavity," Nature **459**, 550 (2009). Axiv:0812.2953.

[255] L. Kipfstuhl, F. Guldner, J. Riedrich-Möller, and C. Becher, "Modeling of optomechanical coupling in a phoxonic crystal cavity in diamond," Opt. Express **22**, 12410–12423 (2014).

[256] J. D. Joannopoulos, S. G. Johnson, R. D. Meade, and J. N. Winn, *Photonic Crystals - Molding the Flow of Light* (Princeton University Press, Princeton, 2008), 2nd ed.

[257] A. Taflove, S. G. Johnson, and A. Oskooi, *Advances in FDTD Computational Electrodynamics: Photonics and Nanotechnology* (Artech House Inc., 2013), chap. 4: Electromagnetic Wave Source Conditions, pp. 65–100.

[258] D. W. Prather, S. Shi, A. Sharkawy, J. Murakowski, and G. J. Schneider, *Photonic crystals - Theory, applications, and fabrication* (John Wiley & Sons, Inc., Hoboken, New Jersey, 2009).

[259] S. G. Johnson and J. D. Joannopoulos, "Block-iterative frequency-domain methods for Maxwell's equations in a planewave basis," Opt. Express **8**, 173–190 (2001).

[260] S. G. Johnson and J. D. Joannopoulos, "MIT Photonic-Bands Package," (2001). Http://ab-initio.mit.edu/mpb/.

[261] X. Letartre, C. Seassal, C. Grillet, P. Rojo-Romeo, P. Viktorovitch, M. L. V. d'Yerville, D. Cassagne, and C. Jouanin, "Group velocity and propagation losses measurement in a single-line photonic-crystal waveguide on InP membranes," Appl. Phys. Lett. **79**, 2312–2314 (2001).

[262] S.-H. Kim, G.-H. Kim, S.-K. Kim, H.-G. Park, Y.-H. Lee, and S.-B. Kim, "Characteristics of a stick waveguide resonator in a two-dimensional photonic crystal slab," J. Appl. Phys. **95**, 411–416 (2004).

[263] J. Vučković, O. Painter, Y. Xu, A. Yariv, and A. Scherer, "Finite-Difference Time-Domain Calculation of the Spontaneous Emission Coupling Factor in Optical Microcavities," IEEE J. Quantum. Electron. **35**, 1168–1175 (1999).

[264] Y. Xu, J. Vučković, R. K. Lee, O. Painter, A. Scherer, and A. Yariv, "Finite-Difference time-domain calculation of spontaneous emission lifetime in a microcavity," J. Opt. Soc. Am. B **16**, 465–474 (1999).

[265] Y. Xu, R. K. Lee, and A. Yariv, "Quantum analysis and the classical analysis of spontaneous emission in a microcavity," Phys. Rev. A **61**, 033807 (2000).

[266] Y. Xu, R. K. Lee, and A. Yariv, "Finite-difference time-domain analysis of spontaneous emission in a microdisk cavity," Phys. Rev. A **61**, 033808 (2000).

[267] M. Fujita, S. Takahashi, Y. Tanaka, T. Asano, and S. Noda, "Simultaneous inhibition and redistribution of spontaneous light emission in photonic crystals," Science **308**, 1296–1298 (2005).

[268] M. Fujita, S. Takahashi, T. Asano, Y. Tanaka, K. Kounoike, M. Yamaguchi, J. Nakanishi, W. Stumpf, and S. Noda, "Controlled spontaneous-emission phenomena in semiconductor slabs with a two-dimensional photonic bandgap," J. Opt. A: Pure Appl. Opt. **8**, S131–S138 (2006).

[269] J. Jackson, *Classical Electrodynamics* (John Wiley & Sons, Inc., New York, New York, 1962).

[270] F. Wijnands, J. Pendry, F. Garcia-Vidal, P. Bell, P. Roberts, and L. Moreno, "Green's functions for Maxwell's equations: application to spontaneous emission," Opt. Quantum. Electron. **29**, 199–216 (1997).

[271] R. D. Meade, K. D. Brommer, A. M. Rappe, and J. D. Joannopoulos, "Existence of a photonic band gap in two dimensions," Appl. Phys. Lett. **61**, 495–497 (1992).

[272] P. R. Villeneuve and M. Piché, "Photonic band gaps in two-dimensional square and hexagonal lattices," Phys. Rev. B **46**, 4969–4972 (1992).

[273] I. Fushman, D. Englund, and J. Vučković, "Coupling of PbS quantum dots to photonic crystal cavities at room temperature," Appl. Phys. Lett. **87**, 241102 (2005).

[274] J. Riedrich-Möller, E. Neu, and C. Becher, "Design of microcavities in diamond-based photonic crystals by Fourier- and real-space analysis of cavity fields," Photon. Nanostruct.: Fundam. Appl. **8**, 150–162 (2010).

[275] C. Kreuzer, J. Riedrich-Möller, E. Neu, and C. Becher, "Design of photonic crystal microcavities in diamond films," Opt. Express **16**, 1632–1644 (2008).

[276] N. W. Ashcroft and D. N. Mermin, *Festkörperphysik* (Oldenbourg Wissenschaftsverlag München, 2007).

[277] A. Mekis, M. Meier, A. Dodabalapur, R. Slusher, and J. Joannopoulos, "Lasing mechanism in two-dimensional photonic crystal lasers," Appl. Phys. A **69**, 111–114 (1999).

[278] K. Busch and S. John, "Photonic band gap formation in certain self-organizing systems," Phys. Rev. E **58**, 3896–3908 (1998).

[279] Z.-Y. Li, L.-L. Lin, and Z.-Q. Zhang, "Spontaneous Emission from Photonic Crystals: Full Vectorial Calculations," Phys. Rev. Lett. **84**, 4341–4344 (2000).

[280] R. C. McPhedran, L. C. Botten, J. McOrist, A. A. Asatryan, C. M. de Sterke, and N. A. Nicorovici, "Density of states functions for photonic crystals," Phys. Rev. E **69**, 016609 (2004).

[281] D. Cassagne, C. Jouanin, and D. Bertho, "Hexagonal photonic-band-gap structures," Phys. Rev. B **53**, 7134–7142 (1996).

[282] C. G. Bostan and R. M. de Ridder, "Design of photonic cystal slab structures with absolute gaps in guided modes," J. Optoelectron. Adv. Mat. **4**, 921–928 (2002).

[283] W. Kuang, Z. Hou, Y. Liu, and H. Li, "The bandgap of a photonic crystal with triangular dielectric rods in a honeycomb lattice," J. Opt. A: Pure Appl. Opt. **7**, 525 (2005).

[284] G.-Y. Dong, X.-L. Yang, L.-Z. Cai, X.-X. Shen, X.-F. Meng, X.-F. Xu, and H. Zhang, "Six-fold hybrid photonic crystal formed holographically with full band gap for low refractive index," Europhys. Lett. **80**, 14006 (2007).

[285] F. Wen, S. David, X. Checoury, M. E. Kurdi, and P. Boucaud, "Two-dimensional photonic crystals with large complete photonic band gaps in both TE and TM polarizations," Opt. Express **16**, 12278–12289 (2008).

[286] L. C. Andreani and D. Gerace, "Photonic-crystal slabs with a triangular lattice of triangular holes investigated using a guided-mode expansion method," Phys. Rev. B **73**, 235114 (2006).

[287] A. F. Matthews, S. F. Mingaleev, and Y. S. Kivshar, "Band-Gap Engineering and Defect Modes in Photonic Crystals with Rotated Hexagonal Holes," Laser Physics **14**, 631–634 (2004).

[288] C. Kao, S. Osher, and E. Yablonovitch, "Maximizing band gaps in two-dimensional photonic crystals by using level set methods," Appl. Phys. B. **81**, 235–244 (2005).

[289] S. G. Johnson, S. Fan, P. R. Villeneuve, J. Joannopoulos, and L. Kolodziejski, "Guided modes in photonic crystal slabs," Phys. Rev. B **60**, 5751 – 5758 (1999).

[290] A. Mekis, J. C. Chen, I. Kurland, S. Fan, P. R. Villeneuve, and J. D. Joannopoulos, "High Transmission through Sharp Bends in Photonic Crystal Waveguides," Phys. Rev. Lett. **77**, 3787–3790 (1996).

[291] S. G. Johnson, P. R. Villeneuve, S. Fan, and J. D. Joannopoulos, "Linear waveguides in photonic-crystal slabs," Phys. Rev. B **62**, 8212–8222 (2000).

[292] M. Notomi, K. Yamada, A. Shinya, J. Takahashi, C. Takahashi, and I. Yokohama, "Extremely Large Group-Velocity Dispersion of Line-Defect Waveguides in Photonic Crystal Slabs," Phys. Rev. Lett. **87**, 253902 (2001).

[293] E. Yablonovitch and T. Gmitter, "Donor and Acceptor Modes in Photonic Band Structure," Phys. Rev. Lett. **67**, 3380 (1991).

[294] X.-P. Feng and Y. Arakawa, "Defect Modes in Two-Dimensional Triangular Photonic Crystals," Jpn. J. Appl. Phys. **36**, L120–L123 (1997).

[295] I. Bayn and J. Salzman, "Ultra-high-Q photonic crystal nanocavity design: The effect of a low-ϵ slab material," Opt. Express **16**, 4972–4980 (2008).

[296] H. Sekoguchi, Y. Takahashi, T. Asano, and S. Noda, "Photonic crystal nanocavity with a Q-factor of ~ 9 million," Opt. Express **22**, 916–924 (2014).

[297] C. Grillet, C. Monat, C. Smith, B. Eggleton, S. Frédérick, D. Dalacu, P. Poole, J. Lapointe, G. Aers, and R. Williams, "Nanowire coupling to photonic crystal nanocavities for single photon sources," Opt. Express **15**, 1267 (2007).

[298] C. Monat, C. Seassal, X. Letartre, P. Regreny, M. Gendry, P. R. Romeo, P. Viktorovitch, M. Le Vassor d'Yerville, D. Cassagne, J. P. Albert, E. Jalaguier, S. Pocas, and B. Aspar, "Two-dimensional hexagonal-shaped microcavities formed in a two-dimensional photonic crystal on an InP membrane," J. Appl. Phys. **93**, 23–31 (2003).

[299] H. H. J. E. Kicken, I. Barbu, R. W. van der Heijden, F. Karouta, R. Nötzel, E. van der Drift, and H. W. M. Salemink, "Wavelength-sized cavities in high aspect InP/InGaAsP/InP photonic crystals," J. Appl. Phys. **106**, 083106 (2009).

[300] Y. Akahane, T. Asano, B.-S. Song, and S. Noda, "High-Q photonic nanocavity in a two-dimensional photonic crystal," Nature **425**, 944 – 947 (2003).

[301] Z. Zhang and M. Qiu, "Small-volume waveguide-section high Q microcavities in 2D photonic crystal slabs," Opt. Express **12**, 3988–3995 (2004).

[302] M. Nomura, K. Tanabe, S. Iwamoto, and Y. Arakawa, "High-Q design of semiconductor-based ultrasmall photonic crystal nanocavity," Opt. Express **18**, 8144–8150 (2010).

[303] K. Nozaki and T. Baba, "Laser characteristics with ultimate-small modal volume in photonic crystal slab point-shift nanolasers," Appl. Phys. Lett. **88**, 211101 (2006).

[304] O. Painter, J. Vučković, and A. Scherer, "Defect modes of a two-dimensional photonic crystal in an optically thin dielectric slab," J. Opt. Soc. Am. B **16**, 275–285 (1999).

[305] J. Vučković, M. Lončar, H. Mabuchi, and A. Scherer, "Design of photonic crystal microcavities for cavity QED," Phys. Rev. E **65**, 016608 (2001).

[306] H.-G. Park, S.-H. Kim, S.-H. Kwon, Y.-G. Ju, J.-K. Yang, J.-H. Baek, S.-B. Kim, and Y.-H. Lee, "Electrically Driven Single-Cell Photonic Crystal Laser," Science **305**, 1444–1446 (2004).

[307] O. Painter, R. Lee, A. Scherer, A. Yariv, J. O'Brien, P. Dapkus, and I. Kim, "Two-Dimensional Photonic Band-Gap Defect Mode Laser," Science **284**, 1819 (1999).

[308] H.-G. Park, J.-K. Hwang, J. Huh, H.-Y. Ryu, Y.-H. Lee, and J.-S. Kim, "Nondegenerate monopole-mode two-dimensional photonic band gap laser," Appl. Phys. Lett. **79**, 3032–3034 (2001).

[309] M.-K. Seo, K.-Y. Jeong, J.-K. Yang, Y.-H. Lee, H.-G. Park, and S.-B. Kim, "Low threshold current single-cell hexapole mode photonic crystal laser," Appl. Phys. Lett. **90**, 171122 (2007).

[310] J.-H. Kang, M.-K. Seo, S.-K. Kim, S.-H. Kim, M.-K. Kim, H.-G. Park, K.-S. Kim, and Y.-H. Lee, "Polarized vertical beaming of an engineered hexapole mode laser," Opt. Express **17**, 6074–6081 (2009).

[311] H.-Y. Ryu, M. Notomi, and Y.-H. Lee, "High-quality-factor and small-mode-volume hexapole modes in photonic-crystal-slab nanocavities," Appl. Phys. Lett. **83**, 4294–4296 (2003).

[312] K. Hennessy, A. Badolato, P. M. Petroff, and E. Hu, "Positioning photonic crystal cavities to single InAs quantum dots," Photon. Nanostruct.: Fundam. Appl. **2**, 65 (2004).

[313] S. Noda, A. Chutinan, and M. Imada, "Trapping and emission of photons by a single defect in a photonic bandgap structure," Nature **407**, 608–610 (2000).

[314] S. Tomljenovic-Hanic, M. J. Steel, C. M. Sterke, and J. Salzman, "Diamond based photonic crystal microcavities," Opt. Express **14**, 3556 – 3562 (2006).

[315] I. Bayn and J. Salzman, "High-Q photonic crystal nanocavities on diamond for quantum electrodynamics," Eur. Phys. J. Appl. Phys. **37**, 19–24 (2007).

[316] S.-H. Kim, S.-K. Kim, and Y.-H. Lee, "Vertical beaming of wavelength-scale photonic crystal resonators," Phys. Rev. B **73**, 235117 (2006).

[317] M. Shirane, S. Kono, J. Ushida, S. Ohkouchi, N. Ikeda, Y. Sugimoto, and A. Tomita, "Mode identification of high-quality-factor single-defect nanocavities in quantum dot-embedded photonic crystals," J. Appl. Phys. **101**, 073107 (2007).

[318] J. Huh, J.-K. Hwang, H.-Y. Ryu, and Y.-H. Lee, "Nondegenerate monopole mode of single defect two-dimensional triangular photonic band-gap cavity," J. Appl. Phys. **92**, 654–659 (2002).

[319] S.-H. Kim and Y.-H. Lee, "Symmetry relations of two-dimensional photonic crystal cavity modes," IEEE J. Quantum Electron. **39**, 1081–1085 (2003).

[320] O. Painter and K. Srinivasan, "Polarization properties of dipolelike defect modes in photonic crystal nanocavities," Opt. Lett. **27**, 339–341 (2002).

[321] J.-H. Kang, S.-K. Kim, K.-Y. Jeong, Y.-H. Lee, M.-K. Seo, and H.-G. Park, "Polarization-resolved far-field measurement of single-cell photonic crystal lasing modes," Appl. Phys. Lett. **98**, 211116 (2011).

[322] D. Englund, I. Fushman, and J. Vučković, "General recipe for designing photonic crystal cavities," Opt. Express **13**, 5961 – 5975 (2005).

[323] M. Okano, T. Yamada, J. Sugisaka, N. Yamamoto, M. Itoh, K. Sugaya, T. Komori, and M. Mori, "Analysis of two-dimensional photonic crystal L-type cavities with low-refractive-index material cladding," J. Opt. **12**, 075101 (2010).

[324] B. Saleh and M. Teich, *Fundamentals of Photonics* (John Wiley & Sons, Inc., Hoboken, 2007).

[325] P. Lalanne, C. Sauvan, and J.-P. Hugonin, "Photon confinement in photonic crystal nanocavities," Laser & Photon. Rev. **2**, 514–526 (2008).

[326] C. Sauvan, G. Lecamp, P. Lalanne, and J. Hugonin, "Modal-reflectivity enhancement by geometry tuning in Photonic Crystal microcavities," Opt. Express **13**, 245–255 (2005).

[327] C. Sauvan, P. Lalanne, and J. P. Hugonin, "Slow-wave effect and mode-profile matching in photonic crystal microcavities," Phys. Rev. B **71**, 165118 (2005).

[328] P. Lalanne, S. Mias, and J. Hugonin, "Two physical mechanisms for boosting the quality factor to cavity volume ratio of photonic crystal microcavities," Opt. Express **12**, 458–467 (2004).

[329] Y. Akahane, T. Asano, B.-S. Song, and S. Noda, "Fine tuned high-Q photonic crystal nanocavity," Opt. Express **13**, 1202 – 1214 (2005).

[330] C. A. Balanis, *Advanced engineering electromagnetics* (Wiley, New York, 1989).

[331] A. Taflove and S. C. Hagness, *Advances in Computational Electrodynamics* (Artech House Inc., Norwood, 1998).

[332] J. Vučković, M. Lončar, H. Mabuchi, and A. Scherrer, "Optimization of the Q factor in photonic crystal microcavities," IEEE J. Quantum. Electron. **38**, 850 – 856 (2002).

[333] K. Srinivasan and O. Painter, "Momentum Space Design of high-Q photonic crystal optical cavities," Opt. Express **10**, 670–684 (2002).

[334] A. F. Oskooi, D. Roundy, M. Ibanescu, P. Bermel, J. Joannopoulos, and S. G. Johnson, "MEEP: A flexible free-software package for electromagnetic simulations by the FDTD method," Comput. Phys. Commun. **181**, 687–702 (2010).

[335] Lumerical Solutions, Inc. http://www.lumerical.com/tcad-products/fdtd/.

[336] J. Riedrich-Möller, "Experimentelle Realisierung von Faserresonatoren und Simulation von Mikroresonatoren in zweidimensionalen photonischen Kristallen," Master's thesis, Universität des Saarlandes, Saarbrücken (2008).

[337] A. Taflove, "Review of the formulation and applications of the finite-difference time-domain method for numerical modeling of electromagnetic wave interactions with arbitrary structures," Wave motion **10**, 547–582 (1988).

[338] A. Taflove and S. C. Hagness, *Computational Electrodynamics: The Finite-Difference Time-Domain Method* (Norwood, MA: Artech House, 2005), 3rd ed.

[339] J.-M.-. Lourtioz, H. Benisty, V. Berger, J.-M. Gérard, D. Maystre, and A. Tchelnokov, *Photonic Crystals, Towards Nanoscale Photonic Devices* (Springer-Verlag, Berlin, 2005).

[340] K. S. Yee, "Numerical solution of initial boundary value problems involving Maxwell's equations in isotropic media," IEEE Trans. Antennas Propag. **14**, 302–307 (1966).

[341] S. G. Johnson, D. Roundy, M. Ibanescu, P. Bermel, and A. Farjadpour, "MIT Electromagnetic Equation Propagation," http://ab-initio.mit.edu/wiki/index.php/Meep (2006).

[342] A. Farjadpour, D. Roundy, A. Rodriguez, M. Ibanescu, P. Bermel, J. D. Joannopoulos, S. G. Johnson, and G. Burr, "Improving accuracy by subpixel smoothing in FDTD," Opt. Lett. **31**, 2972 – 2974 (2006).

[343] J.-P. Berenger, "A Perfectly Matched Layer for the Absorption of Electromagnetic Waves," J. Comp. Phys. **114**, 185–200 (1994).

[344] V. A. Mandelshtam and H. S. Taylor, "Harmonic inversion of time signals and its applications," J. Chem. Phys. **107**, 6756–6769 (1997).

[345] V. A. Mandelshtam and H. S. Taylor, "Erratum: Harmonic inversion of time signals and its applications," J. Chem. Phys. **107**, 6756 (1997).

[346] G. Turri, Y. Chen, M. Bass, D. Orchard, J. E. Butler, S. Magana, T. Feygelson, D. Thiel, K. Fourspring, R. V. Dewees, J. M. Bennett, J. Pentony, S. Hawkins, M. Baronowski, A. Guenthner, M. D. Seltzer, D. C. Harris, and C. M. Stickley, "Optical absorption, depolarization, and scatter of epitaxial single-crystal chemical-vapor-deposited diamond at 1.064μm," Opt. Eng. **46**, 064002 (2007).

[347] S. Ferro, "Synthesis of diamond," J. Mater. Chem. **12**, 2843–2855 (2002).

[348] S. Gsell, T. Bauer, J. Goldfuß, M. Schreck, and B. Stritzker, "A route to diamond wafers by epitaxial deposition on silicon via iridium/yttria-stabilized zirconia buffer layers," Appl. Phys. Lett. **84**, 4541 (2004).

[349] L. Bergman, B. R. Stoner, K. F. Turner, J. T. Glass, and R. J. Nemanich, "Microphotoluminescence and Raman scattering study of defect formation in diamond films," J. Appl. Phys. **73**, 3951–3957 (1993).

[350] R. Samlenski, C. Haug, R. Brenn, C. Wild, R. Locher, and P. Koidl, "Incorporation of nitrogen in chemical vapor deposition diamond," Appl. Phys. Lett. **67**, 2798–2800 (1995).

[351] H.-C. Liou and J. Pretzer, "Effect of curing temperature on the mechanical properties of hydrogen silsesquioxane thin films," Thin Solid Films **335**, 186–191 (1998).

[352] P. Olivero, S. Rubanov, P. Reichart, B. Gibson, S. Huntington, J. Rabeau, A. Greentree, J. Salzman, D. Moore, D. Jamieson, and S. Prawer, "Ion-Beam-Assisted Lift-Off Technique for Three-Dimensional Micromachining of Freestanding Single-Crystal Diamond," Adv. Mater. **17**, 2427–2430 (2005).

[353] P. Olivero, S. Rubanov, P. Reichart, B. Gibson, S. Huntington, A. Rabeau, A. Greentree, J. Salzman, D. Moore, D. Jamieson, and S. Prawer, "Characterization of three-dimensional microstructures in single-crystal diamond," Diamond Relat. Mater. **15**, 1614–1621 (2006).

[354] B. A. Fairchild, P. Olivero, S. Rubanov, A. Greentree, F. Waldermann, R. A. Taylor, J. M. Smith, S. Huntington, B. Gibson, D. Jamieson, and S. Prawer, "Fabrication of ultrathin single-crystal diamond membranes," Adv. Mater. **20**, 1–6 (2008).

[355] N. R. Parikh, J. D. Hunn, E. McGucken, M. L. Swanson, C. W. White, R. A. Rudder, D. P. Malta, J. B. Posthill, and R. J. Markunas, "Single-crystal diamond plate liftoff achieved by ion implantation and subsequent annealing," Appl. Phys. Lett. **61**, 3124–3126 (1992).

[356] V. S. Drumm, A. D. C. Alves, B. A. Fairchild, K. Ganesan, J. C. McCallum, D. N. Jamieson, S. Prawer, S. Rubanov, R. Kalish, and L. C. Feldman, "Surface damage on diamond membranes fabricated by ion implantation and lift-off," Appl. Phys. Lett. **98**, 231904 (2011).

[357] B. R. Patton, P. R. Dolan, F. Grazioso, M. B. Wincott, J. M. Smith, M. L. Markham, D. J. Twitchen, Y. Zhang, E. Gu, M. D. Dawson, B. A. Fairchild, A. D. Greentree, and S. Prawer, "Optical properties of single crystal diamond microfilms fabricated by ion implantation and lift-off processing," Diamond Relat. Mater. **21**, 16–23 (2011).

[358] O. Gaathon, J. Hodges, E. Chen, L. Li, S. Bakhru, H. Bakhru, D. Englund, and R. Osgood Jr., "Planar fabrication of arrays of ion-exfoliated single-crystal-diamond membranes with nitrogen-vacancy color centers," Opt. Mater. **35**, 361–365 (2013).

[359] J. C. Lee, A. P. Magyar, D. O. Bracher, I. Aharonovich, and E. L. Hu, "Fabrication of thin diamond membranes for photonic applications," Diamond Relat. Mater. **33**, 45 – 48 (2013).

[360] I. Aharonovich, J. C. Lee, A. P. Magyar, B. B. Buckley, C. G. Yale, D. D. Awschalom, and E. L. Hu, "Homoepitaxial Growth of Single Crystal Diamond Membranes for Quantum Information Processing," Adv. Mater. **24**, OP54–OP59 (2012).

[361] J. S. Hodges, L. Li, M. Lu, E. H. Chen, M. E.Trusheim, S. Allegri, X. Yao, O. Gaathon, H. Bakhru, and D. Englund, "Long-lived NV^- spin coherence in high-purity diamond membranes," New J. Phys. **14**, 093004 (2012).

[362] L. Li, M. Trusheim, O. Gaathon, K. Kisslinger, C.-J. Cheng, M. Lu, D. Su, X. Yao, H.-C. Huang, I. Bayn, A. Wolcott, J. Richard M. Osgood, and D. Englund, "Reactive ion etching: Optimized diamond membrane fabrication for transmission electron microscopy," J. Vac. Sci. Technol. B **31**, 06FF01 (2013).

[363] I. Bayn, B. Meyler, J. Salzman, and R. Kalish, "Triangular nanobeam photonic cavities in single crystal diamond," New J. Phys. **13**, 025018 (2011).

[364] M. J. Burek, N. P. de Leon, B. J. Shields, B. J. M. Hausmann, Y. Chu, Q. Quan, A. S. Zibrov, H. Park, M. D. Lukin, and M. Lončar, "Free-Standing Mechanical and Photonic Nanostructures in Single-Crystal Diamond," Nano Lett. **12**, 6084–6089 (2012).

[365] I. Friel, S. Clewes, H. Dhillon, N. Perkins, D. Twitchen, and G. Scarsbrook, "Control of surface and bulk crystalline quality in single crystal diamond grown by chemical vapour deposition," Diamond Relat. Mater. **18**, 808 – 815 (2009).

[366] C. Lee, E. Gu, M. Dawson, I. Friel, and G. Scarsbrook, "Etching and micro-optics fabrication in diamond using chlorine-based inductively-coupled plasma," Diamond Relat. Mater. **17**, 1292 – 1296 (2008).

[367] M. Yoshikawa, G. Katagiri, H. Ishida, A. Ishitani, M. Ono, and K. Matsumura, "Characterization of crystalline quality of diamond films by Raman spectroscopy," Appl. Phys. Lett. **55**, 2608–2610 (1989).

[368] Y. von Kaenel, J. Stiegler, J. Michler, and E. Blank, "Stress distribution in heteroepitaxial chemical vapor deposited diamond films," J. Appl. Phys. **81**, 1726–1736 (1997).

[369] M. Fischer, S. Gsell, M. Schreck, and A. Bergmaier, "Growth sector dependence and mechanism of stress formation in epitaxial diamond growth," Appl. Phys. Lett. **100**, 041906 (2012).

[370] H. Windischmann and K. Gray, "Stress measurement of CVD diamond films," Diamond Relat. Mater. **4**, 837 – 842 (1995).

[371] T. Kobayashi and T. Maki, "Prospects of semiconducting diamond electronics," Diamond Films Technol. **6**, 199 (1996).

[372] L. A. Giannuzzi and F. A. Stevie, eds., *Introduction to focused ion beams - Instrumentation, Theory, Techniques and Practice* (Springer Science + Business Media, Inc., Boston, 2005).

[373] A. A. Tseng, "Recent developments in micromilling using focused ion beam technology," J. Micromech. Microeng. **14**, R15–R34 (2004).

[374] J. F. Ziegler, M. D. Ziegler, and J. P. Biersack, "SRIM-2008.04 The stopping and range of ions in matter," www.srim.org (2008).

[375] A. Stanishevsky, "Patterning of diamond and amorphous carbon films using focused ion beams," Thin Solid Films **398–399**, 560–565 (2001).

[376] J. Orloff, L. W. Swanson, and M. Utlaut, "Fundamental limits to imaging resolution for focused ion beams," J. Vac. Sci. Technol. B **14**, 3759–3763 (1996).

[377] I. A. Dobrinets, "Elektronische Mikrostrukturen aus amorphem Kohlenstoff, hergestellt durch fokussierte Ionenstrahlimplantation auf Diamant," Ph.D. thesis, Ruhr-Universität Bochum (2002).

[378] D. P. Adams, M. J. Vasile, T. M. Mayer, and V. C. Hodges, "Focused ion beam milling of diamond: Effects of H_2O on yield, surface morphology and microstructure," J. Vac. Sci. Technol. B **21**, 2334–2343 (2003).

[379] Y. Kudriavtsev, A. Villegas, A. Godines, and R. Asomoza, "Calculation of the surface binding energy for ion sputtered particles," Appl. Surf. Sci. **239**, 273 – 278 (2005).

[380] W. McKenzie, M. Quadir, M. Gass, and P. Munroe, "Focused Ion beam implantation of diamond," Diamond Relat. Mater. **20**, 1125 – 1128 (2011).

[381] A. Fuchs, "Herstellung von Diamant-Nanokristallen und Hybrid-Integrierten-Einzelphotonenquellen," Master's thesis, Universität des Saarlandes (2014).

[382] H. Demers, N. Poirier-Demers, A. R. Couture, D. Joly, M. Guilmain, N. de Jonge, and D. Drouin, "Three-dimensional electron microscopy simulation with the CASINO Monte Carlo software," Scanning **33**, 135–146 (2011).

[383] "CASINO (monte CArlo SImulation of electroN trajectory in sOlids)," http://www.gel.usherbrooke.ca/casino.

[384] C. Uzan-Saguy, C. Cytermann, R. Brener, V. Richter, M. Shaanan, and R. Kalish, "Damage threshold for ion-beam induced graphitization of diamond," Appl. Phys. Lett. **67**, 1194–1196 (1995).

[385] S. Endo, K. Kimura, M. Irie, C. L. Wang, and T. Ito, "Recovery treatments for ion-induced defects in high-quality homoepitaxial CVD diamond," Diamond Relat. Mater. **10**, 322–326 (2001).

[386] J. O. Orwa, K. W. Nugent, D. N. Jamieson, and S. Prawer, "Raman investigation of damage caused by deep ion implantation in diamond," Phys. Rev. B **62**, 5461–5472 (2000).

[387] J.-i. Fujita, M. Ishida, T. Ichihashi, T. Sakamoto, Y. Ochiai, T. Kaito, and S. Matsui, "Structure and resonant characteristics of amorphous carbon pillars grown by focused-ion-beam-induced chemical vapor deposition," Jpn. J. Appl. Phys. **41**, 4423–4426 (2002).

[388] M. Hamada, T. Teraji, and T. Ito, "Field-induced effects of implanted Ga on high electric field diamond devices fabricated by focused ion beam," Appl. Surf. Sci. **216**, 65–71 (2003).

[389] R. Kometani, S. Ishihara, K. Kanda, Y. Haruyama, T. Kaito, and S. Matsui, "Education position control of incorporated gallium in diamond-like carbon deposited by focused-ion-beam chemical vapor deposition," Jpn. J. Appl. Phys. **47**, 5032–5035 (2008).

[390] S. Osswald, G. Yushin, V. Mochalin, S. O. Kucheyev, and Y. Gogotsi, "Control of sp^2/sp^3 carbon ratio and surface chemistry of nanodiamond powders by selective oxidation in air," J. Am. Chem. Soc. **128**, 11635–11642 (2006).

[391] K.-M. C. Fu, C. Santori, P. E. Barclay, and R. G. Beausoleil, "Conversion of neutral nitrogen-vacancy centers to negatively charged nitrogen-vacancy centers through selective oxidation," Appl. Phys. Lett. **96**, 121907 (2010).

[392] I. Bayn, A. Bolker, C. Cytermann, B. Meyler, V. Richter, J. Salzman, and R. Kalish, "Diamond processing by focused ion beam - surface damage and recovery," Appl. Phys. Lett. **99**, 183109 (2011).

[393] M. V. Hauf, B. Grotz, B. Naydenov, M. Dankerl, S. Pezzagna, J. Meijer, F. Jelezko, J. Wrachtrup, M. Stutzmann, F. Reinhard, and J. A. Garrido, "Chemical control of the charge state of nitrogen-vacancy centers in diamond," Phys. Rev. B **83**, 081304 (2011).

[394] L. Rondin, G. Dantelle, A. Slablab, F. Treussart, P. Bergonzo, S. Perruchas, T. Gacoin, M. Chaigneau, H.-C. Chang, V. Jacques, and J.-F. Roch, "Surface-induced charge state conversion of nitrogen-vacancy defects in nanodiamonds," Phys. Rev. B **82**, 115449 (2010).

[395] J. P. Goss, R. Jones, S. J. Breuer, P. R. Briddon, and S. Öberg, "The Twelve-Line 1.682 eV Luminescence Center in Diamond and the Vacancy-Silicon Complex," Phys. Rev. Lett. **77**, 3041–3044 (1996).

[396] Y. Tanaka, T. Asano, Y. Akahane, B.-S. Song, and S. Noda, "Theoretical investigation of a two-dimensional photonic crystal slab with truncated cone air holes," Appl. Phys. Lett. **82**, 1661–1663 (2003).

[397] T. Jung, "Simulation, Herstellung und Untersuchung von optischen Resonatoren in zweidimensionalen photonischen Kristallen in Diamant," Master's thesis, Universität des Saarlandes (2011).

[398] T. Xu, S. Yang, S. V. Nair, and H. E. Ruda, "Nanowire-array-based photonic crystal cavity by finite-difference time-domain calculations," Phys. Rev. B **75**, 125104 (2007).

[399] C. Hepp, "Spektroskopische Untersuchungen an CVD-Diamantfilmen," Master's thesis, Universität des Saarlandes (2008).

[400] K. Hennessy, A. Badolato, A. Tamboli, P. M. Petroff, E. Hu, M. Atature, J. Dreiser, and A. Imamoglu, "Tuning photonic crystal nanocavity modes by wet chemical digital etching," Appl. Phys. Lett. **87**, 021108 (2005).

[401] S. Mosor, J. Hendrickson, B. C. Richards, J. Sweet, G. Khitrova, H. M. Gibbs, T. Yoshie, A. Scherer, O. B. Shchekin, and D. G. Deppe, "Scanning a photonic crystal slab nanocavity by condensation of xenon," Appl. Phys. Lett. **87**, 141105 (2005).

[402] S. Strauf, M. T. Rakher, I. Carmeli, K. Hennessy, C. Meier, A. Badolato, M. J. A. DeDood, P. M. Petroff, E. L. Hu, E. G. Gwinn, and D. Bouwmeester, "Frequency control of photonic crystal membrane resonators by monolayer deposition," Appl. Phys. Lett. **88**, 043116 (2006).

[403] K. Srinivasan and O. Painter, "Optical fiber taper coupling and high-resolution wavelength tuning of microdisk resonators at cryogenic temperatures," Appl. Phys. Lett. **90**, 031114 (2007).

[404] Y. Tanaka, J. Upham, T. Nagashima, T. Sugiya, T. Asano, and S. Noda, "Dynamic control of the Q factor in a photonic crystal nanocavity," Nature **6**, 862 (2007).

[405] H. S. Lee, S. Kiravittaya, S. Kumar, J. D. Plumhof, L. Balet, L. H. Li, M. Francardi, A. Gerardino, A. Fiore, A. Rastelli, and O. G. Schmidt, "Local tuning of photonic crystal nanocavity modes by laser-assisted oxidation," Appl. Phys. Lett. **95**, 191109 (2009).

[406] K. Hennessy, C. Högerle, E. Hu, A. Badolato, and A. Imamoğlu, "Tuning photonic nanocavities by atomic force microscope nano-oxidation," Appl. Phys. Lett. **89**, 041118 (2006).

[407] S.-R. Jian, T.-H. Fang, and D.-S. Chuu, "Mechanisms of p-GaAs(100) surface by atomic force microscope nano-oxidation," J. Phys. D: Appl. Phys. **38**, 2424 (2005).

[408] D. Sridharan, E. Waks, G. Solomon, and J. T. Fourkas, "Reversible tuning of photonic crystal cavities using photochromic thin films," Appl. Phys. Lett. **96**, 153303 (2010).

[409] A. Faraon, D. Englund, D. Bulla, B. Luther-Davies, B. J. Eggleton, N. Stoltz, P. Petroff, and J. Vučković, "Local tuning of photonic crystal cavities using chalcogenide glasses," Appl. Phys. Lett. **92**, 043123 (2008).

[410] C. L. Smith, U. Bog, S. Tomljenovic-Hanic, M. W. Lee, D. K. Wu, L. O'Faolain, C. Monat, C. Grillet, T. F. Krauss, C. Karnutsch, R. C. McPhedran, and B. J. Eggleton, "Reconfigurable microfluidic photonic crystal slab cavities," Opt. Express **16**, 15887–15896 (2008).

[411] A. C. Bedoya, S. Mahmoodian, C. Monat, S. Tomljenovic-Hanic, C. Grillet, P. Domachuk, E. Mägi, B. J. Eggleton, and R. W. van der Heijden, "Liquid crystal dynamics in a photonic crystal cavity created by selective microfluidic infiltration," Opt. Express **18**, 27280–27290 (2010).

[412] K. Busch and S. John, "Liquid-Crystal photonic-band-gap materials: The tunable electromagnetic vacuum," Phys. Rev. Lett. **83**, 967–970 (1999).

[413] A. Turukhin, C.-H. Liu, A. Gorokhovsky, R. Alfano, and W. Phillips, "Picosecond photoluminescence decay of Si-doped chemical-vapor-deposited diamond films," Phys. Rev. B **54**, 16448–16451 (1996).

[414] D. Englund and J. Vučković, "A direct analysis of photonic nanostructures," Opt. Express **14**, 3474–3483 (2006).

[415] J. Meijer, S. Pezzagna, T. Vogel, B. Burchard, H. H. Bukow, I. W. Rangelow, Y. Sarov, H. Wiggers, I. Plümel, F. Jelezko, J. Wrachtrup, F. Schmidt-Kaler, W. Schnitzler, and K. Singer, "Towards the implanting of ions and positioning of nanoparticles with nm spatial resolution," Appl. Phys. A. **91**, 567–571 (2008).

[416] S. Pezzagna, D. Rogalla, D. Wildanger, J. Meijer, and A. Zaitsev, "Creation and nature of optical centres in diamond for single-photon emission - overview and critical remarks," New J. Phys. **13**, 035024 (2011).

[417] S. Pezzagna and J. Meijer, *Ion Implantation* (InTech, 2012), chap. 1: High-Resolution Ion Implantation from keV to MeV, pp. 1–23.

[418] G. Hobler, "Critical angles and low-energy limits to ion channeling in silicon," Radiat. Eff. Defect. S. **139**, 21–85 (1996).

[419] B. K. Ofori-Okai, S. Pezzagna, K. Chang, M. Loretz, R. Schirhagl, Y. Tao, B. A. Moores, K. Groot-Berning, J. Meijer, and C. L. Degen, "Spin properties of very shallow nitrogen vacancy defects in diamond," Phys. Rev. B **86**, 081406 (2012).

[420] D. Antonov, T. Häußermann, A. Aird, J. Roth, H.-R. Trebin, C. Müller, L. McGuinness, F. Jelezko, T. Yamamoto, J. Isoya, S. Pezzagna, J. Meijer, and J. Wrachtrup, "Statistical investigations on nitrogen-vacancy center creation," Appl. Phys. Lett. **104**, 012105 (2014).

[421] P. Spinicelli, A. Dréau, L. Rondin, F. Silva, J. Achard, S. Xavier, S. Bansropun, T. Debuisschert, S. Pezzagna, J. Meijer, V. Jacques, and J.-F. Roch, "Engineered arrays of nitrogen-vacancy color centers in diamond based on implantation of CN^- molecules through nanoapertures," New J. Phys. **13**, 025014 (2011).

[422] K. T. Koga, J. A. V. Orman, and M. J. Walter, "Diffusive relaxation of carbon and nitrogen isotope heterogeneity in diamond: a new thermochronometer," Phys. Earth Planet. Inter. **139**, 35 – 43 (2003). Diffusion and Partitioning in Planetary Interiors.

[423] J. Meijer, T. Vogel, B. Burchard, I. W. Rangelow, L. Bischoff, J. Wrachtrup, M. Domhan, F. Jelezko, W. Schnitzler, S. A. Schulz, K. Singer, and F. Schmidt-Kaler, "Concept of deterministic single ion doping with sub-nm spatial resolution," Appl. Phys. A. **83**, 321 (2006).

[424] M. Lesik, P. Spinicelli, S. Pezzagna, P. Happel, V. Jacques, O. Salord, B. Rasser, A. Delobbe, P. Sudraud, A. Tallaire, J. Meijer, and J.-F. Roch, "Maskless and targeted creation of arrays of colour centres in diamond using focused ion beam technology," Phys. Status Solidi A **210**, 2055–2059 (2013).

[425] S. Pezzagna, D. Wildanger, P. Mazarov, A. D. Wieck, Y. Sarov, I. W. Rangelow, B. Naydenov, F. Jelezko, S. W. Hell, and J. Meijer, "Nanoscale engineering and optical addressing of single spins in diamond," Small **6**, 2117 (2010).

[426] S. Pezzagna, D. Rogalla, H.-W. Becker, I. Jakobi, F. Dolde, B. Naydenov, J. Wrachtrup, F. Jelezko, C. Trautmann, and J. Meijer, "Creation of colour centres in diamond by collimated ion-implantation through nano-channels in mica," Phys. Status Solidi A **208**, 2017–2022 (2011).

[427] A. Persaud, K. Ivanova, Y. Sarov, T. Ivanov, B. E. Volland, I. W. Rangelow, N. Nikolov, T. Schenkel, V. Djakov, D. W. K. Jenkins, J. Meijer, and T. Vogel,

"Micromachined piezoresistive proximal probe with integrated bimorph actuator for aligned single ion implantation," J. Vac. Sci. Technol. B **24**, 3148–3151 (2006).

[428] I. W. Rangelow, "Scanning proximity probes for nanoscience and nanofabrication," Microelectron. Eng. **83**, 1449 – 1455 (2006).

[429] C. S. Smith, "Piezoresistance Effect in Germanium and Silicon," Phys. Rev. **94**, 42–49 (1954).

[430] F. Waldermann, P. Olivero, J. Nunn, K. Surmacz, Z. Y. Wang, D. Jaksch, R. Taylor, I. Walmsley, M. Draganski, P. Reichart, A. Greentree, D. Jamieson, and S. Prawer, "Creating diamond color centers for quantum optical applications," Diamond Relat. Mater. **16**, 1887–1895 (2007).

[431] D. Gatto Monticone, F. Quercioli, R. Mercatelli, S. Soria, S. Borini, T. Poli, M. Vannoni, E. Vittone, and P. Olivero, "Systematic study of defect-related quenching of NV luminescence in diamond with time-correlated single-photon counting spectroscopy," Phys. Rev. B **88**, 155201 (2013).

[432] S. Pezzagna, B. Naydenov, F. Jelezko, J. Wrachtrup, and J. Meijer, "Creation efficiency of nitrogen-vacancy centres in diamond," New J. Phys. **12**, 065017 (2010).

[433] J. Schwartz, P. Michaelides, C. D. Weis, and T. Schenkel, "In situ optimization of co-implantation and substrate temperature conditions for nitrogen-vacancy center formation in single-crystal diamonds," New J. Phys. **13**, 035022 (2011).

[434] C. D. Weis, A. Schuh, A. Batra, A. Persaud, I. W. Rangelow, J. Bokor, C. C. Lo, S. Cabrini, E. Sideras-Haddad, G. D. Fuchs, R. Hanson, D. D. Awschalom, and T. Schenkel, "Single atom doping for quantum device development in diamond and silicon," J. Vac. Sci. Technol. B **26**, 2596–2600 (2008).

[435] B. Naydenov, V. Richter, J. Beck, M. Steiner, P. Neumann, G. Balasubramanian, J. Achard, F. Jelezko, J. Wrachtrup, and R. Kalish, "Enhanced generation of single optically active spins in diamond by ion implantation," Appl. Phys. Lett. **96**, 163108 (2010).

[436] T. Yamamoto, C. Müller, L. P. McGuinness, T. Teraji, B. Naydenov, S. Onoda, T. Ohshima, J. Wrachtrup, F. Jelezko, and J. Isoya, "Strongly coupled diamond spin qubits by molecular nitrogen implantation," Phys. Rev. B **88**, 201201 (2013).

[437] C. Santori, P. E. Barclay, K.-M. C. Fu, and R. G. Beausoleil, "Vertical distribution of nitrogen-vacancy centers in diamond formed by ion implantation and annealing," Phys. Rev. B **79**, 125313 (2009).

[438] S. Cui and E. L. Hu, "Increased negatively charged nitrogen-vacancy centers in fluorinated diamond," Appl. Phys. Lett. **103**, 051603 (2013).

[439] C. Osterkamp, J. Scharpf, S. Pezzagna, J. Meijer, T. Diemant, R. Jürgen Behm, B. Naydenov, and F. Jelezko, "Increasing the creation yield of shallow single defects in diamond by surface plasma treatment," Appl. Phys. Lett. **103**, 193118 (2013).

[440] T. Staudacher, F. Ziem, L. Häussler, R. Stöhr, S. Steinert, F. Reinhard, J. Scharpf, A. Denisenko, and J. Wrachtrup, "Enhancing the spin properties of shallow implanted nitrogen vacancy centers in diamond by epitaxial overgrowth," Appl. Phys. Lett. **101**, 212401 (2012).

[441] J. Tisler, G. Balasubramanian, B. Naydenov, R. Kolesov, B. Grotz, R. Reuter, J.-P. Boudou, P. A. Curmi, M. Sennour, A. Thorel, M. Börsch, K. Aulenbacher, R. Erdmann, P. R. Hemmer, F. Jelezko, and J. Wrachtrup, "Fluorescence and Spin Properties of Defects in Single Digit Nanodiamonds," ACS Nano **3**, 1959–1965 (2009).

[442] K. Beha, A. Batalov, N. B. Manson, R. Bratschitsch, and A. Leitenstorfer, "Optimum Photoluminescence Excitation and Recharging Cycle of Single Nitrogen-Vacancy Centers in Ultrapure Diamond," Phys. Rev. Lett. **109**, 097404 (2012).

[443] B. Lounis and M. Orrit, "Single-photon sources," Rep. Prog. Phys. **68**, 1129 – 1179 (2005).

[444] P. Siyushev, V. Jacques, I. Aharonovich, F. Kaiser, T. Müller, L. Lombez, M. Atatüre, S. Castelletto, S. Prawer, F. Jelezko, and J. Wrachtrup, "Low temperature optical characterization of near infrared single photon emitter in nanodiamonds," New J. Phys. **11**, 113029 (2009).

[445] M. S. Liu, L. A. Bursill, S. Prawer, and R. Beserman, "Temperature dependence of the first-order Raman phonon line of diamond," Phys. Rev. B **61**, 3391–3395 (2000).

[446] H.-Q. Zhao, M. Fujiwara, and S. Takeuchi, "Suppression of fluorescence phonon sideband from nitrogen vacancy centers in diamond nanocrystals by substrate effect," Opt. Express **20**, 15628–15635 (2012).

[447] M. Frimmer, A. Mohtashami, and A. F. Koenderink, "Nanomechanical method to gauge emission quantum yield applied to nitrogen-vacancy centers in nanodiamond," Appl. Phys. Lett. **102**, 121105 (2013).

[448] A. Mohtashami and A. F. Koenderink, "Suitability of nanodiamond nitrogen-vacancy centers for spontaneous emission control experiments," New J. Phys. **15**, 043017 (2013).

[449] M. Lesik, J.-P. Tetienne, A. Tallaire, J. Achard, V. Mille, A. Gicquel, J.-F. Roch, and V. Jacques, "Perfect preferential orientation of nitrogen-vacancy defects in a synthetic diamond sample," Appl. Phys. Lett. **104**, 113107 (2014).

[450] J. Michl, T. Teraji, S. Zaiser, I. Jakobi, G. Waldherr, F. Dolde, P. Neumann, M. W. Doherty, N. B. Manson, J. Isoya, and J. Wrachtrup, "Perfect alignment and preferential orientation of nitrogen-vacancy centers during chemical vapor deposition diamond growth on (111) surfaces," Appl. Phys. Lett. **104**, 102407 (2014).

[451] T. Fukui, Y. Doi, T. Miyazaki, Y. Miyamoto, H. Kato, T. Matsumoto, T. Makino, S. Yamasaki, R. Morimoto, N. Tokuda, M. Hatano, Y. Sakagawa, H. Morishita, T. Tashima, S. Miwa, Y. Suzuki, and N. Mizuochi, "Perfect selective alignment of nitrogen-vacancy centers in diamond," Appl. Phys. Express **7**, 055201 (2014).

[452] B. Hausmann, M. Khan, T. Babinec, Y. Zhang, K. Martinick, M. McCutcheon, P. Hemmer, and M. Lončar, "Fabrication of diamond nanowires for quantum information processing applications," Diamond Relat. Mater. **19**, 621–629 (2010).

[453] P. Maletinsky, S. Hong, M. Grinolds, B. Hausmann, M. Lukin, R. Walsworth, M. Loncar, and A. Yacoby, "A robust scanning diamond sensor for nanoscale imaging with single nitrogen-vacancy centres," Nature Nanotech. **7**, 320–324 (2012).

[454] P. Rath, S. Khasminskaya, C. Nebel, C. Wild, and W. H. Pernice, "Diamond-integrated optomechanical circuits," Nat. Commun. **4**, 1690– (2013).

[455] S. W. Hell and J. Wichmann, "Breaking the diffraction resolution limit by stimulated emission: stimulated-emission-depletion fluorescence microscopy," Opt. Lett. **19**, 780–782 (1994).

[456] E. Rittweger, K. Y. Han, S. E. Irvine, C. Eggeling, and S. W. Hell, "STED microscopy reveals crystal colour centres with nanometric resolution," Nature Photon. **3**, 144–147 (2009).

[457] K. Y. Han, K. I. Willig, E. Rittweger, F. Jelezko, C. Eggeling, and S. W. Hell, "Three-Dimensional Stimulated Emission Depletion Microscopy of Nitrogen-Vacancy Centers in Diamond Using Continuous-Wave Light," Nano Lett. **9**, 3323–3329 (2009).

[458] T. Karin, S. Dunham, and K.-M. Fu, "Alignment of the diamond nitrogen vacancy center by strain engineering," Appl. Phys. Lett. **105**, 053106 (2014).

[459] P. Ovartchaiyapong, K. W. Lee, B. A. Myers, and A. C. B. Jayich, "Dynamic strain-mediated coupling of a single diamond spin to a mechanical resonator," Nat. Commun. **5**, 4429 (2014).

[460] J. Teissier, A. Barfuss, P. Appel, E. Neu, and P. Maletinsky, "Strain Coupling of a Nitrogen-Vacancy Center Spin to a Diamond Mechanical Oscillator," Phys. Rev. Lett. **113**, 020503 (2014).

[461] A. M. Zaitsev, "Vibronic spectra of impurity-related optical centers in diamond," Phys. Rev. B **61**, 12909–12922 (2000).

[462] P. J. Lin-Chung, "Local vibrational modes of impurities in diamond," Phys. Rev. B **50**, 16905–16913 (1994).

[463] W. Windl, P. Pavone, K. Karch, O. Schütt, D. Strauch, P. Giannozzi, and S. Baroni, "Second-order Raman spectra of diamond from ab initio phonon calculations," Phys. Rev. B **48**, 3164–3170 (1993).

[464] A. A. Gorokhovsky, A. V. Turukhin, R. R. Alfano, and W. Phillips, "Photoluminescence vibrational structure of Si center in chemical-vapor deposited diamond," Appl. Phys. Lett. **66**, 43–45 (1995).

[465] J. Walker, "Optical absorption and luminescence in diamond," Rep. Prog. Phys. **42**, 1606–1658 (1979).

[466] G. Sittas, H. Kanda, I. Kiflawi, and P. Spear, "Growth and characterization of Si-doped diamond single crystals grown by the HTHP method," Diamond Relat. Mater. **5**, 866 – 869 (1996).

[467] C. Lethiec, J. Laverdant, H. Vallon, C. Javaux, B. Dubertret, J.-M. Frigerio, C. Schwob, L. Coolen, and A. Maître, "Measurement of Three-Dimensional Dipole Orientation of a Single Fluorescent Nanoemitter by Emission Polarization Analysis," Phys. Rev. X **4**, 021037 (2014).

[468] S. W. Brown and S. C. Rand, "Site symmetry analysis of the 738 nm defect in diamond," J. Appl. Phys. **78**, 4069–4075 (1995).

[469] E. Neu, "Silicon vacancy color centers in chemical vapor deposition diamond: New insights into promising solid state single photon sources," Ph.D. thesis, Universität des Saarlandes (2012).

[470] J. L. O'Brien, A. Furusawa, and J. Vučković, "Photonic quantum thechnologies," Nature Photon. **3**, 687–695 (2009).

[471] T. M. Babinec, B. J. M. Hausmann, M. Khan, Y. Zhang, J. R. Maze, P. R. Hemmer, and M. Lončar, "A diamond nanowire single-photon source," Nature Nanotech. **5**, 195 – 199 (2010).

[472] R. Beams, D. Smith, T. W. Johnson, S.-H. Oh, L. Novotny, and A. N. Vamivakas, "Nanoscale Fluorescence Lifetime Imaging of an Optical Antenna with a Single Diamond NV Center," Nano Lett. **13**, 3807–3811 (2013).

[473] E. Wu, J. R. Rabeau, G. Roger, F. Treussart, H. Zeng, P. Grangier, S. Prawer, and J.-F. Roch, "Room temperature triggered single-photon source in the near infrared," New J. Phys. **9**, 434 (2007).

[474] E. Neu and C. Becher, *Quantum information processing with diamond* (Woodhead publishing series in electronics and optical materials, 2014), chap. 6: Diamond-based single- photon sources and their application in quantum key distribution, pp. 127–159.

[475] K. Iakoubovskii and G. Adriaenssens, "Optical detection of defect centers in CVD diamond," Diamond Relat. Mater. **9**, 1349–1356 (2000).

[476] F. Inam, M. Steel, and S. Castelletto, "Effects of the hosting nano-environment modifications on NV centres fluorescence emission," Diamond Relat. Mater. **45**, 64 – 69 (2014).

[477] H. Khosravi and R. Loudon, "Vacuum field fluctuations and spontaneous emission in a dielectric slab," Proc. R. Soc. Lond. A **436**, 373–389 (1992).

[478] H. P. Urbach and G. L. J. A. Rikken, "Spontaneous emission from a dielectric slab," Phys. Rev. A **57**, 3913–3930 (1998).

[479] S. Brueck, "Radiation from a dipole embedded in a dielectric slab," IEEE J. Sel. Top. Quant. Electron. **6**, 899–910 (2000).

[480] T. Kojima, K. Kojima, T. Asano, and S. Noda, "Accurate alignment of a photonic crystal nanocavity with an embedded quantum dot based on optical microscopic photoluminescence imaging," Appl. Phys. Lett. **102**, 011110 (2013).

[481] S. M. Thon, M. T. Rakher, H. Kim, J. Gudat, W. T. M. Irvine, P. M. Petroff, and D. Bouwmeester, "Strong coupling through optical positioning of a quantum dot in a photonic crystal cavity," Appl. Phys. Lett. **94**, 111115 (2009).

[482] D. Wildanger, B. R. Patton, H. Schill, L. Marseglia, J. P. Hadden, S. Knauer, A. Schönle, J. G. Rarity, J. L. O'Brien, S. W. Hell, and J. M. Smith, "Solid Immersion Facilitates Fluorescence Microscopy with Nanometer Resolution and Sub-Ångström Emitter Localization," Adv. Mater. **24**, OP309–OP313 (2012).

[483] C. Chu, C. Pan, J. Margrave, and R. Hauge, "F_2, H_2O, and O_2 etching rates of diamond and the effects of F_2, HF and H_2O on the molecular O_2 etching of (110) diamond," Diamond Relat. Mater. **4**, 1317 – 1324 (1995).

[484] T. Evans, *Properties of Diamond* (Academic Press, London, U.K., 1979), chap. Changes produced by high temperature treatment of diamond, pp. 401–424.

[485] E. Gallardo, L. J. Martínez, A. K. Nowak, H. P. van der Meulen, J. M. Calleja, C. Tejedor, I. Prieto, D. Granados, A. G. Taboada, J. M. García, and P. A. Postigo, "Emission polarization control in semiconductor quantum dots coupled to a photonic crystal microcavity," Opt. Express **18**, 13301–13308 (2010).

[486] M. Maragkou, A. K. Nowak, E. Gallardo, H. P. van der Meulen, I. Prieto, L. J. Martinez, P. A. Postigo, and J. M. Calleja, "Controlling the properties of single photon emitters via the Purcell effect," Phys. Rev. B **86**, 085316 (2012).

[487] A. Daraei, D. Sanvitto, J. A. Timpson, A. M. Fox, D. M. Whittaker, M. S. Skolnick, P. S. S. Guimarães, H. Vinck, A. Tahraoui, P. W. Fry, S. L. Liew, and M. Hopkinson, "Control of polarization and mode mapping of small volume high Q micropillars," J. Appl. Phys. **102**, 043105 (2007).

[488] A. D. Boozer, A. Boca, R. Miller, T. E. Northup, and H. J. Kimble, "Reversible State Transfer between Light and a Single Trapped Atom," Phys. Rev. Lett. **98**, 193601 (2007).

[489] M. Hijlkema, B. Weber, H. P. Specht, S. C. Webster, A. Kuhn, and G. Rempe, "A single photon server with just one atom," Nature Phys. **3**, 253 – 255 (2007).

[490] A. Stute, B. Casabone, P. Schindler, T. Monz, P. O. Schmidt, B. Brandstatter, T. E. Northup, and R. Blatt, "Tunable ion-photon entanglement in an optical cavity," Nature **485**, 482–485 (2012).

[491] L.-M. Duan, M. D. Lukin, J. I. Cirac, and P. Zoller, "Long-distance quantum communication with atomic ensembles and linear optics," Nature **414**, 413–418 (2001).

[492] K. Jensen, N. Leefer, A. Jarmola, Y. Dumeige, V. M. Acosta, P. Kehayias, B. Patton, and D. Budker, "Cavity-Enhanced Room-Temperature Magnetometry Using Absorption by Nitrogen-Vacancy Centers in Diamond," Phys. Rev. Lett. **112**, 160802 (2014).

[493] F. Jelezko, "Ultrasensitive Diamond Magnetometers," Physics **7**, 43 (2014).

[494] Y. Tao, J. M. Boss, B. A. Moores, and C. L. Degen, "Single-crystal diamond nanomechanical resonators with quality factors exceeding one million," Nat. Commun. **5**, 3638 (2014).

[495] M. J. Burek, D. Ramos, P. Patel, I. W. Frank, and M. Loncar, "Nanomechanical resonant structures in single-crystal diamond," Appl. Phys. Lett. **103**, 131904 (2013).

List of Publications

Journal Publications

[1] J. Riedrich-Möller, C. Arend, C. Pauly, F. Mücklich, M. Fischer, S. Gsell, M. Schreck, and C. Becher, "Deterministic coupling of a single silicon-vacancy color center to a photonic crystal cavity in diamond," Nano Lett. **14**, 5281–5287 (2014).

[2] L. Kipfstuhl, F. Guldner, J. Riedrich-Möller, and C. Becher, "Modeling of optomechanical coupling in a phoxonic crystal cavity in diamond," Opt. Express **22**, 12410–12423 (2014).

[3] J. Riedrich-Möller, L. Kipfstuhl, C. Hepp, E. Neu, C. Pauly, F. Mücklich, A. Baur, M. Wandt, S. Wolff, M. Fischer, S. Gsell, M. Schreck, and C. Becher, "One- and two-dimensional photonic crystal microcavities in single crystal diamond," Nature Nanotech. **7**, 69–74 (2012).

[4] J. Riedrich-Möller, L. Kipfstuhl, and C. Becher, "Nano-Resonatoren aus Diamant," Physik in unserer Zeit **43**, 58–59 (2012).

[5] E. Neu, D. Steinmetz, J. Riedrich-Möller, S. Gsell, M. Fischer, M. Schreck, and C. Becher, "Single photon emission from silicon-vacancy colour centres in chemical vapour deposition nano-diamonds on iridium," New J. Phys. **13**, 025012 (2011).

[6] J. Riedrich-Möller, E. Neu, and C. Becher, "Design of microcavities in diamond-based photonic crystals by Fourier- and real-space analysis of cavity fields," Photon. Nanostruct.: Fundam. Appl. **8**, 150–162 (2010).

[7] C. Kreuzer, J. Riedrich-Möller, E. Neu, and C. Becher, "Design of photonic crystal microcavities in diamond films," Opt. Express **16**, 1632–1644 (2008).

Conference Papers[1]

[1] • C. Becher, A. Bommer, R. Albrecht, J. Riedrich-Möller, and L. Kipfstuhl, "Coupling of single color centers in bulk-and nano-diamond to optical micro-cavities," in *2014 MRS Spring Meeting*, (San Francisco, California), April 21-25 2014. Invited Paper.

[2] • J. Riedrich-Möller, C. Arend, M. Fischer, S. Gsell, M. Schreck, and C. Becher, "Controlled coupling of a single silicon-vacancy center to a photonic crystal cavity in single crystal diamond," in *Hasselt Diamond Workshop 2014, SBDD XIX*, (Hasselt, Belgium), February 19-21 2014.

[3] J. Riedrich-Möller, L. Kipfstuhl, F. Guldner, and • C. Becher, "Photonic and phononic crystal cavities in diamond," in *SPIE Photonics West*, no. 8994-19 in Conference Digest, (San Francisco, CA, USA), February 1-6 2014. Invited Paper

[4] • J. Riedrich-Möller, S. Pezzagna, J.Meijer, M. Fischer, S. Gsell, M. Schreck, and C. Becher, "Controlled coupling of single color centers to a photonic crystal cavity in monocrystalline diamond," in *Conference on Lasers and Electro-Optics Europe and International Quantum Electronics Conference, CLEO/Europe and IQEC 2013*, no. IH-P.6 THU in Conference Digest, (Munich, Germany), May 12-16 2013.

[5] J. Riedrich-Möller, L. Kipfstuhl, C. Hepp, S. Pezzagna, J. Meijer, M. Fischer, S. Gsell, M. Schreck, and • C. Becher, "Photonic crystal microcavities in single crystal diamond for color center coupling," in *Conference on Lasers and Electro-Optics, CLEO 2012*, (San Jose, CA, USA), May 6-11 2012.

[6] J. Riedrich-Möller, L. Kipfstuhl, C. Hepp, S. Pezzagna, J. Meijer, M. Fischer, S. Gsell, M. Schreck, and • C. Becher, "Coupling of color centers to nanophotonic structures in diamond," in *Hasselt Diamond Workshop 2012, SBDD XVII*, (Hasselt, Belgium), March 14-16 2012. Invited Paper

[7] E. Neu, J. Riedrich-Möller, L. Kipfstuhl, C. Hepp, C. Arend, D. Steinmetz, and • C. Becher, "Bright single photon emission from color centers in diamond and coupling to photonic crystal cavities," in *International Conference on Quantum Information Processing and Communication, QIPC 2011*, (Zürich, Switzerland), September 5-9 2011.

[1] A bullet (•) marks the presenter of the talk/poster.

[8] • J. Riedrich-Möller, L. Kipfstuhl, M. Fischer, S. Gsell, M. Schreck, and C. Becher, "1Dand 2D photonic crystal micro-cavities in quasi single crystal diamond," in *22nd European Conference on Diamond, Diamond-Like Materials, Carbon Nanotubes and Nitrides, Diamond 2011*, (Garmisch-Partenkirchen, Germany), September 4-8 2011.

[9] • J. Riedrich-Möller, L. Kipfstuhl, C. Hepp, M. Fischer, S. Gsell, M. Schreck, and C. Becher, "Fabrication and characterization of photonic crystal microcavities in quasi-single crystal diamond films," in *European Conference on Lasers and Electro-Optics and European Quantum Electronics Conference, CLEO/Europe and EQEC 2011*, no. EI2.2 TUE in Conference Digest, (Munich, Germany), May 22-26 2011.

[10] • E. Neu, D. Steinmetz, C. Arend, J. Riedrich-Möller, M. Fischer, S. Gsell, M. Schreck, and C. Becher, "Narrow-bandwidth high-brightness single photon emission from silicon-vacancy colour centres in CVD-nano-diamonds," in *European Conference on Lasers and Electro-Optics and European Quantum Electronics Conference, CLEO/Europe and EQEC 2011*, no. EI3.4 TUE in Conference Digest, (Munich, Germany), May 22-26 2011.

[11] • E. Neu, D. Steinmetz, C. Arend, J. Riedrich-Möller, M. Fischer, S. Gsell, M. Schreck, and C. Becher, "Narrow-bandwidth high-brightness single photon sources based on silicon-vacancy colour centres in cvd-nano-diamonds," in *Quantum Science and Technologies*, (Rovereto, Italy), May 9-12 2011.

[12] • J. Riedrich-Möller, L. Kipfstuhl, C. Hepp, M. Fischer, S. Gsell, M. Schreck, and C. Becher, "Fabrication of photonic crystal microcavities in heteroepitaxial diamond films," in *Hasselt Diamond Workshop 2011, SBDD XVI*, (Hasselt, Belgium), February 21-23 2011.

[13] • E. Neu, D. Steinmetz, C. Arend, J. Riedrich-Möller, M. Fischer, S. Gsell, M. Schreck, and C. Becher, "Single photon emission from silicon-vacancy colour centres in cvd nano-diamonds," in *Hasselt Diamond Workshop 2011, SBDD XVI*, (Hasselt, Belgium), February 21-23 2011.

[14] • E. Neu, D. Steinmetz, J. Riedrich-Möller, R. Albrecht, S. Gsell, M. Fischer, M. Schreck, and C. Becher, "Color centers in diamond: Artificial atoms for quantum information," in *International workshop of the EU-RTN EMALI*, (Barcelona, Spain), September 23-25 2010.

[15] • R. Albrecht, J. Riedrich-Möller, E. Neu, D. Steinmetz, C. Hepp, B. Sauer, M. Hauschild, and C. Becher, "Towards optical interfaces for color centers in diamond," in *International Conference on Quantum Information Processing and Communication, QIPC 2009*, (Rome, Italy), September 21-25 2009.

[16] • J. Riedrich-Möller, E. Neu, C. Hepp, and C. Becher, "Design of microcavities in diamond-based photonic crystals," in *European Conference on Lasers and Electro-Optics and European Quantum Electronics Conference, CLEO/Europe and EQEC 2009*, no. JSII2.4 FRI in Conference Digest, (Munich, Germany), June 14-19 2009.

[17] • C. Hepp, E. Neu, J. Riedrich-Möller, D. Steinmetz, S. Ghodbane, D. Steinmüller-Nethl, and C. Becher, "Optical properties of nanocrystalline diamond films for photonic crystal microcavities," in *Hasselt Diamond Workshop 2009, SBDD XIV*, (Hasselt, Belgium), March 2-4 2009.

[18] • J. Riedrich-Möller, E. Neu, and C. Becher, "Design of microcavities in diamond-based photonic crystals," in *2nd European Topical Meeting on Nanophotonics and Metamaterials, Nanometa 2009*, no. TUE5s.2 in Conference Digest, (Seefeld in Tirol, Austria), January 5-8 2009.

[19] J. Riedrich-Möller, C. Kreuzer, R. Albrecht, E. Neu, and • C. Becher, "Design of photonic crystal microcavities in diamond films for quantum information," in *Conference on Lasers and Electro-Optics and Quantum Electronics and Laser Science, CLEO/QELS 2008*, no. JThA103 in Conference Digest, (San Jose, CA, USA), May 4-9 2008.

Danke!

Zum Gelingen dieser Arbeit haben sehr viele Menschen beigetragen, denen ich an dieser Stelle ganz herzlich danken möchte. An erste Stelle möchte ich meinem Doktorvater Prof. Dr. Christoph Becher ganz besonders danken für die Chance in seiner Gruppe promovieren zu können zu einem äußerst vielseitigen, spannenden und hochaktuellen Thema. Bedanken möchte ich mich insbesondere für die vielen bereichernden Beiträge und die Korrekturen beim Schreiben von Publikationen und beim Erstellen dieser Arbeit, sowie für die Möglichkeit schon frühzeitig die eigene Arbeit auf Konferenzen vorstellen zu können und für die Freiräume bei der alltäglichen Arbeit.

An zweiter Stelle möchte ich mich ganz besonders bei Prof. Dr. Oliver Benson bedanken, der sich bereit erklärt hat diese Arbeit zu begutachten. Ich freue mich und fühle mich sehr geehrt einen so hochgeachteten und international anerkannten Wissenschaftler auf diesem Gebiet als Zweitgutachter gewonnen zu haben.

Diese Arbeit wäre ohne die Hilfe bei der Herstellung der Diamantproben und deren Prozessierung, sowie bei den Messungen nicht zustande gekommen. Ohne all die Unterstützung wären diese tollen Ergebnisse niemals möglich geworden. Ich möchte mich ganz herzlich bei Christoph Pauly (Lehrstuhl für Funktionswerkstoffe, Universität des Saarlandes) bedanken, der alle photonischen Kristallstrukturen, die in dieser Arbeit verwendet wurden, hergestellt hat. Ich bin ihm unendlich dankbar für die tolle Zusammenarbeit, für die vielen Ideen zur Optimierung des Strukturierungsprozesses und für die investierte Zeit und Begeisterung über viele Jahre hinweg.

Ein großer Dank gilt zudem der Gruppe von Dr. Matthias Schreck (Experimentalphysik IV, Universität Augsburg) für das Wachsen und Polieren der Diamantfilme. Hier möchte ich mich ganz besonders bei Dr. Martin Fischer und Dr. Stefan Gsell bedanken mit deren Diamanten wir so tolle Ergebnisse erzielen konnten.

Ich danke ebenso herzlich Dr. Sandra Wolff, Christian Dautermann und Dr. Bert Lägel (Nanostructuring Center, Universität Kaiserslautern) für den Zugang zum Reinraum, zu den Geräten, den Ätzanlagen und diesem unglaublichen Wissenspool zur Nanofabrikation.

Ein weiter großer Dank gilt Dr. Sébastien Pezzagna, Prof. Dr. Jan Meijer und Nicole Raatz (RUBION, Bochum; aktuelle Adresse: Nukleare Festkörperphysik, Universität Leipzig) für die gezielte Ionenimplantation einzelner Stickstoff-Fehlstellen Zentren in die photonischen Kristalle. Für die Möglichkeit diese tolle Technik für unsere Anwendung nutzen zu können bin ich sehr dankbar.

Zudem möchte ich mich bei Armin Baur und Dr. Michael Wandt (IMTEK, Universität Freiburg) für das Freistellen der Proben bedanken. Ich möchte mich außerdem bei Jörg Schmauch für die vielen unzähligen Elektronenmikroskopaufnahmen bedanken und bei Karin Kretsch für die stetige Hilfe und den Rat beim nasschemischen Ätzen. Außerdem Danke ich Elke Huschens ganz herzlich für die Hilfe bei allen Verwaltungsangelegenheiten. Ich danke zudem Christian Zeitz (AG Jacobs, Universität des Saarlandes) und Stefan Bommer (AG Seeman, Universität des Saarlandes) für die zeitaufwendigen Rasterkraftmikroskopaufnahmen und ebenso Samuel Grandthyll und Hendrik Hähl (AG Jacobs, Universität des Saarlandes) für die anspruchsvollen Ellipsometriemessungen an unseren Diamantproben. Desweiteren Danke ich Stefan Griesing (AG Hartmann, Universität des Saarlandes) für die Mitbenutzung der Sputteranlage. Außerdem danke ich Günter Marchand (AG Seidel, Universität des Saarlandes) für die Unterstützung bei den ersten Bondingversuchen mit Diamant.

Ein ganz großes Dankeschön gilt zudem allen aktuellen und ehemaligen Mitarbeitern unserer Arbeitsgruppe. Ohne die tolle Unterstützung durch meine Kollegen, das angenehme Arbeitsklima und die lustigen Grillabende und Geburtstage wäre die Arbeit sehr viel schwerer gewesen. Ganz besonders bedanken möchte ich mich bei Laura Kipfstuhl und Thomas Jung, die beide während ihrer Diplom- und Staatsexamensarbeit mit mir zusammen am Thema "Photonische Kristalle in Diamant" gearbeitet haben und die die Arbeit nun als Doktoranden in unserer Gruppe fortsetzen. Ich freue mich, dass sie dem Thema neue, eigene Impulse verleihen, es weiter entwickeln und ganz neue Richtungen eröffnen. Ich wünsche Euch beiden für Eure eigenen Doktorarbeiten alles Gute.

Ich möchte mich zudem bei Roland Albrecht und Alexander Bommer für die Hilfe im Labor und die vielen fachlichen und unglaublich hilfreichen Diskussionen zu Emitter-Resonator Kopplung bedanken. Bedanken möchte ich mich zudem bei Carsten Arend für die Lebensdauermessungen und die Hilfe im Labor, sowie bei allen IT-Fragen. Christian Hepp, Elke Neu und David Steinmetz danke ich für die Hilfe bei Problemen mit dem Konfokalaufbau. Sebastian Zaske möchte ich für die moralische Unterstützung während meiner Diplomarbeit und Doktorarbeit danken und für die famose Latex-Vorlage dieser Arbeit. Andreas Lenhard danke ich für die technische Unterstützung und die tollen Fahrten zu Weinfesten. Ein besonderer Dank gilt allen Kollegen, die diese Arbeit Kor-

rektur gelesen haben: Laura, Thomas, Alexander, Carsten, Jonas.

Während meiner Promotion habe ich 2011 die Physikerinnentagung an unserer Universität mit organisiert. Das war ein tolles Erlebnis und hat unheimlich viel Spaß gemacht. In diesem Zusammenhang möchte ich allen Mädels, Laura Kipfstuhl, Susanne Blum, Katharina Rojan, Astrid Niederle, Eva Wollrab, Monika Francois und Frau Prof. Dr. Giovanna Morigi ganz herzlich danken.

Den größten Dank möchte ich ganz zum Schluss meiner Familie und meiner kleinen Niedlichkeit aussprechen. Ich danke ihnen für ihre Liebe und fortwährende Unterstützung bei meinem Studium und meiner Promotion besonders in schwierigen Zeiten. Ich danke Ihnen dafür, dass sie immer für mich da sind, mich aufmuntern und mir Mut und Kraft geben. Ganz, ganz lieben Dank!